Petrology of the Gifford Creek Carbonatite Complex and the Yangibana LREE district, Western Australia: new insights from isotope geochemistry and geochronology

Thesis submitted by

Paul R. Slezak

For the degree of Doctor of Philosophy

To the College of Science and Engineering,

James Cook University

(June 2019)

Statement of Access

I, the undersigned author of this thesis, understand that James Cook University will make this thesis available for the use within the university library and allow access in other approved libraries after its submission and the specified embargo period has passed. All users consulting this thesis will have to sign the following statement:

In consulting this thesis, I agree not to copy or closely paraphrase in whole or in part without written consent of the author, and to make proper public written acknowledgement for any assistance that I have obtained from it.

Beyond this, I do not wish to place any restrictions on this thesis.

Paul Slezak

June 2019

Declaration

I declare this is my own work. I have not submitted it in any form for another degree or diploma at any university or institution of tertiary education. Information derived from the published or unpublished work of others has been acknowledged in the text and a list of references is given.

Every reasonable effort has been made to gain permission and acknowledge the owners of copyrighted material. I would be happy to hear from any copyright owner who has accidentally been omitted or incorrectly acknowledged in this manuscript.

Paul Slezak

June 2019

Acknowledgements

Firstly, I would like to acknowledge the support this project received from James Cook University, Hastings Technology Metal Ltd., the ARC Future Fellowship (FT120100198) to Dr. Carl Spandler, and EGRU.

Secondly, I would like to extend my gratitude towards my primary advisor, Carl Spandler, for his field assistance, his help in data discussions, editing, and for taking me on as his student. I would also like to thank Jan Marten Huizenga for becoming my secondary advisor and providing professional guidance.

Thirdly, I would like to thank Hastings Technology Metals Ltd., especially Andy Border and Kieren Whittock, and Malcom Mason for showing Carl and I the field area, letting us stay in camp, and graciously providing me access to Hastings databases and drill core.

Fourthly, a huge thank you to Kevin Blake, Yi Hu, Shane Askew, Jen Whan, and Brendan Jones at the AAC as well as Christa Placzek for introducing me to all the lab facilities, teaching me proper analytical techniques, and answering my many questions.

Fifthly, I would like to thank Bec Steele and Judy Botting who did all the heavy lifting for project logistics, administrative work, and navigation of JCU systems and policies. Thank you for your patience with me!

Sixthly, I would like to thank Maree Corkeron and Liane Millington for their help in editing for style and impact, as well as their feedback on posters and manuscripts as well as advice on professional outlooks and life beyond a PhD candidacy.

Seventhly, thanks Cassian Pirard and Rob Holm for showing me how to deconvolute my LA-ICP-MS data and for their insightful discussions.

Eighthly, thanks to my family for their support during my candidacy.

Ninthly, I would like to thank all my colleagues at James Cook University for the hilarious discussions, whinge fests, heated debates, computer tricks, and good times in general.

Lastly, I would like to thank the external examiners of this thesis for their comments, criticisms, and recommendations.

Statement of Contribution from Others

Nature of Assistance	Contribution	Contributor Name	Affiliation
Intellectual Support	Supervision	Dr. Carl Spandler Dr. Jan Marten Huizenga	JCU JCU
	Proposal Writing	Dr. Carl Spandler	JCU
	Data Collection	Dr. Kevin Blake Dr. Yi Hu Dr. Shane Askew Dr. Jen Whan Brendan Jones Dr. Christa Placzek	JCU, AAC JCU, AAC JCU, AAC JCU, AAC JCU, AAC JCU
	Reviews and Edits	Dr. Carl Spandler Dr. Jan Marten Huizenga Dr. Maree Corkeron	JCU JCU JCU
	Paper contributions	Dr. Carl Spandler Dr. Kevin Blake	JCU JCU, AAC
Financial Support	Research Funding	ARC Future Fellowship (FT120100198) to Dr. Carl Spandler EGRU Hastings Technology Metals Ltd.	
	Scholarship	JCU PRS	

List of Papers

The main body of the thesis is based on the following papers:

Chapter	Paper on which chapter is based
2	**Slezak, P.**, Spandler, C., (in prep) Petrology and geochemistry of the multi-phase Gifford Creek Carbonatite Complex, Western Australia. Manuscript.
3*	**Slezak, P.**, Spandler, C., Blake, K., (2018) Ghosts of apatite past: using hyperspectral CL and micro-geochemical data to reveal multi-generational apatite in the Gifford Creek Carbonatite Complex, Australia. The Canadian Mineralogist 56, 1-25.
4**	**Slezak, P.**, Spandler, C., (2019) Carbonatites as recorders of mantle-derived magmatism and subsequent tectonic events: an example of the Gifford Creek Carbonatite Complex, Western Australia. Lithos 328-329, 212-227.
5	**Slezak, P.**, Spandler, C., (in prep) Geology and ore genesis of the carbonatite-associated Yangibana LREE district, Gascoyne Province, Western Australia. Manuscript.

*Reprints were made with permission from the Canadian Mineralogist.
**Only the first page of the published article is provided for copyright reasons.

Thesis Abstract

Rare earth elements (REE) are an important series of critical metals used in many modern technologies. They are often hosted in carbonatite complexes, which can comprise a series of igneous carbonate rocks as well as other alkaline and mafic rocks. Carbonatites and other alkaline rocks are relatively uncommon and their genetic relationships are often enigmatic. The aim of this thesis is to improve our understanding of carbonatite complexes, from their mantle origins to their ability to host economic REE minerals, by examining the Gifford Creek Carbonatite Complex (GCCC), Gascoyne Province, Western Australia and the Yangibana LREE district contained within the complex.

Carbonatite complexes consist of a diverse suite of igneous rocks such as mafic and (per)alkaline silicate phases in addition to carbonatites. The GCCC is a preeminent example of this diversity as it contains calcite and dolomite carbonatites (collectively called the Lyons River Sills), ankerite-siderite carbonatites (a.k.a. ferrocarbonatites), magnetite-biotite dykes, silica-rich alkaline veins, and the associated alteration assemblages, which include fenites and glimmerites. Bulk rock Nd isotope studies return a range of compositions from $\varepsilon Nd(t_{1.37Ga})$ = -1.8 to -4.0, which points to an enriched mantle origin for all rock types comprising the GCCC. An enriched mantle source is confirmed by additional Sr and C–O isotopes on carbonate minerals from the Lyons River Sills and ankerite-siderite carbonatites. Though genetically related based on isotopic studies, the mechanisms that connect the Lyons River Sills, magnetite-biotite dykes, and ankerite-siderite carbonatites are still somewhat cryptic due to the lack of field relationships. However, the Lyons River Sills display a clear fractionation trend, decreasing in CaO while increasing in MgO and Fe_2O_3 contents, which is driven by separation of a calcite cumulate from the parent melt. In addition, the silica-rich alkaline veins represent a magmatic-hydrothermal fluid rich in Na, F, and high field strength elements (HFSE), which likely exsolved as an incompatible phase from the magnetite-biotite dykes.

Apatite is an important mineral phase, hosting significant levels of REE and other trace elements that is ideal for a variety of in situ analytical methods such as hyperspectral

cathodoluminescence (CL) studies. Hyperspectral CL provides valuable insight to hidden textures that have the potential to affect other analytical techniques. Apatite hosted in the various GCCC rock types was analysed using hyperspectral CL, electron probe micro-analysis (EPMA), and laser ablation inductively coupled mass spectrometry (LA-ICP-MS). The analyses showed apatite has prominent sharp peaks at ~1.4 eV and ~2.l eV, and a broad peak between 2.3 eV and 3.5 eV, related to the REE activators, Nd^{3+}, Eu^{3+}, Sm^{3+}, and Ce^{3+}. Analyses also showed apatite varies compositionally across the GCCC with samples in the southeast region containing higher Sr and lower λ_3 values compared to apatite from the northwest region, which is interpreted to relate to changes in primary magmatic composition. The study also demonstrated that apatite in a fenite samples actually consisted of two distinct phases, one granitic and one carbonatitic, based on the CL spectra, Mn content, and chondrite-normalised REY (REE + Y) patterns. This suggests the carbonatitic apatite nucleated on the pre-existing granitic apatite, and, if analysed for Sm–Nd isotopes, would result in a mixed signature.

The different rock types of the GCCC host a variety of minerals suitable for radiogenic isotope analyses including zircon, monazite, and apatite, which can provide valuable insights to the age and origin of the complex. Zircon crystals obtained from the silica-rich alkaline veins as well as glimmerite alteration assemblages related to the ankerite-siderite carbonatites returned concordant U-Pb ages of c. 1370 Ma for the GCCC. However, monazite U–Pb ages returned a wide range from c. 1300 to 815 Ma. Samarium–Nd isochron ages from monazite-apatite pairs yielded ages between c. 1310 to 1190 Ma, but all had similar initial $^{143}Nd/^{144}Nd$ values of 0.51078 to 0.51087. The c. 1370 Ma zircon date is interpreted as the primary magmatic age for the GCCC, but it does not correlate to any known mantle plume activity or other tectonic event in the Gascoyne Province. The consistent $^{143}Nd/^{144}Nd$ values suggest the range in younger monazite U-Pb ages is indicative of partial recrystallisation/resetting of REE minerals during the protracted tectonic history of the Western Australia Craton from c. 1300 Ma to 815 Ma and its involvement in the breakup of Nuna and assembly and disassembly of Rodinia.

The GCCC hosts the Yangibana LREE district, which comprises multiple prospects totalling 21 million tonnes at 1.17 wt.% TREO, mainly hosted in monazite, which is found in the

ironstones. The ironstones are weathered and oxidised versions of the other units such as the ankerite-siderite carbonatites and magnetite-biotite dykes in the GCCC. They exhibit dissolution cavities, boxwork and botryoidal textures, and secondary REE-phosphate minerals such as rhabdophane. Isocon diagrams between the ankerite-siderite carbonatites and ironstones show significant mass removal, which has resulted in passive REE ore increase by ~3 to ~17 times. This mass removal and ore tenor upgrade is attributed to extensive carbonate breakdown and weathering of the ankerite-siderite carbonatites by meteoric waters near the surface. Monazite is the main ore mineral and micro-chemical analyses show La and Nd have an inverse relationship in monazite in the GCCC. This relationship translates into the bulk rock drill assay data, which shows the central and southeastern regions have the lowest La/Nd ratios (~ 0.3 to ~1.2) and the northwest region has the highest ratios (~1.5 to >2.5). The La/Nd variation reflects a combination of multi-scale processes including variation in primary magmatic composition, shifts in the system from CO_2 to aqueous dominated magmatic-hydrothermal fluids.

The study of the GCCC and Yangibana LREE district highlight the importance of enriched mantle origins and complex magmatic and hydrothermal processes that lead to the formation of the complex and its REE mineral deposits. The study also provides important insights regarding the importance of diligent analytical work needed to obtain meaningful data from complex alkaline igneous systems, like the GCCC.

Table of Contents

Table of Figures

Table of Tables

Chapter 1

Introduction to Rare Earth Elements, Carbonatites, and the Gifford Creek Carbonatite Complex

1.1 Introduction

1.1.1 Rare earth element chemistry

1.1.1.1 General definitions

The rare earth elements (REE) make up a group of seventeen metals consisting of the lanthanide series (6^{th} row on the periodic table) and two additional elements: Sc and Y. The lanthanide series is comprised of the following metals (in order of increasing atomic number): lanthanum (La), cerium (Ce), praseodymium (Pr), neodymium (Nd), promethium (Pm), samarium (Sm), europium (Eu), gadolinium (Gd), terbium (Tb), dysprosium (Dy), holmium (Ho), erbium (Er), thulium (Tm), ytterbium (Yb), and lutetium (Lu). The elements scandium (Sc) and yttrium (Y) are also included as REE as stated by the International Union of Pure Applied Chemistry (IUPAC; Connelly et al., 2005; Walters et al., 2011; Hoatson et al., 2011). Occasionally in geochemistry, however, Sc is not included when referring to REE because of its distinct chemical behaviour (Henderson, 1984). For the purpose of this thesis, Sc will not be included when referring to REE, and REY (REE + Y) will be used to denote the specific inclusion of Y in normalised plots and diagrams.

REE can be further subdivided into light rare earth elements (LREE) and heavy rare earth elements (HREE). The LREE consist of the elements La, Ce, Pr, Nd, Pm, Sm, and Eu. The HREE comprise Eu, Gd, Tb, Dy, Ho, Er, Tm, Yb, Lu, and Y (Henderson, 1984). This thesis will utilise the terms “LREE” and “HREE” accordingly.

1.1.1.2 Chemical properties

Rare earth elements tend to occur together in nature unlike many other elements, which occur separately. This grouping is caused by the shielding of their outer election *4f* orbitals by their $5s^2$ and $5p^6$ orbitals, which mitigates substantial changes in chemical behaviour. Rare earth elements can form subgroups called tetrads based on the number of electrons filling of the *4f* orbital (i.e., 25%, 50%, 75%, and 100% filled; Peppard et al., 1996). REE tend to have a trivalent (III) oxidation state, except Ce and Eu, which can occur as tetravalent (IV) and divalent (II)

cations, respectively. Additionally, as the atomic number of REE increases, their ionic radius decreases, which is known as "lanthanide contraction." The lanthanide contraction is responsible for slight compatibility differences that lead to the distinction between LREE and HREE. Lastly, REE are considered lithophile elements because they tend to concentrate in silicate melts (Henderson, 1984). However, REE may partition more strongly in to hydrated carbonate (Martin et al., 2013), fluoride, or phosphate melts compared to silicate melts (Veksler et al., 2012). The presence of additional elements and compounds such as F, P, and H_2O in carbonate melts likely plays a role in the economic viability of carbonatite-hosted REE deposits.

1.1.2 REE mining history

Historical mining of REE began in the late 1800s, where they were mainly used for in incandescent mantles in gas lamps (Neary and Highley, 1984; Hoatson et al., 2011). The main ore mineral was monazite, which was mined mainly from placer deposits in Brazil and India. Demand for REE increased in the 1940s, 1950s, and 1960s with the advent of the Atomic Age (Chakhmouradian and Wall, 2012). During this time, placer mining was replaced by hard rock mining (Hoatson et al., 2011). The Mountain Pass carbonatite deposit in California, USA, was the main source of REE until the 1990s when REE production increased in China (Castor, 2008). Today, the top REE-producing countries are China, Australia, and Russia. In 2017, China accounted for 79% of the world's REE production followed by Australia with 15% (Fig. 1.1). However, the total REE reserves tell a different story. Though China accounts for the most significant world REE reserves at 36%, Australia only accounts for 3% (Fig. 1.1; USGS, 2018).

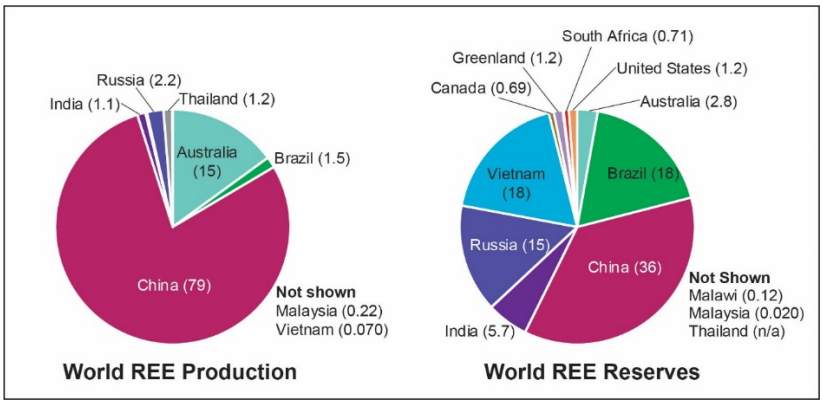

Figure 1.1 World REE production and World REE reserves (USGS, 2018). Note that China and Australia account for most of the world's production, but only have ~36% and ~3% of the total REE reserves.

1.1.2.1 Modern REE uses

Due to their *4f* orbitals shielding, REE have unique chemical and physical properties, making them desirable for use in the technology sector. REE are used in many high technologies such as catalysts, permanent magnets, phosphors, and metal alloys as well as other commodities such as polishing powders, colouring agents, and ceramics (for more uses see Table 1.1; Neary and Highley, 1984; Goonan, 2011; Hoatson et al., 2011; Hatch, 2012). The nature of these technological applications is very specific and there are few, if any, alternative compounds (Goonan, 2011). Despite their necessity and commonplace in modern technologies, the occurrences and controls of REE-bearing mineral deposits are poorly understood.

Table 1.1 Summary of REY elements and their uses.

Application	Examples	REE +Y
Catalysts[1,2,3,4,5]	Automotive catalytic converters, fluid catalytic fracking, air pollution control	La, Ce, Nd, Pr
Metal Alloys[1,2,4]	Steel alloys, magnesium automotive alloys, aluminum alloys	La, Ce, Pr, Nd, Y
Permanent Magnets[2,3,4]	Wind turbine generators, electric motors, cellular phones, computer disc drives, servomotors	Pr, Nd, Sm, Gd, Tb, Dy
Glass and Ceramics[1,2,3,4]	Decolourisation of glass, colouring agents	La, Ce, Pr, Nd, Gd, Ho, Er, Y
Polishing[1,3,4,5]	Touchscreen devices, television and computer screens, optical lenses, silica wafers	La, Ce, Pr
Phosphors[1,2,3,4,5]	LCD, plasma, and CRD displays; fluorescent lighting; LEDs	La, Ce, Eu, Gd, Tb, Y
Batteries[2,3,5]	Nickel-metal-hydride (NiMH) rechargeable batteries	La, Ce, Pr, Nd, Sm
Other[1,2,3,4]	Lasers, satellite systems, fibre optic cables, superconductors	La, Ce, Pr, Nd, Sm, Gd, Y

[1](Neary and Highley, 1984), [2](Goonan, 2011), [3](Hoatson et al., 2011), [4](Walters et al., 2011), [5](Hatch, 2012)

1.2 REE Deposits

1.2.1 Deposit types and examples

The details of REE deposit classification vary amongst authors and government agencies (Table 1.2). Neary and Highley (1984) classify REE deposits by their modes of occurrence and associated rock types. Möller (1989) broadly classifies REE deposits into endogenic (igneous and hydrothermal), exogenic (sedimentary), and metamorphic deposit types. Möller (1989) then

further subdivides each category based on their genetic associations. Long et al. (2010) divides REE into general classes based on rock type. The general classes proposed by Long et al. (2010) are then split into smaller, more detailed groups based on mineralogy, mode of occurrence, and rock chemistry. Walters et al. (2011) divides REE deposits into two main groups: primary deposits and secondary deposits. Primary deposits are those including carbonatites, alkaline igneous rocks, and hydrothermal deposits. Secondary deposits consist of placer deposits (marine, alluvial, and paleo), laterites, and ion-adsorption clays. What is common to all groups is the inclusion of carbonatites and alkaline igneous rocks.

Carbonatite-associated deposits comprise the most commonly mined deposits. Although there are slightly more documented peralkaline associated REE deposits, carbonatite-associated REE are the most commonly mined due to their superior REE recovery rates (Walters et al., 2011). The largest modern-day REE mines, Mountain Pass (USA), Bayan Obo (China), and Mount Weld (Australia) are carbonatite deposits as is the Yangibana LREE deposit, which is the focus of this study.

Table 1.2 Comparison of REE deposit categories.

Neary and Highley, 1984	Möller, 1989		Long et al., 2010 (United States Geological Survey)		Walters et al., 2011 (British Geological Survey)		Hoatson et al., 2011 (Geoscience Australia)		
Alkaline rocks and carbonatites	Endogenic (igneous and hydrothermal mineralisation)	•Alkali-ultrabasic complexes •Carbonatites •Metasomites •Pegmatites •Hydrothermal mineralisation	Peralkaline igneous rocks	•Magmatic (alkali-ultrabasic) •Pegmatite dikes (alkali-ultrabasic) •Pegmatite dikes (peralkaline) •Hydrothermal veins •Volcanic •Metasomatic-albitite	Primary deposits	•Carbonatite-associated •Alkali igneous rock associated •Iron-REE deposits (Iron oxide copper-gold deposits) •Hydrothermal deposits	Magmatic	Orthomagmatic	•Alkaline igneous rocks •Carbonatite •Pegmatite
								Magmatic-hydrothermal	•Albitite •Porphyry •Skarn •Apatite-fluorite vein •Iron oxide breccia
Vein deposits	Exogenic or sedimentary mineralisation	•Weathering •Placer •Other (e.g. phosphorites, bituminous shales, etc.)	Carbonatites	•Magmatic •Dykes and veins •Hydrothermal veins and stockworks •Skarn •Carbonate rock replacement •Metasomatic-fenite	Secondary deposits	•Marine placers •Alluvial placers •Paleoplacers •Lateritic deposits •Ion-adsorption clays	Basinal	Sedimentary	•Placer •Phosphorite •Seafloor manganese nodule •Lignite
								Diagenetic-hydrothermal	•Unconformity-related
Placer deposits	Metamorphic mineralisation	•Skarns	Pegmatites	•Abyssal •Muscovite •REE-allanite-monazite •REE-euxenite •REE-gadolinite •Miarolitic-REE			Regolith	Residual lateritic	•Carbonatite-associated •Ultramafic/mafic rock-associated
								Residual clay	
								Bauxite	
Apatite deposits			Metamorphic	•Migmatised gneiss •Uranium-REE skarn			Metamorphic		•Migmatised gneiss •Calc-silicate
Other			Iron oxide copper-gold	•Magnetite-apatite replacement •Hematite-magnetite replacement					
			Stratiform phosphate residual	•Platform phosphorite •Carbonatite-associated •Granite-associated laterite •Baddeleyite bauxite •Karst bauxite					
			Porphyry-Mo	•Climax-type					
			Paleoplacer	•Uraniferous pyritic quartz pebble conglomerate •Auriferous pyritic quartz pebble conglomerate					
			Placer	•Shoreline Ti-heavy mineral placer •Tin stream placer					

1.2.2 REE-bearing carbonatite complexes

1.2.2.1 General information

Carbonatites are igneous rocks consisting of at least 50% magmatic carbonate minerals and less than 20% SiO_2. Where they contain >20% SiO_2, they are called silicocarbonatites (Le Maitre, 2002). Carbonatites are uncommon igneous rocks with ~500 documented complexes worldwide. They are often associated with alkaline igneous rocks occurring along stable craton margins and in rift zones (Woolley and Kjarsgaard, 2008).

Carbonatite sizes vary considerably and they may occur as plug-like intrusions, dykes, sills, or discontinuous lenses. Often carbonatites are associated with Na and/or K-rich rocks, known as fenites. Fenites are the result of late-stage hydrothermal fluids leaving the carbonatite intrusion and altering the surrounding host rocks (Elliott et al., 2018).

Carbonatites may be enriched in a variety of desirable metals, such as REE and high field strength elements (HFSE) such as Ti, Nb, and Zr (Wall and Zaitsev, 2004; Chakhmouradian and Williams, 2004). Carbonatite-hosted REE are found in the primary minerals phases: monazite [LREE(PO_4)], bastnäsite [LREE(CO_3)F]. However, variable amounts of REE are also be present in apatite [$Ca_5(PO_4)$OH,Cl,F], which may be the only REE-bearing mineral in many carbonatites (Chakhmouradian et al., 2017). The main HFSE-bearing minerals are pyrochlore [$(Na,Ca)_2Nb_2O_6$(OH,F)], columbite [(Fe,Mg,Mn)Nb_2O_6], ilmenite [$FeTiO_3$], zircon [$ZrSiO_4$], baddeleyite [ZrO_2], perovskite [$CaTiO_3$], and titanite [$CaTiO(SiO_4)$] .

1.2.2.2 Gifford Creek Carbonatite Complex

The Gifford Creek Carbonatite Complex (GCCC) is one of three major REE-bearing carbonatites in Australia, including Mount Weld (active mine) and the Cummins Range Carbonatite (prospect; Hoatson et al., 2011). Carbonatites are relatively rare and typically occur in structurally complex intrusive bodies comprising multiple rock types, including various carbonate and silicate alkaline intrusions (Woolley and Kjarsgaard, 2008). The GCCC provides

an opportunity to examine a metalliferous carbonatite-associated critical metal deposit from its origins, to its evolution through time, to the controls on its ore minerals.

The GCCC is a swarm of dykes and sills located in the Gascoyne Province, Western Australia. The Gascoyne Province is the metamorphosed suture zone between the Pilbara and Yilgarn cratons, which comprise much of Western Australia. They range from 0.1 to 1.5 m in width and are continuous for tens of metres up to a few hundred metres. These dykes comprise four main rock types: 1) dolomite and calcite carbonatites (also known as the Lyons River Sills), 2) ankerite-siderite carbonatites, 3) magnetite-biotite dykes, and 4) silica-rich alkaline veins. Four additional phases are also found within the complex: 1) "ironstones"; 2) alkaline amphibole-dolomite veinlets emanating from the dolomite carbonatites; 3) fenites – the produce of wall rock (mainly granite and metasediments) reactions with Na- and K-rich, carbonatite fluids; and 4) glimmerites – the magnetite and biotite-rich products from wall rock and ankerite-siderite carbonatite interaction.

The carbonatites, magnetite-biotite dykes and other associated rocks, especially the ironstones, host LREE mineralisation in a group of prospects collectively known as the Yangibana LREE district. The economic potential of the Yangibana LREE district is being evaluated by Hastings Technology Metals Ltd. and contains significant amounts of Pr and Nd, which contribute to its economic viability. The district contains a Joint Ore Reserves Committee (JORC) resource of 21 million tonnes total rare earth oxide (TREO) grading 1.17%. (Hastings Technology Metals Ltd., 2019).

In addition to being important hosts of REE, monazite and apatite are useful for scientific research. They can be used for U–Pb dating and Sm–Nd isotopic studies (Parrish, 1990; McFarlane and McCulloch, 2007; Fisher et al., 2011). Zircon is also abundant in the GCCC and is the preeminent mineral for U–Pb dating and Lu–Hf isotope studies (Thirlwall and Walder, 1995). The abundance of these mineral phases allows much of the analytical work to be completed in situ, providing petrographic and petrologic context as the mineral is analysed compared to ordinary mineral separates, which may break or become contaminated during mechanical separation.

1.3 Research Objectives and Thesis Structure

This PhD project has been developed to address several large knowledge gaps, both academic and economic such as:

1) The lack of research encompassing all of the rocks types (both primary and secondary) in the GCCC, including petrography, chemistry, in situ analyses of accessory minerals.
2) The genetic links between all the rock types in the magmatic complex are poorly established, including the links between the carbonatites and magnetite-biotite dykes as well as the carbonatites and economically desirable ironstones.
3) Controversies with the age and setting of the GCCC (e.g., potential Warakurna Large Igneous Province or other intraplate causes)
4) A lack of description of the Yangibana LREE district, its mineralisation, and associated alteration.

A challenge to closing these knowledge gaps is a lack of direct field evidence illustrating contact/cross-cutting relationships between rock units. This PhD aims to utilise available field relations (e.g., field mapping and photographic documentation of cross cutting relationships), bulk rock geochemistry, whole rock and accessory mineral isotope geochemistry, and applied mineralogy to determine:

1) the geochemical and isotopic characteristics of the major rock units and essential accessory minerals (Chapter 2, 3, 4);
2) the nature of the relationship (spatial and genetic?) between the carbonatites and magnetite-biotite dykes (Chapter 2);
3) the age and origin of the GCCC (Chapter 4); and
4) the morphology, ore geochemistry, and genetic model of the Yangibana LREE district in addition to potential exploration tools (Chapters 3 and 5).

In order to address these issues, this project aims to provide a “mantle to mine” examination, encompassing the primary origin of the GCCC to its evolution into an economic LREE deposit. The thesis is composed of six chapters, with the main body of the thesis comprising chapters 2

through 5. Each of these chapters represents a journal manuscript. At the time of submission, chapters 3 and 4 have been published. Chapters 2 and 5 are being prepared for submission in 2019. This format of thesis by publication has resulted in some repetition of sections (e.g., geological setting) between chapters. However, each chapter presents an independent body of work, including research methods, results, discussion, and implications sections that are unique for each chapter. The final chapter (Chapter 6) summarises and discusses the completed work and provides suggestions on future research. Some of the methods used in this thesis are abbreviated for journal publication. However, Appendix 1.A contains a list and comprehensive descriptions for the methods employed in this study. In order to present a cohesive document, the appendices are placed at the end of the thesis and appropriately labelled according to the chapter in which they are used.

1.4 References

Castor, S.B., 2008. Rare earth deposits of North America. Resource Geology 58, 337-347.

Chakhmouradian, A.R., Williams, C.T., 2004. Mineralogy of high-field-strength elements (Ti, Nb, Zr, Ta, Hf) in phoscoritic and carbonatitic rocks of the Kola Peninsula, Russia, in: Wall, F., Zaitsev, A.N. (Eds.), Phoscorites and Carbonatites from Mantle to Mine: the Key Example of the Kola Alkaline Province. The Mineralogical Society of Great Britain & Ireland, Cambridge, pp. 293-340.

Chakhmouradian, A.R., Wall, F., 2012. Rare earth elements: minerals, mines, magnets (and more). Elements 8, 333-340.

Connelly, N.G., Damhus, T., Hartshorn, R.M., Hutton, A.T., 2005. Nomenclature of Inorganic Chemistry - IUPAC Recommendations 2005. RSC Publishing, p. 377.

Elliott, H.A.L., Wall, F., Chakhmouradian, A.R., Siegfried, P.R., Dahlgren, S., Weatherley, S., Finch, A.A., Marks, M.A.W., Deady, E., 2018. Fenites associated with carbonatite complexes: a review. Ore Geology Reviews 98, 38-59.

Fisher, C.M., McFarlane, C.R.M., Hanchar, J.M., Schmitz, M.D., Sylvester, P.J., Lam, R., Longerich, H.P., 2011. Sm-Nd isotope systematics by laser ablation-multicollector-

inductively coupled plasma mass spectrometry: methods and potential natural and synthetic reference materials. Chemical Geology 284, 1-20.

Gambogi, J., 2015. Rare earths, Mineral Commodity Summaries, January 2015. U.S. Geological Survey, pp. 128-129.

Goonan, T.G., 2011. Rare earth elements—end use and recyclability: U.S. Geological Survey scientific investigations report 2011–5094, p. 15.

Hatch, G.P., 2012. Dynamics in the global market for rare earths. Elements 8, 341-346.

Hastings Technology Metals, 2019. Yangibana JORC Ore Reserves. Retrieved from https://hastingstechmetals.com/projects/yangibana/yangibana-jorc-resource/ on February 22, 2019.

Henderson, P., 1984. General geochemical properties and abundances of the rare earth elements, in: Henderson, P. (Ed.), Rare Earth Element Geochemistry. Elsevier, Amsterdam, pp. 1-32.

Henderson, P., 1996. The rare earth elements: introduction and review, in: Jones, A.P., Wall, F., Williams, C.T. (Eds.), Rare Earth Minerals: Chemistry, Origin and Ore Deposits. Chapman & Hall, London, pp. 1-19.

Hoatson, D.M., Jaireth, S., Miezitis, Y., 2011. The major rare-earth-element deposits of Australia: geological setting, exploration, and resources. Geoscience Australia, p. 204.

Le Maitre, R.W., 2002. Igneous Rocks: A Classification and Glossary of Terms: recommendations of International Union of Geological Sciences, subcomission on the systematics of igneous rocks. Cambridge University Press, Cambridge.

Long, K.R., Van Gosen, B.S., Foley, N.K., Cordier, D., 2010. The principal rare earth elements deposits of the United States—a summary of domestic deposits and a global perspective: U.S. Geological Survey Scientific Investigations Report 2010–5220, p. 96.

Martin, L.H.J., Schmidt, M.W., Mattsson, H.B., Guenther, D., 2013. Element Partitioning between Immiscible Carbonatite and Silicate Melts for Dry and H2O-bearing Systems at 1–3 GPa. Journal of Petrology 54, 2301-2338.

McFarlane, C.R.M., McCulloch, M.T., 2007. Coupling of in-situ Sm-Nd systematics and U-Pb dating of monazite and allanite with applications to crustal evolution studies. Chemical Geology 245, 45-60.

Möller, P., 1989. Rare earth mineral deposits and their industrial importance, Lanthanides, tantalum and niobium, in: Möller, P., Černý, P., Saupé, F. (Eds.), Lanthanides, Tantalum and Niobium. Springer, pp. 171-188.

Neary, C.R., Highley, D.E., 1984. The economic importance of the rare earth elements, in: Henderson, P. (Ed.), Rare Earth Element Geochemistry. Elsevier, Amsterdam, pp. 423-466.

Parrish, R.R., 1990. U-Pb dating of monazite and its application to geological problems. Canadian Journal of Earth Sciences 27, 1431-1450.

Peppard, D.F., Mason, G.W., Lewey, S., 1969. A tetrad effect in the liquid-liquid extraction ordering of lanthanides(III). Journal of Inorganic Nuclear Chemistry 31, 2271-2272.

Thirlwall, M.F., Walder, A.J., 1995. In situ hafnium isotope ratio analysis of zircon by inductively coupled plasma multiple collector mass spectrometry. Chemical Geology 122, 241-247.

USGS, 2018. Mineral Commodity Summaries: Rare Earths. U.S. Geological Survey, pp. 132-133. Retrieved from https://minerals.usgs.gov/minerals/pubs/commodity/rare_earths/mcs-2018-raree.pdf on June 3, 2018.

Veksler, I.V., Dorfman, A.M., Dulski, P., Kamenetsky, V.S., Danyushevsky, L.V., Jeffries, T., Dingwell, D.B., 2012. Partitioning of elements between silicate melt and immiscible fluoride, chloride, carbonate, phosphate and sulfate melts, with implications to the origin of natrocarbonatite. Geochimica et Cosmochimica Acta 79, 20-40.

Wall, F., Zaitsev, A.N., 2004. Rare earth metals in Kola carbonatites, in: Wall, F., Zaitsev, A.N. (Eds.), Phoscorites and Carbonatites from Mantle to Mine: the Key Example of the Kola Alkaline Province. The Mineralogical Society of Great Britain & Ireland, Cambridge, pp. 341-373.

Walters, A., Lusty, P., Hill, A., 2011. Rare earth elements, British Geological Survey Mineral Profiles, United Kingdom, p. 54.

Woolley, A.R., Kjarsgaard, B.A., 2008. Paragenetic types of carbonatite as indicated by the diversity and relative abundances of associated silicate rocks: evidence from a global database. The Canadian Mineralogist 46, 741-752.

Wu, C., Yuan, Z., Bai, G., 1996. Rare earth deposits in China, in: Jones, A.P., Wall, F., Williams, C.T. (Eds.), Rare Earth Minerals: Chemistry, Origin and Ore Deposits. Chapman and Hall, London, pp. 281-310.

Chapter 2

Petrology and Geochemistry of the Multi-phase Gifford Creek Carbonatite Complex, Western Australia

Abstract

The Gifford Creek Carbonatite Complex (GCCC), Western Australia contains a diverse suite of alkaline igneous rocks, including calcite and dolomite carbonatites (collectively referred to as the Lyons River Sills), ankerite-siderite carbonatites, magnetite-biotite dykes, silica-rich alkaline veins, and the associated alteration assemblages for each rock type. The Lyons River Sills form a swarm of dykes and sills proximal to the regional Lyons River Fault, whereas the ankerite-siderite carbonatites are only found at depth along the Bald Hill Lineament. The magnetite-biotite dykes occur in a few discrete locations, primarily in the southeastern GCCC, and the silica-rich alkaline veins form another dyke/sill swarm in the central GCCC oriented broadly perpendicular to the Lyons River Sills.

The Lyons River Sills are predominantly dolomite carbonatites with subordinate calcite carbonatite occurrences. Fractionation modelling demonstrates the calcite carbonatites are likely a cumulate phase of the carbonatite melt, with the derivative liquids becoming progressively enriched in MgO, Fe_2O_3, TiO_2, and SiO_2. The trend in these residual melts is analogous to the trends represented by bulk rock geochemistry from the dolomite carbonatites. Genetic relationships between the Lyons River Sills and other alkaline igneous units are less clear.

The ankerite-siderite carbonatites are considered to be a magmatic phase, which is supported by their mantle $\delta^{13}C$ isotope values of -6.1 to -7.1‰ and near-mantle $\delta^{18}O$ values of 10.4 to 11.1‰, as well as their similar geochemical characteristics to other known magmatic ferrocarbonatites such as the Swartbooisdrif ferrocarbonatites.

The ankerite-siderite carbonatites share many geochemical characteristics with the magnetite-biotite dikes, such as high LREE and low HFSE contents. Both units contain normalised trace element plots that are antithetic to the silica-rich alkaline veins, which are interpreted to represent magmatic-hydrothermal fluid exsolved from the magnetite-biotite dykes after magmatic differentiation. The silica-rich alkaline veins are enriched in incompatible elements, including Na and F, which facilitated mobility of high field strength elements, such as Zr, Nb, and Ti.

Carbon and O isotope compositions of the carbonate minerals indicate that the carbonatite have a mantle origin, but have undergone hydrothermal alteration. Further Sr-isotope analyses and bulk rock Nd isotopes indicate that both the carbonatites and magnetite-biotite dykes originated from an enriched mantle source. Neodymium isotope model ages range from c. 2100 to 1900 Ma and are interpreted as the age of mantle metasomatism, likely caused by the convergence of the Yilgarn Craton with the Glenburgh Terrane during the 2005 to 1950 Ma Glenburgh Orogeny.

2.1 Introduction

Carbonatites are relatively uncommon igneous rocks that consist of at least 50% primary magmatic carbonate minerals (Le Maitre, 2002). They often form intrusive plugs but also occur as dykes, sills, and extrusive breccias. Compositionally, they can vary significantly in their major element contents. Most carbonatites are Ca- and/or Mg-rich, forming calcite and dolomite carbonatites. Some carbonatites are rich in Fe and form ankerite and/or siderite carbonatites. These ferrocarbonatites are often considered to be late stage and hydrothermal in origin (Le Bas, 1989; Zaitsev et al., 2004). However, some studies have shown that some ferrocarbonatites, such as the Swartbooisdrif and Central Tuva ferrocarbonatites form at temperatures of ~800 °C (Drüppel et al., 2004; Prokopyev et al., 2016) and hence are likely to be magmatic in origin.

Carbonatites of all types are often associated with a wide variety of other rock types including lamprophyres, kimberlites, dunites, pyroxenites, peridotites, syenites, melilites, nephelinites, phonolites, and phoscorites (Woolley and Kjarsgaard, 2008). Of ~500 documented carbonatite complexes worldwide, only a small subset of ~5 to 10% occur with obscure ultramafic rocks known as phoscorites (Krasnova et al., 2004; Woolley and Kjarsgaard, 2008). Phoscorites were originally defined by their magnetite, apatite, and forsterite assemblage (Russel et al., 1954); now the definition can include diopside and phlogopite as additional silicate phases (Krasnova et al., 2004). The genetic relationship between phoscorites and carbonatites is generally poorly understood. Proposed geological processes linking their formation include the segregation of phoscoritic minerals from a carbonatite magma via crystal fractionation (Vartiainen, 1980) and/or

liquid immiscibility (Krasnova et al., 2004). These same separation processes, as well as low degree melting of a fertile, CO_2-rich mantle source, have also been proposed to explain the formation of carbonatite magmas (e.g., Le Bas, 1977; 1989; Lee and Wyllie, 1998; Wyllie and Lee, 1998).

The Gifford Creek Carbonatite Complex (GCCC), Gascoyne Province, Western Australia contains many different alkaline magmatic and hydrothermal phases, many of which are prospective for LREE mineralisation over an area of ~450 km^2. This study outlines the petrology and geochemistry of the alkaline rocks the GCCC, and, in particular, aims to define and establish the origin for the previously documented Lyons River Sills as well as the newly discovered magnetite-biotite dykes and ankerite-siderite carbonatite units. This work provides insights into the potential links between carbonatites and kimberlites, the magmatic origins for the ankerite-siderite carbonatites, and the associations between the variety of magmatic and hydrothermal units in the GCCC.

2.2 Regional Geology and Geologic History

The Gascoyne Province sutures Archean-aged rocks of the Pilbara Craton, Glenburgh Terrane, and Yilgarn Craton to form the Western Australia Craton. It comprises granitic rocks, granitic and metasedimentary gneisses, and metasedimentary rocks that have undergone a 1 b.y. history of terrane assembly and re-working, resulting in seven different tectonic zones. These include (from south to north): the Errabiddy Shear Zone, Paradise Zone, Mooloo Zone, Mutherbukin Zone, Limejuice Zone, Mangaroon Zone, and Boora Zone (Fig 2.1; Sheppard et al., 2010a,b).

The GCCC is located in the northern region of the Mangaroon Zone (Fig. 2.1). The Minga Bar and Collins faults bound the Mangaroon Zone to the south and north, respectively. The Mangaroon Zone comprises the c. 1760 to 1680 Ma Pooranoo Metamorphics, (Sheppard et al., 2010b) and the granitic rocks of the c. 1680 to 1620 Ma Durlacher Supersuite (Pearson et al; 1996). The Mangaroon Zone is unconformably overlain by 1673 to 1455 Ma sedimentary rocks, which make up the Edmund Group (Martin and Thorne, 2004).

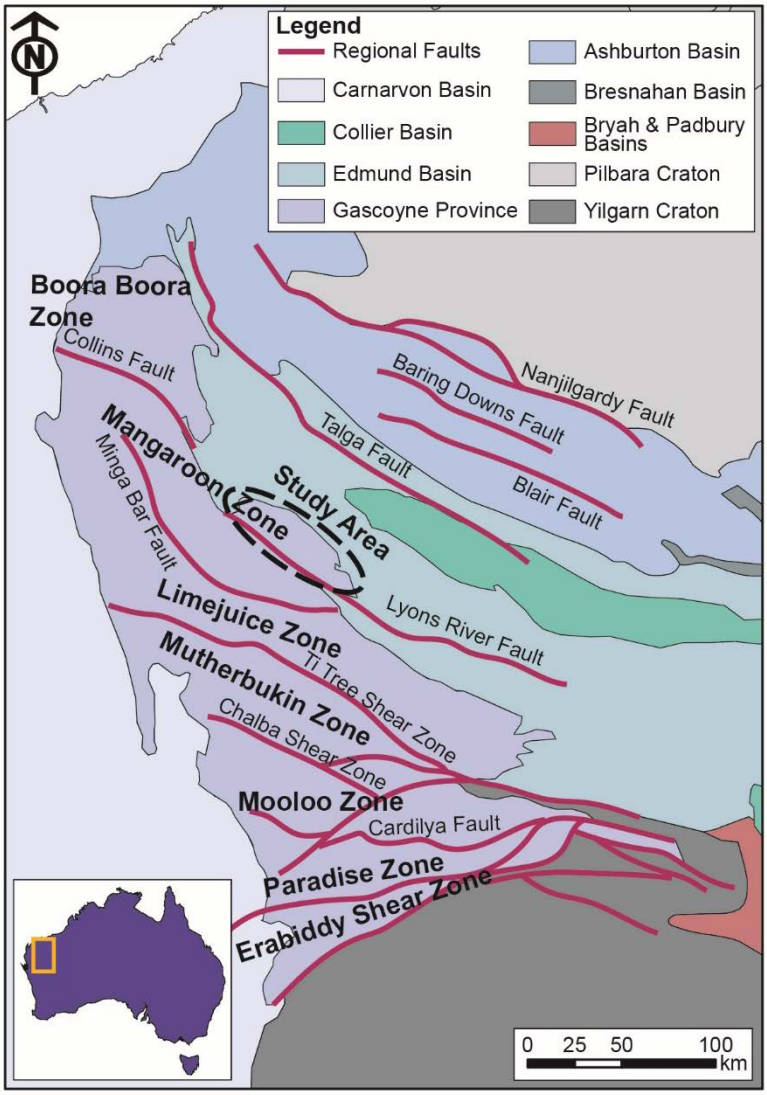

Figure 2.1 Regional tectonic map of the Gascoyne Province and major bounding structures. Note that the Ti Tree Shear Zone and Chalba Shear Zone are faults and not tectonic zones. The GCCC is located in the lobate feature on the northeastern margin of the Mangaroon Zone, constrained by the Lyons River Fault in the southwest and the Edmund Basin in the northeast.

Several orogenic events, potentially associated with supercontinent formation and break-up, affected the Mangaroon Zone evolution. The first of these events was the c. 1680 to 1620 Ma Mangaroon Orogeny. This resulted in regional extension followed by emplacement of the Durlacher Supersuite, medium to high-grade (amphibolite facies) metamorphism, and deformation of the primary sedimentary units of the Pooranoo Metamorphics (Sheppard et al., 2005; 2010a). The region underwent additional metamorphism and fault reactivation related to the c. 1320 to 1170 Ma Mutherbukin Tectonic Event, causing low-grade metamorphism (greenschist facies) and hydrothermal alteration (Korhonen et al., 2015). Following the Mutherbukin Tectonic Event, the region experienced additional low-grade (greenschist facies)

metamorphism during the c. 1030 to 955 Ma Edmundian Orogeny (Martin and Thorne, 2004; Sheppard et al., 2007) as well as fault reactivation and hydrothermal alteration related to the c. 955 to 830 Ma Kuparr Tectonic Event (Cutten and Johnson, 2018; Piechocka et al., 2018; Olierook et al., 2018). Finally, the c. 570 Ma Mulka Tectonic Event caused regional brittle faulting and fault reactivation (Sheppard et al., 2010a; Johnson et al., 2013).

2.3 Local Geology of the Gifford Creek Carbonatite Complex

2.3.1 Host rocks

Locally, the GCCC intrudes the Pooranoo Metamorphics, Durlacher Supersuite, and the Edmund Group metasedimentary rocks. The c. 1760 to 1680 Ma Pooranoo Metamorphics consists mainly of pelitic schists and gneisses as well as metafeldspathic sandstones, representing a metamorphosed, deep marine turbidite sequence (Sheppard et al., 2010b). Metamorphism during Mangaroon Orogeny resulted in localised zones of anatectic granites and deformation of sedimentary strata (Sheppard et al., 2005; 2010a,b).

The c. 1680 to 1620 Ma Durlacher Supersuite comprises several granitoid intrusions: the Pimbyana Granite, the Yangibana Granite, the Dingo Granite, and undifferentiated schlieric granites, all of which intrude the Pooranoo Metamorphics. The Pimbyana Granite is the most abundant granite hosting the GCCC. It has a monzogranitic composition, is coarse to very coarse-grained, and has a strongly porphyritic texture. The Yangibana Granite is a medium-grained, seriate to equigranular syeno- to monzogranite and is coeval with the Pimbyana Granite (Pearson, 1996). The Dingo Granite has a syeno- to monzogranitic composition, is medium to coarse-grained, and has a distinct trachytic texture. It intrudes the Pimbyana Granite and occurs in the northern margin of the GCCC. It is also found outside the GCCC in other regions of the western Mangaroon Zone (Pearson, 1996; Pearson et al., 1996; Sheppard et al., 2005). The schlieric granites are found mainly in the southern half of the GCCC intruding the Pooranoo Metamorphics. Many of the schlieric granites are monzogranitic to granodioritic in composition with enclaves of dark schist and gneiss.

The 1673 to 1455 Ma Edmund Group sedimentary rocks unconformably overlie rocks of the Durlacher Supersuite and Pooranoo Metamorphics. The Edmund Group comprises a large sedimentary package within the extension-related Edmund Basin of the northern Gascoyne Province and Southern Pilbara regions. Around the margins of the GCCC, the Edmund Group consists of quartz sandstones, conglomerates, and siltstones, but there is a significant lateral facies variation in the Edmund Group across the basin (Martin and Thorne, 2004).

2.3.2 Gifford Creek Carbonatite Complex

The GCCC was emplaced c. 1370 Ma (Zi et al., 2017; Slezak and Spandler, 2019*)* into the previously described host rocks. The GCCC is bounded in the south by the northwest-southeast striking Lyons River Fault, a crustal suture between the Archean-Neoarchean Glenburgh Terrane and the Archean Pilbara Craton (Johnson et al., 2013). The Bald Hill Lineament runs subparallel to the Lyons River Fault and separates massive, dextrally sheared granites in the northern region from the complex assortment of schists, granites, and alkaline dykes in the southern region (Fig. 2.2; Pearson, 1996; Pearson et al., 1996). The area between the Bald Hill Lineament and the Lyons River Fault hosts the majority of the alkaline dykes comprising the GCCC.

The GCCC is made up of several different rock types, some of which have been previously defined, creating ambiguity in their identification. The Yangibana Ironstones were first described as such by Gellatly (1975) and the name is still commonly used. The swarm of SE-trending rocks near the Lyons River Fault (Fig. 2.2) have historically been called the Lyons River Sills. These units were first described as ultrabasic sills by Pearson (1996) and Pearson et al. (1996). More recently, the Lyons River Sills have been described as ferrocarbonatites by Pirajno et al. (2014). The work in this thesis has revealed new and undescribed rock types in the GCCC. This chapter describes the new rock units and re-evaluates previously described units (e.g., the Lyons River Sills) based on field associations, mineralogy, and geochemistry. This new evaluation has resulted in four primary rock types:

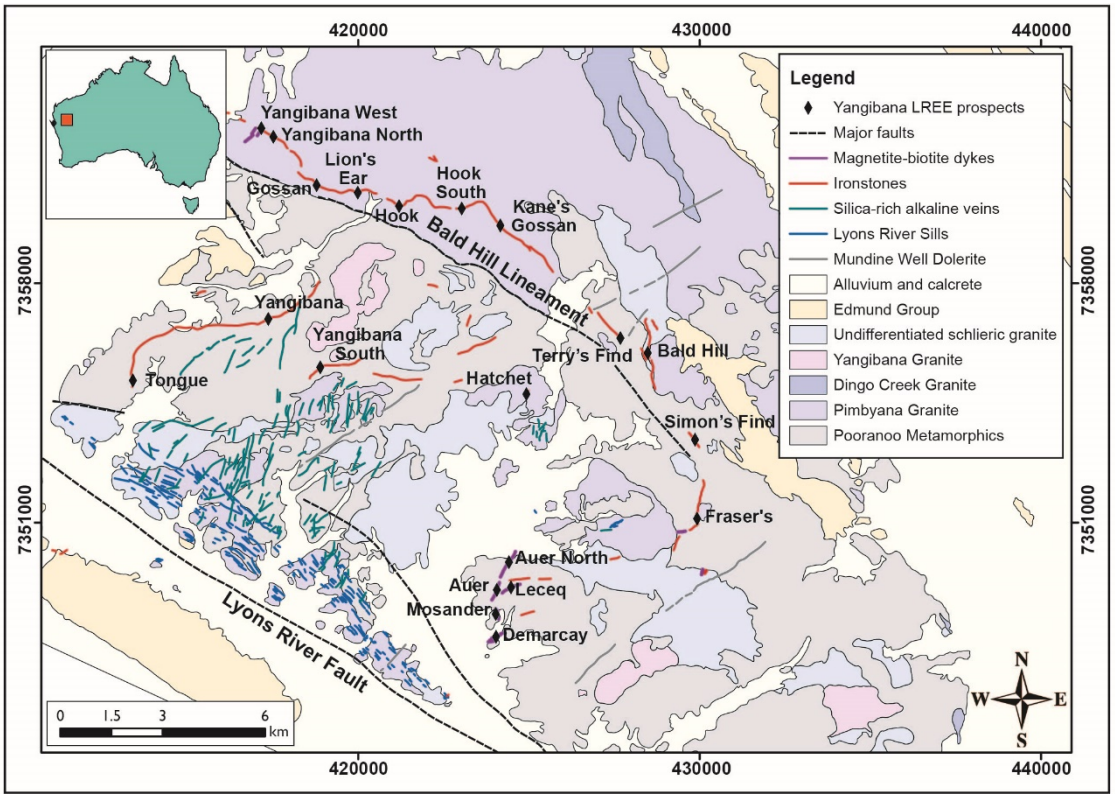

Figure 2.2 District-scale map of the GCCC showing the distribution of the alkaline dyke units, their host rocks, and major mineral deposits that comprise the Yangibana LREE district (modified after Slezak et al., 2018).

1) the Lyons River Sills (Fig. 2.3a,b); 2) magnetite-biotite dykes (Fig. 2.3c); 3) silica-rich alkaline veins (Fig. 2.3d); and 4) ankerite-siderite carbonatites (Fig. 2.3e). In addition, there are three additional rock types related to the primary units: 1) alkaline amphibole-dolomite veins, which emanate from the Lyons River Sills; 2) the Yangibana Ironstones, which host LREE mineralisation of economic interest; 3) fenites (Fig. 2.4a); and 4) glimmerites (Fig. 2.4b). The fenites and glimmerites are the wall rock assemblages created through alteration by alkaline, carbonatite-related fluids.

The Lyons River Sills occur in the southern region of the GCCC mainly as a swarm of dykes and sills, striking subparallel to the Lyons River Fault (i.e., ~130 to 150°) and dipping 30° to 60° SW, but they have also been found in the northeast near the Fraser's deposit (Fig. 2.2). The Lyons River Sills range from 10 cm to 1.5 m in width and occur as continuous dykes/sills for a few tens of metres up to a few hundred metres or more, although individual dykes/sills are rarely traceable for longer distances due to offset by small faults or due to cover by vegetation and surficial sediments. The Lyons River Sills are very fine-grained, have a fresh-surface colour of

blue and green relating to sodic amphiboles and sodic pyroxenes, respectively, and weather buff to dark brown (Fig. 2.3a,b). Some dykes (e.g., LRS-125) have a thick zone of oxidised minerals and may be altered along fractures and joints.

Steeply dipping dykes (Fig. 2.3c) and flat-lying sills composed largely of magnetite and biotite are located in the northwest corner near Yangibana North and Yangibana West, and in the southeast region near Fraser's down to the Demarcay deposits (Fig. 2.2). These units (collectively termed magnetite-biotite dykes) trend northeast to southwest, are 10 cm to 1.5 m thick, and extend for tens to hundreds of metres at the surface. The contacts between the granite and magnetite-biotite dykes are usually sharp, although some small injection veinlets of magnetite and biotite are present, occasionally forming crackle breccias in the granite host rock proximal to the main intruding body. The magnetite-biotite dykes were not observed to cross cut the Lyons River Sills, although at one locality, close to Demarcay, a magnetite-biotite dyke was observed to contain fine-grained quartz, magnetite, and aegirine along its margin (Fig. 2.3c). Fresh magnetite-biotite dykes are black in colour and are composed of coarse-grained magnetite, biotite, apatite, and monazite. Some dykes host 5 to 15 cm-sized pods and bands of apatite and magnetite.

The central region of the GCCC hosts a swarm of silica-rich alkaline veins (Fig. 2.2). They are oriented orthogonally to the Lyons River Sills, striking between 000° to 020°, and dipping subvertically to vertically. There is also a small outcrop of steeply dipping, hydrothermally altered, silica-rich alkaline veins in the east of the complex on "Spider Hill" near the Hatchet deposit (Fig. 2.2; Pearson et al., 1996). Although the veins occur in close proximity to the Lyons River Sills in the southcentral area of the complex, direct field relationships between the two units were not observed. The silica-rich alkaline veins are absent to the north of the Yangibana or Yangibana South mineral deposits (Fig. 2.2). They are typically of limited width, ranging from 3 cm to 50 cm (Fig. 2.3d), but they often extend for tens to several hundreds of metres and are spatially associated with nearby quartz veins of similar orientations. They are usually green to grey to buff in colour when fresh (Fig. 2.3d), although they weather to brown. Additionally, the veins show evidence of multiple fluid pulses and shearing.

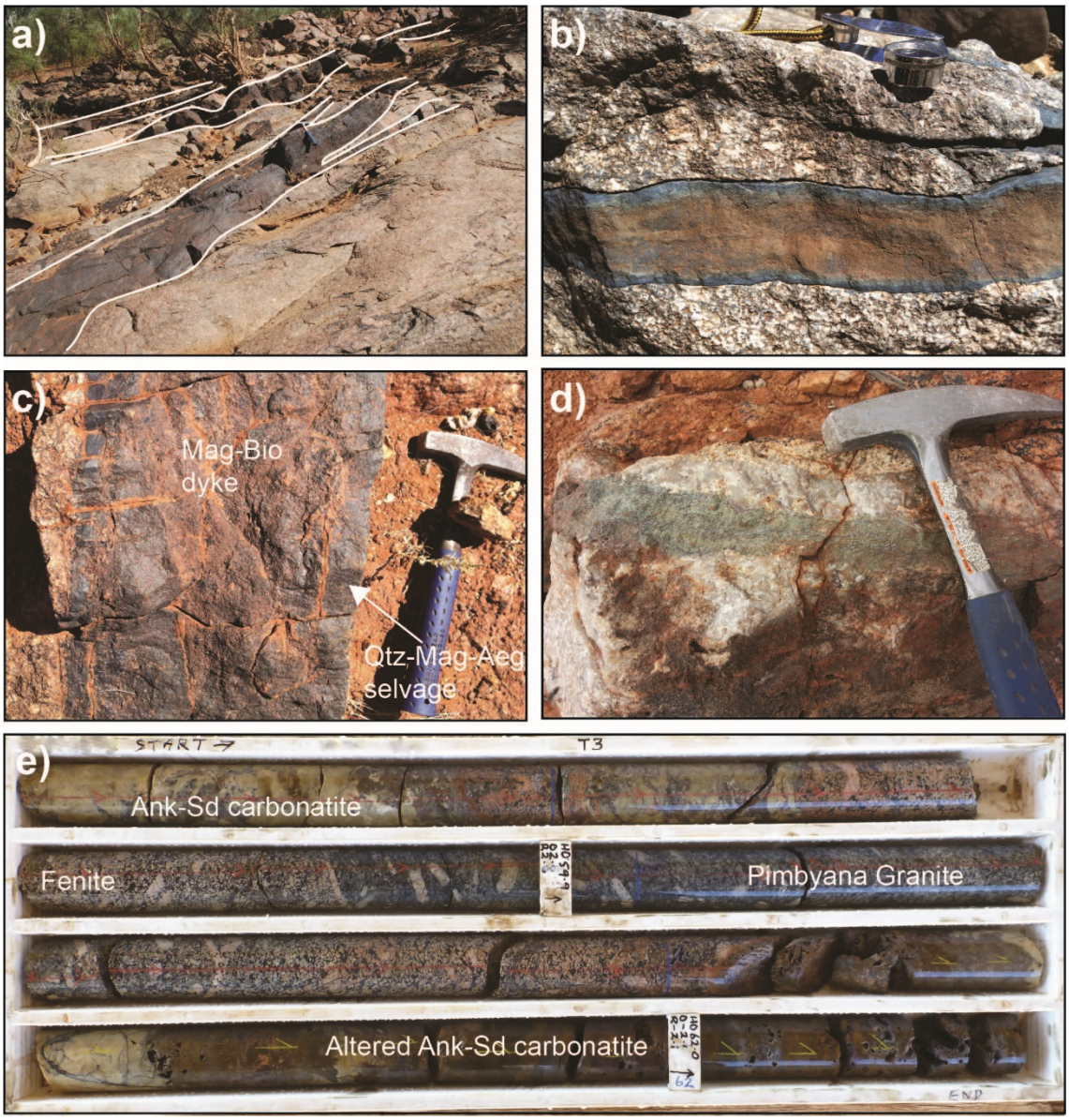

Figure 2.3 Field photos of the various GCCC alkaline intrusive units. a) Lyons River Sills dolomite carbonatite with dark brown weathering patina. b) Lyons River Sills calcite carbonatite with blue, Mg-rich arfvedsonite/riebeckite margins. c) Coarse-grained magnetite-biotite dyke at Demarcay with fine-grained margins similar to the silica-rich alkaline veins in (d). d) Aegirine and HFSE-rich silica-rich alkaline vein in a larger quartz vein hosted in the Pimbyana Granite. The dyke is located in the swarm south of Yangibana South in Figure 2.2. e) Coarse-grained ankerite-siderite carbonatite dyke found in drill hole YN49 at Yangibana North with pink, fenite alteration of the porphyritic Pimbyana Granite host rock. The dyke is altering to a porous, silica and iron-oxide rich rock. Ank = ankerite, Bio = biotite, Mag = magnetite, Sd = siderite.

The ankerite-siderite carbonatites are found at depth beneath the NW-SE trending ironstones subparallel to the Bald Hill Lineament. In drill core, these rocks form dykes 5 cm to 1 m thick (Fig. 2.3e), which crosscut the Yangibana and Pimbyana granites. The ankerite-siderite carbonatites comprise very coarse-grained siderite and ankerite, with enclaves (0.5 to 3 cm in size) of silicate and phosphate minerals. Adjacent to the ankerite-siderite carbonatites are

magnetite and biotite-rich selvages 0.5 to 3 cm thick, which are further enveloped by pink, K-bearing fenites.

In addition to the primary magmatic phases, the GCCC comprises several other phases, including the Yangibana Ironstones, which are significant hosts for LREE mineralisation. These rocks are composed of fine-grained iron oxides, hydroxides, quartz, and phosphate minerals monazite and rhabdophane (Pirajno and González-Álvarez, 2013; Pirajno et al., 2014; Chapter 5). They have vuggy and/or botryoidal textures and often have weathered cavities resembling carbonate parallelepipeds. These rocks are low-temperature alteration products and are not discussed further in this chapter, as they are the subject of Chapter 5.

Small, 3 to 20 mm thick, alkaline amphibole-dolomite veinlets with 1 to 3 cm thick potassium feldspar halos extend up to tens of metres from the parent carbonatite dykes (i.e., the Lyons River Sills). They often follow joint patterns when hosted by granitic units (Fig. 2.4a).

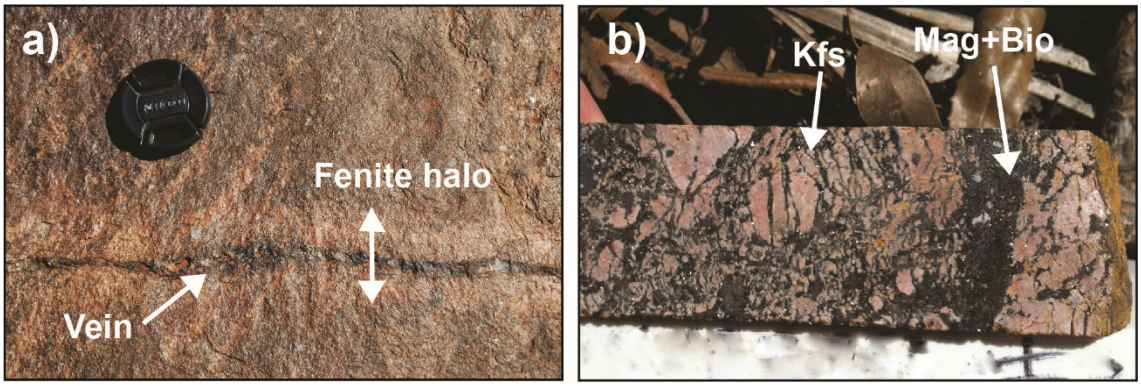

Figure 2.4 Alteration assemblages associated with the alkaline units. a) Alkaline amphibole-dolomite veinlet in joint fracture. Veinlet originates from a dolomite carbonatite dyke. The veinlets (as well as their parent dykes are enclosed by fenite halos. b) Fenitised granite cut by magnetite and biotite alteration selvages (i.e., glimmerites) from Yangibana West.

All rock types are mantled by white to pink halos of fenitised granite and metasediments (e.g., fenites). The fenites are predominantly composed of potassium feldspar, and the extent of alteration is proportional to the size of the dyke, sill, or vein (e.g., 1 cm vein has a 1 to 3 cm fenite halo; a 1 m dyke has a 1 to 3 m fenite halo). Fenites are present in both schists of the Pooranoo Metamorphics and Edmund Group sedimentary rocks but are most obvious in the granitic rocks. Magnetite-biotite alteration selvages are found in conjunction with fenites mantling the ankerite-siderite carbonatites. These selvages fracture fenitised crystals and brecciate the host rock (Fig. 2.4b).

2.4 Analytical Methods

Samples collected for this study are from surface outcrops and diamond drill core. All samples were prepared as polished thin sections and initially examined using a Leica DMRXP optical microscope.

2.4.1 Major element mineral chemistry

The major element composition of biotite were determined on carbon-coated polished pucks (25 mm diameter) using a JEOL JXA-8200 wavelength dispersive (WD) and electron dispersive (ED) combined electron probe micro-analyser (EPMA) at the Advanced Analytical Centre (AAC) at James Cook University (JCU), Townsville, Australia. The beam was set to a 5 μm spot diameter with an accelerating voltage of 15 kV and a current of 20 nA. All elements were analysed for 20 s on peak with 10 s on background. Element concentrations were quantified using well-characterised in-house standards as follows: Ca and Si (wollastonite), Na (albite), Mn (spessartine), Ti (TiO_2), Al (almandine), Mg (olivine), K (orthoclase), Cl (tugtupite), F (SrF_2). All analyses were corrected using the φρz procedure (Armstrong, 1991). Complete results and atoms per formula unit (apfu) calculations can be found in Appendix 2.A.

2.4.2 Bulk rock geochemistry

Bulk rock samples were sent to Bureau Veritas Commodities Canada Ltd in Vancouver, British Columbia. The samples were crushed and split. One sample split was fused into a lithium metaborate/tetraborate bead. The sample bead was dissolved in American Chemical Society (ACS) grade nitric acid dissolution and analysis of the solution conducted via ICP-MS for the following elements: Mg, Al, Si, P, K, Ca, Sc, Ti, V, Cr, Mn, Fe, Ni Ga, Rb, Sr, Y, Zr, Nb, Sn, Cs, Ba, La, Ce, Pr, Nd, Sm, Eu, Gd, Tb, Dy, Ho, Er, Tm, Yb, Lu, Hf, Ta, W, Th, and U. The second sample split was digested in aqua regia and analysed via inductively coupled emission spectroscopy/mass spectroscopy (ES/MS) for the elements Li, Be, B, Cr, Co, Cu, Zn, Ge, As, Se, Mo, Pd, Ag, Cd, In, Sb, Te, Re, Pt, Au, Hg, Tl, Pb, and, Bi. Carbon and S were determined using the LECO method. Fluorine was analysed by sample decomposition by fusion with NaOH

followed by water digestion and acidification using citric acid buffered by an ammonium citrate solution. The fluoride ion was analysed by the potentiometric method.

2.4.3 Carbon-oxygen isotope composition

Sample powders of carbonatite were prepared and analysed for $\delta^{13}C$ and $\delta^{18}O$ at the AAC Environmental Isotope Laboratory. Stable carbon and oxygen isotope compositions were determined using an online ThermoFisher GasBenchIII gas preparation and introduction system coupled to a ThermoFisher DeltaV^{PLUS} isotope ratio mass spectrometer via the ThermoFisher ConFloIV. Carbon dioxide was extracted from carbonate by reaction with 100% orthophosphoric acid in Exetainer vials after atmosphere was replaced with He. Repeat samples of NBS-18 and NBS-19 (as international standards) provided monitoring of accuracy and precision. Standard deviations for internal standards were better than 0.1‰ for both $\delta^{13}C$ and $\delta^{18}O$ values. The $\delta^{13}C$ values are reported relative to Vienna PeeDee Belemnite (VPDB), and the $\delta^{18}O$ values are reported relative to Vienna Standard Mean Ocean Water (VSMOW).

2.4.4 Bulk rock Nd isotopes

Rock samples were prepared at the JCU Mineral Separation Lab. Samples were cut, cleaned, and examined for contaminants such as wall rock clasts. Sample without contamination or alteration were then crushed to a fine powder using a tungsten ring mill. The mill was thoroughly cleaned in between each use. Whole rock isotope analyses of nine samples were performed at the University of Adelaide with a Finnigan MAT 262 thermal ionisation mass spectrometer (TIMS) in static and quadruple cup dynamic measurement modes following the routine in Wade et al. (2006). Between 30 and 200 mg of rock powder were spiked with (^{147}Sm + ^{150}Nd) by initially digesting the samples in a 2 mL 7M HNO_3 + 4 mL 28M HF solution that was evaporated to dryness at 140 °C. Then the samples were digested in a HNO_3-HF solution at 190 °C for at least 96 hours in Parr reaction vessels. The samples were then evaporated to dryness on a hotplate at 140 °C and redissolved in 6 mL 6M HCl. The measurements were corrected for mass fractionation by normalisation to $^{146}Nd/^{142}Nd = 0.7219$. Neodymium and Sm concentrations were corrected for 100 pg and 50 pg blanks, respectively. Reference material JNdi-1 gave 0.512108 ±

8 (2σ) (n = 8). $^{143}Nd/^{144}Nd$ ratios were normalised to the TIMS value of JNdi-1 glass (0.512098 ± 13; Fisher et al., 2011).

2.4.5 Sr isotope composition of carbonate minerals

Carbonatite rocks were sampled for Sr isotope analysis using a dental drill with a titanium burr. Milligram-sized samples were dissolved in 1M acetic acid (Asahara et al., 1995), which leaches Sr from the carbonate component and is not significantly impacted by incorporated silicate detritus. The acid/sample solution was then decanted and evaporated to dryness. Strontium was separated using pre-cleaned Biorad brand micro-columns containing Eichrom strontium-specific resin. Several column volumes of MQ and 3.5M HNO_3 were used to clean the columns, which were equilibrated with 500 µl 3.5M HNO_3. Samples were loaded in 500 µl of 3.5M HNO_3 and washed in four rinses of 300 µl of 3.5M HNO_3. The Sr was then eluted in 500 µl MQ and evaporated to dryness. Evaporated samples were treated with H_2O_2 to ensure removal of any resin and then dissolved in 2 ml 2% HNO_3. A volume corresponding to ~400 ng Sr was placed into 1.5 ml vials containing 2% HNO_3. The Neptune multi collector inductively coupled mass spectrometer (MC-ICP-MS) in the AAC at JCU was used to analyse the samples. Analyses of the SRM-987 standard run in conjunction with the samples yielded a mean ratio of 0.71040 ± 0.000029 (n=5), which is in agreement with the accepted value of the SRM-987 standard of 0.71034 ± 0.00026. Rubidium and Sr contents were determined at the JCU AAC using the trace element methods described in Appendix 1.A to ensure minimal ^{87}Rb impact on the $^{87}Sr/^{86}Sr$ values. Dolomite from the Lyons River Sills had Rb/Sr < 0.01. Siderite and ankerite from the ankerite-siderite carbonatites had Rb/Sr < 0.08 and < 0.0002, respectively. However, these values are an overestimation of the Rb/Sr values due to mineral inclusions within the carbonates, which were not dissolved during sample preparation.

2.5 Petrography

2.5.1 Lyons River Sills

2.5.1.1 Dolomite carbonatites

The Lyons River Sills comprise primarily dolomite carbonatites (Fig. 2.3a) with minor amounts of calcite carbonatite (Fig. 2.3b). The dolomite carbonatites are composed of 50 to 65% Fe-bearing dolomite (determined by EDS); 10 to 30% arfvedsonite and aegirine; minor amounts of biotite, magnetite, ilmenite, and apatite; and trace amounts of monazite, zircon, pyrite, and chalcopyrite. Textural features of the carbonatite sills are heterogeneous, varying between porphyritic, equigranular, and seriate textural varieties. For example, some dolomite carbonatites exhibit a weak porphyritic texture composed of round to elongated carbonate and arfvedsonite (± magnetite) clots (1–2 mm in size; Fig. 2.5a) in a matrix of Mg-bearing biotite, arfvedsonite, dolomite, and magnetite. Other carbonatite sills contain blebs of relatively coarse (100 to 300 μm) subhedral to euhedral dolomite, mantled by a thin hematitic ban. The blebs sit in a matrix of fine-grained (50 to 100 μm) dolomite and silicate minerals (Fig. 2.5b). One arfvedsonite-bearing dolomite carbonatite sample contains micro-brecciated veins/horizons with carbonate clasts in an aegirine-rich matrix.

Relative amounts of aegirine and arfvedsonite vary considerably, even within the same dyke. The abundance of arfvedsonite versus aegirine controls the colour of the dykes in the field. Where arfvedsonite is more abundant, the carbonatites are blue and where aegirine is more abundant, the carbonatites are green. Arfvedsonite occurs as 100 to 500 μm anhedral crystals to euhedral parallelograms throughout the carbonatites, but is most abundant matrix of the porphyritic dolomite carbonatites. Some arfvedsonite displays zones of pleochroism ranging from periwinkle to lavender within the same mineral face, indicative of alteration to riebeckite (Deer et al., 1992). Arfvedsonite shares sharp contacts with dolomite with only minor embayments between the minerals. Arfvedsonite appears to be intergrown with the Mg-bearing biotite in the matrix of some carbonatite samples.

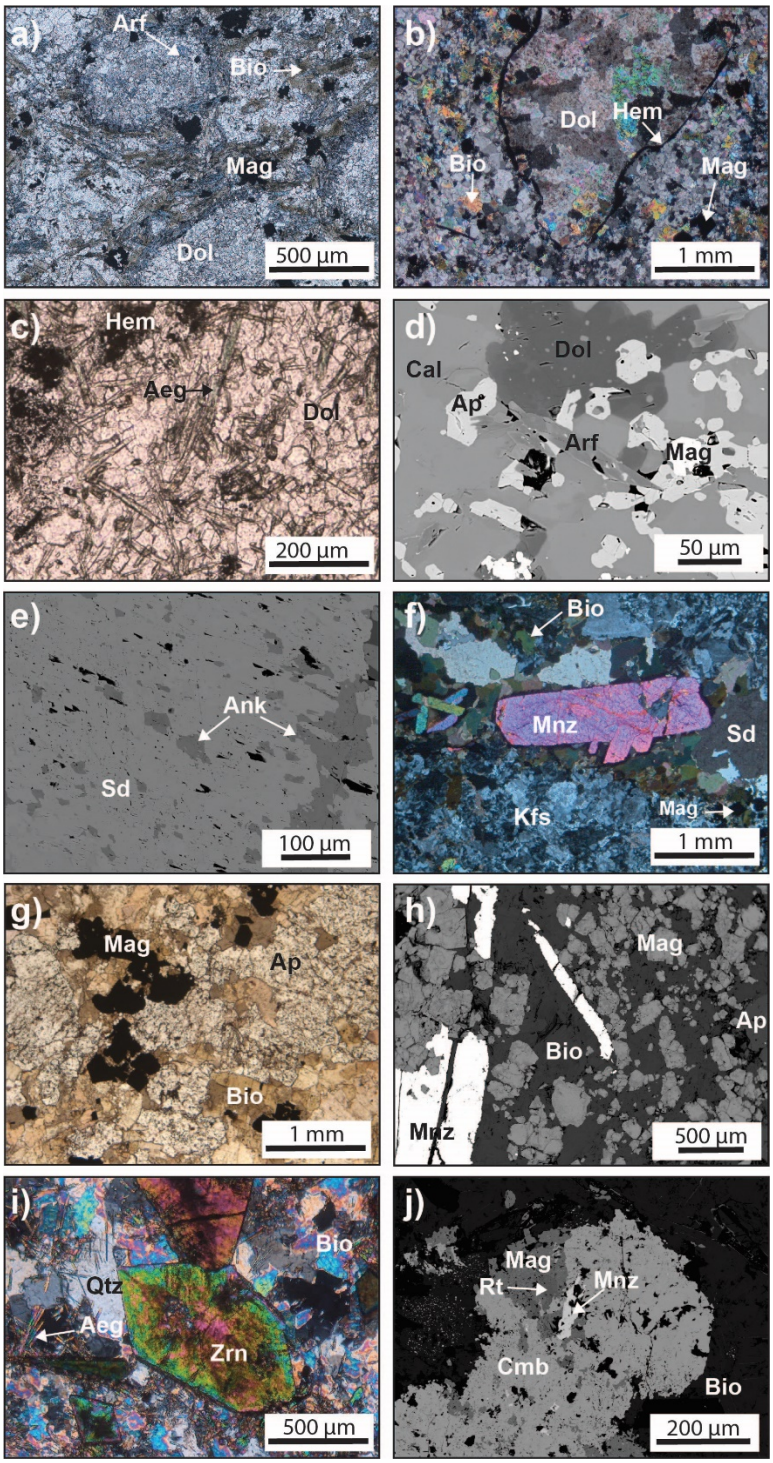

Figure 2.5 Thin section photos of the main rock types comprising the GCCC. PPL = plane polarised light. XPL = cross-polarised light. a) PPL-image of dolomite carbonatite composed of rounded dolomite and arfvedsonite clasts in matrix. b) XPL-image of coarse-grained ferroan dolomite bleb with a thin hematite rim. c) PPL-image of dolomite carbonatite with aegirine needles. d) BSE image of calcite carbonatite with dolomite inclusions. Small specs of calcite are also within the dolomite crystals. e) BSE image of ankerite and siderite intergrowth in an ankerite-siderite carbonatite sample. f) XPL-image of ankerite-siderite carbonatite veinlet containing monazite. Veinlet contact with granite host rock is composed of biotite-magnetite. Granite has been fenitised to K-feldspar. g) XPL-image of a magnetite-biotite dyke with euhedral apatite crystal and euhedral biotite-magnetite. h) BSE image of magnetite-biotite dyke from with large monazite crystals. i) XPL-image of a silica-rich alkaline vein with large, euhedral zircon crystals and fine-grained aegirine needles with quartz and coarser, altered biotite. j) BSE image of columbite with monazite, Ti-bearing magnetite, and Nb-bearing rutile. Aeg = aegirine, Ap = apatite, Arf = arfvedsonite, Bio = biotite, Cal = calcite, Cmb = columbite, Dol = dolomite, Hem = hematite, Kfs = potassium feldspar, Mag = magnetite, Mnz = monazite, Qtz = quartz, Rt = rutile, Sd = siderite, Zrn = zircon.

Aegirine presents as 20 μm wide and up to 100 μm long euhedral needles that seem to overprint dolomite (Fig. 2.5c). Aegirine often occurs as the only silicate phase present in parts of the dolomite carbonatites, but in some samples aegirine was observed to be intergrown with arfvedsonite.

Magnesium-bearing biotite is brownish-olive, anhedral to subhedral, and forms laths and plates up to 300 μm across. The Mg-bearing biotite is most common in the equigranular dolomite carbonatites and in the matrix of the porphyritic carbonatites occurring in abundances between trace to 20% (Fig. 2.5a,b). It is intergrown with dolomite, but often has embayed or ragged crystal margins.

Magnetite comprises 3% to 5% of the dolomite carbonatites and is evenly distributed. It is typically subhedral to euhedral, 20 to 150 μm in size, and partially oxidised to hematite. Ilmenite comprises 1% to 3% of the rock as small, 20 to 100 μm anhedral to subhedral crystals. The subhedral crystals are somewhat tabular in shape, and the anhedral crystals appear to disseminate into the dolomite as an alteration assemblage of hematite and rutile. Apatite is common in the dolomite carbonatites, but its abundance varies greatly between trace amounts to several percent of the rock composition.

Apatite occurs as subhedral to euhedral ovoid grains ranging from 50 to 100 μm in size, forming smooth contacts with dolomite. Trace amounts of monazite and zircon are present as small (<10 μm to 20 μm) crystals in apatite and dolomite, respectively. Pyrite and chalcopyrite are present in some of the dolomite carbonatites samples. Minor apatite banding was observed, but the banding is not as prominent as in the calcite carbonatites (discussed below).

2.5.1.2 Calcite carbonatites

The calcite carbonatites are less common than the dolomite carbonatites, but their mineralogy is similar, being dominated Mg-bearing calcite (determined by EDS), dolomite, arfvedsonite, apatite, and magnetite. Collectively the carbonate minerals comprise approximately 70% to 85% of the rock. Calcite is typically anhedral to subhedral and generally ranges in size from 50 to 100 μm, but it also presents as larger (up to 500 μm) crystals distributed in 1 mm

diameter blebs and horizons within the dykes (Fig. 2.5d). Dolomite is of similar size, but forms subhedral to euhedral crystals and occurs as large clots (1 to 3 mm in diameter) surrounded by calcite. These dolomite clots also contain small crystals of calcite. Dolomite is also present as individual crystals (~50 to 100 μm in size) encompassed by calcite. The contacts between calcite and dolomite are irregular and embayed for both individual crystals and the larger clots.

Apatite in the calcite carbonatites typically occurs as 30 to 100 μm ovoid grains concentrated in horizons (0.5 mm to 10 mm thick) or as disseminated crystals. This banding makes the apatite proportions variable, usually between 5% and 20% of the rock. Many apatite grains contain small inclusions of carbonate minerals (Fig. 2.5d).

Arfvedsonite occurs as subhedral to euhedral tabular grains, 100 to 200 μm in size, and shows slight contrast variations in backscatter electron (BSE) images (Fig. 2.5d) that relate to variations in Ca and Fe contents (as determined by EDS). Arfvedsonite makes up 7% to 10% of the calcite carbonatites. The arfvedsonite crystal margins form straight to irregular contacts with calcite and dolomite. They also often contain small (~5 to 20 μm) apatite inclusions and, rarely, very small (~1 μm) magnetite inclusions.

Magnetite comprises ~3% to 5% of the calcite carbonatites and occurs as 20 to 50 μm anhedral to subhedral crystals disseminated throughout the samples, but is more common where apatite is also present. Magnetite is partially altered to hematite.

2.5.2 Ankerite-siderite carbonatites

No ankerite-siderite carbonatites were found at surface in the GCCC; rather, the samples obtained for analysis were all from drill core. The ankerite-siderite carbonatites comprise siderite, ankerite, calcite, Fe-enriched biotite, magnetite, monazite, apatite, and quartz. Siderite is large, usually >2000 μm in size and contains zones of smaller (20 to 200 μm) ankerite (Fig. 2.5e); however, the proportions of ankerite and siderite can vary considerably within the ankerite-siderite carbonatites. Calcite is similar in size to ankerite, but only present in small quantities proximal to quartz. Quartz forms small domains (~1 cm) within carbonate minerals, sometimes entraining siderite and ankerite crystals. The quartz crystals can be large, up to 1000 μm, and

commonly feature undulose extinction and recrystallised margins. The contact between quartz and ankerite and siderite are often irregular and embayed. Monazite is present as euhedral laths ranging in size from 100 to 1000 μm and often occurs as grain clusters (Fig. 2.5f). Monazite is present within both the carbonate and quartz domains and is observed extending across carbonate-quartz boundaries (Chapter 5). Anhedral to subhedral apatite (200 to 500 μm in size) occurs proximal to monazite. In some samples, apatite crystals occur as aggregates up to 1000 μm in diameter. Magnetite and Fe-enriched biotite co-exist as euhedral crystals (50 to 250 μm in size), which are present mainly along the contacts between the carbonate minerals and granitic host rock (Fig. 2.5f). They are also present along fractures in samples and as isolated crystals within the carbonate minerals.

2.5.3 Magnetite-biotite dykes

The magnetite-biotite dykes are black, equigranular intrusive units composed mainly of magnetite and biotite, which combined make up to 85% to 95% of these rocks. Apatite and monazite comprise the remainder of the magnetite-biotite dykes. Trace quartz was observed with goethite in vugs and in altered samples. Magnetite forms subhedral to euhedral crystals, up to 500 μm in size (Fig. 2.5g) and contains patchy hematite alteration. Magnetite has straight contacts with biotite and may contain inclusions of monazite. Most samples contain both apatite and monazite, but their relative abundances vary greatly even within the same dyke. Platy biotite is present as 100 to 500 μm, subhedral to euhedral crystals (Fig. 2.5g,h) and sometimes presents as an interstitial phase to magnetite and apatite. Apatite forms anhedral to subhedral crystals 50 to 1500 μm in size and often forms large clots (Fig. 2.5g), even aggregating together to create large pods (centimetres in size) within the magnetite-biotite dykes. Apatite ubiquitously hosts small, anhedral monazite inclusions (<10 μm), and under cathodoluminescence (CL), it exhibits complex zonation (Slezak et al., 2018; Chapter 3). Monazite is present in most samples, usually occurring as splayed clusters of large euhedral crystals up to 1000 μm in length (Fig. 2.5h). It can also occur as small inclusions in apatite and magnetite. No carbonate minerals were observed in the magnetite-biotite dykes in thin section or SEM. In one sample from these dykes, aegirine and

quartz were present in significant amounts at the expense of biotite. In addition, much of the magnetite had been altered to hematite and amorphous Fe^{3+}-bearing oxides, presumably goethite.

2.5.4 Silica-rich alkaline veins

The north to northeast striking veins in the centre of the GCCC are variably green to beige in colour. These veins often change in colour and composition along strike, and some veins exhibit evidence of multiple fluid pulses and contain quartz-filled tension gashes, which contributes to their geochemical variability (Appendix 2.B). They comprise variable amounts of phlogopite, aegirine, quartz, goethite, zircon, rutile, magnetite, columbite, arfvedsonite, and monazite. Phlogopite is often anhedral to subhedral, ranging between 100 μm and 500 μm in size. It is heavily altered, exhibiting recrystallised crystal edges and displaying light brown staining along cleavage planes and crystal margins. Quartz is often present as within the veins and also occurs as in cavities and tensions gashes. Quartz occurs as larger (~200 μm), subhedral to anhedral crystals, with recrystallised grain margins, undulose extinction, and small (<5 μm) molybdenite inclusions. Aegirine is present as a groundmass composed of small (10 to 20 μm), euhedral acicular crystals (Fig. 2.5i). Aegirine also forms acicular crystal splays up to 100 μm across in quartz. It was also observed having overgrown phlogopite (Fig. 2.5i).

Titanium-bearing magnetite (as determined by EDS) is present as anhedral to subhedral crystals ranging in size from 20 to 100 μm. It is also contains patchy hematite alteration. In some samples, zircon occurs in significant quantities, presenting as large, feathery clots up to 3 mm in diameter. More often, it presents as euhedral, dipyramids between 150 to 500 μm in size with shortened prismatic faces (Fig. 2.5i). Columbite and rutile appear as anhedral phases (10 to 200 μm in size) associated with similarly-sized (20 to 200 μm), subhedral to euhedral Ti-bearing magnetite (Fig. 2.5j). Columbite also occurs as inclusions within the feathery to fibrous zircon clots. Monazite is rare, forming anhedral laths (50 μm to 200 μm in size), which are occasionally intergrown with the fine-grained, feathery zircon and/or columbite (Fig. 2.5j). Trace amounts of arfvedsonite partially replaced by aegirine were observe, as well.

2.5.5 Alkaline amphibole-dolomite veinlets

The thin (3 to 20 mm wide), alkaline amphibole-dolomite veinlets originating from the dolomite carbonatites are composed of arfvedsonite (60%), Fe^{2+}-bearing dolomite (5 to 20%), rutile (5 to 15%), magnetite (5%), quartz (3 to 5%), apatite (1 to 3%), and monazite (trace). Rutile forms thin, elongate crystals comprising wispy masses up to 500 μm, and it often occurs with fibrous arfvedsonite that forms large masses up to 2 mm in size. The Fe^{2+}-bearing dolomite crystals are anhedral to euhedral and up to 300 μm in size. The dolomite crystal margins and cleavage planes display alteration to hematite. Magnetite and quartz are 100 to 200 μm in size and found in lesser quantities in the veins. Euhedral grains of apatite (100 to 500 μm in size) contain oscillatory zoning with rims enriched in REE (Slezak et al., 2018). Monazite occurs as small (20 to 100 μm), anhedral crystal inclusions within rutile and arfvedsonite.

2.5.6 Fenites

The fenites consist of the wall rocks – usually the Yangibana and Pimbyana granites or schists of the Pooranoo Metamorphics – altered to potassium feldspar, apatite, and minor monazite (Fig. 2.4). In the fenitic alteration halos, plagioclase is pervasively altered to irregularly shaped potassium feldspar (20 to 300 μm) with tartan twinning. Quartz is present as fine-grained (~50 μm) crystals with recrystallised grain boundaries and undulose extinction. Apatite forms anhedral to subhedral crystals (up to 500 μm), many of which are zoned towards REE-rich rims (Slezak et al., 2018; Chapter 3). Monazite occurs as an interstitial phase, filling in voids and fractures in the potassium feldspar and quartz, and as small inclusions (~10 μm) in the apatite.

2.5.7 Magnetite-biotite alteration

In areas immediately adjacent to the ankerite-siderite carbonatites, biotite and magnetite alteration selvages are present as ~1 to 2 cm thick halos (Figs. 2.4b and 2.5f), and also comprise many anastomosing veinlets that fracture the surrounding granitic rocks. These biotite and magnetite alteration assemblages are analogous to glimmerites (Le Maitre, 2002; Elliott et al., 2018). The biotite and magnetite crystals are large (50 to 200 μm) and often euhedral. Large (150

to 500 μm), dipyramid-shaped zircons with short prismatic faces are also present in the glimmerites proximal to the ankerite-siderite carbonatites (Chapter 4).

2.6 Mineral Chemistry

2.6.1 Micas

Biotite-series mica is present in nearly all of the alkaline igneous rocks in the GCCC and displays patchy light and dark texture under BSE (Fig. 2.6). The majority of mica contains intermediate Mg and Fe compositions along the annite-phlogopite solid solution series (Fig. 2.7) and is therefore referred to as "biotite". In general, biotite with higher Mg content is associated with the Lyons River Sills, the magnetite-biotite dykes from the southeast GCCC, and the silica-rich alkaline veins (Fig. 2.7; Appendix 2.A), which are actually closer to tetraferriphlogopite in composition. Iron and Al contents of biotite are highest in the ankerite-siderite carbonatites and associated magnetite-biotite dykes (Fig. 2.7; Appendix 2.A). The darker BSE zones are relatively Mg-rich and also show a shift towards higher F and Si, but lower Al and Cl contents (Figs. 2.7 and Figs. 2.8a,b). Biotite from the magnetite-biotite dykes and ankerite-siderite carbonatites has a range of Fe/(Fe + Mg), overlapping with lower ratios (e.g., ~0.2) exhibited in biotite from the Lyons River Sills as well as higher ratios (e.g., ~0.5), which were measured in biotite from the Pimbyana Granite. The Ti content increases as the Fe/(Fe + Mg) ratio increases (Fig. 2.8c). Biotite with higher Fe also has relatively high K (Figs. 2.8e) contents.

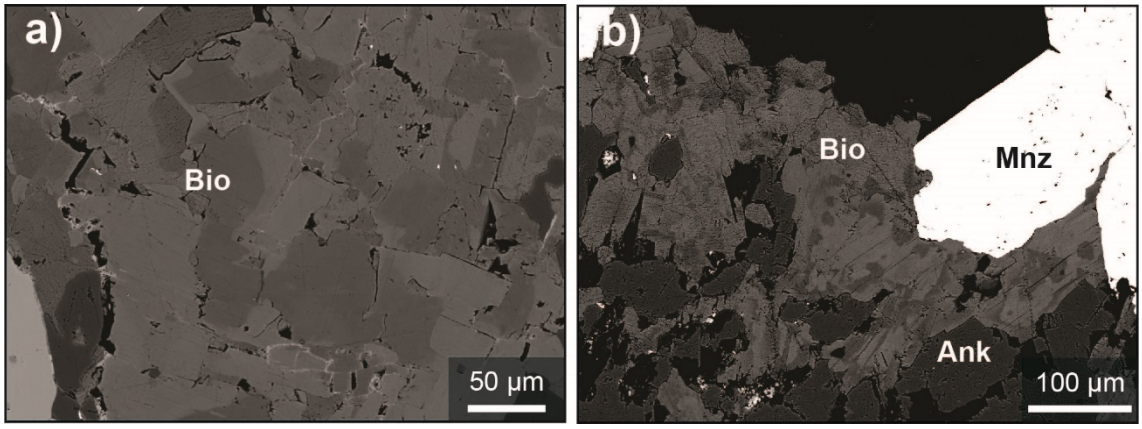

Figure 2.6 Backscattered electron (BSE) images of biotite. Zonation in BSE shows that lighter-coloured zones have more Fe and Al compared to darker-coloured zones, which contain more Mg (Fig. 2.7). a) BSE image from a Demarcay magnetite-biotite dyke. Cleavage planes can be observed passing uninterrupted through both zones. b) BSE image of biotite in an ankerite-siderite carbonatite. Ank = ankerite, Bio = biotite, Mnz = monazite

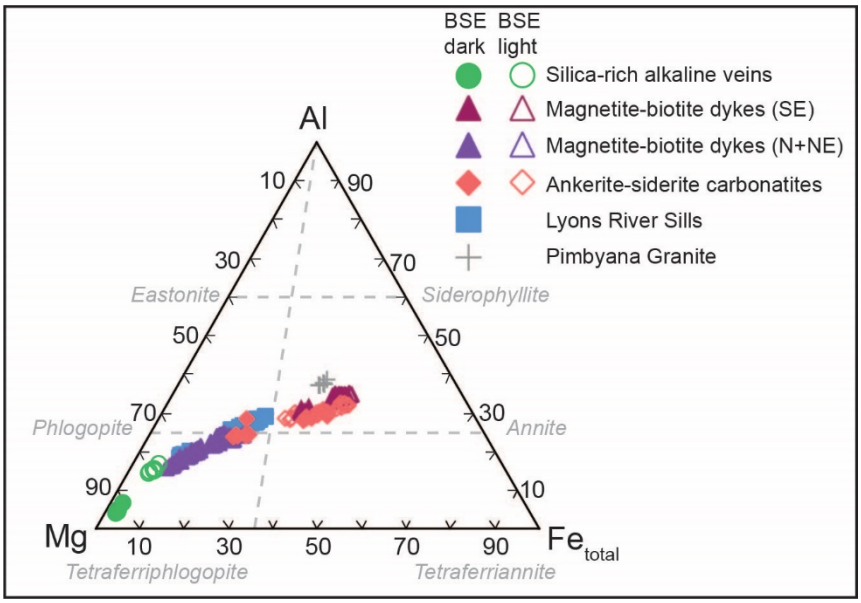

Figure 2.7 Ternary Al-Mg-Fe diagram for biotite. The micas from the silica-rich alkaline veins contain the least Al and Fe, but the most Mg and are likely tetraferriphlogopite. The micas found in the Lyons River Sills and magnetite-biotite dykes rend from tetraferriphlogopite/phlogopite towards more Fe and Al-rich compositions.

Most of the magnetite-biotite dyke analyses have elevated Mn contents compared to their Fe and Mg contents (Fig. 2.8f). Two samples from the northwestern and northern GCCC (YW61 and BH224) have Mn values commensurate with the contents in biotite hosted in ankerite-siderite carbonatites (Fig. 2.8f). The ankerite-siderite carbonatite samples also have slightly higher Cl contents compared to the rest of the analysed biotite (Fig. 2.8d). Biotite from the Lyons River Sills, magnetite-biotite dykes, and silica-rich alkaline veins contains significant F, usually between 3 and 5 wt.% F, but up to nearly 7 wt.% F in some analyses from the silica-rich alkaline veins (Appendix 2.A). These very high F contents exceed the supposed stoichiometric limit (~4.7 wt.% F), but are similar to F-rich biotite reported from Petersen et al. (1982), Valley et al. (1982), and Motoyoshi and Hensen (2001).

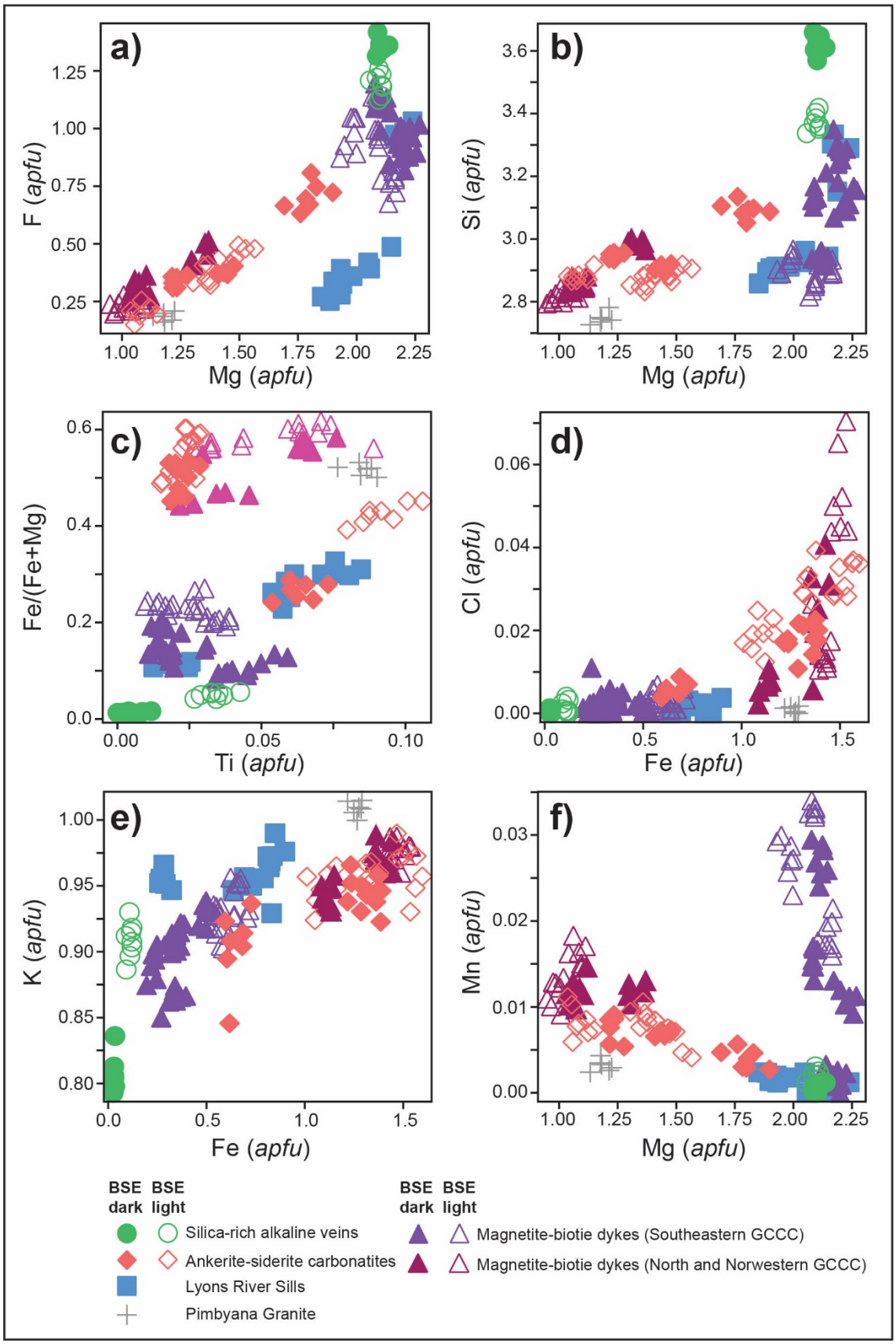

Figure 2.8 Plots of biotite apfu and atomic proportions (Fe/(Fe + Mg)). Closed shapes are dark zones and open shapes are light zones observed under BSE.

2.7 Whole rock chemistry

2.7.1 Lyons River Sills

The complete details of the bulk rock geochemistry can be found in Appendix 2.B. The Lyons River Sills are mainly magnesiocarbonatites with only two samples falling within the calciocarbonatite range (Gittins and Harmer, 1997; Fig. 2.9). In addition, SiO_2 contents reach ~20 wt.% for many of the dolomite-bearing samples (Fig. 2.10a), which also classifies them as silicocarbonatites according to Le Maitre (2002). The calcite carbonatites are rich in CaO and Sr, but contain relatively low TiO_2, Ni, and Cr (Fig. 2.10b-d; Appendix 2.B) compared to the dolomite carbonatites, which tend to have higher MgO contents and higher Mg numbers (Mg# = 54 to 73). As CaO contents decrease, MgO, Fe_2O_3, and SiO_2 contents increase. In addition, K_2O and Ti_2O contents increase with increasing Fe_2O_3 (Fig. 2.10). The calcite carbonatites contain the highest amount of phosphate. Apatite layering was more common in the calcite carbonatite samples, so the high measured phosphate contents may represent a sampling bias. The green (aegirine > arfvedsonite) dolomite carbonatites typically have higher Fe and Na contents than their blue-coloured (aegirine < arfvedsonite) counterparts.

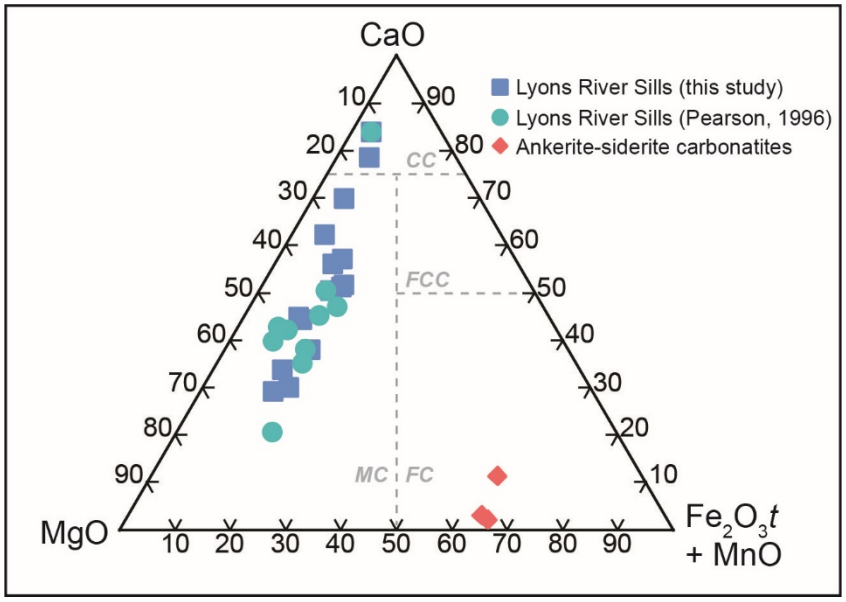

Figure 2.9 Carbonatite classification plot using molar oxides of metals based on bulk rock geochemistry (Gittins and Harmer, 1997). Most of the Lyons River Sills from Pearson (1996) and this study fall within the magnesiocarbonatite field. However, three samples fall in the calciocarbonatite field. As the Lyons River Sills become more Mg-rich, their Fe content also increases. The ankerite-siderite carbonatites plot within the ferrocarbonatite field. CC = calciocarbonatite, DC = Magnesiocarbonatite, FC = ferrocarbonatite, FCC = ferruginous calciocarbonatite

Multi-element spider plots illustrate that the calcite (Fig. 2.11a) and dolomite (Fig. 2.11b) carbonatites show similar patterns, both showing relatively enriched Ba, Th, and REY contents. Both also exhibit troughs at K, Pb, Ti, and have a minor depression at Y. The calcite carbonatites are depleted in Ti and show a negative anomaly for Hf and Zr, but do not feature relative depletion in P (Fig. 2.11a), unlike the dolomite carbonatites (Fig. 2.11b). The Lyons River Sills contain variable amounts of F, ranging from several hundred ppm up to ~9000 ppm. No differences in F content were observed between calcite and dolomite carbonatite varieties.

2.7.2 Ankerite-siderite carbonatites

The ankerite-siderite carbonatites are Fe-rich and contain moderate MgO amounts. They are comparable to the magnetite-biotite dykes in terms of total Fe_2O_3 and MgO contents (Fig. 2.10b,d,e). They are also contain the highest Mn and lowest Sr contents (Fig. 2.10d) compared to other units. The ankerite-siderite carbonatites contain low amounts of SiO_2, CaO, Ba, Nb, Ta, and U, but have variable K/Na, compared to other rock types (Fig. 2.10f). These carbonatites are enriched in Th and LREE, but depleted in Zr, Hf, Ti, and, in some samples, the HREE (Fig. 2.11c).

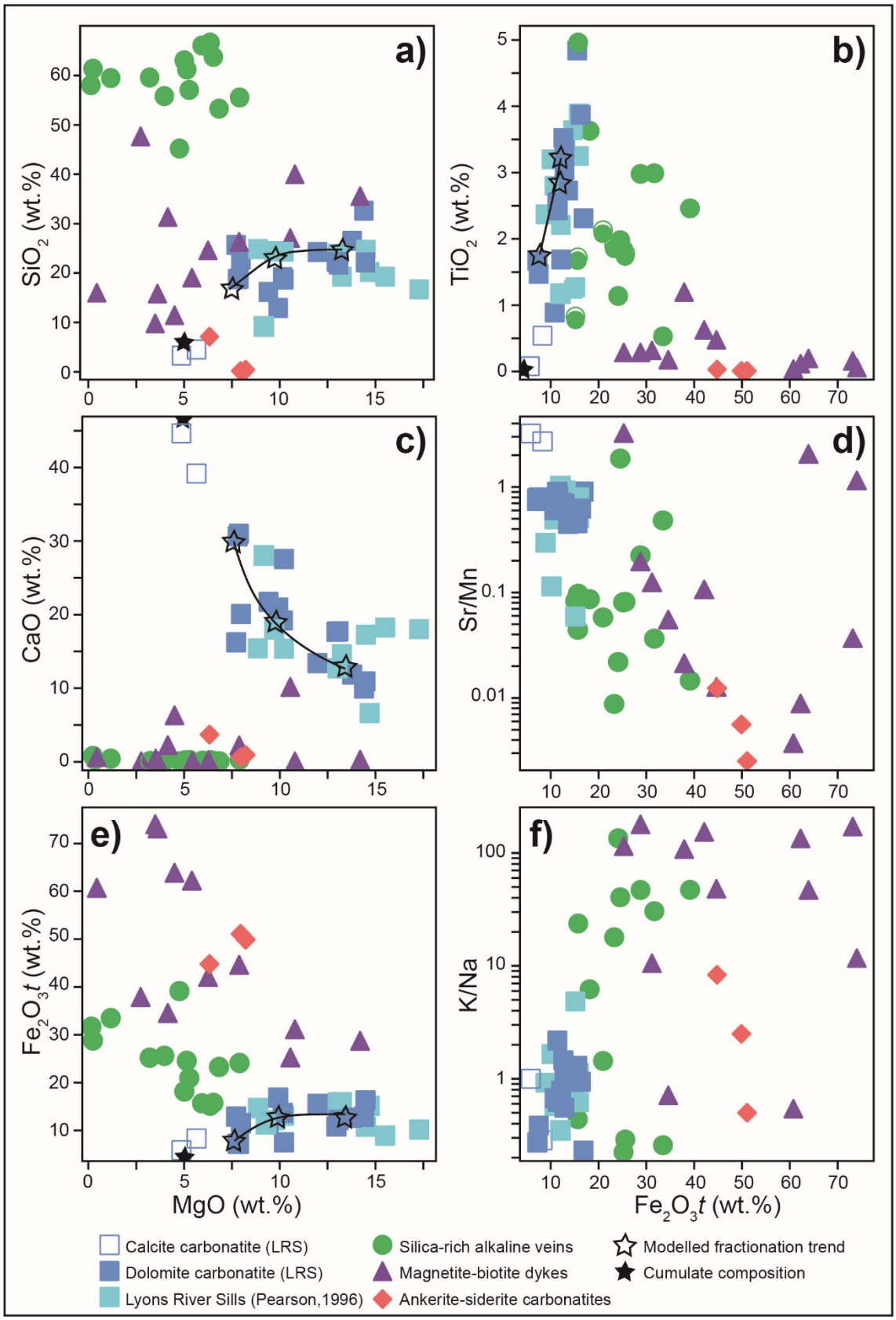

Figure 2.10 Major element X-Y diagrams for the rock types comprising the GCCC. Iron contents are recast as total Fe_2O_3. Open black stars and black lines show calculated fractionation trends when a calcite-rich cumulate phase is separated from a dolomite carbonatite (see Table 2.3).

2.7.3 Magnetite-biotite dykes

The magnetite-biotite dykes contain variable amounts of SiO_2 (Fig. 2.10a) and have low TiO_2 and CaO contents compared to the other rock types (Fig. 2.10b,c). Most of the magnetite-biotite dykes contain more Mn than Sr, except for the three most Mg-rich samples of the magnetite-biotite dyke, which have Sr/Mn >1 (Fig. 2.10d). They are rich in total Fe_2O_3, and generally contain significant K_2O (Fig. 2.10e,f).

Normalised trace element diagrams (Fig. 2.11d) show that the magnetite-biotite dykes are greatly enriched in Th and LREE. They display variable HREE contents that range from slightly depleted to slightly enriched. These units have significant troughs for Nb, Ta, Zr, Hf, and Ti, illustrating depletion in these elements. These rocks also contain significant amounts of F (0.7 to 3.8 wt.%) and Li (~1500 ppm; Appendix 2.B).

2.7.4 Silica-rich alkaline veins

The silica-rich alkaline veins contain 45 to 67 wt.% SiO_2, variable MgO, and high TiO_2 contents (Fig. 2.10a,b). Na_2O and K_2O contents range from 0.02 to 6.5 wt.%, and 0.6 to 4 wt.%, respectively, giving K/Na ranging from ~1 to ~11 (Fig. 2.10f). The Sr/Mn ratios for these rocks fall between the Lyons River Sills and the magnetite-biotite dykes (Fig. 2.10d).

Trace element diagrams show that the silica-rich alkaline veins have a positive Th anomaly, similar to the other rocks in the GCCC (Fig. 2.11e). They also have pronounced Nb enrichment, especially compared to Ta, and notable peaks in Zr and Hf. Most of the silica-rich alkaline vein samples have low Sr, P, and HREE values. Lithium contents range from 16 ppm to greater than 2000 ppm, and F contents reach as high as 2.3 wt. % (Appendix 2.B).

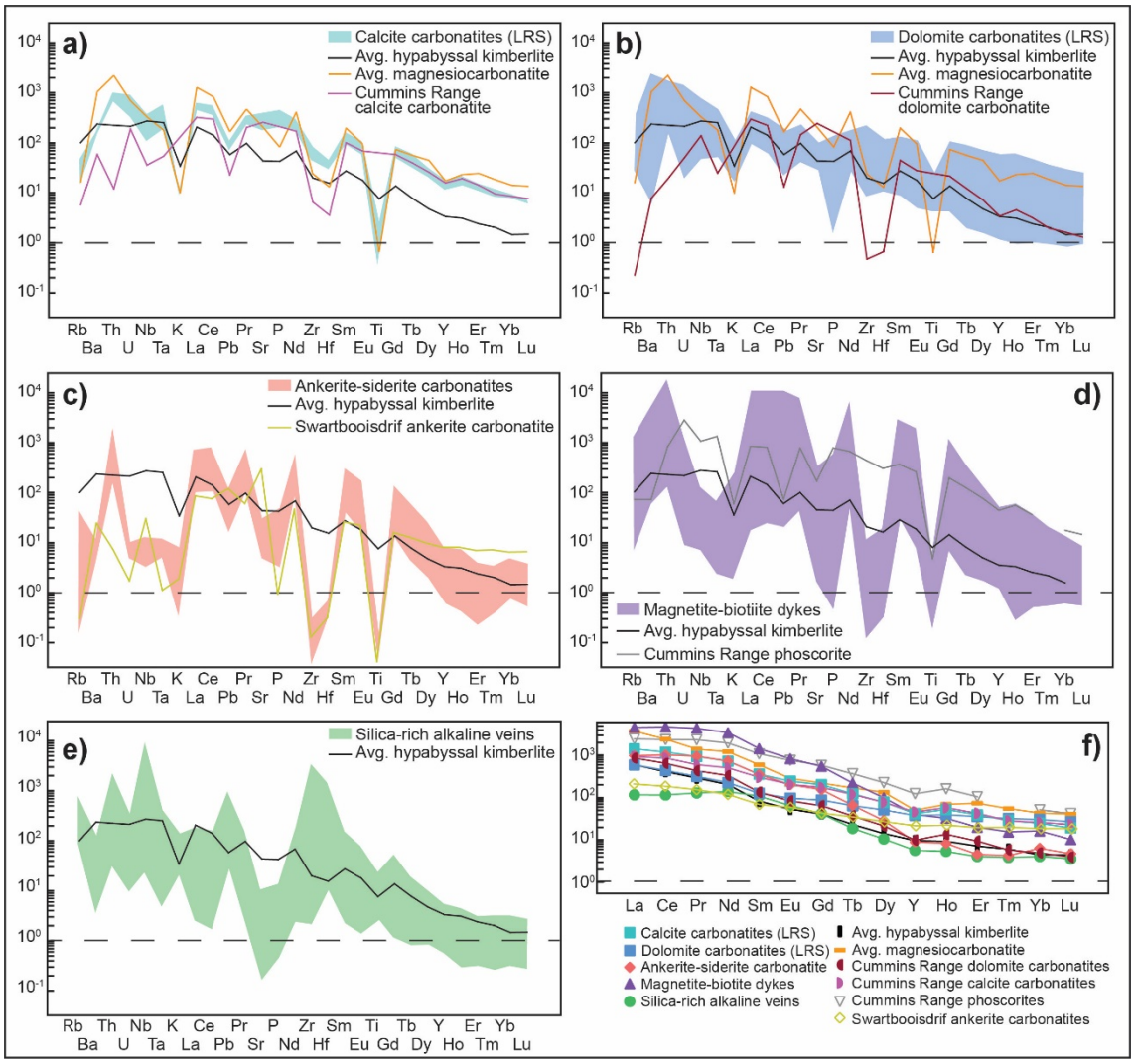

Figure 2.11 a-e) Trace element plots normalised to primitive mantle (Sun and McDonough, 1989). f) Average rock type values normalised to McDonough and Sun (1995). The values for the average hypabyssal kimberlite and average magnesiocarbonatite are from Chakhmouradian et al. (2009). The values for the Cummins Range carbonatites and phoscorites (Australia) are from Downes et al., (2014). Tm is not shown because it is below the detection limit for Cummins Range phoscorites. Swartbooisdrif ankerite carbonatite (South Africa) data is from Thompson et al. (2002).

2.8 Isotope Data

2.8.1 Nd and Sr isotopes

Samarium-Nd isotope compositions were obtained in order to determine the magmatic sources (e.g., mantle or crust) of various rock types of the GCCC. Analyses were conducted on bulk rock samples representative of the different rock types including the Lyons River Sills, magnetite-biotite dykes, ankerite-siderite carbonatites, and silica-rich alkaline veins. A formation age of c. 1370 Ma was used to calculate initial εNd(t) values based on the findings of previous radiogenic isotope dating in the GCCC (Zi et al., 2017; Slezak and Spandler, 2019; Chapter 4).

The εNd($t_{1.37Ga}$) values for the Lyons River Sills, ankerite-siderite carbonatites, magnetite-biotite dykes, and silica-rich alkaline veins of the GCCC range from -1.8 to -4 (Table 2.1). There is some minor regional variability where the rocks near Yangibana North and West have slightly more negative values compared to the rocks near Demarcay and Fraser's (Fig. 2.2). The T_{DM} and T_{CHUR} ages for all samples range from c. 2100 to 1870 Ma and c. 1400 to 1700 Ma, respectively (Table 2.1). The silica-rich alkaline veins samples returned εNd($t_{1.37Ga}$) values consistent with other results (εNd($t_{1.37Ga}$) = -3.62 to -3.90), but the Sm/Nd ratios were abnormally high, resulting in unreasonable T_{CHUR} and T_{DM} ages. One Lyons River Sills sample and two silica-rich alkaline vein samples analysed by Pearson (1996) for Nd isotopes yielded an εNd($t_{1.37Ga}$) value of -1.57 for the Lyons River Sills and an εNd($t_{1.37Ga}$) value of -0.55 and -1.56 for the silica-rich alkaline vein samples (Table 2.1). These silica-rich alkaline vein samples contained lower $^{147}Sm/^{144}Nd$ ratios than the silica-rich alkaline vein samples measured in this study, returning T_{DM} and T_{CHUR} ages consistent with the other units from the GCCC (Table 2.1).

Strontium isotopes were obtained from the carbonate minerals in the Lyons River Sills and the ankerite-siderite carbonatites in the GCCC (Table 2.2). Six dolomite carbonatite analyses resulted in $^{87}Sr/^{86}Sr$ ratios ranging from 0.70570 to 0.71211. Three ankerite-siderite carbonatite samples displayed higher ratios ranging from 0.71465 to 0.71996 (Table 2.2).

Table 2.1 Summary of bulk rock Nd isotope analyses

Sample	Rock Type	Age (Ma)	Nd (µg/g)	Sm (µg/g)	$^{147}Sm/^{144}Nd$	$^{143}Nd/^{144}Nd$	2σ	$^{143}Nd/^{144}Nd$ (*t*)	εNd (*t*)	T_{DM} (Ma)	T_{CHUR} (Ma)
YN49-58.5	ankerite-siderite carbonatite	1370	1080	137	0.076451	0.511431	0.0000032	0.510743	-2.45	1890	1530
YN50-48.6	ankerite-siderite carbonatite	1370	49.0	6.96	0.085773	0.511433	0.0000039	0.510661	-4.07	2030	1650
LRS-16	dolomite carbonatite	1370	92.2	14.7	0.096173	0.511519	0.0000029	0.510654	-4.20	2100	1700
LRS-119	calcite carbonatite	1370	371	64.6	0.10519	0.511706	0.0000030	0.510759	-2.14	2000	1550
YW61-7.7	magnetite-biotite dyke	1370	2370	327	0.083367	0.511467	0.0000027	0.510717	-2.97	1950	1570
MOS-135	magnetite-biotite dyke	1370	121	16.1	0.080447	0.511499	0.0000029	0.510775	-1.83	1870	1490
DMCY-138	magnetite-biotite dyke	1370	801	105	0.079431	0.511485	0.0000022	0.510770	-1.92	1870	1500
YS-104	silica-rich alkaline vein	1370	19.5	7.29	0.22637	0.512722	0.0000023	0.510685	-3.60	-5610	431
YS-105	silica-rich alkaline vein	1370	7.09	2.06	0.17573	0.512250	0.0000029	0.510668	-3.92	3510	2820
P016852*	dolomite carbonatite	1370	57.7	7.79	0.077603	0.511523	n/a	0.510788	-1.57	1860	1480
P17133*	silica-rich alkaline vein	1370	64.8	4.82	0.064086	0.511245	n/a	0.510841	-0.55	1710	1400
P17130*	silica-rich alkaline vein	1370	239	50.7	0.058555	0.511943	n/a	0.510789	-1.56	2130	1550

*Bulk rock Sm-Nd data from Pearson (1996) recalculated to T=1370 Ma.

Table 2.2 Summary of carbonate Sr isotope data obtained from carbonate minerals in the Lyons River Sills and ankerite-siderite carbonatites.

Sample	Rock type	Sr (µg/g)	$^{87}Sr/^{86}Sr$	2σ	εSr(*t*)
YN50-48.6	ankerite-siderite carbonatite	100	0.71881	0.000016	177
YN49-58.5	ankerite-siderite carbonatite	245	0.71464	0.0000090	118
YN49-61.6	ankerite-siderite carbonatite	n/a	0.71985	0.000043	191
LRS-15 A	dolomite carbonatite (green)	1630	0.70644	0.000012	1.58
LRS-23	dolomite carbonatite (blue)	807	0.71115	0.0000085	68.2
LRS-149 A	dolomite carbonatite (green)	1080	0.70569	0.000010	-9.08
LRS-151	dolomite carbonatite (blue)	1370	0.70686	0.000011	7.46
LRS-15 B	dolomite carbonatite (blue)	1540	0.70656	0.0000077	3.22
LRS-149 B	dolomite carbonatite (blue)	1080	0.71209	0.0000080	81.6

2.8.2 C and O isotopes

Several stable isotope populations are present for the various carbonatites in the GCCC (Fig. 2.12; Appendix 2.C). The range of $\delta^{18}O$ values for the main grouping of the Lyons River Sills dolomite carbonatites is 10.2 ‰ to 10.8 ‰, and two Lyons River Sills calcite carbonatite samples yielded $\delta^{18}O$ values of 9.2 ‰ and 10.1 ‰ with both calcite and dolomite carbonatites having $\delta^{13}C$ values between -5.0 ‰ to -5.7 ‰. Two Lyons River Sills analyses yielded $\delta^{18}O$ values of 19.4 ‰ and 26.6 ‰ and $\delta^{13}C$ values of -4.9 ‰ and -4.4 ‰, respectively. The $\delta^{13}C$ values are within the mantle boxes established by both Taylor (1967) and Keller and Hoefs (1995), but the $\delta^{18}O$ values fall just outside of the $\delta^{18}O$ mantle boxes (Fig. 2.12). The ankerite-siderite carbonatites have much more negative $\delta^{13}C$ values ranging from -6.1 ‰ to -7.1 ‰, but similar $\delta^{18}O$ values ranging from 10.2 ‰ to 11.1 ‰.

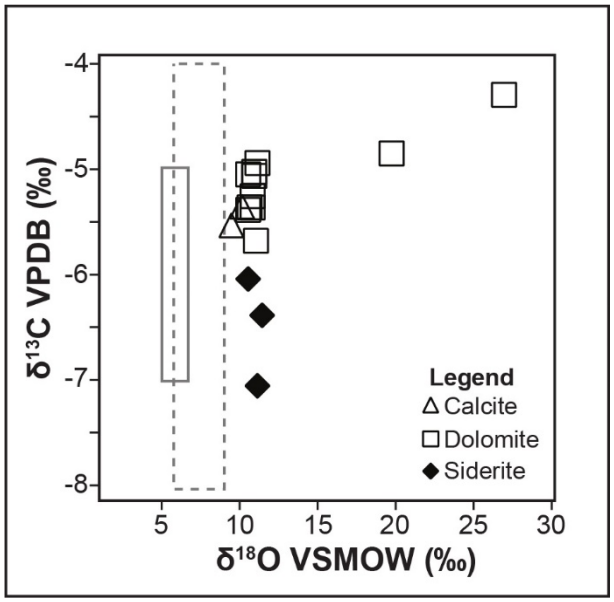

Figure 2.12 C-O isotope plots for the Lyons River Sills and ankerite-siderite carbonatites. Dashed line is the mantle C-O isotope box from Taylor (1967) and the smaller, solid box is the mantle C-O isotope box according to Keller and Hoefs (1995).

2.9 Discussion

2.9.1 Definition and evolution of the Lyons River Sills

Because of their high Si content (~20 wt.% SiO_2) and similar trace element characteristics the Lyons River Sills were originally compared to carbonate-rich samples from the Benfontein kimberlites in South Africa (Pearson, 1996; Pearson and Taylor, 1996; Pearson et al., 1996).

Later, the Lyons River Sills were dubbed the Gifford Creek Ferrocarbonatite Complex by Pirajno et al. (2014) due to the high bulk Fe contents, which is an artifact of the significant magnetite content of these rocks. The trace element analyses confirm the Lyons River Sills are enriched in incompatible elements (Fig. 2.11a,b) as well as Ni and corroborate the similarities between the Lyons River Sills and the carbonate-rich kimberlites from the Benfontein Sills (Pearson, 1996; Pearson and Taylor, 1996; Pearson et al., 1996). Some samples from the Lyons River Sills also contain significant TiO_2 contents (present as ilmenite), which can also be characteristic of kimberlites and carbonate-rich kimberlites (Dawson and Hawthorne, 1973; Le Maitre, 2002 and references therein; Zurevinski and Mitchell, 2011). The Lyons River Sills have Ga/Al ratios (Fig. 2.13) as well as relatively-depleted K and Ti contents (Fig. 2.11a,b) that are similar to hypabyssal kimberlites (Chakhmouradian et al., 2009). The relatively low Na and high K contents of biotite from all rocks in the GCCC also correspond more closely to kimberlites than carbonatites (Reguir et al., 2009). However, other features diagnostic of kimberlites, such as elevated Cr contents, and the presence of perovskite, olivine, and mantle xenoliths were not observed in the Lyons River Sills. Moreover, ilmenite in the Lyons River Sills was determined by Pearson (1996) to have low Mg and Cr contents and high Fe contents, which is more characteristic of carbonatites than kimberlites (Mitchell, 1979). Higher (i.e., ≥ 0.2) Fe/(Fe + Mg) ratios may also be indicative of carbonatite origin (Reguir et al., 2009). Furthermore, the Lyons River Sills have normalised REY contents comparable to an average magnesiocarbonatite, which are nearly an order of magnitude higher than an average hypabyssal kimberlite (Fig. 2.11f; Chakhmouradian et al., 2009). In this thesis, the GCCC was compared to another Proterozoic carbonate complex, the Cummins Range (Halls Creek Orogen, Western Australia) due to its relative proximity to the GCCC in geography and age (Downes et al., 2014). The Lyons River Sills trace element diagrams have similar patterns compared to the Cummins Range dolomite and calcite carbonatites (Fig. 2.11a,b; Downes et al., 2014). However, the Cummins Range carbonatites have lower Ba, Hf, Rb, and Zr contents (Fig. 2.11a,b), which further attests to the ambiguous nature of the Lyons River Sills.

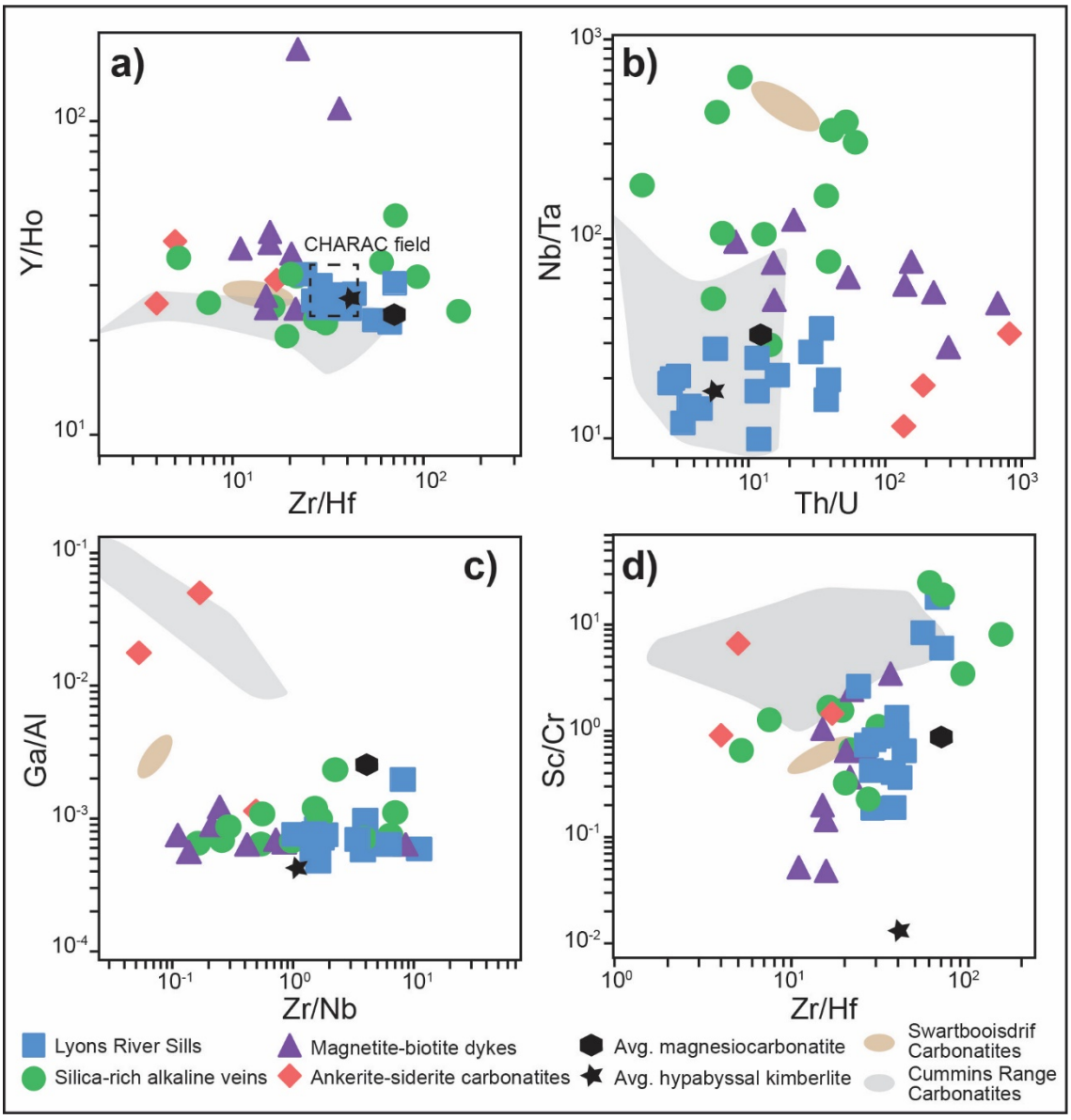

Figure 2.13 Trace element ratios plotted for the different rock types in the GCCC. The average hypabyssal kimberlite and average magnesiocarbonatite values are from Chakhmouradian et al. (2009). The values for the Cummins Range carbonatites and phoscorites (Australia) are from Downes et al., (2014). Swartbooisdrif ankerite carbonatite (South Africa) data is from Thompson et al. (2002). Charge-and-Radius-Controlled (CHARAC) field is from Bau (1996).

According to Le Maitre (2002), "rocks are named based on what they are, not what they might have been". Using this stipulation, the Lyons River Sills are predominantly dolomite carbonatites and subordinate calcite carbonatite based on their total carbonate mineral composition (i.e., >50 modal %). In some cases, these rocks are technically dolomite silicocarbonatites as their SiO_2 contents reach values >20 wt.%. Using molar proportions of oxides (Gittins and Harmer, 1997) and petrography, the Lyons River Sills are geochemically classified as calciocarbonatites and magnesiocarbonatites (Fig. 2.9) and not ferrocarbonatites as proposed by Pirajno et al. (2014). Nevertheless, true ferrocarbonatites are present as ankerite-

siderite carbonatites found in the northwest region of the GCCC (discussed in section 2.9.2). The Lyons River Sills are carbonatites by definition, although they share many geochemical characteristics with hypabyssal kimberlites, such as overlap in Zr/Hf, Th/U, Nb/Ta, Y/Ho, and Zr/Nb values in regards to an average hypabyssal kimberlite (Fig. 2.13; Chakhmouradian et al., 2009). Carbonatites related to kimberlites are often composed of calcite (Mitchell, 1979; Mitchell, 2005); however, some varieties, such as the Benfontein Sills (South Africa) and Tikiusaaq carbonatites (Greenland), can contain appreciable dolomite and ankerite (Dawson and Hawthorne, 1973; Tappe et al., 2009). This geochemical and mineralogical overlap observed in the Lyons River Sills supports the hypothesis that kimberlites, ultramafic lamprophyres, and some carbonatites (i.e., those that are not products of extensive fractionation or related to nepheline volcanism) could be genetically related.

There is significant compositional variation in the Lyons River Sills (Figs. 2.9 and 2.10), despite the fact that they occur congruently as an intrusive swarm subparallel to the Lyons River Fault (Fig. 2.2). Several different mechanisms can account for geochemical variability in carbonatite melts, including wall rock assimilation, reaction with the wall rock, crystal fractionation, and liquid immiscibility. Wall rock assimilation and reaction are considered to be negligible in the Lyons River Sills, as wall rock xenoliths were not observed and the thin carbonatite dykes would have had a low thermal capacity in which to melt granite. In addition, the C, O, Nd, and Sr isotope compositions are indicative of a mantle source, and the high Nd and Sr contents in the Lyons River Sills act as a buffer against isotopic mixing.

For mantle-derived (i.e., Mg-rich) carbonatites, the stability field of calcite increases as pressure decreases (i.e., as the melt ascends), and in many cases, calcite is the liquidus phase (Harmer and Gittins, 1997). At melt compositions less than 30 wt.% MgO for 1 GPa, calcite will begin to crystallise at ~1450 °C to ~1100 °C (depending on MgO contents; Wyllie and Lee, 1998). The low viscosity of a carbonatite melt would facilitate separation of calcite (and other crystallised minerals) from liquid. In this scenario, the Lyons River Sills calcite carbonatites represent crystal cumulates (Harmer and Gittins 1997), and the melt would evolve towards more Fe- and Mg-rich values with progressive calcite-dominated fractionation. By removing various

mineral components (Table 2.3), this study attempts to replicate the major element geochemical variations observed for the Lyons River Sills.

The starting melt composition was an idealised Lyons River Sills dolomite carbonatite with relatively high CaO and low MgO, TiO_2, and Fe_2O_3 contents (Table 2.3; Fig. 2.10). The first phase of fractionation involved crystallisation and removal of calcite, dolomite, Mg-rich arfvedsonite, and apatite from the starting melt in quantities of 29%, 5%, 4%, and 1%, respectively (Table 2.3). These modelled fractionated components represent an early cumulate phase similar in composition to the calcite carbonatite samples (Fig. 2.10), particularly with respect to SiO_2, MgO, CaO, and Fe_2O_3, and TiO_2 contents. The P_2O_5 contents are low in the modelled cumulate phase compared to the actual calcite carbonatite samples, which is likely a result of sampling bias as apatite forms distinct layers within the calcite carbonatites. After removal of the cumulate phase, calcite and additional mineral phases such as phlogopite were further crystallised from the initial residual melt (Residual melt 1 in Table 2.3), which resulted in further melt modification (i.e., Residual melt 2 in Table 2.3). As seen in Figure 2.10, the starting and residual melt compositions mimics the dolomite carbonatite compositional trends observed in the measured samples. During the modelled fractionation, the residual melts become enriched in MgO, Fe_2O_3, SiO_2, Na_2O, K_2O, Ti_2O, and Al_2O_3, which closely mirrors the natural samples.

Because the increasing trends in MgO, Fe_2O_3, and TiO_2 are primarily driven by a loss of CaO as calcite, the calcite carbonatites in the Lyons River Sills likely represent an early cumulate phase. The separation of calcite and apatite as a cumulate phase also accounts for the substantial changes in P_2O_5 between the carbonatites. Biggar (1969) demonstrated that apatite and calcite can crystallise early in carbonatites creating flow banding, which is supported by petrographic reports of apatite banding in East African carbonatites (Le Bas, 1989 and references therein). In addition, calcite as a cumulate phase has been reported in the Kovdor ultramafic alkaline Complex (Harmer and Gittins, 1997; Veksler et al, 1998). Removal of calcite from the carbonatite melt, drives the residual liquid initially to higher Mg and Fe contents, which has been modelled and observed in other carbonatite systems (Wyllie, 1965; Woolley and Kempe, 1989). This trend from Mg-rich to

Fe-rich compositions is also consistent with the Fe/Mg content of biotite (Fig. 2.7 and Fig. 2.8) from these rocks.

Although Na_2O and K_2O values increase through fractionation modelling, the concentration of these elements is variable in the natural samples. The sampled carbonatites likely do not represent pristine melt compositions (Woolley and Church, 2005), and alkali elements are likely to remain incompatible during fractionation (as is consistent with extensive fenitisation of the wall rocks outside of the carbonatites). The model is not expected to accurately represent the alkali element behaviour. The small size and patchy, pervasive nature of aegirine throughout the Lyons River Sills indicates that aegirine is likely a later alteration phase, potentially related to alkali (e.g., K↔Na) exchange with the granite wall rock via fenitising fluids. The aegirine may have overprinted the Lyons River Sills in a processes similar to antiskarn formation, where fluids mobilise elements from the wall rock and react with the intruding carbonatite (Anenburg and Mavrogenes (2018).

Table 2.3 Removal of a calcite-rich cumulate phase form a dolomite carbonatite with continued residual melt fractionation

	Starting composition	**Cumulate phase**	**Residual melt 1**	**Residual melt 2**
SiO_2	16.0	6.17	22.4	24.6
Al_2O_3	0.78	0	1.27	1.00
FeO	7.22	1.02	11.2	11.2
MgO	7.55	5.00	9.29	13.0
CaO	29.8	49.0	18.8	12.8
Na_2O	1.26	1.20	1.33	1.63
K_2O	1.26	0	2.06	1.94
TiO_2	1.72	0	2.82	3.22
P_2O_5	0.43	1.12	0.01	0.01
MnO	0.73	0	1.19	1.4
CO_2	33.2	36.5	29.6	29.2
Total	*100*	*100*	*100*	*100*
Mineral phase	**% subtracted**		**% subtracted**	
Calcite	29		40	
Dolomite	5			
Mg-arfvedsonite	4			
Arfvedsonite			4	
Phlogopite			2	
apatite	1		1	
Total	39		*47*	

2.9.2 Ankerite-siderite carbonatite origins

Ferrocarbonatites are an uncommon type of carbonatite, generally considered as the last to form in a typical carbonatite fractionation sequence (Le Bas, 1977; 1989; Zaitsev et al., 2004). In many cases, ferrocarbonatites – especially those dominated by siderite – are reported to be of hydrothermal origin, occurring at temperatures as low as 150°C (Simonetti and Bell, 1994; Zaitsev et al., 2004). Nonetheless, there are several documented cases of magmatic ferrocarbonatites including the Newania carbonatites in India (Woolley and Buckley, 1993), the Swartbooisdrif ferrocarbonatites in Namibia (Thompson et al., 2002), and the ferrocarbonatites from Central Tuva in Russia (Prokopyev et al., 2016). The Swartbooisdrif ferrocarbonatites have mantle $\delta^{18}O$ values of 7.90 to 8.12‰ (Thompson et al., 2002) and were determined to have formed at temperatures between 420 and 830 (± 200) °C and at pressures of 0.8 (±0.1) GPa based on the calcite-dolomite solvus and biotite-apatite thermometry (Drüppel et al., 2005). Ankerite-calcite carbonatites from Central Tuva were determined to have formed between 790 to 820 °C based on melt inclusion and fluid inclusion homogenisation temperatures (Prokopyev et al., 2016).

Fluorine and estimated OH contents for biotite (this chapter) and apatite (Chapter 3) were used to estimate the formation temperatures based on the petrogenetic model for F-OH biotite-apatite thermometry in Sallet (2000). Though only a rough initial estimate, an approximate temperature range of ~600 to 700 °C was obtained, which falls within the siderite stability field at ~ 1 GPa (Tao et al., 2013) and agrees with the previously discussed ferrocarbonatite formation temperatures. Additionally the ankerite-siderite carbonatites have trace element signatures similar to the Swartbooisdrif ferrocarbonatites as both show depletion in Hf, Rb, Ti, and Zr as well as enrichment in the LREE and overlapping Zr/Hf, Zr/Nb, and Y/Ho values (Fig. 2.11c,f and Fig. 2.13). The Swartbooisdrif ferrocarbonatites have slightly lower $\delta^{18}O$ values (~8 ‰) compared to the ankerite-siderite carbonatites (~10 to 11 ‰). However, both have similar $\delta^{13}C$ values (~ -6 to -7‰). The similar $\delta^{13}C$ values, formation temperatures, and trace element signatures with the Swartbooisdrif ferrocarbonatites are indicative of a magmatic origin for the ankerite-siderite carbonatites in the GCCC.

There are few field observable relations between the ankerite-siderite carbonatites and other primary rock types in the GCCC, making the relationship with other units enigmatic. Other magmatic ferrocarbonatites such as those from Swartbooisdrif and Central Tuva (Russia) occur in alkaline provinces as the predominant carbonatite type (Thompson et al., 2002, Drüppel et al., 2005; Propkoyev et al., 2016) whereas in the GCCC, the ankerite-siderite carbonatites are subordinate to the calcite and dolomite carbonatites of the Lyons River Sills. Woolley (1982) and Le Bas (1989) demonstrated that ferrocarbonatites could be created through multiple fraction paths beginning with calcite carbonatites. However, fractionation modelling from the Lyons River Sills to the ankerite-siderite carbonatites could not resolve the low Si and Ti contents observed in the ankerite-siderite carbonatite whole rock data, which would both be expected to increase with fractionation. The ankerite-siderite carbonatites could be related to the Lyons River Sills by an unidentified intermediate phase at depth. It is also possible the different carbonatites are related to separate, unseen magmatic phases located at depth, which formed because of heterogeneities in mantle source composition.

2.9.3 Magnetite-biotite dykes: connections to carbonatites

Globally, phoscorites are uncommon rocks that are spatially associated with carbonatites, but their genetic relationships are ambiguous. They were originally defined by their magnetite, apatite, and forsterite assemblage at the Phalaborwa carbonatite in South Africa (Russel et al., 1954), but now the definition includes diopside and phlogopite as additional silicate phases. (Krasnova et al., 2004). Glimmerites can be confused with phoscorites as they are dark, potentially igneous rocks occurring spatially with carbonatites, but they consist primarily of biotite (Le Maitre, 2002). Recently the term “glimmerite” has come to suggest a metasomatic origin for these rocks, indicating that glimmerites are a biotite-rich alteration assemblage derived from the alteration of mafic rock types (Elliott et al., 2018).

Compared to the phoscorites in the Cummins Range (Australia; Downes et al., 2014), the magnetite-biotite dykes in the GCCC contain lower Hf, Nb, Ta, and Zr as well as higher Th and LREE contents (Fig. 2.11d). Both the Cummins Range phoscorites and the magnetite-biotite

dykes have negative Ti anomalies and comparable Ba and Pb contents (Fig. 2.11d). The overlaps in trace element composition to the Cummins Range phoscorites, spatial relationship to carbonatites, and equivocal nature of the term "glimmerite" suggests the magnetite-biotite dykes may be more closely related to phoscorites. Though some of the magnetite-biotite dykes contain more monazite than apatite. This could simply reflect more REE than Ca in the system, resulting in monazite precipitation once all available Ca had been used to form apatite. Nevertheless, this thesis refrains from classifying these dykes as phoscorites to avoid genetic implications.

There are two magnetite-biotite dyke localities in the GCCC: 1) southeast, and 2) northern/northwest (Fig. 2.2). The magnetite-biotite dykes in the southeast region contain higher Mg, Ni, and Cr, and lower Fe compared to those of the northwest region. The southeastern magnetite-biotite dykes also contain early apatite with REY patterns enriched in La and Ce, with later apatite zones having REY patterns enriched in Nd and Sm. The north and northwestern magnetite-biotite dykes contain apatite REY patterns enriched in Sm, Eu, and Gd, which is similar to the REY patterns observed in apatite from the ankerite-siderite carbonatites (Slezak et al., 2018; Chapter 3). Biotite from the north and northeastern magnetite-biotite dykes contains higher Fe, Al, and Cl contents than those dykes in the southeastern region (Fig. 2.8). The biotite from these north and northeastern dykes is again similar to the biotite from the ankerite-siderite carbonatites. The magnetite-biotite dykes and ankerite-siderite carbonatites also share similar bulk rock Fe_2O_3 and MgO compositions, have low Sr/Mn ratios (Figs. 2.10d,e), and display similar trace element features (i.e., relative enrichment in Th and REE, and relative depletion in Nb, Ta, Zr, Hf, and Sr; Fig. 2.11c,d,f). Monazite in the ankerite-siderite carbonatites and magnetite-biotite dykes tends to have La_{cn}/Nd_{cn} ratios that transition from $La_{cn}/Nd_{cn} > 1$ in both units to $La_{cn}/Nd_{cn} < 1$ in the magnetite-biotite dykes (Chapter 5). This shift may reflect a shift in the fluid system from one controlled by CO_2 to one controlled by H_2O (Smith et al., 2000). These spatial and geochemical similarities between the magnetite-biotite dykes and ankerite-siderite carbonatites suggests these units might be genetically related. In other instances of coeval carbonatite and phoscorite occurrences, models involving fractionation and/or liquid immiscibility have been proposed to explain their coexistence (Vartiainen, 1980; Kogarko et al., 1997; Krasnova et al., 2004). Overall

there has been very little research on the relationships between these two enigmatic rock types, and direct field relations between the ankerite-siderite carbonatites and magnetite-biotite dykes of the GCCC are lacking. Therefore, the genetic links between these rock units cannot be evaluated any further at present. However, the abundance of monazite and apatite in the GCCC units facilitates additional in situ isotope analyses such as Sm–Nd, which are discussed in detail in Chapter 4.

2.9.4 Origin of the silica-rich alkaline veins

The silica-rich alkaline veins have a wide range in K/Na ratios, consisting broadly of a group with K/Na > 1 and a group with K/Na < 1 (Fig. 2.10f). The difference in K/Na is related to alteration, as much of the primary phlogopite is altered resulting in K loss. The silica-rich alkaline veins with higher K contents tend to contain more phlogopite and higher Rb/Sr values. The silica-rich alkaline veins with higher Na contents contain fine-grained aegirine and are often more altered, exhibiting signs of shearing. Both units contain elevated levels of Si and Nb (as columbite and Nb-bearing rutile) and accommodate significant amounts of Zr (as zircon) and Ti (as rutile), suggesting that these rocks are altered variants of the same unit.

The normalised trace element plots of the silica-rich alkaline veins appear to be antithetic to those of the magnetite-biotite dykes and ankerite-siderite carbonatites (Fig. 2.11c-e). Where the magnetite-biotite dykes (and ankerite-siderite carbonatites) show troughs at Nb, Zr, Hf, and Ti, the silica-rich alkaline veins display peaks, and where the magnetite-biotite dykes show peaks at Ba and REE, the silica-rich alkaline veins display troughs. Because thin silica-, aegirine-, and magnetite-rich veins were observed mantling a magnetite-biotite dyke at Demarcay (Fig. 2.3c), these geochemical associations suggest that the silica-rich alkaline veins represent products of incompatible magmatic-hydrothermal fluid phase related to the magnetite-biotite dykes. After the crystallisation of the magnetite-biotite dykes, this incompatible HFSE- and Fe-rich phase was exsolved into fractures and joints. The HFSE- and Fe-rich phase then likely altered the host rock in a fenitising process, liberating Si and Na.

Though often considered incompatible and immobile, HFSE elements can be incorporated in significant quantities in peralkaline melts (Nicholls and Carmichael, 1969; Watson, 1979), and they can be remobilised under hydrothermal conditions involving Na and F (Rubin et al., 1993; Salvi and Williams-Jones, 1996; Jiang et al., 2005). Zirconium and Ti mobility is enhanced by F complexes such as ZrF_6^{2-} and TiF_6^{2-} (Barsukova et al., 1979; Salvi and Williams-Jones, 1996; Jiang et al., 2005), and Nb is mobile under conditions with increased F activities where it occurs as niobium hydroxyl-fluoride species (Timofeev et al., 2015). The abundance of the alkaline mineral phases, aegirine and arfvedsonite-riebeckite, in the Lyons River Sills may have kept elements such as Ti and Zr sequestered in the early carbonatite melts (Watson, 1979; Rubin et al., 1993). As the magnetite-biotite dyke melts either separated from and/or evolved from the carbonatites, the HFSE likely became increasingly incompatible as the magnetite- and biotite-rich melts crystallised and so were exsolved as a late-stage magmatic-hydrothermal fluids rich in F. These F-rich fluids then incorporated and reacted with the local host rocks (e.g., Pimbyana Granite) causing a decrease in temperature and an increase in Si activity where it has been shown zircon is stable (Salvi and Williams-Jones, 1996; Chakhmouradian et al., 2003; Chakhmouradian and Williams, 2004; Gervasoni et al., 2017). Other Nb-bearing minerals would have crystallised because of decreased F activity (Timofeev et al., 2015), which may have occurred as result of wall rock incorporation into the fluids or incorporation into F-bearing minerals such as phlogopite.

2.9.5 Origins of the GCCC

The GCCC contains a wide array of alkaline rock types that occur together spatially but lack distinct field relationships. Age data from Zi et al. (2017), Slezak and Spandler (2019), and Chapter 3 puts emplacement of all the units in the GCCC at c. 1370 Ma. Bulk rock εNd($t_{1.37Ga}$) values range from -1.83 to -4.20, which is consistent with an enriched mantle source for these rocks (Hart et al., 1992; Stracke et al., 2005; Stracke, 2012). Like the GCCC, the Cummins Range carbonatite complex is also Proterozoic-age and hosted in an orogenic belt (Halls Creek Orogen) in Western Australia (Downes et al., 2014). The dolomite carbonatites from the Cummins and the

Lyons River Sills have comparable Ti values, indicating that their sources were likely enriched in Ti compared to an average magnesiocarbonatite (Fig. 2.11b). Enriched mantle melts (EM2) modelled by Workman et al. (2004) have elevated Ti contents, which may indicate the Lyons River Sills (and the other rocks of the GCCC) as well as the Cummins Range carbonatites were derived from an EM2-like source(s).

The $\delta^{13}C$ and $\delta^{18}O$ values (Fig. 2.12) for the Lyons River Sills and the ankerite-siderite carbonatites are also broadly consistent with a mantle source. The samples with excursions to $\delta^{18}O$ =19.4 ‰ and 26.6 ‰ do not intrude any sedimentary carbonates nor do the heavier $\delta^{18}O$ values correspond to the more fractionated rock-types of the Lyons River Sills (Veizer et al., 1999; Demény et al, 2004). This suggests the samples with elevated $\delta^{18}O$ are underwent post-magmatic, low temperature alteration.

The Sr isotope values for the Lyons River Sills extend along a trend similar to the Phalaborwa carbonatite (Fig. 2.14; Ericksson, 1989; Yuhara et al., 2005) and Group I kimberlites (Smith, 1983), although they contain slightly more radiogenic Nd isotope values, placing them closer to an EM2-type source (Hart et al., 1992; Stracke et al., 2005; Stracke, 2012). The ankerite-siderite carbonatite Sr isotope compositions trend towards extremely radiogenic values without any major changes in Nd isotope composition (Fig. 2.14). These values are far higher than any feasible mantle source and most crustal sources. It is likely that these values reflect resetting caused by tectonically induced recrystallisation of the carbonate minerals. The ankerite-siderite carbonatites contain an order of magnitude less Sr than the Lyons River Sills (e.g., 100s ppm vs 1000s ppm), making them more susceptible to isotopic resetting from fluid interaction and recrystallisation. Recrystallisation and reprecipitation of other minerals such as apatite and monazite has been observed in the complex (Slezak et al., 2018; Slezak and Spandler, 2019; Chapter 3; Chapter 4). In this case, the least radiogenic Sr values in the Lyons River Sills can be regarded as being close to the true source values, which would also be consistent with an enriched mantle source.

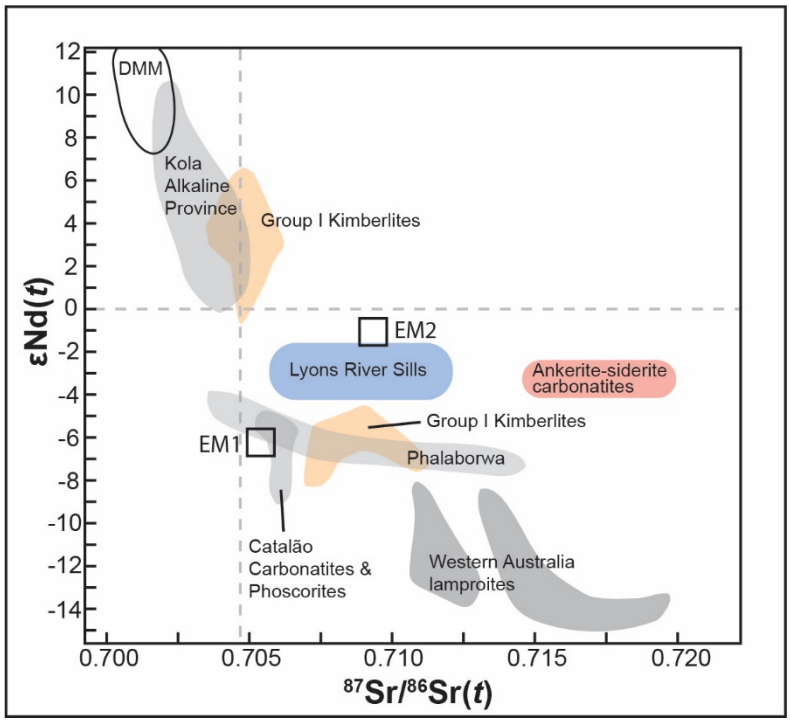

Figure 2.14 Nd vs. Sr isotope plot for GCCC carbonatites. The Lyons River Sills dolomite and calcite carbonatites plot between EM1 and EM2 with Sr values overlapping EM2. They also show a spread in Sr isotope values similar to Phalaborwa. The ankerite-siderite carbonatites have radiogenic Sr values, similar to those found in in Western Australia (WA) lamproites. Kola Alkaline Province, Russia (Zaitsev and Bell, 1995; Dunworth and Bell, 2001); Catalão carbonatites and phoscorites, Brazil (Cordeiro et al., 2010); Phalaborwa, South Africa (Ericksson, 1989; Yuhara et al., 2005); WA lamproites (Nelson et al., 1986); DMM, EM1, EM2 (Hart et al., 1992; Stracke et al., 2005; Stracke, 2012); Group I and II kimberlites (Smith, 1983).

Calculated T_{DM} ages from bulk rock Nd samples are between c. 2100 to 1900 Ma, consistent with timing of convergence and collision of the Yilgarn Craton with the Glenburgh Terrane during the 2005 to 1950 Ma Glenburgh Orogeny (Occhipinti et al., 2004; Sheppard et al., 2004; Johnson et al., 2011). Plate convergence and subduction of hydrated ocean crust beneath the Glenburgh Terrane likely led to subduction-induced mantle metasomatism. This metasomatised mantle was later tapped to produce the carbonatitic parental magmas of the GCCC at c. 1370 Ma (Slezak and Spandler, 2019; Chapter 4). Causes for the alkaline magmatism are unknown. However, magmatism may have been related to far-field stresses associated with the North China Craton separation from the West Australia Craton during Nuna disassembly (Pisarevsky et al., 2014; Slezak and Spandler, 2019; Chapter 4).

2.10 Conclusions

1. The GCCC contains a range of rock types including calcite, dolomite, and ankerite-siderite carbonatites as well as other phases such as magnetite-biotite dykes and silica-rich alkaline veins. In addition to these primary phases, alteration assemblages such as fenites and glimmerites are also present.

2. Geochemical trends in the Lyons River Sills can be explained by fractionation and separation of an early calcite-bearing cumulate phase from the carbonatite melt, leading to Mg and Fe (+ Ti, Si, alkali) enrichment in the melt. However, the relationship between the Lyons River Sills and other units such as the magnetite-biotite dykes and ankerite-siderite carbonatites is still uncertain.

3. The ankerite-siderite carbonatites have mantle-like stable isotope values, trace element trends, and temperatures comparable to other magmatic ferrocarbonatites, pointing to a magmatic origin.

4. The magnetite-biotite dykes and ankerite-siderite carbonatites have similar trace element contents, which suggests they are likely related, but the processes connecting them are still enigmatic.

5. The silica-rich alkaline veins are hydrothermal phases enriched in Na, F, and HFSE that were incompatible with the magnetite-biotite dykes and/or ankerite-siderite carbonatites.

6. The GCCC is comprised of multiple, alkaline magmatic-hydrothermal units that exhibit isotope signatures indicative of an EM2-like source. The convergence of the Yilgarn Craton and Glenburgh Terrane (c. 2000 Ma) may have metasomatised the mantle, which was later tapped to produce the GCCC.

2.11 References

Anenburg, M., Mavrogenes, J.A., 2018. Carbonatitic versus hydrothermal origin for fluorapatite REE-Th deposits: experimental study of REE transport and crustal "antiskarn" metasomatism. American Journal of Science 318, 335-366.

Armstrong, J.T., 1991. Quantitative element analysis of individual microparticles with electron beam instruments, in: Heinrich, K.F.J., Newbury, D.E. (Eds.), Electron Probe Quantification. Plenum Press, New York, pp. 261-315.

Asahara, Y., Tanaka, T., Kamioka, H., Nishimura, A., 1995. Asian continental nature of $^{87}Sr/^{86}Sr$ ratios in north central Pacific sediments. Earth and Planetary Science Letters 133, 105-116.

Barsukova, M.L., Kuznetsov, V.A., Dorofeyva, V.A., Khodakovskiy, L.I., 1979. Measurement of the solubility of rutile TiO_2 in fluoride solutions at elevated temperatures. Geochemistry International 7, 41-49.

Bau, M., 1996. Controls on the fractionation of isovalent trace elements in magmatic and aqueous systems: evidence from Y/Ho, Zr/Hf, and lanthanide tetrad effect. Contributions to Mineralogy and Petrology 123, 323-333.

Biggar, G.M., 1969. Phase relationships in the join $Ca(OH)_2$-$CaCO_3$-$Ca_3(PO_4)$-H_2O at 1000 bars. Mineralogical Magazine 37, 75-82.

Chakhmouradian, A.R., Reguir, E.P., Mitchell, R.H., 2003. Titanite in carbonatitic rocks: genetic dualism and geochemical significance. Periodico di Mineralogia 72, 107-113.

Chakhmouradian, A.R., Williams, C.T., 2004. Mineralogy of high-field-strength elements (Ti, Nb, Zr, Ta, Hf) in phoscoritic and carbonatitic rocks of the Kola Peninsula, Russia, in: Wall, F., Zaitsev, A.N. (Eds.), Phoscorites and Carbonatites from Mantle to Mine: the Key Example of the Kola Alkaline Province. Unwin Hyman, London, pp. 293-340.

Chakhmouradian, A.R., Böhm, C.O., Demény, A., Reguir, E.P., Hegner, E., Creaser, R.A., Halden, N.M., Yang, P., 2009. “Kimberlite” from Wekusko Lake, Manitoba: Actually a diamond-indicator-bearing dolomite carbonatite. Lithos 112, 347-357.

Cordeiro, P.F.O., Brod, J.A., Dantas, E.L., Barbosa, E.S.R., 2010. Mineral chemistry, isotope geochemistry and petrogenesis of niobium-rich rocks from the Catalão I carbonatite-phoscorite complex, Central Brazil. Lithos 118, 223-237.

Cutten, H.N., Johnson, S.P., 2018. Kuparr Tectonic Event (KU): WA Geology Online, Explanatory Notes Extract. Geological Survey of Western Australia.

Dawson, J.B., Hawthorne, J.B., 1973. Magmatic sedimentation and carbonatitic differentiation in kimberlite sills at Benfontein, South Africa. Journal of Geological Society of London 129, 61-85.

Deer, W.A., Howie, R.A., Zussman, J., 1992. An Introduction to the rock-forming Minerals, 2nd ed. Longman, Essex.

Demény, A., Sitnikova, M.A., Karchevsky, P.I., 2004. Stable C and O isotope compositions of carbonatite complexes of the Kola Alkaline Province: phoscorite-carbonatite relationships and source compositions, in: Wall, F., Zaitsev, A.N. (Eds.), Phoscorites and Carbonatites from Mantle to Mine: the Key Example of the Kola Alkaline Province. Mineralogical Society of Great Britain and Ireland, London, pp. 407-429.

Downes, P.J., Demény, A., Czuppon, G., Jaques, A.L., Verall, M., Sweetapple, M., Adams, D., McNaughton, N.J., Gwalani, L.G., Griffin, B.J., 2014. Stable H-C-O isotope and trace element geochemistry of the Cummins Range Carbonatite Complex, Kimberley region, Western Australia: implications for hydrothermal REE mineralization, carbonatite evolution and mantle source regions. Mineralium Deposita 49, 905-932.

Drüppel, K., Hoefs, J., M., O., 2004. Fenitizing Processes Induced by Ferrocarbonatite Magmatism at Swartbooisdrif, NW Namibia. Journal of Petrology 46, 377-406.

Dunworth, E.A., Bell, K., 2001. The Turiy Massif, Kola Peninsula, Russia: isotopic and geochemical evidence for multi-source evolution. Journal of Petrology 42, 377-405.

Elliott, H.A.L., Wall, F., Chakhmouradian, A.R., Siegfried, P.R., Dahlgren, S., Weatherley, S., Finch, A.A., Marks, M.A.W., Deady, E., 2018. Fenites associated with carbonatite complexes: a review. Ore Geology Reviews 98, 38-59.

Eriksson, S.C., 1989. Phalaborwa: a saga of magmatism, metasomatism and miscibility, in: Bell, K. (Ed.), Carbonatites: Genesis and Evolution. Unwin Hyman, London, pp. 221-254.

Fisher, C.M., McFarlane, C.R.M., Hanchar, J.M., Schmitz, M.D., Sylvester, P.J., Lam, R., Longerich, H.P., 2011. Sm-Nd isotope systematics by laser ablation-multicollector-inductively coupled plasma mass spectrometry: methods and potential natural and synthetic reference materials. Chemical Geology 284, 1-20.

Gellatly, D.C., 1975. Yangibana Creek U-Th-REE-base metal prospect, Gascoyne Goldfield, W.A., Amax Exploration (Australia) Inc.

Gervasoni, F., Klemme, S., Rohrbach, A., Brutzner, T., Berndt, J., 2017. Experimental constraints on the stability of baddeleyite and zircon in carbonate- and silicate-carbonate melts. American Mineralogist 102, 860-866.

Gittins, J., Harmer, R.E., 1997. What is ferrocarbonatite? A revised classification. Journal of African Earth Sciences 25, 159-168.

Harmer, R.E., Gittins, J., 1997. The origin of dolomitic carbonatites: field and experimental constraints. Journal of African Earth Sciences 25, 5-28.

Hart, S.R., Hauri, E.H., Oschmann, L.A., Whitehead, J.A., 1992. Mantle plumes and entrainment: isotopic evidence. Science 256, 517-520.

Jiang, S.Y., Wang, R.C., Xu, X.S., Zhao, K.D., 2005. Mobility of high field strength elements (HFSE) in magmatic-, metamorphic-, and submarine-hydrothermal systems. Physics and Chemistry of the Earth 30, 1020-1029.

Johnson, S.P., Sheppard, S., Rasmussen, B., Wingate, M.T.D., Kirkland, C.L., Muhling, J.R., Fletcher, I.R., Belousova, E.A., 2011. Two collisions, two sutures: punctuated pre-1950 Ma assembly of the West Australian Craton during the Ophthalmian and Glenburgh Orogenies. Precambrian Research 189, 239-262.

Johnson, S.P., Thorne, A.M., Tyler, I.M., Korsch, R.J., Kennett, B.L.N., Cutten, H.N., Goodwin, J., Blay, O., Blewett, R.S., Joly, A., Dentith, M.C., Aitken, A.R.A., Holzschuh, J., Salmon, M., Reading, A., Heinson, G., Boren, G., Ross, J., Costelloe, R.D., Fomin, T., 2013. Crustal architecture of the Capricorn Orogen, Western Australia and associated metallogeny. Australian Journal of Earth Sciences 60, 681-705.

Keller, J., Hoefs, J., 1995. Stable isotope characteristics of recent natrocarbonatites from Oldoinyo Lengai, in: Bell, K., Keller, J. (Eds.), Carbonatite Volcanism. Springer, Berlin, pp. 113-123.

Korhonen, F.J., Johnson, S.P., Fletcher, I.R., Rasmussen, B., Sheppard, S., Muhling, J.R., Dunkley, D.J., Wingate, M.T.D., Roberts, M.P., Kirkland, C.L., 2015. Pressure-temperature-time evolution of the Mutherbukin Tectonic Event, Capricorn Orogen: Geological Survey of Western Australia, Report 146, p. 64.

Krasnova, N.I., Petrov, T.G., Balaganskaya, E.G., Garcia, D., Moutte, J., Zaitsev, A.N., Wall, F., 2004. Introduction to phoscorites: occurrence, composition, nomenclature and petrogenesis, in: Wall, F., Zaitsev, A.N. (Eds.), Phoscorites and Carbonatites from Mantle to Mine: the Key Example of the Kola Alkaline Province. The Mineralogical Society of Great Britain and Ireland, London, pp. 45-74.

Le Bas, M.J., 1977. Carbonatite-nephelinite volcanism. Wiley, London, 347 p.

Le Bas, M.J., 1989. Diversification of carbonatite, in: Bell, K. (Ed.), Carbonatites: Genesis and Evolution. Unwin Hyman, London, pp. 428-447.

Le Maitre, R.W., 2002. Igneous Rocks: A Classification and Glossary of Terms: recommendations of International Union of Geological Sciences, subcommission on the systematics of igneous rocks. Cambridge University Press, Cambridge.

Lee, W.-J., Wyllie, P.J., 1998. Petrogenesis of carbonatite magmas from mantle to crust, constrained by the system CaO-(MgO+FeO*)-(Na_2O+K_2O)-(SiO_2+Al_2O_3+TiO_2)-CO_2. Journal of Petrology 39, 495-517.

Martin, D.M., Thorne, A.M., 2004. Tectonic setting and basin evolution of the Bangemall Supergroup in the northwestern Capricorn Orogen. Precambrian Research 128, 385-409.

McDonough, W.F., Sun, S.s., 1995. The composition of the Earth. Chemical Geology 120, 223-253.

Mitchell, R.H., 1979. The alleged kimberlite-carbonatite relationship: additional contrary mineralogical evidence. American Journal of Science 279, 570-589.

Motoyoshi, Y., Hensen, B.J., 2001. F-rich phlogopite stability in ultra-high-temperature metapelites from the Napier Complex, East Antarctica. American Mineralogist 86, 1404-1413.

Nelson, D.R., McCulloch, M.T., Sun, S.-S., 1986. The origins of ultrapotassic rocks as inferred from Sr, Nd and Pb isotopes. Geochimica et Cosmochimica Acta 50, 231-245.

Nicholls, J., Carmichael, J.S.E., 1969. Peralkaline acid liquids: a petrological study. Contributions to Mineralogy and Metrology 20, 268-294.

Occhipinti, S.A., Sheppard, S., Passchier, C., Tyler, I.M., Nelson, D.R., 2004. Palaeoproterozoic crustal accretion and collision in the southern Capricorn Orogen: the Glenburgh Orogeny. Precambrian Research 128, 237-255.

Olierook, H.K.H., Agangi, A., Plavsa, D., Reddy, S.M., Yao, W., Clark, C., Occhipinti, S.A., Kylander-Clark, A.R.C., 2019. Neoproterozoic hydrothermal activity in the West Australian Craton related to Rodinia assembly or breakup? Gondwana Research 68, 1-12.

Pearson, J.M., 1996. Alkaline rocks of the Gifford Creek Complex, Gascoyne Province, Western Australia: their petrogenetic and tectonic significance, Department of Geology and Geophysics. University of Western Australia, p. 219.

Pearson, J.M., Taylor, W.R., 1996. Mineralogy and geochemistry of fenitized alkaline ultrabasic sills of the Gifford Creek Complex, Gascoyne Province, Western Australia. The Canadian Mineralogist 34, 201-219.

Pearson, J.M., Taylor, W.R., Barley, M.E., 1996. Geology of the alkaline Gifford Creek Complex, Gascoyne Complex, Western Australia. Australian Journal of Earth Sciences 43, 299-309.

Petersen, E.U., Essene, E.J., Peacor, D.R., Valley, J.W., 1982. Fluorine end-member micas and amphiboles. American Mineralogist 67, 538-544.

Piechocka, A.M., Sheppard, S., Fitzsimons, I.C.W., Johnson, S.P., Rasmussen, B., Jourdan, F., 2018. Neoproterozoic $^{40}Ar/^{39}Ar$ mica ages mark the termination of a billion years of intraplate reworking in the Capricorn Orogen, Western Australia. Precambrian Research 310, 391-406.

Pirajno, F., González-Álvarez, I., 2013. The ironstone veins of the Gifford Creek ferrocarbonatite complex, Gascoyne Province: Geological Survey of Western Australia, Record 2013/12, p. 19.

Pirajno, F., González-Álvarez, I., Chen, W., Kyser, K.T., Simonetti, A., Leduc, E., leGras, M., 2014. The Gifford Creek Ferrocarbonatite Complex, Gascoyne Province, Western Australia: Associated fenitic alteration and a putative link with the ~1075 Ma Warakurna LIP. Lithos 202–203, 100-119.

Pisarevsky, S.A., Wingate, M.T.D., Li, Z.-X., Wang, X.-C., Tohver, E., Kirkland, C.L., 2014. Age and paleomagnetism of the 1210Ma Gnowangerup–Fraser dyke swarm, Western Australia, and implications for late Mesoproterozoic paleogeography. Precambrian Research 246, 1-15.

Prokopyev, I.R., Borisenko, A.S., Borovikov, A.A., Pavlova, G.G., 2016. Origin of REE-rich ferrocarbonatites in southern Siberia (Russia): implications based on melt and fluid inclusions. Mineralogy and Petrology 110, 845-859.

Reguir, E.P., Chakhmouradian, A.R., Halden, N.M., Malkovets, V.G., Yang, P., 2009. Major- and trace-element compositional variation of phlogopite from kimberlites and carbonatites as a petrogenetic indicator. Lithos 112, 372-384.

Rubin, J.N., Henry, C.D., Price, J.G., 1993. The mobility of zirconium and other "immobile" elements during hydrothermal alteration. Chemical Geology 110, 29-47.

Russel, H.D., Hiemstra, S.A., Groenevelf, D., 1954. The mineralogy and petrology of the carbonatite at Loolekop, Eastern Transvaal. Transactions of the Geological Society of South Africa 57, 197-208.

Sallet, R., 2000. Fluorine as a tool in the petrogenesis of quartz-bearing magmatic associations: applications of an improved F–OH biotite–apatite thermometer grid. Lithos 50, 241-253.

Salvi, S., Williams-Jones, A.E., 1996. The role of hydrothermal processes in concentrating high-field strength elements in the Strange Lake peralkaline complex, northeastern Canada. Geochimica et Cosmochimica Acta 60, 1917-1932.

Sheppard, S., Occhipinti, S.A., Nelson, D.R., 2005. Intracontinental reworking in the Capricorn Orogen, Western Australia: the 1680-1620 Ma Mangaroon Orogeny. Australian Journal of Earth Sciences 52, 443-460.

Sheppard, S., Rasmussen, B., Muhling, J.R., Farrell, T.R., Fletcher, I.R., 2007. Grenvillian-aged orogenesis in the Palaeoproterozoic Gascoyne Complex, Western Australia: 1030-950 Ma reworking of the Proterozoic Capricorn Orogen. Journal of Metamorphic Geology 25, 477-494.

Sheppard, S., Bodorkos, S.P., Johnson, S.P., Wingate, M.T.D., Kirkland, C.L., 2010a. The Paleoproterozic Capricorn Orogeny: intracontinental reworking not continent-continent collision. Geological Survey of Western Australia, Report 108, p. 33.

Sheppard, S., Johnson, S.P., Wingate, M.T.D., Kirkland, C.L., Pirajno, F., 2010b. Explanatory notes for the Gascoyne Province: Geological Survey of Western Australia, p. 336.

Simonetti, A., Bell, K., 1994. Isotopic and geochemical investigation of the Chilwa Island Carbonatite Complex, Malawi: evidence for a depleted mantle source region, liquid immiscibility, and open system behaviour. Journal of Petrology 35, 1597-1621.

Slezak, P., Spandler, C., 2016. Age and origin of the Yangibana LREE deposit and associated ferrocarbonatites, Gascoyne Province, Western Australia, Goldschmidt 2016. Geochemical Society, Yokohama, Japan, June 26-July 1, p. 2888.

Slezak, P., Spandler, C., Blake, K., 2018. Ghosts of apatite past: using hyperspectral cathodoluminescence and micro-geochemical data to reveal multi-generational apatite in the Gifford Creek Carbonatite Complex, Australia. The Canadian Mineralogist 56, 1-25.

Slezak, P., Spandler, C., 2019. Carbonatites as recorders of mantle-derived magmatism and subsequent tectonic events: an example of the Gifford Creek Carbonatite Complex, Western Australia. Lithos 328-329, 212-227.

Smith, C.B., 1983. Pb, Sr and Nd isotopic evidence for sources of southern African Cretaceous kimberlites. Nature 304, 51-54.

Smith, M.P., Henderson, P., Campbell, L.S., 2000. Fractionation of the REE during hydrothermal processes: Constraints from the Bayan Obo Fe-REE-Nb deposit, Inner Mongolia, China. Geochimica et Cosmochimica Acta 64, 3141-3160.

Stracke, A., 2012. Earth's heterogeneous mantle: A product of convection-driven interaction between crust and mantle. Chemical Geology 330-331, 274-299.

Stracke, A., Hofman, A.W., Hart, S.R., 2005. FOZO, HIMU, and the rest of the mantle zoo. Geochemistry Geophysics Geosystems 6, 1-20.

Sun, S.s., McDonough, W.F., 1989. Chemical and isotopic systematics of oceanic basalts: implications for mantle composition and processes, in: Saunders, A.D., Norry, M.J. (Eds.), Magmatism in the ocean basins. Geological Society Special Publication, London, pp. 313-345.

Tao, R., Fei, Y., Zhang, L., 2013. Experimental determination of siderite stability at high pressure. American Mineralogist 98, 1565-1572.

Tappe, S., Steenfelt, A., Heaman, L.M., Simonetti, A., 2009. The newly discovered Jurassic Tikiusaaq carbonatite-aillikite occurrence, West Greenland, and some remarks on carbonatite–kimberlite relationships. Lithos 112S, 385-399.

Taylor, H.P., Frechen, J., Degens, E., 1967. Oxygen and carbon isotope studies of carbonatites from the Laacher See District, West Germany and the Alnö District, Sweden. Geochimica et Cosmochimica Acta 31, 407-430.

Thompson, R.N., Smith, P.M., Gibson, S.A., Mattey, D.P., Dickin, A.P., 2002. Ankerite carbonatite from Swartbooisdrif, Namibia: the first evidence for magmatic ferrocarbonatite. Contributions to Mineralogy and Petrology 143, 377-395.

Timofeev, A., Migdisov, A.A., Williams-Jones, A.E., 2015. An experimental study of the solubility and speciation of niobium in fluoride-bearing aqueous solutions at elevated temperature. Geochimica et Cosmochimica Acta 158, 103-111.

Valley, J.W., Petersen, E.U., Essene, E.J., Bowman, J.R., 1982. Fluorphlogopite and fluortremolite in Adirondack marbles and calculated C-O-H-F fluid compositions. American Mineralogist 67, 545-557.

Vartiainen, H., 1980. The petrography, mineralogy and petrochemistry of the Sokli carbonatite massif, northern Finland. Geological Survey of Finland, p. 126.

Veizer, J., Ala, D., Azmy, K., Bruckschen, P., Buhl, D., Bruhn, F., Carden, G.A.F., Diener, A., Ebneth, S., Godderis, Y., Jasper, T., Korte, C., Pawellek, F., Podlaha, O.G., Strauss, H., 1999. 87Sr/86Sr, δ13C and δ18O evolution of Phanerozoic seawater. Chemical Geology 161, 59-88.

Veksler, I.V., Nielsen, T.F.D., Sokolov, S.V., 1998. Mineralogy of Crystallized Melt Inclusions from Gardiner and Kovdor Ultramafic Alkaline Complexes: Implications for Carbonatite Genesis. Journal of Petrology 39, 2015-2031.

Wade, B.P., Barovich, K.M., Hand, M., Scrimgeour, I.R., Close, D.F., 2006. Evidence of early Mesoproterozoic arc magmatism in the Musgrave Block, central Australia: Implications for Proterozoic crustal growth and tectonic reconstructions of Australia. Journal of Geology 114, 43-63.

Watson, E.B., 1979. Zircon saturation in felsic liquids: experimental results and applications to trace element geochemistry. Contributions to Mineralogy and Metrology 70, 407-419.

Woolley, A.R., 1982. A discussion of carbonatite evolution and nomenclature, and the generation of sodic and potassic fenites. Mineralogical Magazine 46, 13-17.

Woolley, A.R., Buckley, H.A., 1993. Magnesite-siderite series carbonates in the Nkombwa and Newania carbonatite complexes. South African Journal of Geology 96, 126-130.

Woolley, A.R., Kempe, D.R.C., 1989. Carbonatites: nomenclature, average chemical compositions, and element distribution, in: Bell, K. (Ed.), Carbonatites: Genesis and Evolution. Unwin Hyman, London, pp. 1-14.

Woolley, A.R., Church, A.A., 2005. Extrusive carbonatites: a brief review. Lithos 85, 1-14.

Woolley, A.R., Kjarsgaard, B.A., 2008. Paragenetic types of carbonatite as indicated by the diversity and relative abundances of associated silicate rocks: evidence from a global database. The Canadian Mineralogist 46, 741-752.

Workman, R.K., Hart, S.R., Jackson, M., Regelous, M., Farley, K.A., Blusztajn, J., Kurz, M., Staudigel, H., 2004. Recycled metasomatized lithosphere as the origin of Enriched Mantle II (EM2) end-member: Evidence from the Samoan Volcanic Chain. Geochemistry, Geophysics, Geosystems 5, 1-44.

Wyllie, P.J., 1965. Melting relationships in the system CaO-MgO-CO_2-H_2O, with petrological applications. Journal of Petrology 6, 101-123.

Wyllie, P.J., Lee, W.-J., 1998. Model system controls on conditions for formation of magnesiocarbonatite and calciocarbonatite magmas from the mantle. Journal of Petrology 39, 1885-1893.

Yuhara, M., Hirahara, Y., Nishi, N., Kagami, H., 2005. Rb-Sr, Sm-Nd ages of the Phalaborwa Carbonatite Complex, South Africa. Polar Geoscience18, 101-113.

Zaitsev, A.N., Bell, K., 1995. Sr and Nd isotope data of apatite, calcite and dolomite as indicators of source, and the relationships of phoscorites and carbonatites from the Kovdor massif, Kola peninsula, Russia. Contributions to Mineralogy and Petrology 121, 324-335.

Zaitsev, A.N., Sitnikova, M.A., Subbotin, V.V., Fernandez-Suarez, J., Jeffries, T.E., 2004. Sallanlatvi Complex-a rare example of magnesite and siderite carbonatites, in: Wall, F., Zaitsev, A.N. (Eds.), Phoscorites and Carbonatites from Mantle to Mine: the Key Example of the Kola Alkaline Province. Geological Society of Great Britain and Ireland, London, pp. 201-245.

Zi, J.W., Gregory, C., Rasmussen, B., Sheppard, S., Muhling, J.R., 2017. Using monazite geochronology to test the plume model for carbonatites: The example of Gifford Creek Carbonatite Complex, Australia. Chemical Geology 463, 50-60.

Zurevinski, S.E., Mitchell, R.H., 2011. Highly evolved hypabyssal kimberlite sills from Wmindji, Quebec, Canada: insights into the process of flow differentiation in kimberlite magmas. Contributions to Mineralogy and Petrology 161, 765-776.

Chapter 3

Ghosts of apatite past: Using Hyperspectral CL and Micro-geochemical Data to Reveal Multi-generational Apatite in the Gifford Creek Carbonatite Complex, Australia

Abstract

Apatite can host significant levels of trace elements, including REE, within its crystal lattice, making it particularly useful for deciphering geological events and processes. This study employs hyperspectral cathodoluminescence (CL) and in situ micro-chemical techniques to identify and characterize various generations of apatite found in the magnetite-biotite dykes, carbonatites, and fenites of the Gifford Creek Carbonatite Complex (GCCC), Western Australia. Hyperspectral CL analysis revealed that apatite in all samples has complex internal zoning, including multiple distinct generations, with zones of relatively bright CL generally having more complex spectra compared to darker CL zones. Most of the CL spectra have prominent sharp peaks at ~1.4 eV and ~2.l eV, and a broad peak between 2.3 eV and 3.5 eV, which are relate to REE activators, or groups of activators, in apatite, particularly Nd^{3+}, Eu^{3+}, Sm^{3+} and Ce^{3+}.

Trace element analyses of apatite confirm the relative enrichment in REE of the CL brighter zones. Most apatite generations have concave-down to sinusoidal REE patterns that lack Eu anomalies, but often feature distinct negative Y anomalies. The depletion in LREE is interpreted to be due to LREE sequestration into monazite, which is relatively abundant in most of the samples. Most apatite samples contain very low Si contents, but appreciable Na, so REE incorporation into apatite was primarily via a coupled substitution of REE + Na replacing 2Ca, which is consistent with the highly alkaline, low SiO_2 environment under which the apatite formed. Based on the combined trace element signatures and CL textures, the multiple generations of apatite are interpreted to reflect growth from alkaline magmas followed by recrystallization during subsequent metamorphic/hydrothermal events. The notable exception is the apatite core domains from a fenite sample that contain relatively high Si and Mn contents, low Sr, and relatively HREE-enriched REE patterns with distinct negative Eu anomalies. This apatite is interpreted to be relict from the granitic precursor to fenitization.

The apatite samples also show systematic compositional variations across the GCCC, with apatite from magnetite-biotite dyke samples from the southeast of the complex containing higher Sr, lower Gd/Ce, and lower λ_3 values (normalised REE pattern inflections) compared to

apatite from the northwest. Recognition of these spatial variations in apatite compositions from the intra-grain micro-scale through to the district scale, demonstrate the utility of combining advanced petrographic methods, such as hyperspectral CL, with micro-chemical analysis to reveal complex geological records preserved in apatite. As apatite is a common accessory mineral, these techniques may be more broadly applicable to igneous source tracing, understanding metamorphic and/or metasomatic processes, provenance studies from detrital mineral records, and studies of the evolution of ore systems.

3.1 Introduction

Apatite [$Ca_5(PO_4)_3(OH,Cl,F)$] is a common accessory mineral in many rock types as well as a significant biogenic mineral in teeth and bone. The crystal structure of apatite allows numerous substitutions including Na, Mn, Y, REE, As, Si, F, Cl, OH^-, and CO_3^{2-}, as well as radio-isotope tracers Sr, U, Pb and Nd (Pan and Fleet, 2002; Hughes and Rakovan, 2015). Apatite also readily undergoes recrystallisation during post-formation hydrothermal alteration (Harlov and Förster, 2003; Harlov, 2015). This susceptibility to recrystallisation together with affinity for trace elements means that apatite geochemistry has great potential to monitor geological processes and events. In particular, radiogenic isotope ratios of apatite can be used to determine crystallisation ages, model ages, and source rock compositions (De Paolo, 1981; Nelson and De Paolo, 1985). The REE geochemistry of apatite can be used to decipher the environment and conditions of mineral formation and recrystallisation.

The incorporation of REE into the apatite crystal lattice can occur via the following coupled substitutions (Portnov and Gorobets, 1969; Roeder et al., 1987; Rønsbo 1989; Hughes et al., 1991; Fleet and Pan, 1995; Mitchell et al., 1997; Cherniak 2000; Chen et al., 2002; Pan and Fleet, 2002):

$$REE^{3+} + Si^{4+} = Ca^{2+} + P^{5+} \quad (1)$$

$$REE^{3+} + Na^{+} = 2Ca^{2+} \quad (2)$$

$$2REE^{3+} + \square = 3Ca^{2+} \quad (3)$$

$$REE^{3+} + O^{2-} = Ca^{2+} + F^{-} \quad (4)$$

where □ corresponds to a site vacancy. At the individual grain scale, these substitutions may manifest as zoning or growth textures related to either primary apatite formation or recrystallisation during secondary metamorphic or hydrothermal events. These secondary events may also present themselves as dissolution-reprecipitation of apatite to form a new generation of apatite and/or other minerals (e.g., monazite or xenotime; Pan et al., 1993; Pan, 1997; Harlov and Förster, 2003; Harlov, 2015). Careful documentation of these textural features can provide insights to the causative geological events, provided the textures are appropriately interpreted with respect to the whole-rock phase petrology: In this case, detailed study of each phase of apatite is required.

Cathodoluminescence (CL) is electromagnetic radiation emission produced by electron excitation of luminescent material (Marshall, 1988; Pagel et al., 2000; Waychunas, 2002; Götze et al., 2013). Cathodoluminescence can reveal hidden or cryptic textures in luminescent minerals that normally appear homogenous under optical microscope or in backscattered electron (BSE) images (Marshall, 1988; Pagel et al., 2000; Waychunas, 2002; Götze, 2012; Götze et al., 2013). Apatite is among the more luminescent rock-forming minerals due to its capacity to incorporate REE and Mn into its crystal structure, elements that are considered the primary cause of luminescence in many minerals (Marshall, 1988; Mitchell et al., 1997; Pagel et al., 2000; Waychunas, 2002; Gaft et al., 2015). Additionally, apatite may luminesce due to defects in the crystal structure, which hereafter is referred to as "intrinsic" luminescence after MacRae and Wilson (2008). This luminescent character of apatite means that CL imaging can be used in complement to optical petrography, BSE, or element concentration mapping to delineate the micro-scale textural and chemical zoning in apatite.

Optical microscope CL and some SEM-CL setups operate in the visible spectrum. However, many minerals, especially apatite, emit luminescent bands in the ultraviolet (UV) and near infrared (NIR) spectrum, which are not visible to the human eye. Hyperspectral CL mapping with false colour overlays gives the benefit of allowing one to visualise UV and NIR spectral data (MacRae et al., 2005; 2012; 2013; Edwards et al., 2007; Edwards and Lee, 2014). For example, hyperspectral CL mapping was used to identify and help quantify Nd^{3+} in apatite, whose

luminescence occurs in the NIR spectrum (MacRae et al., 2012). Nevertheless, application of these techniques to natural apatite samples is in its infancy, and further work is required to better understand the geochemical/crystallographic controls on CL signatures of natural apatite for various geological settings.

This study conducted hyperspectral CL mapping in combination with in situ geochemical analyses (e.g., WDS EPMA and LA-ICP-MS) of apatite from the Gifford Creek Carbonatite Complex (GCCC) in Western Australia. The study focuses on multiple generations of apatite formed under different magmatic/hydrothermal conditions, with the primary goal of reaching a better understanding of trace element incorporation into – and the corresponding CL response of – apatite from alkaline magmatic/hydrothermal environments. The findings of this study have broad implications for REE mobility, Sm-Nd isotope systematics, and potential mechanisms for increasing ore tenor in REE deposits.

3.2 Geologic Setting and Sample Description

The GCCC is located the Proterozoic Gascoyne Province of Western Australia (Fig. 3.1). The GCCC primarily consists of a series or swarms of narrow dykes, sills, and veins that cut Mesoproterozoic metasedimentary and granitic rocks of the Pooranoo Metamorphics and Durlacher Supersuite, respectively. They also cut the Neoproterozoic Edmund Group Metasediments that unconformably overlay the Mesoproterzoic rocks. Emplacement of the GCCC was controlled by regional faults such as the Lyons River Fault and the Bald Hill Lineament (Fig. 3.1; Pearson et al., 1996; Sheppard et al., 2010). Age determinations for the GCCC span a wide range from 1380 Ma to 900 Ma based on U-Th-Pb dating of zircon and monazite (Slezak and Spandler, 2016; Zi et al., 2017): this age range covers the initial onset of alkaline magmatism and multiple metamorphic and tectonic events, such as the Mutherbukin Tectonic Event (1320 to 1170 Ma; Korhonen et al., 2015), the Warakurna Large Igneous Province (c.1076 Ma; Wingate et al., 2004), and the Edmundian Orogeny (1030 to 950 Ma; Sheppard et al., 2007).

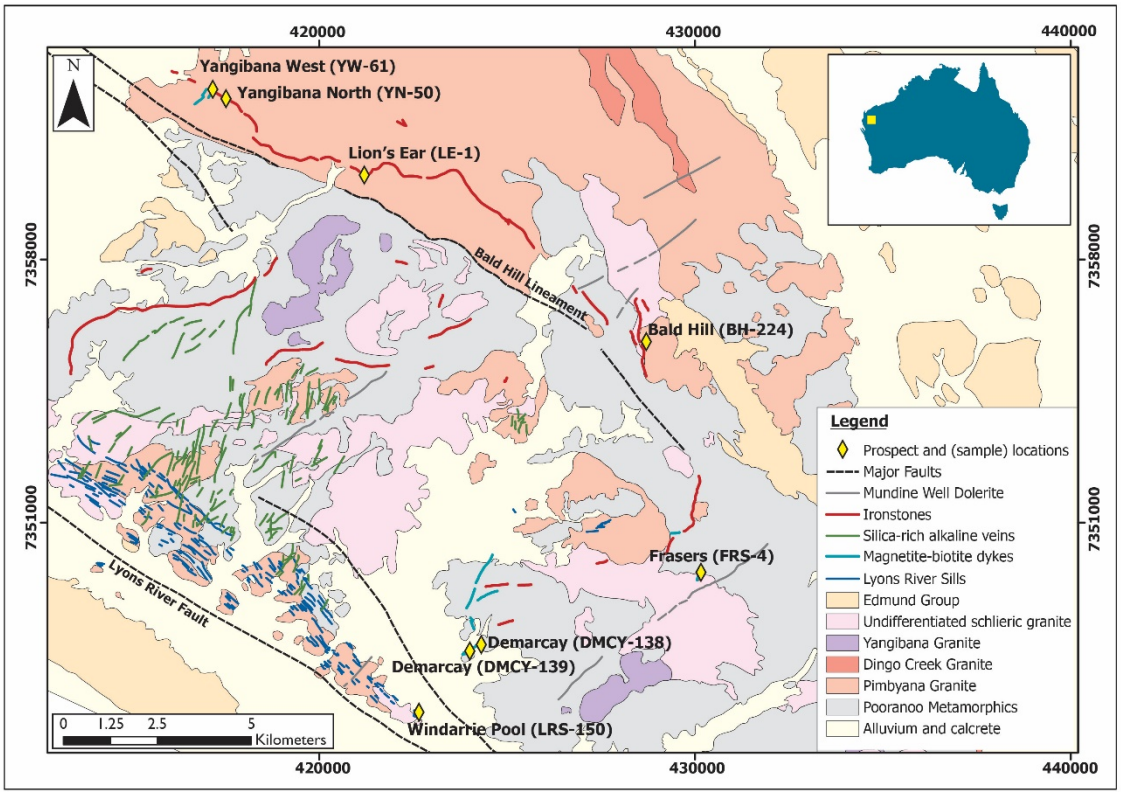

Figure 3.1 Geologic map of the Gifford Creek Carbonatite Complex (modified from Pearson 1996).

The area is of economic interest as dykes/sills located along the Bald Hill Lineament and in the southeast area of the complex (Fig. 3.1) contain significant resources of LREE (particularly Nd and Pr), which totals 21 million tonnes of ore at 1.17% total rare earth oxides (Hastings Technology Metals Limited, 2017). The LREE are hosted mainly in monazite and apatite (Pirajno et al., 2014), and there is a distinct spatial variation in the REE ore compositions, with orebodies in the northwest of the GCCC (along the Bald Hill Lineament; Fig. 3.1) having lower Nd/La values than those in the southeast (Fig. 3.2).

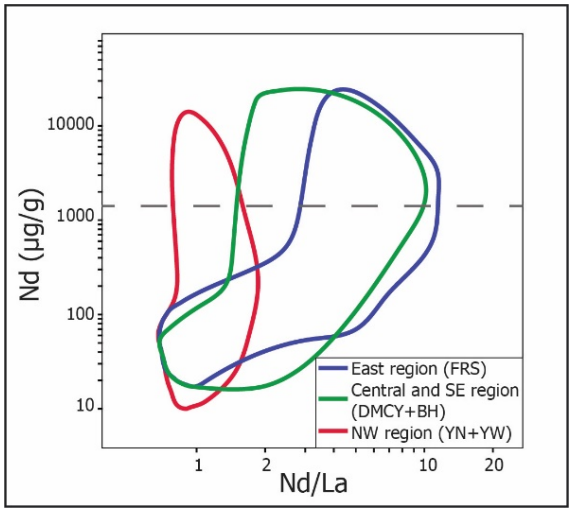

Figure 3.2 Neodymium versus Nd/La of ore samples from the Gifford Creek Carbonatite Complex. Note the variation in ore composition with location across the GCCC, with ore samples from the northwest of the complex (Yangibana North: YN and Yangibana West: YW) having relatively low Nd/La values compared to ore samples from the center (Bald Hill: BH) and southeast (Demarcay; DMCY) of the complex, which in turn have lower Nd/La than ores from the easternmost (Frasers; FRS) regions of the complex. The dashed gray line is the minimum ore grade cut off. Ore composition fields were constructed from 15,272 analyses of drill core provided by Hastings Technology Metals Ltd.

The GCCC consists of four primary rock types: 1) dolomitic carbonatites (also known as the Lyons River Sills); 2) Silica-rich alkaline veins; 3) magnetite-biotite dykes, and; 4) ankerite-siderite carbonatites. Associated with these four main rock types are fenitised wall rocks (a.k.a. "fenites") and alkaline amphibole-dolomite veinlets that emanate from carbonatite dykes/sills. Weathered and oxidised surface outcrops of the four main rock types form "ironstones" (Fig. 3.1) rich in Fe-oxides and hydroxides, Fe-rich carbonates, and quartz. Although the precise protolith of each ironstone unit is difficult to ascertain, these rocks are of economic interest as they are the main host of REE mineralisation. Detailed descriptions of these all of these rock types are presented in Chapter 2. Here, the geochemical and textural analysis of apatite from eight rock samples is presented including: three magnetite-biotite dykes samples collected from outcrop (DMCY-138, DMCY-139, FRS-4), two magnetite-biotite dyke samples and one ankerite-siderite carbonatite sample taken from drill core (YW-61, BH-224, and YN-50, respectively), one sample of a alkaline amphibole-dolomite veinlet (LRS-150) taken from surface outcrop, and one sample taken from a surface outcrop of fenite adjacent to an ironstone (LE-1). These samples were selected for their apatite size, abundance, and proximity to the LREE deposits.

3.2.1 Magnetite-biotite dykes

The magnetite-biotite dykes form thin (0.1 cm to 1.5 m) dykes and sills throughout the field area, but are most abundant in the southeast and northwest corners of the complex, around the Demarcay/Frasers and Yangibana West prospects, respectively (Fig. 3.1). The magnetite-biotite dykes are seriate to equigranular and composed of biotite (phlogopite-annite series), magnetite, apatite, and monazite, although proportions of apatite and monazite vary greatly. Mineralogy and location of the samples examined here is presented in Table 3.1 and Figure 3.1. Apatite is a major constituent of all samples and, generally, is present as large (up to 500 μm) anhedral to euhedral grain aggregates or clots. These apatite clots often contains inclusions of monazite and magnetite. In places, apatite grains are cut by small veinlets and fractures filled with iron oxides. The biotite ranges in size from 100 μm to 2 mm, and often features radiation damage from included monazite. Biotite may be present as euhedral coarse grains or as an interstitial

phase to the apatite and magnetite (e.g., sample DMCY-139). Magnetite tends to be anhedral to subhedral (except sample FRS-4, where magnetite is euhedral) and may be up to 500 μm in size. Magnetite in variably altered to hematite along grain margins. Monazite is present in all samples and occurs both as large (up to 1 mm), anhedral to euhedral crystals, either individually or as splayed clusters of crystals, or as small (<10 μm) inclusions within the apatite. Minor amounts of late-stage quartz and iron oxides (most likely hematite and goethite) are occasionally present as infill between the magnetite, biotite, and phosphate minerals. These are considered post-magmatic alteration phases. Additional mineral phases include minor amounts of ragged and irregular potassium feldspar grains in sample BH-224, which likely represent entrained grains from the fenitised host rock, and fine (~10 μm) blebs of aegirine in sample FRS-4.

Table 3.1 Location, rock type, and mineralogy of the rock samples analysed in this study.

Sample #	Rock Type	Nearest Prospect	Latitude	Longitude	Primary Mineralogy (in order of abundance)
DMCY-139	Magnetite-biotite dyke	Demarcay	424026	7347653	Mag, Ap, Bio, Mnz
DMCY-138	Magnetite-biotite dyke	Demarcay	424026	7347653	Bio, Ap, Mag, Mnz, Qtz
FRS-4	Magnetite-biotite dyke	Fraser's	430083	7349554	Mag, Aeg, Qtz, Hem, Mnz, Ap, Bio
BH-224	Magnetite-biotite dyke	Bald Hill	428503	7355090	Bio, Mag, Kfs, Ap, Mnz
YW-61	Magnetite-biotite dyke	Yangibana West	416152	7363045	Mag, Bio, Mnz, Ap
YN-50	Ankerite-siderite carbonatite	Yangibana North	417402	7362065	Sid, Ank, Bio, Mag, Mnz, Qtz, Ap, Kfs
LRS-150	Alkaline amphibole-dolomite veinlet	Windarrie Pool*	422586	7345898	Rbk, Arf, Rt, Dol, Qtz, Ap, Mag, Mnz
LE-1	Fenite	Lion's Ear	419997	7360600	Kfs, Qtz, Ap, Mnz, Hem, Zrn

Notes: Locations are recorded in UTM zone 51. Bio = biotite, Mag = magnetite, Mnz = monazite, Ap = apatite, Qtz = quartz, Aeg = aegirine, Rbk = riebeckite, Arf = arfvedsonite, Rt = rutile, Sid = siderite, Ank = ankerite, Cal = calcite, Dol = dolomite, Kfs = potassium feldspar, Hem = hematite, Zrn = zircon. Abbreviations from Whitney & Evans (2010).
*Not a prospect, location name taken from Pearson (1996).

3.2.2 Ankerite-siderite carbonatites

Fresh ankerite-siderite carbonatites are only found as 5 cm veins to 1 m thick dykes at depth in drill core along the Bald Hill Lineament (Fig. 3.1). The veins and dykes are mantled by fenitic, potassium feldspar alteration of the host granitic and metasedimentary rocks. Sample YN-50 is a ankerite-siderite carbonatite taken from drill core from the Yangibana North prospect. The main rock constituent is macro-crystalline (> 2 mm) subhedral to euhedral siderite that transitions

to finer ankerite (20 μm to 200 μm) and then calcite (20 μm to 200 μm) proximal to a phosphate-silicate enclave found within the sample. The enclave is composed of magnetite, biotite, monazite, apatite, quartz, and trace plagioclase. Euhedral magnetite and biotite occur together along the contact between the carbonates and the enclave and range in size from 50 μm to 250 μm. Quartz crystals are typically large (>1000 μm), but have recrystallised along the grain margins as revealed by undulatory extinction. Apatite occurs as small, anhedral to subhedral crystals (200 μm to 500μm in length) that are proximal to monazite, which itself occurs as large (up to 500 μm) lathlike crystals. Monazite is often found in the quartz, but in some cases, the laths extend beyond the silicate enclave into the carbonate domain.

3.2.3 Alkaline amphibole-dolomite veinlets

The dolomitic carbonatites sills (known as the Lyon River Sills) that crop out to the north-east of the Lyons River Fault (Fig. 3.1) often have thin (typically 3 mm to 2 cm wide) veins and veinlets that emanate from the sill into the fenitised wall rock over a distance of several tens of meters. These veins – known herein as alkaline amphibole-dolomite veinlets – have distinct pink potassium feldspar alteration halos that extends 1 cm to 3 cm outward from the veins. The alkaline amphibole-dolomite veinlet sample studied here (LRS-150) is composed of fine, feathery rutile (crystal masses up to 500 μm) and fine, fibrous riebeckite-arfvedsonite (crystal masses up to 2 mm) with lesser amounts of Fe-bearing dolomite (100 μm to 200 μm in size) and iron oxides, mainly euhedral to subhedral magnetite (~100 μm in size) partly altered to hematite. Subhedral quartz (up to 200 μm μm) and euhedral apatite (100 μm to 500 μm) are present, as is trace amounts of anhedral monazite as small (<100 μm) inclusions within the rutile and riebeckite-arfvedsonite.

3.2.4 Fenites

The magnetite-biotite dykes, ironstones, carbonatites, and related alkaline amphibole-dolomite veinlets are enveloped by K-rich fenite zones within the host metasedimentary or granitic rocks. The width of the fenite zones are commensurate with the size of the dykes and veins (i.e., 1 m to 2 m dykes tend to have distinct fenite halos of 2 m to 3 m width, while a 1 cm vein will tend to have a 1 cm to 3 cm fenite halo).

Sample LE-1 is fenite taken from an alteration zone of precursor granite around an ironstone dike near the Lions Ear prospect (Fig. 3.1). LE-1 is primarily composed of potassium feldspar with lesser amounts of plagioclase, apatite, monazite, quartz, zircon, and hematite. Most of the primary plagioclase has been altered to ragged, irregular potassium feldspar grains that range from 20 μm to 300 μm in size. Quartz is mostly fine-grained (<50 μm) and exhibits undulose extinction and extensively recrystallised grain boundaries. Apatite grains are relatively large (500 μm in length) and subhedral to euhedral in form. Monazite (up to 200 μm) occurs throughout the sample as interstitial grains to potassium feldspar, as fracture fillings, and as small inclusions (10 to 20 μm) in apatite. Hematite is present as veinlets that cross cut the sample. Accessory zircon with oscillatory zoning is also present in this sample.

3.3 Methods

All samples were prepared as polished thin sections and 25 mm diameter polished pucks, which contained the rock offcuts for the polished thin sections. Both thin sections and polished pucks were examined using a Leica DMRXP optical microscope. The apatite grains hosted in the rock samples (mounted in the polished pucks) were then analysed in situ by electron probe microanalysis (EPMA) and laser ablation inductively coupled plasma mass spectrometry (LA-ICP-MS) at the Advanced Analytical Centre at James Cook University, Townsville, Australia. Details for EPMA and LA-ICP-MS analyses are presented in Appendices 3.A and 3.B, respectively.

In order to ascertain the nature of the apatite in each sample (e.g., heterogeneity or homogeneity of spectra), a large region, usually 1.5 mm x 1.5 mm, was scanned using hyperspectral cathodoluminescence according to the methods described below. Following this, higher resolution CL scans were conducted on 2–3 individual apatite grains. One image and corresponding CL spectra for each sample that best illustrated the overall textures observed is presented in Figures 3.5-3.12.

Cathodoluminescence analyses of apatite were conducted using a JEOL XM-86440 CL spectrometer connected to the JEOL JXA-8200 EPMA via a 200 μm optic fiber cable. The

effective wavelength range of the spectrometer is 350 nm to 1200 nm (i.e., 3.54 eV to 1.03 eV). At >1200 nm the signal-to-noise ratio is too high for meaningful interpretation (MacRae et al., 2005). Samples were mapped in situ using a 1 µm to 5 µm spot size and 1 µm to 5 µm step (depending on apatite size) with a dwell time of 20 ms to 50 ms per spot. The beam was set to 20 kV and 20 nA. These data were then compiled into raster images, and then RGB false colour images using the xCLent software from CSIRO, and Chimage software, respectively (Harrowfield et al., 1993). Wavelength spectra for the different zones within the apatite were obtained using the XCL-image software. Deconvolution of these spectra was conducted using the Optical Fit 17.07 software from CSIRO (Fig. 3.3; Torpy and Wilson, 2008). Each CL spectrum is considered the sum of a number of CL peaks with Gaussian distributions produced by the presence of CL activators. The Optical Fit software is used to approximate a "best fit" to the CL spectrum by assuming Gaussian peak profiles and matching peak locations to known activator band locations for apatite from the CSIRO luminescence database (Fig. 3.3; MacRae and Wilson, 2008).

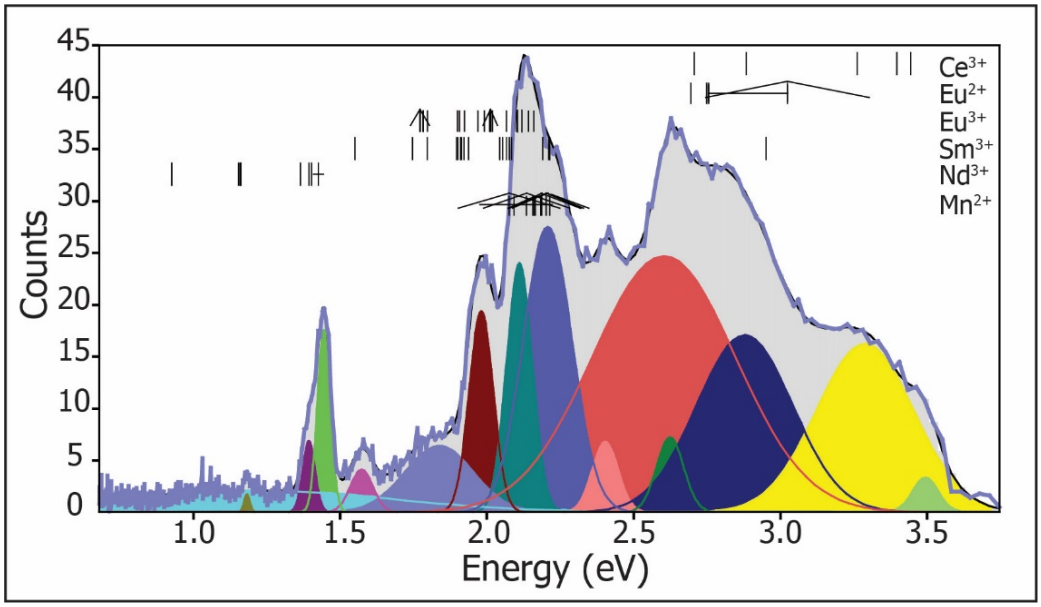

Figure 3.3 A deconvoluted hyperspectral CL curve for the mottled pink and purple zones in the apatite from LE-1, constructed using the Optical Fit 17.07 software from CSIRO (Torpy and Wilson, 2008). The total curve (purple) comprises the sum of Gaussian distributed peaks (multiple colours) of possible CL activators present across the energy spectra. Thin vertical lines indicate single activator locations. Thin horizontal lines indicate an activator present over a range of band values, and triangular hats depict the full width at half maximum (FWHM) for an activator (where the data are available). The locations of the apatite activators are taken from MacRae and Wilson (2008) and references therein. More activators are present in apatite, but only these were shown in the interest of simplicity.

After CL analysis, the samples were polished to remove the top few micrometers of the exposed surface of the samples in order to avoid potential electron beam damage from the previous analysis (see below). The samples were then carbon-coated again and analysed for major/minor elements using a JEOL JXA-8200 WD/ED combined electron probe micro-analyser. Analysis locations were selected on various CL zones across multiple apatite grains within the regional CL maps acquired for each sample. The beam was set to a 2 μm to 5 μm spot size with an accelerating voltage of 15 kV and a current of 20 nA. All elements were analysed for 20s on peak with 10s on background, except for F and Sr, which were analysed using 40s on peak with 20s on background and 30s on peak with 15s on background, respectively. Element concentrations were quantified using well-characterised in-house standards as follows: Ca and Si (wollastonite), Na (albite), P and Ce ($CePO_4$), Nd ($NdPO_4$), F and Sr (SrF_2), and Cl (tugtupite). Analyses were then subject to a ZAF matrix correction procedure for data quantification. This method better fit the data due to the substantial levels of REE in some apatites. The EPMA results are presented in Appendix 3.A.

The analysis of halogens in apatite is highly dependent on crystal orientation and electron beam exposure. Fluorine in particular is susceptible to migration in the apatite crystal lattice due to exposure to an electron beam (Stormer et al., 1993; Pyle et al., 2002). For example, X-ray counts of F in apatite tend to increase substantially when F is analysed by an electron beam parallel to the *c*-axis of the crystal (Stormer et al., 1993; Goldoff et al., 2012). This migration of F can lead to erroneous values greater than 1.0 apfu or 3.77 wt.% F in fluorapatite (Pyle et al., 2002; Chakhmouradian et al., 2017). To monitor and correct for potential F migration during analysis, F counts were recorded with analysis time using a chart recorder. These time-resolved data were then used to extrapolate back to the F counts at time zero, as stipulated by Stormer and Pierson (1993), McCubbin et al. (2010), and Goldoff et al. (2012). The zero intercept value was then used as the raw F count rate for the analysis prior to ZAF correction to calculated final element concentration values.

Transmitted light, CL images, and the EPMA WDS spot locations were used to determine suitable areas of apatite for trace element spot analysis by LA-ICP-MS. For each sample, multiple

apatites and their correlating CL zones were analysed using laser spot analyses. As laser spot analyses also sample at depth, Sr and REE counts were monitored during data reduction and the appropriate signal intervals selected according to each CL zone analysed with EPMA and based on the CL images. Trace element analyses were conducted using a Coherent GeoLasPro 193nm Excimer laser coupled to a Varian (now Bruker) 820-MS quadrupole ICP-MS. Laser spot sizes varied from 24 to 44 μm depending on the size of the target apatite zone. Samples were ablated using a surface energy density of 4 J/cm^2, as measured at the site of ablation, and a repetition rate of 10 Hz. The rate of oxide production and plasma fractionation were monitored by keeping ThO/Th to around 0.5%, and $^{238}U/^{232}Th$ sensitivity ≈ 1, respectively. The synthetic glasses NIST SRM 610 and 612 were used as the primary and secondary standards, respectively,

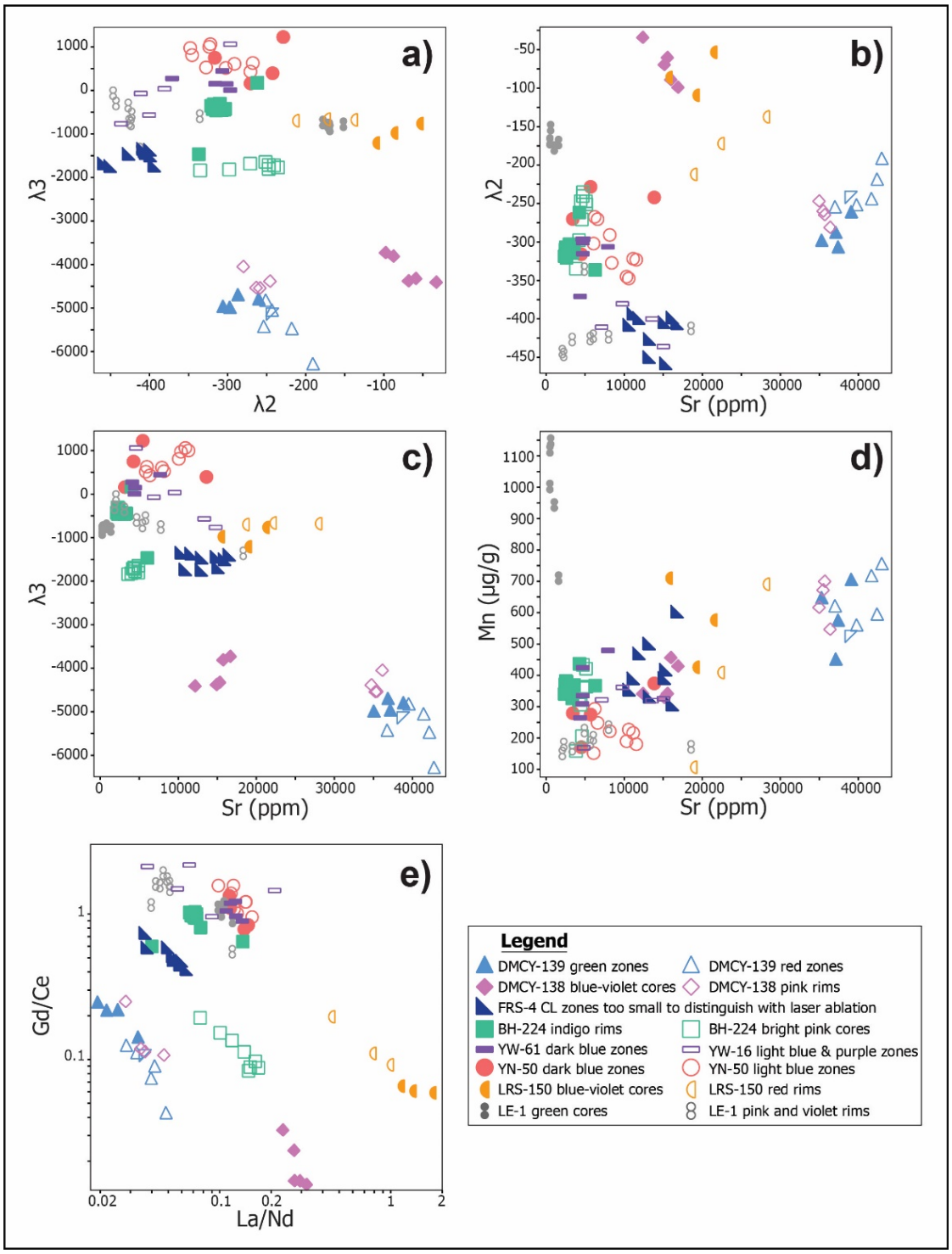

Figure 3.4 Trace element characteristics of apatite from the GCCC. a) REE compositional parameters λ_2 versus λ_3 of apatite. Definitions of λ_2 and λ_3 are outlined in O'Neill (2016). Both DMCY magnetite-biotite dyke samples from the southeastern region have low λ_3 values compared to other samples from this study. The blue-violet cores from DMCY-138, the green cores from fenite sample LE-1, and the magmatic-hydrothermal apatite from LRS-150 have relatively high λ_2 values. b) Sr versus λ_2 of apatite. Apatites from the southeast of the GCCC (DMCY-138, DMCY-139, and LRS-150) have the highest Sr values. c) λ_3 versus Sr of apatite. Note the high Sr and low λ_3 of the magnetite-biotite dyke samples from the southeast of the GCCC. d) Sr versus Mn concentration of apatite. The green CL apatite cores from the fenite (LE-1) have low Sr and high Mn, whereas apatite from the southeast magnetite-biotite dyke from the southeast of the Complex has high Sr and moderate Mn contents. e) Gd/Ce versus La/Nd of apatite. Samples from the southeastern region of the GCCC and the bright apatite cores from Bald Hill (BH-224) have much lower Gd/Ce ratios than the other samples.

with reference values taken from Spandler et al. (2011). The Ca content as determined by EPMA WDS was used as an internal standard, and data reduction was carried out using the SILLS program (Guillong et al., 2008). The error and detection limit were calculated in SILLS using the methods from Luo et al. (2007) and Pettke et al. (2012), respectively. The following isotopes were chosen for analysis: ^{27}Al, ^{31}P, ^{43}Ca, ^{44}Ca, ^{49}Ti, ^{55}Mn, ^{66}Zn, ^{75}As, ^{85}Rb, ^{88}Sr, ^{89}Y, ^{90}Zr, ^{93}Nb, ^{118}Sn, ^{133}Cs, ^{137}Ba, ^{139}La, ^{140}Ce, ^{141}Pr, ^{143}Nd, ^{147}Sm, ^{151}Eu, ^{157}Gd, ^{159}Tb, ^{163}Dy, ^{165}Ho, ^{167}Er, ^{169}Tm, ^{171}Yb, ^{175}Lu, ^{178}Hf, ^{181}Ta, ^{208}Pb, ^{232}Th, and ^{238}U.

The examination of this REE data utilises standard chondrite-normalised REE plots, as well as the methods introduced by O'Neill (2016), who fitted polynomial equations to REE patterns and arranged the data in orthogonal form such that the coefficients of the equations (expressed as λ_n) represent a shape of the normalised REE pattern. O'Neill (2016) defined five coefficients that can be used to effectively describe the shape of REE patterns: λ_0 describes the overall height of the REE pattern (i.e., the average concentration of REE); λ_1 describes the slope of the REE pattern; λ_2 describes the quadratic curvature of the REE pattern, and; λ_3 describes the inflections at either end of the REE patterns; and λ_4 describes the W-shape of the pattern. Analysis of the REE data revealed that λ_2 and λ_3 were effective at illustrating the differences across the apatite samples in this study (Fig. 3.4).

3.4 Results

3.4.1 Cathodoluminescence and REY patterns

One of the advantages of hyperspectral CL over other CL methods is the ability to apply a false colour overlay to the measured CL spectra, including UV and IR wavelengths. Red, green, and blue colours can be applied over specific CL wavelengths in order to highlight changes in peak position and intensity. In this study, red was mapped to the wavelengths ~830 to 930 nm (i.e., 1.49 to 1.33 eV), green was mapped to ~525 to 650 nm (i.e., 2.36 to 1.91 eV), and blue was mapped to ~350 to 500 nm (i.e., 3.54 to 2.48 eV). In this study, "brighter" zones refer to the longer wavelengths and correlate to the reds, pinks, and lighter colour shades; "darker" zones refer to the observed deep blues, greens, and indigos.

Overall, the CL spectra of the brighter zones have more peaks, greater peak intensity, and more complex spectra (Table 3.2). The darker zones (greens and blues) display spectra that have fewer, less intense peaks than the pink to light purple zones. Accordingly, the overall REE + Y contents for the brighter CL zones tend to be higher than for the CL dark zones.

3.4.1.1 Magnetite-biotite dyke sample DMCY-139

Backscattered electron imaging reveals two distinct domains of apatite in sample DMCY-139 (Fig. 3.5a). The inner cores of the apatite grains are coloured bright red/pink in CL (using the RGB coding in this study). Although some aspects of the primary oscillatory zoning can be observed (Fig. 3.5b), much of this phase of apatite is heavily embayed. The red core zones are mantled by CL green-coloured apatite, which also exhibits distinct oscillatory zoning. Both the darker green and brighter red zones have comparable CL spectra; however, the red zones have more distinct peaks (e.g., ~1.4 eV, ~2.1 eV, near 3.5eV) of greater intensity (Fig. 3.5c; Table 3.2).

Chondrite-normalised REE+Y (REY) patterns for both of these apatite domains feature a sinusoidal shape with an inflection from concave downward between La to Eu, to concave upward from Gd to Lu (Fig. 3.5d), giving distinctly low λ_3 values (O'Neill 2016; Fig. 3.4a). The two domains have similar REY patterns and similar CL peak patterns, although the darker, green CL zones have slightly lower LREE contents (and lower CL peak heights) than the brighter, red CL zones.

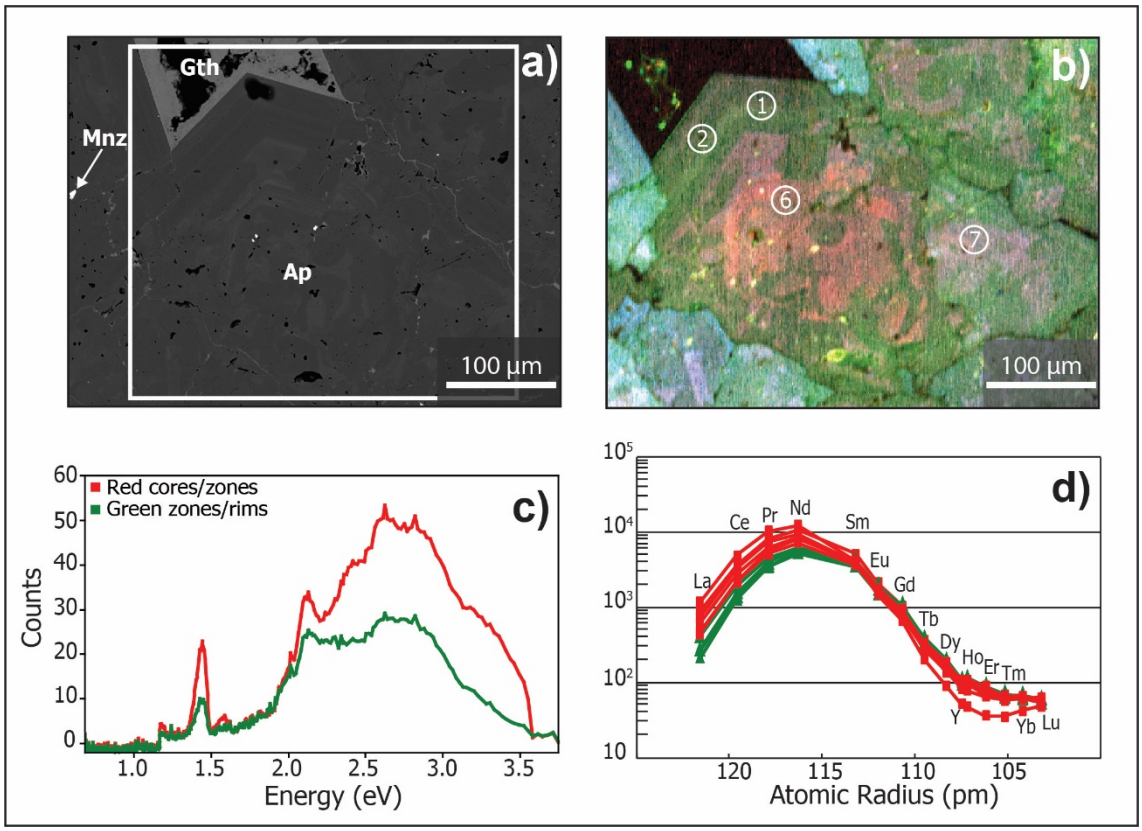

Figure 3.5 a) Backscattered electron image of apatite from the magnetite-biotite dyke sample DMCY-139. b) Hyperspectral CL image of apatite showing zonation and internal variation, possibly from dissolution, in the apatite grain. Circles and numbers denote laser sampling location (Appendix 3.B) and sample number present in this image. Circles are actual spot size. c) CL spectra of the apatite in (b). The red zones have slightly higher count rates and a more pronounced shoulder from 3.1eV to 3.5eV. The line colour of the spectra correlates to the apatite colour in (b). d) Chondrite-normalised REY patterns for both CL zones. Colours correspond to CL in (b). There is overlap in the zones, indicating only slight variations REY content. Mineral abbreviations can be found in Table 3.1. Chondrite values are from Sun and McDonough (1995) and REY are plotted according to atomic radius assuming a coordination number of nine for apatite.

3.4.1.2 Magnetite-biotite dyke sample DMCY-138

Apatite grains from sample DMCY-138 show nearly uniform BSE signals (Fig. 3.6a) Nevertheless, hyperspectral CL reveals two distinct apatite generations: blue-violet core zones that are mantled by bright pink rim zones that occasionally display oscillatory zoning (Fig. 3.6b). The darker, blue-violet cores have relatively simple CL spectra with a small peak at 1.35 eV to 1.48 eV and a very wide and tall peak that spans from 2.3 eV to 3.6 eV (Fig. 3.6c; Table 3.2). The pink zones have distinct CL spectra with taller peaks at 1.35 eV to 1.48 eV and at around 2.1 eV, but with shorter and wider peaks in the 2.3 eV to 3.6eV range (Fig. 3.6c; Table 3.2).

As with sample DMCY-139, both apatite zones have sinusoidal REY patterns with inflections near Nd, low λ_3 values (Fig. 3.4a) and small, negative Y anomalies (Fig. 3.6d). The

pink CL zones are enriched in the elements Sm to Lu, but relatively depleted in La and Ce compared to the blue-violet CL zones.

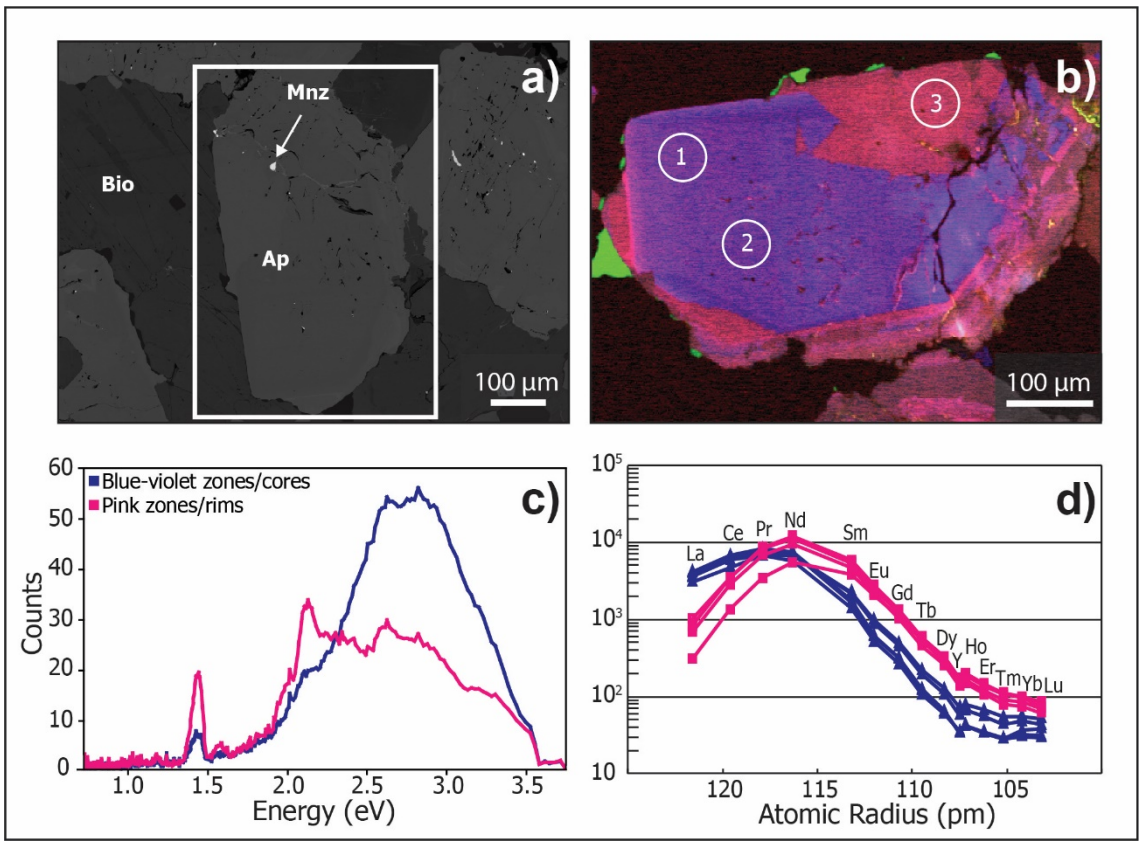

Figure 3.6 a) Backscattered electron image of apatite from the magnetite-biotite dyke sample DMCY-138. b) Hyperspectral CL image of apatite highlighting zonation. Circles and numbers denote laser sampling location and sample number present in this image. Circles are actual spot size. c) CL spectra of the apatite in (b). The bright pink rim has higher counts near 1.4eV and 2.1eV. The blue-violet core has higher counts from 2.5eV to 3.5eV. The line colour of the spectra correlates to the apatite colour in (b). d) Chondrite-normalised REY patterns for both CL zones. Colours correspond to CL in (b). The blue-violet core is enriched in La and Ce whereas the pink rim is enriched in the REY from Nd to Lu. See Figure 3.5 for details on mineral abbreviations and REY plot style.

3.4.1.3 Magnetite-biotite dyke sample FRS-4

Despite a fairly homogenous BSE response (Fig. 3.7a), CL analysis of apatite from FRS-4 reveals a wispy and mottled texture composed of bright pink zones swirled with darker, purple zones (Fig. 3.7b). Also present are bright pink zones with oscillatory zoning. The apatite with this zoning is interpreted as relict primary apatite. Some discrete blue zones are found in the center of the apatite grains (e.g., Fig. 3.7b). The blue zone and the bright pink zones appear to be luminescent end members of the wispy, mottled pink and purple apatite textures.

Regarding CL spectra, the blue zones have a small peak from 1.35 eV to 1.48 eV and a tall, wide peak from 2.3 eV to 3.6 eV. The bright pink zones have more peaks that are distinct in their CL spectra (Fig. 3.7c; Table 3.2), with higher intensity peaks at approximately 1.4 eV, 1.6

eV, 2.0 eV and 2.2 eV. By contrast, blue zones have greater peak intensities from 2.3 eV to 3.3 eV.

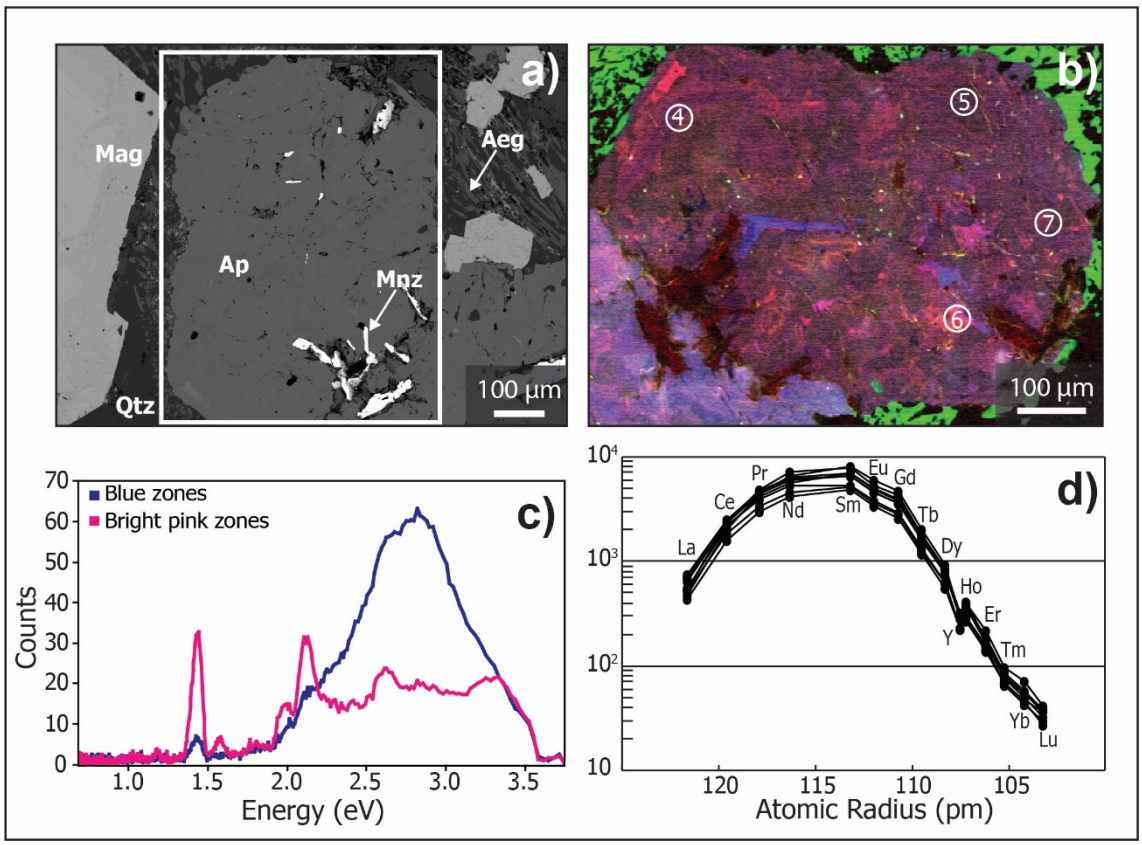

Figure 3.7 a) Backscattered electron image of apatite from the magnetite-biotite dyke sample FRS-4. b) Hyperspectral CL image of apatite revealing complex internal structure. Circles and numbers denote laser sampling location and sample number present in this image. Circles are actual spot size. c) CL spectra of the apatite in (b). The bright pink zones have higher counts at peaks near 1.4 eV, 2.0 eV, and 2.1 eV. The blue-violet cores have higher counts from 2.3 eV to 3.3 eV. The line colour of the spectra correlates to the apatite colour in (b). d) Chondrite-normalised REY patterns for the apatite sample. See Figure 3.5 for details on mineral abbreviations and REY plot style.

The trace element concentrations of the luminescent end-member apatite zones could not be determined due to their complex nature and small size. The mottled (mixed?) zone has a strongly concave downward REY pattern (i.e., low λ_2 values; Fig. 3.4a) with the apex of the curve between Nd and Sm (Fig. 3.7d). There is a small Y anomaly as well as a very slight downward inflection at Eu.

3.4.1.4 Magnetite-biotite dyke sample BH-224

Apatite grains in this sample contain core zones with monazite inclusions (~10 µm), mantled by BSE-darker, monazite-free apatite (Fig. 3.8a). The monazite-bearing core zones are bright pink in their CL response. The core zones are elongated and euhedral but appear to be fragmented and broken (Fig. 3.8b). In BSE, the darker apatite zones correspond to dark, indigo

colour under CL. The bright pink zones have greater peak intensities, and more complex spectra, compared to the darker indigo zones that have simple spectra (i.e., only two main peaks at 2.2 eV and 2.7 eV). The bright pink zones also feature a large peak centered at 2.5 eV to 2.7 eV that has multiple ledges on either side (Fig. 3.8c; Table 3.2).

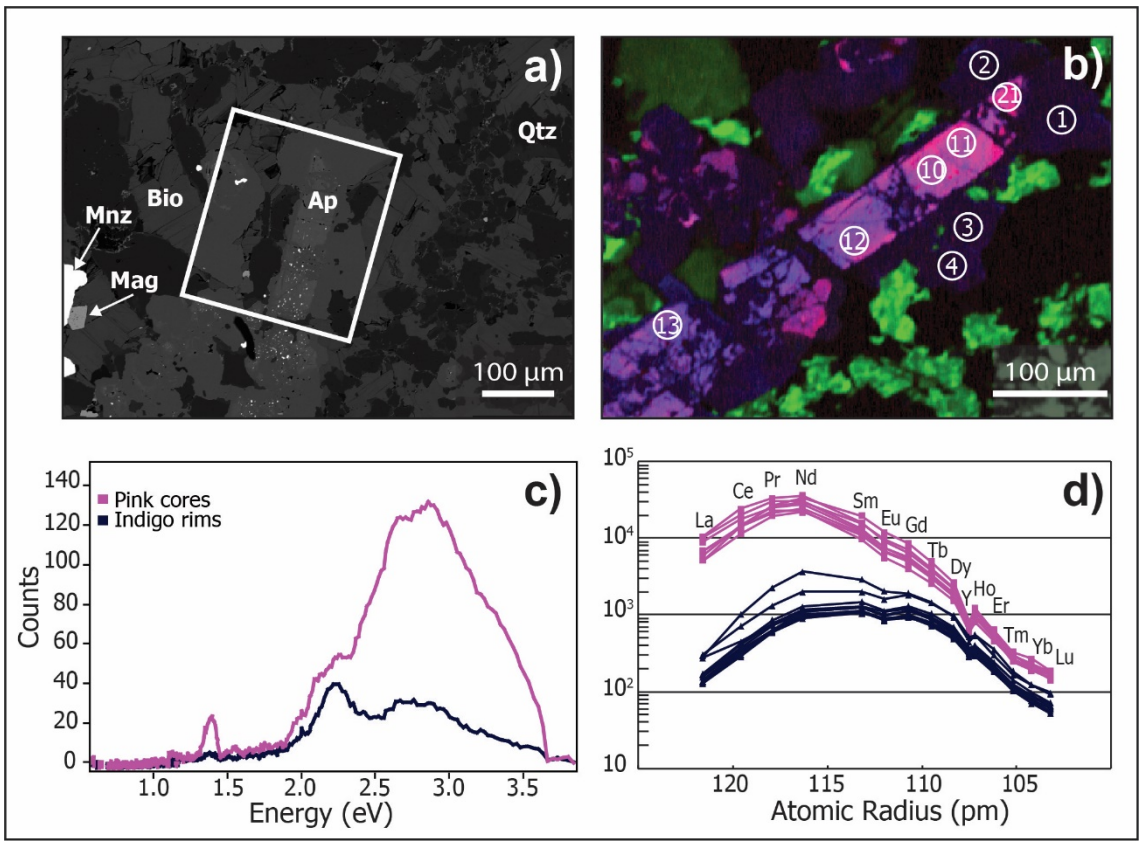

Figure 3.8 a) Backscattered electron image of apatite from the magnetite-biotite dyke sample BH-224. b) Hyperspectral CL image of apatite showing bright pink cores with dark indigo rims. Circles and numbers denote laser sampling location and sample number present in this image. Circles are actual spot size. c) CL spectra of the apatite in (b). The bright pink core has much higher counts over the entire spectra compared to the dark indigo rim. The line colour of the spectra correlates to the apatite colour in (b). d) Chondrite-normalised REY patterns for both CL zones. Colours correspond to CL in (b). The pink core is enriched in the REY compared to the darker, indigo zone. See Figure 3.5 for details on mineral abbreviations and REY plot style.

The REY patterns for the bright and dark CL zones both have concave downward patterns, with the apex around Nd, and higher λ_3 values than the samples from Demarcay prospect described above. However, the brighter, pink CL zones are distinctly enriched in LREE compared to the indigo zones (Fig. 3.8d). Both zones lack Eu anomalies, but do have a distinct negative Y anomaly.

3.4.1.5 Magnetite-biotite dyke sample YW-61

Much of the apatite in sample YW-61 appears homogenous in optical microscope and BSE images (Fig. 3.9a). By contrast, CL imaging reveals a heterogeneous texture within apatite grains and clusters. Small (<40 µm wide) light blue and lavender zones of apatite mottle the more common dark blue apatite zones (Fig. 3.9b). The dark blue zones display simpler CL spectra compared to the brighter, lavender zones. The lavender zones have many more distinct peaks (e.g., the peaks at 1.35 eV to 1.48eV and 1.75 eV to 1.85eV) with much higher counts (Fig. 3.9c; Table 3.2).

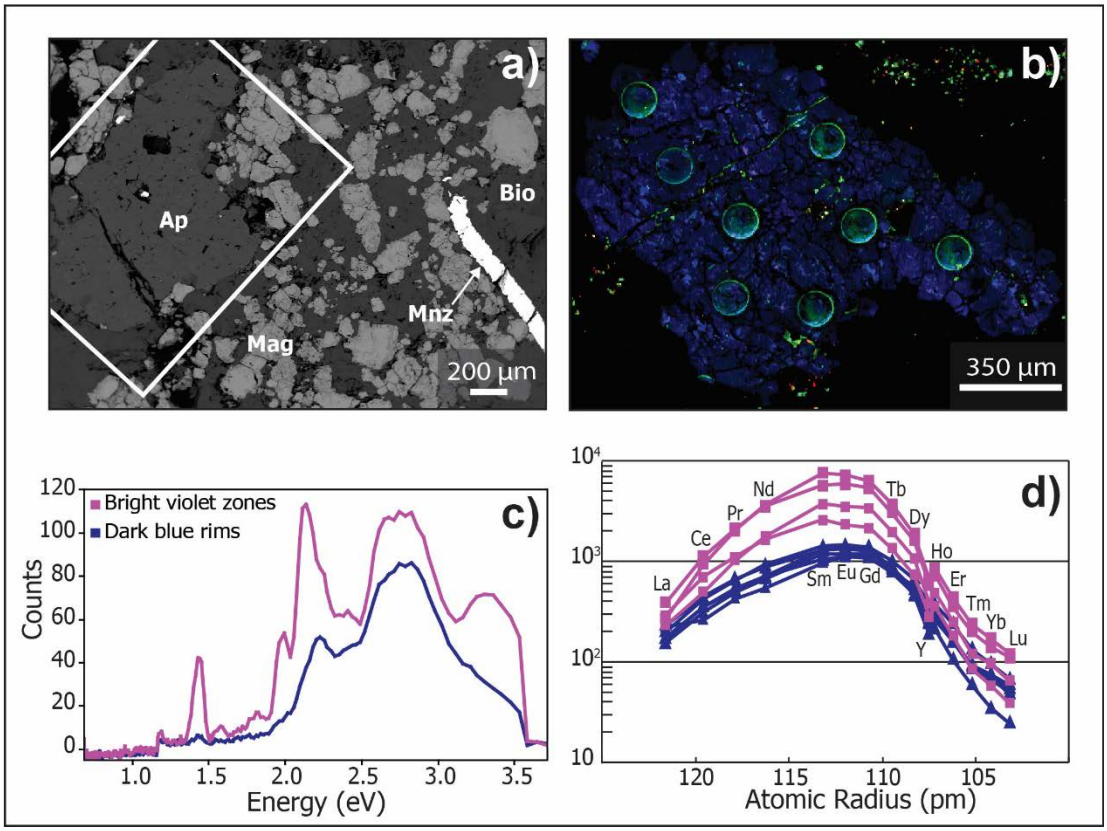

Figure 3.9 a) Backscattered electron image of apatite from the magnetite-biotite dyke sample YW-61. b) Hyperspectral CL image of apatite showing internal zonation. Bubbles are laser spots for LA-MC-ICP-MS analyses for Sm-Nd isotopes. Trace element analyses were conducted on other apatite with the same CL spectra within the same rock sample. c) CL spectra of the apatite in (b). The light violet zones have overall higher counts than the dark blue zones. The line colour of the spectra correlates to the apatite colour in (b). d) Chondrite-normalised REY patterns for both CL zones. Colours correspond to CL in (b). The light violet cores are enriched in all REY. See Figure 3.5 for details on mineral abbreviations and REY plot style.

The dark blue and brighter violet CL zones share similar overall REY pattern shapes. Both zones display REY patterns that are concave downward with an apex centered on Eu and both zones have a distinct negative Y anomaly (Fig. 3.9d) and high λ_3 values. The brighter

lavender zones, however, are more enriched in REY, especially LREE, compared to the dark blue zones.

3.4.1.6 Ankerite-siderite carbonatite sample YN-50

The apatite in the ankerite-siderite carbonatite sample YN-50 has dark blue and light blue CL signals, based on the RGB colour scheme used in this study. The texture of these apatite grains can be described at mottled, with minor growth rims (Fig. 3.10a,b). This dark blue apatite has two broad peaks; one from 2.1 eV to 2.5 eV with a small shoulder at 2.4 eV; and another from 2.5 eV to 3.1 eV. The light blue zones display a slight increase in the relative peak intensities and exhibit more peaks than the dark blue zones (Fig. 3.10c; Table 3.2).

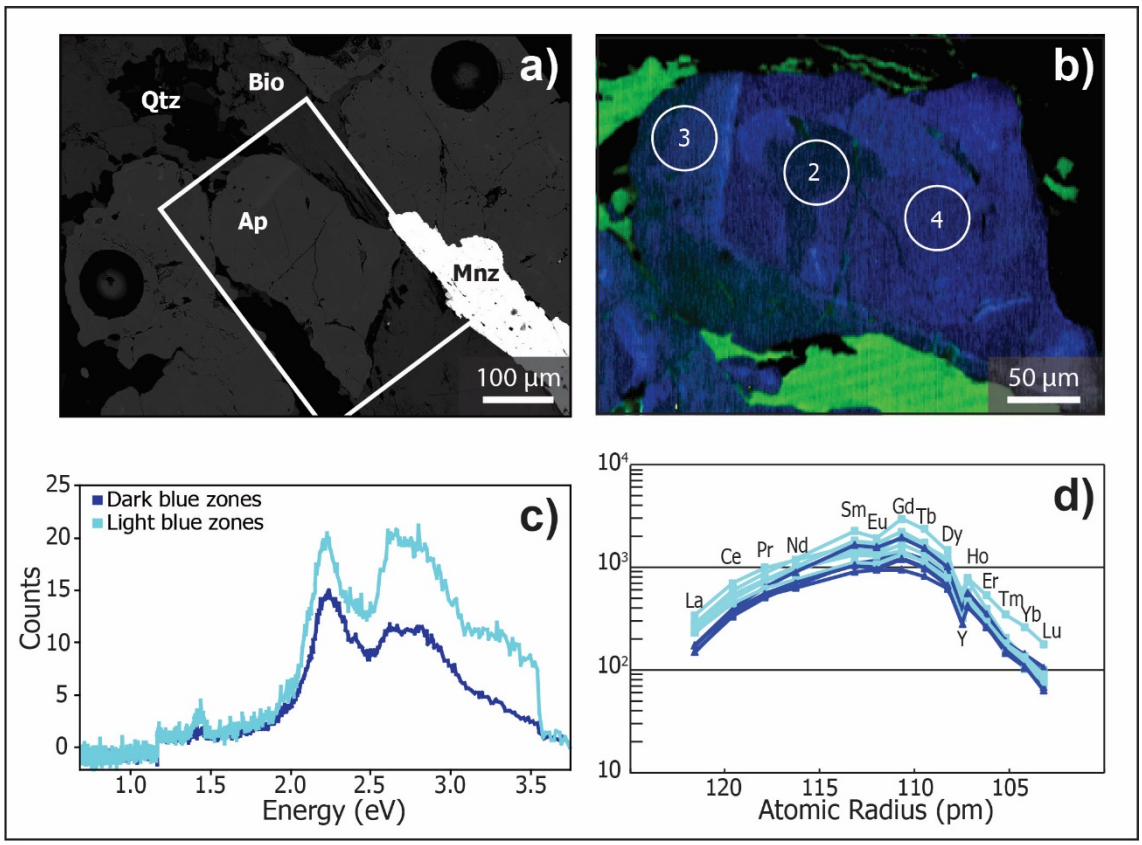

Figure 3.10 a) Backscattered electron image of apatite from the ankerite-siderite carbonatite sample YN-50. Dark bubbles are laser spots for LA-MC-ICP-MS analyses for Sm-Nd isotopes. b) Hyperspectral CL image of apatite showing minor zonation and slight internal variation in the apatite grain. Circles and numbers denote laser sampling location and sample number present in this image. Circles are actual spot size. c) CL spectra of the apatite in panel (b). The light blue zones have slightly higher count rates; however, the overall counts for this sample are extremely low compared to other samples in this study. The line colour of the spectra correlates to the apatite colour in (b). d) Chondrite-normalised REY patterns for both CL zones. Colours correspond to CL in (b). There is some overlap in the zones, indicating only slight variations REY content.

The REY patterns for YN-50 apatite are concave downward with the apex of the curve near Gd, and a small negative Y anomaly (Fig. 3.10d). These patterns are similar in shape to those of magnetite-biotite dyke sample YW-61, but overall have a flatter shape and are not as HREE depleted (i.e., higher λ_2 and λ_3 than YW-61). Furthermore, the YN-50 apatite REY patterns also have a slight negative Eu anomaly. The light blue CL zones are slightly enriched in REY compared to the darker blue zones, but the differences are not as distinct when compared to other samples.

3.4.1.7 Alkaline amphibole-dolomite veinlet sample LRS-150

Apatite grains from the alkaline amphibole-dolomite veinlet (sample LRS-150; Fig. 3.11a) show a distinct CL colour transition from dark blue-violet cores to a bright red rims (Fig. 3.11b). This transition is also evident in BSE images as slightly brighter rim zones compared to the cores (Fig. 3.11a). The CL spectrum for the dark blue-violet cores displays a simple spectrum with one large broad peak from 2.0 eV to 3.5 eV (Fig. 3.11c). The red rims have more complicated spectra with multiple peaks (Table 3.2).

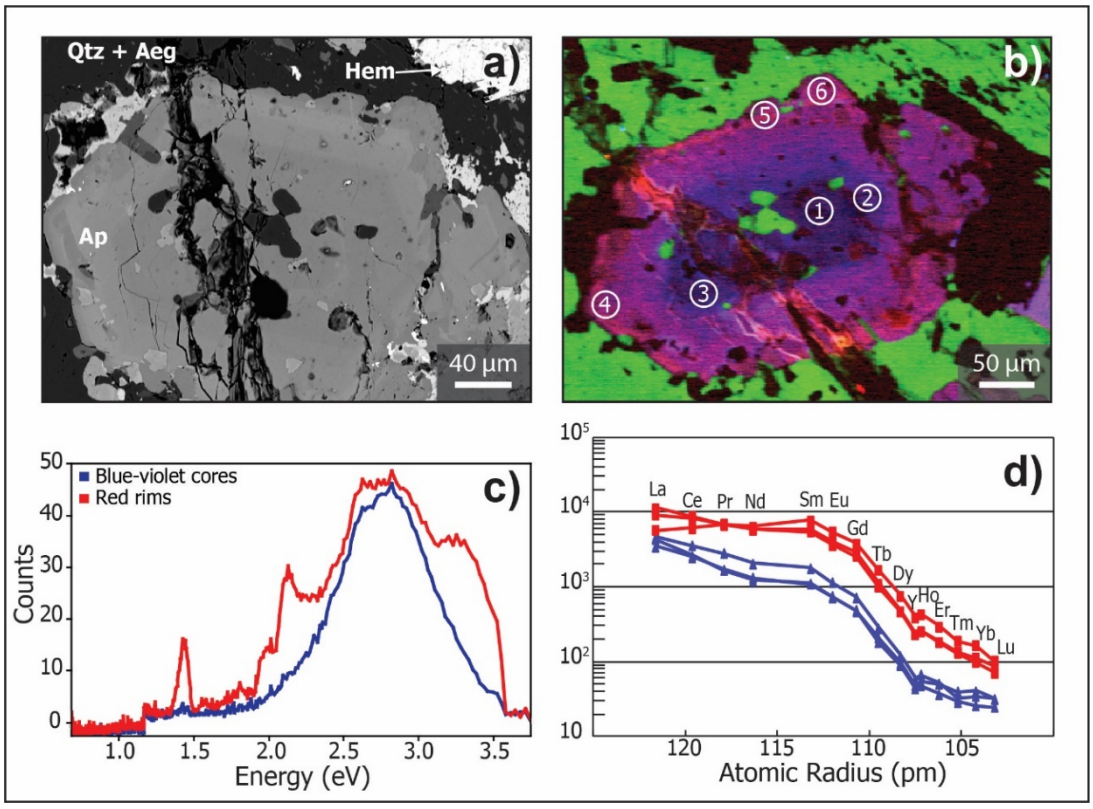

Figure 3.11 a) BSE images of apatite from the alkaline amphibole-dolomite veinlet sample (LRS-150; mineral abbreviations can be found in Table 3.1). b) Hyperspectral CL image of apatite depicting zonation from a dark blue-violet core to a brighter pink/red rim. Circles and numbers denote laser sampling location and sample number present in this image. Circles are actual spot size. c) CL spectra of the apatite in (b). The red/pink rims have many more peaks (e.g. 1.4 eV) compared to the darker, blue-violet core. The line colour of the spectra correlates to the apatite colour in (b). d) REY-normalised pattern for both CL. Colours correspond to CL in (b). The red rims are enriched in all REY compared to the darker blue-violet cores.

The REY patterns for both the red and blue-violet apatite zones are distinctively LREE rich and less concave (i.e., high λ_2; Fig. 3.4a) compared to other studied apatite samples. Despite the similar pattern shape, the red CL zones are more enriched in all REY compared to the blue-violet zones.

3.4.1.8 Fenite sample LE-1

Apatite grains in the fenitised granite sample LE-1 appear homogenous in their BSE signal (Fig. 3.12a), whereas two distinct types are apparent from CL imaging: rounded, green CL cores that are mantled by mottled pink and violet coloured apatite marked by fractures and occasional monazite inclusions (Fig. 3.12b). The green cores have simple CL spectra with one substantial peak from 2.0 eV to 2.5 eV. This peak (in green) is offset to the right from the distinct peak (in purple) at ~2.1 eV to ~2.2 eV. This 2.1 eV to 2.2 eV peak is often present in the bright

pink-red/violet apatite zones of LE-1 and other samples. The pink/violet mottled rims in sample LE-1 have more complex spectra with multiple, taller peaks (Fig. 3.12c; Table 3.2).

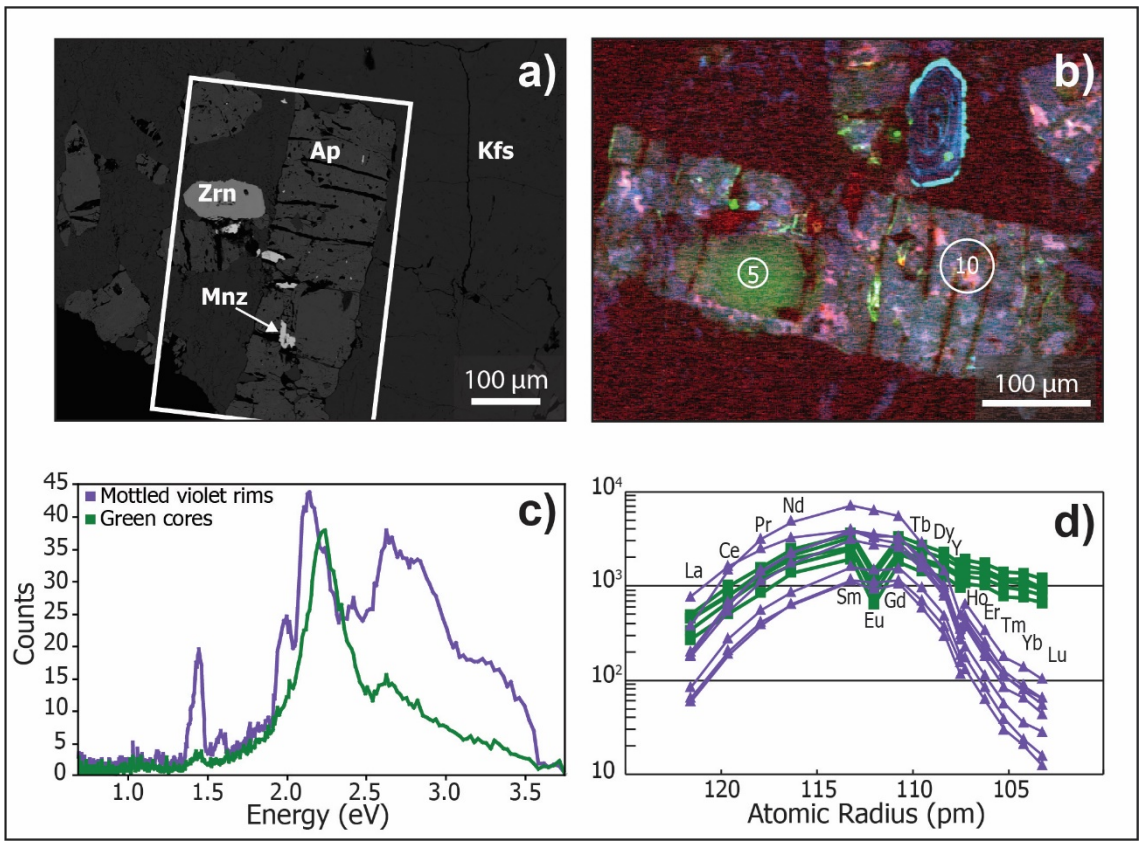

Figure 3.12 a) BSE images of apatite from the fenite sample (LE-1; mineral abbreviations can be found in Table 3.1). b) Hyperspectral CL image of A highlighting the green apatite core and the mottled pink and violet rims. Circles and numbers denote laser sampling location and sample number present in this image. Circles are actual spot size. c) CL spectra of the apatite in (b). The green core has fewer peaks and the main peak is offset to the right of the main peak from the pink and violet rims. The line colour of the spectra correlates to the apatite colour in (b). d) REY-normalised pattern for both CL zones. Colours correspond to CL in (b).The green core shows a much flatter pattern, enriched in HREE.

The two apatite domains have very different REY patterns. The green CL apatite cores have REY patterns that are atypical of other apatite examined in this study; they are enriched in HREE compared to the LREE, with a large, negative Eu anomaly (Fig. 3.12d) and relatively high λ_2 (Fig. 3.4a). The mottled CL pink/violet apatite rim zones have a concave downward REY patterns with an apex at Sm, no significant Eu anomaly, and a much more pronounced negative Y anomaly (Fig. 3.12d). These rims are also depleted in HREE compared to the green cores.

3.4.2 Other minor and trace elements

Average F contents of the analysed apatite range from 3.8 wt.% to 4.4 wt.% (at or above stoichiometric limit), and Cl was at or below detection limit (Appendix 3.A), which classifies all

samples as fluorapatite. These values are greater than the expected stoichiometric value of 3.77 wt.% but are consistent with previously reported fluorapatite compositions (Bühn et al., 2001; Luo et al., 2011; Chakhmouradian et al., 2017). REY contents negatively correlate with Ca + Sr (Fig. 3.13a), but show a positive correlation with Na content, with atomic Na to atomic (total) REY ratios near 1:1 (Fig. 3.13b). Apatite zones with brighter and more complex CL responses tend to have higher REY (and Na) contents. SiO_2 contents are below or near detection limits (approximately 0.01 wt.% to 0.05 wt.% SiO_2) in all samples except in the green apatite cores from LE-1, where the average SiO_2 value is 0.24 wt.% (Fig. 3.13c, Appendix 3.A).

Table 3.2 Summary of descriptions and peak intensities comprising the CL spectra of apatite domains. Peak width domains are compared relative to each other within each sample. Intensity is compared across samples. Darker shaded boxes are indicative of peak heights (i.e., intensity, with darker colours corresponding to tall peaks).

Sample	Rock type	Hyperspectral CL colour	1.16–1.22	1.35–1.48	1.53–1.63	1.75–1.85	1.9–2.03	2.05–2.2	2.05–2.37	2.2–2.44	2.44–3.1	2.3–3.6	2.5–2.7	3.1–3.6
DMCY-139	Magnetite-biotite dyke	Red cores	NP	NP	NP		NS	NP		WS	WP			WS
		Green rim	NP	NP	NP		NS	NP		NS	WP			
DMCY-138	Magnetite-biotite dyke	Pink rims	NP	NP	NP		NS	NP		WP	WP			WS
		Blue-violet cores	NP	NP			WS	WS				VWP		
FRS-4	Magnetite-biotite dyke	Pink zones	NP	NP	NP	WP	NP	NP		WP			NP	WP
		Blue zones		NP			WS	WS				VWP		WS
BH-224	Magnetite-biotite dyke	Pink core	NP	NP	NP		WS		WS			VWP		WS
		Indigo rim		NP			WS		WP		WP			
YW-61	Magnetite-biotite dyke	Light violet zones	NP	NP	NP	WP	NP	NP		NS	WP			WP
		Blue rims	NP	NP	WP		WP		NP		WP			WS
YN-50	Ankerite-siderite carbonatite	Light blue zones		NP			NS		NP		WP			WS
		Dark blue zones							WP		WP			
LRS-150	Alkaline amphibole-dolomite veinlet	Red rim	NP	NP	NP	WP	NS	NP			WP			WP
		Blue-violet core		NP								VWP		
LE-1	Fenite	Pink and purple rims	NP	NP	NP		NP	NP		NS	WP			WS
		Green cores		NP					NP				NP	

Note: W=wide, N= narrow, V = very, S = shoulder to a peak (i.e., "exposed" side peak), P = Peak

Strontium contents of the analysed apatite can reach up to 5 wt.% with samples from the south-east of the study area (LRS-150, DMCY-138, DMCY-139) having the highest Sr contents, and apatite cores from fenite sample LE-1 having the lowest Sr (Fig. 3.4b). Strontium shows a weak, positive correlation with LREE content and a negative correlation with λ_3 (Fig. 3.4c), but does not display any significant correlations with HREE. Within each sample, the bright CL zones contain Sr and the LREE in greater amounts than the dark CL zones. Lead, Ba, and LREE all have a moderate positive correlations, with the brighter CL zones (e.g., pinks and reds) typically having higher contents of these elements than the darker CL zones (e.g., dark blues and indigos). Thorium and Ba also show a positive correlation trend; however, the distinction between different CL zones is not apparent. Arsenic was near, or below, detection limits for all samples. Manganese did not correlate with any examined elements and overall contents were low except for the green-luminescing apatite cores in sample LE-1.

3.5 Discussion

3.5.1 Cathodoluminescence of apatite

Cathodoluminescence imaging has proved highly effective for identifying internal zonation and textural variations in luminescent minerals (Götze, 2012; Götze et al., 2013), as also demonstrated by the results for apatite in this study. The CL images reveal complex internal zonation in all of the examined apatite, even though many samples (DMCY-138, YW-61, FRS-4, and LE-1) show no significant variation in their BSE signals. Therefore, CL can be much more effective than BSE for imaging intra-grain chemical variations in apatite. Hyperspectral CL analysis, as used here, may provide yet more information on the chemical composition and lattice structure of apatite, provided the distinct features of CL spectra can be directly related to specific elemental or crystallographic features of apatite.

The CL spectral line is the total CL spectra combined over a range of wavelengths. In order to determine individual activators from a sample, the spectrum must be deconvoluted. Deconvolution involves transforming and scaling the spectra emitted by the sample from wavelength (nm) to energy (eV) using the Planck-Einstein relation:

$$E = \frac{hc}{\gamma} \qquad (5)$$

where E is energy, h is Planck's constant, c is the speed of light, and λ is wavelength. This transformation transposes and scales the x-axis allowing the spectra to be expressed as a sum of Gaussian distributions. Each of individual curves represents a probability of a luminescent center within the mineral, which allows identification of potential activators (Marshall, 1988; Townsend and Rowlends, 2000; Barbarand and Pagel, 2001; MacRae et al., 2013).

For many minerals, apatite being a preeminent example, a CL spectrum can be quite complicated as it involves multiple activators. For instance, in apatite, Eu^{3+}, Sm^{3+}, Pr^{3+}, and Mn^{2+} are all potential activators near 1.9 eV (Roeder et al., 1987; Gaft et al., 1998; 2015; Götze, 2000; Barbarand and Pagel, 2001). Some activators such as Nd^{3+} and Yb^{3+} do not share overlapping activation energies with other activators, making their presence in apatite easily discernable in CL spectra. Activators such as Ce^{3+} have a wide spread of activation energies. Some of these energy bands may overlap with many other possible activators (e.g., Ce^{3+} at 2.88 eV overlaps with Eu^{2+}, Yb^{2+}, and one band of intrinsic luminescence; Gaft et al., 1998; 2015; Dorenbos, 2003). Other energy bands may overlap with few or no other activators (e.g., Ce^{3+} at 3.39 eV is very close to Tm^{3+}at 3.40 eV but Ce^{3+} at 3.54 eV is alone; Gaft et al., 1998; Barbarand and Pagel, 2001). To further complicate matters, some REY within apatite may have a synergistic effect that causes other activators to increase in intensity (Waychunas, 2002). These overlapping bands make deconvolution of CL spectra in apatite better for some elements than others, particularly when examining natural samples. However, the peak interpretation can be assisted by trace element chemistry (especially REY), which is the approach taken in this study.

In the samples examined here, the apatite grains with pink, purple, and red (bright) colours all exhibit CL spectra with more peaks and with greater intensities than the CL spectra observed in the apatite with blue and indigo (dark) colours. In these brighter zones, the peaks at 1.16 eV to 1.22 eV and 1.35 eV to 1.48 eV can be attributed to Nd^{3+} (MacRae et al., 2013). The peak from 1.35 eV to 1.48 eV is actually a composite of two overlapping Gaussian distributions related to Nd^{3+} as specific energy bands at 1.364 eV, 1.393 eV, 1.403 eV, and as a range from

1.40 eV to 1.44 eV (see Fig. 3.3 as an example of overlap). The small peaks at 1.16 eV to 1.22 eV have distribution curves that suggest that the peak is also caused by the Nd^{3+} energy bands at 1.161 eV and 1.163 eV (Table 3.3; Gaft et al., 1998; 2015; Kempe and Götze, 2002).

Many of the bright zones also exhibit a distinct peak from 1.53eV to 1.63eV as well as a "shoulder" from 1.9 eV to 2.03 eV. The peak from 1.53 eV to 1.63 eV has a probability distribution related to Sm^{3+} (Table 3.3), which has a known band at 1.55 eV (Kempe and Götze, 2002). The shoulder at 1.9 eV to 2.03 eV has a distribution that is likely related to Eu^{3+} and/or Mn^{2+}, but it may also be affected and/or related to Sm^{3+} and Pr^{3+}, which also have energy bands near that location (Table 3.3; Roeder et al., 1987; Gaft et al., 1998; 2015; Götze, 2000, Barbarand and Pagel, 2001). There is a notable increase in intensity of the peak(s) in the region between 2.5 eV and 3.0 eV in the bright pink, purple, and red zones. There are many activators in this area such as Ce^{3+}, Dy^{3+}, Eu^{2+}, Tb^{3+}, Tm^{3+}, UO_2^{2+}, as well as several intrinsic luminescence bands (Table 3.3; Portnov and Gorobets, 1969; Mariano and Ring, 1975; Marshall, 1988; Gaft et al.,1998; Götze, 2000; Barbarand and Pagel, 2001; Kempe and Götze, 2002; Dorenbos, 2003; Czaja et al., 2010; 2013; Gaft et al., 2015). Due to the significant overlap of activators in this spectral region, it is difficult to determine the specific REE responsible for luminescence.

Table 3.3 Summary of discernable CL activators and their emission peak locations in apatite from this study.

Activator	Peak Location (eV)
Ce^{3+}	2.5–3.0, 3.1–3.6
Pr^{3+}	1.9–2.03
Nd^{3+}	1.16–1.22, 1.35–1.48
Sm^{3+}	1.53–1.63, 1.9–2.03
Eu^{2+}	2.5–3.0
Eu^{3+}	1.9–2.03
Tb^{3+}	2.5–3.0
Dy^{3+}	2.5–3.0
Tm^{3+}	2.5–3.0, 3.1–3.6
Mn^{2+}	1.9–2.03, 2.22
UO_2^{2+}	2.5–3.0
Intrinsic	3.1–3.6

The shoulder from 3.1 eV to 3.6 eV consists of several overlapping Gaussian distributions that may be attributed to Ce^{3+}, Tm^{3+}, and/or an intrinsic luminescence (Table 3.3). These activators have energy band locations at 3.263 eV, 3.397 eV, 3.444 eV, and 3.542 eV for Ce^{3+}; 3.406 eV and 3.416 eV for Tm^{3+}; and 3.289 eV for the intrinsic luminescence (Portnov and Gorobets, 1969; Gaft et al., 1998; 2015; Barbarand and Pagel, 2001; Kempe and Götze, 2002).

The darker CL apatite rim zones (blue and indigo) tend to have simpler spectra overall, with only one or two large peaks (e.g., YN-50 dark blue zone in Fig. 3.10b and LRS-150 blue zone in Fig. 3.11b). However, the peaks are located in spectral regions with the most activator overlap (2.0 eV to 3.0eV). Attempts to deconvolute these spectra result in fewer Gaussian curves than in the brighter red zones. Nevertheless, the curves have a much wider distribution that captures multiple CL activators, resulting in similar difficulties in deciphering specific activators.

The green apatite cores from the fenite sample LE-1 have a main peak centered at 2.22 eV, which is shifted to slightly higher energies relative to the peak at 2.03 eV to 2.17 eV (Fig. 3.12c) observed in the pink/violet rims. As previously mentioned, this region contains multiple REE activators in addition to Mn^{2+} (Mariano and Ring, 1975; Marshall, 1988; Gaft et al., 1998; 2015; Götze, 2000; Kempe and Götze, 2002). However, this peak shift is interpreted to be the result of Mn^{2+} exhibiting greater influence on the CL spectra than the REE in this region, as the trace element data collected in this study shows that the green-luminescing CL cores in the fenitic apatite contain more Mn than the other samples in this study (Fig. 3.4d; Appendix 3.B).

Overall, apatite domains with higher CL counts across the spectra (i.e., brighter CL signals) tend to have higher overall REE contents (or λ_0 of O'Neill 2016), which means that hyperspectral CL analysis can be used as a qualitative tool for determining relative REE contents between apatite domains.

3.5.2 Element substitution mechanisms in apatite

Using Chapter 3's geochemical dataset, this section evaluates likely mechanisms of trace element substitution in apatite. The Si content is quite low for most of the apatite samples, and there is a clear positive relationship between REY and Na (Fig. 3.13b), as well as a negative

correlation between REY and Ca. These features support REY incorporation in apatite by the reaction $REY^{3+} + Na^{+} = 2Ca^{2+}$, rather than through the substitution mechanism $REY^{3+} + Si^{4+} = Ca^{2+} + P^{5+}$ (Fig. 3.13c; Portnov and Gorobets, 1969; Rønsbo, 1989; Hughes et al., 1991; Fleet and Pan, 1995; Mitchell et al., 1997). Some compositions fall above the 1:1 line for (atomic) REY versus Na, indicating that other substitution mechanisms may also be responsible for incorporating REY into the apatite structure. No correlation between REY and F was observed, which indicates that the reaction $REY^{3+} + O^{2-} = Ca^{2+} + F$ is unlikely to be important in this case. Instead, it is suggested that the reaction $2REY^{3+} + \square = 3Ca^{2+}$ (Fig. 3.13c; Pan and Fleet, 2002) may account for the additional REY substitution in nearly all the samples (except the apatite cores in LE-1; see below). Other minor mechanisms may also account for some REY substitution in apatite, but evaluation of these mechanisms is beyond the scope of this study.

The green apatite cores in fenite sample LE-1 contain higher SiO_2 and lower Na_2O and Sr values than the other analysed apatite. These samples also plotted above the 1:1 line in atomic REY versus Na space (Fig. 3.13b), and hence have excess REY compared to Na. With high SiO_2 contents, it is suggested that the reaction $REY^{3+} + Si^{4+} = Ca^{2+} + P^{5+}$ plays a role in REY incorporation in these apatite cores.

Roeder et al., (1987) and Rønsbo (1989) established that silica activity and alkalinity of fluid can affect REY incorporation into precipitating apatite. For example, in a silica-saturated system, the reaction $REY^{3+} + Si^{4+} = Ca^{2+} + P^{5+}$ will be the dominant mechanism of REE substitution in apatite, whereas in a silica-undersaturated, alkaline system, $REY^{3+} + Na^{+} = 2Ca^{2+}$ will be the dominant REY substitution mechanism. In this study, most of the examined grains are from ankerite-siderite carbonatites and magnetite-biotite dykes, which are alkaline melts (or fluids) with low silica activity. These apatite grains contain low Si and incorporate REY primarily via the substitution by $REY^{3+} + Na^{+} = 2Ca^{2+}$. The apatite cores from the fenite, LE-1 are interpreted to be relict apatite grains from the granitic host rock (see below), and hence originally formed from silica-saturated granitic melt. In this case, the $REY^{3+} + Si^{4+} = Ca^{2+} + P^{5+}$ substitution plays an important role in REY incorporation into apatite. If these findings are more generally applicable, then Na-Si-REY systematics of apatite may be used to evaluate the chemical

environment from which the apatite crystallised, and may therefore be a powerful provenance-tracing tool.

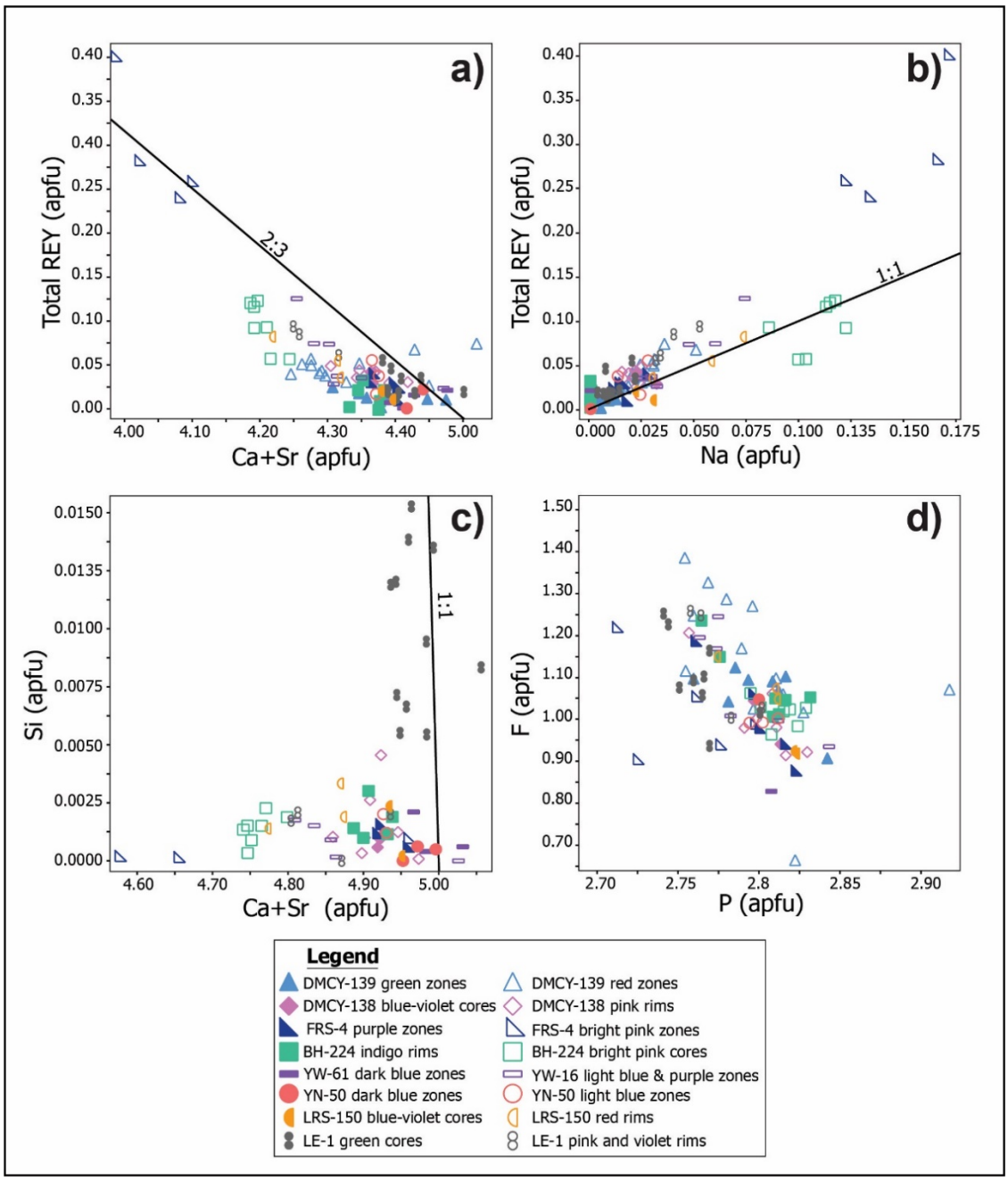

Figure 3.13 a) Atomic Ca + Sr versus atomic total REE + Y (REY) of apatite compositions. The 2:3 slope for some samples (e.g., FRS-4) suggests some REY incorporation via a $2REY^{3+} + \square = 3Ca^{2+}$ mechanism. b) Atomic Na versus atomic total REE + Y (REY) for apatite samples examined in this study. Compositions that plot close to the 1:1 line indicate REY incorporation into apatite via a $REY^{3+} + Na^{+} = 2Ca^{2+}$ substitution. Compositions plotting above the 1:1 line require an additional REY substitution mechanism. c) Atomic Ca + Sr versus atomic Si of apatite compositions. All samples have low Si contents, except the core zones of apatite from fenite sample LE-1. d) Atomic F versus atomic P of apatite compositions. The negative slope suggests that F and another anion (possibly CO_3^{2-} due to the carbonatite association) are substituting for PO_4^{3-}. This may account for the excess F (>1.0 *apfu*) measured in apatite in this study. Atomic formula unit values are presented in Appendix 3.A.

The high Sr content is a commonly observed characteristic of apatite from peralkaline and carbonatitic rocks. Strontium, Ba, and Pb are divalent, and thus can substitute for Ca without charge balance issues (Pan and Fleet, 2002 and references therein, Chakhmouradian et al., 2002). Thorium correlates with these 2+ ions as well as the LREE and may be substituting for Ca via the process $Th^{4+} + \square = 2Ca^{2+}$ (Hughson and Sen Gupta, 1964; Baumer et al., 1983; Pan and Fleet, 2002).

Based on the general apatite formula [$Ca_5(PO_4)_3(OH,Cl,F)$], the end member fluorapatite is able to accommodate about 3.77 wt.% F (1.0 *apfu*) into "channel sites" dictated by the PO_4^{3-} tetrahedron and the $Ca(I)O_9$ and $Ca(II)O_6$ polyhedra (Hughes et al., 1989; 1990). The incorporation of F^- is usually at the expense of Cl^- and/or OH^-. Fluorine values above the presumed stoichiometric limit of 3.77 wt.% may be due to F incorporation into sites other than the nominal fluorine site of apatite. The coupled substitution of $F^- + CO_3^{2-} = PO_4^{3-}$ (Binder and Troll, 1989; Fleet and Liu, 2008; Yi et al., 2013) is supported by the negative correlation between F and P_2O_5 in Figure 3.13d, and therefore is proposed to account for the high F values in the apatite analyses.

3.5.3 Composition and origin of apatite in the GCCC

The CL imaging and chemical analysis reveal multiple generations of apatite present in alkaline magmatic/hydrothermal rocks from across the GCCC. These features are consistent with other reports of multiphase apatite from alkaline igneous rocks and REE ore deposits (Kempe and Götze, 2002; Schoneveld et al., 2015; Chakhmouradian et al., 2017; Song et al., 2018). Chakhmouradian *et al*. (2017) describes several different cases to explain core-rim compositional variations within apatite from carbonatites: 1) precipitation of different, non-phosphate mineral phases within a magma that cause re-saturation of apatite within the melt, creating REY-rich apatite rims; 2) hydrothermal fluid alteration of apatite either by in situ alteration or dissolution/re-precipitation onto existing grains, and; 3) multiple intrusions of alkaline melt that precipitates re-equilibrated apatite onto the pre-existing cores.

The zoning features of the GCCC apatite are a cryptic record of apatite crystallisation and recrystallisation: Some zones in the grain interiors with regular or oscillatory zoning can be

ascribed to original magmatic apatite, while the mottled or irregular rims and zones are likely to have formed via subsequent (and possibly multiple) recrystallisation events related to later hydrothermal or magmatic activity. In many cases, a hydrothermal origin for the apatite rim zones can be inferred based on textural features (e.g., mottled textures) and the presence of hydrothermal quartz and Fe-oxides (± K-feldspar, ± aegirine) in fractures and pores in apatite.

The concept of multiple events forming different generations of apatite is consistent with the protracted (>300 m.y.) geological history of the GCCC (Slezak and Spandler, 2016; Zi et al., 2017) that records the effects of an assortment of regional-scale tectonic events including the 1320 to 1170 Ma Mutherbukin Tectonic Event (Korhonen et al., 2015), the c. 1076 Ma Warakurna Large Igneous Province (Wingate et al., 2004), and the 1030 to 950 Ma Edmundian Orogeny (Sheppard et al., 2007). It is proposed that initial magmatism, followed by metamorphism or hydrothermal activity associated with these events is responsible for forming the multiple apatite domains in the samples.

Despite these complexities, there are some commonalities in apatite between samples. Apatite from most samples feature convex down REY pattern (or negative λ_2 values: Fig. 3.4a), with relatively low HREE contents, a notable negative Y anomaly, and a very small to negligible Eu anomaly (Figs. 3.5-12). This convex down pattern (negative λ_2) is consistent with the apatite/carbonatite melt partition coefficients that favour the middle REE over both LREE and HREE (Klemme and Dalpé, 2003). At first, the depleted LREE patterns appear anomalous given these rocks lie within a LREE ore field, but all analysed apatite samples, except sample LRS-150, coexist with abundant monazite, which preferentially sequesters the LREE and is the dominant ore mineral of the GCCC. Only apatite from hydrothermal vein sample LRS-150 is enriched in LREE, and this sample only contains very rare monazite. Most of the samples are magnetite-biotite dykes, which have not previously been reported from the GCCC and are described in Chapter 3. Some of the distinctive features of apatite from the magnetite-biotite dykes are shared by apatite from the carbonatite (concave REY pattern, Y anomaly; Fig. 3.10d), which may be evidence to support direct genetic links between these rock units.

A more detailed evaluation of REY and other trace elements from this sample set reveals some systematic differences between samples. The REY patterns for DMCY-139 and DMCY-138 (Figs. 3.5d and 3.6d, respectively) both exhibit sinusoidal shapes (for both CL defined zones), giving distinctly lower λ_3 values, but somewhat higher λ_2 values compared to other samples (Fig. 3.4a). The alkaline amphibole-dolomite veinlet sample (LRS-150; Fig. 3.11) also has relatively high λ_2 (Fig. 3.4a). All three samples are enriched in Sr and Mn, and they have lower Gd/Ce compared to the other samples (Fig. 3.4b-d). These three samples were collected from the southeast of the study area (Fig. 3.1), and, together with the spatial variation observed in ore composition (Fig. 3.2), are interpreted to reflect primary compositional variations in the alkaline magmatic rocks across the GCCC. The origin of this spatial variation in chemistry is examined in detail using bulk rock geochemical and isotopic data (Chapters 2 and 4; Slezak and Spandler, 2019).

Apatite grains from fenite sample LE-1 have notably different CL spectra and REY patterns. The dark green apatite core zones have simple CL spectra that suggest Mn^{2+} is also key activator. The trace element composition of these apatite crystals is quite distinct from all other samples: they are relatively enriched in HREE, Mn, and Si (Figs. 3.12d, 3.4d, 3.13c, respectively), depleted in Sr (Fig. 3.4b,c), and have distinct negative Eu anomalies. These cores lack the more complex multi-peak CL spectra and negative Y anomalies observed for most other apatite samples examined in this study. The REY pattern with the negative Eu anomaly of the green apatite is characteristic of apatite crystallised from a granitic melt in which apatite and feldspar crystallised from the same melt (Möller and Muecke, 1984; Sha and Chappell, 1999). The high SiO_2 content is consistent with apatite crystallised from silica-saturated magma (Rønsbo, 1989; Sha and Chappell, 1999). By contrast, the negative Y anomaly and HREE depletion in the mottled bright pink/violet apatite that envelopes the green apatite is consistent with a carbonatite-magnetite-biotite dyke origin for these apatite rims as documented in this study (Figs. 3.5 to 3.10) and in Chakhmouradian et al. (2017). The zoning in these apatite grains is interpreted to be the result of crystallisation of apatite related to alkaline magmatism (i.e., fenitisation) preferentially onto pre-existing apatite of the granitic protolith. This complex grain history is not made apparent from

optical microscope or BSE imaging, which further highlights the value of hyperspectral CL imaging as a petrographic tool to guide micro-scale geochemical analysis, such as using LA-ICP-MS.

3.6 Applications

Apatite is common in many rock types and forms in many geological environments, and can incorporate a large range of trace elements that can be used for petrogenetic tracing and geochronology. However, apatite is also reactive to hydrothermal processes, and recrystallisation may not be immediately apparent from routine petrographic analysis. Techniques such as optical or monochromatographic CL provide researchers with the ability to identify alteration, growth zoning, and multiple generations in luminescent minerals, such as apatite. More advanced methods, such as hyperspectral CL mapping combined with elemental micro-analysis, hold even greater promise for understanding igneous and hydrothermal histories of rocks, or for provenance studies that use "out of context" minerals, such as detrital components of sediments or sedimentary rocks (e.g., Morton, 1991). For example, apatite grains in fenite samples LE-1 comprise two domains each with distinct CL spectra and chemical compositions that are interpreted to have formed from two very different sources (granitic and carbonatitic), as described above.

These techniques may also be used to improve understanding of ore systems and hence, assist mineral exploration efforts. Despite the broad similarities in the CL spectra and composition of most apatite samples analysed here, apatite collected from the southeast and east of the GCCC (Demarcay and Fraser's, respectively) could be distinguished from the apatite in Bald Hill and Yangibana in the north and northwest (Fig. 3.1). This spatial distinction is also seen in the REY tenor of ore samples from the region (Fig. 3.2), with the more sought-after Nd-rich ores (i.e., high Nd/La) found in the southeast. This coincidence of apatite and bulk ore chemistry across the region strongly indicates that the distinct REY compositions of the ores are inherited from protolithic igneous and hydrothermal rocks, rather than being a product of ironstone-forming weathering and alteration processes. In this case, analysis of apatite from suitable indicator rocks

for mineralisation (carbonatites, magnetite-biotite dykes) may aid in targeting the most prospective areas for exploration.

Accurate identification of different mineral generations and origins may also be crucial for guiding further in situ analysis such as Sm–Nd, Rb–Sr, and/or U–Pb isotope measurments for age dating and source tracing (e.g., De Paolo, 1981). This is particularly relevant for REE-rich minerals such as apatite and monazite, as these minerals can now be analysed in situ for their Sm-Nd isotope composition via LA-MC-ICP-MS (Fisher et al., 2011). Samarium–Nd isotope values determined for coexisting mineral phases, or rocks, can be used for age determinations provided that the minerals (or rocks) were crystallised at the same time from a source with uniform isotopic composition, and provided that isotopic ratios were not disturbed by subsequent metamorphic and hydrothermal events.

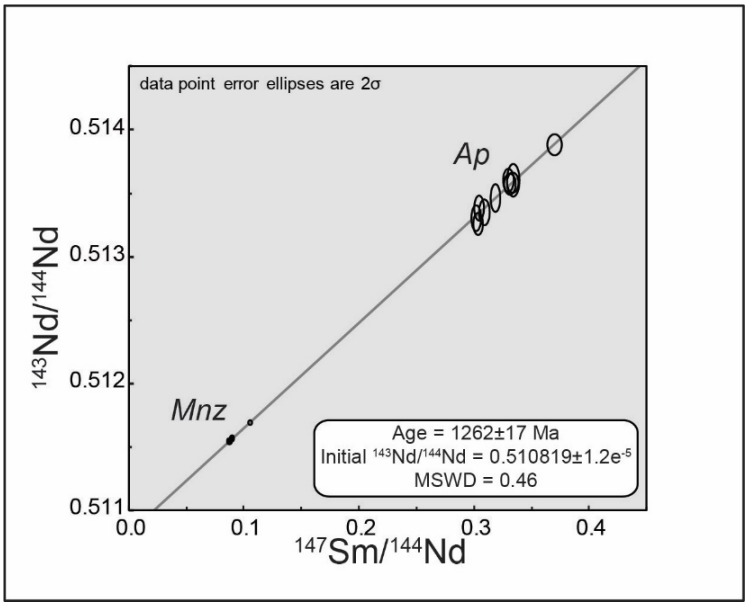

Figure 3.14 Sm-Nd isochron for sample YN-50 using isotopic data obtained in situ from coexisting apatite and monazite.

In this study, apatite and monazite from carbonatite sample YN-50 were interpreted to be co-genetic, based on their textural relationship, trace element content and CL signatures (Fig. 3.10). The inferred contemporaneous formation and contrasting Sm/Nd ratio of these two minerals makes them well suited for Sm–Nd isochron dating via in situ micro-scale Sm–Nd isotope analyses. Guided by micro-textural features of these minerals, in situ Sm–Nd isotope analyses of monazite and apatite from YN-50 was conducted following the methodology of Hammerli et al., (2014). The analyses produced an isochron age of 1262 ± 17 Ma (Fig. 3.14),

which is in agreement with the U-Pb age of 1250 ± 15 Ma for monazite from the same sample (Chapter 4; Slezak and Spandler, 2019), and previous age determinations for the GCCC (c. 1370; Zi et al., 2017, Slezak and Spandler, 2019; Chapter 4). This consistency of age determinations demonstrates the utility of in situ Sm–Nd isotope microanalysis of REE minerals for dating, provided co-genetic mineral phases can be accurately identified. This latter point is most effectively achieved with the aid of micro-textural/micro-chemical characterisation of REE minerals, such as that outlined in this paper.

3.7 References

Barbarand, J., Pagel, M., 2001. Cathodoluminescence study of apatite crystals. American Mineralogist 86, 473-484.

Baumer, A., Caruba, R., Bizzouard, H., Peckett, A., 1983. Chlorapatite de synthesis: substitution et inclusions de Mn, Ce, U et Th traces. Canadian Mineralogist 21, 567-573.

Binder, G., Troll, G., 1989. Coupled anion substitution in natural carbon-bearing apatites. Contributions to Mineralogy and Petrology 101, 394-401.

Bühn, B., Wall, F., Le Bas, M.J., 2001. Rare-earth element systematics of carbonatitic fluorapatites and their significance for carbonatite magma evolution. Contributions to Mineralogy and Petrology 141, 572-591.

Chakhmouradian, A.R., Reguir, E.P., Mitchell, R.H., 2002. Strontium-apatite: new occurrences and the extent of Ca-Sr substitution in apatite-group minerals. Canadian Mineralogist 40, 121-136.

Chakhmouradian, A.R., Reguir, E.P., Zaitsev, A.N., Coueslan, C., Xu, C., Kynicky, J., Mumin, A.H., Yang, P., 2017. Apatite in carbonatitic rocks: compositional variation, zoning, element partitioning and petrogenetic significance. Lithos 274-275, 188-213.

Cherniak, D.J., 2000. Rare earth element diffusion in apatite. Geochimica et Cosmochimica Acta 64, 3871-3885.

Czaja, M., Bodyl, S., Lisiecki, R., Mazurak, Z., 2010. Luminescence properties of Pr^{3+} and Sm^{3+} ions in natural apatite. Physics and Chemistry of Minerals 37, 425-433.

Czaja, M., Bodyl-Gajowska, S., Mazurak, Z., 2013. Steady-state luminescence measurement for qualitative identification of rare earth ions in minerals. Journal of Mineralogical and Petrological Sciences 108, 47-54.

De Paolo, D.J., 1981. Neodymium isotopes in the Colorado Front Range and crust-mantle evolution in the Proterozoic. Nature 291, 193-196.

Dorenbos, P., 2003. Anomalous luminescence of Eu^{2+} and Yb^{2+} in inorganic compounds. Journal of Physics: Condensed Matter 15, 2645-2665.

Edwards, P.R., Lee, M.R., 2014. Cathodoluminescence hyperspectral imaging in geoscience, Cathodoluminescence and its application to geoscience. Mineralogical Association of Canada, Quebec, pp. 29-45.

Edwards, P.R., Martin, R.W., Lee, M.R., 2007. Combined cathodoluminescence hyperspectral imaging and wavelength dispersive X-ray analysis of minerals. American Mineralogist 92, 235-242.

Fisher, C.M., McFarlane, C.R.M., Hanchar, J.M., Schmitz, M.D., Sylvester, P.J., Lam, R., Longerich, H.P., 2011. Sm-Nd isotope systematics by laser ablation-multicollector-inductively coupled plasma mass spectrometry: methods and potential natural and synthetic reference materials. Chemical Geology 284, 1-20.

Fleet, M.E., Liu, X., 2008. Accommodation of the carbonate ion in fluorapatites synthesized at high pressure. American Mineralogist 93, 1460-1469.

Fleet, M.E., Pan, Y., 1995. Site preference of rare earth elements in fluorapatite. American Mineralogist 80, 329-335.

Gaft, G., Reisfeld, R., Panczer, G., 2015. Modern luminescence spectroscopy of minerals and materials, 2nd ed. Springer Mineralogy, Cham, Switzerland, 606 p.

Gaft, M., Reisfeld, R., Panczer, G., Blank, P., Boulon, G., 1998. Laser-induced time-resolved luminescence of minerals. Spectrochimica Acta 54, 2163-2175.

Goldoff, B., Webster, J.D., Harlov, D.E., 2012. Characterization of fluor-chlorapatites by electron probe microanalysis with a focus on time-dependent intensity variation of halogens. American Mineralogist 97, 1103-1115.

Götze, J., 2000. Materials characterisation by cathodoluminescence microscopy and spectroscopy, Proceedings of the Sixth International Congress on Applied Mineralogy in Research, Economy, Technology, Ecology and Culture, Gottingen, Germany, pp. 783-786.

Götze, J., 2012. Application of cathodoluminescence microscopy and spectroscopy in geosciences. Microscopy and Microanalysis 18, 1270-1284.

Götze, J., Schertl, H.P., Neuser, R.D., Kempe, U., Hanchar, J.M., 2013. Optical microscope-cathodoluminescence (OM-CL) imaging as a powerful tool to reveal internal textures of minerals. Mineralogy and Petrology 107, 373-392.

Guillong, M., Meier, D.L., Allan, M.M., Heinrich, C.A., Yardley, B.W.D., 2008. SILLS: a MATLAB-based program for the reduction of laser ablation ICP-MS data of homogenous materials and inclusions in: Sylvester, P. (Ed.), Laser ablation ICP-MS in the Earth Sciences: current practices and outstanding issues. Mineralogical Association of Canada, Vancouver, BC, pp. 328-333.

Hammerli, J., Kemp, A.I.S., Spandler, C., 2014. Neodymium isotope equilibration during crustal metamorphism revealed by in situ microanalysis of REE-rich accessory minerals. Earth and Planetary Science Letters 392, 133-142.

Harlov, D.E., 2015. Apatite: a fingerprint for metasomatic processes. Elements 11, 171-176.

Harlov, D.E., Förster, H.J., 2003. Fluid-induced nucleation of (Y+REE)-phosphate minerals within apatite: nature and experiment. Part II. Fluorapatite. American Mineralogist 88, 1209-1229.

Harrowfield, I.R., MacRae, C., Wilson, N.C., 1993. Chemical imaging in electron microprobes, Proceedings of the 27th Annual Microbeam Analysis Society (MAS) Meeting, pp. 547-548.

Hughes, J.M., Cameron, M., Crowley, K.D., 1989. Structural variations in natural F, OH, and Cl apatites. American Mineralogist 74, 870-876.

Hughes, J.M., Cameron, M., Crowley, K.D., 1990. Crystal structures of natural ternary apatites: solid solution in the $Ca_5(PO_4)_3X$ (X=F,OH,CL) system. American Mineralogist 75, 295-304.

Hughes, J.M., Cameron, M., Mariano, A.N., 1991. Rare-earth-element ordering and structural variations in natural rare-earth-bearing apatites. American Mineralogist 76, 1165-1173.

Hughes, J.M., Rakovan, J., 2015. Structurally robust, chemically diverse: apatite and apatite supergroup minerals. Elements 11, 165-170.

Hughson, M.R., Sen Gupta, J.G., 1964. A thorian intermediate member of the britholite-apatite series. American Mineralogist 49, 937-951.

Kempe, U., Götze, J., 2002. Cathodoluminescence (CL) behavior and crystal chemistry of apatite from rare-metal deposits. Mineralogical Magazine 66, 151-172.

Klemme, S., Dalpé, C., 2003. Trace-element partitioning between apatite and carbonatite melt. American Mineralogist 88, 639-646.

Korhonen, F.J., Johnson, S.P., Fletcher, I.R., Rasmussen, B., Sheppard, S., Muhling, J.R., Dunkley, D.J., Wingate, M.T.D., Roberts, M.P., Kirkland, C.L., 2015. Pressure-temperature-time evolution of the Mutherbukin Tectonic Event, Capricorn Orogen: Geological Survey of Western Australia, Report 146, p. 64.

Luo, Y., Gao, S., Longerich, H.P., Gunter, D., Wunderli, S., Yuan, H.-L., Liu, X.-M., 2007. The uncertainty budget of the multi-element analysis of glasses using LA-ICP-MS. Journal of Analytical Spectrometry 22, 122-130.

Luo, Y., Rakovan, J., Tang, Y., Lupulescu, M., Hughes, J.M., Pan, Y., 2011. Crystal chemistry of Th in fluorapatite. American Mineralogist 96, 23-33.

MacRae, C., Wilson, N.C., Torpy, A., 2013. Hyperspectral cathodoluminescence. Mineralogy and Petrology 107, 429-440.

MacRae, C., Wilson, N.C., Torpy, A., Davidson, C.J., 2012. Hyperspectral cathodoluminescence imaging and analysis extending from ultraviolet to near infrared. Microscopy and Microanaysis 18, 1239-1245.

MacRae, C.M., Wilson, N.C., 2008. Luminescence database I - minerals and materials, Microscopy and Microanalysis. Cambridge University Press, Cambridge, U.K., pp. 184-204.

MacRae, C.M., Wilson, N.C., Johnson, S.A., Phillips, P.L., Otsuki, M., 2005. Hyperspectral mapping-combining cathodoluminescence and X-ray collection in an electron microprobe. Microscopy Research and Technique 67, 271-277.

Mariano, A.N., Ring, P.J., 1975. Europium-activated cathodoluminescence in minerals. Geochimica et Cosmochimica Acta 39, 649-660.

Marshall, D.J., 1988. Cathodoluminescence of geological materials. Unwin Hyman, Boston.

McCubbin, F.M., Steele, A., Nekvasil, H., Schnieders, A., Rose, T., Fries, M., Carpenter, P.K., Jolliff, B.L., 2010. Detection of structurally bound hydroxyl in fluorapatite from Apollo Mare basalt 15058,128 using TOF-SIMS. American Mineralogist 95, 1141-1150.

McDonough, W.F., Sun, S.s., 1995. The composition of the Earth. Chemical Geology 120, 223-253.

Mitchell, R.H., Xiong, J., Mariano, A.N., Fleet, M.E., 1997. Rare-earth-element-activated cathodoluminescence in apatite. The Canadian Mineralogist 35, 979-998.

Möller, P., Muecke, G.K., 1984. Significance of Europium anomalies in silicate melts and crystal-melt equilibria: a review. Contributions to Mineralogy and Metrology 87, 242-2850.

Morton, A.C., 1991. Geochemical studies of detrital heavy minerals and their application to provenance research, in: Morton, A.C., Todd, S.P., Haughton, P.D.W. (Eds.), Developments in Sedimentary Provenance Studies. Geological Society Special Publications, London, pp. 31-45.

Nelson, B.K., De Paolo, D.J., 1985. Rapid production of continental crust 1.7 to 1.9 b.y. ago: Nd isotopic evidence from the basement of the North American mid-continent. Geological Society of America Bulletin 96, 746-754.

O'Neill, H.S.C., 2016. The smoothness and shapes of chondrite-normalized rare earth element patterns in basalts. Journal of Petrology 57, 1463-1508.

Pagel, M., Barbin, V., Blanc, P., Ohnenstetter, D., 2000. Cathodoluminescence in geosciences: an introduction, in: Pagel, M., Barbin, V., Blanc, P., Ohnenstetter, D. (Eds.), Cathodoluminescence in Geoscience. Springer, Berlin, pp. 1-21.

Pan, Y., 1997. Zircon- and monazite-forming metamorphic reactions at Manitouwadge, Ontario. Canadian Mineralogist 35, 105-118.

Pan, Y., Fleet, M.E., 2002. Compositions of the apatite-group minerals: substitution mechanisms and controlling factors, in: Kohn, B.P., Rakovan, J., Hughes, J.M. (Eds.), Phosphates - Geochemical, Geobiological, and Materials Importance. Mineralogical Society of America, Washington, D.C., pp. 13-49.

Pan, Y., Fleet, M.E., MaCRae, N.D., 1993. Oriented monazite inclusions in apatite porphyroblasts from the Hemlo gold deposit, Ontario, Canada. Mineralogical Magazine 57, 697-707.

Pearson, J.M., 1996. Alkaline rocks of the Gifford Creek Complex, Gascoyne Province, Western Australia: their petrogenetic and tectonic significance, Department of Geology and Geophysics. University of Western Australia, p. 219.

Pearson, J.M., Taylor, W.R., Barley, M.E., 1996. Geology of the alkaline Gifford Creek Complex, Gascoyne Complex, Western Australia. Australian Journal of Earth Sciences 43, 299-309.

Pettke, T., Oberlie, F., Audétat, A., Guillong, M., Simon, A.C., Hanley, J.J., Klemm, L.M., 2012. Recent developments in element concentration and isotope ratio analysis of individual fluid inclusions by laser ablation single and multiple collector ICP-MS. Ore Geology Reviews 44, 10-38.

Pirajno, F., González-Álvarez, I., Chen, W., Kyser, K.T., Simonetti, A., Leduc, E., leGras, M., 2014. The Gifford Creek Ferrocarbonatite Complex, Gascoyne Province, Western Australia: Associated fenitic alteration and a putative link with the ~1075 Ma Warakurna LIP. Lithos 202–203, 100-119.

Pyle, J.M., Spear, F.S., Wark, D.A., 2002. Electron microprobe analysis of REE in apatite, monazite, and xenotime: protocalls and pitfalls, in: Kohn, M.J., Rakovan, J., Hughes, J.M. (Eds.), Phosphates - Geochemical, Geobiological, and Materials Importance. Mineralogical Society of America, pp. 337-362.

Roeder, P.L., MacArthur, D., Ma, X., Palmer, G.R., Mariano, A.N., 1987. Cathodoluminescence and microprobe study of rare-earth elements in apatite. American Mineralogist 72, 801-811.

Rønsbo, J.G., 1989. Couple substitutions involving REEs and Na and Si in apatites in alkaline rocks from the Ilimaussag intrusion, South Greenland and the petrological implications. American Mineralogist 74, 896-901.

Schoneveld, L., Spandler, C., Hussey, K., 2015. Genesis of the central zone of the Nolans Bore rare earth element deposit, Northern Territory, Australia. Contributions to Mineralogy and Petrology 170, 1-22.

Sha, L.-K., Chappell, B.W., 1999. Apatite chemical composition, determined by electron microprobe and laser-ablation inductively coupled plasma mass spectrometry, as a probe into granite petrogenesis. Geochimica et Cosmochimica Acta 63, 3861-3881.

Sheppard, S., Johnson, S.P., Wingate, M.T.D., Kirkland, C.L., Pirajno, F., 2010. Explanatory notes for the Gascoyne Province: Geological Survey of Western Australia, p. 336.

Sheppard, S., Rasmussen, B., Muhling, J.R., Farrell, T.R., Fletcher, I.R., 2007. Grenvillian-aged orogenesis in the Palaeoproterozoic Gascoyne Complex, Western Australia: 1030-950 Ma reworking of the Proterozoic Capricorn Orogen. Journal of Metamorphic Geology 25, 477-494.

Slezak, P., Spandler, C., 2016. Age and origin of the Yangibana LREE deposit and associated ferrocarbonatites, Gascoyne Province, Western Australia, Goldschmidt 2016. Geochemical Society, Yokohama, Japan, June 26-July 1, p. 2888.

Slezak, P. and Spandler, C. 2019. Carbonatites as recorders of mantle-derived magmatism and subsequent tectonic events: An example of the Gifford Creek Carbonatite Complex, Western Australia. Lithos, 328-329, 212-227.

Song, W., Xu, C., Smith, M.P., Chakhmouradian, A.R., Brenna, M., Kynicky, J., Chen, N., Yang, Y., Deng, M., Tang, H., 2018. Genesis of the world's largest rare earth element deposit, Bayan Obo, China: Protracted mineralization evolution over ~1b.y. Geology 46, 323-326.

Spandler, C., Pettke, T., Rubatto, D., 2011. Internal and external fluid sources for eclogite-facies veins in the Monviso meta-ophiolite, Western Alps: Implications for fluid flow in subduction zones. Journal of Petrology 52, 1207-1236.

Stormer, J., J.C., Pierson, M.L., 1993. Variation of F and Cl X-ray intensity due to anisotropic diffusion and electron microprobe analysis of apatite: An addendum. American Mineralogist Supplemental Data.

Stormer, J., J.C., Pierson, M.L., Tacker, R.C., 1993. Variation of F and Cl on X-ray intensity due to anisotropic diffusion in apatite during electron microprobe analysis. American Mineralogist 78, 641-648.

Torpy, A., Wilson, N.C., 2008. OpticalFit Software by CSIRO Australia.

Townsend, P.D., Rowlands, A.P., 2000. Information encoded in cathodoluminescence emission spectra, in: Pagel, M., Barbin, V., Blanc, P., Ohnenstetter, D. (Eds.), Cathodoluminescence in Geosciences. Springer, Germany, pp. 41-57.

Waychunas, G.A., 2002. Apatite luminescence, in: Kohn, M.J., Rakovan, J., Hughes, J.M. (Eds.), Phosphates - Geochemical, Geobiological, and Materials Importance. Mineralogical Society of America, Washington, D.C., pp. 701-742.

Whitney, D.L., Evans, B.W., 2010. Abbreviations for names of rock-forming minerals. American Mineralogist 95, 185-187.

Wingate, M.T.D., Pirajno, F., Morris, P.A., 2004. Warakurna large igneous province: A new Mesoproterozoic large igneous province in west-central Australia. Geology 32, 105-108.

Yi, H., Balan, E., Gervais, C., Segalen, L., Fayon, F., Roche, D., Person, A., Morin, G., Guillaumet, M., Blanchard, M., Lazzeri, M., Baboneau, F., 2013. A carbonate-fluoride defect model for carbonate-rich fluorapatite. American Mineralogist 98, 1066-1069.

Zi, J.W., Gregory, C., Rasmussen, B., Sheppard, S., Muhling, J.R., 2017. Using monazite geochronology to test the plume model for carbonatites: The example of Gifford Creek Carbonatite Complex, Australia. Chemical Geology 463, 50-60.

Chapter 4

Carbonatites as Recorders of Mantle-derived Magmatism and Subsequent Tectonic Events: An Example of the Gifford Creek Carbonatite Complex, Western Australia

Abstract

The Gifford Creek Carbonatite Complex (GCCC), Western Australia contains a diverse suite of alkaline igneous rocks, including dolomite carbonatites, ankerite-siderite carbonatites, magnetite-biotite dykes, fenites, glimmerites, silica-rich alkaline veins, and ironstones. This study employs U–Pb, Sm–Nd, and Lu–Hf radiogenic isotope techniques on monazite, apatite, and zircon to determine the origin, age, and history of the GCCC.

Zircon crystals in glimmerite alteration selvages adjacent to ankerite-siderite carbonatites exhibit pyramidal crystal morphologies, εHf(*t*) values of -1.8 to -4.3, high Th/U, and variable Zr/Hf, all of which are likely indicative of carbonatitic zircon sourced from an enriched mantle component. Uranium–Pb dating of these zircons returned a crystallisation age of c. 1370 Ma for the GCCC. Monazite hosted in the ankerite-siderite carbonatites, magnetite-biotite dykes, and fenite alteration assemblages yielded variable U–Pb ages ranging from c. 1250 Ma to 815 Ma. Samarium–Nd isochrons determined from coexisting monazite and apatite gave dates between c. 1310 Ma to c. 1190 Ma, but all with similar initial $^{143}Nd/^{144}Nd$ values of 0.51078 – 0.51087.

The c. 1370 Ma age of the GCCC does not correspond to any known mantle plume activity, but does broadly correlate with the separation of known break-up events in supercontinent Nuna. The monazite and apatite εNd(*t*) data illustrate that the multiple younger U–Pb monazite and Sm–Nd isotope isochron dates do not record multiple magmatic emplacement events, but rather represent in situ partial recrystallisation/resetting of REE-bearing minerals during the protracted tectonic history of the Western Australia Craton from c. 1300 Ma to 815 Ma, and its involvement in the breakup of Nuna and assembly and disassembly of Rodinia.

The age variability in the U–Pb and the Sm–Nd isotope systems in monazite and apatite reveal that tectonically-induced hydrothermal alteration can contribute to the isotopic resetting of phosphate minerals. This isotopic resetting, if properly identified, can be used as a thorough geochronological record of tectonism affecting alkaline igneous complexes after initial magmatic emplacement.

4.1 Introduction

Carbonatites are uncommon igneous rocks that contain >50% primary carbonate minerals (Le Maitre, 2000). Owing to their mantle origins, carbonatites are excellent recorders of mantle processes, mantle sources (Bell and Simonetti, 2010), and the tectonic processes that allow their emplacement in the crust (Woolley and Bailey, 2012). Therefore, the preserved carbonatite record has the potential to provide information on mantle upwelling and/or tectonic processes through time. This record may be particularly beneficial for understanding the Proterozoic Era, as Proterozoic carbonatites and their associated rock types are found in many cratons (Woolley and Bailey, 2012) where other evidence of contemporary mantle magmatism may be lacking. As well as their petrological significance, carbonatite complexes are prospective for metals, such as LREE, Nb, Ta, and Zr in addition to other commodities such as P and Fe (Mariano, 1989).

To fully exploit the petrological, tectonic, and mineralogical record of carbonatites, accurate temporal constraints on carbonatite formation are needed. However, carbonatite complex geochronology has been problematic and the subject of debate in the literature. Efforts to date prominent rare metal-bearing carbonatite complexes using different dating methods have returned significant age discrepancies. For instance, Bayan Obo, the world's largest REE deposit, has been repeatedly dated using different methods (e.g., $^{40}Ar/^{39}Ar$, Rb–Sr, Re–Os, U–Pb, Th–Pb, Sm–Nd, La–Ba) over the last 25 years, with each radiogenic system returning different ages, ranging from mid Proterozoic to Devonian (Le Bas et al., 2007; Yang et al., 2011; Zhu et al., 2015; Yang et al., 2017; Song et al., 2018). The southern Canadian Cordillera carbonatites include fourteen carbonatite bodies, several of which, such as the Upper Fir carbonatites, are prospective for Nb and Ta resources (Mitchell et al., 2017). Efforts to date these complexes using U–Pb zircon analyses produced discordant data with upper intercept dates denoting events at 800 – 700 Ma, c.500 Ma, and c.360 – 340 Ma; however, there is a significant spread in dates obtained from different zones within the same zircon grains (Millonig et al., 2012). Dating of the Cummins Range Carbonatite (Australia) returned a range of dates including c. 1040 to 1000 Ma (U–Pb on zircon; Downes et al., 2016), c. 1010 Ma (Pb–Pb on zirconolite; Downes et al., 2016), 905 Ma

(Rb–Sr isochron; Sun et al., 1986), and c.900 – 590 Ma (U–Th–Pb on monazite; Downes et al., 2016).

In many cases, the large range in dates for carbonatites is interpreted to represent post-emplacement modification or resetting of carbonatite minerals including the accessory phase chronometers (Downes et al., 2016; Song et al., 2018). On a provincial scale, Woolley and Bailey (2012) argue that the multiple ages for carbonatites are due to repeated episodes of carbonatite magmatism caused by changes in plate-wide stress regimes. This scenario would imply that carbonatites are not exclusively associated with deep seated mantle plumes (Bell and Simonetti, 2010), but rather represent the products of reactivation of crustal weak zones, allowing upwelling of low degree melts from the subcontinental lithospheric mantle (SCLM; Woolley and Bailey, 2012). Similar debates are ongoing around the origin and significance of kimberlites and other mantle-derived alkaline rocks (Tappe et al., 2017). Despite the ambiguity in dating carbonatites and their origins, many of these complexes contain abundant REE, U, and/or Th-bearing accessory phases amenable for age determination and isotope tracking (e.g., zircon and monazite).

Zircon and monazite are the most widely used accessory phases for U–Pb dating of geologic events. They contain significant U and Th contents and low common Pb, and are retentive of U and Pb diffusion at high temperatures (i.e., 900°C to 1000°C; Parrish, 1990; Harrison et al., 2002; Cherniak and Watson, 2003; Cherniak et al., 2004; Cherniak, 2010). In addition, zircon is mechanically durable and contains significant amounts of Hf and low Lu, which also make it an excellent mineral for Lu–Hf isotope analysis (Thirlwall and Walder, 1995). Unlike zircon, monazite does not become metamict due to radiation damage, but it may develop domains with discrete ages through the processes of dissolution-reprecipitation (Seydoux-Guillaume et al., 2002; 2004; Rasmussen and Muhling, 2007, Rasmussen et al., 2007). Being a REE-bearing phosphate, monazite (together with apatite) is also suitable for in situ Sm–Nd isotope analysis via LA-MC-ICP-MS (Foster and Vance, 2006; McFarlane and McCulloch, 2007; Fisher et al., 2011).

The Gifford Creek Carbonatite Complex (GCCC) in Western Australia is a Proterozoic carbonatite complex. It sits in the Proterozoic rocks of the Gascoyne Province. The Gascoyne

Province records over 1 b.y. of tectonism and connects the Archean Pilbara and Yilgarn cratons to form the West Australia Craton. The GCCC comprises a diverse suite of alkaline rock types, and is endowed with significant LREE phosphate mineralisation, which makes up the Yangibana LREE district (Chapter 5). The complex falls into the long lived carbonatite complex category, with previously determined ages spanning 400 m.y. (Pirajno et al., 2014; Zi et al., 2017). These previous studies have largely focused on dating the dominant alkaline igneous rock unit – the Lyons River Sills – leaving many other alkaline magmatic units undated. These rocks contain a suite of minerals that are amenable to isotope analysis including carbonatitic zircon, monazite, and apatite. This study has been conducted to analyse Sm–Nd, U–Pb, and Lu–Hf in accessory/minor minerals from multiple alkaline rock types to better constrain the formation history and evolution of the GCCC. The emplacement of the complex has been affirmed and the evolution of the complex has been extended. It has also been demonstrated that the GCCC was not created by multiple magmatic events but rather formed via one initial magmatic event and was reworked or recrystallised by subsequent tectonic events.

4.2 Regional Geology and Geologic History

The Gascoyne Province records the suturing of the Archean-aged rocks of the Pilbara Craton, Glenburgh Terrane, and Yilgarn Craton to form the Western Australia Craton as well as over 1 b.y. of re-working through seven known orogenic events, resulting in seven different tectonic zones (Johnson et al., 2017). These tectonic zones include (from south to north): the Errabiddy Zone, Paradise Zone, Mooloo Zone, Mutherbukin Zone, Limejuice Zone, Mangaroon Zone (in which the study area is located), and the Boora Boora Zone (Fig. 4.1; Johnson et al., 2013). The first of multiple orogenic events that led to the formation of Gascoyne Province (Table 4.1) was the collision of the Archean Pilbara Craton with the Neoarchean Glenburgh Terrane. This collisional/accretionary event occurred during the 2215 to 2145 Ma Ophthalmia Orogeny (Rasmussen et al., 2005; Johnson et al., 2011). The Lyons River Fault is the suture zone between these two terranes (Fig. 4.1; Johnson et al., 2013). Collision of the combined Pilbara-Glenburgh block with the Archean Yilgarn Craton followed during the 2005 to 1950 Ma Glenburgh Orogeny,

forming the Western Australia Craton (Occhipinti et al. 2004, Sheppard et al., 2004; Johnson et al., 2011). The suture zone between the Yilgarn and the Pilbara-Glenburgh is interpreted as the Cardilya Fault (Johnson et al., 2013). The 1820 to 1770 Ma Capricorn Orogeny saw extensive crustal reworking and the emplacement of the 1820 to 1775 Ma Moorarie Supersuite.

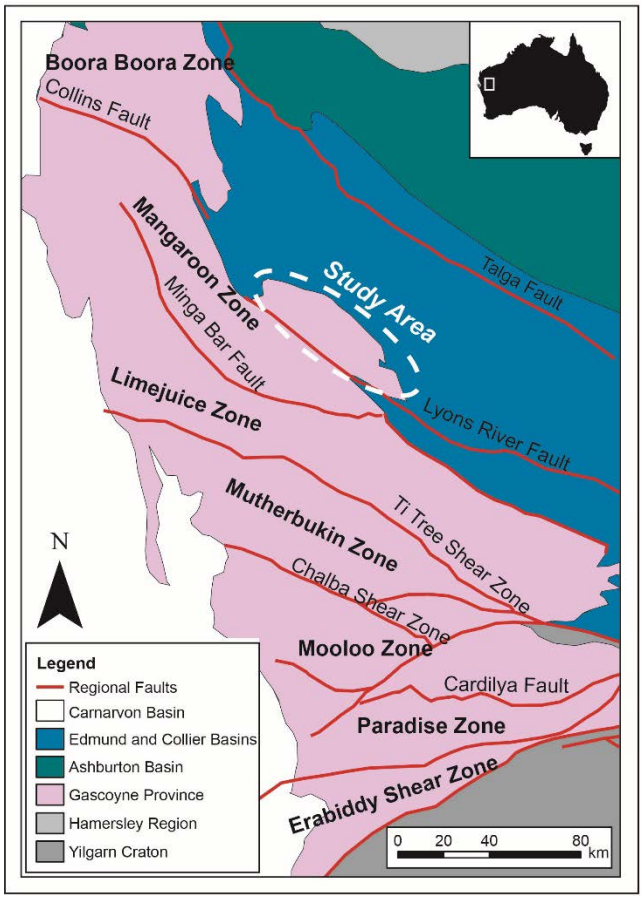

Figure 4.1 Regional geologic map of the Gascoyne Province (Western Australia). The Gascoyne Province is divided into seven tectonic zones, each bounded by major faults. The Lyons River Fault and Cardilya Fault have been traced to the Moho using seismic reflection surveys (Johnson et al., 2013).

The 1690 to 1620 Ma Mangaroon Orogeny was responsible for emplacement of the granitic Durlacher Supersuite, amphibolite-facies metamorphism, and deformation of sedimentary units that now comprise the Pooranoo Metamorphics (Sheppard et al., 2005). The Gascoyne Province underwent metamorphism and fault reactivation during the 1320 to 1170 Ma Mutherbukin Tectonic Event (Korhonen et al., 2015). The region experienced greenschist-facies metamorphism during the 1030 to 955 Ma Edmundian Orogeny (Martin and Thorne, 2004; Sheppard et al., 2007) as well as fault reactivation and hydrothermal alteration related to the c. 955 to 830 Ma Kuparr Tectonic Event (Cutten and Johnson, 2018; Piechocka et al., 2018;

Olierook et al., 2018). Most recently, the Gascoyne Province underwent regional brittle faulting and fault reactivation during the c. 570 Ma Mulka Tectonic Event (Johnson et al., 2013).

Table 4.1 Tectonic history of the Gascoyne Province, Western Australia.

Orogenic Event	Age (Ma)	Immediate Cause	References
Ophthalmia Orogeny	2215–2145	Collision between the Pilbara Craton and Glenburgh Terrane. Suture is the Lyons River Fault.	Rasmussen et al. (2005), Johnson et al. (2011; 2013)
Glenburgh Orogeny	2005–1950	Collision between the Pilbara-Glenburgh craton and the Yilgarn Craton to create the Western Australia Craton. Suture is at the Cardilya Fault.	Occhipinti et al. (2004), Sheppard et al. (2004), Johnson et al. (2013)
Capricorn Orogeny	1820–1770	Intracontinental reworking due to far-field stresses from the West Australia-North Australian craton collision (Nuna assembly)	Sheppard et al. (2010a), Johnson et al. (2017)
Mangaroon Orogeny	1690–1620	Intracontinental extension, rifting, and magmatism possibly due to far-field stresses relating to West, North, and South Australia cratonic assembly	Sheppard et al. (2005), Johnson et al. (2013), this study
Mutherbukin Tectonic Event	1320–1170	Crustal thickening and transpression correlates with other orogenic events along the margins of the Western Australia Craton related to the break-up of Nuna	Korhonen et al. (2015)
Edmundian Orogeny	1030–950	Intracontinental reworking (i.e., compression followed by extension), possibly caused by oblique collision of Proterozoic Australia with other terrane(s)	Sheppard et al. (2007)
Kuparr Tectonic Event	955–830	Intracontinental reworking related, in part, to Rodinia disassembly	Cutten and Johnson (2018), Olierook et al. (2018)
Mulka Tectonic Event	c. 570	Intracontinental reworking due to assembly of Gondwana	Sheppard et al. (2010b)

4.3 Geology of the Gifford Creek Carbonatite Complex

The GCCC comprises a series of alkaline magmatic dykes and sills that crop out along the northeastern margin of the Mangaroon Zone within the Gascoyne Province (Fig. 4.1). The alkaline rocks intrude the granitic rocks of the Mesoproterozoic Durlacher Supersuite as well as the pelitic schists, arkosic schists, gneisses, and migmatites of the older Pooranoo Metamorphics (Fig. 4.2). The northwest striking Lyons River Fault bounds the GCCC to the south. Metasedimentary units belonging to the Mesoproterzoic Edmund Group lie unconformably on the Durlacher Supersuite at the northern margin of the GCCC. These metasedimentary rocks are also intruded by the GCCC alkaline dykes (Pearson, 1996; this study). The Bald Hill Lineament

runs subparallel to the Lyons River Fault and separates massive, dextrally-sheared granitic rocks in the northern region from the complex assortment of schists, granites, and alkaline dykes in the southern region (Fig. 4.2; Pearson 1996; Pearson et al., 1996). The southern area hosts anatectic granitic pods within metamorphic units, schlieric granites, and an abundance of carbonatitic dykes from the GCCC (Pearson, 1996; Pearson et al., 1996; Sheppard et al., 2005).

Four main rock types comprise the GCCC (Fig. 4.2): 1) the Lyons River Sills (LRS), 2) magnetite-biotite dykes, 3) ankerite-siderite carbonatites, and 4) silica-rich alkaline veins. Additional phases are found within the complex include: 1) alkaline amphibole-dolomite veinlets emanating from the dolomite carbonatites; 2) highly oxidised "ironstones" hosting significant LREE mineralisation of economic interest; and 3) alteration assemblages consisting of glimmerites and fenites – the altered wall rocks (mainly granite and metasediments) caused by alkaline fluids emitted from the ankerite-siderite carbonatites.

The Lyons River Sills (LRS) are a swarm of dolomite and calcite carbonatite dykes and sills (0.2 to 2 m thick) that run subparallel to the Lyons River Fault in the southern GCCC (Fig. 4.2). The LRS comprise fine-grained dolomite to Fe-bearing dolomite, subordinate Mg-bearing calcite and minor amounts of either aegirine (green dykes/sills) or arfvedsonite altering to riebeckite (blue dykes/sills). Both varieties contain fine-grained magnetite altering to hematite, ilmenite, variable apatite, and trace monazite. Mg-rich biotite is present in some samples, but is not ubiquitous in the LRS. Occasionally, the LRS exhibit weak porphyritic textures, but the porphyroblasts are completely altered to iron oxides (Pearson et al., 1996).

Most magnetite-biotite dykes occur in the southeast region of the GCCC, but there are also magnetite-biotite dykes located in the northwest corner of the complex (Fig. 4.2). These units occur as dykes and sills. They range from 0.1 to 1.5 m in thickness, extend for several hundreds of meters in length, and are coarse-grained with seriate to equigranular textures (Slezak et al., 2018). They consist of coarse biotite of annite-phlogopite composition, magnetite partially altered to hematite, apatite, and monazite.

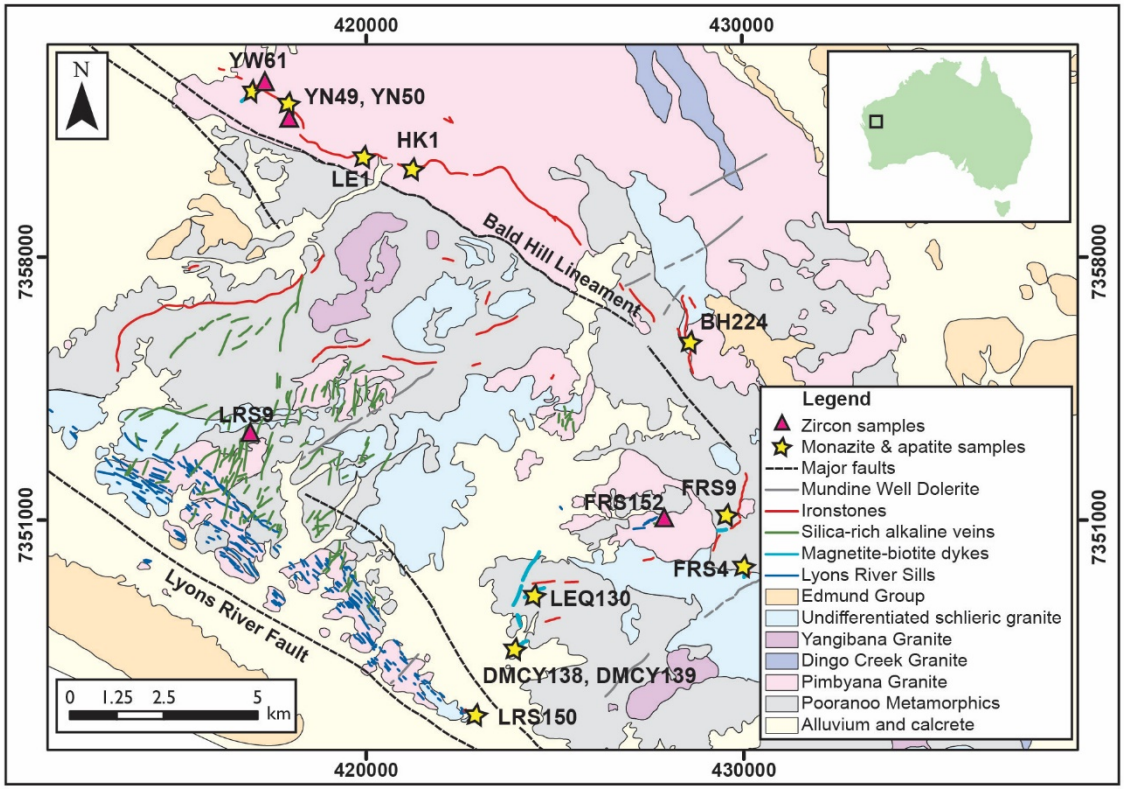

Figure 4.2 Geologic map of the Gifford Creek Carbonatite Complex with marked zircon, apatite, and monazite sample locations (modified after Slezak et al., 2018).

The ankerite-siderite carbonatites have, to date, only been identified from the subsurface below the ironstones along the Bald Hill Lineament (Fig. 4.2) and at the Fraser's deposit (FRS9 in Fig. 4.2). The extent of the ankerite-siderite carbonatites is not well resolved due to non-exposure, but they typically express as 0.1 to 2 m thick dykes in drill core. Large, macro-crystalline siderite with lesserr ankerite inclusions and accessory calcite make up the ankerite-siderite carbonatites. Within the large carbonate realms there are small quartz-biotite-magnetite domains that contain large euhedral monazite and apatite, with monazite crystals growing across the silica-carbonate boundaries. In addition, small biotite-magnetite veins occasionally containing trace pyrite and chalcopyrite cross cut the carbonate minerals (Slezak et al., 2018).

The silica-rich alkaline veins are magmatic-hydrothermal veins that strike perpendicular to the LRS in the south-central and central regions of the GCCC (Fig. 4.2). These rarely exceed 1 metre in width, but can be several hundred of metres in length. The silica-rich alkaline veins comprise fine-grained aegirine, magnetite, quartz, and zircon, with minor amounts of phlogopite, riebeckite, Nb-bearing rutile, columbite, and very rarely, trace monazite (Chapter 2).

Also present in the GCCC are other minor magmatic-hydrothermal phases including small veinlets (1 to 5 cm in width), which are exuded from the LRS. Fibrous rutile and riebeckite, in addition to magnetite and dolomite, make up these veinlets. Apatite and minor amounts of monazite are also present in small concentrations.

At surface, the ironstones comprise the LREE deposits (Fig. 4.2) and are an alteration phase. They consist mainly of fine-grained Fe oxides, Fe hydroxides (e.g., hematite and goethite), amorphous silica, and minor Mn oxides (Pirajno and González-Álvarez, 2013). The also contain monazite, though it can fractured and partially altered to rhabdophane.

Glimmerites are present immediately adjacent to the ankerite-siderite carbonatite dykes as small veins, crackle breccia infill, and occasionally as pervasive alteration halos in the metamorphic and granitic country rock. The glimmerites consist of biotite, magnetite, zircon, and are considered to be products of carbonatitic fluids reacting with the granitic host rocks. Fenites are alteration assemblages that envelope all the previously discussed rock types and alteration. They consist of K-feldspar, apatite, monazite, hematite, and occasionally minor fine-grained quartz. The extent of fenitisation is proportional to the size of their associated intruding bodies (i.e., veins have millimeter to centimeter-scale fenite halos, dykes/sills have decimeter to meter-scale fenite halos; Slezak et al., 2018).

4.4 Previous Geochronological Work on the GCCC

Previous work on the GCCC by Pearson (1996) produced multiple, poorly constrained U–Pb ages and was inconclusive as to the precise age of carbonatite magmatism. However, Pearson (1996) did determine a c.1690 Ma crystallisation age for the Durlacher Supersuite granitic rocks that host the complex, as well as a zircon $^{207}Pb/^{206}Pb$ age of c.1360 Ma obtained from a fenitised granite sample. Pirajno et al. (2014) analysed several LRS samples and reported U–Pb ages of 1073 ± 35 Ma for apatite and 1050 ± 24 Ma for monazite. These authors suggested a connection between the formation of the LRS and 1075 Ma Warakurna Large Igneous Province (LIP), relating the LRS to mantle plume activity. Zi et al. (2017) analysed monazite from several LRS carbonatite and fenite samples from Pearson's 1996 PhD study, obtaining multiple monazite

U–Th–Pb SHRIMP ages spanning c.1360 Ma to 900 Ma and concluding that the GCCC did not form because of the Warakurna LIP mantle plume activity. These authors demonstrated that the GCCC is a long lived carbonatite complex, and suggested that the range of monazite dates may reflect episodic monazite growth related to tectonic or magmatic events that affected the GCCC.

The ankerite-siderite carbonatites, magnetite-biotite dykes, and fenites are major hosts for monazite and apatite where as the silica-rich alkaline veins and glimmerites contain appreciable levels of zircon. Combined textural constraints and isotopic dating of these minerals helps to resolve the temporal evolution not only of the LRS, but of all of the rock-types in the GCCC.

4.5 Analytical Techniques

All samples were prepared as polished thin sections and 25 mm diameter polished pucks and examined using a Leica DMRXP optical microscope. Selected samples were subsequently examined using backscattered electron (BSE) imaging and energy dispersive spectrometry (EDS) using a JEOL-JXA8200 super probe at the Advanced Analytical Centre (AAC) at James Cook University (JCU), Townsville, Australia. The samples were then analysed in situ by laser ablation ICP-MS at the AAC at JCU.

4.5.1 Trace element analysis

Trace element analysis of zircon was conducted using a Coherent GeoLasPro 193nm Excimer laser coupled to a Varian (now Bruker) 820-MS quadrupole ICP-MS. Laser spot sizes varied from 24 to 44 μm depending on the size of the desired target. Samples were ablated in a large volume cell (Fricker et al., 2011) using a repetition rate of 10 Hz and surface energy density (measured at the site of ablation) of 6 J/cm^2. The ablated material was carried in high purity He gas then mixed with Ar before being introduced to the ICP-MS. The rate of oxide production and plasma fractionation were monitored by keeping ThO/Th at, or below, 0.5% and keeping $^{238}U/^{232}Th$ sensitivity ≈ 1 (Pettke, 2008). The synthetic glasses NIST SRM 610 and 612 were used as the primary and secondary standards, respectively, with reference values taken from Spandler et al. (2011). Stoichiometric Zr (43.14 wt.%) was used for internal standardisation. Data reduction

was carried out using the SILLS program (Guillong et al., 2008) with uncertainties and detection limits calculated in SILLS using the methods from Luo et al. (2007) and Pettke et al. (2012), respectively. The following isotopes were chosen for analysis: ^{7}Li, ^{23}Na, ^{24}Mg, ^{27}Al, ^{29}Si, ^{31}P, ^{43}Ca, ^{44}Ca, ^{49}Ti, ^{53}Cr, ^{55}Mn, ^{57}Fe, ^{66}Zn, ^{75}As, ^{85}Rb, ^{88}Sr, ^{89}Y, ^{90}Zr, ^{93}Nb, ^{118}Sn, ^{133}Cs, ^{137}Ba, ^{139}La, ^{140}Ce, ^{141}Pr, ^{143}Nd, ^{147}Sm, ^{151}Eu, ^{157}Gd, ^{159}Tb, ^{163}Dy, ^{165}Ho, ^{167}Er, ^{169}Tm, ^{171}Yb, ^{175}Lu, ^{178}Hf, ^{181}Ta, ^{208}Pb, ^{232}Th, and ^{238}U.

4.5.2 In situ U–Pb isotope analysis

Zircon mineral separates and monazite grains, either in thin sections or in polished rock sample pucks, were analysed in situ for U–Pb isotopes using the same set up as described for the trace element analysis, except spot sizes of 24 µm, 32 µm, and 44 µm were used for zircon and monazite. Data were collected for ^{29}Si, ^{90}Zr, ^{202}Hg, ^{204}Pb, ^{206}Pb, ^{207}Pb, ^{208}Pb, ^{232}Th, ^{235}U, and ^{238}U for zircon. For monazite, ^{31}P was substituted for ^{29}Si and ^{90}Zr. Due to the use of high purity He and Ar gases with a gold trap placed in the carrier gas line before the inlet into the sample cell, ^{202}Hg was always below the detection limit (in the gas background and during mineral ablation). Data reduction was conducted using Iolite v3.5 (Hellstrom et al., 2008; Paton et al., 2010; 2011). Age calibration and instrumental drift were monitored by analysis of GJ1 zircon (Jackson et al., 2004) and Manangotry monazite (Horstwood et al., 2003) as primary standards. The 91500 (Wiedenbeck et al., 1995) and FC1 zircons (Paces and Miller, 1993) and the Namaqualand (Liu et al., 2012) and Bananeira monazites (Gonçlaves et al., 2016) were used as secondary zircon and monazite standards, respectively. Standards were analysed at the beginning and end of each session as well as after analyses of 10 unknowns. To account for discordance and common Pb, the results were plotted in Isoplot/Ex 4.15 (Ludwig, 2009) using Tera-Wasserburg Concordia plots (Tera and Wasserburg, 1972; Jackson et al., 2004). The secondary zircon standards, 91500 and FC1, returned ^{206}Pb/^{238}U weighted mean dates of 1056 ± 5.6 Ma and 1114 ± 16 Ma, respectively, which agrees reasonably well with the reference ages of 1065.4 ± 0.3 Ma for 91500 (Wiedenbeck et al., 1995) and 1099 ± 0.6 Ma for FC1 (Paces and Miller, 1993). The Bananeira monazite returned a ^{206}Pb/^{238}U weighted mean date of 505 ± 2.4 Ma within uncertainty of the

reference age of 507.7 ± 1.3 Ma (Gonçlaves et al., 2016). The Namaqualand monazite returned a $^{206}Pb/^{238}U$ weighted mean date of 1029.4 ± 4.2 Ma in agreement with its reference age of c.1033 Ma (Knoper et al., 2000; Hokada and Motoyoshi, 2006).

4.5.3 Mineral Sm–Nd isotope analysis

In situ Sm–Nd isotope analysis of monazite and apatite was undertaken at the AAC, JCU, using a Coherent GeoLasPro 193nm Excimer laser ablation system coupled with a Thermo-Scientific NEPTUNE MC-ICP-MS. The NEPTUNE Faraday cup configuration is the same set up used by McFarlane and McCulloch (2007) with interference and mass bias corrections made according to Fisher et al. (2011). Laser spot sizes were 24 μm for monazite and between 44 and 60 μm for apatite. Each analysis consisted of data acquisition for 60s on background, 60s data acquisition, and a 60s washout time between analyses. Samples were ablated in a large volume cell (Fricker et al., 2011) using a repetition rate of 4 Hz and surface energy density (measured at the site of ablation) of 4 J/cm^2. The ablated material was carried via He gas (flow rate of 2.5 l/min) to a bulb with a volume of 2.5 cm^3 where it was mixed with Ar (flow of 0.95 l/min) and N_2 (0.01 l/min) before being carried to the MC-ICP-MS. A synthetic LREE-doped glass (ID-TIMS; $^{147}Sm/^{144}Nd = 0.2451 \pm 7$) and a Nd-doped glass (JNdi-1; ID-TIMS $^{143}Nd/^{144}Nd = 0.512098 \pm 13$) were used as primary standards to monitor and correct for drift in unknown $^{147}Sm/^{144}Nd$ and $^{143}Nd/^{144}Nd$ values (Fisher et al., 2011). This chapter's results for JNdi-1 glass are $^{143}Nd/^{144}Nd = 0.512091 \pm 15$ (n = 28) and for LREE glass are $^{147}Sm/^{144}Nd = 0.2442 \pm 2$ (n = 28), agreeing with the ID-TIMS results from Fisher et al. (2011) of 0.512098 and 0.2451, respectively. As a quality control measure, Otter Lake apatite and Mae Klang monazite were used as secondary standards. The results for Otter Lake apatite (n = 24; $^{143}Nd/^{144}Nd = 0.511908 \pm 23$ and $^{147}Sm/^{144}Nd = 0.0807 \pm 5$) align with the average values ($^{143}Nd/^{144}Nd = 0.511942 \pm 45$ and $^{147}Sm/^{144}Nd = 0.0827 \pm 21$) reported for Otter Lake (Yang et al., 2014). The results for Mae Klang monazite (n=25; $^{143}Nd/^{144}Nd = 0.512638 \pm 17$ and $^{147}Sm/^{144}Nd = 0.0925 \pm 7$) also concur with those published by Fisher et al. (2011; $^{143}Nd/^{144}Nd = 0.512646 \pm 10$ and $^{147}Sm/^{144}Nd = 0.0978 \pm 227$).

4.5.4 Zircon Lu–Hf isotope analysis

In situ Lu–Hf isotope micro-analysis of zircon was conducted using the laser ablation and MC-ICP-MS instrumentation and gas flow setting as outlined above. Lutetium–Hf sample spots were selected over, or adjacent to, the U–Pb spots. The NEPTUNE Faraday cup configuration and isobaric interference corrections are carried out according to Woodhead et al. (2004) and Kemp et al. (2009). Each analysis consisted of 60s on background and 60s data acquisition with a 60s washout time between analyses. Samples were ablated using a repetition rate of 4 Hz, a surface energy density of 6 J/cm^2, and a spot size of 90 μm. FC1 zircon was used as a secondary standard for quality assurance. Average values of $^{176}Hf/^{177}Hf = 0.282495 \pm 6$ were obtained for Mud Tank and $^{176}Hf/^{177}Hf = 0.282164 \pm 8$ for FC1. This is within uncertainty of the solution value of 0.282184 ± 16 (Woodhead and Hergt, 2005) and indistinguishable from the LA-MC-ICP-MS values of $^{176}Hf/^{177}Hf = 0.282499 \pm 17$ and $^{176}Hf/^{177}Hf = 0.282176 \pm 22$ for Mud Tank and FC1, respectively (Kemp et al., 2009). Depleted mantle (DM) ages and εHf(*t*) values were calculated using ^{176}Lu (λ) = 0.00001867 (Scherer et al., 2001; Söderlund et al., 2004), $^{176}Hf/^{177}Hf = 0.28325$, and $^{176}Lu/^{177}Hf = 0.0384$ (Griffin et al., 2000).

4.6 Results

4.6.1 Monazite and apatite

4.6.1.1 Petrographic description

Monazite is common in most alkaline rock types in the GCCC, often occurring in greater abundance than apatite, the other major phosphate containing REE found in the complex. Anhedral to rarely euhedral monazite (10 to 20 μm in size) occurs in trace amounts in the dolomite and calcite carbonatites of the LRS. Because of its small size, this study did not undertake in situ LA-ICP-MS analyses on monazite in the LRS. It becomes slightly larger and more abundant in the alkaline amphibole-dolomite veinlets that stem from the LRS, where it occurs as small (20 to 40 μm), anhedral grains and as larger, tabular euhedral grains (up to 200 μm in size) associated with arfvedsonite and rutile.

Cream to buff coloured monazite (in hand specimen) makes up between ~1% and ~10% of the magnetite-biotite dykes, ankerite-siderite carbonatites, and their alteration assemblages (i.e., fenites and glimmerites). Monazite from the Magnetite-biotite dykes and ankerite-siderite carbonatites commonly occurs as large (up to 2 mm) subhedral to euhedral lath-shaped crystals, forming clusters that create tabular crystal splays (Fig. 4.3). Some monazite may occur as small inclusions (~10 μm) in apatite, possibly due to exsolution (Slezak et al., 2018; Chapter 3). In high-contrast BSE images, the monazite in these rocks exhibits dark and light zonation and oscillatory growth zones (Fig. 4.3) on the outer margins. The lighter BSE zones are typically associated with higher Th and/or Nd contents and lower La contents, as determined by EDS semi-quantitative analyses.

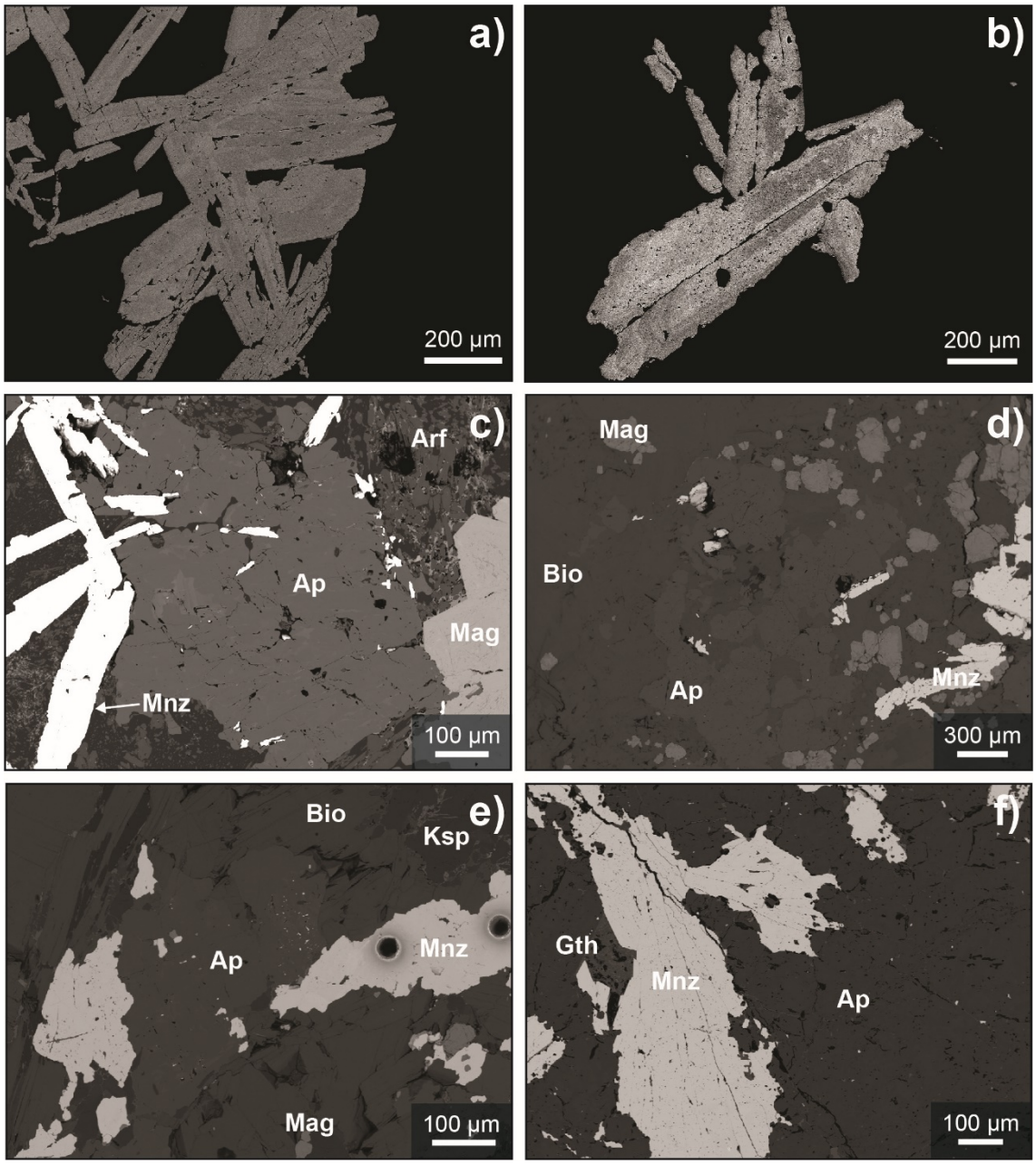

Figure 4.3 a) Backscattered electron (BSE) image of monazite hosted in the magnetite-biotite dyke sample FRS4. Note the subtle light and dark patchy zonation. b) BSE image of monazite from ankerite-siderite carbonatite sample YW49. Note the patchy light and dark zones as well as the oscillatory growth zones on the lower left crystal margin. c) Magnetite-biotite dyke sample FRS4 illustrating the straight contacts and lack of monazite exsolution in apatite. Also present are magnetite, aegirine, and quartz. d) Magnetite-biotite dyke sample YW61 with a seriate texture. Monazite and apatite coexist in this sample, but rarely are observed in direct contact with each other. e) Magnetite-biotite dyke sample BH224. Some small inclusions of monazite are present in apatite. The spots in monazite are 32 µm laser ablation pits for U–Pb dating. f) Magnetite-biotite dyke sample DMCY139 with intergrown monazite and apatite. Mineral abbreviations: Arf = arfvedsonite, Ap = Apatite, Bio = biotite, Gth = goethite, Ksp = potassium feldspar, Mag = magnetite, Mnz = monazite.

In hand specimen, apatite grains are translucent white to opaque sandy brown in colour. They are anhedral to subhedral and occasionally euhedral, occurring as large 200 to 500 µm crystals or crystal clusters (Fig. 4.3). Apatite is occasionally intergrown with monazite and often intergrown with biotite and magnetite (Fig. 4.3c,e), forming seriate to equigranular textures.

Small, rare inclusions of monazite occur in most apatite grains (Fig. 4.3c-f). Monazite and apatite typically display relatively smooth contacts with each other (Fig. 4.3c). In one magnetite-biotite dyke sample, DMCY139, monazite and apatite are intergrown with some apatite occurring as inclusions in monazite and vice versa (Fig. 4.5f). Hyperspectral CL conducted on GCCC apatite by Slezak et al. (2018) revealed textural and chemical variability within apatite, including the existence of multiple zones with differing CL spectra and varying REE contents. Slezak et al. (2018) demonstrated that the apatite geochemistry could distinguish different magmatic origins (i.e., carbonatite vs. granite) for apatite in the GCCC. The apatites analysed in this study were of only of carbonatite origin based on the REY diagrams obtained in Slezak et al. (2018).

4.6.1.2 U–Pb geochronology of monazite

The results of U–Pb isotope analysis of monazite from four ankerite-siderite carbonatites (YN49, HK01, YN50, FRS9), five magnetite-biotite dykes (DMCY139, LEQ130, FRS4, YW61, BH224), one fenite (LE1), and one alkaline amphibole-dolomite veinlet (LRS150) are presented in Table 4.2, Figure 4.4, and Appendix 4.A. All samples exhibit common Pb mixing trends in Tera-Wasserburg diagrams, but the majority of samples plot near concordia (e.g., BH224 and DMCY139 in Fig. 4.4f,h). The lower concordia intercept is interpreted as crystallisation age of monazite. The upper intercept on concordia is at $^{207}Pb/^{206}Pb$ values of between 0.8-1.0 for most samples, which is broadly consistent with the primordial Pb isotope composition (Stacey and Kramers, 1975). Collectively, the calculated monazite U–Pb dates span a substantial time period from c. 1250 to 815 Ma. Monazite from each sample provides a well-constrained lower intercept age, suggesting that the analysed monazite within a single sample crystallised at the same time. The linear dispersion of analyses are related to the proportions of common-Pb in each sample. The dates obtained from the monazite are often outside uncertainty when comparing different samples. Even samples collected in close proximity gave very different ages; ankerite-siderite carbonatite samples YN49 and YN50 were collected from two adjacent drill holes only 100 metres apart and at similar depths, but returned dates of 1054 ± 20 Ma and 1252 ± 14 Ma (Fig. 4.4a,b), respectively.

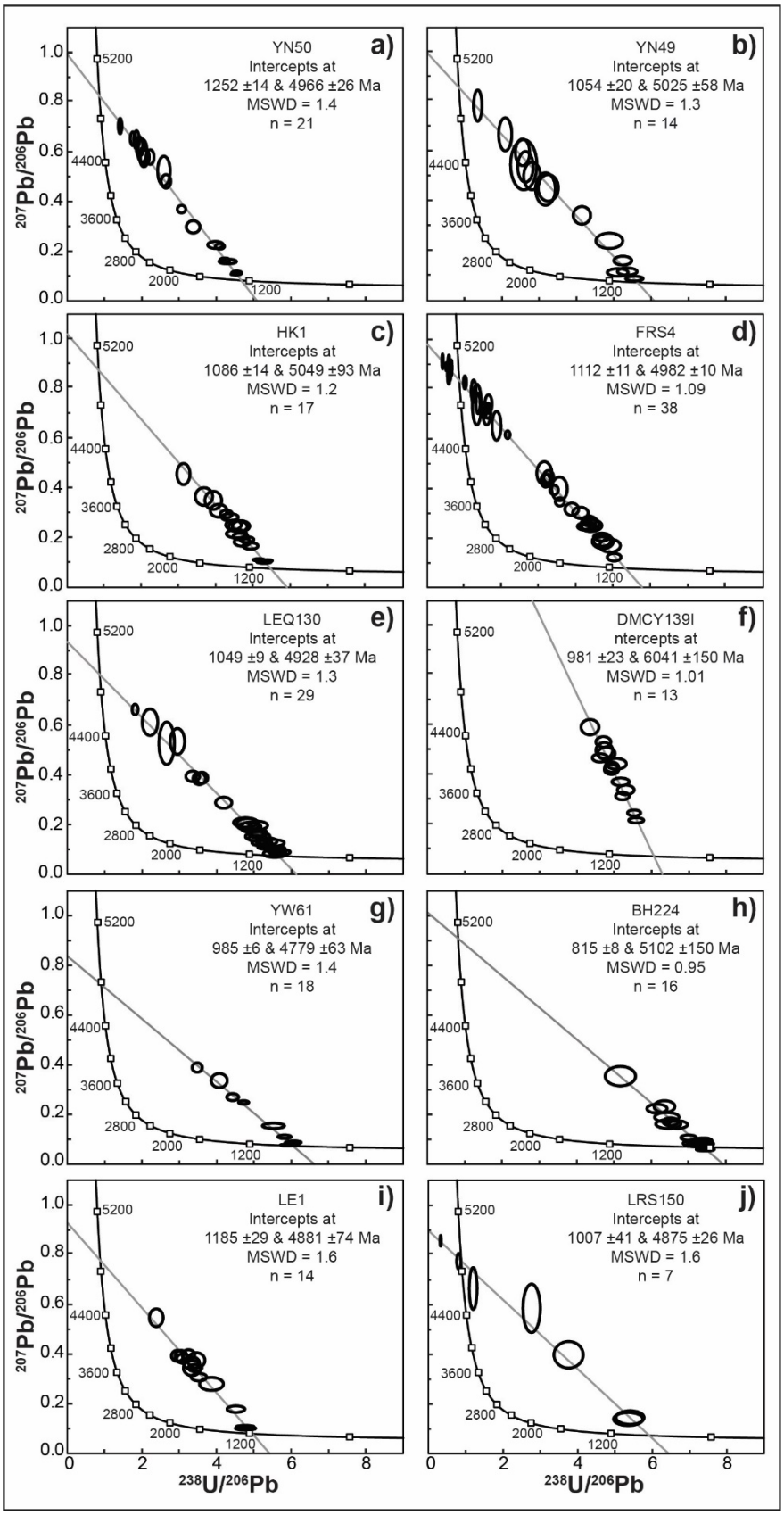

Figure 4.4 Tera-Wasserburg U–Pb plots of monazite analyses. The lower intercept to concordia is interpreted to be the monazite crystallisation age. a) YN50: ankerite-siderite carbonatite. b) YN49: ankerite-siderite carbonatite. c) HK1: ankerite-siderite carbonatite. d) FRS4: phoscorite. e) LEQ130: magnetite-biotite dyke. f) DMCY139: magnetite-biotite dyke. g) YW61: magnetite-biotite dyke. h) BH224: magnetite-biotite dyke. i) LE1: fenitised granite. j) LRS150: magmatic hydrothermal vein originating from a Lyons River Sill dolomite carbonatite.

4.6.1.3 Sm–Nd isotope analysis of monazite and apatite

Samples selected for analysis contained coeval monazite and apatite based on the primary petrographic textures and in CL signatures (Slezak et al., 2018). Therefore, the Sm–Nd isotope compositions of these phases can be used to construct isochrons for dating (Fig. 4.5; Appendix 4.B). Bulk rock Nd isotopes for several of the same samples were used as a quality control measure to check for disequilibrium.

In one magnetite-biotite dyke sample without significant monazite, DMCY138, there are significant differences in Sm/Nd ratios (Fig. 4.5i) between CL zones of individual euhedral apatite grains (see Figure 3.6 in Chapter 3). Nevertheless, the Sm–Nd isotope systematics of this apatite varies consistently, allowing for an in situ Sm–Nd isochron age. In two ankerite-siderite carbonatite samples (YN49 and FR9), only monazite is present, but zoning in this monazite involves sufficient differences in Sm/Nd to allow calculation of acceptable Sm–Nd isochrons (Fig. 4.6g,h).

The Sm–Nd isochron ages range from c. 1300 to 1200 Ma (Fig. 4.5, Table 4.2) except for one magnetite-biotite dyke sample (YW61), which returned a younger date of 1085 ± 15 Ma (Fig. 4.5b, Table 4.2). Calculated uncertainties range from ±77 Ma to ±9 Ma, and MSWD values fall within the range of 0.3 to 2.1. All initial $^{143}Nd/^{144}Nd$ ratios are between 0.51078 and 0.51087 (Table 4.2).

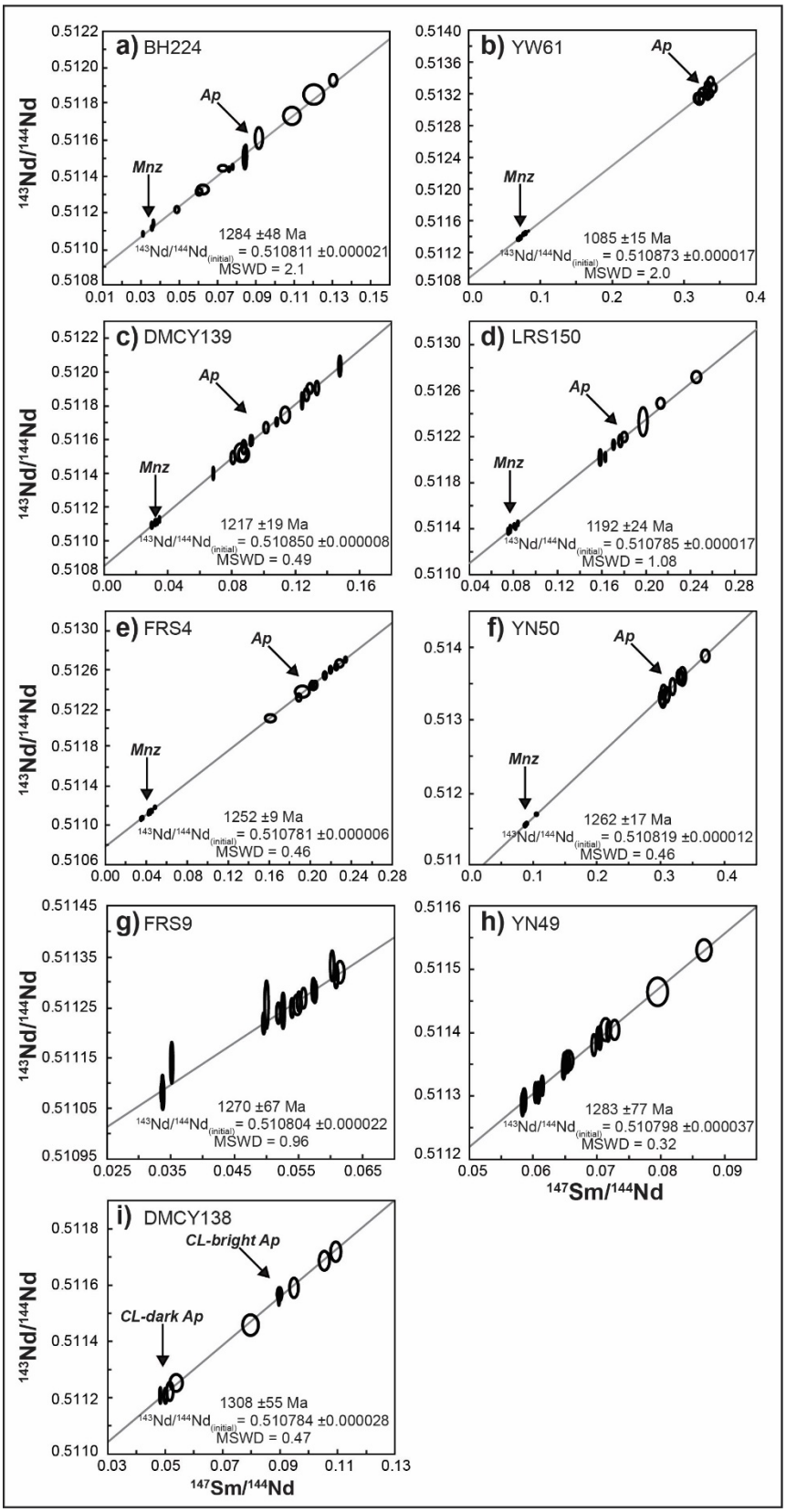

Figure 4.5 Sm–Nd isochron plots. a) BH224: magnetite-biotite dyke monazite and apatite. b) YW61: phoscoritic monazite and apatite. c) DMCY139: magnetite-biotite dyke monazite and apatite. d) LRS150: magmatic hydrothermal vein from dolomite carbonatite (LRS) apatite and monazite pair. e) FRS4: magnetite-biotite dyke apatite and monazite. f) YN50: ankerite-siderite carbonatite apatite and monazite. g) FRS9: ankerite-siderite carbonatite monazite only. h) YN49: monazite only. i) DMCY138: bright and dark CL zones, forming a Sm–Nd isochron pair.

Table 4.2 Monazite U–Pb ages and Sm–Nd isochron ages for monazite-apatite pairs.

Sample	Rock type	Latitude	Longitude	U–Pb age (monazite)	U–Pb analyses (n)	U–Pb MSWD	Sm–Nd isochron age	Initial $^{143}Nd/^{144}Nd$ (isochron)	Sm–Nd analyses (n)	Sm–Nd MSWD
YW61	Magnetite-biotite dyke	416152	7363045	985 ± 6	18	1.4	1085 ± 15	0.510873 ± 0.000017	23	2.0
YN50	Ankerite-siderite carbonatite	417402	7345898	1252 ± 14	21	1.4	1262 ± 17	0.510819 ± 0.000012	20	0.46
YN49*	Ankerite-siderite carbonatite	417512	7362069	1054 ± 20	14	1.3	1283 ± 77	0.510798 ± 0.000034	17	0.32
HK1	Ankerite-siderite carbonatite	421578	7360296	1086 ± 14	17	1.2	n/a	n/a	n/a	n/a
LE1	Fenitised granite	419997	7360600	1185 ± 29	14	1.6	n/a	n/a	n/a	n/a
BH224	Magnetite-biotite dyke	428503	7355090	815 ± 8	16	0.95	1284 ± 48	0.510811 ± 0.00021	15	2.1
FRS4	Magnetite-biotite dyke	430083	7349554	1112 ± 11	38	1.09	1252 ± 9	0.510782 ± 0.000006	24	0.46
FRS9*	Magnetite-biotite dyke	429717	7350888	n/a	n/a	n/a	1270 ± 67	0.510804 ± 0.000022	19	0.96
LEQ130	Magnetite-biotite dyke	424481	7349108	1049 ± 9	29	1.3	n/a	n/a	n/a	n/a
DMCY139	Magnetite-biotite dyke	424026	7347653	981 ± 23	13	1.01	1217 ± 19	0.510850 ± 0.000008	24	0.49
DMCY138†	Magnetite-biotite dyke	424026	7347653	n/a	n/a	n/a	1308 ± 55	0.510784 ± 0.000028	10	0.47
LRS150	Alkaline amphibole-dolomite veinlet	422586	7345898	1007 ± 41	7	1.6	1192 ± 24	0.510785 ± 0.00017	14	1.08

*monazite only Sm–Nd isochron; †apatite only Sm–Nd isochron

4.6.2. Zircon

4.6.2.1 Petrographic description

Zircon crystals were obtained from two samples from a glimmerite alteration assemblage associated with ankerite-siderite carbonatites (YW61-12 and YN50-50) and two samples from the silica-rich alkaline veins (LRS9 and FRS152). In all of the samples, zircon appears opaque, greyish-pink to dark peach in colour, and exhibits a dipyramidal morphology with a shorter aspect ratio compared to typical granitic zircons (Fig. 4.6; Corfu et al., 2003). The zircon grains are large, ranging from 150 to 500 μm in size, with some grains reaching nearly 1 mm along the *c* axis (Fig. 4.6a). In BSE, the glimmerite-hosted zircons display faint and truncated oscillatory zoning (Fig. 4.6b). Zircon crystals from the silica-rich alkaline vein (LRS9) are relatively homogenous in BSE, but some grains contain embayed margins, fractures, pits, and may occasionally exhibit fibrous textures. Hyperspectral CL of all samples returned little to no luminescence.

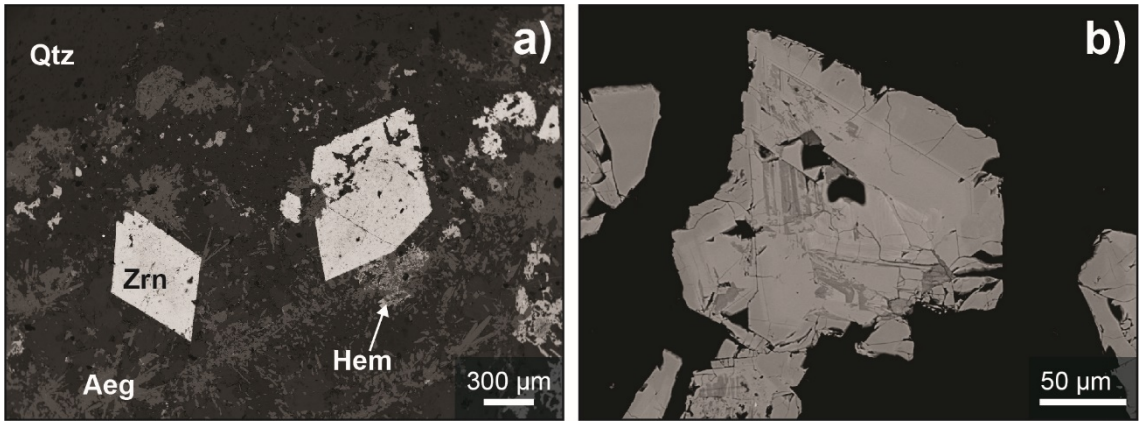

Figure 4.6 a) Backscattered electron (BSE) image of homogenous zircon with aegirine, quartz, and hematite in silica-rich alkaline vein sample LRS9. b) BSE image of zircon from glimmerite sample YN50-50 that represents an alteration halo around ankerite-siderite carbonatite sample YN50. Note the distinct zoning and fractured nature of the zircon grains. Aeg = aegirine, Hem = hematite, Qtz = quartz, Zrn = zircon.

4.6.2.2 Trace element contents

Zircon is highly enriched in Th (mostly >1000 ppm; Fig. 4.7a). Uranium contents are variable (14 to 1000 ppm), with the silica-rich alkaline vein sample (LRS9) having the lowest U contents (~14 to 20 ppm; Appendix 4.C). The Th/U ratios in the studied zircon are typically >1 and the sample from the silica-rich alkaline vein (LRS9) has Th/U ~200 (Fig. 4.7b). All zircon samples contain considerable Nb (500 to 5000 ppm; Fig. 4.7c) and several tens of ppm Ta (Fig. 4.7c). The zircon samples frm the silica-rich alkaline viens (LRS9 and FRS152) have Nb/Ta > 80

and the zircon samples from the glimmerites (YN50-50 and YW61-12) have Nb/Ta = 10 to 30. Hafnium contents range between 2,000 and 18,000 ppm and the Zr/Hf ratios span a wide range from 25 to 200. Zircons form the silica-rich alkaline vein (LRS9) have much higher Nd (440 to 700 ppm) and Sm (270 to 350 ppm) contents, but much lower HREE (e.g., only 0.2 to 0.4 ppm Lu) and Y than the zircons from other samples (Fig. 4.8). Nevertheless, all samples have Y/Ho = 21 to 29 (Fig. 4.7c).

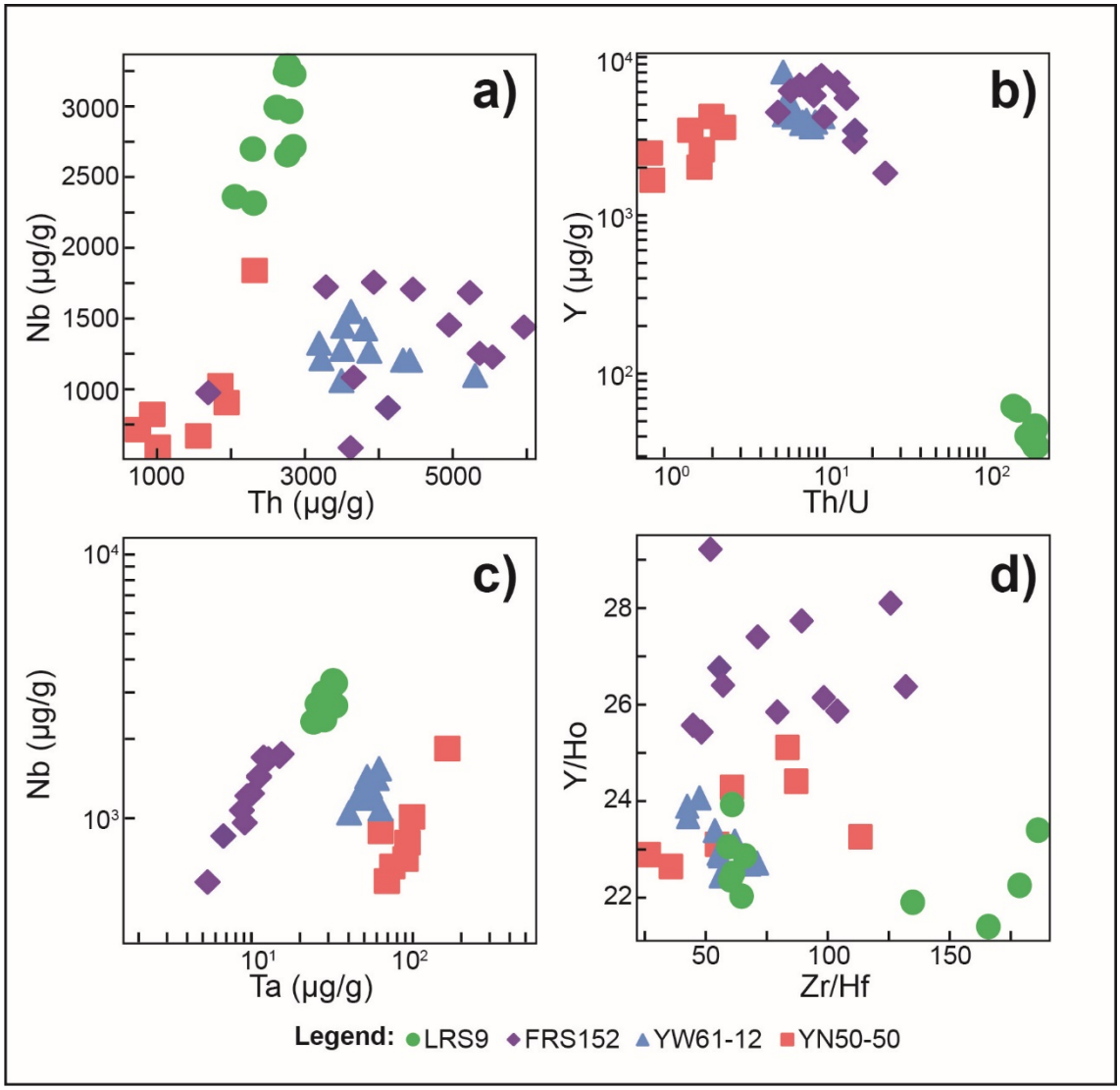

Figure 4.7 Zircon trace element plots. Silica-rich alkaline vein-hosted zircons are samples LRS9 and FRS152. Glimmerite-hosted zircons are samples YN50-50 and YW61-12. a) Plot of Th vs. Nb. Note that all samples have high Th contents and silica-rich alkaline vein zircon sample LRS9 contains the highest Nb content. b) Plot of Th/U vs. Y. All samples contain Th/U ≥ 1, with most being significantly greater than 1. c) Plot of Nb vs. Ta. The zircons in the silica-rich alkaline vein have a higher Nb/Ta ratio than the zircons in the glimmerite alteration. d) Plot of Y/Ho vs. Zr/Hf. Most samples plot near the chondritic Y/Ho defined by Bau (1996). However, Zr/Hf has a large spread of values, with higher Zr/Hf corresponding to higher Nb/Ta.

Due to the high amounts of Nd and Sm, the LRS9 zircons have a REY-normalised pattern with a steep, positive slope from La to Sm, followed by a negative slope from Sm to Y, and a flat-lying pattern from Y to Lu (Fig. 4.8). The REY-normalised patterns of the zircon from the glimmerite samples (YN61-12 and YN50-50) and silica-rich alkaline vein sample FRS152 feature gentle, positive slope from Nd to Tb and flat HREE patterns. All zircon samples have no Eu anomalies, but some exhibit very small negative Y anomalies (Fig. 4.8).

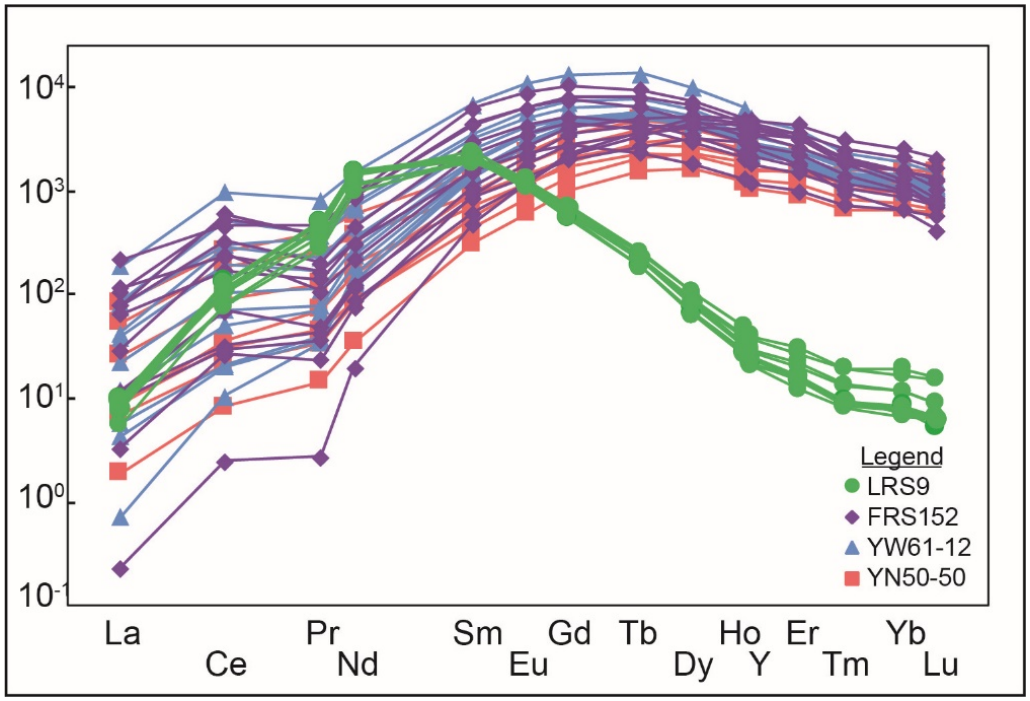

Figure 4.8 REY-normalised plot of zircon samples silica-rich alkaline vein-hosted zircons (LRS9 and FRS152) and glimmerite-hosted zircons (YN50-50 and YW61-12). The LRS9 (green) zircons have an REY pattern slope inflection at Nd-Sm, whereas all other samples have slope inflections at Gd-Tb, and are more enriched in HREE. REE are normalised using chondritic values of McDonough and Sun (1995) using CN=6. Note that with a CN=6, Y and Ho are transposed because their similar ionic radii (Y=90 pm, Ho=90.1 pm; Shannon, 1976).

4.6.2.3 U–Pb geochronology

Zircon U–Pb isotope data are summarised in Figure 4.9, Table 4.3, and Appendix 4.D. Two samples of glimmerites (YN61-12 and YN50-50) and one sample of a silica-rich alkaline vein with magnetite-biotite dyke inclusions (FRS152) yielded concordant ages (Fig. 4.9a-c) of 1361 ± 11 Ma (YN61-12), 1362 ± 11 Ma (Y50-50), and 1373 ± 8 Ma (FR152). Zircon from the silica-rich alkaline vein sample LRS9 yielded a discordant data with a lower intercept (interpreted as the age of crystallisation) of 1381 ± 16 Ma (Fig. 4.9d).

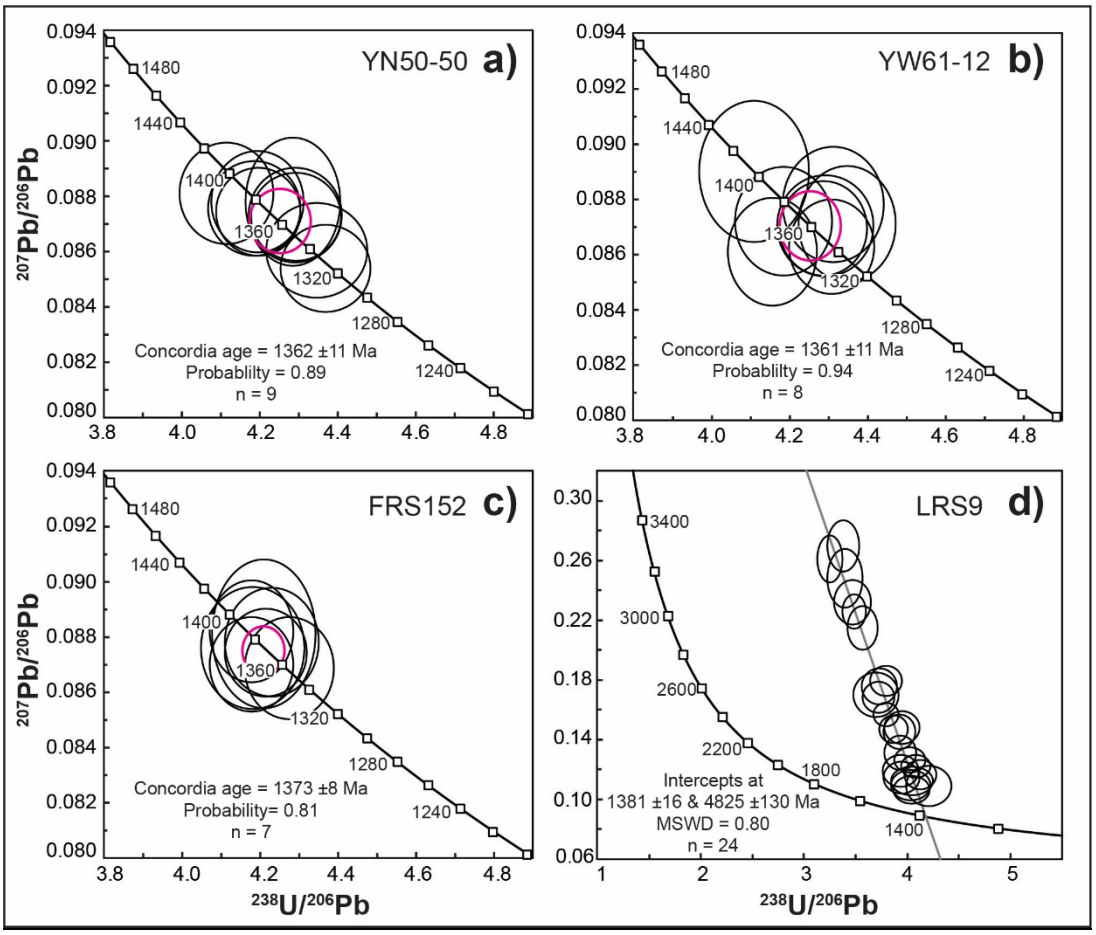

Figure 4.9 Tera-Wasserburg U–Pb zircon plots. a) Concordant zircon age in glimmerite YN50-50. b) Concordant zircon age in glimmerite sample YW61-12. c) Concordant zircon age from zircons in silica-rich alkaline vein sample FRS152. d) Concordia intercept age for zircon from silica-rich alkaline vein sample LRS9. The discordia array for this sample is consistent with variable components of common lead in the analyses.

4.6.2.4 Lu–Hf isotopes

Lutetium–Hf isotope results for zircon are presented in Table 4.3 and Appendix 4.E. Initial zircon εHf(t) values were calculated to 1370 Ma, based on average U–Pb zircon data. εHf($t_{1.37Ga}$) values for the glimmerite samples are -4.15 ± 0.62 (YN61-12) and -3.67 ± 0.68 (YN50-50), whereas the silica-rich alkaline vein samples (LRS9 and FR152) have slightly higher εHf($t_{1.37Ga}$) values of -2.55 ± 0.51 and -1.55 ± 0.56, respectively.

Table 4.3 Zircon U–Pb and Lu–Hf results.

Sample	Rock type	Latitude	Longitude	U–Pb age	Average εHf($t_{1.37Ga}$)
LRS9	Silica-rich alkaline vein	416009	7352640	1381 ± 16	-2.55 ± 0.51
FRS152	Silica-rich alkaline vein	427668	7351034	1373 ± 8	-1.55 ± 0.56
YW61-12	Glimmerite	416152	7363045	1361 ± 11	-4.15 ± 0.62
YN50-50	Glimmerite	417402	7345898	1362 ± 11	-3.67 ± 0.68

4.7 Discussion

The collective geochronology dataset presented here spans some 550 m.y. from c. 1370 Ma to c. 815 Ma, with various mineral chronometers – even from the same sample – returning different age ranges (Fig. 4.10). A similar range of dates was obtained by Zi et al. (2017) based on Th–Pb dating of monazites from the LRS and their associated fenites from the GCCC. Although such a large age range for a single magmatic complex may seem unusual, these results are consistent with the broad range of ages obtained from some other REE-rich carbonatite complexes (Song et al., 2018; Downes et al., 2016). Below, the temporal evolution of the GCCC is evaluated with respect to regional geological events, and discuss some implications of this chapter's results for interpreting the tectonic processes and events based on the geological record of carbonatites.

4.7.1 Primary magmatic age and origin of the GCCC

The oldest dates from this dataset are the U–Pb zircon ages of 1362 ± 11 Ma, 1361 ± 11 Ma, 1373 ± 8 Ma, and 1381 ± 16 Ma (Figs. 4.9 and 4.10). These ages derive from both glimmerites associated with ankerite-siderite carbonatites and silica-rich alkaline veins from across the GCCC and are all within uncertainty of each other. The dated zircons occur as large euhedral crystals with dipyramidal morphologies, and they lack distinct cathodoluminescence zoning. They also have unusual trace element compositions with distinctly high Th/U and Zr/Hf, high LREE, and low HREE (Figs. 4.7 and 4.8) compared to typical granitoid zircons (Belousova et al., 2002; Hoskin and Schaltegger, 2003). Moreover, the lack of Eu anomalies indicates crystallisation in the absence of plagioclase. These morphological and geochemical features are characteristics of carbonatitic zircon (Belousova et al., 2002; Corfu et al., 2003; Hoskin and Schaltegger 2003; Zhang et al., 2017), and so the formation of these zircons is interpreted to be contemporaneous with primary carbonatite magmatism of the GCCC. Given the exceptional resilience of zircon to post-crystallisation alteration (Cherniak and Watson, 2003; Cherniak, 2010), the c. 1370 Ma zircon age is regarded to be the age of igneous emplacement of the GCCC. This age is consistent with a $^{207}Pb/^{206}Pb$ date of 1362 ± 20 Ma for high Th/U zircons from a fenitised granitic rock

reported by Pearson (1996), and the oldest U–Pb monazite dates (1361 ± 10 Ma) reported by Zi et al. (2017) for the complex.

Bulk rock Nd isotope data for the GCCC carbonatites and magnetite-biotite dykes (Chapter 2) calculated to 1370 Ma give εNd($t_{1.37Ga}$) values of -1.83 to -4.20, which is consistent with derivation from an enriched mantle source (Chapter 2), as is typical for carbonatites worldwide (Bell and Simonetti, 2010). The Hf isotope compositions of the c. 1370 Ma zircons (εHf($t_{1.37Ga}$) ~ -1.6 to -4.2), is also consistent with enriched mantle source. Assuming Nd and Hf isotopes accord to the mantle array (Vervoort et al., 1999; Chauvel et al., 2008), the equivalent εNd($t_{1.37Ga}$) values calculated from these Hf isotope compositions are between ~ -2 and -4, which further supports a primary mantle origin for these zircons.

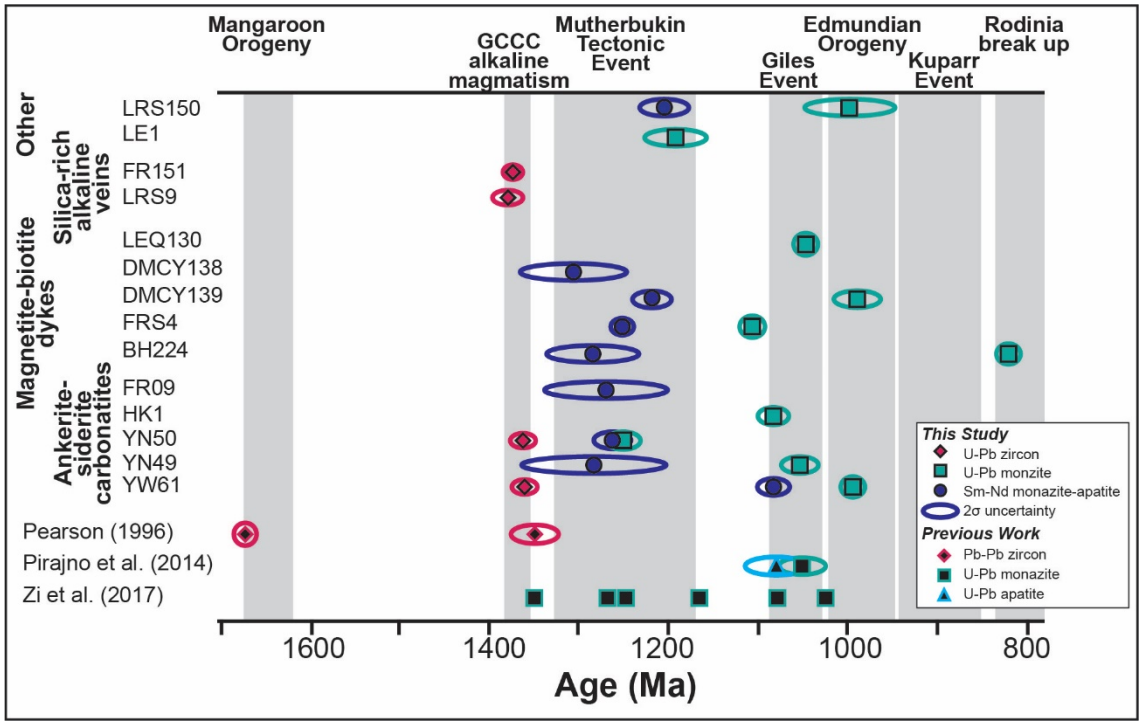

Figure 4.10 Compilation of zircon U–Pb ages, monazite U–Pb ages, Sm–Nd isochron ages from monazite-apatite pairs from this study, as well as $^{207}Pb/^{206}Pb$ granite and fenite zircon ages from Pearson (1996), SHRIMP U–Th monazite ages from Zi et al. (2017), and apatite/monazite Pirajno et al. (2014). Note the decoupling of U–Pb and Sm–Nd ages in monazite. The monazite U–Pb age and Sm–Nd ages are significantly younger that the U–Pb zircon ages and correspond to regional tectonic/magmatic events (Mangaroon Orogeny: Sheppard et al., 2005; Mutherbukin Tectonic Event: Korhonen et al., 2015; Giles Event: Smithies et al., 2015; Edmundian Orogeny: Sheppard et al., 2007), including potential links to Rodinia disassembly (Li et al., 2008).

Emplacement of the GCCC at c. 1370 Ma is rather enigmatic, as this time period does not correspond to any known magmatic or tectonic event on the Australian continent. While a mode of 1380 to 1340 Ma detrital zircons has been identified from the Arid Basin of the Albany

Fraser Orogen (southeastern Western Australia), their source remains unrecognised (Spaggiari et al., 2015). This time period postdates the c. 1410 Ma Loongana Arc of the Madura Province, and predates the Albany Fraser (stage 1) Orogeny (1330 to 1280 Ma; Spaggiari et al., 2015) as well as the Mutherbukin Tectonic Event (Table 4.1; Korhonen et al., 2015). The only other c. 1370 Ma date from the region is a $^{207}Pb/^{206}Pb$ monazite age of 1375 ± 14 Ma from the Abra polymetallic deposit (Zi et al., 2015) located approximately 250 km west-southwest of the GCCC, and – like the GCCC – situated immediately adjacent to the Lyons River Fault system. The coincidence of these two ages indicates the Lyons River Fault was active at this time, and may have permitted tapping of carbonatitic melts from the mantle into the crust to form the GCCC.

In the absence of local tectonism, the Lyons River Fault system and formation of the GCCC were likely activated by far field stresses. The most accepted plate reconstructions for the early Mesoproterozoic place the North China Craton immediately outboard of the northwestern margin of the West Australian Craton (Pisarevsky et al., 2014) or along the western margin of the Northern Australian Craton (Zhang et al., 2012). Apparent polar wander paths indicate that the North China Craton separated from the West Australian Craton between 1400 Ma and 1350 Ma, as part of the greater breakup of the supercontinent Nuna (Pisarevsky et al., 2014). Rifting of these continental fragments is cited as the driver for emplacement of the extensive 1.33 to 1.30 Ga Yanliao mafic sills and the carbonatite-associated 1.30 Ga Bayan Obo REE-Nb-Fe deposit of the North China Craton (Zhang et al., 2017). On the opposite end of the West Australia Craton, this rifting event is proposed to have had an earlier magmatic imprint of intrusion of the 1.39 Ga Biberkine dyke swarm in the Yilgarn Craton (Stark et al., 2018), and possibly emplacement of the GCCC at 1.37 Ga.

4.7.2 Post emplacement evolution of the GCCC

All of the Sm–Nd isochron dates determined from monazite and apatite fall within the range of 1300 Ma to 1200 Ma (Fig. 4.10), except one magnetite-biotite dyke sample (YW61) that has a Sm–Nd isochron age of 1085 ± 15 Ma. The U–Pb monazite dates are also younger than the magmatic age of the GCCC, falling into several groups: c. 1250–1200 Ma, c. 1100–1050 Ma, c.

1000 Ma, and c. 815 Ma. This range of ages, except the youngest date, was also recognised in previous dating studies of the LRS (Pirajno et al., 2014; Zi et al., 2017). Before discussing the regional tectonic significance of these ages, this chapter evaluates whether the ages correspond to local resetting of the Sm–Nd and U–Pb geochronometers, or whether these ages record primary crystallisation of REE mineral during repeated episodes of carbonatite/alkaline magmatism.

The LREE enriched nature of the alkaline rocks of the GCCC translates to a significantly lower Sm/Nd ratio of 0.0867 (Chapter 2) compared with putative enriched mantle sources (Sm/Nd = 0.1786 of model EM2; Workman et al. 2004). Therefore, the GCCC evolved to much less radiogenic Nd isotope compositions with time compared to its enriched mantle source (Fig. 4.11). This isotopic divergence allows for the determination of whether the post 1370 Ma ages obtained from apatite and monazite correspond to new inputs of enriched mantle-derived magma into the complex, which should have relatively juvenile εNd(t) values, or whether they represent resetting ages, in which case the Nd isotope compositions should fall on the GCCC isotope evolution line. Rather strikingly, all of the monazite and apatite data (at their respective U–Pb and/or Sm–Nd isochron ages) plot very close to, or along, the GCCC Nd isotope evolution line (Fig. 4.11), demonstrating that the younger ages represent isotope disturbance or recrystallisation of apatite and monazite, rather than repeated episodes of magmatism.

Many carbonatites are spatially and temporally contemporaneous with the emplacement of large igneous provinces (LIPs; Ernst and Bell, 2010 and references therein), implying a possible genetic link between the two. Based on the c. 1050 to 1075 Ma apatite and monazite ages, Pirajno et al. (2014) concluded the similarly aged Warakurna LIP was the progenitor of the GCCC. However, the Nd isotope data demonstrate that there was no addition of juvenile mantle during that time. Furthermore, U–Pb age data from Zi et al. (2017) and this study demonstrate that the magmatic origins of the GCCC significantly predate the Warakurna LIP.

Although not magmatic, the post 1370 Ma ages of the GCCC can be related to local and regional orogenic events. The 1300 to 1200 Ma ages correlate with the 1320 to 1170 Ma Mutherbukin Tectonic Event, which was a period of transpression and crustal thickening in the Gascoyne Province, reaching peak metamorphic conditions of ~0.3 to 0.6 GPa and temperatures

of 400 to 700 °C in the Mutherbukin Zone. The event was very long lived, keeping mid-crustal temperatures elevated for ~100 m.y. (Korhonen et al., 2015) and also causing regional hydrothermal alteration (Olierook et al., 2018).

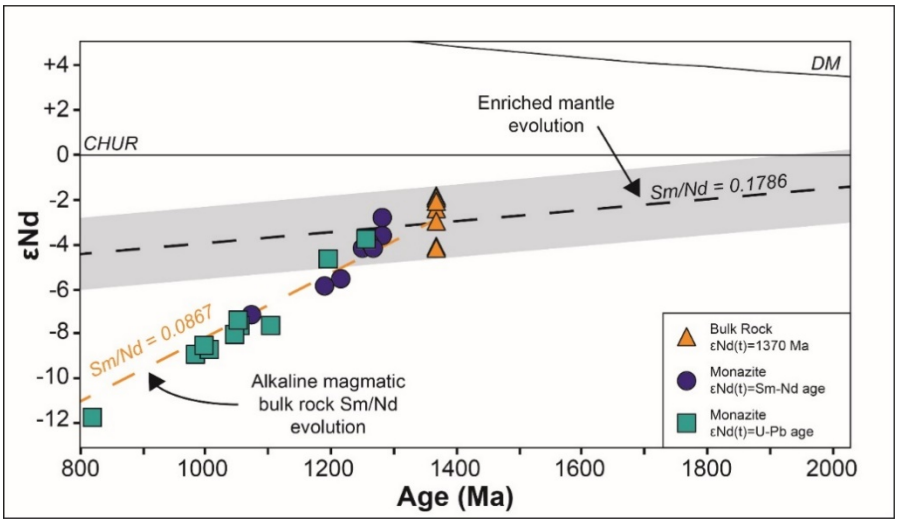

Figure 4.11 εNd versus time plot for mineral and bulk-rock data for the GCCC. The black dashed line is the modelled isotope evolution of the depleted mantle source that formed the GCCC at 1370 Ma, using an initial Sm/Nd of 0.1786 for a model enriched mantle (EM2 from Workman et al., 2004) and the average bulk rock εNd(*t*) of carbonatite samples of the GCCC (Chapter 2). The yellow dashed line is the modelled isotope evolution of the GCCC starting from the bulk rock εNd($t_{1.37Ga}$) and using an average Sm/Nd of GCCC carbonatites of 0.0867. Note the isotopic compositions of monazite closely correspond to the isotope evolution model of the GCCC.

The c.1100 to 1050 Ma U–Pb monazite ages and one Sm–Nd isochron broadly correlate with the c. 1076 Warakurna Large Igneous Province (Wingate et al., 2004, Pirajno et al., 2014). However, as stated above, the Nd isotope data exclude a mantle input at this stage (Fig. 4.11). Instead, these ages are considered to correspond to the 1090 to 1040 Ma Giles Event (Edgoose et al., 2004), which Smithies et al. (2015) attributed to destabilisation of lithospheric mantle caused by the abutment of the Musgrave thermal anomaly against cooler lithosphere of the Capricorn Orogen. The strike-slip motion on the Mundrabilla Shear Zone coupled with regional extension occurring within the adjacent the Capricorn Orogen, created a tectonic channel that focused the Warakurna LIP into the extensional basins of the Capricorn Orogen (Smithies et al., 2015).

The c.1000 to 980 Ma U–Pb (this study) and Th–Pb (Zi et al., 2017) monazite dates fit well with the Edmundian Orogeny, a period of initial compression followed by extension, possibly caused by oblique continental collisions, resulting in greenschist-facies metamorphism in the central Gascoyne Province (Sheppard et al., 2007).

The 815 ± 8 Ma age returned from the monazite from Bald Hill sample BH224 is the youngest age recorded in the GCCC. It is over 100 m.y. younger than the Edmundian Orogeny. Other areas of Australia, such as the Kimberley region, experienced alkaline magmatism c. 815 Ma, such as the Skerring kimberlite (800 ±10 Ma), Pteropus Creek kimberlite (805 ± 10 Ma), Aries Kimberlite (815 ± 4 Ma), and Bow Hill lamprophyre (815 ± 20 Ma; Pidgeon et al., 1989; Downes et al., 2006). During this time, the c. 827 Ma Gairdner Dyke Swarm was emplaced across the Gawler Craton, the Musgrave block, and parts of the Western Australia Craton (Wingate et al., 1998; Pirajno and Hoatson, 2012), with some dykes occurring as far east as Olympic Dam (c. 820 to 830 Ma; Huang et al., 2015). This time is coincident with the c. 825 Ma "super plume" activity and the initial break-up of Rodinia (Li et al. 2008; Pirajno and Hoatson, 2012). The new age within the GCCC is interpreted to represent an expression of hydrothermalism related to far field stresses associated with Rodina disassembly (Fig. 4.10).

4.7.3 Mechanisms for U–Pb and Sm–Nd resetting in monazite and apatite

Monazite is prized for its ability to resist age resetting due to slow diffusion of U, Th, and Pb (Cherniak et al., 2004; Gardés et al., 2006; 2007; McFarlane and Harrison, 2007; Cherniak, 2010), and it is relative insolubility in water and dilute solutions at high temperatures and pressures (e.g., Ayers and Watson, 1991; Pourtier et al., 2010). However, a number of studies have shown that acidic and saline hydrothermal fluids, as well as alkaline fluids, can induce dissolution-precipitation of monazite, and hence alteration of U–Pb and Sm–Nd isotopic systems (Teufel and Heinrich, 1997; Seydoux-Guillaume et al., 2002; Rasmussen and Muhling, 2007; Rassmussen et al., 2007; Hetherington et al., 2010). These findings are consistent with the work of Downes et al. (2014) and Millonig et al. (2012, 2013) who demonstrated that monazite recrystallised at temperatures from ~250 to 400 °C during greenschist-facies metamorphism of the Cummins Range carbonatites, and ~500 to 700 °C during amphibolite-facies metamorphism of the southern Canadian Cordillera carbonatites, respectively.

The carbonatites and magnetite-biotite dykes of the GCCC are enriched in F^-, CO_3^{2-}, K, and Na (Chapter 2.), which under greenschist facies conditions, may have provided a suitable

chemical environment to preferentially recrystallize monazite, inducing Pb loss. There is textural evidence, such as the zonation within monazite and apatite, and alteration of primary biotite, to suggest that the ankerite-siderite carbonatites, magnetite-biotite dykes, and silica-rich alkaline veins were hydrothermally altered after igneous emplacement (Slezak et al., 2018; this thesis).

Despite the evidence for tectonically-induced U–Pb resetting in monazite, the Nd isotope values from monazite and apatite are typically homogenous with very low uncertainties. The isochron ages are, however, younger than the U–Pb zircon ages, with most being contemporaneous with the Mutherbukin Tectonic Event between c.1300 to 1200 Ma. REE diffusion in apatite is expected to be very slow under metamorphic conditions (Cherniak, 2000), and there are no experimentally-derived REE diffusion data for monazite. Nevertheless, empirical evidence from metamorphic rocks indicates relatively slow rates of REE diffusion in both apatite and monazite at temperatures up to at least 700 °C (Spandler et al., 2018). The Mutherbukin Tectonic Event likely only reached greenschist-facies metamorphic conditions in the Edmund Basin adjacent to the GCCC (Korhonen et al., 2015), although the relatively high content of Th and other radioactive elements in the GCCC may have provide additional radiogenic heat during this time. This protracted (e.g., ~100 m.y.) metamorphic heating, additional radiogenic heat, and regional hydrothermalism (Zi et al., 2015) likely allowed resetting of the Nd isotope system for monazite and apatite during this event. A similar situation has been proposed for post emplacement resetting of radiogenic isotope systems in the Nolan's Bore REE fluorapatite deposit of central Australia (Huston et al., 2016). The lower metamorphic grades and shorter time spans for subsequent tectonic events in the GCCC prevented subsequent Nd isotope resetting for most samples, except one that was reset during the Edmundian Orogeny. This resetting is likely responsible for the high MSWD in two samples, BH224 and YW61 (MSWD = 2.0 and 2.1, respectively) suggesting these are errorchrons with additional uncertainty (Wendt and Carl, 1991). The resetting of the Sm–Nd system by geologic events is the likely source for these values.

4.7.4 Implications for dating carbonatite magmatism

A number of previous carbonatite studies, including Bayan Obo (Zhang et al., 2017), Cummins Range (Downes et al., 2016), as well as the GCCC have reported wide age ranges, which tempts interpretation that these are long-lived magmatic systems. These protracted ages then give rise to the debate over the mechanisms that can cause multiple carbonatite magmatic intrusions. One hypothesis points to protracted periods of melting and magmatism associated with mantle plumes (Bell and Simonetti, 2010), whereas Woolley and Bailey (2012) suggest that repeated magmatic events are related to lithospheric focusing, entrainment, and carbonatite magma release during tectonism (as also proposed for kimberlites; Tappe et al., 2017). Though both concepts have merit in the potential origins and mechanisms for carbonatite emplacement, it is noted that the previously mentioned well-dated carbonatite complexes are not protracted magmatic systems. Instead, mineral geochronometers such as apatite and monazite were partially or completely altered due to metamorphic and/or radiogenic heating, and/or hydrothermal dissolution-reprecipitation. Particularly comparable to this study's results, Song et al. (2018) demonstrated that monazites from Bayan Obo were reset during post-emplacement events (913 to 361 Ma) after initial ore formation at 1.3 Ga. In some instances, carbonatites may record potential plume-related events, such as the Gairdner Dyke Swarm or Warakurna LIP ages expressed in the GCCC. However, in many of these cases, these large magmatic events are not the cause of carbonatite magmatism, but instead provide the tectonic/metamorphic conditions to induce isotopic resetting.

Carbonatites often contain a variety of minerals suitable for geochronology. Utilising multiple minerals and multiple radiogenic isotope systems in combination with detailed petrographic evaluation (e.g., Slezak et al., 2018) is paramount to establishing a proper magmatic age and appropriate tectonic history of the complex. Millonig et al. (2013) determined that the most robust minerals in terms of Pb retention (from most robust to least robust) are as follows: baddeleyite, zircon, apatite, titanite, zirconolite, monazite, and pyrochlore. This study supports their findings that zircon is a more robust recorder of magmatic ages than apatite and monazite. However, the susceptibility of these latter minerals to isotopic resetting during hydrothermal

events makes them useful recorders of post-formation alteration events. These post-magmatic geochronometers may be particularly beneficial when applied to ancient carbonatite complexes in Precambrian terranes (such as the GCCC), where tectonic histories are complex and poorly known.

4.8 Conclusions

Carbonatite complexes, such as the GCCC, can be excellent recorders of time owing to their propensity for hosting radiogenic isotope-bearing minerals. Based on U–Pb zircon analysis, the emplacement age of the GCCC is c. 1370 Ma, a time of relative tectonic quiescence in the Gascoyne Province. Younger isotopic dates (c. 1300 to 815 Ma) determined for monazite and apatite reflect isotopic resetting of these minerals due to multiple hydrothermal/tectonic events affecting the complex, rather than multiple magmatic injections. This isotopic resetting can be advantageous in detecting the effects of widespread, low-grade hydrothermalism associated with distal orogenic events or localised major tectonic events such as the Mutherbukin Tectonic Event, the Giles Event, or the Edmundian Orogeny. In order to obtain meaningful emplacement ages for ancient carbonatite complexes the use of a multi-mineral and/or multi-isotopic approach is advised.

4.9 References

Ayers, J.C., Watson, E.B., 1991. Solubility of apatite, monazite, zircon, and rutile in supercritical aqueous fluids with implications for subduction zone geochemistry. Philosophical Transactions of the Royal Society of London A 335, 335-375.

Bau, M. 1996 Controls on the fractionation of isovalent trace elements in magmatic and aqueous systems: evidence from Y/Ho, Zr/Hf, and lanthanide tetrad effect. Contributions to Mineralogy and Petrology 123, 323-333.

Bell, K., Simonetti, A., 2010. Source of parental melts to carbonatites - critical isotopic constraints. Mineralogy and Petrology 98, 77-89.

Belousova, E.A., Griffin, W.L., O'Reilly, S.Y., Fisher, N.I., 2002. Igneous zircon: trace element composition as an indicator of source rock type. Contributions to Mineralogy and Petrology 143, 602-622.

Cawood, P.A., Tyler, I.M., 2004. Assembling and reactivating the Proterozoic Capricorn Orogen: lithotectonic elements, orogenies, and significance. Precambrian Research, 128 201-218.

Chauvel, C., Lewin, E., Carpentier, M., Arndt, N.T., Marini, J.C., 2008. Nature Geoscience 1, 64-67.

Cherniak, D.J., 2000. Rare earth element diffusion in apatite. Geochimica et Cosmochimica Acta 64, 3871-3885.

Cherniak, D.J., 2010. Diffusion in accessory minerals: zircon, titanite, apatite, monazite and xenotime, in: Zhang, Y., Cherniak, D.J. (Eds.), Diffusion in Minerals and Melts. Reviews in Mineralogy and Geochemistry. Mineralogical Society of America and Geochemical Society, pp. 827-869.

Cherniak, D.J., Watson, E.B., 2003. Diffusion in zircon, in: Hanchar, J.M., Hoskin, P.W.O. (Eds.), Zircon. Reviews in Mineralogy and Geochemistry. Mineralogical Society of America and Geochemical Society, pp. 113-143.

Cherniak, D.J., Watson, E.B., Grove, M., Harrison, T.M., 2004. Pb diffusion in monazite: A combined RBS/SIMS study. Geochimica et Cosmochimica Acta 68, 829-840.

Corfu, F., Hanchar, J.M., Hoskin, P.W.O., Kinny, P., 2003. Atlas of zircon textures, in: Hanchar, J.M., Hoskin, P.W.O. (Eds.), Zircon. Reviews in Mineralogy and Geochemistry. Mineralogical Society of America and Geochemical Society, pp. 460-500.

Cutten, H.N., Johnson, S.P., 2018. Kuparr Tectonic Event (KU): WA Geology Online, Explanatory Notes Extract. Geological Survey of Western Australia.

Downes, P.J., Wartho, J.-A., Griffin, B.J., 2006. Magmatic Evolution and Ascent History of the Aries Micaceous Kimberlite, Central Kimberley Basin, Western Australia: Evidence from Zoned Phlogopite Phenocrysts, and UV Laser 40Ar/39Ar Analysis of Phlogopite–Biotite. Journal of Petrology 47, 1751-1783.

Downes, P.J., Demény, A., Czuppon, G., Jaques, A.L., Verall, M., Sweetapple, M., Adams, D., McNaughton, N.J., Gwalani, L.G., Griffin, B.J. 2014. Stable H-C-O isotope and trace element geochemistry of the Cummins Range Carbonatite Complex, Kimberley region, Western Australia: implications for hydrothermal REE mineralization, carbonatite evolution and mantle source regions. Mineralium Deposita 49, 905-932.

Downes, P.J., Dunkley, D.J., Fletcher, I.R., McNaughton, N.J., Rasmussen, B., Jaques, A.L., Verall, M., Sweetapple, M.T., 2016. Zirconolite, zircon and monazite-(Ce) U-Th-Pb age constraints on the emplacement, deformation and alteration history of the Cummins Range Carbonatite Complex, Halls Creek Orogen, Kimberley region, Western Australia. Mineralogy and Petrology 110, 199-222.

Edgoose, C.J., Scrimgeour, I.R., Close, D.F., 2004. Geology of the Musgrave Block, Northern Territory, Northern Territory Geological Survey, Report 15.

Ernst, R.E., Bell, K., 2010. Large igneous provinces (LIPs) and carbonatites. Mineralogy and Petrology 98, 55-76.

Fisher, C.M., McFarlane, C.R.M., Hanchar, J.M., Schmitz, M.D., Sylvester, P.J., Lam, R., Longerich, H.P., 2011. Sm-Nd isotope systematics by laser ablation-multicollector-inductively coupled plasma mass spectrometry: Methods and potential natural and synthetic reference materials. Chemical Geology 284, 1-20.

Foster, G.L., Vance, D., 2006. In situ Nd isotopic analysis of geologic materials by laser ablation MC-ICP-MS. Journal of Analytical Spectrometry 21, 288-296.

Fricker, M.B., Kutscher, D., Aeschlimann, B., Frommer, J., Dietiker, R., Bettmer, J., Gunther, D., 2011. High spatial resolution trace element analysis by LA-ICP-MS using a novel ablation cell for multiple large samples. International Journal of Mass Spectrometry 307, 39-45.

Gardés, E., Jaoul, O., Montel, J.M., Seydoux-Guillame, A.M., Wirth, R., 2006. Pb diffusion in monazite: An experimental study of Pb2+ + Th4+ = 2Nd3+ interdiffusion. Geochimica et Cosmochimica Acta 70, 2325-2336.

Gardés, E., Montel, J.M., Seydoux-Guillame, A.M., Wirth, R., 2007. Pb diffusion in monazite: new constraints from the experimental study of Pb2+ = Ca2+ interdiffusion. Geochimica et Cosmochimica Acta 71, 4036-4043.

Gonçlaves, G.O., Lana, C., Scholz, R., Buick, I.S., Gerdes, A., Kamo, S.L., Corfu, F., Marinho, M.M., Chaves, A.O., Valeriano, C., Nalini Jr., H.A., 2016. An assessment of monazite from the Itambé pegmatite district for use as U-Pb isotope reference material for microanalysis and implications for the origin of the "Moacyr" monazite. Chemical Geology 424, 30-50.

Griffin, W.L., Pearson, N.J., Belousova, E., Jackson, S.E., van Achterbergh, E., O'Reilly, S.Y., Shee, S.R., 2000. The Hf isotope composition of cratonic mantle: LAM-MC-ICPMS analysis of zircon megacrysts in kimberlites. Geochimica et Cosmochimica Acta 64, 133-147.

Guillong, M., Meier, D.L., Allan, M.M., Heinrich, C.A., Yardley, B.W.D., 2008. Appendix A6: SILLS: A MATLAB-based program for the reduction of laser ablation ICP-MS dating of homogenous materials and inclusions, in: Sylvester, P. (Ed.), Laser ablation ICP-MS in the Earth Sciences: Current Practices and Outstanding Issues. Mineralogical Association of Canada Short Course Series. Mineralogical Association of Canada, Vancouver, BC, pp. 328-333.

Harrison, T.M., Catlos, E.J., Montel, J.M., 2002. U-Th-Pb of phosphate minerals, in: Kohn, M.J., Rakovan, J., Hughes, J.M. (Eds.), Phosphates - Geochemical, Geobiological, and Materials Importance. Reviews in Mineralogy and Geochemistry. Mineralogical Society of America, Washington, D.C., pp. 523-558.

Hellstrom, J., Paton, C., Woodhead, J.D., Hergt, J.M., 2008. Iolite: software for spatially resolved LA-(quad and MC) ICPMS analysis, in: Sylvester, P. (Ed.), Laser Ablation ICP–MS in the Earth Sciences: Current Practices and Outstanding Issues. Mineralogical Association of Canada Short Course series 40, pp. 343-348.

Hetherington, C.J., Harlov, D.E., Budzyn, B., 2010. Experimental metasomatism of monazite and xenotime: mineral stability, REE mobility and fluid composition. Mineralogy and Petrology 99, 165-184.

Hokada, T., Motoyoshi, Y., 2006. Electron microprobe technique for U-Th-Pb and REE chemistry of monazite, and its implications for pre-, peak- and post-metamorphic events of the Lutzow-Holm Complex and the Napier Complex, East Antarctic. Polar Geoscience 19, 118-151.

Hoskin, P.W.O., Schaltegger, U., 2003. The composition of zircon and igneous and metamorphic petrogenesis, in: Hanchar, J.M., Hoskin, P.W.O. (Eds.), Zircon. Reviews in Mineralogy and Geochemistry. Mineralogical Society of America and Geochemical Society, pp. 27-62.

Horstwood, M.S.A., Foster, G.L., Parrish, R.R., Noble, S.R., Nowell, G.M., 2003. Common-Pb corrected in situ U-Pb accessory mineral geochronology by LA-MC-ICP-MC. Journal of Analytical Atomic Spectrometry 18, 837-846.

Huang, Q., Kamenetsky, V.S., McPhie, J., Ehrig, K., Meffre, S., Maas, R., Thompson, J., Kamenetsky, M., Chambefort, I., Apukhtina, O., Hu, Y., 2015. Neoproterozoic (c. 820-830 Ma) mafic dykes at Olympic Dam, South Australia: links with the Gardiner Large Igneous Province. Precambrian Research 271, 160-172.

Huston, D.L., Maas, R., Cross, A., Hussey, K.J., Mernagh, T.P., Fraser, G., Champion, D.C., 2016. The Nolans Bore rare-earth element-phosphorus-uranium mineral system: geology, origin and post-depositional modifications. Mineralium Deposita 51, 797-822.

Jackson, S.E., Pearson, N.J., Griffin, W.L., Belousova, E.A., 2004. The application of laser ablation-inductively coupled plasma-mass spectrometry to in situ U-Pb zircon geochronology. Chemical Geology 211, 47-69.

Johnson, S.P. et al., 2011. Two collisions, two sutures: Punctuated pre-1950 Ma assembly of the West Australian Craton during the Ophthalmian and Glenburgh Orogenies. Precambrian Research 189, 239-262.

Johnson, S.P., Thorne, A.M., Tyler, I.M., Korsch, R.J., Kennett, B.L.N., Cutten, H.N., Goodwin, J., Blay, O., Blewett, R.S., Joly, A., Dentith, M.C., Aitken, A.R.A., Holzschuh, J., Salmon, M., Reading, A., Heinson, G., Boren, G., Ross, J., Costelloe, R.D., Fomin, T., 2013. Crustal architecture of the Capricorn Orogen, Western Australia and associated metallogeny. Australian Journal of Earth Sciences 60, 681-705.

Johnson, S.P., Korhonen, F.J., Kirkland, C.L., Cliff, J.B., Belousova, E.A., Sheppard, S., 2017. An isotopic perspective on growth and differentiation of Proterozoic orogenic crust: From subduction magmatism to cratonization. Lithos 268-271, 76-86.

Kemp, A.I.S., Foster, G.L., Schersten, A., Whitehouse, M.J., Darling, J., Storey, C., 2009. Concurrent Pb-Hf isotope analysis of zircon by laser ablation multi-collector ICP-MS, with

implications for the crustal evolution of Greenland and the Himalayas. Chemical Geology 261, 244-260.

Knoper, M., Armstrong, R.A., Andreoli, M.A.G., Ashwal, L.D., 2000. The Steenkampskraal monazite vein: a subhorizontal stretching shear zone indicating extensional collapse of Namaqualand at 1033 Ma? Journal of African Earth Sciences 31 (suppl.), 38-39.

Korhonen, F.J., Johnson, S.P., Fletcher, I.R., Rasmussen, B., Sheppard, S., Muhling, J.R., Dunkley, D.J., Wingate, M.T.D., Roberts, M.P., Kirkland, C.L., 2015. Pressure-temperature-time evolution of the Mutherbukin Tectonic Event, Capricorn Orogen, Geological Survey of Western Australia, Report 146.

Le Bas, M.J., Xueming, Y., Taylor, R.N., Spiro, B., Milton, J.A., Peishan, Z., 2007. New evidence from a calcite-dolomite carbonatite dyke for the magmatic origin of the massive Bayan Obo ore-bearing dolomite marble, Inner Mongolia, China. Mineralogy and Petrology 90, 223-248.

Le Maitre, R.W., 2002. Igneous Rocks: A Classification and Glossary of Terms: recommendations of International Union of Geological Sciences, subcommission on the systematics of igneous rocks. Cambridge University Press, Cambridge.

Li, Z.X., Bogdanova, S.V., Collins, A.S., Davidson, A., De Waele, B., Ernst, R.E., Fitzsimons, I.C.W., Fuck, R.A., Gladkochub, D.P., Jacobs, J., Karlstrom, K.E., Lu, S., Natapov, L.M., Pease, V., Pisarevsky, S.A., Thrane, K., Vernikovsky, V., 2008. Assembly, configuration, and break-up history of Rodinia: a synthesis. Precambrian Research 160, 179-210.

Liu, Z-C., Wu, F-Y., Yang, Y-H., Yang, J-H., Wilde, S.A., 2012. Neodymium isotopic compositions of the standard monazites used in U-Th-Pb geochronology. Chemical Geology 334, 221-239.

Ludwig, K.R., 2009. Isoplot v.3.71 a geochronological toolkit for Microsoft Excel. Berkeley Geochronology Center Special Publication No. 4, Berkeley.

Luo, Y., Gao, S., Longerich, H.P., Gunter, D., Wunderli, S., Yuan, H-L., Liu, X-M., 2007. The uncertainty budget of the multi-element analysis of glasses using LA-ICP-MS. Journal of Analytical Spectrometry 22, 122-130.

Mariano, A.N., 1989. Nature of economic mineralization in carbonatites and related rocks, in: Bell, K. (Ed.), Carbonatites. Unwin Hyman, London, pp. 149-176.

Martin, D.M., Thorne, A.M., 2004. Tectonic setting and basin evolution of the Bangemall Supergroup in the northwestern Capricorn Orogen. Precambrian Research 128, 385-409.

Martin, D.M., Sheppard, S., Thorne, A.M., 2005. Geology of the Maroonah, Ullawarra, Capricorn, Mangaroon, Edmund, and Elliott Creek 1:100 000 sheets, Western Australia Geological Survey, 1:100 000 Geological Series Explanatory Notes.

McDonough, W.F., Sun, S.s., 1995. The composition of the Earth. Chemical Geology 120, 223-253.

McFarlane, C.R.M., Mark Harrison, T., 2006. Pb-diffusion in monazite: Constraints from a high-T contact aureole setting. Earth and Planetary Science Letters 250, 376-384.

McFarlane, C.R.M., McCulloch, M.T., 2007. Coupling of in-situ Sm-Nd systematics and U-Pb dating of monazite and allanite with applications to crustal evolution studies. Chemical Geology 245, 45-60.

Millonig, L.J., Gerdes, A., Groat, L.A., 2012. U-Th-Pb geochronology of meta-carbonatites and meta-alkaline rocks in the southern Canadian Cordillera: a geodynamic perspective. Lithos 152, 202-2017.

Millonig, L.J., Gerdes, A., Groat, L.A., 2013. The effect of amphibolite facies metamorphism on the U-Th-Pb geochronology of accessory minerals from meta-carbonatites and associated meta-alkaline rocks. Chemical Geology 353, 199-209.

Mitchell, R.H., Chudy, T., McFarlane, C.R.M., Wu, F.Y., 2017. Trace element and isotopic composition of apatite in carbonatites from the Blue River area (British Columbia, Canada) and mineralogy of associated silicates rocks. Lithos 286-287, 75-91.

Occhipinti, S.A., Sheppard, S., Passchier, C., Tyler, I.M., Nelson, D.R., 2004. Palaeoproterozoic crustal accretion and collision in the southern Capricorn Orogen: the Glenburgh Orogeny. Precambrian Research 128, 237-255.

Olierook, H.K.H., Agangi, A., Plavsa, D., Reddy, S.M., Yao, W., Clark, C., Occhipinti, S.A., Kylander-Clark, A.R.C., 2018. Neoproterozoic hydrothermal activity in the West Australian Craton related to Rodinia assembly or breakup? Gondwana Research 68, 1-12.

Paces, J.B., Miller, J.D., 1993. Precise U-Pb ages of Duluth Complex and related mafic intrusions, northeastern Minnesota: geochronological insights to physical, petrogenetic, paleomagmatic, and tectonomagmatic processes associated with the 1.1 Ga Midcontinent Rift System. Journal of Geophysical Research 98, 13997-14013.

Parrish, R.R., 1990. U-Pb dating of monazite and its application to geological problems. Canadian Journal of Earth Sciences 27, 1431-1450.

Paton, C., Woodhead, J., Hellstrom, J., Hergt, J., Greig, A., Maas, R., 2010. Improved laser ablation U-Pb zircon geochronology through robust down-hole fractionation correction. Geochemistry, Geophysics, Geosystems 11.

Paton, C., Hellstrom, J., Paul, B., Woodhead, J., Hergt, J., 2011. Iolite: Freeware for the visualisation and processing of mass spectrometric data. Journal of Analytical Atomic Spectrometry 26, 2508.

Pearson, J.M., 1996. Alkaline rocks of the Gifford Creek Complex, Gascoyne Province, Western Australia: their petrogenetic and tectonic significance. PhD thesis, University of Western Australia, 219 p.

Pearson, J.M., Taylor, W.R., Barley, M.E., 1996. Geology of the alkaline Gifford Creek Complex, Gascoyne Complex, Western Australia. Australian Journal of Earth Sciences 43, 299-309.

Pettke, T., 2008. Analytical protocols for element concentration and isotope ratio measurements in fluid inclusions by LA-(MC)-ICP-MS, in: Sylvester, P. (Ed.), Laser ablation ICP-MS in earth sciences: current practices and outstanding issues. Mineral Association of Canada Short Course Series. Mineral Association of Canada, Vancouver, pp. 189-218.

Pettke, T., Oberlie, F., Audétat, A., Guillong, M., Simon, A.C., Hanley, J.J., Klemm, L.M., 2012. Recent developments in element concentration and isotope ratio analysis of individual fluid inclusions by laser ablation single and multiple collector ICP-MS. Ore Geology Reviews 44, 10-38.

Pidgeon, R.T., Smith, C.B., Fanning, C.M., 1989. Kimberlite and lamproite emplacement ages in Western Australia. In: Ross, J. et al. (Eds.), Kimberlites and related rocks: their composition, occurrence, origin and emplacement. Geological Society of Australia Special Publication No. 14. Blackwell Scientific Publications, Carlton, Australia, pp. 369-381.

Piechocka, A.M., Sheppard, S., Fitzsimons, I.C.W., Johnson, S.P., Rasmussen, B., Jourdan, F., 2018. Neoproterozoic 40Ar/39Ar mica ages mark the termination of a billion years of intraplate reworking in the Capricorn Orogen, Western Australia. Precambrian Research 310, 391-406.

Pirajno, F., González-Álvarez, I., 2013. The ironstone veins of the Gifford Creek ferrocarbonatite complex, Gascoyne Province: Geological Survey of Western Australia, Record 2013/12, p. 19.

Pirajno, F., González-Álvarez, I., Chen, W., Kyser, K.T., Simonetti, A., Leduc, E., leGras, M., 2014. The Gifford Creek Ferrocarbonatite Complex, Gascoyne Province, Western Australia: associated fenitic alteration and a putative link with the ~1075 Ma Warakurna LIP. Lithos 202-203, 100-119.

Pirajno, F., Hoatson, D.M., 2012. A review of Australia's Large Igneous Provinces and associated mineral systems: implications for mantle dynamics through geological time. Ore Geology Reviews 48, 2-54.

Pisarevsky, S.A., S.A., Wingate, M.T.D., Li, Z-X., Wang, X-C., Tohver, E., Kirkland, C.L., 2014. Age and paleomagnetism of the 1210 Ma Gnowangerup–Fraser dyke swarm, Western Australia, and implications for late Mesoproterozoic paleogeography. Precambrian Research 246, 1-15.

Pourtier, E., Devidal, J.L., Gibert, F., 2010. Solubility measurements of synthetic neodymium monazite as a function of temperature at 2 kbars, and aqueous neodymium speciation in equilibrium with monazite. Geochimica et Cosmochimica Acta 74, 1872-1891.

Rasmussen, B., Fletcher, I.R., Sheppard, S., 2005. Isotopic dating of the migration of a low- grade metamorphic front during orogenesis. Geology 33, 773-776.

Rasmussen, B., Muhling, J.R., 2007. Monazite begets monazite: evidence for dissolution of detrital monazite and reprecipitation of syntectonic monazite during low-grade regional metamorphism. Contributions to Mineralogy and Petrology 154, 675-689.

Rasmussen, B., Fletcher, I.R., Muhling, J.R., 2007. In situ U–Pb dating and element mapping of three generations of monazite: Unravelling cryptic tectonothermal events in low-grade terranes. Geochimica et Cosmochimica Acta 71, 670-690.

Seydoux-Guillame, A.M., Paquette, J.L., Wiedenbeck, M., Montel, J.M., Heinrich, W., 2002. Experimental resetting of the U-Th-Pb systems in monazite. Chemical Geology 191, 165-181.

Seydoux-Guillame, A.M., Wirth, R., Deutsch, A., Schärer, U., 2004. Microstructure of 24-1928 Ma concordant monazites; implications for geochronology and nuclear waste deposits. Geochimica et Cosmochimica Acta 68, 2517-2527.

Scherer, E., Münker, C., Mezger, K., 2001. Calibration of the Lutetium-Hafnium Clock. Science 293, 683.

Shannon, R.D., 1976. Revised effective ionic radii and systematic studies of interatomic distances in halides and chalcogenides. Acta Crystallographica Section A 32, 752-767.

Sheppard, S., Occhipinti, S.A., Nelson, D.R., 2005. Intracontinental reworking in the Capricorn Orogen, Western Australia: the 1680-1620 Ma Mangaroon Orogeny. Australian Journal of Earth Sciences 52, 443-460.

Sheppard, S., Occhipinti, S.A., Tyler, I.M., 2004. A 2005–1970 Ma Andean-type batholith in the southern Gascoyne Complex, Western Australia. Precambrian Research 128, 257-277.

Sheppard, S., Rasmussen, B., Muhling, J.R., Farrell, T.R., Fletcher, I.R., 2007. Grenvillian-aged orogenesis in the Palaeoproterozoic Gascoyne Complex, Western Australia: 1030-950 Ma reworking of the Proterozoic Capricorn Orogen. Journal of Metamorphic Geology 25, 477-494.

Sheppard, S., Bodorkos, S.P., Johnson, S.P., Wingate, M.T.D., Kirkland, C.L., 2010a. The Paleoproterozic Capricorn Orogeny: intracontinental reworking not continent-continent collision. Geological Survey of Western Australia, Report 108, p. 33.

Sheppard, S., Johnson, S.P., Wingate, M.T.D., Kirkland, C.L., Pirajno, F., 2010b. Explanatory notes for the Gascoyne Province: Geological Survey of Western Australia, p. 336.

Slezak, P.R., Spandler, C., and Blake, K. 2018. Ghosts of apatite past: using hyperspectral CL and micro-geochemical data to reveal multi-generational apatite in the Gifford Creek Carbonatite Complex, Australia. The Canadian Mineralogist 56, 773-797.

Smithies, R.H., Kirkland, C.L., Korhonen, F.J., Aitken, A.R.A., Howard, H.M., Maier, W.D., Wingate, M.T.D., Quentin de Gromard, R., Gessner, K., 2015. The Mesoproterozoic thermal evolution of the Musgrave Province in central Australia - plume vs. the geological record. Gondwana Research 27, 1419-1429.

Söderlund, U., Patchett, P.J., Vervoort, J.D., Isachsen, C.E., 2004. The 176Lu decay constant determined by Lu–Hf and U–Pb isotope systematics of Precambrian mafic intrusions. Earth and Planetary Science Letters 219, 311-324.

Song, W., Xu, C., Smith, M.P., Chakhmouradian, A.R., Brenna, M., Kynický, J., Chen, N., Yang, Y., Deng, M., Tang, H., 2018. Genesis of the world's largest rare earth element deposit, Bayan Obo, China: Protracted mineralization evolution over ~1b.y. Geology 46, 323-326.

Spaggiari, C.V., Kirkland, C.L., Smithies, R.H., Wingate, M.T.D., Belousova, E.A., 2015. Transformation of an Archean craton margin during Proterozoic basin formation and magmatism: The Albany–Fraser Orogen, Western Australia. Precambrian Research, 266, 440-466.

Spandler, C., Hammerli, J., Pirard, C., 2018. Neodymium isotope disequilibria in subducted sediments, and potential consequences for subduction zone recycling. Geology 46, 815-818.

Spandler, C., Pettke, T., Rubatto, D., 2011. Internal and external fluid sources for eclogite-facies veins in the Monviso meta-ophiolite, Western Alps: implications for fluid flow in subduction zones. Journal of Petrology 52, 1207-1236.

Stacey, J.S., Kramers, J.D., 1975. Approximation of terrestrial lead isotope evolution by a two-stage model. Earth and Planetary Science Letters 26, 207-221.

Stark, J.C., Wang, X-C., Li, Z-X., Denyszyn, S., Rasmussen, B., Zi, J-W., 2018. 1.39 Ga mafic dyke swarm in southwestern Yilgarn Craton marks Nuna to Rodinia transition in the West Australian Craton. Precambrian Research 316, 291-304.

Sun, S.S., Jaques, A.L., McCulloch, M.T., 1986. Isotopic evolution of the Kimberley block, Western Australia, Abstracts of 4th International Kimberlite Conference. Geological Society of Australia, Perth, pp. 346-348.

Tappe, S., Brand, N. B., Stracke, A., van Acken, D., Liu, C. Z., Strauss, H., et al. 2017. Plates or plumes in the origin of kimberlites: U/Pb perovskite and Sr-Nd-Hf-Os-CO isotope constraints from the Superior craton (Canada). Chemical Geology 455, 57-83.

Tera, F., Wasserburg, G.J., 1972. U-Th-Pb systematics in three Apollo 14 basalts and the problem of initial Pb in lunar rocks. Earth and Planetary Science Letters 14, 281-304.

Teufel, S., Heinrich, H., 1997. Partial resetting of the U-Pb isotope system in monazite through hydrothermal experiments: An SEM and U-Pb isotope study. Chemical Geology 137, 273-281.

Thirlwall, M.F., Walder, A.J., 1995. In situ Hf isotope ratio analysis of zircon by inductively coupled plasma multi collector mass spectrometry. Chemical Geology 122, 241-247.

Vervoort, J.D., Patchett, P.J., Blichert-Toft, J., Albarède, F., 1999. Relationships between Lu–Hf and Sm–Nd isotopic systems in the global sedimentary system. Earth and Planetary Science Letters 168, 79-99.

Wendt, I., Carl, C., 1991. The statistical distribution of the mean squared weighted deviation. Chemical Geology: Isotope Geoscience section 86, 275-285.

Wiedenbeck, M., Alle, P., Corfu, F., Griffin, W.L., Meier, M., Oberli, F., von Quadt, A., Roddick, J.C., Spiegel, W., 1995. Three natural zircon standards for U-Th-Pb, Lu-Hf, trace element and REE analyses. Geostandards Newsletter 19, 1-23.

Wingate, M.T.D., Campbell, I.H., Composton, W., Gibson, G.M., 1998. Ion microprobe U-Pb ages for Neoproterozoic basaltic magmatism in south-central Australia and implications for the breakup of Rodinia. Precambrian Research 87, 138-159.

Wingate, M.T.D., Pirajno, F., Morris, P.A., 2004. Warakurna large igneous province: A new Mesoproterozoic large igneous province in west-central Australia. Geology 32, 105-108.

Woodhead, J., Hergt, J., Shelley, M., Eggins, S., Kemp, R., 2004. Zircon Hf-isotope analysis with an excimer laser, depth profiling, ablation of complex geometries, and concomitant age estimation. Chemical Geology 209, 121-135.

Woodhead, J.D., Hergt, J.M., 2005. A preliminary appraisal of seven natural zircon reference materials for in situ Hf isotope determination. Geostandards and Geoanalytical Research 29, 183-195.

Woolley, A.R., Bailey, D.K., 2012. The crucial role of lithospheric structure in the generation and release of carbonatites: geological evidence. Mineralogical Magazine 76, 259-270.

Woolley, A.R., Kjarsgaard, B.A., 2008. Paragenetic types of carbonatite as indicated by the diversity and relative abundances of associated silicate rocks: evidence from a global database. The Canadian Mineralogist 46, 741-752.

Workman, R.K. et al., 2004. Recycled metasomatized lithosphere as the origin of Enriched Mantle II (EM2) end-member: Evidence from the Samoan Volcanic Chain. Geochemistry, Geophysics, Geosystems 5, 1-44.

Yang, K-F., Fan, H-R., Santosh, M., Hu, F-F., Wang, K-Y., 2011. Mesoproterozoic mafic and carbonatitic dykes from the northern margin of the North China Craton: implications for the final breakup of Columbia supercontinent. Tectonophysics 498, 1-10.

Yang, X., Lai, X., Pirajno, F., Liu, Y., Ling, M., Sun, W., 2017. Genesis of the Bayan Obo Fe-REE-Nb formation in Inner Mongolia, North China craton: a perspective review. Precambrian Research 288, 39-71.

Yang, Y-H., Wu, F-Y., Yang, J-H., Chew, D.M., Xie, L-W., Chu, Z-Y., Zhang, Y-B., Huang, C., 2014. Sr and Nd isotopic compositions of apatite reference materials used in U-Th-Pb geochronology. Chemical Geology 385, 35-55.

Zhang, S., Li, Z.-X., Evans, D.A.D., Wu, H., Li, H., Dong, J., 2012. Pre-Rodinia supercontinent Nuna shaping up: A global synthesis with new paleomagnetic results from North China. Earth and Planetary Science Letters 353-354, 145-155.

Zhang, S.H., Zhao, Y., Liu, Y., 2017. A precise zircon Th-Pb age of carbonatite sills from the world's largest Bayan Obo deposit: Implications for timing and genesis of REE-Nb mineralization. Precambrian Research 291, 202-219.

Zhu, X., Sun, J., Pan, C., 2015. Sm-Nd isotopic constraints on rare-earth mineralization in the Bayan Obo ore deposit, Inner Mongolia, China. Ore Geology Reviews 64, 543-553.

Zi, J.W., Gregory, C., Rasmussen, B., Sheppard, S., Muhling, J.R., 2017. Using monazite geochronology to test the plume model for carbonatites: The example of Gifford Creek Carbonatite Complex, Australia. Chemical Geology 463, 50-60.

Zi, J.W., Rasmussen, B., Muhling, J.R., Fletcher, I.R., 2015. In situ U-Pb geochronology of xenotime and monazite from the Abra polymetallic deposit in the Capricorn Orogen, Australia: Dating hydrothermal mineralization and fluid flow in a long-lived crustal structure. Precambrian Research 260, 91-112.

Chapter 5

Geology and Ore Genesis of the Carbonatite-associated Yangibana LREE District, Gascoyne Province, Western Australia

Abstract

Carbonatites are important sources of critical metals, particularly rare earth elements (REE), which are used in advanced technologies and manufacturing. However, carbonatite complexes are often highly heterogeneous, which complicates exploration strategies and comparisons with other carbonatite-hosted mineral deposits. This study examines the ore mineralogy and ore genesis of the Yangibana LREE district, hosted in the Gifford Creek Carbonatite Complex (GCCC), Western Australia.

The Yangibana LREE district consists of multiple mineral prospects/deposits hosted within the GCCC, which comprises a range of rock types including calcite carbonatites, dolomite carbonatites, magnetite-biotite dykes, ankerite-siderite carbonatites, silica-rich alkaline veins, fenites, glimmerites, and what have historically been called “ironstones”. Structural analyses indicate the dykes/sills comprising the GCCC were emplaced during a period of extension and/or transtension, possibly utilising existing structures. The Yangibana LREE prospects/deposits are located along many of these structures, particularly along the prominent Bald Hill Lineament.

The primary ore mineral is monazite, which is contained within the ironstone, ankerite-siderite carbonatites, and magnetite-biotite dykes. The ironstones comprise boxwork-textured Fe-oxides/hydroxides, quartz, chalcedony, and LREE-phosphate minerals, which mainly consists of monazite and subordinate rhabdophane. Carbonate mineral-shaped cavities in the ironstones, fenite and glimmerite alteration mantling the ironstone units, and ankerite-siderite carbonatite dykes altering to ironstone-like assemblages in drill core indicate the ironstones are derived from the ankerite-siderite carbonatites: this premise is further supported by similar bulk rock Nd isotope compositions of the ironstones and other alkaline igneous rocks of the GCCC. Isocon diagrams between the ankerite-siderite carbonatites and ironstones show significant mass removal, which has resulted in passive REE ore increase by ~3 to ~17 times. This mass removal and ore tenor upgrade is attributed to extensive carbonate breakdown and weathering of the ankerite-siderite carbonatites by meteoric waters near the surface.

Monazite from the ironstones has strong positive and negative correlations between Pr and Nd, and Nd and La, respectively. These relationships are reflected in the bulk rock drill assays, which display substantial variation in the La/Nd ratios throughout the GCCC. The changes in La/Nd are attributed to multiple factors including variations in primary magmatic composition, shifts in the magmatic-hydrothermal systems related to CO_2- versus water-dominated fluid phases, and changes in temperature.

5.1 Introduction

Carbonatites – peralkaline-alkaline igneous rocks containing ≥ 50% primary carbonate minerals (Le Maitre, 2002) – are the most important primary sources for critical metals such as rare earth elements (REE) and high field strength elements (HFSE) (Chakhmouradian and Zaitsev, 2012; Wall, 2014; Goodenough et al., 2016). Although, REE deposits associated with peralkaline-alkaline silicate igneous rocks typically contain higher tonnages, they often have lower grades than carbonatite-hosted REE deposits, which also provide superior REE recovery (Walters et al., 2011; Wall, 2014). Not surprisingly, the largest currently-producing mines for REE (Bayan Obo, China; Maoniuping, China; and Mt. Weld, Australia) and Nb (Araxá, Brazil; Catalão I & II, Brazil; and St. Honoré, Canada) are all carbonatite-associated critical metal deposits (Mitchell, 2015; Elliott et al., 2018). In many cases, the economic viability of mining carbonatite deposits relies on natural post-magmatic enrichment processes such as lateritisation to concentrate Nb and REE to ore grades (Moreteani and Preinfalk, 1996).

Australia hosts a variety of different REE deposits (Fig. 5.1), including several carbonatite deposits such as Mt. Weld, Cummins Range, and the Yangibana LREE district (Jaireth et al., 2014). The Yangibana LREE district, owned by Hastings Technology Metals Ltd., contains 21 million tonnes of ore grading 1.17% TREO. It is hosted by the Gifford Creek Carbonatite Complex (GCCC) of Western Australia, and is a collective of small deposits/prospects found in dykes and sills throughout the complex. The deposits are particularly rich in Pr and Nd, which are hosted mainly in monazite within ironstone dykes (Hastings Technology Metals Ltd., 2019). The ironstone dykes or “ironstones”, as they have historically been called, are not Fe-rich sedimentary

rocks as their name might imply; they occur as anastomosing dykes and sills that crosscut the Paleo to Mesoproterozoic granitic, metasedimentary, and sedimentary rocks in the area. Previous work on the complex has provided descriptions of a calcite and dolomite carbonatite dyke/sill complex known as the Lyons River Sills (Pearson, 1996; Pearson and Taylor, 1996; Pearson et al., 1996) and has attempted to establish links between the Lyons River Sills and REE mineralisation (Pirajno et al., 2014). However, it was not until recently that fresh ankerite-siderite carbonatites (a.k.a. true ferrocarbonatites) as well as magnetite-biotite dykes were reported in the GCCC (Slezak et al., 2018; Slezak and Spandler, 2019; Chapter 2). These newly recognised rock types are of additional significance, as they also host considerable monazite mineralisation. Recent geochronology work yielded a range of dates related to formation and resetting (Zi et al., 2017; Slezak and Spandler, 2019). This additional age and geochemical context warrants a re-evaluation of the ore genesis of the GCCC by bringing together new geochemical, petrographical, and isotopic data.

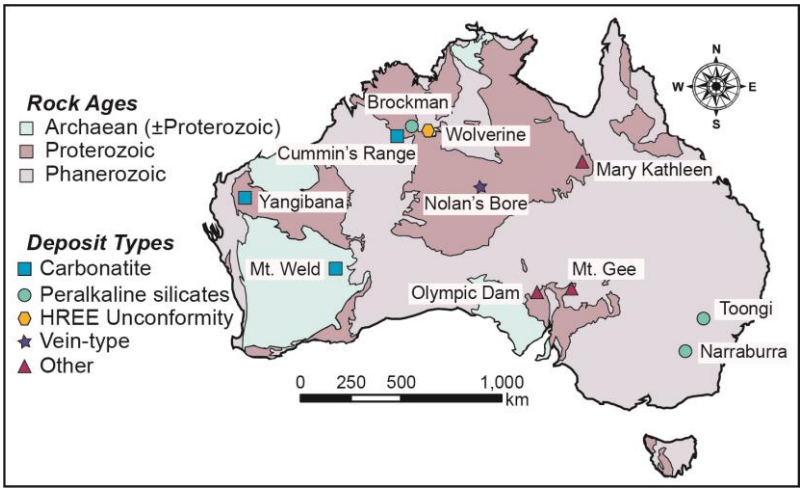

Figure 5.1 Map of major REE deposit types in Australia (modified from Jaireth et al., 2014).

This chapter combines previous data with field mapping, bulk rock geochemistry, and monazite chemistry data to better characterise and understand the Yangibana LREE deposits and prospects. The distribution of ore metals across the complex is examined and the mechanisms for increases in ore tenor through weathering is evaluated. This chapter presents a new ore genesis model for the district and compares Yangibana to other critical metal-bearing carbonatites worldwide.

5.2 Regional Geology and Geologic History

The Yangibana LREE deposit is hosted by the GCCC in the Gascoyne Province of Western Australia. The Gascoyne Province comprises granitic rocks, gneisses, and metasedimentary rocks that have undergone over 1 b.y. of terrane assembly and re-working related to at least seven major orogenic events, creating multiple large-scale faults that delineate different crustal zones in the Gascoyne Province (Sheppard et al., 2010a,b; Johnson et al., 2013; 2017; Chapter 2; Chapter 4).

The GCCC sits adjacent to the Lyons River Fault, which has been determined via seismic reflection surveys to extend down to – and offset – the Mohorovičić Discontinuity (Johnson et al., 2013). The Lyons River Fault is a major shear zone, which sutured the Neoarchean Glenburgh Terrane with the Archean Pilbara Craton during the 2215 to 2145 Ma Ophthalmia Orogeny (Sheppard et al., 2005; Johnson et al., 2011; 2013). It was later reactivated as an extensional structure prior to and after the 1680 to 1620 Ma Mangaroon Orogeny (Sheppard et al., 2005), and again as a reverse fault system during the 1320 to 1170 Ma Mutherbukin Tectonic Event (Korhonen et al., 2015; Johnson et al., 2013).

The GCCC mainly intrudes the Durlacher Supersuite and Pooranoo Metamorphics in the region between the Lyons River Fault and the Bald Hill Lineament (Fig. 5.2a). However, some small dykes are present south of the Lyons River Fault in the Edmund Group, and several different alkaline dykes and sills have been found immediately to the north of the Bald Hill Lineament (Fig. 5.2).

After emplacement of the GCCC, the region was subjected to several major tectonomagmatic events, including the 1320 to 1170 Ma Mutherbukin Tectonic Event (Korhonen et al., 2015), the 1090 to 1040 Ma Giles Event (Smithies et al., 2015), the 1030 to 950 Ma Edmundian Orogeny (Martin and Thorne, 2004; Sheppard et al. 2007), the 955 to 830 Ma Kuparr Tectonic Event (Cutten and Johnson, 2018; Olierook et al., 2018), and the 570 Ma Mulka Tectonic Event, (Sheppard et al., 2010a). Some of these events are recorded by U–Pb ages of GCCC

monazite and Sm–Nd isochrons from monazite and apatite that have undergone dissolution and precipitation (Zi et al., 2017; Slezak and Spandler, 2019; Chapter 4).

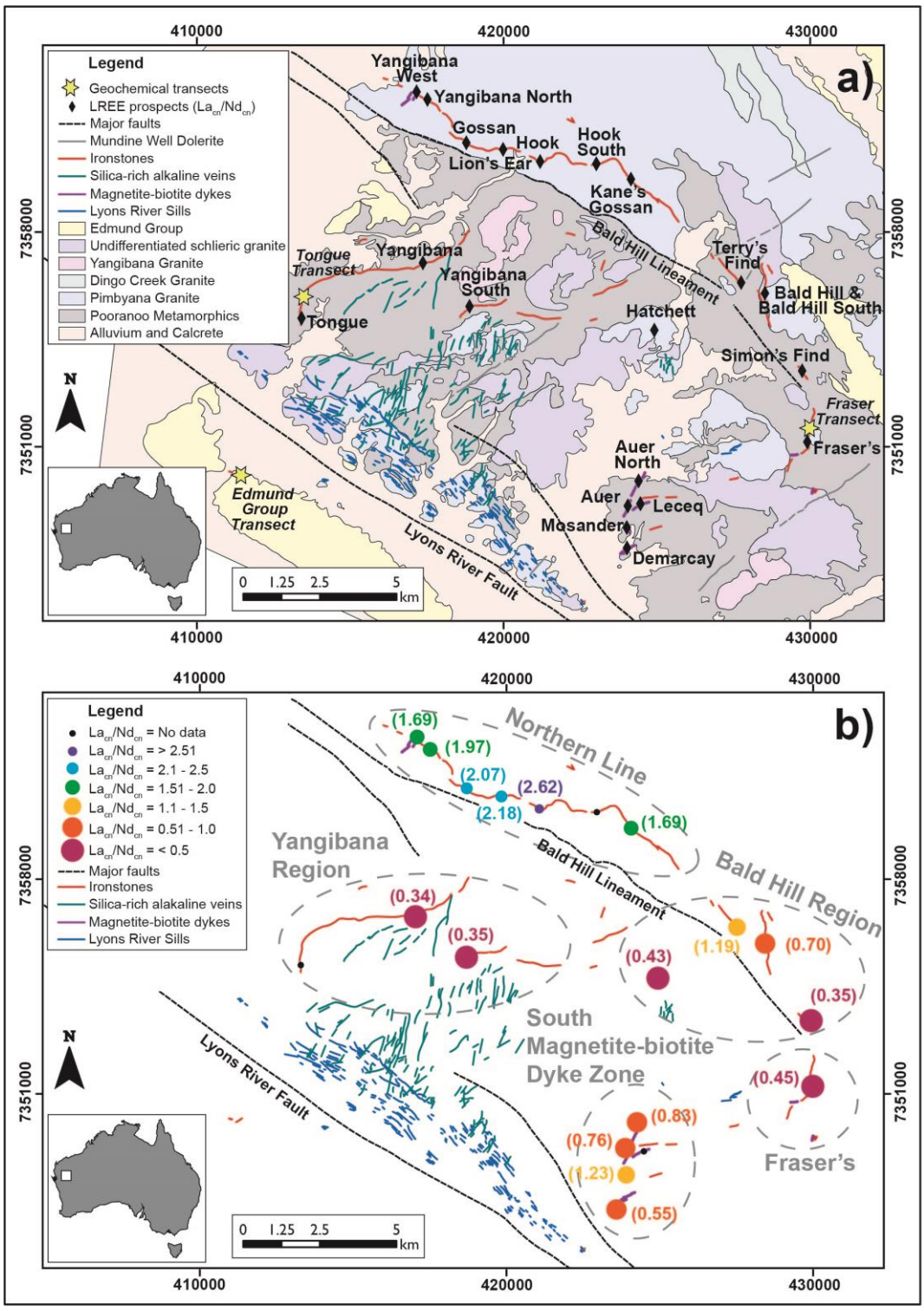

Figure 5.2 a) Geologic map of the Gifford Creek Carbonatite Complex (GCCC) with prospect locations and sampling transect locations. b) Distribution of La_{cn}/Nd_{cn} values based on Hasting Technology Metals drill assay data. Five major deposit/prospect regions are circled. The lowest La_{cn}/Nd_{cn} (highest Nd concentrations) are located in the central and east central regions of the GCCC (modified after Slezak et al., 2018).

5.3 Analytical Techniques

5.3.1 Cathodoluminescence and major element analyses of ore minerals

All REE ore samples were prepared as polished thin sections and 25 mm diameter polished pucks, both of which were examined using a Leica DMRXP optical microscope. Subsequent cathodoluminescence (CL) analyses of the ore mineral, monazite, were conducted using a JEOL XM-86440 CL spectrometer connected to the JEOL JXA-8200 WD/ED electron probe micro-analyzer (EPMA) at the Advanced Analytical Centre (AAC) at James Cook University (JCU), Townsville, Australia, using the same setup and conditions as those in Slezak et al. (2018) and Chapter 3. Deconvolution of these spectra was conducted using the Optical Fit 17.07 software from CSIRO (Torpy and Wilson, 2008).

After CL analysis, the samples were re-polished, carbon-coated again, and analysed for major/minor elements in monazite and rhabdophane using the JEOL JXA-8200 EPMA at JCU. The electron beam was set to spot size of 2 to 5 μm, with the accelerating voltage and beam current set to 15 kV and 20 nA, respectively. All elements were analysed for 20s on peak with 10s on background. Element concentrations were quantified using well-characterised, in-house standards as follows: Ca and Si (wollastonite), Sr (SrF_2), P and Ce ($CePO_4$), Nd ($NdPO_4$), Sm ($SmPO_4$), Pr ($PrPO_4$), Y (YPO_4), Gd ($GdPO_4$), Dy ($DyPO_4$), La ($LaPO_4$), and Th (Th metal). The φρz procedure was used to correct the analyses (Armstrong, 1991).

5.3.2 Trace element analysis of monazite

Trace elements analyses of monazite were conducted using a Coherent GeoLasPro 193nm Excimer laser coupled to a Varian (now Bruker) 820-MS quadrupole ICP-MS at the AAC, JCU. Monazite grains were ablated in a large volume cell (Fricker et al., 2011), using a 24 μm spot size, repetition rate of 10 Hz, and surface energy density (measured at the site of ablation) of 4 J/cm^2. The ablated material was carried in high purity He gas then mixed with Ar before being introduced to the ICP-MS. The rate of oxide production and plasma fractionation were monitored by keeping ThO/Th at or below 0.5%, and $^{238}U/^{232}Th$ sensitivity ≈ 1 (Pettke, 2008). The synthetic glasses NIST SRM 610 and 612 were used as the primary and secondary standards, respectively,

with reference values taken from Spandler et al. (2011). The Ce contents, as determined by EPMA WDS, were used as internal standards for monazite. Data reduction was carried out using the SILLS program (Guillong et al., 2008), employing the errors and detection limits calculation methods of Luo et al. (2007) and Pettke et al. (2012), respectively. The isotopes chosen for analysis include: ^{27}Al, ^{29}Si, ^{31}P, ^{43}Ca, ^{44}Ca, ^{49}Ti, ^{55}Mn, ^{66}Zn, ^{75}As, ^{85}Rb, ^{88}Sr, ^{89}Y, ^{90}Zr, ^{93}Nb, ^{118}Sn, ^{133}Cs, ^{137}Ba, ^{139}La, ^{140}Ce, ^{141}Pr, ^{143}Nd, ^{147}Sm, ^{151}Eu, ^{157}Gd, ^{159}Tb, ^{163}Dy, ^{165}Ho, ^{167}Er, ^{169}Tm, ^{171}Yb, ^{175}Lu, ^{178}Hf, ^{181}Ta, ^{208}Pb, ^{232}Th, and ^{238}U.

5.3.3 Bulk rock Sm-Nd isotope analysis

Whole rock Sm-Nd isotope analyses of five samples (three ironstones, one fenite, one Pimbyana Granite) were performed at the University of Adelaide with a Finnigan MAT262 thermal ionisation mass spectrometer (TIMS) in static and quadrupole cup dynamic measurement modes following the routine described in Wade et al. (2006). The measurements were corrected for mass fractionation by normalisation to ^{146}Nd/^{142}Nd = 0.7219 and ^{143}Nd/^{144}Nd ratios were normalised to the TIMS value of JNdi-1 glass (0.512098 ± 13; Fisher et al. 2011).

5.3.4 Bulk rock transect samples

Sampling transects were completed across the ironstone dykes at the Fraser's deposit (FT) and Tongue prospect (TT), which cross-cut the Pimbyana Granite and Pooranoo Metamorphics, respectively (Fig. 5.2a). A third sample transect was taken across a subeconomic ironstone dyke intruding the Edmund Group (EGT). Samples were taken directly from the ironstone, which was considered the origin (0 m). Additional samples were taken at available outcrops including the contact between the ironstone and the fenite, within the fenite (centimetres to metres from the origin), and in the least-altered host rock (metres to tens of metres from the origin). Any visible surficial weathering rinds were trimmed and discarded from the collected samples. The purpose was to identify the extent of alteration related to the ironstone intrusions and to assess geochemical exchange between the host rocks and ironstones (or rather their precursor igneous intrusion). The location, sample type, and geochemical summary are found in Appendix 5.A. Bulk rock mass

balance data were calculated according to the methods of Gresen (1967) and Grant (1986) using the EASYGRESGRANT Excel macros and spreadsheets (López-Moro, 2012).

All samples were crushed and then milled to a fine powder using a tungsten carbide ring mill. The Fraser's transect samples were analysed for major element composition from Li borate fusion glasses in the AAC at JCU, using a Bruker-AXS S4 Pioneer X-ray Fluorescence Spectrometer. The glasses were then mounted into 25 mm diameter epoxy pucks and analysed using the LA-ICP-MS setup described previously. In addition to the afore mentioned isotopes chosen for monazite, the following analytes were measured for the glasses: ^{9}Be, ^{27}Al, ^{45}Sc, ^{49}Ti, ^{52}Cr, ^{53}Cr, ^{57}Fe, ^{59}Co, ^{60}Ni, ^{65}Cu, ^{66}Zn, ^{69}Ga, ^{72}Ge, ^{85}Rb, ^{98}Mo, ^{121}Sb, and ^{133}Cs. The data were reduced using Glitter software (Van Achterbergh et al., 2001).

Samples from the Tongue and Edmund Group ironstone transects were analysed for 53 elements by Bureau Veritas Commodities Canada Ltd in Vancouver, British Columbia where the samples were split. One sample split was fused into a lithium metaborate/tetraborate bead. The sample bead was dissolved in American Chemical Society (ACS) grade nitric acid dissolution and analysis of the solution conducted via ICP-MS for the following elements: Mg, Al, Si, P, K, Ca, Sc, Ti, V, Cr, Mn, Fe, Ni Ga, Rb, Sr, Y, Zr, Nb, Sn, Cs, Ba, La, Ce, Pr, Nd, Sm, Eu, Gd, Tb, Dy, Ho, Er, Tm, Yb, Lu, Hf, Ta, W, Th, and U. The second sample split was digested in aqua regia and analysed via inductively coupled emission spectroscopy/mass spectroscopy (ES/MS) for the elements Li, Be, B, Cr, Co, Cu, Zn, Ge, As, Se, Mo, Pd, Ag, Cd, In, Sb, Te, Re, Pt, Au, Hg, Tl, Pb, and, Bi. Carbon and S were determined using the LECO method.

5.4 Overview of the Gifford Creek Carbonatite Complex

5.4.1 Rock types of the GCCC

The GCCC comprises several different types of intrusive bodies, hydrothermal units, and associated alteration assemblages. The primary magmatic-hydrothermal units are the Lyons River Sills, ankerite-siderite carbonatites, magnetite-biotite dykes, silica-rich alkaline veins as well as the in situ alteration assemblages for these units, which include fenites and glimmerites (see Chapter 2).

5.4.1.1 Lyons River Sills

The Lyons River Sills (Fig. 5.3a,b) mainly occur as a swarm of carbonatite dykes/sills trending NW-SE in the area immediately to the north of the Lyons River Fault. The Lyons River Sills are composed of fine-grained, Fe-bearing dolomite and occasionally calcite, minor amounts of Mg- and F-rich arfvedsonite, aegirine, Mg-bearing biotite, magnetite, ilmenite, and fluorapatite in addition to trace amounts of monazite, zircon, pyrite, and chalcopyrite (Pearson, 1996; Pearson and Taylor, 1996; Pearson et al., 1996; Chapter 2). The Lyons River Sills strike northwest and dip variably 30 to 60° SW (Fig. 5.4a), subparallel with the Lyons River Fault and Bald Hill Lineament (Fig. 5.2). Outcrop scale features such as veins, veinlets, and joints (Fig. 5.4) display orientations and morphologies analogous to district scale dykes and faults (Fig. 5.2). For example, the small, outcrop scale ironstone veinlets are located orthogonal to the Lyons River Fault (Fig. 5.4b,c) whereas the carbonatite veinlets are oriented along joint sets parallel to the Lyons River Fault (Fig. 5.4c). The silica-rich alkaline veins (Fig. 5.2) also broadly correspond to the N-S joint sets recorded at the outcrop scale (Fig. 5.4b). Step-over patterns and veinlet pinch outs are also common among the Lyons River Sills at both a district and outcrop scales (Figs. 5.2, 5.3b, and 5.4d).

5.4.1.2 Ankerite-siderite carbonatites

The ankerite-siderite carbonatites (Fig. 5.3c) have only been observed in drill core at depths of 40 to 50 m in the northwestern corner of the GCCC along the Bald Hill Lineament. They occur as 0.05 to 1 m thick dykes (Fig. 5.3c) composed of coarse-grained siderite and ankerite, with minor calcite and with enclaves of magnetite, biotite, monazite, apatite, and quartz (Fig. 5.3d; Slezak et al., 2018; Chapter 2; Chapter 3).

5.4.1.3 Magnetite-biotite dykes

Magnetite-biotite dykes (Fig. 5.3e) are present mainly in the southeast region between the Fraser's deposit and Demarcay prospect (Fig. 5.2). They comprise magnetite, biotite, apatite, and monazite (Fig. 5.3f; Chapter 2; Chapter 3). Many magnetite-biotite dykes, particularly at Auer North prospect, do not crop out, but were discovered during exploration drilling Hastings Technology

Metals Ltd. The units that appear at the surface, like at Demarcay and Mosander, dip to the west-northwest. Some localities, like Mosander, are nearly flat lying sills (Fig. 5.3e) and others, such as Demarcay, are steeply dipping dykes. The thickness of the magnetite-biotite dykes is variable, ranging from 0.1 to 1.5 m.

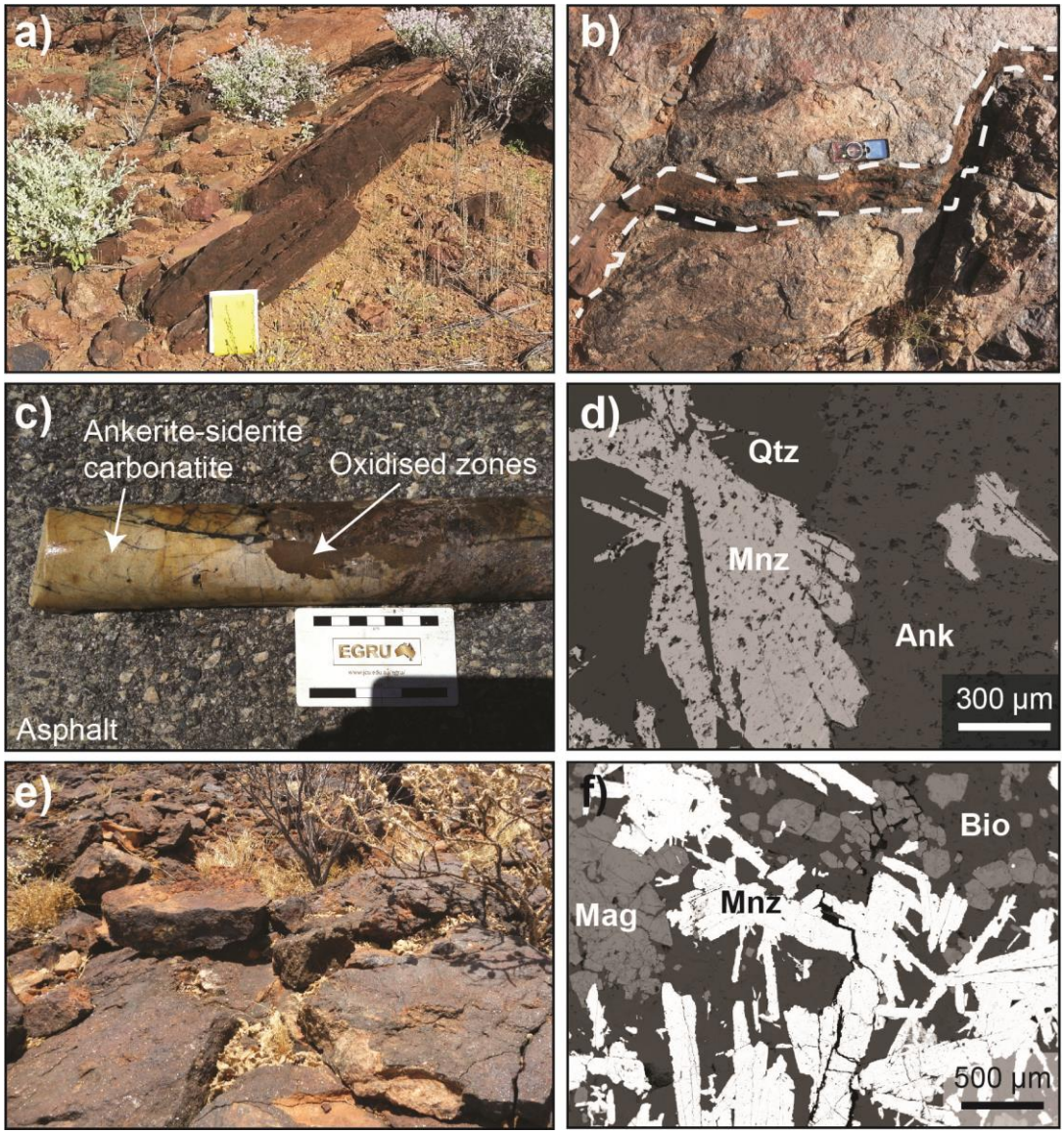

Figure 5.3 Field photos and backscattered electron (BSE) images of GCCC rock types. a) Lyons River Sill dolomite carbonatite with typical dark brown weathering surface and dipping southwest towards the Lyons River Fault. b) Lyons River Sills with a 'z'-shaped step over and deflection of the dyke by a pegmatitic section of schlieric granite. c) True ferrocarbonatite composed of ankerite and siderite from Yangibana North with patchy alteration to iron oxides, similar to the ironstones. d) BSE image of monazite growing in both the quartz and ankerite domains of the ankerite-siderite carbonatites. There is a narrow Fe-oxide rim surrounding the monazite in the ankerite. e) Course-grained magnetite-biotite dyke at Mosander with a flat-lying, sill morphology. f) BSE image of magnetite-biotite dyke with large, tabular, euhedral monazite intergrown with subhedral to euhedral biotite and subhedral to euhedral magnetite.

5.4.1.4 Silica-rich alkaline veins

The silica-rich alkaline veins (Fig. 5.5a) are most abundant as a steeply-dipping, N to NNE trending swarm in the central region of the GCCC. Some display evidence of multiple fluid

pulses and minor shearing along the vein margins. Individual veins can be up to 50 cm in width, several hundred metres in length, and tend to be heterogeneous in mineralogy and texture. The dominant mineralogy is aegirine, quartz, zircon, rutile, magnetite, columbite, monazite, and phlogopite (Chapter 2). These units strike north-northeast, roughly orthogonal to the Lyons River Sills (Figs. 5.2) and tend to follow regional cleavage fabrics and joint planes (Fig. 5.4c).

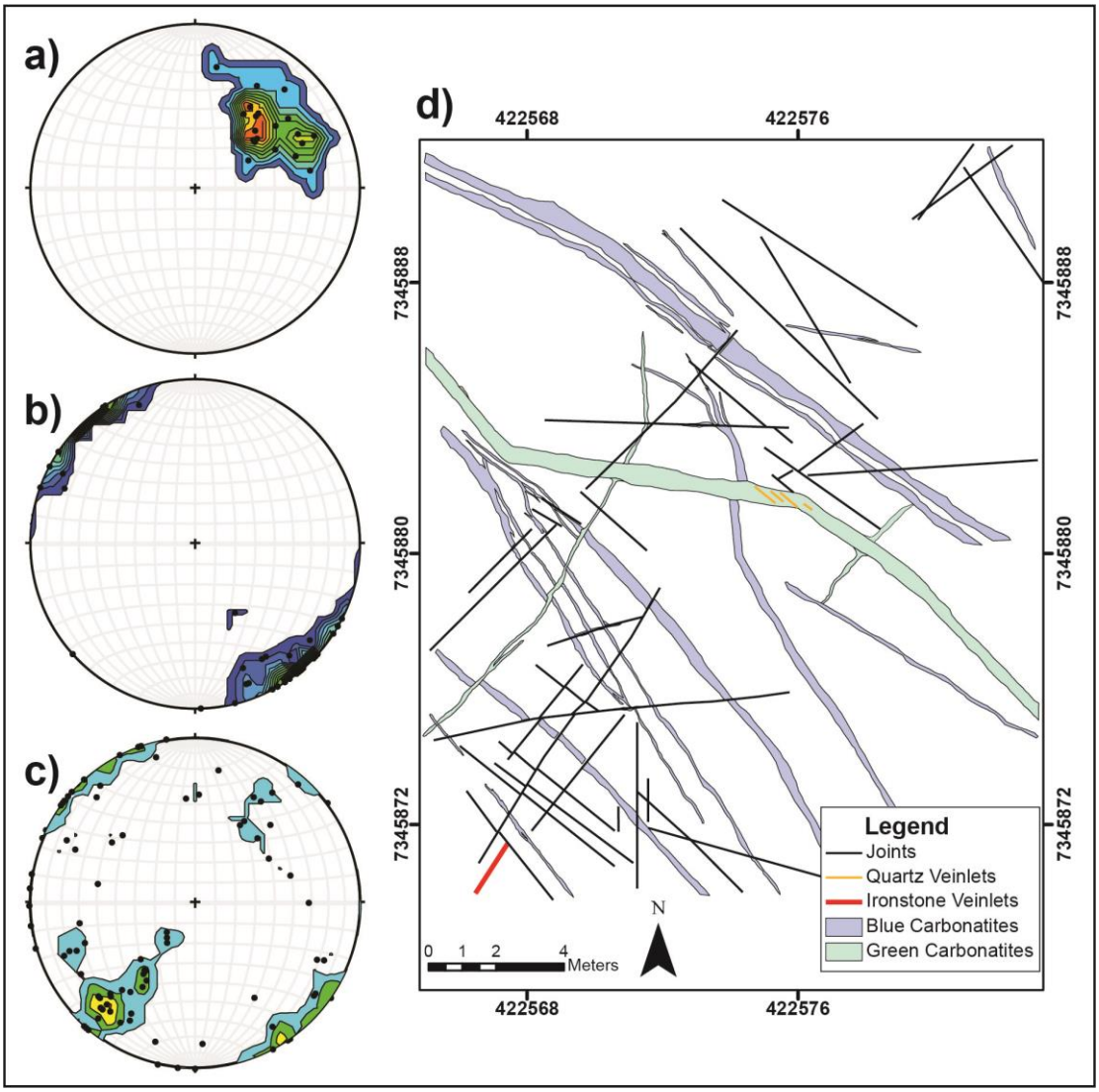

Figure 5.4 Outcrop-scale structural measurements of the Lyons River Sills, ironstones, and joint/fault planes in granite in the southeastern GCCC. a) Stereonet of the pole to planes for the strike and dip of the Lyons River Sills. b) Plot of pole to planes for the ironstone veinlets originating from the Lyons River Sills in outcrop. c) Plot of poles to planes for the joint sets in the schlieric granite hosting the Lyons River Sills. d) Outcrop map of the Lyons River Sills detailing their morphology and showing their relationships with the ironstones and joint sets. White background is granite host rock.

5.4.1.5 Ironstone dykes

Other rock-types present in the GCCC including the voluminous and economically important ironstones, as well as the minor quartz and quartz-magnetite veins and various

alteration assemblages (i.e., fenites and glimmerites). In the Yangibana LREE district, the ironstones specifically refer to large (up to several metres wide) dyke-like structures that protrude from the landscape (Fig. 5.5b). They are mainly located subparallel to the Bald Hill Lineament and along the eastern and western flanks of the GCCC (Fig. 5.2). The ironstones comprise fine-grained hematite with relict magnetite cores, recrystallised quartz, occasional barite, monazite, apatite, rhabdophane, and Mn oxides (Pirajno and González-Álvarez, 2013; this study). The ironstones do not exhibit any primary igneous textures. Most features relate to low temperature mineral precipitation and include botryoidal banding of Mn oxides and hydrous Fe oxides, such as goethite, minor chalcedony banding around open spaces, and Mn oxide crusts (Pirajno and González-Álvarez, 2013, this study). Evidence of carbonate dissolution is present in some ironstone outcrops (Fig. 5.5c). The ironstones contain significant vugs and void spaces at surface and in drill core. Small veinlets, reminiscent of the larger ironstones, are also observed to emanate from the Lyons River Sills (Figs. 5.4d and 5.5d). These veinlets have a northeast-southwest strike and dip subvertically to vertically. They are often composed of Fe oxide minerals, but occasionally exhibit a primary mineral assemblage comprising riebeckite, rutile, carbonate, magnetite, apatite, and monazite.

5.4.1.6 Quartz-magnetite veins

Large quartz and brecciated quartz-magnetite veins (Fig. 5.5e) occasionally crop out in the GCCC. They form wide (~5 to 7 m), prominent white ridges in the landscape, but are only continuous for a few tens of metres. These veins are mainly located in the central GCCC, near Yangibana South. Some of these quartz veins are spatially associated with and subparallel to mineralised ironstones (e.g., Yangibana North). Others are found in close proximity to the silica-rich alkaline veins in the southcentral region. Northeast-southwest trending brecciated quartz-magnetite veins (Fig. 5.5e) are relatively narrow (10 to 70 cm wide) and occur near the ironstones along the Bald Hill Lineament and occasionally near the magnetite-biotite dykes in the southern GCCC.

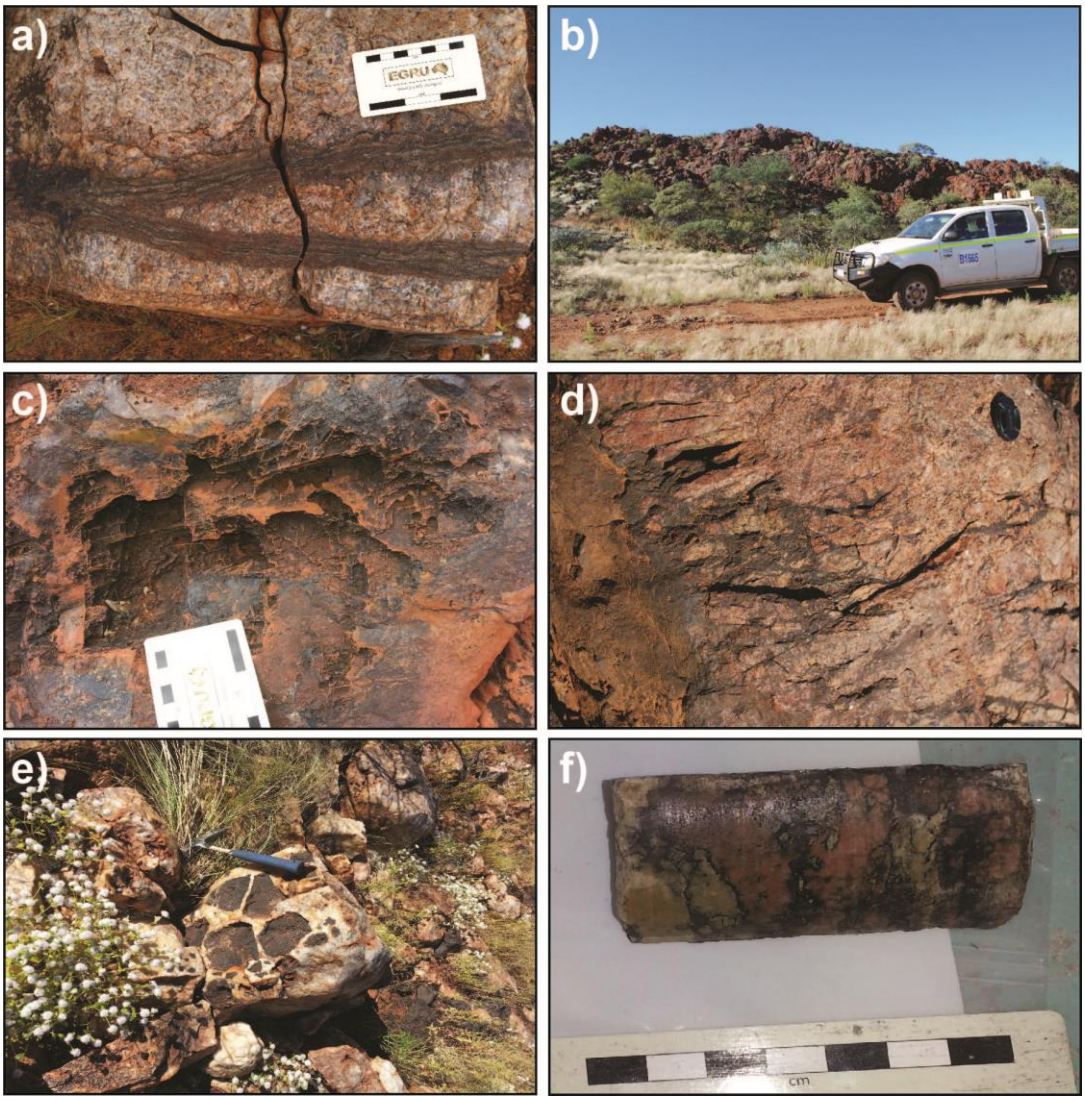

Figure 5.5 Field photos of GCCC rock types and alteration assemblages. a) Silica-rich alkaline vein from the central GCCC with multiple arfvedsonite-riebeckite (dark) and aegirine (light) layers. These dykes contain high amounts of Zr, Ti, and Nb. b) Ironstone outcrop at the Fraser's deposit. c) Ironstone with parallelepiped-shaped dissolution cavities morphologically similar to crystalline carbonate minerals. d) Alkaline amphibole-dolomite veinlets emanating from a Lyons River Sill intrusive dyke. The veins are intruding and fenitising the host granite. e) Quartz-magnetite vein with large magnetite clasts. f) Drill core sample from Yangibana North where the ankerite-siderite carbonatites have extensively fenitised the host granite forming a pink fenite rich in potassium feldspar. The contact between the fenite and the ironstone is composed of glimmerite comprising magnetite, biotite, monazite, and zircon.

5.4.1.7 Alteration assemblages

The two most common alteration assemblages in the GCCC are fenites and glimmerites. The fenites are pink (Fig. 5.5d,f) to white and mainly comprise potassium feldspar with lesser amounts of apatite, monazite, and rarely, microcrystalline quartz. They are pervasive and envelope all of the alkaline rock phases in the complex, but are most conspicuous around the ironstones, ankerite-siderite carbonatites, and the Lyons River Sills. The width of the fenite alteration zone tends is proportional to the width of the dyke/sill (Slezak et al., 2018; Chapter 2; Chapter 3).

Glimmerites composed of biotite, magnetite, monazite, and zircon are present as narrow, contact alteration halos between the fenitised wall rock and the ankerite-siderite carbonatite dykes. They may also form a series of small veinlets, creating crackle breccia in the host rocks (Fig. 5.5f; Chapter 2).

5.4.2 Yangibana LREE deposits and prospects

Multiple mineral deposits and prospects collectively comprise the Yangibana LREE district. The district can be divided into five sections based on location within the GCCC (Fig. 5.2b):

1) Yangibana Region
2) Northern Line
3) Bald Hill Region
4) Fraser's
5) Southern magnetite-biotite zone

The prospects appear to be controlled by pre-existing structures. The Yangibana region comprises the Yangibana, Yangibana South, and Tongue prospects, all of which crop out as large, north-northwest dipping, ironstones hosted in the metasedimentary rocks of the Pooranoo Metamorphics. The geometry of the prospects is controlled by the Mangaroon Orogen-aged S_1 compositional layering and F_1 folding within the host rocks, which are later overprinted by a S_2 crenulation cleavage (Sheppard et al., 2005). Small, brittle faults locally offset the Tongue–Yangibana ironstone and truncate the Tongue prospect to the south. At the time of publication, the unaltered protolith of these ironstones has not been recognised.

The Northern Line comprises seven prospects that occur along a nearly continuous, anastomosing ironstone outcrop that runs subparallel to the Bald Hill Lineament. The ironstone dykes intrude the Pimbyana and Yangibana Granites, and mineralisation occurs where the ironstone outcrops are the most prominent at surface, dipping variably to the south-southwest. Ankerite-siderite carbonatites and magnetite-biotite dykes have been encountered at depth in drill core in the Yangibana West and Yangibana North deposits (Fig. 5.3c).

The Bald Hill region consists of the Bald Hill and Bald Hill South deposits as well as Terry's Find, Simon's Find, and Hatchet prospects. The largest deposits, Bald Hill and Bald Hill South, are made up of two shallowly dipping (15 to 30° SW) ironstones hosted in schlieric Pimbyana Granite near surface and emplaced at depth into pelitic metasedimentary rocks (likely the Pooranoo Metamorphics) at depth. The mineralised zones are contained mainly in the ironstones and in subordinate magnetite-biotite rock assemblages.

The easternmost deposit, Fraser's, consists of one large (Fig. 5.5b), steeply dipping (55 to 65°W) ironstone that contains altered ankerite-siderite carbonatite at depth (~100 m below surface). Several small magnetite-biotite and carbonatite dykes also occur in this region. The Fraser's deposit intrudes along a contact between Pimbyana Granite and schists of the Pooranoo Metamorphics.

The Southern magnetite-biotite dyke zone is currently the southernmost mineralised occurrence. The region consists of the Auer, Auer North, Leceq, Mosander, and Demarcay prospects, which are hosted mainly in schists of the Pooranoo Metamorphics. These prospects comprise both ironstones and magnetite-biotite dykes. Several prospects such as Auer and Auer North do not outcrop at surface and were delineated through drilling and magnetic geophysical surveys.

5.5 Geochemistry and Sm-Nd Isotope Composition of the Ironstones

5.5.1 Ironstones compared to least-altered host rocks

Sampling transects were conducted across three different ironstone outcrops (Fig. 5.2a) in three different rock types as described in Section 5.3.4. A summary comparing the ironstone and host rock chemistry is provided in Figs. 5.6. The complete geochemical data are presented in Appendix 5.A.

The ironstone samples have lower SiO_2, MgO, Al_2O_3, Na_2O, and K_2O contents, but much higher MnO, P_2O_5, and Fe_2O_3 levels compared to the least-altered host rocks samples (Fig. 5.6a-d). The granite-hosted (FT) and schist-hosted ironstone samples have lower TiO_2 contents compared to the least-altered samples, but the quartzite-hosted ironstone (EGT) has higher TiO_2

contents compared to the unaltered quartzite (Fig. 5.6e). The ironstone samples contain higher Be, Ni, Cu, Zn, Ge, Mo, Sr, REE, Pb, Th, and U (Fig. 5.6f) contents than to the fresh and altered rock in which they intrude. Overall, the ironstone samples have lower Cs, Rb, and in the granite-hosted ironstones, Ta, compared to the least-altered host rocks.

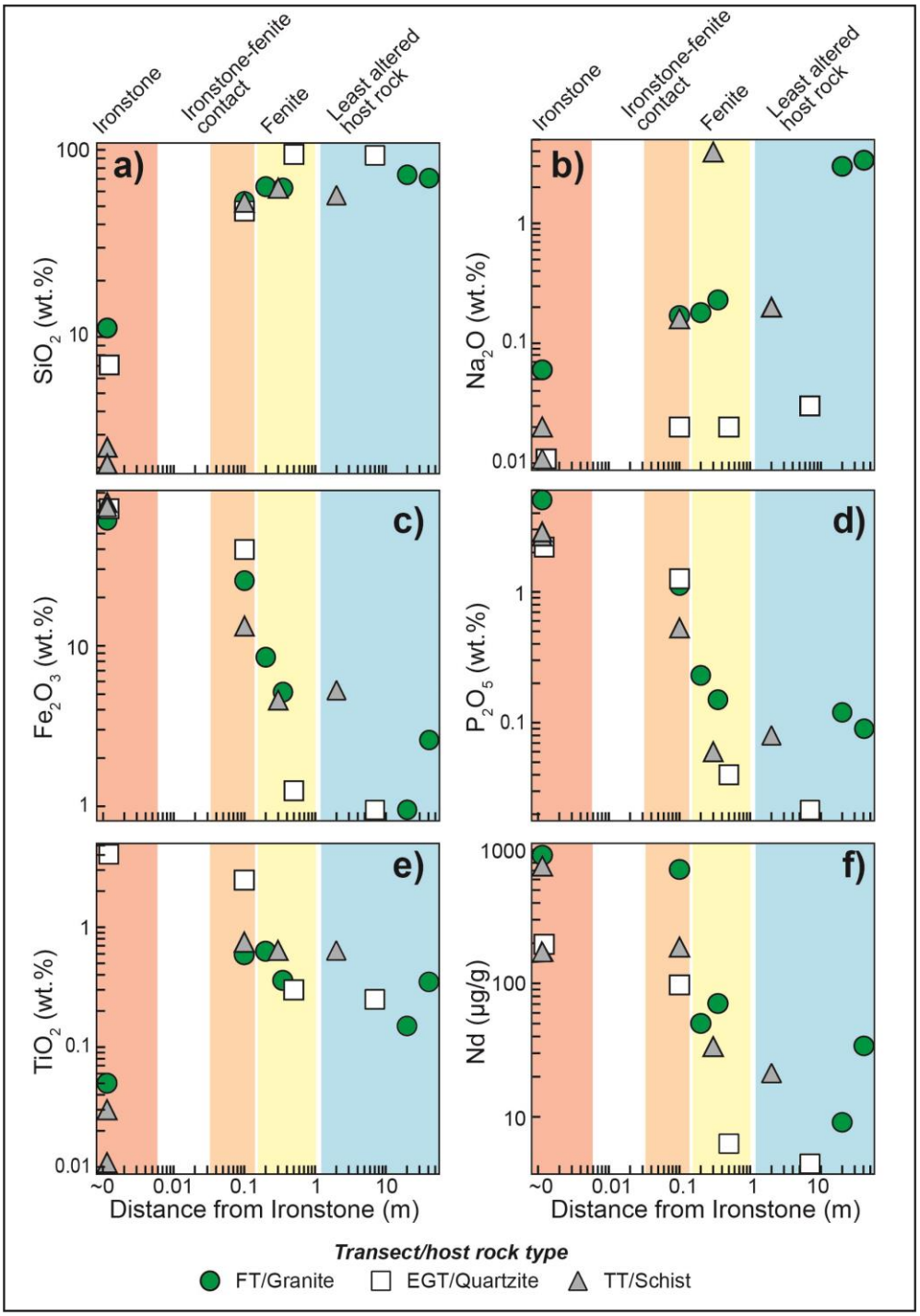

Figure 5.6 FT = Fraser's Transect, EGT = Edmund Group Transect, and TT = Tongue Transect. Shaded regions show distribution of elements in ironstone dykes, ironstone-fenite contacts, fenites, and least-altered host rock. All values plotted against distance (log scale).

Moving away from the ironstones, the fenites show an increase in major elements such as SiO_2 and Na_2O; however, the concentrations of these oxides are typically less than the least-altered host rocks (Fig. 5.6a,b). Other components such as Fe_2O_3, P_2O_5, and Nd decrease in concentration in the fenites moving away from the ironstones (Fig. 5.6c,d,f). Oxides and elements such as TiO_2, Nb, and Ta decrease in concentration as distance from the ironstones increases. Other HFSE elements such as Zr and Hf vary within the fenite samples.

Isocon plots were attempted with the fenite samples compared to the least-altered host rocks. Unfortunately, elements normally considered immobile for constructing isocon diagrams (e.g., Al, HFSE, and REY) did not fall on linear arrays (Grant, 1986) and are considered mobile in these fenites. Nevertheless, mass balance calculations indicate the fenites underwent relatively small mass and volume changes (e.g., 1 to 5%), suggesting that direct comparison (Fig. 5.6) is reasonable. Plots of fenite and least-altered host rocks with lines of constant mass can be found in Supplementary Figure 1 (Appendix 5.A). The plots show that fenite compositions vary in major element losses/gains depending on the host rock being fenitised and are overall enriched in REE.

Mass balance calculations and isocon diagrams were used to compare unaltered ankerite-siderite carbonatite core samples and an average of REE-enriched ironstone samples at the Yangibana North prospect. This comparison was conducted as there is textural and field evidence indicating the ironstones are genetically related to the ankerite-siderite carbonatites. This isocon also clarifies the increase in ore tenor related ironstone alteration (see section 5.7 Discussion). The ironstone data was obtained from bulk rock assay data provided by Hastings Technology Metals Ltd. The elements Nb, Ta, and Zr formed a linear array and are immobile during low temperature alteration (MacLean and Kranidiotis, 1987), so these element were chosen to define the isochon (Grant, 1986). This isocon has a slope ~10:1 (Fig. 5.7), indicative of ~90 % loss of mass during alteration of the ankerite-siderite carbonatites to REE-ore ironstones. The LREE and other elements such as Ba, Pb, and Th also plot near the isocon (Fi. 5.7). Major oxides such as MnO, MgO, CaO, and Fe_2O_3 plot well to the right of the isocon (Fig. 5.7), indicating these elements were lost during conversion of ankerite-siderite carbonatite to ironstone.

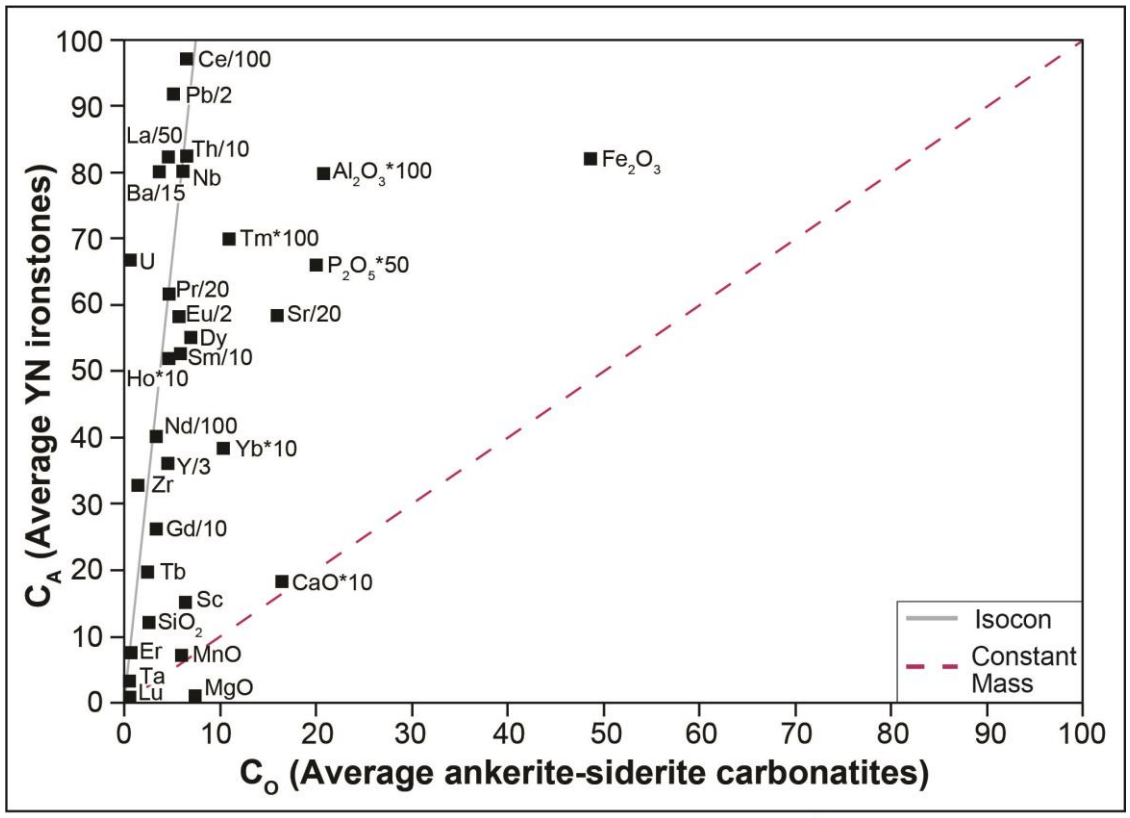

Figure 5.7 Isocon diagrams comparing an average of the least-altered ankerite-siderite carbonatite samples (Yangibna North area) and an average of Yangibana North ironstones based on bulk rock assays from Hastings Technology Metals Ltd. Isocon is defined by Nb, Ta, and Zr.

Chondrite normalised REY patterns were plotted for the average ankerite-siderite carbonatite (Chapter 2) and an average of ironstone drill samples from Yangibana North obtained from Hastings Technology Metals Ltd. The ironstones contain greater overall concentrations of REY compared to the ankerite-siderite carbonatites, but both have similar overall shapes showing relatively flat to slightly arcuate patterns from La to Nd followed by steep downward slopes to Ho where the patterns become more flat-lying (Fig. 5.8)

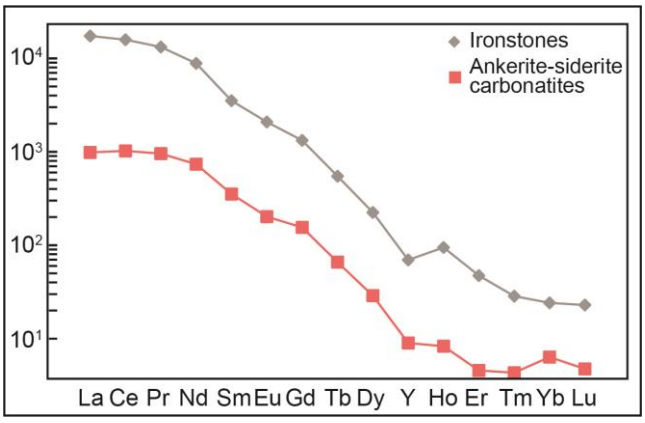

Figure 5.8 Chondrite normalised REY patterns (McDonough and Sun, 1995) for the average ankerite-siderite carbonatites (found at Yangibana North) and the average Yangibana North ironstones.

5.5.2 Sm-Nd isotopes

Five bulk rock samples (three ironstones, one fenite, one Pimbyana Granite) were analysed for Sm–Nd isotope abundances. A summary of the results can be found in Table 5.1. The ironstone samples have low $^{147}Sm/^{144}Nd$ ratios (~0.06 to 0.08) compared to the Pimbyana Granite and fenitised Pimbyana Granite samples (~0.1). The ironstones from Fraser's, Lion's Ear, and Yangibana North have εNd($t_{1.37Ga}$) values of -1.55, -1.83, and -3.24 (Slezak and Spandler, 2019; Chapter 4), respectively. The bulk rock Nd isotope measurements fall within the range of bulk rock εNd($t_{1.37Ga}$) values (-0.55 to -4.20) for the Lyons River Sills, magnetite-biotite dykes, and silica-rich alkaline dykes reported in Chapter 2 and Pearson (1996). The fenitised Pimbyana Granite sample has an εNd($t_{1.37Ga}$) (i.e., fenitisation age) of -2.26, or εNd($t_{1.68Ga}$) (i.e., granite crystallisation age) = 1.27 compared to unaltered Pimbyana Granite which has an εNd($t_{1.68Ga}$) (i.e., crystallisation age) = -6.07.

Table 5.1 Bulk rock Sm–Nd isotope results for ironstones, fenites, and the Pimbyana Granite.

Sample	LE-1	YN-1	FT-1	FT-3	FT-7
Rock Type	Ironstone	Ironstone	Ironstone	Fenitised Pimbyana Granite	Pimbyana Granite
Rock age *t* (Ma)	1370	1370	1370	1370/1680*	1680*
Nd µg/g	4140	1520	1020	82.4	34.8
Sm µg/g	531	161	98.7	14.8	5.76
$^{147}Sm/^{144}Nd$	0.0776	0.0641	0.0586	0.0109	0.100
$^{143}Nd/^{144}4Nd$	0.511474	0.511280	0.511316	0.511730	0.511261
$^{143}Nd/^{144}Nd(t)$	0.510775	0.510703	0.510789	0.510753	0.510156
εNd(*t*)	-1.83	-3.24	-1.55	-2.26/1.27*	-6.07
T_{DM} (Ma)	1860	1890	1790	2040	2500
T_{CHUR} (Ma)	1490	1560	1460	1570	2160

*1680 Ma date based on Pearson et al. (1996) and indicates granite crystallization age.

5.5.3 REY geochemistry of mineralised zones

Bulk rock geochemistry of drill core provided by Hastings Technology Metals Ltd. shows REY enrichment, especially in LREE, in all prospects of the GCCC (Fig. 5.9). All prospects have similar MREE and HREE patterns with small negative Y anomalies. However, there are significant variations in the first tetrad (La to Nd) in the five Yangibana LREE groupings (Fig. 5.9). The prospects along the Northern Line show $La_{cn} > Nd_{cn}$, resulting in a more flat-lying REY pattern, whereas the other regions show $La_{cn} < Nd_{cn}$, creating a convex upward curve in the LREE

(Fig. 5.9). Moving east along the Northern Line away from Yangibana North, prospects such as Kane's Gossan show decreasing La_{cn}/Nd_{cn} (Fig. 5.2b and Fig. 5.9).

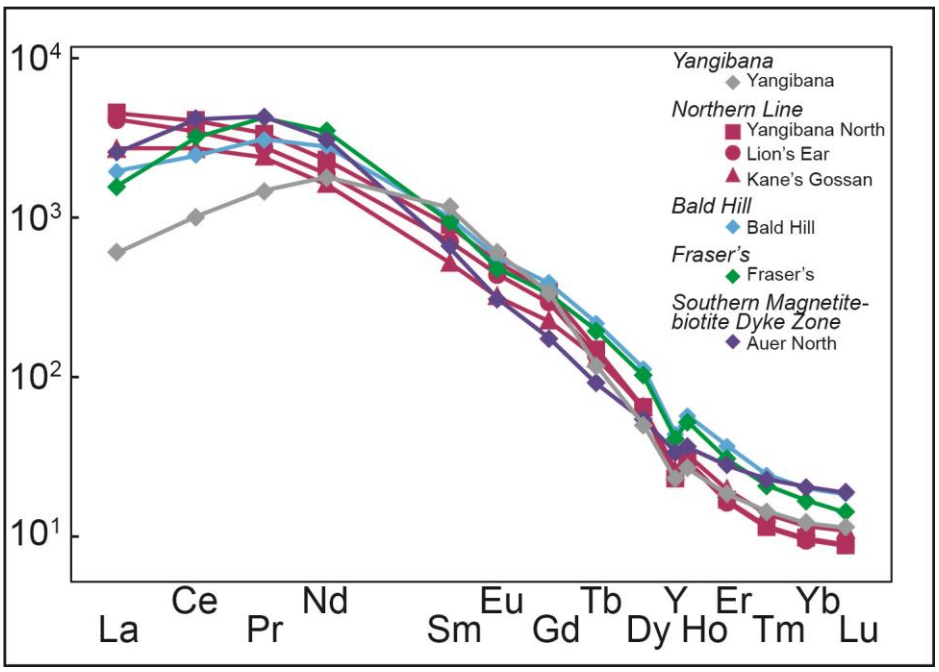

Figure 5.9 Normalised REY pattern using chondrite values from McDonough and Sun (1995). The Northern Line shows greater normalised La values compared to the other LREE than the other regions, which have higher normalised Ce, Pr, and Nd values. The Northern Line shows a decrease in normalised La values moving east so that Kane's Gossan has lower La_{cn}/Nd_{cn} compared to Yangibana North. The REY are spaced according to their ionic radius (Shannon, 1976).

Drill hole date from all prospects and deposits show a consistent range in La/Nd ~0.2 to 1.5 when the total REY ≤ 800 ppm (Fig. 5.10). The Yangibana North and West deposits show a higher density of La/Nd values from ~0.75 to 1.5 and total REY contents below 800 ppm (Fig. 5.10a) compared to the other prospects and deposits. The other deposits and prospects have a larger proportion of La/Nd values between ~0.1 to ~0.5 (Fig. 5.10b-e) and overall higher total REY contents ranging from ~800 ppm up to 10,000 ppm (Fig. 5.10b-e). The general trend for most prospects of the GCCC (Fig. 5.10f) is that as total REY contents increase, the La/Nd ratio decreases.

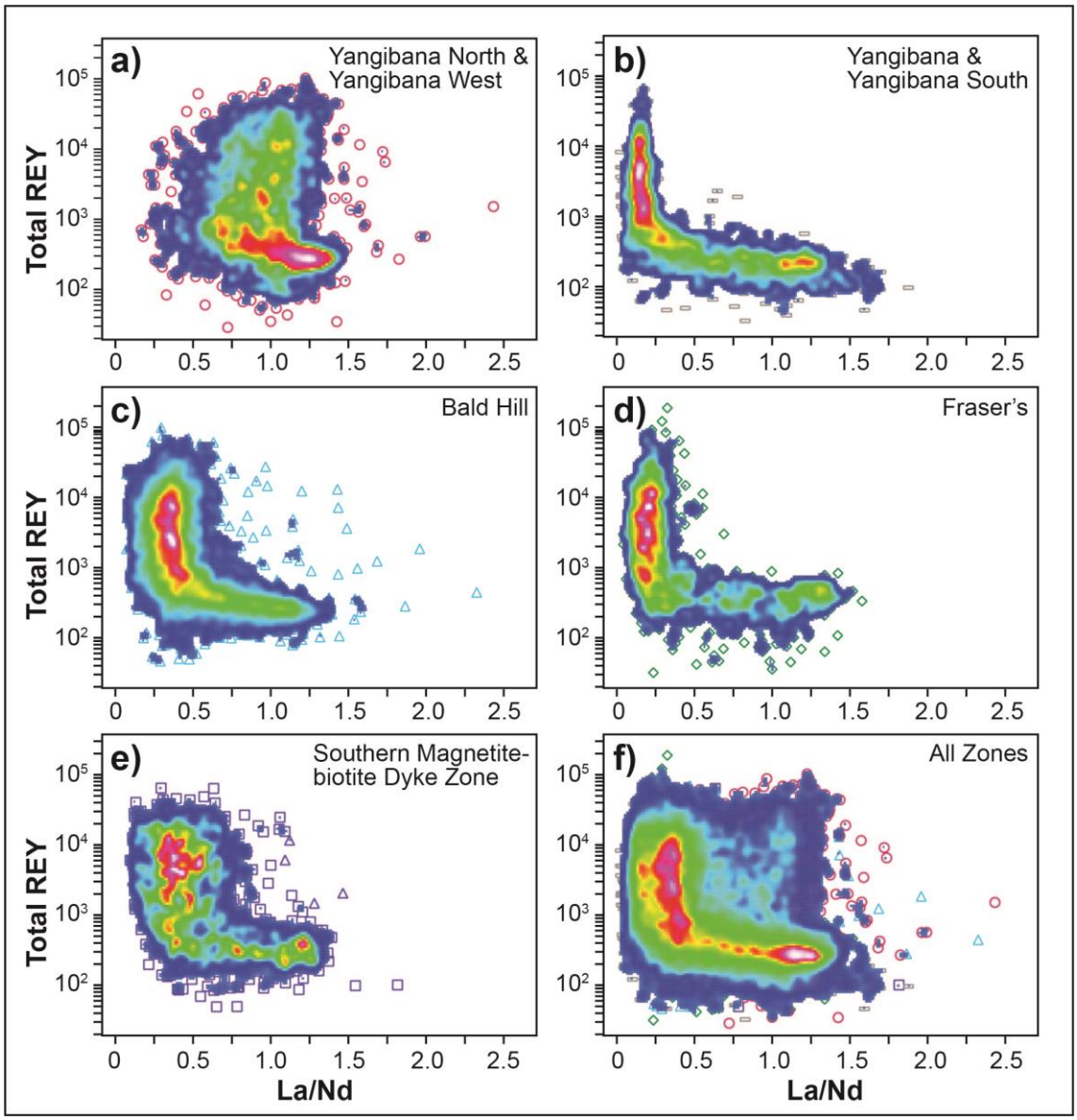

Figure 5.10 Density plots of Hasting's REY drill assays from representative prospects of the different regions in the Yangibana LREE district. White, pink, red (i.e., warm colours) represent a high data point density. Cooler colours (e.g., blue) represent low data point density. a) Yangibana North and Yangibana West sample data: n = 2,061. b) Yangibana and Yangibana South prospects sample data: n = 3,176. c) Bald Hill deposit sample data: n = 5262. d) Fraser's deposit sample data: n = 1,504. e) South Magnetite-biotite Dyke Zone sample data: n = 2,061. Data points include Auer, Auer North, Demarcay, and Mosander deposits/prospects. f) Overlay of all zones showing the regional trend of La/Nd vs. total REY. See Figure 5.2 for prospect locations.

5.6 Ore Mineralogy and Chemistry

Monazite is the main ore mineral at Yangibana and the majority consists primarily the (Ce)-monazite variety, though some grains transition to (Nd)-monazite (Appendix 5.B). For simplicity, this study simply uses the term "monazite" without a compositional prefix. In the GCCC, monazite is found in highest concentrations in the ironstone deposits, magnetite-biotite dykes, and ankerite-siderite carbonatites. Trace amounts of monazite are also present in the silica-

rich alkaline veins, occurring coevally with more abundant zircon. Monazite is only present as trace amounts in the Lyons River Sills, which instead contain greater amounts of apatite.

Monazite in the magnetite-biotite dykes, ankerite-siderite carbonatites, and their alteration assemblages (i.e., fenites and glimmerites) occurs in significant quantities, making up between ~1% and ~10% of the rock by volume. It is often cream to peach colour in hand specimen and forms large (~2 mm) clusters of subhedral to euhedral tabular crystals. Less commonly, monazite forms small, anhedral inclusions (~10 μm) in apatite, possibly produced by exsolution (Slezak et al., 2018; Chapter 2; Chapter 3). In high-contrast backscattered electron (BSE) and cathodoluminescence (CL) images, monazite often exhibits patchy, irregular dark and light zonation (Fig. 5.11a) as well as occasional oscillatory growth zones (Fig. 5.11b). The lighter BSE zones are typically associated with somewhat higher Th contents (as determined by EDS). Large monazite grains hosted in the ironstones also have a tabular morphology similar to the monazite in the ankerite-siderite carbonatites and magnetite-biotite dykes. However, these large monazite crystals are often fractured, have irregular margins, and are occasionally mantled by a slightly darker (in BSE) REE-bearing mineral phases (Fig. 5.11c). This mineral mantling monazite has an amorphous to acicular crystal habit (Fig. 5.11c,d) and based on its morphology, high CaO contents, and low EPMA totals (Appendix 5.B) is likely rhabdophane [$(REE,Ca,Th)PO_4 \cdot nH_2O$]. The low EPMA totals are likely attributed to the incorporation of water into the crystal structure. This mineral is often found together with botryoidal and boxwork-textured iron oxides and hydroxides like goethite (Fig. 5.11d).

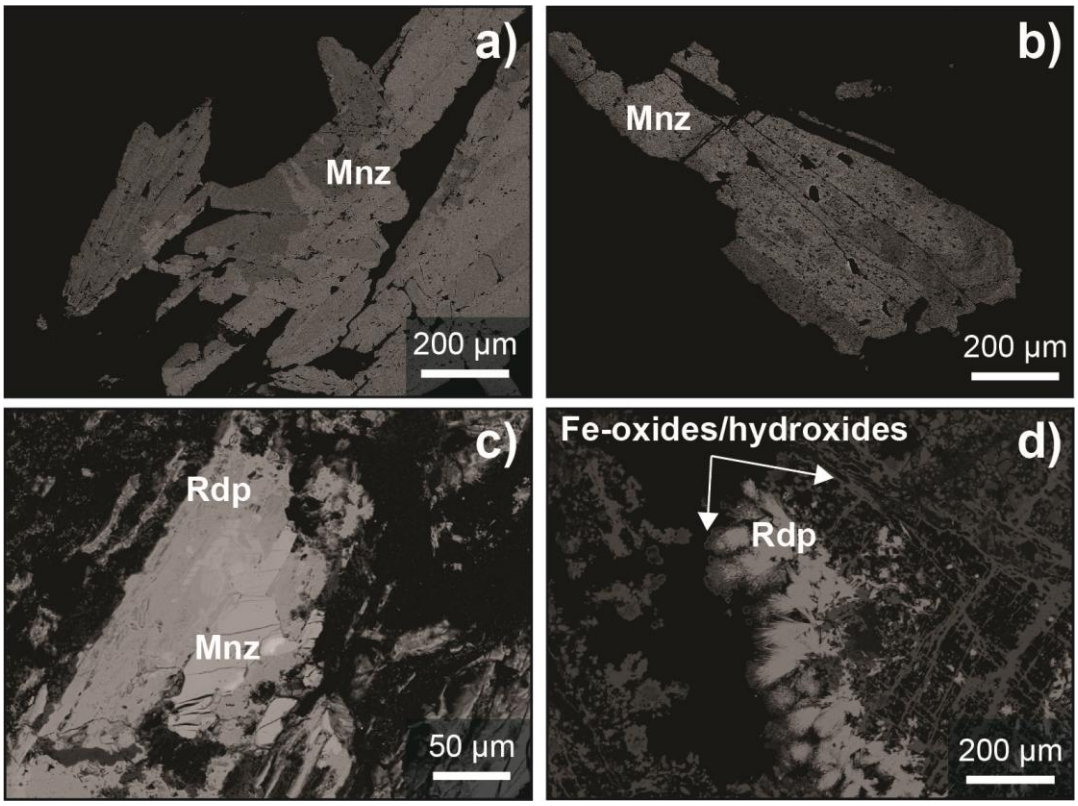

Figure 5.11 Backscatter electron (BSE) images of the main ore minerals, monazite and rhabdophane. a) Monazite from a magnetite-biotite dyke near Fraser's with patchy, dark zonation in large, tabular monazite crystals. Zones are related mainly to changes in Th content. b) Monazite from Yangibana North with oscillatory zoning on the crystal margins. c) Fractured monazite altering to slightly darker rhabdophane in a drill cutting sample from Fraser's ironstone. d) Fibrous rhabdophane radially growing in an ironstone sample with boxwork Fe-oxide texture. Sample is from the Fraser's deposit.

5.6.1 Monazite mineral chemistry

False colour overlays were applied to the monazite CL spectra as follows: blue = 449 to 549 nm, green = 553 to 638 nm, and red = 771 to 912 nm. These false colour overlays allow the near-infra red spectra luminescence of monazite to be observed. Under CL, monazite displays patchy zonation in cores and rims (Fig. 5.12a). Counts are elevated from ~350 nm up to ~600 nm and distinct peaks occur at 784 nm, 857 nm, and 1048 nm (Fig. 5.12b). Both light and dark CL zones have similar spectral shapes, but the lighter zones show higher counts at the 857 nm peak. The full width at half maximum (FWHM) and eV values for the probable peak locations can be found in Supplementary Figure 2 and Supplementary Table 1 in Appendix 5.C.

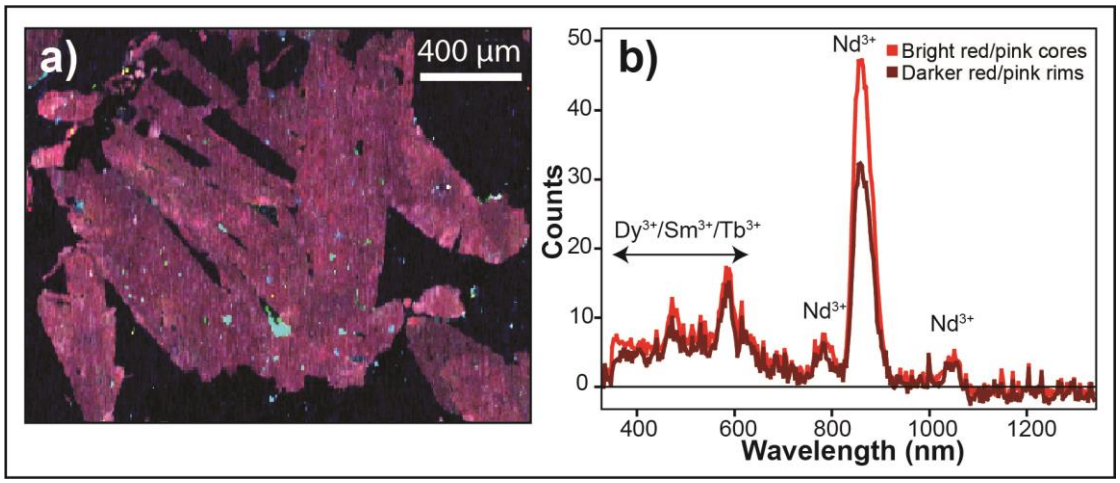

Figure 5.12 Monazite CL image and associated spectra. a) False colour, hyperspectral CL image of monazite showing slightly patchy texture. The red colour, in particular, highlights the prominence of the 857 nm peak from Nd^{3+} in the sample. b) Spectral image of light and dark zones in the monazite. Both zones have the same patterns, but darker zones have lower counts related to slight changes in REE content.

Monazite has low Si (<1 wt.% SiO_2), low Ca (<1 wt.% CaO), and variable Th (0.5 to10 wt.% ThO_2; Appendix 5.B). Thorium and Ca correspond to a decrease in total REY (REE + Y; Fig. 5.13a). Additionally, Si and Th correlate with a decrease in REY and P content in monazite (Fig. 5.13b). No correlations were observed between Th and individual REY. Monazite in the Lyons River Sills and their associated alkaline amphibole-dolomite veinlets contains higher amounts of Ca, Th, and Si compared to the monazite hosted in the ankerite-siderite carbonatites and magnetite-biotite dykes (Fig. 5.13a,b).

Lanthanum and Nd show a strong, negative correlation with monazite. The alkaline amphibole-dolomite veinlets and Lyons River Sills have the highest La contents and lowest Nd contents (Fig. 5.13c). Cerium and Nd show no correlation, though there are minor regional variations in Ce contents (e.g., the western region contains more Ce-rich monazite). Neodymium shows a strong positive correlation with Pr (Fig. 5.13d) and a moderate positive correlation with Sm (Fig. 5.13e). Monazite from the ironstones and fenites have the highest contents of REE such as Pr, Nd, and Sm.

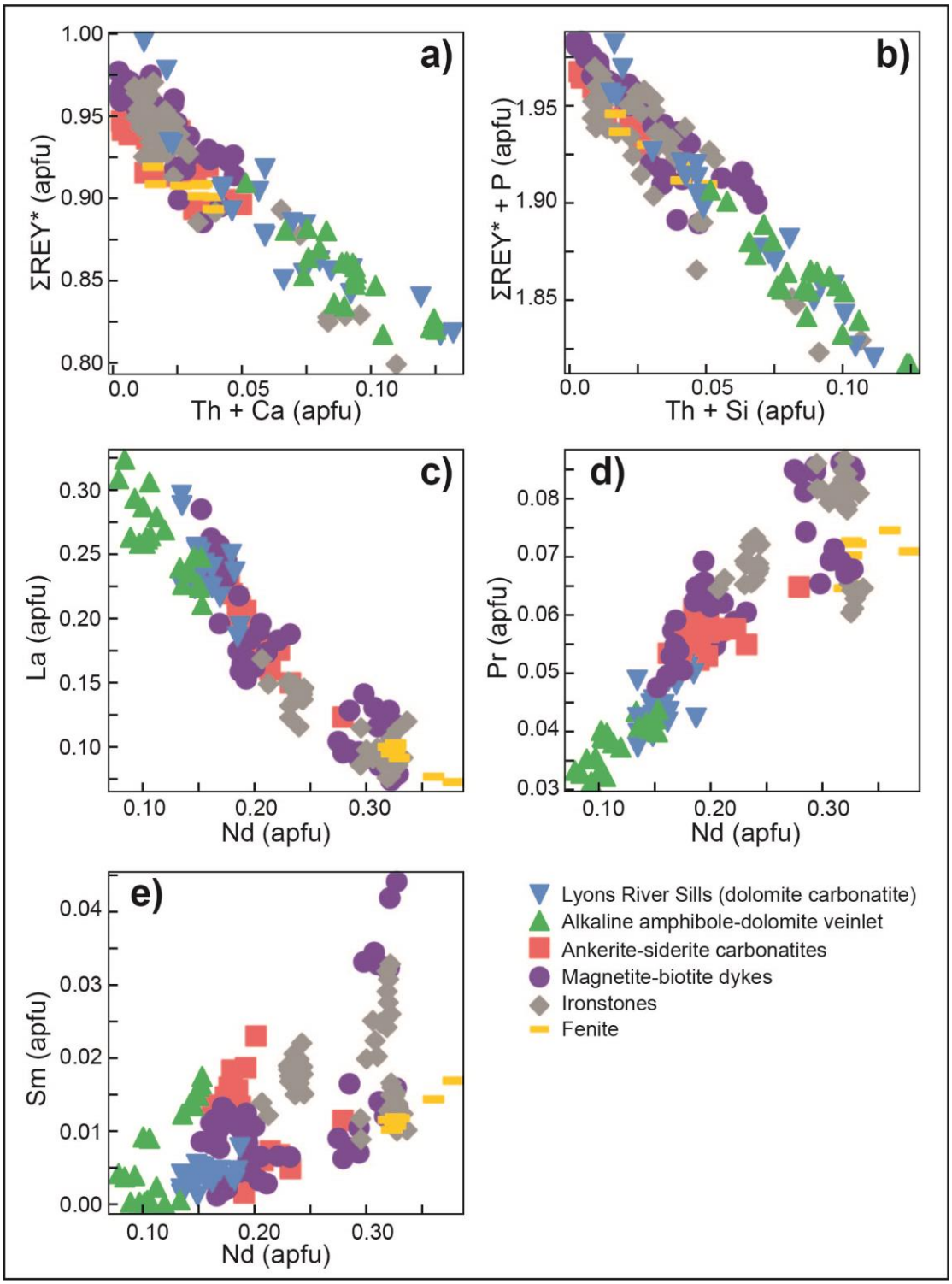

Figure 5.13 Atoms per formula unit plots (from EPMA analyses) of monazite based on rock type. ΣREY* = La-Sm, Y, and, for some samples, Dy and Gd data (see Appendix 5.B for details). Note the concentrations in Dy and Gd do not significantly increase the total REY contents in these monazite analyses.

Arsenic and Nd contents have a strong, positive correlation (Fig. 5.14a), but As and Yb show no correlation (Fig. 5.14b). Strontium correlates with both Th and Pb and reaches contents up to 20,000 ppm (Fig. 5.14c; Appendix 5.D). Monazite in the alkaline amphibole-dolomite veinlets has the highest Sr contents and lowest Yb contents. The monazite hosted in the fenites, ankerite-siderite carbonatites, and magnetite-biotite dykes tends to have higher HREE contents and lower Sr contents (Fig. 5.14d). Lead correlates strongly with Th and is typically present at the hundreds of ppm level, but may be up to 8000 ppm (Appendix 5.D). Uranium contents in monazite range from 1 to 90 ppm (Appendix 5.D) and show little correlation with Th or Pb.

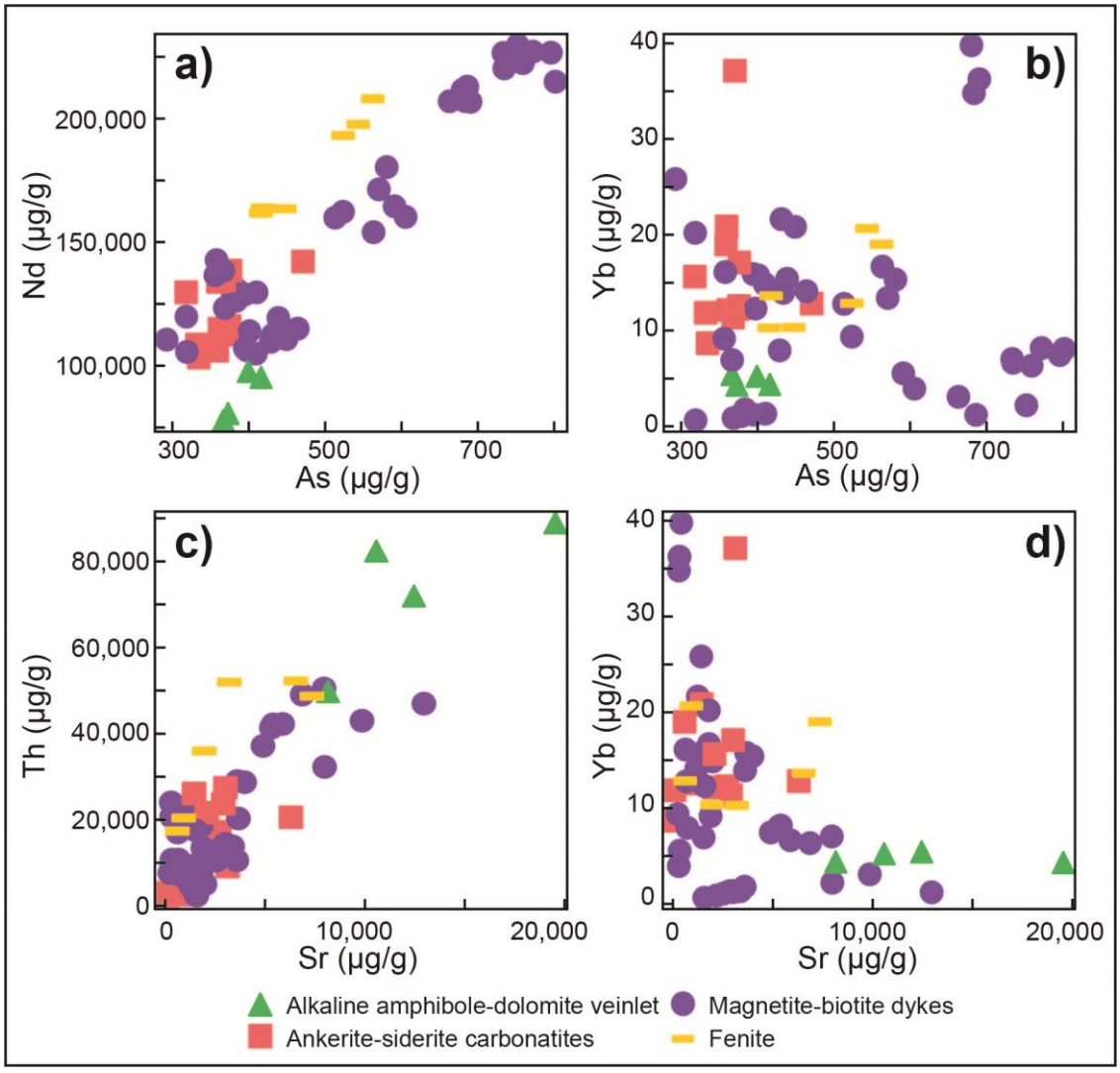

Figure 5.14 X-Y plots illustrating major and trace elements for monazite based on LA-ICP-MS data.

Normalised REY plots from in situ LA-ICP-MS analyeses show that monazite has two main patterns: 1) plots with relatively straight and flat to downward slopes from La to Sm as illustrated by the monazite in the ankerite-siderite carbonatites, alkaline amphibole-dolomite veinlet, and some magnetite-biotite dykes (Fig. 5.15a-c); and 2) patterns with curved, positive slopes from La to Pr and/or Nd, followed by an inflection and gentle, negative slopes from Sm to Gd, as seen in some of the magnetite-biotite dykes and fenitised granite monazite samples (Fig. 5.15c,d). All samples display a steep, negative slope from Gd to Lu with a small, negative Y anomaly. The magnetite-biotite dyke samples show the greatest variability in REY trends with shifts in the normalised La contents as well as variable HREE concentrations (Fig. 5.15c). The REY patterns for the fenite-hosted monazite shows high contents of Nd to Tb, creating a more arcuate shape (Fig. 5.15d).

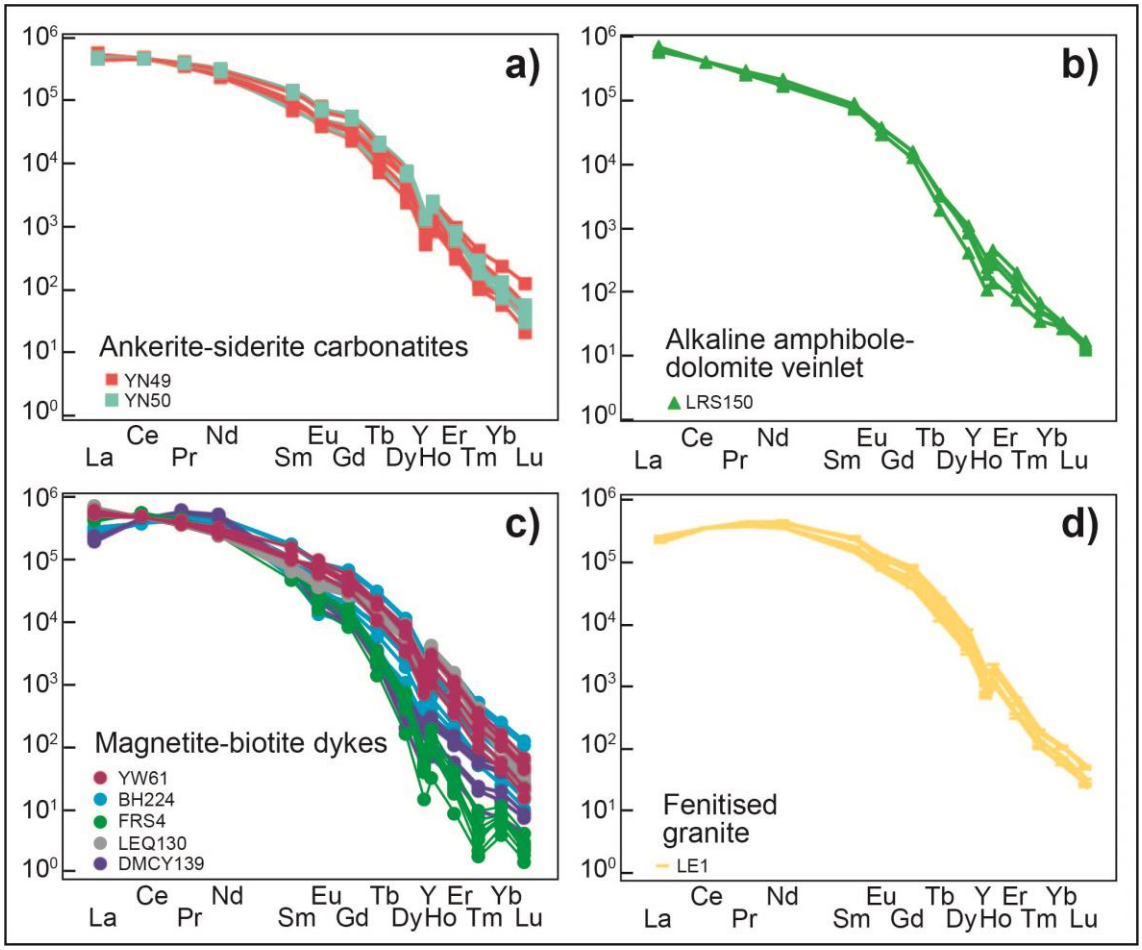

Figure 5.15 Chondrite normalised REY patterns (McDonough and Sun, 1995), plotted according to ionic radius with a nine-fold coordination number (Shannon, 1976). Data is from in situ LA-ICP-MS analyses on monazite.

5.6.2 Rhabdophane mineral chemistry

The amorphous to acicular mineral mantling monazite, identified as rhabdophane (Fig. 5.11c,d) has high Ca contents (~2.5 to ~5.5 wt.% CaO; Appendix 5.B). In the analysed rhabdophane, there is a negative correlation between Th + Ca and the total measured REY contents. There is a strong correlation between Nd, Pr, and Sm contents, but no correlation between Nd, La, or Ce. Furthermore, the La/Nd ratio is similar to that of monazite analysed in the same sample. The Y contents are low and there is little correspondence between REE + P and Th + Si.

5.7 Discussion

Based on petrology, geochemistry, and isotopic systematics, the GCCC is considered to have formed via emplacement of evolving, mantle-derived, alkaline magma at mid to upper crustal levels. The variation in rock-types across the complex is interpreted to reflect magma evolution via fractionation (with or without liquid immiscibility) melt wall-rock reaction, and hydrothermal alteration (Chapters 2-4). The LREE rich ironstones that comprise the Yangibana ore field are considered to have direct genetic links with these alkaline igneous rocks. This chapter henceforth examines the mechanisms for GCCC emplacement, the genetic links between the ironstones and the other GCCC rock types, and the cause of the spatial trends in LREE signatures across the complex. With reference to these aspects of the mineralisation, the final section compares the Yangibana ore field with other major critical metal-bearing carbonatite deposits.

5.7.1 Tectonic and structural conditions of emplacement of the GCCC

Zircon U–Pb dating demonstrates that the GCCC was emplaced c. 1370 Ma in a singular magmatic event (Chapter 4). Subsequent to emplacement, the complex underwent multiple tectonic re-working events as demonstrated by the various monazite U–Pb and Sm–Nd ages (Zi et al., 2017; Slezak and Spandler, 2019; Chapter 4). However, this magmatic event does not correlate with any known tectonic event in the Gascoyne Province, so large-scale mechanisms controlling carbonatite magma intrusion are unknown. Motion along the Lyons River Fault may have been caused by far-field stresses related to the separation of the North China Craton from

the West Australia Craton around 1400 to 1350 Ma (Pisarevsky et al., 2014; Slezak and Spandler, 2019) or by far-field stresses related to the incipient convergence of the Mawson Craton with the southeastern margin (present day) of the West Australia Craton (Aitken et al., 2016; Stark et al., 2018).

The W to NW orientation of many of the units – subparallel to the Lyons River Fault and Bald Hill Lineament – suggest extension/transtention in the N to NE directions to allow for dyke emplacement along the pre-existing structures. The step-over veins (Figs. 5.4 d and 5.5d), orthogonal orientation of the GCCC units (Fig. 5.2), and close correlation between dyke morphology and pre-existing structures (Figs. 5.2 and 5.4) indicate that the area was subjected to extensional stresses, which allowed the low viscosity carbonatite melts to permeate the crust. Neither extensive brecciation/explosive features nor intrusive plugs are observed in the GCCC units. The lack of these features and prevalence of fine-grained dyke morphologies suggest a hypabyssal (i.e., mid to upper crust) emplacement setting (Barker, 1989). Carbonatite melts typically have low viscosities (Treiman, 1989), and in the case of the GCCC, may also be of low volumes. These features suggests that the GCCC likely did not have the capacity to pond within the crust (Brett et al., 2015) to form substantial intrusive plugs or volcanic pipes, occurring instead as relatively thin dykes and sills along pre-existing structures. Vaughan and Scarrow (2003) demonstrated that lithospheric transtensional faulting may trigger localised mantle magmatism and additional work by Jelsma et al. (2004) showed that large regional structures act as emplacement corridors for small volume, mantle-derived melts. A similar scenario is proposed where the Lyons River Fault underwent extension/transtension at c. 1370 Ma, allowing for the migration of alkaline melts from the mantle to hypabyssal emplacement into the crust, forming the GCCC.

5.7.2 Origins of the ironstone

The bulk rock chemistry of the ironstones is very different compared to the other rock types found in the complex, as they are almost entirely composed of Fe_2O_3 and SiO_2 with subordinate phosphate mineralisation. The geochemical transects across the ironstones into the

country rock show the ironstones contain higher amounts of elements common to alkaline magmatic systems such as REE, P, Th, and U (Fig. 5.6; Woolley and Kempe, 1989) in contrast to the rocks in which they intrude (i.e., quartzite, pelitic schist, and granite). The ironstones are also enveloped by fentite and glimmerite alteration styles analogous to those observed in the ankerite-siderite carbonatites and Lyons River Sills (e.g., Fig. 5.5d,f). In addition, the ironstones have bulk-rock Nd isotope compositions (Table 5.2) that are similar to other units of the GCCC (Chapter 2), indicating they have a common (enriched mantle) source.

At several ironstone outcrops carbonate mineral dissolution cavities (Fig. 5.5c) and Fe-oxides/hydroxides pseudomorphing carbonate minerals were observed. In drill core, the ankerite siderite carbonatite is partially altered and oxidised to a porous, hematite-rich rock similar to the ironstones observed at surface (Fig. 5.3c). These field observations are consistent with the original hypothesis of Gellatly (1975) that the ironstones are likely the product of dissolution of carbonate minerals. Pearson et al. (1996) indicated that the ironstones may be analogous to "rødberg", an iron-rich, low temperature, calcite-dolomite-iron oxide rock that forms as a result of metasomatism from hydrothermal fluids (Andersen, 1984; Le Bas, 1989). The rødberg rocks, originally described in the Fen Complex (Norway), were formed by low temperature (200 to 300°C) hydrothermal, oxidising (above hematite-magnetite buffer) fluids, which altered the existing ankerite-siderite carbonatites to calcite, dolomite, and hematite via the reactions:

$$4FeCO_3 + O_2 = 2Fe_2O_3 + 4CO_2 \quad (1)$$

$$10Ca(Mg_{0.6}Fe_{0.4})(CO_3)_2 + O_2 = 2Fe_2O_3 + 6CaMg(CO_3)_2 + 4\ CaCO_3 + 4CO_2 \quad (2)$$

as described by Andersen (1984). However, the textures reported included intergrowths of calcite and dolomite, fine-grained platy hematite, as well as resorption features in ankerite (Andersen, 1984). In the GCCC, Pirajno and González-Álvarez (2013) observed hematite development along carbonate lamellae, and hematite veins cross-cutting other textures, both of which were interpreted as higher temperature rødberg reactions. However, these distinct, euhedral crystal features were rarely observed in this study, and it is speculated these relatively higher temperature

characteristics have been overprinted by meteoric, low temperature features such as botryoidal hematite, boxwork textures (Fig. 5.11d), and vugs (Fig. 5.5c).

The transformation of monazite to rhabdophane (Fig. 5.11c,d) occurs under low temperature hydrothermal conditions, as rhabdophane is only stable at T < 400 °C at 0.05 GPa and T < 200 °C at 0.1 GPa (Akers et al., 1993). Rhabdophane has also been reported to form at temperatures as low as 5 °C and under acidic, REE-saturated fluid conditions (Roncal-Herrero et al., 2011). Based on the available textural and mineralogical evidence, the ironstones likely formed by rødberg-style alteration of the ankerite-siderite carbonatites (and possibly magnetite-biotite dykes) that was subsequently overprinted by meteoric fluid interactions (Fig. 5.16), which dissolved the carbonate mineral phases and precipitated low temperature goethite, hematite, other Fe-Mn oxides/hydroxides, and silica (Pirajno and González-Álvarez, 2013; this study).

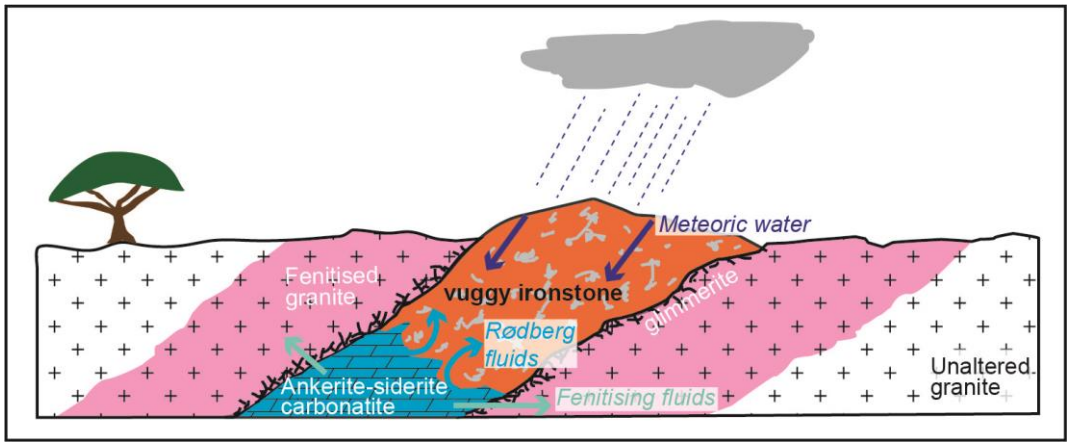

Figure 5.16 Schematic of the creation of vuggy ironstone through alteration of the ankerite-siderite dykes by Rødberg and meteoric fluids. Formation of the fenites and glimmerites is also shown.

The West Australia Craton has episodically undergone subaerial exposure since the late Proterozoic, though much of it underwent extensive regolith development from the Paleogene until the mid-Miocene (Anand and Paine, 2002; Pillans, 2007). The extended length of subaerial exposure of the GCCC has provided ample time for meteoric waters to infiltrate and alter the dykes, forming the present day ironstones (Fig. 5.16). This is supported by ankerite-siderite carbonatite altering to ironstone in core samples (Fig. 5.3c) and fresh ankerite-siderite carbonatite only occurring in drill core from depths ≥ 40 metres below the areas where the ironstones crop out at the surface. The depth of meteoric fluid infiltration was likely controlled and/or enhanced

by porosity generation via carbonate dissolution and internal structures (e.g., joints, faults, wall rock contacts) in the carbonatites.

5.7.3 Ironstone LREE ore genesis

Weathering and laterite formation are important processes that can improve the ore tenor of carbonatite deposits. The largest Nb deposits in the world occur in Brazil and include the pyrochlore-rich carbonatite deposits Araxá, Catalão, and Morro do Seis Lagos, which have all undergone extensive lateritisation (Chakhmouradian et al., 2015; Mitchell, 2015; Giovannini et al., 2017). However, the laterites mainly increase the ore tenor by weathering through eluvial enrichment where carbonate minerals are dissolved or remobilised, leaving the immobile pyrochlore as residual material (Mariano, 1989).

The REE-bearing minerals behave differently in the laterite environment compared to pyrochlore. In the cases of Araxá and Catalão I, primary REE-bearing minerals (including phosphates) are dissolved, liberating REE, which are then incorporated into Al-phosphates such as gorceixte and, to a lesser extent, bound to Fe hydroxides (Morteani and Preinfalk, 1996). Extensive supergene enrichment via lateritisation has also occurred at the Mount Weld REE deposit, where breakdown of primary REE-bearing minerals (e.g., monazite and apatite) has liberated REE to form REE-bearing oxyhydroxides, secondary monazite, churchite, cerianite, and a suite of REE-rich hydrated aluminophosphate (plumbogummite group) minerals. This lateritisation has enriched LREE concentrations by ~5 to 200 times compared to the average carbonatite LREE contents (Lottermoser, 1990).

Comparison of the Yangibana ironstones with likely precursor rocks (e.g., Figs. 5.7 and 5.8) indicate an average upgrade in ore tenor of ~3 to ~17 times during supergene alteration. Overall the ankerite-siderite carbonatites and the ironstones have comparable normalised REY patterns (Fig. 5.8), which is consistent with their genetic relationship and indicative of an environment involving little fractionation between REE (Morteani and Preinfalk, 1996). The ironstones of the Yangibana LREE district demonstrate that some monazite has been altered and remobilised to form rhabdophane and possibly REE-bearing Fe-oxides/hydroxides, similar to the

processes at Araxá, Catalão I, and Mount Weld. However, this REE-remobilisation has occurred to a much lesser extent as primary monazite and apatite remain the predominant REE-bearing minerals in the district.

The steep slope of the isocon (~10:1) in Figure 5.7 indicates the original ankerite-siderite carbonatites lost ~90% of their original mass, which is evident by the loss of the carbonate-forming elements CaO, Fe_2O_3, MgO (Fig. 5.7), CO_2, and the extensive voids and vugs in the ironstones. The considerable amount of remnant primary REE-bearing phosphate minerals (i.e., monazite) suggest the ironstones were upgraded through eluvial supergene processes similar to those involving pyrochlore at the carbonatite deposits in Brazil as opposed to the chemical breakdown and concentration of primary REE-bearing phases (Morteani and Preinfalk, 1996).

5.7.4 Ore mineral chemistry and LREE trends

Monazite in the Yangibana LREE district luminesces in the infrared spectrum with peaks at approximately 784 nm, 857 nm, and 1048 nm (Fig. 5.12b); these peaks have been shown to be associated with Nd^{3+} (Richter et al. 2008; Lenz et al., 2013; Gaft et al. 2015). Other small peaks near 474 nm and 583 nm with elevated counts down to 350 nm are most likely associated with Dy^{3+}, Sm^{3+}, and/or Tb^{3+} (Gorobets and Rogojine, 2001; Richter et al., 2008). Variation in the CL intensities in the dark and light pink zones (in the false colour maps) are related to varying REE contents, particularly Nd^{3+}, which can be seen in the variations in the 857 nm peak (Fig. 5.12b).

Though low in overall Ca and Si contents, the monazite in the Yangibana LREE district shows strong correlations between Th, Si, Ca, REE, and P, indicative of the common coupled substitutions of $Th^{4+} + Ca^{2+} = 2REE^{3+}$ and $Th^{4+} + Si^{4+} = REE^{3+} + P^{5+}$ related to cheralite and huttonite solid solutions, respectively (Fig. 5.13a,b; Grammaccioli and Segalstad, 1978; Van Emden et al., 1997). The high Sr content of monazite from the alkaline amphibole-dolomite veinlet is likely due to Sr^{2+} cheralite-type substitution, which can be attributed to the higher Sr contents in the Lyons River Sills (Chapter 2). The correlation between As and Nd is likely related to the presence of AsO_4^3, which can substitute for PO_4^{3-} (Clavier et al., 2011). However, La and Nd show an intriguing inverse relationship where monazite from the Lyons River Sills and their

associated alkaline amphibole-dolomite veinlets have high La_{cn}/Nd_{cn} (Fig. 5.15b) compared to other rock types, which show increasing Pr, Nd, and Sm (Fig. 5.13c-d) contents with decreasing La contents. This relationship is also reflected in the REY normalised apatite patterns (Slezak et al., 2018; Chapter 3) and in the bulk rock REY plots (Figs. 5.9 and 5.10). In addition to these variations by rock type, there are regional variations in La_{cn}/Nd_{cn} (Fig. 5.2b), which show monazite in the Yangibana, Bald Hill, Fraser's, and Southern magnetite-biotite dyke zones is more enriched Nd (Figs. 5.9 and 5.10). Moreover, the total REY contents in these areas is much higher compared in these areas compared to the Yangibana North and West regions (Figs. 5.52b and 5.10). The shift from La to Nd enriched carbonatite phases has also been documented by Zaitsev et al. (1998) and Moore et al. (2015), who observed higher Nd contents in REE carbonate minerals, which the authors surmised were indicative of more evolved units. In addition, high Th contents in monazite are indicative of higher formation temperatures (Wall and Zaitsev, 2004). The monazite in the Lyons River Sills and their associated alkaline amphibole-dolomite veinlets has much higher Th, Sr, and La contents compared to monazite occurring in the other rock types (Figs. 5.13a-c and 5.14d), which suggests these units may have formed early during the emplacement of the GCCC. The Nd-rich monazite and higher Fe contents observed in the magnetite-biotite dykes and ankerite-siderite carbonatites suggests these units may be paragenetically later and more evolved than the Lyons River Sills.

In addition to magmatic effects on LREE distribution, the observed shifts from La to Nd-enriched rocks can also be caused by LREE fractionation in hydrothermal environments related to changes in fluid type and temperature (Smith et al., 2000; Migdisov et al., 2016). Changes in fluid type (i.e., CO_2 vs. H_2O) can contribute to REE fractionation within a system. In the monazite-aegirine hydrothermal veins at Bayan Obo, high La values in monazite were indicative of greater La (and Ce) solubility in CO_2-rich fluids compared to Nd and Sm, which were more likely to be associated with aqueous fluids (Smith et al., 2000). The ironstone bulk rock REY patterns from the Lion's Ear prospect show $La_{cn}>Nd_{cn}$ (Fig. 5.2b and Fig. 5.10). However, in situ monazite REY patterns from fenite sample (LE1) display greater curvature in the first tetrad with $La_{cn}<Nd_{cn}$ (Fig. 5.15d). This change could be linked to a switch from a CO_2 magmatic-hydrothermal system (i.e.,

ankerite-siderite carbonatite) towards an H_2O-dominated, fenitising fluid and/or a decrease in the fluid temperature as the fluids infiltrate the cold granite host rock (Smith et al., 2000; Migdisov et al., 2016).

Migdisov et al. (2016) demonstrated that that LREE were more mobile than HREE at lower hydrothermal temperatures and that REE could also be variably fractionated based on solubility in the presence of F and Cl-bearing fluids, the latter providing more effective transport mechanisms for REE. Chlorine contents in biotite from the ankerite-siderite carbonatites are higher that biotite from other units (Chapter 2); the higher Cl in the ankerite-siderite carbonatites may have contributed to fractionated LREE contents (Migdisov et al., 2016) in these rocks, and their alteration products.

The general La/Nd trends exhibited by the GCCC are likely caused by multi-scale variables. First order regional changes in REY observed in the monazite ore within the Yangibana LREE district are likely due to the evolution of the entire carbonatite system, which is demonstrated by the higher La/Nd ratio and Th contents in monazite from the Lyons River Sills compared to monazite in the ankerite-siderite carbonatites and magnetite-biotite dykes. Second order effects may be caused by changes related to the fluid nature of the systems, such as shifts in CO_2 and H_2O-dominated systems. Third order causes are likely attributed to changes in ligand type/concentration (e.g., F^-, Cl^-) and changes in hydrothermal temperatures. Low temperature weathering (i.e., lateritisation) does not necessarily cause extensive REE fractionation as demonstrated by the similar REE-normalised laterite and host rock profiles in this study (Fig. 5.8) and at Araxá, Catalão I, and Mount Weld (Lottermoser, 1990; Morteani and Preinfalk, 1996).

5.7.5 Comparison with other mineralised carbonatite complexes

The Yangibana LREE district has many similarities compared to other pre-eminent carbonatite-hosted deposits. For example, carbonatite complexes – and their associated metal deposits – are often located in extensional zones in or along old craton margins, which may also host other alkaline igneous phases such as lamprophyres and kimberlites (Table 5.2; Woolley et al., 1989 Gomes et al., 1990; Gibson, 1995; Pearson, 1996; Graham, 2004; Duke, 2009; Cordeiro

et al., 2011; Chakhmouradian et al., 2015). In many cases, such as the Morro do Seis Lagso, Araxá, Catalão I, Mount Weld, and Yangibana deposits, weathering and laterisation can upgrade the ore tenor by removing gangue minerals and/or remobilising and concentrating metals such as REE (Lottermoser, 1990; Morteani and Preinfalk, 1996; this study).

Despite their similar tectonic settings, alkaline rock associations, and amenability to enrichment though lateritisation, carbonatite-hosted metal deposits are quite diverse with respect to their ages, isotopic mantle signatures, metal type, and ore endowment (Table 5.2). The emplacement ages for carbonatites vary considerably ranging from modern day and extending back to the Archean (Woolley, 1989). Some metalliforous carbonatites such as Mount Weld are likely Paleoproterozoic in age (Table 5.2), whereas others such as Bear Lodge are much younger (e.g., Tertiary age; Duke, 2009). The isotopic compositions of carbonatite-hosted metal deposits also vary yielding both depleted and enriched mantle signatures. For instance, Mount Weld has an $\varepsilon Nd(t_{2.025Ga})$ = 0.1 to 1.6, but Catalão has more negative values of $\varepsilon Nd(t_{0.081Ga})$ = -7.9 to -9.8 (Table 5.2; Graham et al., 2004; Guarino et al., 2017). The Yangibana LREE district falls between these two units with $\varepsilon Nd(t_{1.37Ga})$ = -1.55 to -4.2 (Table 5.2; Chapter 2; Chapter 5).

Carbonatite-hosted metal deposits can also differ in the type of metal in which they are endowed. For example, Mount Weld, Bear Lodge and Yangibana are enriched mainly in LREE whereas Tomtor, Catalão I, Araxá, and Morro dos Seis Lagos are enriched mainly in Nb, but often both REE- and HFSE-bearing minerals are present to some degree at most deposits. Traditionally ferrocarbonatites are often considered good candidates for REE-enrichment as they are often considered the latest and most-fractionated carbonatite phase (Le Bas, 1989; Zaitsev et al., 2004). However, this might not necessarily be true as Yangibana is LREE-bearing and Morro dos Seis Lagos is Nb-bearing, but both deposits contain appreciable ferrocarbonatites (Mitchell 2015; Giovanni et al., 2017; this study). Conversely, Araxá and Mount Weld contain fresh calcite and dolomite carbonatites but are Nb and REE-bearing, respectively (Lottermoser, 1990; Cordeiro et al., 2011; Jaireth et al., 2014; Chakhmouradian et al., 2015).

Table 5.2 Comparison of carbonatite-associated REE and HFSE deposits (non-exhaustive summary).

Deposit	Location	Size & grade	Metals	Ore minerals	Host rocks	Associated rocks	Geologic setting	Age (Ma)	εNd(*t*)
Yangibana	Australia	21 Mt @ 1.17% TREO[1]	LREE	monazite (primary & secondary)	Weathered and fresh ankerite-siderite carbonatites, magnetite-biotite and ironstone dykes[2]	Magnetite-biotite dykes, Magmatic-hydrothermal silica-rich alkaline veins, dolomite (±calcite) carbonatites[2]	Gifford Creek Carbonatite Complex in localised extensional zone[2,3] near cratonic suture zone	~1370 (U–Pb, zircon & monazite)[4]	-4.2 to -1.6[2,4]
Mt. Weld	Australia	23.2 Mt @ 7.5 %TREO[6]	LREE, Sm, Eu (±Dy, Tb, Zr, Ti, Nb, Ta, P)[5,6]	Monazite (primary & secondary), synchesite, churchite, plumbogummite-group minerals[6,7]	Lateritisation of carbonatite intrusive plug[6,7]	Melnoites, kimberlites (regional association)[8]	Eastern Goldfields Province near Yilgarn cratonic margin[8]	~2025 (Re–Os)[9]	0.1 to 1.6[8]
Catalaõ I	Brazil	Fresh - 29 Mt @ 1.22 % Nb_2O_5 Supergene – 19Mt @ 1.08% Nb_2O_5[9]	Nb[9]	Pyrochlore[9]	Laterite and fresh dolomite carbonatites and phoscorite as dykes and plugs[9,10]	Alkaline ultrapotassic rocks – kamafugites, minor kimberlites and lamproites[9,10]	Alto Paranaíba Igneous Province along Saõ Francisco cratonic margin, Trindade Mantle Plume?[9,11]	~81 (U–Pb, baddeleyite)[10]	-7.9 to -9.8*[10]
Bull Hill/Bear Lodge	United States	13.3 Mt @ 3.22% TREO[12]	LREE[12]	Basnäsite, parisite, synchysite, ancylite, monazite, cerianite[12]	Oxide and fresh rocks in carbonatite diatreme breccia[12]	Phonolite, syenite, trachyte[12]	Bear Lodge alkaline complex near the Wyoming Craton-Proterozoic basement transition, back-arc extension related to subduction[13]	~51 to 52 (Ar–Ar; biotite, orthoclase)[14]	0.2 to 0.5[12]
Tomtor	Russia	1.18 Mt @ 6.71% Nb_2O_5[15]	Nb, REE, Y, Sc[15,16]	Pyrochlore, goyazite, monazite[15,16]	Weathered and laterised dolomite-calcite carbonatites[15]	Nepheline syenites, subalkaline gabbro, phoscorites, jakupirangite-urtite, lamprophyres[17,18]	Tomtor Alkaline Ultrabasic Massif in Siberian Craton[15,18]	~660 to 510?[19]	n/a
Morro dos Seis Lagos	Brazil	2897.9 Mt @ 2.81% Nb_2O_5[20]	Nb	Pyrochlore, Nb-brookite, Nb-rich rutile[21]	Extensive laterites from siderite and dolomite carbonatite[22]	n/a	Guyana Shield in the Amazon Craton[23]	1300[21]	n/a
Araxá	Brazil	462 Mt @ 2.48% Nb_2O_5[9]	Nb	Pyrochlore, Nb-rich rutile[15,22]	Laterite from dolomite, calcite carbonatites[15]	Phoscorites, pyroxenites, lamprophyres[23]	Paranaíba Arch along margin of São Francisco Craton[23]	98 to 77	n/a

[1]Hastings Technology Metals Ltd. (2019), [2]this study, [3]Pearson (1996), [4]Slezak and Spandler (2019), [5]Lynas Corporation (2015), [6]Jaireth et al. (2014), [7]Lottermoser (1990), [8]Graham et al. (2004), [9]Cordeiro et al. (2011), [10]Guarino et al. (2017), [11]Gibson et al. (1995), [12]Moore et al. (2015), [13] Duke (2009), [14]Anderson et al. (2013), [15]Chakhmouradian et al. (2015) [16]Lazareva et al. (2015), [17]Kravechenko and Pokrovsky (1995), [18]Panina et al. (2016), [19]Entin et al. (1990), [20]Justo and Souza (1986), [21]Giovannini et al. (2017), [22]Mitchell (2015), [23]Gomes et al. (1990)
*Sm–Nd data recalculated to T = 81 Ma

5.7.6 Guidelines for Exploration

The GCCC-hosted Yangibana LREE district (and other carbonatite-hosted rare metal deposits) highlight the importance that major crustal structures play in carbonatite emplacement, especially in old, stable cratons. Smaller structures, like the Bald Hill Lineament, are also important for controlling carbonatite morphology and exposing intrusive bodies. Periods of regional tectonic extension are critical as potential triggers for carbonatite magmatism (Vaughan and Scarrow, 2003) as well as mechanisms for carbonatite melt ascension through the crust (Jelsma et al., 2004). Other alkaline igneous rocks, such as kimberlites, lamproites, syenites, etc. may be indicative of associated carbonatite magmatism.

Carbonatite alteration assemblages are typically commensurate with the size of the intruding body (i.e., relatively small for GCCC units), so regional bulk rock geochemical sampling may not be useful unless a high sample density is collected. Furthermore, unaltered host rock should be sampled to provide background in which to compare potential alteration assemblages and potential outlier intrusive units. In the Yangibana LREE district, Pb and Zn are greatly enriched in the fenitised granites and quartzites, but depleted in the fenitised schists (Appendix 5.A). Conversely, Na_2O is depleted in the fenitised granites but enriched in the fenitised schists (Fig. 5.6b), but the opposite is true for K_2O. Isocons are useful for determining enrichment in weathered zones, provided fresh protolith is discovered. However, the mobility of most elements in fenite alteration halos means that isocons may not always be appropriate.

At Yangibana, the dykes present as high U and Th features mantled by high K zones (in the fenitised granites). The high K concentrations in some fenites and the high U and/or Th contents in the carbonatites make airborne and ground-based radiometric surveys useful exploration tools. Magnetic and gravimetric geophysical surveys may also prove useful in distinguishing magnetite and mafic mineral-rich carbonatite complexes, which should exhibit sharp couplings of high magnetism and high density rocks with low magnetism and low density rocks. These methods may also be useful in identifying additional ore bodies at depth as

demonstrated in Hastings' discovery of Auer and Auer North Hastings Technology Metals Ltd., pers. commun.).

5.9 Conclusions

1. The GCCC was emplaced in a transtensional/extensional setting.

2. The LREE-rich ironstones are genetically related to the other magmatic units in the GCCC, showing analgous enriched mantle Nd isotope values to the fresh alkaline intrusive rocks.

3. Røberg-style alteration followed by weathering and oxidation via meteoric fluids of the ankerite-siderite carbonatites created the ironstones.

4. The ironstones' REY mineralisation was enriched ~3 to ~17 times mainly by eluvial processes.

5. There is spatial variation in La/Nd in the rocks at the GCCC related to petrologic differences as well as changes in the magmatic-hydrothermal system with respect to CO_2 and temperature.

6. The GCCC shows many similarities with other major critical metal-bearing carbonatites such as its tectonic setting, enriched mantle component, and increase in ore tenor through weathering and lateritisation.

5.10 References

Aitken, A.R.A., Betts, P.G., Young, D.A., Blankenship, D.D., Roberts, J.L., Siegert, M.J., 2016. The Australo-Antarctic Columbia to Gondwana transition. Gondwana Research 29, 136-152.

Akers, W.T., Grove, M., Harrison, T.M., Ryerson, F.J., 1993. The instability of rhabdophane and its unimportance in monazite paragenesis. Chemical Geology 110, 169-176.

Anand, R.R., Paine, M., 2002. Regolith geology of the Yilgarn Craton, Western Australia: Implications for exploration. Australian Journal of Earth Sciences 49, 3-162.

Andersen, T., 1984. Secondary processes in carbonatites: petrology of 'rødberg' (hematite-calcite-dolomite carbonatite) in the Fen central complex, Telmark (South Norway). Lithos 17, 227-245.

Anderson, A.K., Cosca, M.A., Larson, P.B., 2013. Timing of carbonatite magmatism in the Bear Lodge alkaline complex. Geological Society of America Abstracts 45, 499.

Armstrong, J.T., 1991. Quantitative element analysis of individual microparticles with electron beam instruments, in: Heinrich, K.F.J., Newbury, D.E. (Eds.), Electron Probe Quantification. Plenum Press, New York, pp. 261-315.

Barker, D.S., 1989. Field relations of carbonatites, in: Bell, K. (Ed.), Carbonatites: Genesis and Evolution. Unwin Hyman, London, pp. 38-69.

Brett, R.C., Russell, J.K., Andrews, G.D.M., Jones, T.J., 2015. The ascent of kimberlite: Insights from olivine. Earth and Planetary Science Letters 424, 119-131.

Chakhmouradian, A.R., Zaitsev, A.N., 2012. Rare earth mineralization in igneous rocks: sources and processes. Elements 8, 347-353.

Chakhmouradian, A.R., Reguir, E.P., Kressall, R.D., Crozier, J., Pisiak, L.K., Sidhu, R., Yang, P., 2015. Carbonatite-hosted niobium deposit at Aley, northern British Columbia (Canada): mineralogy, geochemistry and petrogenesis. Ore Geology Reviews 64, 642-666.

Clavier, N., Podor, R., Dacheux, N., 2011. Crystal chemistry of the monazite structure. Journal of the European Ceramic Society 31, 941-976.

Cordeiro, P.F.O., Brod, J.A., Palmieri, M., Oliveira, C.G.O., Barbosa, E.S.R., Santos, R.V., Gaspar, J.C., Assis, L.C., 2011. The Catalão I niobium deposit, central Brazil: resources, geology and pyrochlore chemistry. Ore Geology Reviews 41, 112-121.

Cutten, H.N., Johnson, S.P., 2018. Kuparr Tectonic Event (KU): WA Geology Online, Explanatory Notes Extract. Geological Survey of Western Australia.

Duke, G.I., 2009. Black Hills–Alberta carbonatite–kimberlite linear trend: Slab edge at depth? Tectonophysics 464, 186-194.

Elliott, H.A.L., Wall, F., Chakhmouradian, A.R., Siegfried, P.R., Dahlgren, S., Weatherley, S., Finch, A.A., Marks, M.A.W., Deady, E., 2018. Fenites associated with carbonatite complexes: A review. Ore Geology Reviews 98, 38-59.

Entin, A.R., Zaitzev, A.J., Nenashev, N.J., 1990. About the range of the geological events related to the ultramafic alkaline rock intrusion of the Tomtor massif (NM Yakutija). Geology and Geophysics 12, 42-51 (in Russian).

Fisher, C.M., McFarlane, C.R.M., Hanchar, J.M., Schmitz, M.D., Sylvester, P.J., Lam, R., Longerich, H.P., 2011. Sm-Nd isotope systematics by laser ablation-multicollector-inductively coupled plasma mass spectrometry: methods and potential natural and synthetic reference materials. Chemical Geology 284, 1-20.

Fricker, M.B., Kutscher, D., Aeschlimann, B., Frommer, J., Dietiker, R., Bettmer, J., Gunther, D., 2011. High spatial resolution trace element analysis by LA-ICP-MS using a novel ablation cell for multiple large samples. International Journal of Mass Spectrometry 307, 39-45.

Gaft, G., Reisfeld, R., Panczer, G., 2015. Modern luminescence spectroscopy of minerals and materials. Springer Mineralogy, Cham, p. 606.

Gellatly, D.C., 1975. Yangibana Creek U-Th-REE-base metal prospect, Gascoyne Goldfield, W.A., Amax Exploration (Australia) Inc.

Gibson, S.A., Thompson, R.N., Leonardos, O.H., Dickin, A.P., Mitchell, J.G., 1995. The Late Cretaceous impact of the Trindade Mantle Plume: evidence from large-volume, mafic, potassic magmatism in SE Brazil. Journal of Petrology 36, 189-229.

Giovannini, A.L., Bastos Neto, A.C., Porto, C.G., Pereira, V.P., Takehara, L., Barbanson, L., Bastos, P.H.S., 2017. Mineralogy and geochemistry of laterites from the Morro dos Seis Lagos Nb (Ti, REE) deposit (Amazonas, Brazil). Ore Geology Reviews 88, 461-480.

Gomes, C.B., Ruperti, E., Morbidelli, L., 1990. Carbonatite complexes from Brazil: A review. Journal of South American Earth Sciences 3, 51-63.

Goodenough, K.M., Schilling, J., Jonsson, E., Kalvig, P., Charles, N., Tuduri, J., Deady, E.A., Sadeghi, M., Schiellerup, H., Müller, A., Bertrand, G., Arvanitidis, N., Eliopoulos, D.G., Shaw, R.A., Thrane, K., Keulen, N., 2016. Europe's rare earth element resource potential: an overview of REE metallogenetic provinces and their geodynamic setting. Ore Geology Reviews 72, 838-856.

Gorobets, B.S., Rogojine, A., 2001. Luminescent spectra of minerals. RPC VIMS, Moscow, p. 300 (in Russian).

Graham, S., Lambert, D., Shee, S., 2004. The petrogenesis of carbonatite, melnoite and kimberlite from the Eastern Goldfields Province, Yilgarn Craton. Lithos 76, 519-533.

Gramaccioli, C.M., Segalstad, T.M., 1978. A uranium-and thorium-rich monazite from a south-alpine pegmatite at Piona, Italy. The American mineralogist 63, 757-761.

Grant, J.A., 1986. The isocon diagram-a simple solution to Gresens' equation for metasomatic alteration. Economic Geology 81, 1976-1982.

Gresens, R.L., 1967. Composition-volume relationships of metasomatism. Chemical Geology 2, 47-65.

Guarino, V., Wu, F.-Y., Melluso, L., Gomes, C.B., Tassinari, C.C.G., Ruberti, E., Brilli, M., 2017. U-Pb ages, geochemistry, C-O-Nd-Sr-Hf isotopes and petrogenesis of the Catalão II carbonatite complex (Alto Paranaíba Igneous Province, Brazil): implications for regional-scale heterogeneities in the Brazilian carbonatite associations. International Journal of Earth Sciences 106, 1963-1989.

Guillong, M., Meier, D.L., Allan, M.M., Heinrich, C.A., Yardley, B.W.D., 2008. SILLS: a MATLAB-based program for the reduction of laser ablation ICP-MS data of homogenous

materials and inclusions in: Sylvester, P. (Ed.), Laser ablation ICP-MS in the Earth Sciences: current practices and outstanding issues. Mineralogical Association of Canada, Vancouver, BC, pp. 328-333.

Hastings Technology Metals, 2019. Yangibana JORC Ore Reserves. Retrieved from https://hastingstechmetals.com/projects/yangibana/yangibana-jorc-resource/ on February 22, 2019.

Jaireth, S., Hoatson, D.M., Miezitis, Y., 2014. Geological setting and resources of the major rare-earth-element deposits in Australia. Ore Geology Reviews 62, 72-128.

Jelsma, H.A., de Wit, M.J., Thiart, C., Dirks, P.H.G.M., Viola, G., Basson, I.J., Anckar, E., 2004. Preferential distribution along transcontinental corridors of kimberlites and related rocks of Southern Africa. South African Journal of Geology 107, 301-324.

Johnson, S.P., Sheppard, S., Rasmussen, B., Wingate, M.T.D., Kirkland, C.L., Muhling, J.R., Fletcher, I.R., Belousova, E.A., 2011. Two collisions, two sutures: punctuated pre-1950 Ma assembly of the West Australian Craton during the Ophthalmia and Glenburgh Orogenies. Precambrian Research 189, 239-262.

Johnson, S.P., Thorne, A.M., Tyler, I.M., Korsch, R.J., Kennett, B.L.N., Cutten, H.N., Goodwin, J., Blay, O., Blewett, R.S., Joly, A., Dentith, M.C., Aitken, A.R.A., Holzschuh, J., Salmon, M., Reading, A., Heinson, G., Boren, G., Ross, J., Costelloe, R.D., Fomin, T., 2013. Crustal architecture of the Capricorn Orogen, Western Australia and associated metallogeny. Australian Journal of Earth Sciences 60, 681-705.

Johnson, S.P., Korhonen, F.J., Kirkland, C.L., Cliff, J.B., Belousova, E.A., Sheppard, S., 2017. An isotopic perspective on growth and differentiation of Proterozoic orogenic crust: From subduction magmatism to cratonization. Lithos 268-271, 76-86.

Justo, L.J.E.C., Souza, M.M., 1986. Jazida de nióbio do Morro dos Seis Lagos, Amazonas, in: Schobbenhaus, C., Coelho, C.E.S. (Eds.), Principais Depósitos Minerais do Brasil - Ferro e Metais da Indústria do Aço. Departmento Nacional da Produção Mineral, pp. 463-468 (in Portuguese).

Korhonen, F.J., Johnson, S.P., Fletcher, I.R., Rasmussen, B., Sheppard, S., Muhling, J.R., Dunkley, D.J., Wingate, M.T.D., Roberts, M.P., Kirkland, C.L., 2015. Pressure-temperature-

time evolution of the Mutherbukin Tectonic Event, Capricorn Orogen: Geological Survey of Western Australia, Report 146, p. 64.

Kravchenko, S.M., Pokrovsky, B.G., 1995. The Tomtor Alkaline Ultrabasic Massif and related REE-Nb deposits, Northern Siberia. Economic Geology 90, 676-689.

Lazareva, E.V., Zhmodik, S.M., Dobretsov, N.L., Tolstov, A.V., Shcherbov, B.L., Karmanov, N.S., Gerasimov, E.Y., Bryanskaya, A.V., 2015. Main minerals of abnormally high-grade ores of the Tomtor deposit (Arctic Siberia). Russian Geology and Geophysics 56, 844-873.

Le Bas, M.J., 1989. Diversification of carbonatite, in: Bell, K. (Ed.), Carbonatites Genesis and Evolution. Unwin Hyman Ltd, London, pp. 428-447.

Le Maitre, R.W., 2002. Igneous Rocks: A Classification and Glossary of Terms: recommendations of International Union of Geological Sciences, subcommission on the systematics of igneous rocks. Cambridge University Press, Cambridge.

Lenz, C., Nasdala, L., Talla, D., Hauzenberger, C., Seitz, R., Kolitsch, U., 2015. Laser-induced REE^{3+} photoluminescence of selected accessory minerals - an "advantageous artefact" in Raman spectroscopy. Chemical Geology 415, 1-16.

López-Moro, F.J., 2012. EASYGRESGRANT—A Microsoft Excel spreadsheet to quantify volume changes and to perform mass-balance modelling in metasomatic systems. Computers & Geosciences 39, 191-196.

Lottermoser, B.G., 1990. Rare-earth element mineralisation within the Mt. Weld carbonatite laterite, Western Australia. Lithos 24, 151-167.

Luo, Y., Gao, S., Longerich, H.P., Gunter, D., Wunderli, S., Yuan, H.-L., Liu, X.-M., 2007. The uncertainty budget of the multi-element analysis of glasses using LA-ICP-MS. Journal of Analytical Spectrometry 22, 122-130.

Lynas Corporation LTD., 2015. Mount Weld mineral resource and ore reserve update 2015, p. 24. Retrieved from https://www.lynascorp.com/PublishingImages/Pages/Mt-Weld-Resources-and-Reserves/ASX%20Announcement%20-%20Ore%20Reserves%20and%20Resources%20FINAL%20051015.pdf on August 8, 2018.

MacLean, W.H., Kranidiotis, P., 1987. Immobile elements as monitors of mass transfer in hydrothermal alteration; Phelps Dodge massive sulfide deposit, Matagami, Quebec. Economic Geology 82, 951-962.

Mariano, A.N., 1989. Nature of economic mineralization in carbonatites and related rocks, in: Bell, K. (Ed.), Carbonatites: Genesis and Evolution. Unwin Hyman, London, pp. 149-176.

Martin, D.M., Thorne, A.M., 2004. Tectonic setting and basin evolution of the Bangemall Supergroup in the northwestern Capricorn Orogen. Precambrian Research 128, 385-409.

McDonough, W.F., Sun, S.s., 1995. The composition of the Earth. Chemical Geology 120, 223-253.

Migdisov, A., Williams-Jones, A.E., Brugger, J., Caporuscio, F.A., 2016. Hydrothermal transport, deposition, and fractionation of the REE: experimental data and thermodynamic calculations. Chemical Geology 439, 13-42.

Mitchell, R.H., 2015. Primary and secondary niobium mineral deposits associated with carbonatites. Ore Geology Reviews 64, 626-641.

Moore, M., Chakhmouradian, A.R., Mariano, A.N., Sidhu, R., 2015. Evolution of rare-earth mineralization in the Bear Lodge carbonatite, Wyoming: Mineralogical and isotopic evidence. Ore Geology Reviews 64, 499-521.

Morteani, G., Preinfalk, C., 1996. REE distribution and REE carriers in laterites formed on the alkaline complexes of Araxa and Catalao (Brazil), in: Jones, A.P., Wall, F., Williams, C.T. (Eds.), Rare Earth Minerals: Chemistry, Origin and Ore Deposits. Chapman and Hall, London.

Olierook, H.K.H., Agangi, A., Plavsa, D., Reddy, S.M., Yao, W., Clark, C., Occhipinti, S.A., Kylander-Clark, A.R.C., 2018. Neoproterozoic hydrothermal activity in the West Australian Craton related to Rodinia assembly or breakup? Gondwana Research 68, 1-12.

Panina, L.I., Rokosova, E.Y., Isakova, A.T., Tolstov, A.V., 2016. Lamprophyres of the Tomtor Massif: A result of mixing between potassic and sodic alkaline mafic magmas. Petrology 24, 608-625.

Pearson, J.M., 1996. Alkaline rocks of the Gifford Creek Complex, Gascoyne Province, Western Australia: their petrogenetic and tectonic significance, Department of Geology and Geophysics. University of Western Australia, p. 219.

Pearson, J.M., Taylor, W.R., 1996. Mineralogy and geochemistry of fenitized alkaline ultrabasic sills of the Gifford Creek Complex, Gascoyne Province, Western Australia. The Canadian Mineralogist 34, 201-219.

Pearson, J.M., Taylor, W.R., Barley, M.E., 1996. Geology of the alkaline Gifford Creek Complex, Gascoyne Complex, Western Australia. Australian Journal of Earth Sciences 43, 299-309.

Pettke, T., 2008. Analytical protocols for element concentration and isotope ratio measurements in fluid inclusions by LA-(MC)-ICP-MS, in: Sylvester, P. (Ed.), Laser ablation ICP-MS in earth sciences: current practices and outstanding issues. Mineral Association of Canada, Vancouver, pp. 189-218.

Pettke, T., Oberlie, F., Audetat, A., Guillong, M., Simon, A.C., Hanley, J.J., Klemm, L.M., 2012. Recent developments in element concentration and isotope ratio analysis of individual fluid inclusions by laser ablation single and multiple collector ICP-MS. Ore Geology Reviews 44, 10-38.

Pillans, B., 2007. Pre-Quaternary landscape inheritance in Australia. Journal of Quaternary Science 22, 439-447.

Pirajno, F., González-Álvarez, I., 2013. The ironstone veins of the Gifford Creek ferrocarbonatite complex, Gascoyne Province: Geological Survey of Western Australia, Record 2013/12, p. 19.

Pirajno, F., González-Álvarez, I., Chen, W., Kyser, K.T., Simonetti, A., Leduc, E., leGras, M., 2014. The Gifford Creek Ferrocarbonatite Complex, Gascoyne Province, Western Australia: associated fenitic alteration and a putative link with the ~1075 Ma Warakurna LIP. Lithos 202–203, 100-119.

Pisarevsky, S.A., Wingate, M.T.D., Li, Z.-X., Wang, X.-C., Tohver, E., Kirkland, C.L., 2014. Age and paleomagnetism of the 1210Ma Gnowangerup–Fraser dyke swarm, Western Australia, and implications for late Mesoproterozoic paleogeography. Precambrian Research 246, 1-15.

Richter, D.K., Görgen, P., Götte, T., 2008. Monazite cathodoluminescence - a new tool for heavy mineral analysis of siliciclastic rocks. Sedimentary Geology 209, 36-41.

Roncal-Herrero, T., Rodríguez-Blanco, J.D., Oelkers, E.H., Benning, L.G., 2011. The direct precipitation of rhabdophane ($REEPO_4 \cdot nH_2O$) nano-rods from acidic aqueous solutions at 5–100 °C. Journal of Nanoparticle Research 13, 4049-4062.

Rukhlov, A.S., Chudy, T.C., Arnold, H., Miller, D., 2018. Field trip guidebook to the Upper Fir carbonatite-hosted Ta-Nb deposit, Blue River area, east-central British Columbia, p. 67.

Shannon, R.D., 1976. Revised effective ionic radii and systematic sutdies of interatomic distances in halides and chalcogenides. Acta Crystallographica Section A 32, 752-767.

Sheppard, S., Occhipinti, S.A., Nelson, D.R., 2005. Intracontinental reworking in the Capricorn Orogen, Western Australia: the 1680-1620 Ma Mangaroon Orogeny. Australian Journal of Earth Sciences 52, 443-460.

Sheppard, S., Rasmussen, B., Muhling, J.R., Farrell, T.R., Fletcher, I.R., 2007. Grenvillian-aged orogenesis in the Palaeoproterozoic Gascoyne Complex, Western Australia: 1030-950 Ma reworking of the Proterozoic Capricorn Orogen. Journal of Metamorphic Geology 25, 477-494.

Sheppard, S., Bodorkos, S.P., Johnson, S.P., Wingate, M.T.D., Kirkland, C.L., 2010a. The Paleoproterozic Capricorn Orogeny: intracontinental reworking not continent-continent collision. Geological Survey of Western Australia, Report 108, p. 33.

Sheppard, S., Johnson, S.P., Wingate, M.T.D., Kirkland, C.L., Pirajno, F., 2010b. Explanatory notes for the Gascoyne Province: Geological Survey of Western Australia, p. 336.

Slezak, P., Spandler, C., Blake, K., 2018. Ghosts of apatite past: using hyperspectral cathodoluminescence and micro-geochemical data to reveal multi-generational apatite in the Gifford Creek Carbonatite Complex, Australia. The Canadian Mineralogist 56, 773-797.

Slezak, P., Spandler, C., 2019. Carbonatites as recorders of mantle-derived magmatism and subsequent tectonic events: an example of the Gifford Creek Carbonatite Complex, Western Australia. Lithos 328-329, 212-227.

Smith, M.P., Henderson, P., Campbell, L.S., 2000. Fractionation of the REE during hydrothermal processes: Constraints from the Bayan Obo Fe-REE-Nb deposit, Inner Mongolia, China. Geochimica et Cosmochimica Acta 64, 3141-3160.

Smithies, R.H., Kirkland, C.L., Korhonen, F.J., Aitken, A.R.A., Howard, H.M., Maier, W.D., Wingate, M.T.D., Quentin de Gromard, R., Gessner, K., 2015. The Mesoproterozoic thermal evolution of the Musgrave Province in central Australia - plume vs. the geological record. Gondwana Research 27, 1419-1429.

Spandler, C., Pettke, T., Rubatto, D., 2011. Internal and external fluid sources for eclogite-facies veins in the Monviso meta-ophiolite, Western Alps: Implications for fluid flow in subduction zones. Journal of Petrology 52, 1207-1236.

Stark, J.C., Wang, X-C., Li, Z-X., Denyszyn, S., Rasmussen, B., Zi, J-W., 2018. 1.39 Ga mafic dyke swarm in southwestern Yilgarn Craton marks Nuna to Rodinia transition in the West Australian Craton. Precambrian Research 316, 291-304.

Torpy, A., Wilson, N.C., 2008. OpticalFit Software by CSIRO Australia.

Treiman, A.H., 1989. Carbonatite magma: properties and processes, in: Bell, K. (Ed.), Carbonatites: Genesis and Evolution. Unwin Hyman, London, pp. 89-104.

Van Achterbergh, E., Ryan, C.C., Jackson, S.E., Griffin, W.L., 2001. Data reduction software for LA-ICP-MS, in: Sylvester, P.J. (Ed.), Laser-Ablation-ICP-MS in the Earth Sciences: Principles and Applications. Mineral Association of Canada, pp. 239-243.

Van Emdem, B., Thornber, M.R., Graham, J., Lincoln, F.J., 1997. The incorporation of actinides in monazite and xenotime from placer deposits in Western Australia. The Canadian Mineralogist 35, 95-104.

Vaughan, A.P.M., Scarrow, J.H., 2003. K-rich mantle metasomatism control of localization and initiation of lithospheric strike-slip faulting. Terra Nova 15, 163-169.

Wade, B.P., Barovich, K.M., Hand, M., Scrimgeour, I.R., Close, D.F., 2006. Evidence of early Mesoproterozoic arc magmatism in the Musgrave Block, central Australia: Implications for Proterozoic crustal growth and tectonic reconstructions of Australia. Journal of Geology 114, 43-63.

Wall, F., 2014. Rare earth elements, in: Gunn, A.G. (Ed.), Critical Metals Handbook. John Wiley & Sons, pp. 312-339.

Wall, F., Zaitsev, A.N., 2004. Rare earth metals in Kola carbonatites, in: Wall, F., Zaitsev, A.N. (Eds.), Phoscorites and Carbonatites from Mantle to Mine: the Key Example of the Kola Alkaline Province. The Mineralogical Society of Great Britain & Ireland, Cambridge, pp. 341-373.

Walters, A., Lusty, P., Hill, A., 2011. Rare earth elements, British Geological Survey Mineral Profiles, United Kingdom, p. 54.

Woolley, A.R., 1989. The spatial and temporal distribution of carbonatites, in: Bell, K. (Ed.), Carbonatites: Genesis and Evolution. Unwin Hyman, London, pp. 15-37.

Woolley, A.R., Kempe, D.R.C., 1989. Carbonatites: nomenclature, average chemical compositions, and element distribution, in: Bell, K. (Ed.), Carbonatites: Genesis and Evolution. Unwin Hyman Ltd, London, pp. 1-14.

Zaitsev, A.N., Frances, W., Le Bas, M.J., 1998. REE-Sr-Ba minerals from the Khibina carbonatites, Kola Peninsula, Russia: their mineralogy, paragenesis and evolution. Mineralogical Magazine 62, 225-250.

Zaitsev, A.N., Sitnikova, M.A., Subbotin, V.V., Fernandez-Suarez, J., Jeffries, T.E., 2004. Sallanlatvi Complex-a rare example of magnesite and siderite carbonatites, in: Wall, F., Zaitsev, A.N. (Eds.), Phoscorites and Carbonatites from Mantle to Mine: the Key Example of the Kola Alkaline Province. Geological Society of Great Britain and Ireland, London, pp. 201-245.

Zi, J.W., Gregory, C., Rasmussen, B., Sheppard, S., Muhling, J.R., 2017. Using monazite geochronology to test the plume model for carbonatites: The example of Gifford Creek Carbonatite Complex, Australia. Chemical Geology 463, 50-60.

Chapter 6

Thesis Summary and Future Work

6.1 Summary discussion

The aims of this thesis were to study the mineralised Gifford Creek Carbonatite Complex (GCCC) in order to:

1) Evaluate the heterogeneous rock types with respect to their petrology, which comprise carbonatite complexes, especially the novel magnetite-biotite dykes, ankerite-siderite carbonatites, silica-rich alkaline veins, alteration assemblages;
2) Elucidate the origins of the GCCC, particularly with respect to age, origin, and tectonic history; and
3) Describe the genesis of the carbonatite-associated Yangibana LREE district in the context of the GCCC, creating a revised model for the district.

These tasks were completed using a combination of bulk rock and in situ geochemical and isotopic techniques in order to overcome the lack of crosscutting field relationships in the complex.

Chapter 2 discussed the primary rock types found in the GCCC such as the dolomite and calcite carbonatites of the Lyons River Sills, magnetite-biotite dykes, ankerite-siderite carbonatites, and silica-rich alkaline veins. Through the use of bulk rock geochemistry, EPMA analyses on biotite, and isotopic analyses, the GCCC was determined to have originated from an enriched mantle source, potentially metasomatised during prior convergent tectonic processes involved in assembling the West Australia Craton. Furthermore, the inverse relationship between CaO and other major element compositions (e.g., Fe_2O_3, MgO, TiO_2, etc.) in the Lyons River Sills was shown to be driven by crystallisation of calcite-rich cumulate phase followed by melt evolution via fractionation. In addition, the ankerite-siderite carbonatites were demonstrated to potentially be magmatic in origin. Though the precise nature of the ankerite-siderite carbonatites and magnetite-biotite dykes is still uncertain, they have similar trace element signatures and may have a genetic link. Based on the anithetic relationship between trace element plots for the magnetite-biotite dykes and silica-rich alkaline veins, the silica-rich alkaline veins were determined to be a late F and Na-rich magmatic-hydrothermal phase, which mobilised Ti, Nb, and Zr.

Hyperspectral CL analyses on apatite (Chapter 3) determined that there were episodes of REE mobilisation in apatite on the scale of individual crystals, which affected the CL spectra. The apatite crystals from different rock types all had spectral peaks at 1.4 eV, 2.l eV, and 2.3 – 3.5 eV, related primarily to the REE activators, Nd^{3+}, Eu^{3+}, Sm^{3+} and Ce^{3+}. Quantitative techniques such as EPMA and LA-ICP-MS corroborate these findings and demonstrate that there are variations in primary magmatic composition based on apatite REY patterns. Further examination shows that in the fenite sample, carbonatitic apatite with high REY and Sr contents precipitated on granitic apatite with high SiO_2 and Mn contents. By conducting these detailed studies, it was shown that hyperspectral CL is useful for apatite provenance determination and potentially mineral exploration as well as triage for further in situ isotopic analytical techniques.

Based on U–Pb dates obtained from carbonatitic zircon crystals from glimmerites (which are associated with the ankerite-siderite carbonatites) and silica-rich alkaline vein samples (Chapter 4), it is concluded that the GCCC was emplaced at c. 1370 Ma, during a single magmatic event. The Hf isotope values ($\varepsilon Hf(t_{1.37Ga})$ = -1.6 to -4.2), which agree with the bulk rock Nd values ($\varepsilon Nd(t_{1.37Ga})$ = -1.8 to -4.2), agreeing with an enriched mantle as the source for the magmas. Uranium–Pb dating of monazite from the GCCC yielded dates younger than those of zircon at 1250 to 1200 Ma, 1100 to 1050 Ma, c. 1000 Ma, and c. 815 Ma. Samarium–Nd isochron dates from monazite, apatite, and monazite-apatite pairs also resulted in younger ages with a much tighter spread from c. 1300 to 1200 Ma, but with consistent initial $^{143}Nd/^{144}Nd$ values (0.51078 to 0.51087) and a lower Sm/Nd ratio of 0.0867. Plotting the εNd values of the GCCC samples at their respective U–Pb and Sm–Nd ages resulted in an isotopic evolution trend that correlates with the increasingly nonradiogenic Nd values for the GCCC at the given dates. This isotopic trend is much steeper that the projected trend for an enriched mantle model (EM2), indicating that the GCCC had formed during one magmatic event at c. 1370 Ma and subsequently underwent tectonic reworking, causing partial recrystallisation and resetting of the U–Pb and Sm–Nd isotope systems both in monazite and apatite. The age of emplacement of the GCCC (c. 1370 Ma) does not correlate with any known magmatism in the region, but does broadly correspond with the breakup of the Nuna supercontinent. The subsequent U–Pb dates are attributed to major tectonic events

that affected the GCCC, such as the Mutherbukin Tectonic Event, Giles Event, Edumundian Orogeny, and Rodinia disassembly.

Chapter 5 demonstrated the dykes/sills of the GCCC were likely emplaced during a period of extension and/or transtension, allowing for the low viscosity alkaline melts to permeate the crust via pre-existing structures such as the Lyons River Fault, Bald Hill Lineament, and other subordinate structures. The ironstones, which are of REE economic interest, were evaluated to establish their relationship with the other units of the GCCC. Obvious dissolution features, low temperature minerals and textures (e.g., botryoidal Fe-oxides/hydroxides), enrichments in REE and Th, and bulk rock Nd isotopes ($\varepsilon Nd(t_{1.37Ga})$ = -1.55 to -3.24) show the ironstones are genetically related to the ankerite-siderite carbonatites (and likely other alkaline igneous units in the GCCC), which were altered by low temperature, oxidising fluids such as meteoric waters. Isocon analysis between the ankerite-siderite carbonatites and ironstones also show that the ironstones are enriched in REE contents by ~3 to ~17 times, though they have loss a considerable percentage of mass, resulting in their vuggy texture. The main ore mineral, monazite showed an inverse relationship between La and Nd, which was reflected in both in situ analyses and bulk rock drill assays. This La/Nd ratio varies across the GCCC and influences the prospectivity of the mineral deposits of the Yangibana LREE district. The northwest region has the higher La/Nd ratio (La/Nd = 1.5 to 2) compared to the central region (La/Nd = 0.3 to 0.5). The cause for this variation is believed to relate to changes in the primary melt compositions (as reflected in the different rock types) as well as changes regarding CO_2 activity in the later stage magmatic-hydrothermal fluids. Chapter 5 also compares the Yangibana LREE district to several other preeminent carbonatite mineral deposits, prospective for REE and HFSE. The comparison highlights the importance of extensional stress regimes along cratonic margins for carbonatite complex emplacement. It also demonstrates that laterisation is important in concentrating critical metals in carbonatite systems.

6.2 Future work

Despite the extensive analytical work conducted in this thesis, several questions remain. For example, carbonatites and other phases such as the magnetite-biotite dykes which share some

similarities to phoscorites, may be genetically related, but what are the exact chemical/physical mechanisms that connect them? In addition, carbonatites, depending on their composition, can form over a wide range of temperatures. A rough temperature estimate for the ankerite-siderite carbonatites has been established, but the uncertainty is large. What are the precise formation temperatures and pressures of the GCCC units? Lanthanum and Nd often have a positive correlation, but they are inversely related in the monazite from the GCCC. Under what conditions do La and Nd separate from each other and what are the geologic implications of this relationship? To answer these additional questions, the following work is proposed:

1) Piston cylinder and/or cold seal experiments on carbonatite-phoscorite melts to examine the major components of these rocks such as CaO, MgO, FeO/Fe_2O_3, P_2O_5, SiO_2, K_2O, Na_2O, CO_2, H_2O, REE_2O_3, and F to emulate derivation from a mantle melt and subsequent changes pressure, temperature, and composition.

2) Oxygen isotope temperature/pressure calculations based on quartz-magnetite, biotite-magnetite, and/or apatite-biotite pairs. Caution would be required in using quartz-carbonate phases, as Sr resetting was observed in some carbonate samples in the ankerite-siderite carbonatites in this study.

3) Mg and Ca isotope studies on the carbonatites may provide additional insights regarding the mechanisms for genesis and evolution (i.e., fractionation, immiscibility, contamination) of the Lyons River Sills and ankerite-siderite carbonatites.

4) Lower temperature experiments (< 700 ºC) focussing on La and Nd species in magmatic and/or hydrothermal settings with respect to F, Cl, K_2O, Na_2O, H_2O, CO_2, P_2O_5 and potential effects on La vs. Nd mobility and their partitioning into monazite.

5) If/when ground is broken for mining in the Yangibana LREE district, evaluation of newly exposed cross cutting relationships between the rocks should be evaluated, particularly in the context of the geochemical database created during this work.

6) As stated in Chapter 5, many of the dykes and sills are associated with structural features of varying scales (large faults down to joints). A regional structural analysis combined with previous geochronology work (e.g., this thesis) may provide insights regarding the stress regimes imparted by far-field stresses affecting the West Australia Craton that likely contributed to the emplacement of the GCCC.

Appendices

Chapter 1 Appendices

Appendix 1.A – Thesis Analytical Methods

1.A.1 Sample Preparation

Samples selected for micro-analysis were prepared as 27mm x 46 mm polished thin sections to a thickness of 30 μm. Offcuts these thin sections were then prepared as 25 mm diameter polished pucks. Both pucks and thin sections were polished to microprobe quality (i.e., 1 μm). Thin sections and polished pucks were examined and imaged using a Leica DMRXP optical microscope. Except for some zircon samples, which were prepared as grain mounts, all micro-analyses were conducted in situ within the pucks and/or thin sections.

Zircon grain mounts were prepared by crushing samples to a size of ~500 to 1000 μm with a tungsten-carbide disk mill at the JCU Mineral Separation Lab. Crushed samples were run through a Wilfley table, creating light and heavy separates. The heavy mineral separates underwent further density separation using LST Heavy Liquid, which consists of a solution of hydrated lithium heteropolytungstates and has a specific gravity of 2.85 g/cm^3 at standard temperature and pressure. After density separation, the magnetic minerals were removed with a standard ferromagnet. The separates were then run through a Frantz Isodynamic Magnetic Separator. Zircons hand-picked from the final batch of mineral separates after density and magnetic separation, then mounted in a 25 mm epoxy puck.

1.A.2 Cathodoluminescence (CL) Analyses

Sample pucks and thin sections were carbon-coated and then tested for cathodoluminescence (CL) using a JEOL JSM-5410LV scanning electron microscope (SEM) with a monochromatic Robinson photomultiplier CL detector. Images were captured using JEOL SEMAFORE 4.0.2. The kV was adjusted to elicit a CL response, usually ~15 kV. Images were captured using a contrast setting of 38-45% and a filter of 100 kHz. Monochromatic images were captured in order to determine textural variations not observable under transmitted and reflected light microscopy.

After panchromatic CL and BSE imaging, the top few microns of the sample were polished away to ensure a fresh analytical surface. The samples were re-carbon coated and

analysed using JEOL XM-86440 CL spectrometer connected to the JEOL JXA-8200 WD/ED combined electron probe micro-analyser (EPMA) via a 200 μm optic fibre cable. The effective wavelength range of the spectrometer is 350 nm to 1200 nm (i.e., 3.54 eV to 1.03 eV). At >1200 nm the signal-to-noise ratio is too high for meaningful interpretation (MacRae et al., 2005). Samples were mapped in situ using a 1 μm to 5 μm spot size and 1 μm to 5 μm step (depending on grain size) with a dwell time of 20 ms to 50 ms per spot. The beam was set to 20 kV and 20 nA. These data were then compiled into raster images, and then RGB false colour images using the xCLent software from CSIRO, and Chimage software, respectively (Harrowfield et al., 1993). Wavelength spectra for the different zones within the mineral were obtained using the XCL-image software.

In order to determine individual activators from a sample, the spectrum must be deconvoluted. Deconvolution involves transforming and scaling the spectra emitted by the sample from wavelength (nm) to energy (eV) using the Planck-Einstein relation:

$$E = \frac{hc}{\gamma} \qquad (1)$$

where E is energy, h is Planck's constant, c is the speed of light, and λ is wavelength. This transformation transposes and scales the x-axis allowing the spectra to be expressed as a sum of Gaussian distributions. Each of individual curves represents a probability of a luminescent centre within the mineral, which allows identification of potential activators (Marshall, 1988; Townsend and Rowlends, 2000; Barbarand and Pagel, 2001; MacRae et al., 2013).

Deconvolution of these spectra was conducted using the Optical Fit 17.07 software from CSIRO (Fig. 1.A.1; Torpy and Wilson, 2008). Each CL spectrum is considered the sum of a number of CL peaks with Gaussian distributions produced by the presence of CL activators. The Optical Fit software is used to approximate a best fit line to the CL spectrum by assuming Gaussian peak profiles and matching probable peak locations to known activator band locations from the CSIRO luminescence database (Fig. 1.A.1; MacRae and Wilson, 2008).

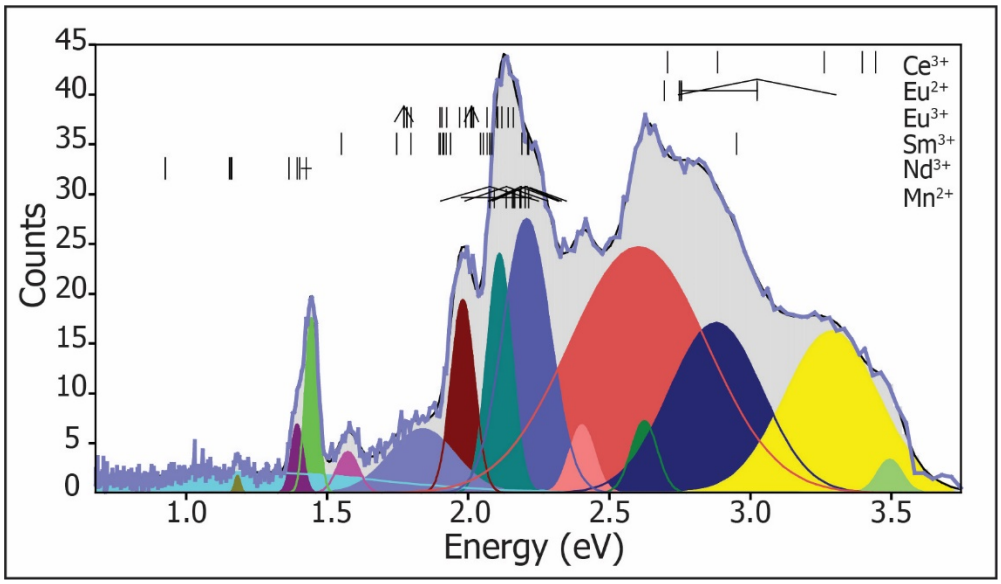

Figure 1.A.1 A deconvoluted hyperspectral CL curve for the mottled pink and purple zones in the apatite from LE-1, constructed using the Optical Fit 17.07 software from CSIRO (Torpy and Wilson, 2008). The total curve (purple) comprises the sum of Gaussian distributed peaks (multiple colours) of possible CL activators present across the energy spectra. Thin vertical lines indicate single activator locations. Thin horizontal lines indicate an activator present over a range of band values, and triangular hats depict the full width at half maximum (FWHM) for an activator (where the data are available). The locations of the apatite activators are taken from MacRae and Wilson (2008) and references therein. More activators are present in apatite, but only these were shown in the interest of simplicity.

1.A.3 Wavelength Dispersive (WD) Analyses

After CL analyses, the samples were polished to remove the top few micrometres of the exposed surface of the samples in order to avoid potential electron beam damage from the previous analysis, particularly for apatite. The samples were then carbon-coated again and analysed for major/minor elements using a JEOL JXA-8200 WD/ED EPMA. In the case of apatite and monazite, analysis locations were selected on various CL zones across multiple grains within the regional CL maps acquired for each sample. The beam was set to a 2 µm to 5 µm spot size with an accelerating voltage of 15 kV and a current of 20 nA. All elements were analysed for 20s on peak with 10s on background, except for F and Sr, which were analysed using 40s on peak with 20s on background and 30s on peak with 15s on background, respectively. Element concentrations were quantified using well-characterised in-house standards as follows: Ca and Si (wollastonite), Na (albite), F and Sr (SrF_2), Cl (tugtupite), Mn (spessartine), Ti (TiO_2), Al (almandine), Mg (olivine), K (orthoclase), Sm ($SmPO_4$), P and Ce ($CePO_4$), Nd ($NdPO_4$), Pr ($PrPO_4$), Y (YPO_4), Gd ($GdPO_4$), Dy ($DyPO_4$), La ($LaPO_4$), and Th (Th metal).

Apatite analyses were then subject to a ZAF matrix correction procedure for data quantification because this correction best fit the data due to the substantial levels of REE in some apatites. The φρz procedure was used to correct all other minerals (Armstrong, 1991).

The analysis of halogens in apatite is highly dependent on crystal orientation and electron beam exposure. Fluorine in particular is susceptible to migration in the apatite crystal lattice due to electron beam exposure (Stormer et al., 1993; Pyle et al., 2002). For example, X-ray counts of F in apatite tend to increase substantially when F is analysed by an electron beam parallel to the *c*-axis of the crystal (Stormer et al., 1993; Goldoff et al., 2012). This migration of F can lead to erroneous values greater than 1.0 apfu or 3.77 wt.% F in fluorapatite (Pyle et al., 2002; Chakhmouradian et al., 2017). To monitor and correct for potential F migration during analysis, F counts were recorded along with analysis time, using a chart recorder. These time-resolved data were then plotted in MS Excel and extrapolated back to the F counts at time zero using a best fit line as stipulated by Stormer and Pierson (1993), McCubbin et al. (2010), and Goldoff et al. (2012). The Y-intercept value from the line of best fit was then used as the new raw F count rate and background subtracted from this value. The background (in counts per second) for this correction is calculated by:

$$\left(\frac{\left[\frac{(BG_l+BG_u)}{2}\right]}{1000}\right) \times \mathrm{E} = BG(\mathrm{E})$$

Where BG_l = lower background intercept in cps/nA, BG_u = upper background intercept in cps/nA, E = probe current in nA, and BG = background in cps at the specified probe current. Once background is subtracted, the resulting value (in cps) is entered back into the microprobe to calculate final element concentration values for use in the ZAF correction (in the case of apatite).

1.A.4 Trace Elements (LA-ICP-MS)

Transmitted light, CL images, and the EPMA WDS spot locations were used to determine suitable areas of minerals for trace element spot analysis by laser ablation inductively coupled mass spectrometry (LA-ICP-MS). Where CL zones were analysed, multiple grains and their correlating CL zones were analysed using laser spot analyses. Trace element analyses were conducted using a Coherent GeoLasPro 193nm Excimer laser coupled to a Varian (now Bruker)

820-MS quadrupole ICP-MS. Laser spot sizes typically varied from 24 to 44 μm depending on the size of the target apatite zone. Samples were ablated using a surface energy density of 4 J/cm^2 for phosphate minerals and 6 J/cm^2 for silicate minerals as measured at the site of ablation, and a repetition rate of 10 Hz. The rate of oxide production and plasma fractionation were monitored by keeping ThO/Th to around 0.5%, and $^{238}U/^{232}Th$ sensitivity ≈ 1, respectively. The synthetic glasses NIST SRM 610 and 612 were used as the primary and secondary standards, respectively, with reference values taken from Spandler et al. (2011). Internal values as determined by EPMA WDS were used as internal standards for trace element analyses. For example, Ca and Ce were used for apatite and monazite, respectively (Chapter 3; Chapter 5). In some cases, stoichiometric values were used, such as 43.14 wt.% Zr for zircon (Chapter 4). Data reduction was carried out using the ETH (Zurich, Switzerland) Signal Integration for Laboratory Laser Systems (SILLS) program (Guillong et al., 2008). Signal selection in SILLS was completed by first identifying and, if necessary, removing spikes. All analysed isotopes (see chapters for mineral-specific isotopes) were plotted in SILLS. Background and signal time intervals were selected for primary standards (NIST 610), secondary standards (NIST 612), and unknown values (Fig. 1.A.2). Intervals were selected based on the best overall smoothness for the longest period of time (up to three separate intervals) of the curve for germane elements (e.g., REE in monazite and apatite).

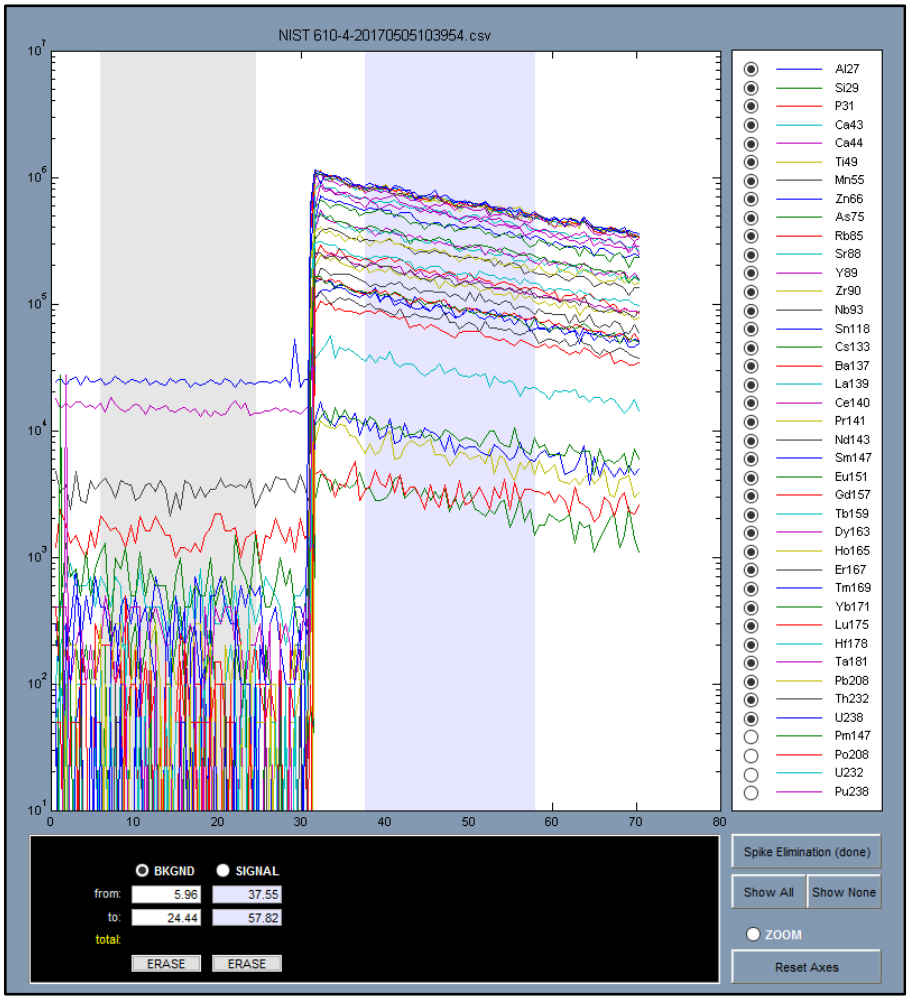

Figure 1.A.2 An example of element isotope plots and signal selection in SILLS (Guillong et al., 2008) for NIST 610. Background selection is grey and analysis is periwinkle..

Because SILLS is able to plot all of the isotopes analysed on a log scale, mineral inclusions are more easily avoided (e.g., monazite inclusion in apatite). SILLS also allows up to three separate intervals to be selected in the sample analysis section, but only one interval may be selected for background (Fig. 1.A.2). As laser spot analyses also sample at depth various elements were monitored during interval selection and the appropriate signal intervals selected according to each CL zone analysed with EPMA and based on the CL images. Element drift was plotted and elements showing the least drift over the analyses were selected. The error and detection limit were calculated in SILLS using the methods from Luo et al. (2007) and Pettke et al. (2012), respectively.

1.A.5 U–Pb

Zircon mineral separates and monazite grains, either in thin sections or in polished rock sample pucks, were analysed in situ for U–Pb isotopes using the same laser ablation set up as described for the trace element analysis, except spot sizes of 24 µm, 32 µm, and 44 µm were used for zircon and monazite. Data were collected for ^{29}Si, ^{90}Zr, ^{202}Hg, ^{204}Pb, ^{206}Pb, ^{207}Pb, ^{208}Pb, ^{232}Th, ^{235}U, and ^{238}U for zircon. For monazite, ^{31}P was substituted for ^{29}Si and ^{90}Zr. Due to the use of high purity He and Ar gases with a gold trap placed in the carrier gas line before the inlet into the sample cell, ^{202}Hg was always below the detection limit (in the gas background and during mineral ablation). Age calibration and instrumental drift were monitored by analysis of GJ1 zircon (Jackson et al., 2004) and Manangotry monazite (Horstwood et al., 2003) as primary standards. The 91500 (Wiedenbeck et al., 1995) and FC1 zircons (Paces and Miller, 1993) and the Namaqualand (Liu et al., 2012) and Bananeira monazites (Gonçlaves et al., 2016) were used as secondary zircon and monazite standards, respectively. Standards were analysed at the beginning and end of each session as well as after analyses of 10 unknowns.

Iolite v3.5, which plots the data as time-resolved mass spectra, was used for data reduction (Hellstrom et al., 2008; Paton et al., 2010; 2011). Data reduction consisted of establishing baseline values for all mass isotopes for all analyses. Outliers outside of two standard deviations were removed from background and sample signals to reduce spikes. Signals were trimmed and selected for primary standards, which were then calibrated to the published isotope values for the standards used. Downhole fractionation corrections were applied using exponential or exponential plus linear models. The U and Pb isotope analyte signals were then plotted for the unknown analyses in Iolite. The spectra plot similarly to those in Figure 1.A.2. Smooth, consistent curves were selected for unknowns. The VisualAge UcomPbine algorithm was used to account for common ^{207}Pb/^{206}Pb values in the primary standards for monazite analyses. The U–Pb_Geochron4 algorithm (Paton et al., 2010) was used in calculating the isotope ratios for zircon analyses. Uncertainties were obtained using the methods of Paton et al. (2010), which account for excess analytical uncertainty calculated in quadrature. These propagated uncertainties as well as the calculated U–Th–Pb isotope values and ratios were then exported into MS Excel and plotted

using Isoplot/EX 4.15 (Ludwig, 2009). To account for discordance and incorporation of common Pb, the results were plotted using Tera-Wasserburg Concordia plots (Tera and Wasserburg, 1972; Jackson et al., 2004) and compared with values from the 2-stage Pb model from Stacey and Kramers (1975).

The secondary zircon standards, 91500 and FC1, returned ages of 1056 ± 5.6 Ma and 1114 ± 16 Ma, respectively, which agrees reasonably well with the reference ages of 1065.4 ± 0.3 Ma for 91500 (Wiedenbeck et al., 1995) and 1099 ± 0.6 Ma for FC1 (Paces and Miller, 1993). The Bananeira monazite returned an age of 505 ± 2.4 Ma within uncertainty of the reference age of 507.7 ± 1.3 Ma (Gonçlaves et al., 2016). The Namaqualand monazite returned a date of 1029.4 ± 4.2 Ma in agreement with its reference age of c.1033 Ma (Knoper et al., 2000; Hokada and Motoyoshi, 2006).

1.A.6 Sm–Nd

In situ Sm–Nd isotope analysis of monazite and apatite was undertaken at the AAC, JCU, using a Coherent GeoLasPro 193nm Excimer laser ablation system coupled with a Thermo-Scientific NEPTUNE MC-ICP-MS. The NEPTUNE Faraday cup configuration is the same set up used by McFarlane and McCulloch (2007) with interference and mass bias corrections made according to Fisher et al. (2011). Laser spot sizes were 24 μm for monazite and between 44 and 60 μm for apatite. Each analysis consisted of data acquisition for 60s on background, 60s data acquisition, and a 60s washout time between analyses. Samples were ablated in a large volume cell (Fricker et al., 2011) using a repetition rate of 4 Hz and surface energy density (measured at the site of ablation) of 4 J/cm^2. The ablated material was carried via He gas (flow rate of 2.5 l/min) to a bulb with a volume of 2.5 cm^3 where it was mixed with Ar (flow of 0.95 l/min) and N_2 (0.01 l/min) before being carried to the MC-ICP-MS. A synthetic LREE-doped glass (ID-TIMS; $^{147}Sm/^{144}Nd = 0.2451 \pm 7$) and a Nd-doped glass (JNdi-1; ID-TIMS $^{143}Nd/^{144}Nd = 0.512098 \pm 13$) were used as primary standards to monitor and correct for drift in unknown $^{147}Sm/^{144}Nd$ and $^{143}Nd/^{144}Nd$ values (Fisher et al., 2011).

Data reduction was carried out in MS Excel. Multi-collector data for the Sm–Nd analyses was extracted, collated, and plotted in Excel using an in-house macro. Background for the measured isotopes are assumed to be zero. The $^{143}Nd/^{144}Nd$ and $^{147}Sm/^{144}Nd$ ratios were plotted against time for the 60 s data acquisition. Outliers were eliminated from the ratio plots. The average value and standard error were calculated for each analysis. The measured values for the primary standards were averaged and normalised against the published values. The unknown data was then corrected based on the normalised data. The initial $^{143}Nd/^{144}Nd$ value and $\varepsilon Nd(t)$ values were calculated using $^{143}Nd/^{144}Nd_{CHUR} = 0.512638$, $^{147}Sm/^{144}Nd_{CHUR} = 0.1966$, and $\lambda = 6.54 \times 10^{-12}$, based on the Nd isotopic correction of $^{146}Nd/^{144}Nd = 0.7219$ (De Paolo, 1981; Patchet, 1989). Progressive errors (2σ) were obtained by calculating the measured uncertainties in quadrature.

The results for JNdi-1 glass are $^{143}Nd/^{144}Nd = 0.512091 \pm 15$ (n = 28) and for LREE glass are $^{147}Sm/^{144}Nd = 0.2442 \pm 2$ (n = 28), agreeing with the ID-TIMS results from Fisher et al. (2011) of 0.512098 and 0.2451, respectively. As a quality control measure, Otter Lake apatite and Mae Klang monazite were used as secondary standards. This study's results for Otter Lake apatite (n = 24; $^{143}Nd/^{144}Nd = 0.511908 \pm 23$ and $^{147}Sm/^{144}Nd = 0.0807 \pm 5$) align with the average values ($^{143}Nd/^{144}Nd = 0.511942 \pm 45$ and $^{147}Sm/^{144}Nd = 0.0827 \pm 21$) reported for Otter Lake (Yang et al., 2014). The results for Mae Klang monazite (n=25; $^{143}Nd/^{144}Nd = 0.512638 \pm 17$ and $^{147}Sm/^{144}Nd = 0.0925 \pm 7$) also concur with those published by Fisher et al. (2011; $^{143}Nd/^{144}Nd = 0.512646 \pm 10$ and $^{147}Sm/^{144}Nd = 0.0978 \pm 227$).

1.A.7 Lu–Hf

In situ Lu–Hf isotope micro-analysis of zircon was conducted using the laser ablation and MC-ICP-MS instrumentation and gas flow setting as outlined above for Sm-Nd. Lutetium–Hf sample spots were selected over or adjacent to the U–Pb spots. The NEPTUNE Faraday cup configuration and isobaric interference corrections were carried out according to Woodhead et al. (2004) and Kemp et al. (2009). Each analysis consisted of 60s on background and 60s data

acquisition with a 60s washout time between analyses. Samples were ablated using a repetition rate of 4 Hz, a surface energy density of 6 J/cm^2, and a spot size of 90 μm.

Data reduction was carried out in MS Excel Multi-collector data for the Lu–Hf was extracted, collated, and plotted in Excel using an in house macro. Background for the measured isotopes were assumed to be zero. The $^{176}Hf/^{177}Hf$ and $^{175}Lu/^{177}Hf$ ratios were plotted against time for the 60 s data acquisition. Outliers were eliminated from the ratio plots. The average value and standard error were calculated for each analysis. The measured values $^{176}Hf/^{177}Hf$ for the Mud Tank Zircon (MTZ) were averaged then normalised against the published values. The unknown analyses were then corrected based on the normalised $^{176}Hf/^{177}Hf$ values for the measured MTZ. The $^{175}Lu/^{177}Hf$ value was calculated to $^{176}Lu/^{177}Hf$ based on isotopic abundance ($^{176}Lu/^{175}Lu$ = 0.26549) for all samples. The initial εHf(*t*) values were calculated using $^{176}Hf/^{177}Hf_{CHUR}$ = 0.282785, $^{176}Lu/^{177}Hf$ = 0.0.0336, and $\lambda = 1.867 \times 10^{-5}$ (Bouvier et al., 2008; Scherer et al., 2001; Söderlund et al., 2004). Depleted mantle (DM) ages were calculated using λ = 01.867 x 10^{-5} (Scherer et al., 2001; Söderlund et al., 2004), $^{176}Hf/^{177}Hf$ = 0.28325, and $^{176}Lu/^{177}Hf$ = 0.0384 (Griffin et al., 2000). Progressive errors (2σ) were obtained by calculating the measured uncertainties in quadrature.

An average value of $^{176}Hf/^{177}Hf$ = 0.282495 ± 6 was obtained for the primary standard, Mud Tank, and an average value of $^{176}Hf/^{177}Hf$ = 0.282164 ± 8 was obtained for the secondary standard, FC1. This is within uncertainty of the solution value of 0.282184 ± 16 (Woodhead and Hergt, 2005) and indistinguishable from the LA-MC-ICP-MS values of $^{176}Hf/^{177}Hf$ = 0.282499 ± 17 and $^{176}Hf/^{177}Hf$ = 0.282176 ± 22 for Mud Tank and FC1, respectively (Kemp et al., 2009).

1.A.8 Rb–Sr

Carbonatite rocks were sampled for Sr isotope analysis using a dental drill with a titanium burr. The drill bit was first cleaned by submersion into 10% HNO_3, followed by 18.2 miliOhm water (MQ), and ethanol. The drill bit was dried and the sample was abraded. All acids utilised for dissolution were made using Seastar Analytic brand ultrapure acid and MQ water. Samples ranging from 8 to 16 g were dissolved in 1 M acetic acid (Asahara et al., 1995), which leaches Sr

from the carbonate component and is not significantly affected by incorporated silicate detritus. Following addition of 3 ml of acetic acid, samples were placed in an ultrasonic bath for 0.5 hours, and then allowed to stand for ~12 hours. Samples were then briefly (~5 minutes) agitated again in the ultrasonic bath and centrifuged for 20 minutes at 20,000 rotations per minute. The acid/sample solution was then decanted and evaporated to dryness. Strontium was separated using pre-cleaned Biorad brand micro-columns containing Eichrom strontium-specific resin. Several column volumes of MQ and 3.5M HNO_3 was used to clean the columns, which were equilibrated with 500 µl 3.5M HNO_3 prior to sample loading. Samples were loaded in in 500 µl of 3.5M HNO_3 and washed in four rinses of 300 ul of 3.5M HNO_3. The Sr was then eluted in 500 µl MQ and evaporated to dryness. Evaporated samples were treated with a few drops Seastar brand H_2O_2 to ensured removal of any resin. Samples were dissolved in 2 ml 2% HNO_3. A volume corresponding to ~400 ng Sr was placed in to1.5 ml vials containing 2% HNO_3. The Neptune MC-ICP-MS in the AAC at JCU was used to analyse the samples. Total runtime was ~16 min for most samples. Negligible corrections for Kr and Rb interferences were observed. The $^{87}Sr/^{86}Sr$ ratio was corrected for mass bias from $^{86}Sr/^{88}Sr$ and normalised to 0.1194. Analyses of the SRM-987 standard run in conjunction with the samples yielded a mean ratio of 0.71040 ± 0.000029 (n=5), which is in agreement with the accepted value of the SRM-987 standard of 0.71034 ± 0.00026.

1.A.9 Stable C & O isotopes

Sample powders of carbonatite were prepared and analysed for $\delta^{13}C$ and $\delta^{18}O$ at the AAC Environmental Isotope Laboratory. Stable carbon and oxygen isotope compositions were determined using an online ThermoFisher GasBenchIII gas preparation and introduction system coupled to a ThermoFisher DeltaV^{PLUS} isotope ratio mass spectrometer via the ThermoFisher ConFloIV. Carbon dioxide was extracted from carbonate by reaction with 100% orthophosphoric acid in Exetainer vials after atmosphere was replaced with He. Repeat samples of NBS-18 and NBS-19 (as international standards) provided monitoring of accuracy and precision. Standard deviations for internal standards were better than 0.1‰ for both $\delta^{13}C$ and $\delta^{18}O$ values. The $\delta^{13}C$

values are reported relative to Vienna PeeDee Belemnite (VPDB), and the $\delta^{18}O$ values are reported relative to Vienna Standard Mean Ocean Water (VSMOW).

1.A.10 Bulk Rock Nd isotopes

Rock samples were crushed at the JCU Mineral Separation Lab. Samples were cut, cleaned, and examined for contaminants such as wall rock clasts. Sample without contamination or alteration were then crushed to a fine powder using a tungsten ring mill. The mill was thoroughly cleaned in between each use. Whole rock isotope analyses of nine samples were performed at the University of Adelaide with a Finnigan MAT 262 thermal ionisation mass spectrometer (TIMS) in static and quadruple cup dynamic measurement modes following the routine in Wade et al. (2006). Between 30 and 200 mg of rock powder were spiked with (^{147}Sm + ^{150}Nd) by initially digesting the samples in a 2 mL 7M HNO_3 + 4 mL 28M HF solution that was evaporated to dryness at 140 °C. Then the samples were digested in a HNO_3-HF solution at 190 °C for at least 96 hours in Parr reaction vessels. The samples were then evaporated to dryness on a hotplate at 140 °C and redissolved in 6 mL 6M HCl. The measurements were corrected for mass fractionation by normalisation to $^{146}Nd/^{142}Nd = 0.7219$. Neodymium and Sm concentrations were corrected for 100 pg and 50 pg blanks, respectively. Reference material JNdi-1 gave 0.512108 ± 8 (2σ) (n = 8). $^{143}Nd/^{144}Nd$ ratios were normalised to the TIMS value of JNdi-1 glass (0.512098 ± 13; Fisher et al., 2011).

1.A.11 Bulk Rock Geochemistry

1.A.11.1 JCU AAC

The major element compositions of rock samples were analysed from Li borate fusion glasses in the AAC, JCU, using a Bruker-AXS S4 Pioneer X-ray Fluorescence Spectrometer. The fusion glasses were then mounted into 25 mm diameter epoxy pucks and analysed at JCU using the LA-ICP-MS setup described previously. Multiple laser spots were analysed for each glass. The data were reduced using Glitter software (Van Achterbergh et al., 2001) by selecting the smoothest signals for all elements. An average value and standard error for the analyses were then calculated.

1.A.11.2 Bureau Veritas Ltd.

Bulk rock samples were sent to Bureau Veritas Commodities Canada Ltd in Vancouver, British Columbia. The samples were crushed and split. The first sample split was fused into a lithium metaborate/tetraborate bead. The sample bead was dissolved in American Chemical Society (ACS) grade nitric acid dissolution and analysis of the solution conducted via ICP-MS for the following elements: Mg, Al, Si, P, K, Ca, Sc, Ti, V, Cr, Mn, Fe, Ni Ga, Rb, Sr, Y, Zr, Nb, Sn, Cs, Ba, La, Ce, Pr, Nd, Sm, Eu, Gd, Tb, Dy, Ho, Er, Tm, Yb, Lu, Hf, Ta, W, Th, and U. The second sample split was digested in aqua regia and analysed via inductively coupled emission spectroscopy/mass spectroscopy (ES/MS) for the elements Li, Be, B, Cr, Co, Cu, Zn, Ge, As, Se, Mo, Pd, Ag, Cd, In, Sb, Te, Re, Pt, Au, Hg, Tl, Pb, and, Bi. Carbon and S were determined using the LECO method. Fluorine was analysed by sample decomposition by fusion with NaOH followed by water digestion and acidification using citric acid buffered by an ammonium citrate solution. The fluoride ion was analysed by the potentiometric method.

1.A References

Armstrong, J. T. (1991). Quantitative element analysis of individual microparticles with electron beam instruments. In: Heinrich, K. F. J. & Newbury, D. E. (eds.) Electron Probe Quantification. New York: Plenum Press, 261-315.

Asahara, Y., Tanaka, T., Kamioka, H. & Nishimura, A. (1995). Asian continental nature of87Sr/86Sr ratios in north central Pacific sediments. Earth and Planetary Science Letters 133, 105-116.

Barbarand, J. & Pagel, M. (2001). Cathodoluminescence study of apatite crystals. American Mineralogist 86, 473-484.

Bouvier, A., Vervoort, J. D. & Patchett, P. J. (2008). The Lu–Hf and Sm–Nd isotopic composition of CHUR: constraints from unequilibrated chondrites and implications for the bulk composition of terrestrial planets. Earth and Planetary Science Letters 273, 48-57.

Chakhmouradian, A. R., Reguir, E. P., Zaitsev, A. N., Coueslan, C., Xu, C., Kynicky, J., Mumin, A. H. & Yang, P. (2017). Apatite in carbonatitic rocks: compositional variation, zoning, element partitioning and petrogenetic significance. Lithos 274-275, 188-213.

De Paolo, D. J. (1981). Neodymium isotopes in the Colorado Front Range and crust-mantle evolution in the Proterozoic. Nature 291, 193-196.

Fisher, C. M., McFarlane, C. R. M., Hanchar, J. M., Schmitz, M. D., Sylvester, P. J., Lam, R. & Longerich, H. P. (2011). Sm-Nd isotope systematics by laser ablation-multicollector-inductively coupled plasma mass spectrometry: methods and potential natural and synthetic reference materials. Chemical Geology 284, 1-20.

Fricker, M. B., Kutscher, D., Aeschlimann, B., Frommer, J., Dietiker, R., Bettmer, J. & Gunther, D. (2011). High spatial resolution trace element analysis by LA-ICP-MS using a novel ablation cell for multiple large samples. International Journal of Mass Spectrometry 307, 39-45.

Goldoff, B., Webster, J. D. & Harlov, D. E. (2012). Characterization of fluor-chlorapatites by electron probe microanalysis with a focus on time-dependent intensity variation of halogens. American Mineralogist 97, 1103-1115.

Gonçlaves, G. O., Lana, C., Scholz, R., Buick, I. S., Gerdes, A., Kamo, S. L., Corfu, F., Marinho, M. M., Chaves, A. O., Valeriano, C. & Nalini Jr., H. A. (2016). An assessment of monazite from the Itambe pegmatite district for use as U-Pb isotope reference material for microanalysis and implications for the origin of the "Moacyr" monazite. Chemical Geology 424, 30-50.

Griffin, W. L., Pearson, N. J., Belousova, E., Jackson, S. E., van Achterbergh, E., O'Reilly, S. Y. & Shee, S. R. (2000). The Hf isotope composition of cratonic mantle: LAM-MC-ICPMS analysis of zircon megacrysts in kimberlites. Geochimica et Cosmochimica Acta 64, 133-147.

Guillong, M., Meier, D. L., Allan, M. M., Heinrich, C. A. & Yardley, B. W. D. (2008). SILLS: a MATLAB-based program for the reduction of laser ablation ICP-MS data of homogenous materials and inclusions In: Sylvester, P. (ed.) Laser ablation ICP-MS in the Earth Sciences: current practices and outstanding issues. Vancouver, BC: Mineralogical Association of Canada, 328-333.

Harrowfield, I. R., MacRae, C. & Wilson, N. C. (1993). Chemical imaging in electron microprobes. Proceedings of the 27th Annual Microbeam Analysis Society (MAS) Meeting, 547-548.

Hellstrom, J., Paton, C., Woodhead, J. D. & Hergt, J. M. (2008). Iolite: software for spatially resolved LA-(quad and MC) ICPMS analysis. In: Sylvester, P. (ed.) Laser Ablation ICP–MS in the Earth Sciences: Current Practices and Outstanding Issues: Mineralogical Association of Canada Short Course series 40, 343-348.

Hokada, T. & Motoyoshi, Y. (2006). Electron microprobe technique for U-Th-Pb and REE chemistry of monazite, and its implications for pre-, peak- and post-metamorphic events of the Lutzow-Holm Complex and the Napier Complex, East Antarctica. Polar Geoscience 19, 118-151.

Horstwood, M. S. A., Foster, G. L., Parrish, R. R., Noble, S. R. & Nowell, G. M. (2003). Common-Pb corrected in situ U-Pb accessory mineral geochronology by LA-MC-ICP-MC. Journal of Analytical Atomic Spectrometry 18, 837-846.

Jackson, S. E., Pearson, N. J., Griffin, W. L. & Belousova, E. A. (2004). The application of laser ablation-inductively coupled plasma-mass spectrometry to in situ U-Pb zircon geochronology. Chemical Geology 211, 47-69.

Kemp, A. I. S., Foster, G. L., Schersten, A., Whitehouse, M. J., Darling, J. & Storey, C. (2009). Concurrent Pb-Hf isotope analysis of zircon by laser ablation multi-collector ICP-MS, with implications for the crustal evolution of Greenland and the Himalayas. Chemical Geology 261, 244-260.

Knoper, M., Armstrong, R. A., Andreoli, M. A. G. & Ashwal, L. D. (2000). The Steenkampskraal monazite vein: a subhorizontal stretching shear zone indicating extensional collapse of Namaqualand at 1033 Ma? Journal of African Earth Sciences 31 (suppl.), 38-39.

Liu, Z.-C., Wu, F-Y., Yang, Y-H., Yang, J-H, Widle, S.A. (2012). Neodymium isotopic compositions of the standard monazites used in U-Th-Pb geochronology. Chemical Geology 334, 221-239.

Ludwig, K. R. (2009). Isoplot v.3.71 a geochronological toolkit for Microsoft Excel. Berkeley.

Luo, Y., Gao, S., Longerich, H. P., Gunter, D., Wunderli, S., Yuan, H.-L. & Liu, X.-M. (2007). The uncertainty budget of the multi-element analysis of glasses using LA-ICP-MS. Journal of Analytical Spectrometry 22, 122-130.

MacRae, C., Wilson, N. C. & Torpy, A. (2013). Hyperspectral cathodoluminescence. Mineralogy and Petrology 107, 429-440.

MacRae, C. M. & Wilson, N. C. (2008). Luminescence database I - minerals and materials. Microscopy and Microanalysis. Cambridge, U.K.: Cambridge University Press, 184-204.

MacRae, C. M., Wilson, N. C., Johnson, S. A., Phillips, P. L. & Otsuki, M. (2005). Hyperspectral mapping-combining cathodoluminescence and X-ray collection in an electron microprobe. Microscopy Research and Technique 67, 271-277.

Marshall, D. J. (1988). Cathodoluminescence of geological materials. Boston: Unwin Hyman.

McCubbin, F. M., Steele, A., Nekvasil, H., Schnieders, A., Rose, T., Fries, M., Carpenter, P. K. & Jolliff, B. L. (2010). Detection of structurally bound hydroxyl in fluorapatite from Apollo Mare basalt 15058,128 using TOF-SIMS. American Mineralogist 95, 1141-1150.

McFarlane, C. R. M. & McCulloch, M. T. (2007). Coupling of in-situ Sm-Nd systematics and U-Pb dating of monazite and allanite with applications to crustal evolution studies. Chemical Geology 245, 45-60.

Paces, J. B. & Miller, J. D. (1993). Precise U-Pb ages of Duluth Complex and related mafic intrusions, northeastern Minnesota: geochronological insights to physical, petrogenetic, paleomagmatic, and tectonomagmatic processes associated with the 1.1 Ga Midcontinent Rift System. Journal of Geophysical Research 98, 13997-14013.

Patchett, P. J. (1989). Radiogenic isotope geochemistry of rare earth elements. In: Lipin, B. R. & McKay, G. A. (eds.) Geochemistry and Mineralogy of Rare Earth Elements. Washington, D.C.: Mineralogical Society of America, 25-44.

Paton, C., Hellstrom, J., Paul, B., Woodhead, J. & Hergt, J. (2011). Iolite: Freeware for the visualisation and processing of mass spectrometric data. Journal of Analytical Atomic Spectrometry 26, 2508-2518.

Paton, C., Woodhead, J., Hellstrom, J., Hergt, J., Greig, A. & Maas, R. (2010). Improved laser ablation U-Pb zircon geochronology through robust down-hole fractionation correction. Geochemistry, Geophysics, Geosystems 11.

Pettke, T., Oberlie, F., Audetat, A., Guillong, M., Simon, A. C., Hanley, J. J. & Klemm, L. M. (2012). Recent developments in element concentration and isotope ratio analysis of individual fluid inclusions by laser ablation single and multiple collector ICP-MS. Ore Geology Reviews 44, 10-38.

Pyle, J. M., Spear, F. S. & Wark, D. A. (2002). Electron microprobe analysis of REE in apatite, monazite, and xenotime: protocalls and pitfalls. In: Kohn, M. J., Rakovan, J. & Hughes, J. M. (eds.) Phosphates: Geochemical, Geobiological, and Materials Importance: Mineralogical Society of America, 337-362.

Scherer, E., Münker, C. & Mezger, K. (2001). Calibration of the Lutetium-Hafnium Clock. Science 293, 683.

Söderlund, U., Patchett, P. J., Vervoort, J. D. & Isachsen, C. E. (2004). The 176Lu decay constant determined by Lu–Hf and U–Pb isotope systematics of Precambrian mafic intrusions. Earth and Planetary Science Letters 219, 311-324.

Spandler, C., Pettke, T. & Rubatto, D. (2011). Internal and external fluid sources for eclogite-facies veins in the Monviso meta-ophiolite, Western Alps: Implications for fluid flow in subduction zones. Journal of Petrology 52, 1207-1236.

Stacey, J. S. & Kramers, J. D. (1975). Approximation of terrestrial lead isotope evolution by a two-stage model. Earth and Planetary Science Letters 26, 207-221.

Stormer, J., J.C. & Pierson, M. L. (1993). Variation of F and Cl X-ray intensity due to anisotropic diffusion and electron microprobe analysis of apatite: An adendum. American Mineralogist Supplemental Data.

Stormer, J., J.C., Pierson, M. L. & Tacker, R. C. (1993). Variation of F and Cl on X-ray intensity due to anisotropic diffusion in apatite during electron microprobe analysis. American Mineralogist 78, 641-648.

Tera, F. & Wasserburg, G. J. (1972). U-Th-Pb systematics in three Apollo 14 basalts and the problem of initial Pb in lunar rocks. Earth and Planetary Science Letters 14, 281-304.

Torpy, A. & Wilson, N. C. (2008). OpticalFit Software by CSIRO Australia.

Townsend, P. D. & Rowlands, A. P. (2000). Information encoded in cathodoluminescence emission spectra. In: Pagel, M., Barbin, V., Blanc, P. & Ohnenstetter, D. (eds.) Cathodoluminescence in geosciences. Springer, pp. 41-57.

Van Achterbergh, E., Ryan, C. C., Jackson, S. E. & Griffin, W. L. (2001). Data reduction software for LA-ICP-MS. In: Sylvester, P. J. (ed.) Laser-Ablation-ICP-MS in the Earth Sciences: Principles and Applications: Mineral Association of Canada, 239-243.

Wade, B. P., Barovich, K. M., Hand, M., Scrimgeour, I. R. & Close, D. F. (2006). Evidence of early Mesoproterozoic arc magmatism in the Musgrave Block, central Australia: Implications for Proterozoic crustal growth and tectonic reconstructions of Australia. Journal of Geology 114, 43-63.

Wiedenbeck, M., Alle, P., Corfu, F., Griffin, W. L., Meier, M., Oberli, F., von Quadt, A., Roddick, J. C. & Spiegel, W. (1995). Three natural zircon standards for U-Th-Pb, Lu-Hf, trace element and REE analyses. Geostandards Newsletter 19, 1-23.

Woodhead, J., Hergt, J., Shelley, M., Eggins, S. & Kemp, R. (2004). Zircon Hf-isotope analysis with an excimer laser, depth profiling, ablation of complex geometries, and concomitant age estimation. Chemical Geology 209, 121-135.

Woodhead, J. D. & Hergt, J. M. (2005). A preliminary appraisal of seven natural zircon reference materials for in situ Hf isotope determination. Geostandards and Geoanalytical Research 29, 183-195.

Yang, Y. H., Wu, F. Y., Yang, J. H., Chew, D. M., Xie, L. W., Chu, Z. Y., Zhang, Y. B. & Huang, C. (2014). Sr and Nd isotopic compositions of apatite reference materials used in U-Th-Pb geochronology. Chemical Geology 385, 35-55.

Chapter 2 Appendices

Appendix 2.A – Biotite EPMA Analyses

Spot analysis	LR18BLC Bio 1	LR18BLC Bio 2	LR18BLC Bio 3	LR18BLC Bio 4	LR18BLC Bio 5	LR18BLC Bio 6	LR23 Bio4 dk	LR23 Bio5 dk	LR23 Bio2
Mineral	biotite	biotite	biotite	biotite	biotite	biotite	biotite dolomite carbonatite	biotite dolomite carbonatite	biotite dolomite carbonatite
Predominant rock type	granite	granite	granite	granite	granite	granite			
BSE zone	n/a	n/a	n/a	n/a	n/a	n/a	n/a	n/a	n/a
F	0.818	0.853	0.660	0.759	0.764	0.692	1.80	2.11	1.17
Na2O	0.0319	0.0374	0.0421	0.00640	0.0166	0.0278	0.0840	0.0433	0.0087
MgO	10.3	10.7	10.3	9.8	10.3	10.5	18.7	19.8	17.2
Al2O3	16.9	16.6	16.9	17.2	16.9	16.3	11.7	11.5	12.4
SiO2	35.7	35.6	35.7	35.2	35.9	36.0	40.3	40.4	38.4
Cl	0.00310	0.0119	0.0137	bdl	bdl	0.00970	0.00220	bdl	0.00290
K2O	10.3	10.2	10.4	10.2	10.2	10.3	10.2	10.2	10.1
CaO	bdl	bdl	bdl	bdl	bdl	bdl	0.0410	0.0753	0.0446
TiO2	1.53	1.46	1.32	1.44	1.50	1.55	1.09	1.05	1.33
MnO	0.0667	0.0448	0.0507	0.0366	0.0537	0.0396	0.0381	0.0143	0.0190
FeO	19.9	19.4	20.1	19.9	19.8	18.8	11.3	10.4	13.2
Total	95.6	94.8	95.5	94.5	95.5	94.2	95.2	95.6	93.9
-O=(F,Cl)2	0.345	0.362	0.281	0.319	0.322	0.294	0.758	0.888	0.493
new Total	95.3	94.5	95.2	94.2	95.2	93.9	94.4	94.7	93.5
APFU									
F	0.198	0.208	0.160	0.186	0.185	0.169	0.419	0.487	0.279
Na	0.00474	0.00559	0.00627	0.000962	0.00246	0.00417	0.0120	0.00612	0.00127
Mg	1.18	1.22	1.18	1.13	1.18	1.21	2.05	2.15	1.93
Al	1.53	1.51	1.53	1.57	1.53	1.49	1.01	0.991	1.10
Si	2.74	2.74	2.74	2.73	2.75	2.78	2.96	2.94	2.90
Cl	0.000402	0.001554	0.001783	0	0	0.00127	0.000274	0	0.000371
K	1.01	1.01	1.01	1.01	1.00	1.01	0.957	0.947	0.973
Ca	0	0	0	0	0	0	0.00323	0.00588	0.00360
Ti	0.0882	0.0845	0.0765	0.0840	0.0866	0.0902	0.0601	0.0574	0.0754
Mn	0.00433	0.00292	0.00330	0.00240	0.00348	0.00259	0.00237	0.000883	0.00121
Fe	1.27	1.25	1.29	1.29	1.27	1.22	0.692	0.636	0.834

Spot analysis	LR23 Bio3	LR23 Bio 7	LR23 Bio 8	LR23 Bio 9	LR23 Bio 101	LR23 Bio 102	LR23 Bio 103	LR23 Bio 10
Mineral	biotite	biotite	biotite	biotite	biotite	biotite	biotite	biotite
Predominant rock type	dolomite carbonatite	dolomite carbonatite	dolomite carbonatite	dolomite carbonatite	dolomite carbonatite	dolomite carbonatite	dolomite carbonatite	dolomite carbonatite
BSE zone	n/a	n/a	n/a	n/a	n/a	n/a	n/a	n/a
F	1.37	1.68	1.41	1.28	1.13	1.66	1.53	1.06
Na2O	0.0447	0.0572	0.0772	0.0514	0.0526	0.0507	0.0329	0.0227
MgO	17.3	18.7	16.9	17.3	16.4	17.4	17.9	16.9
Al2O3	12.7	12.1	12.5	12.4	13.1	12.4	12.3	12.7
SiO2	38.6	39.6	38.5	39.0	37.8	38.8	39.2	38.6
Cl	0.00720	0.0251	bdl	0.0193	0.0294	0.00500	0.0136	bdl
K2O	9.71	10.1	10.1	10.2	10.1	10.2	10.1	10.3
CaO	0.0336	0.0207	0.0101	0.0944	0.0429	0.0240	0.0479	0.0413
TiO2	1.09	0.97	1.27	1.26	1.33	1.44	1.05	1.50
MnO	0.0273	bdl	0.0214	0.0320	0.0373	0.0202	0.0285	0.0368
FeO	13.3	11.8	12.9	13.2	14.2	13.2	12.7	13.5
Total	94.1	95.0	93.7	94.8	94.2	95.1	94.9	94.6
-O=(F,Cl)2	0.578	0.713	0.594	0.543	0.482	0.700	0.647	0.446
new Total	93.6	94.3	93.1	94.3	93.7	94.4	94.2	94.2
APFU								
F	0.325	0.393	0.337	0.302	0.270	0.391	0.360	0.252
Na	0.00650	0.00819	0.0113	0.00744	0.00772	0.00732	0.00474	0.00330
Mg	1.94	2.06	1.90	1.93	1.85	1.93	1.98	1.89
Al	1.12	1.05	1.11	1.09	1.16	1.08	1.08	1.12
Si	2.89	2.93	2.91	2.91	2.86	2.89	2.91	2.89
Cl	0.000915	0.003143	0	0.00244	0.00377	0.000631	0.00171	0
K	0.929	0.950	0.972	0.968	0.976	0.964	0.956	0.990
Ca	0.00270	0.00164	0.00082	0.00755	0.00348	0.00191	0.00381	0.00332
Ti	0.0614	0.0538	0.0721	0.0710	0.0756	0.0805	0.0585	0.0846
Mn	0.00173	0	0.00137	0.00202	0.00239	0.00127	0.00179	0.00234
Fe	0.831	0.730	0.812	0.824	0.899	0.819	0.789	0.849

Spot analysis	LR 27 Bio 2	LR 27 Bio 3	LR 27 Bio 4	LR 27 Bio 5	LR 27 Bio 6	dmcy138_bio_1	dmcy138_bio_2	dmcy138_bio_3
Mineral	biotite	biotite	biotite	biotite	biotite	biotite	biotite	biotite
Predominant rock type	dolomite carbonatite	dolomite carbonatite	dolomite carbonatite	dolomite carbonatite	dolomite carbonatite	mag-bio dyke	mag-bio dyke	mag-bio dyke
BSE zone	n/a	n/a	n/a	n/a	n/a	dark	dark	light
F	4.47	4.78	4.52	4.38	4.35	5.09	5.34	4.13
Na2O	0.0691	0.0848	0.0597	0.0852	0.0889	0.0844	0.0561	0.0259
MgO	21.1	22.0	21.5	21.1	21.7	20.5	20.6	18.4
Al2O3	7.47	7.32	7.59	7.29	8.20	7.91	7.87	10.5
SiO2	48.0	48.2	47.9	48.3	46.5	45.8	46.1	40.7
Cl	bdl	0.0159	bdl	0.00510	bdl	0.0357	0.00520	0.0496
K2O	10.8	11.0	11.0	10.8	11.0	10.6	10.5	10.2
CaO	0.138	0.0510	bdl	0.00330	0.0123	bdl	bdl	0.00340
TiO2	0.493	0.243	0.341	0.472	0.269	0.251	0.328	0.503
MnO	0.00300	0.0216	0.0156	0.00960	0.0252	0.254	0.269	0.498
FeO	5.04	4.70	4.92	4.51	5.69	6.45	6.08	11.9
Total	97.6	98.4	97.8	96.9	97.8	96.9	97.1	96.9
-O=(F,Cl)2	1.88	2.02	1.90	1.85	1.83	2.15	2.25	1.75
new Total	95.7	96.4	95.9	95.1	96.0	94.8	94.8	95.2
APFU								
F	0.974	1.03	0.982	0.957	0.932	1.10	1.15	0.927
Na	0.00923	0.0112	0.00795	0.0114	0.0117	0.0112	0.00739	0.00357
Mg	2.16	2.24	2.20	2.17	2.19	2.09	2.08	1.95
Al	0.606	0.589	0.615	0.593	0.654	0.637	0.630	0.877
Si	3.30	3.29	3.29	3.33	3.15	3.13	3.13	2.89
Cl	0	0.00184	0	0.000597	0	0.00413	0.000599	0.00597
K	0.951	0.956	0.966	0.952	0.947	0.922	0.913	0.926
Ca	0.0102	0.00373	0	0	0.000892	0	0	0
Ti	0.0255	0.0125	0.0176	0.0245	0.0137	0.0129	0.0167	0.0269
Mn	0.000175	0.00125	0.000908	0.000561	0.00145	0.0147	0.0154	0.0299
Fe	0.290	0.268	0.283	0.260	0.322	0.368	0.345	0.706

Spot analysis	dmcy138_bio_4	dmcy138_bio_5	dmcy138_bio_6	dmcy138_bio_7	dmcy138_bio_8	dmcy138_bio_9	dmcy138_bio_10	dmcy138_bio_11	dmcy138_bio_12
Mineral	biotite	biotite	biotite	biotite	biotite	biotite	biotite	biotite	biotite
Predominant rock type	mag-bio dyke	mag-bio dyke	mag-bio dyke	mag-bio dyke	mag-bio dyke	mag-bio dyke	mag-bio dyke	mag-bio dyke	mag-bio dyke
BSE zone	light	light	light	light	light	light	dark	dark	dark
F	3.87	4.68	4.35	3.94	4.66	4.67	5.13	5.13	5.64
Na2O	0.102	0.0177	0.0659	0.0523	0.0690	0.0428	0.0775	0.0247	0.0518
MgO	18.2	19.0	18.7	18.7	18.7	18.8	20.6	20.5	20.8
Al2O3	10.5	9.75	10.1	10.1	10.1	9.61	8.19	7.89	7.84
SiO2	40.8	42.0	41.1	41.2	41.1	41.6	45.6	45.7	46.6
Cl	0.0281	0.0290	0.0416	0.0378	0.0259	0.0319	0.0156	0.0261	0.0261
K2O	10.3	10.1	9.91	9.99	10.1	9.99	10.6	10.4	10.5
CaO	bdl	bdl	bdl	bdl	bdl	0.00470	bdl	bdl	bdl
TiO2	0.566	0.329	0.534	0.489	0.441	0.502	0.273	0.301	0.319
MnO	0.485	0.385	0.475	0.449	0.427	0.450	0.296	0.290	0.259
FeO	12.0	9.29	9.80	10.3	9.87	9.65	6.77	6.40	6.21
Total	96.8	95.6	95.1	95.2	95.4	95.4	97.5	96.6	98.3
-O=(F,Cl)2	1.64	1.98	1.84	1.67	1.97	1.97	2.16	2.17	2.38
new Total	95.2	93.6	93.2	93.6	93.5	93.4	95.3	94.4	95.9
APFU									
F	0.872	1.05	0.982	0.892	1.05	1.05	1.10	1.11	1.19
Na	0.0141	0.00242	0.00912	0.00726	0.00951	0.00589	0.0102	0.00328	0.00673
Mg	1.93	2.00	1.99	2.00	1.98	1.99	2.08	2.09	2.08
Al	0.885	0.812	0.851	0.851	0.845	0.804	0.657	0.636	0.619
Si	2.90	2.97	2.93	2.95	2.92	2.95	3.10	3.13	3.12
Cl	0.00339	0.00347	0.00503	0.00459	0.00312	0.00384	0.00180	0.00303	0.00296
K	0.932	0.914	0.903	0.913	0.918	0.905	0.921	0.904	0.901
Ca	0	0	0	0	0	0	0	0	0
Ti	0.0303	0.0175	0.0287	0.0264	0.0236	0.0268	0.0140	0.0155	0.0161
Mn	0.0293	0.0230	0.0287	0.0273	0.0257	0.0270	0.0170	0.0168	0.0147
Fe	0.716	0.549	0.585	0.616	0.587	0.573	0.385	0.366	0.348

Spot analysis	dmcy138_bio_13	dmcy138_bio_14	leq130_bio_1	leq130_bio_2	leq130_bio_3	leq130_bio_4	leq130_bio_5	leq130_bio_6	leq130_bio_7
Mineral	biotite	biotite	biotite	biotite	biotite	biotite	biotite	biotite	biotite
Predominant rock type	mag-bio dyke	mag-bio dyke	mag-bio dyke	mag-bio dyke	mag-bio dyke	mag-bio dyke	mag-bio dyke	mag-bio dyke	mag-bio dyke
BSE zone	dark	dark	dark	dark	dark	dark	dark	dark	dark
F	5.28	4.52	4.95	4.87	4.2	4.35	4.64	4.75	4.5
Na2O	0.0630	0.0863	0.0561	0.0353	0.0504	0.0114	0.0144	0.0523	0.0320
MgO	20.7	20.4	23.4	22.8	22.5	21.5	22.9	22.7	22.4
Al2O3	7.60	8.21	7.91	8.78	7.97	9.05	8.57	8.39	8.85
SiO2	46.8	45.3	48.6	47.2	47.1	45.3	47.5	47.7	47.0
Cl	0.0119	0.0313	bld	0.000700	0.0194	0.0439	0.0186	0.0320	0.0320
K2O	10.6	10.4	10.3	10.5	10.0	10.0	10.3	10.4	10.3
CaO	bdl	0.0598	bdl	bdl	bdl	bdl	bdl	bdl	bdl
TiO2	0.214	0.367	0.403	0.351	0.355	0.610	0.394	0.373	0.612
MnO	0.229	0.285	0.205	0.188	0.161	0.228	0.202	0.185	0.214
FeO	5.74	6.31	4.97	6.20	5.50	6.97	6.27	6.10	6.71
Total	97.3	95.9	101	101	97.8	98.0	101	101	101
-O=(F,Cl)2	2.23	1.91	2.08	2.05	1.77	1.84	1.96	2.01	1.90
new Total	95.0	94.0	98.7	98.9	96.1	96.2	98.9	98.7	98.7
APFU									
F	1.13	0.988	1.02	1.01	0.894	0.933	0.961	0.984	0.937
Na	0.00826	0.0116	0.00706	0.00448	0.00658	0.00150	0.00183	0.00665	0.00409
Mg	2.09	2.10	2.27	2.23	2.26	2.17	2.24	2.22	2.20
Al	0.606	0.669	0.605	0.677	0.632	0.723	0.661	0.648	0.687
Si	3.17	3.13	3.16	3.09	3.17	3.07	3.11	3.12	3.09
Cl	0.00136	0.00367	0	0.0000776	0.00221	0.00504	0.00206	0.00355	0.00357
K	0.914	0.915	0.850	0.874	0.862	0.866	0.863	0.870	0.865
Ca	0	0.00443	0	0	0	0	0	0	0
Ti	0.0109	0.0191	0.0197	0.0173	0.0180	0.0311	0.0194	0.0184	0.0303
Mn	0.0131	0.0167	0.0113	0.0104	0.00920	0.0131	0.0112	0.0103	0.0120
Fe	0.325	0.365	0.270	0.339	0.310	0.395	0.343	0.334	0.370

Spot analysis	leq130_bio_8	leq130_bio_9	leq130_bio_10	leq130_bio_11	leq130_bio_12	leq130_bio_13	leq130_bio_14	leq130_bio_15	mos135_bio_1
Mineral	biotite	biotite	biotite	biotite	biotite	biotite	biotite	biotite	biotite
Predominant rock type	mag-bio dyke	mag-bio dyke	mag-bio dyke	mag-bio dyke	mag-bio dyke	mag-bio dyke	mag-bio dyke	mag-bio dyke	mag-bio dyke
BSE zone	light	light	light	light	light	light	light	light	dark
F	3.77	3.6	3.53	3.32	3.1	3.61	3.77	3.66	5.44
Na2O	0.0449	0.0929	0.0735	0.0885	0.134	0.0601	0.0301	0.0352	0.0853
MgO	21.2	20.7	21.0	21.1	20.8	21.3	21.2	21.3	21.7
Al2O3	11.2	11.3	11.0	11.4	11.3	10.9	11.2	11.1	9.86
SiO2	42.3	42.8	42.6	41.9	42.3	43.0	42.3	42.5	44.3
Cl	0.0141	0.0200	0.0504	0.0222	0.0592	0.0230	0.0496	0.0267	0.00890
K2O	10.7	10.7	10.7	10.4	10.6	10.6	10.7	10.7	11.1
CaO	bdl	bdl	bdl	bdl	bdl	bdl	bdl	bdl	bdl
TiO2	0.591	0.608	0.758	0.683	0.748	0.736	0.661	0.646	0.238
MnO	0.291	0.305	0.333	0.368	0.295	0.277	0.299	0.344	0.506
FeO	9.43	9.91	9.61	9.82	9.93	9.00	9.60	9.40	9.23
Total	99.5	99.9	99.7	99.2	99.3	99.4	99.7	99.8	102
-O=(F,Cl)2	1.59	1.52	1.50	1.40	1.32	1.53	1.60	1.55	2.29
new Total	97.9	98.4	98.2	97.7	97.9	97.9	98.1	98.2	100
APFU									
F	0.816	0.777	0.764	0.724	0.676	0.779	0.815	0.790	1.13
Na	0.00596	0.0123	0.00975	0.0118	0.0179	0.00795	0.00399	0.00466	0.0109
Mg	2.16	2.11	2.14	2.17	2.14	2.16	2.16	2.16	2.13
Al	0.899	0.906	0.889	0.923	0.916	0.875	0.902	0.896	0.766
Si	2.89	2.92	2.91	2.89	2.92	2.93	2.89	2.90	2.92
Cl	0.00163	0.00231	0.00585	0.00259	0.00692	0.00266	0.00574	0.00309	0.000994
K	0.930	0.927	0.934	0.918	0.934	0.918	0.928	0.935	0.930
Ca	0	0	0	0	0	0	0	0	0
Ti	0.0304	0.0312	0.0390	0.0354	0.0388	0.0378	0.0340	0.0332	0.0118
Mn	0.0169	0.0176	0.0193	0.0215	0.0172	0.0160	0.0173	0.0199	0.0282
Fe	0.540	0.566	0.550	0.566	0.572	0.514	0.549	0.537	0.508

Spot analysis	mos135_bio_2	mos135_bio_3	mos135_bio_4	mos135_bio_5	mos135_bio_6	mos135_bio_7	mos135_bio_8	mos135_bio_9	mos135_bio_10
Mineral	biotite	biotite	biotite	biotite	biotite	biotite	biotite	biotite	biotite
Predominant rock type	mag-bio dyke	mag-bio dyke	mag-bio dyke	mag-bio dyke	mag-bio dyke	mag-bio dyke	mag-bio dyke	mag-bio dyke	mag-bio dyke
BSE zone	dark	dark	dark	dark	dark	dark	light	light	light
F	5.19	5.07	5.27	5.18	5.26	5.39	4.53	4.46	4.29
Na2O	0.0743	0.0427	0.0540	0.0660	0.0765	0.00290	0.0305	0.0535	0.0379
MgO	21.0	21.6	21.3	21.5	21.6	21.3	20.8	20.8	20.7
Al2O3	9.95	9.70	9.83	9.75	9.6	9.96	10.7	10.6	10.7
SiO2	44.3	44.1	44.4	44.5	45.0	44.4	42.2	42.5	42.1
Cl	0.00440	0.00370	0.0170	0.0185	0.0289	0.0141	0.0221	0.00740	0.00890
K2O	11.0	11.0	10.8	10.9	11.1	11.1	11.1	11.1	11.0
CaO	bdl	bdl	bdl	bdl	bdl	bdl	bdl	bdl	bdl
TiO2	0.307	0.280	0.443	0.347	0.331	0.324	0.379	0.362	0.283
MnO	0.524	0.459	0.426	0.514	0.458	0.479	0.580	0.567	0.576
FeO	9.66	8.97	8.25	8.98	8.8	9.02	11.5	11.0	11.8
Total	102	101	101	102	102	102	102	101	102
-O=(F,Cl)2	2.19	2.14	2.22	2.18	2.22	2.27	1.91	1.88	1.81
new Total	99.8	99.1	98.6	99.5	100.0	99.8	99.9	99.5	99.7
APFU									
F	1.09	1.07	1.11	1.09	1.10	1.13	0.968	0.954	0.921
Na	0.00955	0.00552	0.00697	0.00848	0.00977	0.00037	0.00400	0.00702	0.00499
Mg	2.08	2.15	2.11	2.12	2.12	2.10	2.09	2.09	2.09
Al	0.778	0.762	0.771	0.762	0.745	0.775	0.854	0.845	0.858
Si	2.94	2.94	2.95	2.95	2.96	2.93	2.85	2.87	2.86
Cl	0.000495	0.000418	0.00192	0.00208	0.00323	0.00158	0.00253	0.000849	0.00102
K	0.930	0.933	0.919	0.917	0.935	0.939	0.952	0.956	0.951
Ca	0	0	0	0	0	0	0	0	0
Ti	0.0153	0.0140	0.0222	0.0173	0.0164	0.0161	0.0193	0.0184	0.0144
Mn	0.0295	0.0259	0.0240	0.0289	0.0255	0.0268	0.0332	0.0325	0.0331
Fe	0.536	0.500	0.459	0.498	0.485	0.498	0.652	0.622	0.670

Spot analysis	mos135_bio_11	mos135_bio_12	mos135_bio_13	mos135_bio_14	bh224_bio_1	bh224_bio_2	bh224_bio_3	bh224_bio_4	bh224_bio_5
Mineral	biotite	biotite	biotite	biotite	biotite	biotite	biotite	biotite	biotite
Predominant rock type	mag-bio dyke	mag-bio dyke	mag-bio dyke	mag-bio dyke	mag-bio dyke	mag-bio dyke	mag-bio dyke	mag-bio dyke	mag-bio dyke
BSE zone	light	light	light	light	dark	dark	dark	dark	dark
F	4.64	4.64	5.39	4.65	1.49	1.36	1.02	1.39	1.11
Na2O	0.0683	0.0477	0.0336	0.0209	0.0750	0.0108	0.0267	0.0405	0.0341
MgO	20.6	20.7	20.8	20.7	9.64	9.33	8.89	9.10	9.34
Al2O3	10.8	10.6	10.9	10.7	14.0	14.3	14.5	14.0	14.2
SiO2	41.8	42.3	42.2	42.2	37.1	37.2	36.4	37.0	36.6
Cl	0.00880	0.00660	0.0243	0.0103	0.149	0.167	0.234	0.248	0.190
K2O	11.1	11.0	10.9	10.7	9.91	9.92	9.91	9.83	9.73
CaO	bdl	bdl	bdl	bdl	bdl	bdl	bdl	bdl	bdl
TiO2	0.206	0.187	0.273	0.327	1.17	1.10	1.30	1.14	1.06
MnO	0.593	0.580	0.576	0.560	0.175	0.149	0.175	0.187	0.184
FeO	11.9	11.3	11.5	11.3	21.4	21.1	22.2	20.8	21.2
Total	102	101	102	101	95.1	94.5	94.6	93.7	93.7
-O=(F,Cl)2	1.96	1.95	2.27	1.96	0.661	0.610	0.482	0.641	0.510
new Total	99.7	99.4	100	99.2	94.4	93.9	94.1	93.1	93.2
APFU									
F	0.995	0.994	1.14	0.996	0.362	0.332	0.251	0.342	0.274
Na	0.00898	0.00626	0.00435	0.00274	0.0112	0.00161	0.00403	0.00610	0.00516
Mg	2.08	2.09	2.07	2.09	1.10	1.07	1.03	1.05	1.09
Al	0.861	0.847	0.853	0.851	1.27	1.30	1.33	1.28	1.31
Si	2.84	2.86	2.82	2.86	2.85	2.87	2.83	2.88	2.86
Cl	0.00101	0.000757	0.00275	0.00118	0.0194	0.0219	0.0309	0.0326	0.0252
K	0.956	0.946	0.926	0.928	0.971	0.976	0.984	0.975	0.969
Ca	0	0	0	0	0	0	0	0	0
Ti	0.0105	0.0095	0.0137	0.0167	0.0677	0.0640	0.0761	0.0668	0.0624
Mn	0.0340	0.0333	0.0325	0.0321	0.0114	0.00974	0.0115	0.0123	0.0122
Fe	0.673	0.639	0.640	0.641	1.37	1.36	1.44	1.35	1.39

Spot analysis	bh224_bio_6	bh224_bio_7	bh224_bio_8	bh224_bio_9	bh224_bio_10	bh224_bio_11	bh224_bio_12	bh224_bio_13	bh224_bio_14
Mineral	biotite	biotite	biotite	biotite	biotite	biotite	biotite	biotite	biotite
Predominant rock type	mag-bio dyke	mag-bio dyke	mag-bio dyke	mag-bio dyke	mag-bio dyke	mag-bio dyke	mag-bio dyke	mag-bio dyke	mag-bio dyke
BSE zone	dark	dark	light	light	light	light	light	light	light
F	1.22	1.14	0.8958	0.8322	0.8886	0.9604	0.9694	0.789	1.13
Na2O	0.0541	0.0493	0.0867	0.0716	0.0443	0.0853	0.0377	bdl	0.0687
MgO	9.04	9.14	8.70	8.28	8.56	8.09	8.35	8.23	8.70
Al2O3	14.5	14.4	14.8	14.8	14.7	14.8	14.5	14.9	14.4
SiO2	36.7	36.4	35.6	35.5	35.7	35.5	35.7	35.7	36.6
Cl	0.311	0.237	0.338	0.329	0.375	0.529	0.486	0.391	0.333
K2O	9.80	9.68	9.77	9.73	9.83	9.77	9.50	9.69	9.79
CaO	bdl	bdl	bdl	bdl	bdl	bdl	bdl	0.00490	bdl
TiO2	1.12	1.10	1.07	1.06	1.18	1.19	0.99	1.25	1.10
MnO	0.156	0.195	0.201	0.193	0.184	0.165	0.190	0.151	0.139
FeO	22.0	22.2	22.9	23.3	22.3	23.3	22.5	22.9	22.4
Total	94.9	94.5	94.3	94.1	93.8	94.3	93.2	94.0	94.7
-O=(F,Cl)2	0.584	0.533	0.454	0.425	0.459	0.524	0.518	0.421	0.551
new Total	94.3	94.0	93.9	93.7	93.3	93.8	92.6	93.6	94.2
APFU									
F	0.298	0.280	0.222	0.208	0.221	0.239	0.243	0.196	0.278
Na	0.00811	0.00743	0.0132	0.0110	0.00676	0.0130	0.00579	0	0.0103
Mg	1.04	1.06	1.02	0.974	1.00	0.949	0.986	0.966	1.01
Al	1.32	1.32	1.36	1.38	1.36	1.37	1.35	1.38	1.32
Si	2.83	2.83	2.80	2.80	2.81	2.79	2.82	2.81	2.84
Cl	0.0407	0.0312	0.0450	0.0440	0.0500	0.0705	0.0652	0.0522	0.0438
K	0.967	0.961	0.978	0.980	0.987	0.980	0.960	0.973	0.970
Ca	0	0	0	0	0	0	0	0	0
Ti	0.0650	0.0641	0.0632	0.0628	0.0697	0.0707	0.0592	0.0741	0.0645
Mn	0.0102	0.0128	0.0134	0.0129	0.0123	0.0110	0.0128	0.0101	0.00913
Fe	1.43	1.44	1.50	1.54	1.47	1.53	1.49	1.51	1.46

Spot analysis	bh224_bio_15	yn49-61_bio_1	yn49-61_bio_2	yn49-61_bio_3	yn49-61_bio_4	yn49-61_bio_5	yn49-61_bio_6	yn49-61_bio_7	yn49-61_bio_8
Mineral	biotite	biotite	biotite	biotite	biotite	biotite	biotite	biotite	biotite
Predominant rock type	mag-bio dyke	ank-sid carbonatite	ank-sid carbonatite	ank-sid carbonatite	ank-sid carbonatite	ank-sid carbonatite	ank-sid carbonatite	ank-sid carbonatite	ank-sid carbonatite
BSE zone	light	dark	dark	dark	dark	light	light	light	light
F	1.28	3.31	2.94	3.22	2.94	1.72	1.67	1.81	2.08
Na2O	0.0593	0.0708	0.0356	0.0934	0.0620	0.0161	0.0344	0.0756	0.0651
MgO	9.18	17.2	16.7	17.9	15.9	13.0	13.0	13.1	13.4
Al2O3	14.1	9.55	9.93	9.67	11.3	12.6	12.5	12.7	12.0
SiO2	36.9	43.5	42.3	43.5	43.4	38.1	38.1	37.7	38.7
Cl	0.201	0.0423	0.0574	0.0379	0.0495	0.151	0.0965	0.192	0.150
K2O	9.80	9.99	10.2	9.88	9.27	9.64	9.93	9.76	9.81
CaO	bdl	0.00330	bdl	0.00330	bdl	bdl	bdl	bdl	bdl
TiO2	1.53	1.16	1.10	1.01	1.12	1.61	1.54	1.53	1.70
MnO	0.184	0.0769	0.0478	0.0455	0.0780	0.117	0.108	0.113	0.112
FeO	20.9	10.4	12.1	10.2	10.3	17.5	17.7	17.0	16.9
Total	94.1	95.3	95.3	95.6	94.4	94.4	94.7	93.9	94.8
-O=(F,Cl)2	0.584	1.40	1.25	1.36	1.25	0.758	0.725	0.805	0.910
new Total	93.5	93.9	94.1	94.2	93.2	93.6	93.9	93.1	93.9
APFU									
F	0.314	0.746	0.671	0.723	0.665	0.412	0.400	0.435	0.493
Na	0.00892	0.00978	0.00498	0.0129	0.00860	0.00236	0.00505	0.0111	0.00947
Mg	1.06	1.83	1.80	1.90	1.69	1.46	1.47	1.48	1.50
Al	1.29	0.802	0.845	0.809	0.951	1.12	1.12	1.14	1.06
Si	2.86	3.10	3.05	3.09	3.11	2.88	2.88	2.86	2.90
Cl	0.0264	0.00511	0.00702	0.00456	0.00600	0.0193	0.0124	0.0248	0.0191
K	0.970	0.908	0.936	0.895	0.846	0.931	0.959	0.947	0.939
Ca	0	0	0	0	0	0	0	0	0
Ti	0.0890	0.0621	0.0599	0.0538	0.0601	0.0916	0.0876	0.0876	0.0959
Mn	0.0121	0.00464	0.00292	0.00274	0.00472	0.00753	0.00689	0.00726	0.00712
Fe	1.36	0.622	0.728	0.604	0.617	1.11	1.12	1.08	1.06

Spot analysis	yn49-61_bio_9	yn49-61_bio_10	yn49-61_bio_11	yn49-61_bio_12	yn49-61_bio_13	yn49-61_bio_14	yn49-61_bio_15	frs4_bio_1	frs4_bio_2	frs4_bio_3
Mineral	biotite	biotite	biotite	biotite	biotite	biotite	biotite	biotite	biotite	biotite
Predominant rock type	ank-sid carbonatite	ank-sid carbonatite	ank-sid carbonatite	ank-sid carbonatite	ank-sid carbonatite	ank-sid carbonatite	ank-sid carbonatite	mag-bio dyke	mag-bio dyke	mag-bio dyke
BSE zone	light	light	light	light	dark	dark	dark	n/a	n/a	n/a
F	2.01	1.81	1.54	2.02	3.09	3.6	2.79	4.54	4.44	4.73
Na2O	0.0073	0.0442	0.0335	0.0309	bdl	0.0151	0.0801	0.0874	0.028	0.0785
MgO	13.6	12.5	12.5	14.0	16.8	17.1	16.5	21.6	21.9	22.1
Al2O3	11.8	12.2	12.4	12.1	9.92	9.58	9.5	5.83	6.44	6.23
SiO2	38.8	38.1	38.1	38.8	43.3	43.6	43.8	49.7	48.9	49.1
Cl	0.122	0.151	0.178	0.134	0.0723	0.0318	0.0398	0.0117	0.0204	bdl
K2O	9.62	9.82	9.98	10.0	10.1	10.2	9.91	10.2	10.5	10.4
CaO	0.00540	bdl	bdl	bdl	bdl	bdl	bdl	bdl	bdl	bdl
TiO2	1.51	1.77	1.86	1.42	1.22	1.28	1.36	0.673	0.740	0.897
MnO	0.074	0.130	0.132	0.0648	0.0499	0.0664	0.0933	0.0368	0.0260	bdl
FeO	16.7	18.4	18.3	16.1	11.6	10.0	11.4	3.47	4.08	3.91
Total	94.3	94.9	95.0	94.7	96.1	95.5	95.5	96.1	97.0	97.5
-O=(F,Cl)2	0.874	0.796	0.689	0.881	1.32	1.52	1.18	1.91	1.87	1.99
new Total	93.4	94.1	94.3	93.9	94.8	93.9	94.3	94.2	95.2	95.5
APFU										
F	0.479	0.433	0.369	0.478	0.695	0.808	0.631	0.968	0.944	0.999
Na	0.00107	0.00648	0.00492	0.00448	0	0.00208	0.0111	0.0114	0.00365	0.0102
Mg	1.53	1.41	1.41	1.57	1.78	1.81	1.76	2.17	2.19	2.20
Al	1.05	1.09	1.10	1.06	0.832	0.801	0.801	0.463	0.510	0.490
Si	2.92	2.88	2.89	2.91	3.08	3.09	3.13	3.35	3.29	3.28
Cl	0.0156	0.0193	0.0229	0.0170	0.00872	0.00382	0.00482	0.00134	0.00232	0
K	0.924	0.948	0.965	0.957	0.914	0.923	0.904	0.875	0.898	0.889
Ca	0	0	0	0	0	0	0	0	0	0
Ti	0.0854	0.101	0.106	0.0797	0.0654	0.0680	0.0732	0.0341	0.0374	0.0451
Mn	0.00469	0.00836	0.00844	0.00411	0.00301	0.00399	0.00565	0.00210	0.00148	0
Fe	1.05	1.16	1.16	1.01	0.687	0.594	0.682	0.196	0.229	0.218

Spot analysis	frs4_bio_4	frs4_bio_5	frs4_bio_6	frs4_bio_7	frs4_bio_8	frs4_bio_9	frs4_bio_10	frs4_bio_11	YW61-8_bio_1	YW61-8_bio_2
Mineral	biotite	biotite	biotite	biotite	biotite	biotite	biotite	biotite	biotite	biotite
Predominant rock type	mag-bio dyke	mag-bio dyke	mag-bio dyke	mag-bio dyke	mag-bio dyke	mag-bio dyke	mag-bio dyke	mag-bio dyke	mag-bio dyke	mag-bio dyke
BSE zone	n/a	n/a	n/a	n/a	n/a	n/a	n/a	n/a	light	dark
F	4.76	4.07	4.56	4.28	4.6	3.8	3.89	4.01	1.26	1.15
Na2O	0.0473	0.113	0.0466	0.0598	0.0416	0.0261	0.0239	0.0707	0.126	0.0855
MgO	21.9	21.9	21.8	21.7	21.8	21.7	20.9	21.4	9.76	10.0
Al2O3	6.71	6.27	6.77	6.38	6.28	6.88	7.43	7.40	15.5	14.9
SiO2	48.3	48.2	48.1	48.7	49.1	47.8	46.8	46.3	37.7	38.4
Cl	0.0145	0.0952	0.0232	0.00800	0.0189	0.0391	0.0507	0.0391	0.0971	0.0442
K2O	10.3	10.4	10.5	10.4	10.5	10.4	10.4	10.3	10.4	10.3
CaO	bdl	0.00210	bdl	0.000400	bdl	bdl	bdl	bdl	bdl	bdl
TiO2	0.905	0.775	0.786	0.750	0.696	0.974	1.06	1.14	0.574	0.524
MnO	0.0142	0.0396	0.0455	0.0248	0.0266	0.0165	0.0565	0.0200	0.259	0.230
FeO	4.38	4.18	4.4	4.21	4.06	5.05	5.77	5.59	23.0	21.7
Total	97.2	96.0	97.0	96.5	97.1	96.7	96.4	96.2	98.7	97.3
-O=(F,Cl)2	2.01	1.73	1.93	1.80	1.94	1.61	1.65	1.70	0.552	0.494
new Total	95.2	94.3	95.1	94.7	95.1	95.1	94.7	94.5	98.1	96.8
APFU										
F	1.01	0.878	0.973	0.916	0.977	0.818	0.844	0.871	0.297	0.273
Na	0.00615	0.0150	0.00609	0.00784	0.00541	0.00345	0.00318	0.00941	0.0181	0.0124
Mg	2.19	2.23	2.19	2.19	2.18	2.21	2.14	2.19	1.08	1.12
Al	0.531	0.504	0.538	0.509	0.497	0.552	0.601	0.599	1.36	1.32
Si	3.24	3.29	3.24	3.30	3.29	3.25	3.21	3.18	2.81	2.88
Cl	0.00165	0.0110	0.00265	0.000917	0.00215	0.00451	0.00589	0.00455	0.0123	0.00562
K	0.879	0.900	0.905	0.894	0.898	0.905	0.908	0.899	0.986	0.988
Ca	0	0	0	0	0	0	0	0	0	0
Ti	0.0457	0.0398	0.0399	0.0381	0.0351	0.0499	0.0546	0.0591	0.0322	0.0296
Mn	0.000807	0.00229	0.00260	0.00142	0.00151	0.000952	0.00328	0.00116	0.0164	0.0146
Fe	0.246	0.238	0.248	0.238	0.228	0.288	0.331	0.321	1.43	1.36

Spot analysis	YW61-8_bio_3	YW61-8_bio_4	YW61-8_bio_5	YW61-8_bio_6	YW61-8_bio_7	YW61-8_bio_8	YW61-8_bio_9	YW61-8_bio_10	YW61-8_bio_11
Mineral	biotite	biotite	biotite	biotite	biotite	biotite	biotite	biotite	biotite
Predominant rock type	mag-bio dyke	mag-bio dyke	mag-bio dyke	mag-bio dyke	mag-bio dyke	mag-bio dyke	mag-bio dyke	mag-bio dyke	mag-bio dyke
BSE zone	dark	dark	dark	dark	dark	dark	light	light	light
F	1.96	2.24	1.84	2.19	1.83	1.76	1.01	1.15	1.29
Na2O	0.0942	0.086	0.0996	0.0963	0.0139	0.0708	0.195	0.104	0.146
MgO	12.5	12.7	11.9	12.5	11.9	12.0	9.82	9.99	9.46
Al2O3	12.8	13.3	13.3	12.8	13.0	13.0	15.3	15.3	15.5
SiO2	40.9	41.1	40.8	41.4	40.8	41.0	38.1	38.1	37.4
Cl	0.059	0.0181	0.0854	0.0431	0.0618	0.0528	0.105	0.0831	0.104
K2O	10.0	10.3	10.2	10.2	10.3	10.0	10.0	10.3	10.1
CaO	bdl	bdl	0.0131	bdl	bdl	bdl	0.00860	bdl	bdl
TiO2	0.366	0.398	0.626	0.485	0.680	0.832	0.463	0.493	0.579
MnO	0.189	0.213	0.204	0.193	0.182	0.167	0.232	0.230	0.287
FeO	18.5	18.0	18.7	18.0	18.8	18.5	22.5	22.3	22.7
Total	97.4	98.4	97.8	97.9	97.5	97.3	97.8	98.0	97.6
-O=(F,Cl)2	0.838	0.947	0.794	0.932	0.784	0.753	0.449	0.503	0.567
new Total	96.6	97.4	97.0	97.0	96.7	96.6	97.3	97.4	97.0
APFU									
F	0.453	0.511	0.425	0.502	0.424	0.407	0.240	0.272	0.307
F	0.0134	0.0120	0.0141	0.0135	0.00197	0.0100	0.0284	0.0150	0.0212
Na	1.36	1.37	1.30	1.35	1.29	1.31	1.10	1.11	1.06
Mg	1.11	1.13	1.14	1.10	1.13	1.12	1.35	1.34	1.38
Al	2.99	2.96	2.98	3.00	2.99	3.00	2.85	2.85	2.81
Si	0.00731	0.00221	0.0106	0.00529	0.00767	0.00655	0.0133	0.0105	0.0132
Cl	0.935	0.950	0.948	0.941	0.958	0.931	0.959	0.979	0.972
K	0	0	0.00102	0	0	0	0.000691	0	0
Ca	0.0201	0.0216	0.0344	0.0264	0.0375	0.0458	0.0261	0.0277	0.0327
Ti	0.0117	0.0130	0.0126	0.0118	0.0113	0.0103	0.0147	0.0146	0.0183
Mn	1.13	1.08	1.14	1.09	1.15	1.13	1.41	1.39	1.43

Spot analysis	YW61-8_bio_12	YW61-8_bio_13	YW61-8_bio_14	YW61-8_bio_15	ys7_bio_1	ys7_bio_2	ys7_bio_3	ys7_bio_4	ys7_bio_5
Mineral	biotite	biotite	biotite	biotite	biotite	biotite	biotite	biotite	biotite
Predominant rock type	mag-bio dyke	mag-bio dyke	mag-bio dyke	mag-bio dyke	Sil-alk vein	Sil-alk vein	Sil-alk vein	Sil-alk vein	Sil-alk vein
BSE zone	light	light	light	light	dark	dark	dark	dark	dark
F	0.9814	1.08	0.8734	0.9073	6.78	6.97	7.01	7.37	7
Na2O	0.0671	0.0817	0.071	0.0913	0.0772	0.0407	0.0279	0.0112	0.0273
MgO	9.73	9.92	9.20	9.66	22.8	23.0	23.0	23.0	23.3
Al2O3	15.5	15.0	15.4	14.8	1.51	1.61	1.67	1.76	1.69
SiO2	37.7	37.8	37.4	37.6	59.7	59.5	59.1	59.2	58.7
Cl	0.110	0.118	0.136	0.0852	0.0113	0.0120	0.00780	bdl	bdl
K2O	10.1	10.2	10.2	10.2	10.2	10.2	10.4	10.4	10.3
CaO	bdl	bdl	bdl	bdl	bdl	bdl	bdl	bdl	bdl
TiO2	0.569	0.581	0.767	0.753	0.0851	0.129	0.0907	0.188	0.0426
MnO	0.228	0.268	0.253	0.234	0.0109	0	0.00640	0	0.0230
FeO	22.1	22.7	22.9	22.6	0.654	0.496	0.559	0.598	0.550
Total	97.0	97.7	97.1	96.8	102	102	102	103	102
-O=(F,Cl)2	0.438	0.481	0.398	0.401	2.86	2.94	2.95	3.10	2.95
new Total	96.6	97.2	96.7	96.4	99.0	99.0	98.9	99.5	98.7
APFU									
F	0.234	0.257	0.210	0.218	1.31	1.35	1.36	1.42	1.36
Na	0.00982	0.0119	0.0104	0.0135	0.00918	0.00483	0.00332	0.00132	0.00325
Mg	1.09	1.11	1.04	1.09	2.09	2.10	2.10	2.09	2.14
Al	1.38	1.33	1.38	1.33	0.109	0.116	0.121	0.126	0.122
Si	2.84	2.84	2.84	2.85	3.66	3.64	3.63	3.60	3.61
Cl	0.0141	0.0151	0.0174	0.0110	0.00117	0.00124	0.000811	0	0
K	0.968	0.977	0.983	0.987	0.798	0.793	0.813	0.805	0.806
Ca	0	0	0	0	0	0	0	0	0
Ti	0.0323	0.0329	0.0438	0.0431	0.00392	0.00591	0.00418	0.00858	0.00197
Mn	0.0146	0.0171	0.0162	0.0150	0.000566	0	0.000332	0	0.00120
Fe	1.39	1.43	1.45	1.43	0.0336	0.0254	0.0287	0.0304	0.0282

Spot analysis	ys7_bio_6	ys7_bio_7	ys7_bio_8	ys7_bio_9	ys7_bio_10	ys7_bio_11	ys7_bio_12	ys7_bio_13	ys7_bio_14
Mineral	biotite	biotite	biotite	biotite	biotite	biotite	biotite	biotite	biotite
Predominant rock type	Sil-alk vein	Sil-alk vein	Sil-alk vein	Sil-alk vein	Sil-alk vein	Sil-alk vein	Sil-alk vein	Sil-alk vein	Sil-alk vein
BSE zone	dark	dark	light	light	light	light	light	light	light
F	7.05	6.95	6.09	5.87	5.94	5.85	5.67	6.29	6.05
Na2O	0.0769	0.0605	0.0184	0.0596	0.0398	0.0623	0.0493	0.0401	0.035
MgO	22.9	23.2	22.1	22.1	21.4	22.2	22.2	22.2	21.9
Al2O3	2.31	1.41	5.66	5.58	6.08	5.60	5.16	5.35	5.50
SiO2	58.1	59.6	52.3	52.5	51.9	52.6	53.7	53.5	52.8
Cl	0.00780	0.00920	0.0373	0.00560	0.0302	0.00560	0.0225	0.00920	0.000700
K2O	10.7	10.3	11.0	11.1	11.2	11.4	11.2	11.0	11.1
CaO	bdl	bdl	bdl	bdl	bdl	bdl	bdl	bdl	bdl
TiO2	0.256	0.000900	0.600	0.730	0.882	0.768	0.719	0.562	0.680
MnO	0.0121	0.0219	0.0459	0.0287	0.0212	0.0390	0.0281	0.0178	0.0391
FeO	0.670	0.534	2.06	2.25	2.26	2.02	1.70	1.73	2.26
Total	102	102	99.8	100	99.8	101	101	101	100
-O=(F,Cl)2	2.97	2.93	2.57	2.47	2.51	2.46	2.39	2.65	2.55
new Total	99.1	99.1	97.3	97.8	97.3	98.1	98.2	98.0	97.9
APFU									
F	1.37	1.34	1.23	1.19	1.21	1.18	1.14	1.26	1.22
Na	0.00916	0.00718	0.00229	0.00739	0.00496	0.00771	0.00608	0.00492	0.00433
Mg	2.10	2.11	2.11	2.11	2.06	2.11	2.11	2.10	2.09
Al	0.167	0.102	0.427	0.421	0.461	0.421	0.387	0.399	0.413
Si	3.57	3.65	3.35	3.36	3.34	3.36	3.42	3.38	3.37
Cl	0.000812	0.000954	0.00405	0.000607	0.00329	0.000606	0.00243	0.000987	0.0000757
K	0.836	0.801	0.897	0.908	0.918	0.930	0.912	0.886	0.903
Ca	0	0	0	0	0	0	0	0	0
Ti	0.0118	0.0000414	0.0289	0.0351	0.0427	0.0369	0.0344	0.0268	0.0326
Mn	0.000629	0.00113	0.00249	0.00156	0.00116	0.00211	0.00151	0.000954	0.00211
Fe	0.0344	0.0273	0.110	0.120	0.122	0.108	0.090	0.092	0.121

Spot analysis	ys7_bio_15	yn50-49_bio_1	yn50-49_bio_2	yn50-49_bio_3	yn50-49_bio_4	yn50-49_bio_5	yn50-49_bio_6	yn50-49_bio_7	yn50-49_bio_8
Mineral	biotite	biotite	biotite	biotite	biotite	biotite	biotite	biotite	biotite
Predominant rock type	Sil-alk vein	ank-sid carbonatite	ank-sid carbonatite	ank-sid carbonatite	ank-sid carbonatite	ank-sid carbonatite	ank-sid carbonatite	ank-sid carbonatite	ank-sid carbonatite
BSE zone	light	dark	dark	dark	dark	light	light	light	light
F	5.56	1.56	1.6	1.74	1.56	1.44	1.75	1.36	1.41
Na2O	0.0442	0.0886	0.101	0.130	0.200	0.158	0.121	0.0728	0.116
MgO	22.0	12.8	13.0	13.5	13.1	12.2	12.4	12.4	11.8
Al2O3	5.41	12.8	12.7	12.6	12.9	13.3	13.7	13.2	13.7
SiO2	53.2	39.3	39.4	39.8	38.9	38.7	38.3	38.8	38.3
Cl	0.00490	0.173	0.143	0.137	0.134	0.228	0.259	0.230	0.312
K2O	11.2	10.1	10.2	10.0	10.0	10.1	10.1	10.2	10.1
CaO	bdl	bdl	bdl	bdl	bdl	0.0217	bdl	bdl	bdl
TiO2	0.681	0.379	0.392	0.338	0.421	0.279	0.282	0.270	0.324
MnO	0.0568	0.105	0.115	0.118	0.105	0.167	0.148	0.130	0.150
FeO	2.19	20.9	19.9	19.9	19.9	21.1	21.5	21.0	22.1
Total	100	98.2	97.6	98.2	97.1	97.7	98.5	97.7	98.3
-O=(F,Cl)2	2.34	0.696	0.706	0.764	0.687	0.658	0.795	0.624	0.664
new Total	98.0	97.5	96.8	97.5	96.5	97.0	97.7	97.0	97.7
APFU									
F	1.12	0.364	0.375	0.403	0.367	0.339	0.409	0.321	0.332
Na	0.00548	0.0127	0.0144	0.0185	0.0288	0.0228	0.0173	0.0105	0.0167
Mg	2.09	1.41	1.44	1.48	1.45	1.36	1.36	1.38	1.30
Al	0.408	1.12	1.11	1.08	1.13	1.17	1.19	1.16	1.20
Si	3.40	2.90	2.92	2.92	2.89	2.88	2.83	2.89	2.85
Cl	0.000531	0.0217	0.0179	0.0170	0.0169	0.0288	0.0324	0.0290	0.0393
K	0.915	0.950	0.966	0.938	0.952	0.955	0.951	0.967	0.960
Ca	0	0	0	0	0	0.00173	0	0	0
Ti	0.0327	0.0210	0.0219	0.0186	0.0235	0.0156	0.0157	0.0151	0.0181
Mn	0.00308	0.00656	0.00721	0.00732	0.00664	0.0106	0.00925	0.00820	0.00944
Fe	0.117	1.29	1.23	1.22	1.24	1.31	1.33	1.31	1.38

Spot analysis	yn50-49_bio_9	yn50-49_bio_10	yn50-51_bio-mag_vein_1	yn50-51_bio-mag_vein_2	yn50-51_bio-mag_vein_3	yn50-51_bio-mag_vein_4	yn50-51_bio-mag_vein_5	yn50-51_bio-mag_vein_6	yn50-51_bio-mag_vein_7
Mineral	biotite	biotite	biotite	biotite	biotite	biotite	biotite	biotite	biotite
Predominant rock type	ank-sid carbonatite	ank-sid carbonatite	glimmerite	glimmerite	glimmerite	glimmerite	glimmerite	glimmerite	glimmerite
BSE zone	light	light	n/a	n/a	n/a	n/a	n/a	n/a	n/a
F	1.44	1.72	0.9455	1.07	0.8137	1.08	0.9836	1.02	0.8261
Na2O	0.131	0.0962	0.0641	0.124	0.125	0.0695	0.0651	0.0499	0.0816
MgO	12.4	12.1	8.93	9.79	9.26	9.66	9.88	9.75	9.79
Al2O3	13.4	13.2	14.5	14.4	14.4	14.4	14.4	14.3	14.0
SiO2	38.3	38.2	37.8	38.0	38.4	37.8	38.1	38.0	37.9
Cl	0.214	0.263	0.333	0.284	0.201	0.296	0.234	0.216	0.273
K2O	10.1	10.2	10.1	9.75	9.94	10.2	10.2	10.0	10.1
CaO	bdl	bdl	bdl	0.0200	0.0173	bdl	bdl	bdl	bdl
TiO2	0.356	0.486	0.461	0.486	0.387	0.469	0.466	0.543	0.409
MnO	0.140	0.121	0.158	0.145	0.130	0.126	0.143	0.151	0.184
FeO	21.8	21.5	23.7	23.7	23.6	24.1	24.1	24.0	24.6
Total	98.2	97.8	97.0	97.8	97.3	98.1	98.5	98.0	98.1
-O=(F,Cl)2	0.655	0.784	0.473	0.515	0.388	0.522	0.467	0.478	0.410
new Total	97.6	97.0	96.5	97.3	96.9	97.6	98.1	97.6	97.7
APFU									
F	0.339	0.406	0.228	0.255	0.195	0.258	0.233	0.243	0.198
Na	0.0189	0.0139	0.00947	0.0180	0.0184	0.0102	0.00947	0.00729	0.0120
Mg	1.37	1.35	1.01	1.10	1.05	1.09	1.11	1.10	1.11
Al	1.17	1.16	1.31	1.28	1.29	1.28	1.28	1.27	1.25
Si	2.85	2.85	2.88	2.86	2.91	2.85	2.86	2.86	2.87
Cl	0.0270	0.0332	0.0430	0.0363	0.0258	0.0378	0.0297	0.0275	0.0351
K	0.955	0.968	0.985	0.937	0.961	0.976	0.972	0.965	0.974
Ca	0	0	0	0.00161	0.00140	0	0	0	0
Ti	0.0199	0.0272	0.0264	0.0275	0.0221	0.0266	0.0263	0.0308	0.0233
Mn	0.00880	0.00762	0.0102	0.00924	0.00836	0.00804	0.00906	0.00963	0.0118
Fe	1.35	1.34	1.51	1.49	1.49	1.52	1.51	1.52	1.56

Spot analysis	yn50-51_bio-mag_vein_8	yn50-51_bio_1	yn50-51_bio_2	yn50-51_bio_3	yn50-51_bio_4	yn50-51_bio_5	yn50-51_bio_6	yn50-51_bio_7	yn50-51_bio_8
Mineral	biotite	biotite	biotite	biotite	biotite	biotite	biotite	biotite	biotite
Predominant rock type	glimmerite	ank-sid carbonatite	ank-sid carbonatite	ank-sid carbonatite	ank-sid carbonatite	ank-sid carbonatite	ank-sid carbonatite	ank-sid carbonatite	ank-sid carbonatite
BSE zone	n/a	dark	dark	dark	dark	dark	dark	dark	light
F	0.9961	1.31	1.41	1.48	1.52	1.51	1.31	1.54	0.9052
Na2O	0.116	0.160	0.0892	0.112	0.0746	0.0808	0.131	0.0313	0.0756
MgO	9.92	11.0	11.0	11.2	11.0	11.2	11.1	11.5	9.89
Al2O3	14.2	13.1	13.1	13.2	13.2	12.8	13.3	13.1	14.0
SiO2	38.0	39.6	39.7	39.8	39.5	40.0	39.5	39.7	37.7
Cl	0.251	0.179	0.160	0.114	0.144	0.141	0.166	0.086	0.218
K2O	9.99	10.1	10.0	9.96	9.98	9.79	9.88	9.80	9.57
CaO	bdl	0.0110	bdl	0.000800	0.0126	bdl	bdl	bdl	bdl
TiO2	0.433	0.322	0.448	0.515	0.361	0.446	0.362	0.439	0.450
MnO	0.150	0.121	0.0904	0.139	0.135	0.137	0.143	0.086	0.109
FeO	24.3	22.0	22.4	22.1	22.0	22.4	21.0	20.7	24.1
Total	98.3	97.8	98.5	98.6	98.0	98.5	96.9	97.0	97.0
-O=(F,Cl)2	0.476	0.592	0.630	0.649	0.672	0.668	0.589	0.668	0.430
new Total	97.8	97.2	97.9	97.9	97.3	97.8	96.3	96.3	96.6
APFU									
F	0.237	0.309	0.330	0.345	0.357	0.353	0.310	0.363	0.218
Na	0.0169	0.0231	0.0128	0.0160	0.0107	0.0116	0.0190	0.0045	0.0112
Mg	1.11	1.22	1.22	1.23	1.21	1.23	1.23	1.28	1.12
Al	1.26	1.15	1.15	1.15	1.16	1.12	1.17	1.15	1.26
Si	2.86	2.95	2.94	2.93	2.94	2.95	2.96	2.96	2.87
Cl	0.0321	0.0226	0.0201	0.0142	0.0181	0.0176	0.0211	0.0108	0.0282
K	0.960	0.958	0.946	0.938	0.946	0.923	0.943	0.930	0.930
Ca	0	0.000879	0	0	0.00100	0	0	0	0
Ti	0.0245	0.0180	0.0250	0.0286	0.0202	0.0248	0.0204	0.0246	0.0258
Mn	0.00954	0.00762	0.00567	0.00869	0.00849	0.00855	0.00906	0.00539	0.00704
Fe	1.53	1.37	1.39	1.36	1.37	1.39	1.31	1.29	1.54

Spot analysis	yn50-51_bio_9	yn50-51_bio_10	yn50-51_bio_11	yn50-51_bio_12	yn50-51_bio_13	yn50-51_bio_14	yn50-51_bio_15	yn50-51bio_in_cbt_vn_1	yn50-51bio_in_cbt_vn_2	yn50-51bio_in_cbt_vn_3
Mineral Predominant rock type	biotite ank-sid carbonatite	biotite ank-sid carbonatite	biotite ank-sid carbonatite	biotite ank-sid carbonatite	biotite ank-sid carbonatite	biotite ank-sid carbonatite	biotite ank-sid carbonatite	biotite ank-sid carbonatite	biotite ank-sid carbonatite	biotite ank-sid carbonatite
BSE zone	light	light	light	light	light	light	light	n/a	n/a	n/a
F	0.8142	0.7832	0.6191	0.8728	1.06	0.843	0.9334	0.8159	0.7447	0.8997
Na2O	0.0941	0.117	0.0972	0.159	0.104	0.155	0.0864	0.115	0.0854	0.0939
MgO	10.2	9.51	9.30	9.18	9.56	9.36	9.86	8.03	7.89	7.36
Al2O3	13.7	14.2	14.4	14.1	14.2	14.3	14.0	13.3	13.4	13.6
SiO2	38.7	37.8	37.7	38.1	38.0	38.0	37.9	37.4	37.4	36.8
Cl	0.221	0.281	0.280	0.288	0.224	0.239	0.274	0.284	0.307	0.241
K2O	10.3	9.80	9.87	10.1	10.0	10.1	10.0	9.99	9.99	9.83
CaO	0.000800	bdl	0.00270	0.00700	bdl	0.0164	0.00120	bdl	bdl	0.0210
TiO2	0.397	0.506	0.409	0.423	0.468	0.491	0.418	1.50	1.64	1.88
MnO	0.115	0.121	0.159	0.174	0.125	0.0922	0.132	0.125	0.193	0.164
FeO	23.3	24.6	25.1	24.8	23.2	24.0	23.6	26.3	26.4	26.1
Total	97.7	97.8	98.0	98.1	96.9	97.6	97.3	97.8	98.0	96.9
-O=(F,Cl)2	0.393	0.393	0.324	0.432	0.497	0.409	0.455	0.408	0.383	0.433
new Total	97.3	97.4	97.6	97.7	96.4	97.2	96.8	97.4	97.6	96.5
APFU										
F	0.194	0.188	0.149	0.209	0.255	0.202	0.224	0.198	0.180	0.220
Na	0.0138	0.0172	0.0143	0.0233	0.0153	0.0228	0.0127	0.0171	0.0127	0.0141
Mg	1.15	1.08	1.05	1.04	1.08	1.06	1.12	0.919	0.901	0.849
Al	1.22	1.27	1.29	1.26	1.27	1.28	1.26	1.20	1.21	1.24
Si	2.92	2.87	2.87	2.88	2.88	2.88	2.88	2.87	2.87	2.85
Cl	0.0283	0.0362	0.0361	0.0369	0.0289	0.0306	0.0352	0.0369	0.0398	0.0316
K	0.990	0.948	0.957	0.973	0.971	0.977	0.971	0.978	0.977	0.970
Ca	0	0	0	0.000568	0	0.00133	0	0	0	0.00174
Ti	0.0225	0.0289	0.0234	0.0241	0.0268	0.0280	0.0239	0.0864	0.0944	0.109
Mn	0.00733	0.00775	0.0103	0.0111	0.00805	0.00592	0.00851	0.00813	0.0125	0.0108
Fe	1.47	1.56	1.60	1.57	1.47	1.52	1.50	1.69	1.69	1.69

Appendix 2.B – Bulk Rock Geochemistry

2.B.1 – Bulk rock geochemistry data

Notes: *Sample data from Pearson (1996) PhD thesis for the Lyons River Sills.

Sample		LRS-119	LRS-121	**P17128***	LRS-001	LRS-003	LRS-015A
Rock type		calcite carbonatite	calcite carbonatite	calcite carbonatite	dolomite carbonatite	dolomite carbonatite	dolomite carbonatite
SiO2	wt.%	3.29	4.53	7.78	18.8	18.7	22.8
Al2O3	wt.%	0.160	0.300	0.570	0.810	0.830	2.17
Fe2O3	wt.%	5.4	8.3	13.7	7.2	7.51	11.5
MgO	wt.%	4.86	5.65	8.70	7.80	10.2	7.97
CaO	wt.%	44.6	39.2	28.6	30.7	27.6	20.1
Na2O	wt.%	0.260	0.910	1.51	2.31	2.16	3.12
K2O	wt.%	0.260	0.260	0.410	0.630	0.830	1.95
TiO2	wt.%	0.0800	0.540	1.24	1.68	1.47	2.43
P2O5	wt.%	9.08	4.41	2.81	0.430	0.0800	3.27
MnO	wt.%	0.150	0.190	0.270	0.110	0.160	0.260
Cr2O3	wt.%	bdl	0.00300		0.0310	0.0260	0.0460
Sum	wt.%	98.3	99.1		99.7	99.3	99.4
Ba	µg/g	1010	998	404	256	125	207
Sc	µg/g	18.0	16.0	12.2	9.00	15.0	25.0
Cs	µg/g	0.400	bdl		bdl	bdl	0.200
Ga	µg/g	bdl	1.20		2.50	2.50	8.00
Hf	µg/g	13.0	9.00	11.0	3.50	6.90	10.0
Nb	µg/g	76.2	261	339	60.5	111	112
Rb	µg/g	28.0	9.30	21.0	12.2	18.4	64.4
Sn	µg/g	3.00	4.00		4.00	2.00	4.00
Sr	µg/g	3910	3990	2420	627	989	1630
Ta	µg/g	7.70	21.9	30.3	3.20	5.40	5.40
Th	µg/g	80.9	56.7	150	12.8	21.5	73.3
U	µg/g	6.80	17.1	29.00	4.8	7.00	4.50
V	µg/g	36.0	88.0	248	124	84.0	259
W	µg/g	bdl	0.90		2.70	1.80	1.70
Zr	µg/g	867	498	655	92.8	165	394
Y	µg/g	77.6	54.1	173	5.90	5.20	144
La	µg/g	390	285	224	62.0	119	164
Ce	µg/g	868	595	471	111	225	307
Pr	µg/g	107	68.1		11.3	21.0	37.0
Nd	µg/g	408	254	210	34.4	61.8	144
Sm	µg/g	66.5	39.7	36.3	4.03	4.35	34.5
Eu	µg/g	17.1	10.5	11.00	0.890	0.860	11.2
Gd	µg/g	50.2	30.2		3.32	2.52	38.0
Tb	µg/g	5.47	3.43	4.95	0.340	0.210	5.25
Dy	µg/g	23.2	15.2		1.59	1.10	30.0
Ho	µg/g	3.40	2.33	5.93	0.220	0.160	5.29
Er	µg/g	7.19	5.41		0.650	0.470	13.5

Sample		LRS-119	LRS-121	**P17128***	LRS-001	LRS-003	LRS-015A
Rock type		calcite carbonatite	calcite carbonatite	calcite carbonatite	dolomite carbonatite	dolomite carbonatite	dolomite carbonatite
Tm	µg/g	0.790	0.630		0.0700	0.0700	1.79
Yb	µg/g	4.20	3.76	10.9	0.560	0.430	9.59
Lu	µg/g	0.470	0.480	1.44	0.0800	0.0700	1.12
Ni	µg/g	bdl	bdl	27	274	272	179
Mo	µg/g	0.210	0.850		0.270	1.07	0.460
Cu	µg/g	21.8	17.1	27.000	11.9	7.05	124
Pb	µg/g	13.4	17.1	32.0	4.15	5.32	10.5
Zn	µg/g	27.7	49.9	92.0	12.1	30.2	31.5
Ag	µg/g	88.0	214		42.0	25.0	50.0
Co	µg/g	10.9	23.3		21.6	9.10	28.2
As	µg/g	4.70	4.70		5.30	1.20	1.80
Au	µg/g	N.A.	N.A.		0.500	1.00	bdl
Cd	µg/g	0.160	0.170		0.130	0.140	0.120
Sb	µg/g	0.0700	0.190		0.0500	0.0400	0.0700
Bi	µg/g	bdl	0.100		0.0300	0.0400	0.0400
Cr	µg/g	1.00	1.90	70.0	12.2	5.70	18.6
B	µg/g	bdl	bdl		3.00	3.00	bdl
Tl	µg/g	0.110	0.0200		bdl	0.0200	bdl
Hg	µg/g	bdl	bdl		bdl	9.00	5.00
Se	µg/g	bdl	bdl		bdl	bdl	0.300
Te	µg/g	0.0900	0.100		0.0200	0.0500	0.0800
Ge	µg/g	0.200	bdl		bdl	bdl	0.100
In	µg/g	0.0500	0.0400		bdl	bdl	bdl
Re	µg/g	bdl	1.00		bdl	bdl	bdl
Be	µg/g	1.30	0.300		0.500	0.800	0.800
Li	µg/g	10.3	0.800		10.2	9.60	8.70
Pd	µg/g	25.0	39.0		21.0	bdl	bdl
Pt	µg/g	3.00	bdl		2.00	bdl	bdl
F	µg/g	8210	3540	4800	3340	2620	2890
TOT/C	wt.%	8.56	10.1		8.13	8.42	6.52
TOT/S	wt.%	0.0200	0.0600		0.0400	0.0500	0.0100
LOI	wt.%	30.0	34.8		29.2	29.8	23.8

Sample		LRS-015B	LRS-016	LRS-023	LRS-027	LRS-115	LRS-117
Rock type		dolomite carbonatite	dolomite carbonatite	dolomite carbonatite	dolomite carbonatite	dolomite carbonatite	dolomite carbonatite
SiO2	wt.%	22.3	12.9	24.3	16.2	32.6	26.5
Al2O3	wt.%	1.39	0.680	3.37	2.40	1.53	3.06
Fe2O3	wt.%	10.8	16.9	15.5	11.4	12.9	12.7
MgO	wt.%	13.0	9.92	12.0	9.41	14.4	13.8
CaO	wt.%	17.7	21.0	13.4	21.7	9.96	11.9
Na2O	wt.%	2.39	2.71	1.93	0.990	3.46	2.16
K2O	wt.%	1.61	0.530	2.52	2.16	1.92	3.15
TiO2	wt.%	0.890	2.31	4.84	2.55	3.34	3.52
P2O5	wt.%	0.170	0.0300	1.08	2.74	0.0400	0.360
MnO	wt.%	0.330	0.270	0.230	0.260	0.200	0.170
Cr2O3	wt.%	0.0380	0.0110	0.0620	0.0240	0.0700	0.0720
Sum	wt.%	99.5	99.0	99.1	98.9	98.6	99.5
Ba	µg/g	42.0	340	2470	2190	17300	52.0
Sc	µg/g	14.0	41.0	28.0	26.0	13.0	22.0
Cs	µg/g	0.400	bdl	4.30	0.300	6.00	1.30
Ga	µg/g	4.70	7.10	12.7	9.80	6.80	9.40
Hf	µg/g	5.30	33.8	11.1	17.7	6.20	12.3
Nb	µg/g	32.8	286	238	500	110	98.6
Rb	µg/g	50.1	15.2	190	57.9	227	103
Sn	µg/g	2.00	10.00	4.00	4.00	3.00	2.00
Sr	µg/g	1540	1890	807	1810	1070	824
Ta	µg/g	2.10	19.7	9.40	17.8	5.60	7.00
Th	µg/g	44.4	98.6	76.2	141	15.4	17.7
U	µg/g	1.20	26.8	6.60	24.7	0.400	4.00
V	µg/g	131	270	196	153	147	181
W	µg/g	0.500	6.50	11.3	7.20	18.00	9.50
Zr	µg/g	209	2390	422	768	179	384
Y	µg/g	18.2	58.0	64.4	250	12.6	9.30
La	µg/g	113	161	264	286	119	77.1
Ce	µg/g	190	298	537	544	214	148
Pr	µg/g	19.7	31.9	62.3	62.0	20.8	15.7
Nd	µg/g	63.7	106	224	234	60	52.2
Sm	µg/g	7.57	14.7	36.5	53.8	6.42	5.86
Eu	µg/g	1.86	3.60	10.1	17.9	1.00	1.33
Gd	µg/g	5.22	10.3	29.8	58.2	5.53	3.92
Tb	µg/g	0.620	1.18	3.47	9.12	0.580	0.400
Dy	µg/g	3.65	7.84	16.4	52.4	2.81	1.93
Ho	µg/g	0.660	1.91	2.30	8.88	0.420	0.370
Er	µg/g	1.79	7.68	5.62	21.6	1.26	1.1
Tm	µg/g	0.3000	1.51	0.710	2.62	0.200	0.170
Yb	µg/g	1.81	11.7	4.31	13.9	1.29	1.26
Lu	µg/g	0.260	1.86	0.530	1.69	0.170	0.170
Ni	µg/g	457	25.0	283	50.0	592	449
Mo	µg/g	0.140	0.110	1.02	0.0800	0.110	0.430

Sample		LRS-015B	LRS-016	LRS-023	LRS-027	LRS-115	LRS-117
Rock type		dolomite carbonatite	dolomite carbonatite	dolomite carbonatite	dolomite carbonatite	dolomite carbonatite	dolomite carbonatite
Cu	µg/g	65.4	34.3	95.3	126	11.4	182
Pb	µg/g	4.40	16.3	16.5	26.5	7.03	4.26
Zn	µg/g	32.5	135	92.6	53.2	61.1	25.9
Ag	µg/g	27.0	46.0	50.0	74.0	22.0	88.0
Co	µg/g	29.0	41.0	42.4	30.1	31.0	67.7
As	µg/g	0.600	4.70	0.800	0.100	0.500	5.60
Au	µg/g	0.700	bdl	bdl	bdl	1.80	bdl
Cd	µg/g	0.130	0.370	0.250	0.150	0.100	0.0900
Sb	µg/g	0.0300	0.0900	0.0300	0.120	0.0500	0.0500
Bi	µg/g	bdl	0.0800	0.0700	0.0600	0.0400	0.0300
Cr	µg/g	14.9	6.80	148	40.00	69.4	24.7
B	µg/g	bdl	bdl	bdl	bdl	bdl	4.00
Tl	µg/g	0.0200	bdl	0.430	0.0300	0.610	0.130
Hg	µg/g	bdl	bdl	bdl	bdl	bdl	bdl
Se	µg/g	bdl	bdl	0.200	0.200	bdl	bdl
Te	µg/g	0.100	0.0800	0.0500	0.100	0.0200	bdl
Ge	µg/g	bdl	bdl	0.300	0.200	0.200	bdl
In	µg/g	bdl	0.0800	bdl	0.110	bdl	bdl
Re	µg/g	bdl	bdl	bdl	bdl	bdl	bdl
Be	µg/g	0.700	1.00	6.50	1.60	7.40	0.700
Li	µg/g	19.3	0.90	135	54.1	315	11.4
Pd	µg/g	bdl	bdl	bdl	bdl	bdl	20.0
Pt	µg/g	bdl	6.00	bdl	bdl	bdl	bdl
F	µg/g	3270	132	4920	2760	9040	2810
TOT/C	wt.%	7.83	9.12	5.33	8.08	4.30	6.31
TOT/S	wt.%	bdl	0.150	0.0500	0.0500	0.470	0.220
LOI	wt.%	28.9	31.8	19.9	29.1	16.2	22.1

Sample Rock type		LRS-118 dolomite carbonatite	LRS-125-BRCBT carbonatite	LRS-140 dolomite carbonatite	LRS-149 dolomite carbonatite	LRS-151 dolomite carbonatite
SiO2	wt.%	22.2	1.76	25.7	19.2	21.7
Al2O3	wt.%	2.02	0.16	3.70	1.98	1.37
Fe2O3	wt.%	16.3	16.21	12.9	13.7	12.2
MgO	wt.%	14.5	15.9	7.72	10.2	13.1
CaO	wt.%	10.9	25.13	16.2	19.2	17.7
Na2O	wt.%	2.30	0.03	3.29	1.39	2.19
K2O	wt.%	2.16	0.22	3.31	1.78	1.72
TiO2	wt.%	3.87	0.3	3.04	2.73	1.69
P2O5	wt.%	1.04	0.44	1.83	0.650	1.17
MnO	wt.%	0.190	0.64	0.240	0.310	0.250
Cr2O3	wt.%	0.0640	0.014	0.0110	0.0430	0.0580
Sum	wt.%	99.4	99.5	99.3	99.4	99.0
Ba	µg/g	770	326	64.0	535	171
Sc	µg/g	18.0	20	24.0	23.0	24.0
Cs	µg/g	1.70	0.4	bdl	bdl	1.20
Ga	µg/g	10.4	bdl	12.0	7.60	5.50
Hf	µg/g	11.4	3.3	8.10	15.5	5.70
Nb	µg/g	105	322	149	402	153
Rb	µg/g	87.7	23.8	74.2	35.8	79.7
Sn	µg/g	2.00	2	4.00	10.00	3.00
Sr	µg/g	919	301.7	1390	1080	1370
Ta	µg/g	6.10	2.4	3.00	14.8	4.30
Th	µg/g	33.6	16.3	269	152	30.8
U	µg/g	2.90	5.9	3.70	5.30	0.900
V	µg/g	191	23	207	219	170
W	µg/g	9.50	0.5	5.30	4.00	4.50
Zr	µg/g	429	103.8	307	637	161
Y	µg/g	32.1	12.6	468	101	23.9
La	µg/g	123	225	181	132	77.4
Ce	µg/g	255	464.8	393	262	143
Pr	µg/g	30.2	55.93	52.3	29.0	15.7
Nd	µg/g	115	220.9	226	108	58.3
Sm	µg/g	18.4	31.56	74.9	30.2	14.1
Eu	µg/g	5.20	6.73	30.1	10.1	4.20
Gd	µg/g	15.5	15.14	122	33.3	12.5
Tb	µg/g	1.89	0.99	22.9	4.77	1.44
Dy	µg/g	8.42	3.49	119	24.3	6.13
Ho	µg/g	1.27	0.4	19.1	3.99	0.940
Er	µg/g	3.17	0.83	39.2	8.96	2.09
Tm	µg/g	0.400	0.14	3.72	0.960	0.300
Yb	µg/g	2.25	0.9	18.3	4.94	1.86
Lu	µg/g	0.280	0.12	2.08	0.620	0.260
Ni	µg/g	bdl	42	58.0	200	369
Mo	µg/g	0.890	23.84	3.13	0.200	0.310

Sample		LRS-118	LRS-125-BRCBT	LRS-140	LRS-149	LRS-151
Rock type		dolomite carbonatite	carbonatite	dolomite carbonatite	dolomite carbonatite	dolomite carbonatite
Cu	µg/g	113.3	2.39	191	82.8	67.2
Pb	µg/g	8.41	40.77	25.2	21.5	12.8
Zn	µg/g	53.0	48	45.6	48.7	39.2
Ag	µg/g	37.0	69	39.0	47.0	28.0
Co	µg/g	62.7	16.2	27.1	38.2	33.2
As	µg/g	2.30	3.9	4.60	0.500	6.00
Au	µg/g	bdl	0.9	bdl	bdl	bdl
Cd	µg/g	0.0900	0.18	0.190	0.120	0.100
Sb	µg/g	0.0300	bdl	0.0500	0.0200	0.0400
Bi	µg/g	0.0200	0.45	0.0600	0.0300	bdl
Cr	µg/g	44.4	86.9	4.90	63.2	56.4
B	µg/g	bdl	12	bdl	bdl	bdl
Tl	µg/g	0.170	0.05	bdl	bdl	0.180
Hg	µg/g	bdl	16	bdl	bdl	bdl
Se	µg/g	bdl	bdl	bdl	bdl	bdl
Te	µg/g	0.0300	bdl	0.0500	0.0200	0.0400
Ge	µg/g	0.200	0.2	bdl	bdl	bdl
In	µg/g	bdl	0.41	bdl	0.0500	0.0200
Re	µg/g	bdl	1	2.00	bdl	bdl
Be	µg/g	1.50	1.6	0.500	0.800	2.90
Li	µg/g	17.0	14.2	2.10	7.90	65.5
Pd	µg/g	17.0	bdl	bdl	12.0	19.0
Pt	µg/g	bdl	bdl	2.00	2.00	3.00
F	µg/g	3310	1353	1350	667	5160
TOT/C	wt.%	6.83	38.7	6.04	8.04	7.23
TOT/S	wt.%	0.0200	10.4	0.0100	0.0100	0.0200
LOI	wt.%	23.8	bdl	21.4	28.2	25.7

Sample		**P01019***	**P01089***	**P01090***	**P16852***	**P17119***	**P17120***
Rock type		dolomite carbonatite	dolomite carbonatite	dolomite carbonatite	dolomite carbonatite	dolomite carbonatite	dolomite carbonatite
SiO2	wt.%	23.9	20.2	16.7	24.7	19.3	24.9
Al2O3	wt.%	2.40	1.92	1.26	1.29	1.53	2.60
Fe2O3	wt.%	15.9	15.2	10.2	10.8	15.9	14.7
MgO	wt.%	13.0	14.7	17.3	14.5	13.3	8.86
CaO	wt.%	12.7	6.62	18.0	17.3	14.6	15.4
Na2O	wt.%	2.14	0.570	1.39	1.97	2.47	3.59
K2O	wt.%	2.41	2.76	2.30	1.13	1.53	2.33
TiO2	wt.%	3.89	1.27	3.20	2.80	3.25	3.64
P2O5	wt.%	0.740	0.370	0.0100	0.510	1.74	1.61
MnO	wt.%	0.240	0.600	0.210	0.220	0.200	0.210
Cr2O3	wt.%						
Sum	wt.%						
Ba	µg/g	1600	623	3150	494	137	3790
Sc	µg/g	21.7	59.7	21.9	12.2	13.7	21.3
Cs	µg/g						
Ga	µg/g						
Hf	µg/g	8.50	5.40	11.4	5.60	7.10	11.6
Nb	µg/g	156	263	602	94.0	94.0	166
Rb	µg/g	98.0	291	174	147	44.0	66.0
Sn	µg/g						
Sr	µg/g	939	275	186	843	1240	1200
Ta	µg/g	9.40	6.90	25.0	7.30	13.3	9.80
Th	µg/g	30.7	109	5.30	17.6	21.4	43.6
U	µg/g	6.00	7.00	1.00	5.00	3.00	1.00
V	µg/g						
W	µg/g						
Zr	µg/g	255	139	654	235	325	478
Y	µg/g	29.0	1.00	1.00	19.5	14.0	31.0
La	µg/g	177	788	7.24	118	122	142
Ce	µg/g	371	1620	21.6	246	266	296
Pr	µg/g						
Nd	µg/g	152	545	14.9	102	101	113
Sm	µg/g	21.5	48.2	2.70	15.4	14.1	17.4
Eu	µg/g	4.63	8.33	0.520	3.80	2.90	4.09
Gd	µg/g						
Tb	µg/g	1.47	1.37	0.230	1.36	1.10	1.65
Dy	µg/g		4.73	1.20		5.72	8.38
Ho	µg/g	1.41	0.670	0.200	1.29	1.05	1.76
Er	µg/g						
Tm	µg/g						
Yb	µg/g	3.17	0.710	0.290	1.46	1.97	3.64
Lu	µg/g	0.460	0.0900	0.0300	0.180	0.220	0.520
Ni	µg/g	477	220	236	419	326	326
Mo	µg/g						

Sample		**P01019***	**P01089***	**P01090***	**P16852***	**P17119***	**P17120***
Rock type		dolomite carbonatite	dolomite carbonatite	dolomite carbonatite	dolomite carbonatite	dolomite carbonatite	dolomite carbonatite
Cu	µg/g	26.0	33.0	52.0	79.0	161	170
Pb	µg/g	9.000	47.0	13.0	20.0	14.0	13.0
Zn	µg/g	172	175	105	93.0	112	86.0
Ag	µg/g						
Co	µg/g						
As	µg/g						
Au	µg/g						
Cd	µg/g						
Sb	µg/g						
Bi	µg/g						
Cr	µg/g	411	520	462	390	468	564
B	µg/g						
Tl	µg/g						
Hg	µg/g						
Se	µg/g						
Te	µg/g						
Ge	µg/g						
In	µg/g						
Re	µg/g						
Be	µg/g						
Li	µg/g						
Pd	µg/g						
Pt	µg/g						
F	µg/g	5400	10000	8200	4800	4000	30000
TOT/C	wt.%						
TOT/S	wt.%						
LOI	wt.%						

Sample **Rock type**		**P17122*** dolomite carbonatite	**P17140*** dolomite carbonatite	**P17141*** dolomite carbonatite	YN50-49 ank-sid carbonatite	YN49-58 ank-sid carbonatite
SiO2	wt.%	24.4	24.3	19.3	7.13	0.44
Al2O3	wt.%	2.54	2.95	1.04	0.530	0.0800
Fe2O3	wt.%	12.1	13.1	8.91	44.8	49.9
MgO	wt.%	9.71	10.2	15.5	6.33	8.22
CaO	wt.%	18.0	15.4	18.3	3.69	0.930
Na2O	wt.%	2.70	2.97	2.19	0.0300	0.0200
K2O	wt.%	2.26	2.94	2.02	0.250	0.0500
TiO2	wt.%	2.21	3.41	2.37	0.0300	bdl
P2O5	wt.%	2.62	0.370	0.120	1.05	0.0700
MnO	wt.%	0.230	0.180	0.180	6.67	5.64
Cr2O3	wt.%				0.00300	bdl
Sum	wt.%				99.4	99.7
Ba	µg/g	277	866	9400	77.0	56.0
Sc	µg/g	24.5	18.6	8.10	8.00	8.00
Cs	µg/g				1.40	0.500
Ga	µg/g				3.20	7.50
Hf	µg/g	10.6	8.80	5.30	0.200	bdl
Nb	µg/g	141	104	103	6.70	9.20
Rb	µg/g	93.0	101	38.0	27.0	5.30
Sn	µg/g				bdl	bdl
Sr	µg/g	907	1300	413	640	244.9
Ta	µg/g	9.60	9.40	8.80	0.200	0.500
Th	µg/g	47.9	31.9	67.5	163	19.0
U	µg/g	4.00	7.00	6.00	0.200	bdl
V	µg/g				bdl	bdl
W	µg/g				0.500	bdl
Zr	µg/g	468	313	182	3.40	0.500
Y	µg/g	164	5.00	1.00	35.2	2.90
La	µg/g	142	143	143	512	65.1
Ce	µg/g	299	302	261	1390	187
Pr	µg/g				196	28.8
Nd	µg/g	142	107	72.6	755	113
Sm	µg/g	29.3	12.7	6.10	125	15.0
Eu	µg/g	8.77	2.37	0.960	27.2	2.95
Gd	µg/g				77.0	7.13
Tb	µg/g	4.11	0.650	0.420	6.01	0.470
Dy	µg/g				17.9	1.42
Ho	µg/g	4.89	0.560	0.430	1.13	0.0700
Er	µg/g				1.83	0.110
Tm	µg/g				0.260	0.0300
Yb	µg/g	8.29	0.690	0.70	2.35	0.360
Lu	µg/g	0.970	0.0900	0.0900	0.260	0.0500
Ni	µg/g	186	323	615	127	80.0
Mo	µg/g				6.61	2.31

Sample **Rock type**		**P17122*** dolomite carbonatite	**P17140*** dolomite carbonatite	**P17141*** dolomite carbonatite	YN50-49 ank-sid carbonatite	YN49-58 ank-sid carbonatite
Cu	µg/g	158	126	317	134.5	0.930
Pb	µg/g	18.0	21.0	24.0	21.6	3.08
Zn	µg/g	75.0	103	292	232	278
Ag	µg/g				9.00	10.0
Co	µg/g				51.7	81.7
As	µg/g				2.00	0.300
Au	µg/g				0.600	1.80
Cd	µg/g				0.140	0.0600
Sb	µg/g				0.0700	bdl
Bi	µg/g				0.360	0.03
Cr	µg/g	419	650	447	5.50	1.20
B	µg/g				bdl	bdl
Tl	µg/g				0.140	0.0300
Hg	µg/g				bdl	bdl
Se	µg/g				0.200	bdl
Te	µg/g				0.0400	0.0300
Ge	µg/g				0.400	0.400
In	µg/g				0.670	0.990
Re	µg/g				1.00	bdl
Be	µg/g				0.600	bdl
Li	µg/g				21.1	7.60
Pd	µg/g				bdl	bdl
Pt	µg/g				bdl	bdl
F	µg/g	4400	700	3000	976	167
TOT/C	wt.%				9.89	11.9
TOT/S	wt.%				0.590	bdl
LOI	wt.%				28.9	34.4

Sample Rock type		YN50-48 ank-sid carbonatite	LRS-008 Sil-alk vein	DMCY-137FG Sil-alk vein	FR-152 Sil-alk vein	FR-153 Sil-alk vein	SHS-002 Sil-alk vein
SiO2	wt.%	0.19	59.6	59.5	61.2	63.8	66.1
Al2O3	wt.%	0.0200	0.510	0.820	1.94	2.48	0.7400
Fe2O3	wt.%	51.1	25.2	33.5	24.6	15.8	15.7
MgO	wt.%	7.95	3.2	1.17	5.14	6.53	5.94
CaO	wt.%	0.600	0.0600	0.420	0.0700	0.0700	0.100
Na2O	wt.%	0.0200	6.21	2.44	0.0600	0.120	3.47
K2O	wt.%	bdl	1.31	0.630	2.43	2.85	1.52
TiO2	wt.%	bdl	1.84	0.530	1.98	4.96	1.72
P2O5	wt.%	0.0700	0.0600	0.290	0.0500	0.0100	0.0400
MnO	wt.%	5.38	0.0200	0.0600	0.0100	0.0200	0.0300
Cr2O3	wt.%	bdl	0.0130	0.148	0.0600	0.0840	0.0620
Sum	wt.%	99.7	98.9	99.8	98.3	98.5	98.2
Ba	µg/g	28.0	252	681	824	189	289
Sc	µg/g	3.00	460	319	261	64.0	107
Cs	µg/g	bdl	1.90	1.10	2.10	3.90	0.500
Ga	µg/g	5.30	6.30	5.20	8.90	8.90	3.40
Hf	µg/g	bdl	62.6	3.20	11.8	11.8	35.6
Nb	µg/g	2.30	1650	15.4	403	318	620
Rb	µg/g	bdl	128	50.5	216	287	92.8
Sn	µg/g	1.00	4.00	351	9.00	5.00	11.00
Sr	µg/g	100.4	12.5	224	144	15.1	10.3
Ta	µg/g	0.200	10.0	0.200	1.70	10.8	5.80
Th	µg/g	13.7	104	7.70	86.2	30.2	17.4
U	µg/g	bdl	2.80	0.200	0.600	2.1	2.70
V	µg/g	bdl	351	450	511	276	128
W	µg/g	bdl	2.30	0.700	0.700	6.60	2.10
Zr	µg/g	0.400	3780	24.0	381	320	186
Y	µg/g	4.20	18.1	2.90	18.2	10.8	4.40
La	µg/g	123	119	11.7	84.3	22.0	15.4
Ce	µg/g	306	267	39.9	239	41.6	46.9
Pr	µg/g	41.3	40.5	10.2	42.7	5.64	8.69
Nd	µg/g	142	190	47.6	252	26.2	48.2
Sm	µg/g	16.8	48.3	6.10	63.5	9.41	6.61
Eu	µg/g	4.00	12.1	1.04	13.1	2.72	1.08
Gd	µg/g	8.36	28.7	2.07	27.3	6.20	2.11
Tb	µg/g	0.650	2.07	0.180	1.97	0.670	0.180
Dy	µg/g	1.95	6.42	0.82	6.33	2.76	0.950
Ho	µg/g	0.160	0.510	0.110	0.510	0.460	0.120
Er	µg/g	0.250	0.80	0.250	0.970	1.08	0.380
Tm	µg/g	0.0300	0.130	0.0300	0.130	0.180	0.0500
Yb	µg/g	0.360	1.02	0.270	0.930	1.25	0.360
Lu	µg/g	0.0400	0.130	0.0400	0.100	0.190	0.0500
Ni	µg/g	83.0	53.0	bdl	214	359	309
Mo	µg/g	81.0	3.04	1.17	5.54	0.200	2.80

Sample		YN50-48	LRS-008	DMCY-137FG	FR-152	FR-153	SHS-002
Rock type		ank-sid carbonatite	Sil-alk vein	Sil-alk vein	Sil-alk vein	Sil-alk vein	Sil-alk vein
Cu	µg/g	0.780	15.3	4.07	5.83	6.54	10.8
Pb	µg/g	3.99	83.6	4.75	46.3	11.2	100.0
Zn	µg/g	218	508	109	573	173	714
Ag	µg/g	28.0	212	11.0	28.0	7.00	39.0
Co	µg/g	80.4	15.8	4.80	52.8	44.6	24.4
As	µg/g	0.200	0.500	0.500	0.400	0.200	1.60
Au	µg/g	1.70	bdl	0.900	bdl	bdl	bdl
Cd	µg/g	0.180	0.590	bdl	0.0200	bdl	bdl
Sb	µg/g	bdl	0.100	0.0500	0.0300	0.0300	0.0300
Bi	µg/g	0.480	0.270	0.0700	0.470	0.0700	0.100
Cr	µg/g	3.30	18.4	251	145	280	163
B	µg/g	bdl	2.00	bdl	1.00	bdl	1.00
Tl	µg/g	bdl	0.190	0.0800	0.430	0.690	0.170
Hg	µg/g	10.00	110	bdl	bdl	bdl	7.00
Se	µg/g	bdl	bdl	bdl	bdl	bdl	bdl
Te	µg/g	0.0200	bdl	bdl	0.0300	bdl	0.0200
Ge	µg/g	0.300	0.500	1.00	0.500	0.300	0.500
In	µg/g	0.700	0.330	0.470	0.100	0.170	0.740
Re	µg/g	3.00	bdl	bdl	bdl	bdl	bdl
Be	µg/g	bdl	24.4	2.70	16.3	17.4	33.2
Li	µg/g	1.90	1200	180	968	917	702
Pd	µg/g	bdl	N.A.	bdl	bdl	bdl	bdl
Pt	µg/g	2.00	bdl	bdl	3.00	bdl	bdl
F	µg/g	78.0	9550	3910	12900	13800	14200
TOT/C	wt.%	11.9	0.020	0.0200	0.0400	0.0300	0.0200
TOT/S	wt.%	bdl	0.0100	bdl	0.0300	bdl	0.0300
LOI	wt.%	34.4	N.A.	0.200	0.600	1.70	2.80

Sample		SHS-003	YS-004	YS-006	YS-007	YS-009	YS-101
Rock type		sil-alk vein	sil-alk vein	sil-alk vein	sil-alk vein	sil-alk vein	sil-alk vein
SiO2	wt.%	66.7	45.2	57.1	53.3	55.8	61.4
Al2O3	wt.%	2.31	2.11	3.48	1.67	0.850	2.93
Fe2O3	wt.%	15.2	39.1	20.9	23.3	25.6	28.8
MgO	wt.%	6.36	4.76	5.27	6.83	3.97	0.240
CaO	wt.%	0.140	0.0300	0.170	0.0100	0.0600	0.0300
Na2O	wt.%	2.16	0.0500	3.20	0.180	6.35	0.0500
K2O	wt.%	2.25	2.36	4.60	3.23	1.84	2.35
TiO2	wt.%	0.830	2.46	2.13	1.90	1.78	2.98
P2O5	wt.%	0.0600	0.0200	0.0100	0.0400	bdl	bdl
MnO	wt.%	0.0200	0.0600	0.0400	0.0500	0.0500	bdl
Cr2O3	wt.%	0.0700	0.108	0.0390	0.0770	0.0340	0.0890
Sum	wt.%	98.8	97.2	98.1	91.9	97.1	99.7
Ba	µg/g	500	147	79.0	26.0	384	658
Sc	µg/g	75.0	1290	579	653	628	587
Cs	µg/g	3.20	9.50	6.40	8.00	2.70	0.800
Ga	µg/g	8.70	12.1	14.8	9.80	4.50	10.1
Hf	µg/g	10.9	23.5	105	407	58	6.00
Nb	µg/g	55.1	6290	3860	5250	2420	691
Rb	µg/g	224	287	340	363	184	64.9
Sn	µg/g	3.00	26.0	14.0	18.0	9.0	30.0
Sr	µg/g	12.9	6.80	18.0	3.40	31.6	17.4
Ta	µg/g	1.10	16.3	14.7	17.2	6.90	1.60
Th	µg/g	42.6	82.7	95.4	182	28.6	5.90
U	µg/g	7.70	1.60	1.10	3.00	0.700	1.00
V	µg/g	262	1060	838	582	703	1180
W	µg/g	1.10	14.6	13.7	22.4	3.60	13.3
Zr	µg/g	220	3600	7860	37900	4150	116
Y	µg/g	14.0	5.70	6.70	23.3	2.50	3.30
La	µg/g	15.3	42.3	8.10	34.4	12.1	2.70
Ce	µg/g	38.5	79.1	22.4	127	36.2	6.60
Pr	µg/g	5.09	10.4	4.8	24.8	6.2	1.27
Nd	µg/g	25.2	39.4	32.7	159	32.0	6.70
Sm	µg/g	5.75	8.26	14.2	48.6	6.43	2.09
Eu	µg/g	1.53	2.33	3.55	10.4	1.32	0.510
Gd	µg/g	3.94	7.22	8.07	22.5	2.82	1.14
Tb	µg/g	0.450	0.570	0.640	1.82	0.190	0.160
Dy	µg/g	2.54	2.06	2.15	7.37	0.680	0.880
Ho	µg/g	0.430	0.230	0.210	0.730	0.0500	0.160
Er	µg/g	1.1	0.40	0.460	1.5	0.150	0.340
Tm	µg/g	0.160	0.0600	0.0700	0.220	0.0200	0.0600
Yb	µg/g	0.970	0.370	0.500	1.57	0.150	0.310
Lu	µg/g	0.150	0.0500	0.0600	0.190	0.0200	0.0400
Ni	µg/g	622	50.0	38.0	99.0	84.0	99.0
Mo	µg/g	2.63	433	225	651	6.47	1.59

Sample		SHS-003	YS-004	YS-006	YS-007	YS-009	YS-101
Rock type		sil-alk vein	sil-alk vein	sil-alk vein	sil-alk vein	sil-alk vein	sil-alk vein
Cu	µg/g	14.3	3.87	3.29	2.07	16.0	11.1
Pb	µg/g	14.8	13.0	15.9	20.0	164	20.3
Zn	µg/g	295	176	169	198	2570	25.8
Ag	µg/g	21.0	10.0	50.0	90.0	6.00	23.0
Co	µg/g	52.8	14.3	11.3	23.5	15.6	14.3
As	µg/g	2.00	0.600	0.800	0.800	0.300	3.80
Au	µg/g	bdl	0.800	3.60	8.60	1.00	bdl
Cd	µg/g	0.0200	0.190	0.320	0.410	0.0500	0.0200
Sb	µg/g	bdl	0.0400	0.0600	0.0500	0.0400	0.0800
Bi	µg/g	0.280	1.08	0.700	4.43	0.990	0.190
Cr	µg/g	232	159	71.0	189	32.9	377
B	µg/g	2.00	bdl	3.00	2.00	1.00	1.00
Tl	µg/g	0.510	0.590	0.310	0.370	0.220	0.0600
Hg	µg/g	8.00	bdl	bdl	bdl	9.00	bdl
Se	µg/g	bdl	bdl	bdl	bdl	bdl	bdl
Te	µg/g	bdl	bdl	bdl	bdl	bdl	bdl
Ge	µg/g	0.200	0.500	1.10	0.900	0.300	0.300
In	µg/g	0.240	0.170	0.470	2.65	0.190	0.0700
Re	µg/g	bdl	bdl	bdl	bdl	bdl	bdl
Be	µg/g	18.0	4.00	18.1	18.7	132	0.700
Li	µg/g	251	844	>2000	>2000	1460	46.7
Pd	µg/g	bdl	bdl	bdl	N.A.	bdl	bdl
Pt	µg/g	bdl	bdl	bdl	bdl	bdl	bdl
F	µg/g	9780	11500	11500	20300	12200	534
TOT/C	wt.%	0.0300	0.0200	0.0700	0.0200	0.0200	0.0300
TOT/S	wt.%	0.0500	0.0100	bdl	0.0300	0.0300	0.0300
LOI	wt.%	2.60	0.700	N.A.	1.20	0.600	0.700

Sample Rock type		YS-102 sil-alk vein	YS-105 sil-alk vein	YS-107 sil-alk vein	AUR-128 mag-bio dyke	BH-110 mag-bio dyke	DMCY-137CG mag-bio dyke	DMCY-138 mag-bio dyke
SiO2	wt.%	58.1	63.1	55.6	9.84	47.7	11.5	27.1
Al2O3	wt.%	2.84	2.62	3.05	2.73	3.20	2.53	5.98
Fe2O3	wt.%	31.7	18.2	24.1	74.0	37.9	63.9	25.3
MgO	wt.%	0.130	5.01	7.90	3.49	2.73	4.50	10.6
CaO	wt.%	0.510	0.130	0.0100	0.400	0.0300	6.34	10.2
Na2O	wt.%	0.0800	0.540	0.0300	0.170	0.0300	0.0500	0.0500
K2O	wt.%	2.44	3.35	4.05	2.00	3.26	2.36	5.76
TiO2	wt.%	2.99	3.63	1.14	0.0600	1.20	0.200	0.290
P2O5	wt.%	bdl	0.0500	bdl	3.08	bdl	5.19	8.14
MnO	wt.%	0.0300	0.0200	0.0300	0.0300	0.710	0.250	0.260
Cr2O3	wt.%	0.0860	0.0570	0.118	0.00700	0.0580	0.0360	0.0310
Sum	wt.%	99.7	98.6	97.6	98.3	98.8	97.8	95.1
Ba	µg/g	152	128	186	744	7320	2140	3590
Sc	µg/g	688	187	221	4.00	135	8.00	6.00
Cs	µg/g	0.700	4.40	12.4	13.3	4.10	1.70	12.9
Ga	µg/g	10.3	8.90	12.1	17.7	12.6	8.90	20.3
Hf	µg/g	6.30	8.40	6.40	bdl	5.30	0.300	0.300
Nb	µg/g	388	465	21.1	5.90	87.4	5.40	7.70
Rb	µg/g	61.1	277	439	235	207	176	535
Sn	µg/g	63.00	6.00	14.00	4.00	31.00	12.00	13.00
Sr	µg/g	8.50	13.4	5.10	269	118	4000	7510
Ta	µg/g	0.600	2.50	0.200	0.100	0.700	bdl	bdl
Th	µg/g	5.20	3.00	2.60	139	19.3	114	62.2
U	µg/g	0.600	1.80	0.200	1.00	0.900	0.500	0.400
V	µg/g	150	347	457	149	401	109	53.0
W	µg/g	12.5	2.40	1.90	bdl	2.50	3.90	bdl
Zr	µg/g	103	259	139	1.50	108	4.70	3.30
Y	µg/g	4.10	8.40	3.20	246	5.30	38.9	47.6
La	µg/g	1.70	5.70	2.10	545	34.6	230	92.2
Ce	µg/g	3.00	11.5	4.40	2330	176	1030	596
Pr	µg/g	0.690	1.61	0.680	412	32.4	255	160
Nd	µg/g	2.90	7.90	3.70	1790	150	1250	892
Sm	µg/g	0.990	2.25	0.990	248	12.2	128	122
Eu	µg/g	0.320	0.670	0.230	55.8	1.47	19.1	21.9
Gd	µg/g	0.920	2.36	0.700	148	3.87	36.8	36.8
Tb	µg/g	0.170	0.390	0.0900	17.1	0.260	2.74	3.12
Dy	µg/g	0.880	2.01	0.600	73.0	1.32	11.0	12.1
Ho	µg/g	0.160	0.370	0.100	9.70	0.140	0.950	1.21
Er	µg/g	0.380	1.00	0.320	17.85	0.310	2.30	2.63
Tm	µg/g	0.0600	0.130	0.0400	1.55	0.0500	0.320	0.440
Yb	µg/g	0.370	0.900	0.360	7.25	0.370	1.92	2.64
Lu	µg/g	0.0500	0.110	0.0500	0.620	0.0500	0.230	0.320
Ni	µg/g	79.0	240	168	117	101	110	96.0
Mo	µg/g	50.5	1.26	0.380	0.560	25.9	0.740	0.270

Sample		YS-102	YS-105	YS-107	AUR-128	BH-110	DMCY-137CG	DMCY-138
Rock type		sil-alk vein	sil-alk vein	sil-alk vein	mag-bio dyke	mag-bio dyke	mag-bio dyke	mag-bio dyke
Cu	µg/g	10.6	22.2	5.96	3.73	82.0	5.11	2.79
Pb	µg/g	108.8	12.7	5.87	4.04	719	25.2	14.5
Zn	µg/g	167	232	120	90.6	147	774	1090
Ag	µg/g	104	9.00	11.0	39.0	746	12.0	12.0
Co	µg/g	15.4	18.5	12.1	22.1	37.0	47.5	68.9
As	µg/g	0.500	0.200	0.600	0.100	0.200	2.20	0.600
Au	µg/g	0.500	0.600	bdl	bdl	6.00	1.10	0.900
Cd	µg/g	0.350	0.0100	bdl	0.0200	0.310	0.0500	0.0300
Sb	µg/g	0.0800	0.0200	0.0600	bdl	0.0400	0.0300	0.0200
Bi	µg/g	0.620	0.320	0.120	bdl	0.150	0.0300	bdl
Cr	µg/g	411	170	332	3.80	207	55.0	115
B	µg/g	2.00	bdl	bdl	bdl	bdl	2.00	bdl
Tl	µg/g	0.0200	0.330	0.630	0.820	0.510	0.230	0.890
Hg	µg/g	bdl	bdl	bdl	6.00	bdl	bdl	13.0
Se	µg/g	bdl	bdl	bdl	bdl	bdl	bdl	bdl
Te	µg/g	bdl	bdl	bdl	bdl	bdl	0.120	0.140
Ge	µg/g	0.300	0.300	0.400	0.700	0.800	1.50	0.900
In	µg/g	0.170	0.410	0.110	bdl	0.220	0.0400	0.140
Re	µg/g	bdl	bdl	bdl	bdl	bdl	bdl	bdl
Be	µg/g	1.30	16.8	8.20	5.00	6.80	2.00	4.80
Li	µg/g	16.3	1120	1900	255	802	409	1010
Pd	µg/g	16.00	bdl	bdl	bdl	bdl	bdl	bdl
Pt	µg/g	bdl	bdl	bdl	bdl	bdl	2.00	3.00
F	µg/g	284	11900	23000	9150	8590	16400	37700
TOT/C	wt.%	0.100	0.0500	0.0300	0.0300	0.0400	0.0300	0.0400
TOT/S	wt.%	0.0100	bdl	bdl	bdl	0.1600	bdl	0.0200
LOI	wt.%	0.700	1.90	1.50	2.30	1.10	0.700	1.10

Sample Rock type		FR-154 mag-bio dyke	LEQ-130 mag-bio dyke	MOS-135 mag-bio dyke	MOS-136 mag-bio dyke	FRS-003 mag-bio dyke	FRS-004 mag-bio dyke	YW-145 mag-bio dyke
SiO2	wt.%	26.3	15.9	35.6	40.0	31.4	16.1	19.1
Al2O3	wt.%	2.67	1.82	7.72	5.90	1.21	0.260	1.23
Fe2O3	wt.%	44.7	73.2	28.8	31.2	34.6	60.8	62.3
MgO	wt.%	7.88	3.61	14.2	10.8	4.15	0.440	5.41
CaO	wt.%	2.25	0.0200	0.0200	0.0800	2.28	0.650	0.0700
Na2O	wt.%	0.0800	0.0100	0.040	0.540	1.55	0.110	0.0200
K2O	wt.%	3.87	1.72	7.51	5.72	1.11	0.0600	2.70
TiO2	wt.%	0.480	0.160	0.290	0.320	0.180	0.0400	0.120
P2O5	wt.%	2.00	0.390	0.250	0.390	12.85	1.92	0.0300
MnO	wt.%	2.20	0.120	0.370	0.210	3.43	7.92	3.77
Cr2O3	wt.%	0.0400	0.0170	0.0440	0.0550	0.00300	0.00600	0.00600
Sum	wt.%	96.8	98.1	95.9	97.1	98.4	96.8	97.4
Ba	µg/g	4100	409	2240	2910	37800	4430	596
Sc	µg/g	48.0	12.0	9.00	25.0	22.0	12.0	11.0
Cs	µg/g	7.30	5.60	19.0	15.0	1.60	bdl	5.60
Ga	µg/g	12.7	6.70	31.2	20.0	4.10	3.60	4.90
Hf	µg/g	0.700	0.400	0.700	5.70	4.90	0.900	0.100
Nb	µg/g	68.4	14.3	9.90	9.70	18.9	8.90	19.3
Rb	µg/g	390	153	582	463	157	4.60	297
Sn	µg/g	19.00	7.00	7.00	34.00	18.00	5.00	1.00
Sr	µg/g	218	34.4	567	204	1480	229.5	260
Ta	µg/g	0.900	0.300	0.200	bdl	0.900	0.400	0.300
Th	µg/g	91.3	134	10.8	12.9	29.7	291	150
U	µg/g	6.00	0.200	0.700	1.60	4.00	24.8	2.80
V	µg/g	151	113	74.0	146	35.00	100	48.0
W	µg/g	bdl	bdl	0.500	bdl	0.700	0.600	8.80
Zr	µg/g	15.0	10.6	11.0	85.5	99.00	14.8	2.20
Y	µg/g	42.7	41.2	7.10	25.0	11.4	37.3	8.50
La	µg/g	12.4	1950	85.4	123	205	2680	612
Ce	µg/g	44.1	3990	299	439	637	8640	2420
Pr	µg/g	11.3	493	47.7	74.3	76.8	1090	232
Nd	µg/g	61.9	1570	195	321	229	3500	753
Sm	µg/g	11.8	140	19.7	42.9	19.5	329	70.2
Eu	µg/g	2.92	30.3	3.34	7.93	4.54	59.4	11.2
Gd	µg/g	9.11	93.6	7.83	20.2	10.2	145	32.2
Tb	µg/g	1.45	7.39	0.480	1.72	0.770	7.08	1.30
Dy	µg/g	8.58	22.9	1.41	6.91	2.86	16.7	3.03
Ho	µg/g	1.69	1.59	0.160	0.900	0.330	0.170	0.0500
Er	µg/g	3.99	1.39	0.430	2.35	0.750	0.980	0.240
Tm	µg/g	0.450	0.160	0.0400	0.310	0.0900	0.190	0.0700
Yb	µg/g	2.51	1.18	0.320	2.10	0.490	1.96	0.510
Lu	µg/g	0.290	0.100	0.0400	0.270	0.0600	0.150	0.0600
Ni	µg/g	235	90.0	139	125	61.0	98.0	121
Mo	µg/g	3.39	0.0600	0.250	0.320	21.7	57.7	1.32

Sample		FR-154	LEQ-130	MOS-135	MOS-136	FRS-003	FRS-004	YW-145
Rock type		mag-bio dyke	mag-bio dyke	mag-bio dyke	mag-bio dyke	mag-bio dyke	mag-bio dyke	mag-bio dyke
Cu	µg/g	133	3.44	2.11	4.34	5.42	13.2	2.57
Pb	µg/g	516	40.8	10.4	14.2	998	2070	14.1
Zn	µg/g	1560	337	576	470	1400	4010	542
Ag	µg/g	447	36.0	9.00	42.0	30.0	12.0	25.0
Co	µg/g	57.4	27.4	60.8	37.1	40.5	35.8	43.4
As	µg/g	0.700	0.300	0.600	0.300	0.600	3.30	1.30
Au	µg/g	1.4	bdl	0.200	bdl	0.900	bdl	0.200
Cd	µg/g	0.750	0.0200	bdl	0.0100	0.720	2.07	0.150
Sb	µg/g	bdl	bdl	bdl	bdl	0.0300	0.0800	0.0400
Bi	µg/g	0.0500	0.0200	bdl	bdl	1.47	2.67	0.0400
Cr	µg/g	130	18.4	187	125	8.20	3.00	4.50
B	µg/g	3.00	bdl	bdl	bdl	bdl	48.00	2.00
Tl	µg/g	0.680	0.330	0.930	0.710	0.700	0.2000	0.380
Hg	µg/g	6.00	bdl	bdl	6.00	93.0	bdl	bdl
Se	µg/g	bdl	bdl	bdl	bdl	bdl	bdl	bdl
Te	µg/g	bdl	bdl	bdl	bdl	0.0400	bdl	bdl
Ge	µg/g	0.700	0.500	0.500	0.500	0.400	0.100	1.50
In	µg/g	0.420	bdl	0.0400	0.110	1.02	1.2	0.380
Re	µg/g	bdl	bdl	bdl	bdl	3.00	bdl	bdl
Be	µg/g	16.8	2.50	2.20	2.40	25.1	4.60	13.6
Li	µg/g	1520	280	515	561	712	6.50	1240
Pd	µg/g	bdl	bdl	bdl	bdl	bdl	bdl	bdl
Pt	µg/g	4.00	bdl	bdl	bdl	bdl	bdl	bdl
F	µg/g	25700	3840	37000	26700	8370	777	19700
TOT/C	wt.%	0.0500	0.0300	0.0300	0.0300	0.0800	0.110	0.0400
TOT/S	wt.%	0.0300	bdl	0.0100	0.0100	0.150	0.210	0.0100
LOI	wt.%	3.90	1.10	0.800	1.50	1.40	8.10	2.60

Sample Rock type		FR-154 mag-bio dyke	LEQ-130 mag-bio dyke	MOS-135 mag-bio dyke	MOS-136 mag-bio dyke	FRS-003 mag-bio dyke	FRS-004 mag-bio dyke	YW-145 mag-bio dyke
SiO2	wt.%	26.3	15.9	35.6	40.0	31.4	16.1	19.1
Al2O3	wt.%	2.67	1.82	7.72	5.90	1.21	0.260	1.23
Fe2O3	wt.%	44.7	73.2	28.8	31.2	34.6	60.8	62.3
MgO	wt.%	7.88	3.61	14.2	10.8	4.15	0.440	5.41
CaO	wt.%	2.25	0.0200	0.0200	0.0800	2.28	0.650	0.0700
Na2O	wt.%	0.0800	0.0100	0.040	0.540	1.55	0.110	0.0200
K2O	wt.%	3.87	1.72	7.51	5.72	1.11	0.0600	2.70
TiO2	wt.%	0.480	0.160	0.290	0.320	0.180	0.0400	0.120
P2O5	wt.%	2.00	0.390	0.250	0.390	12.85	1.92	0.0300
MnO	wt.%	2.20	0.120	0.370	0.210	3.43	7.92	3.77
Cr2O3	wt.%	0.0400	0.0170	0.0440	0.0550	0.00300	0.00600	0.00600
Sum	wt.%	96.8	98.1	95.9	97.1	98.4	96.8	97.4
Ba	µg/g	4100	409	2240	2910	37800	4430	596
Sc	µg/g	48.0	12.0	9.00	25.0	22.0	12.0	11.0
Cs	µg/g	7.30	5.60	19.0	15.0	1.60	bdl	5.60
Ga	µg/g	12.7	6.70	31.2	20.0	4.10	3.60	4.90
Hf	µg/g	0.700	0.400	0.700	5.70	4.90	0.900	0.100
Nb	µg/g	68.4	14.3	9.90	9.70	18.9	8.90	19.3
Rb	µg/g	390	153	582	463	157	4.60	297
Sn	µg/g	19.00	7.00	7.00	34.00	18.00	5.00	1.00
Sr	µg/g	218	34.4	567	204	1480	229.5	260
Ta	µg/g	0.900	0.300	0.200	bdl	0.900	0.400	0.300
Th	µg/g	91.3	134	10.8	12.9	29.7	291	150
U	µg/g	6.00	0.200	0.700	1.60	4.00	24.8	2.80
V	µg/g	151	113	74.0	146	35.00	100	48.0
W	µg/g	bdl	bdl	0.500	bdl	0.700	0.600	8.80
Zr	µg/g	15.0	10.6	11.0	85.5	99.00	14.8	2.20
Y	µg/g	42.7	41.2	7.10	25.0	11.4	37.3	8.50
La	µg/g	12.4	1950	85.4	123	205	2680	612
Ce	µg/g	44.1	3990	299	439	637	8640	2420
Pr	µg/g	11.3	493	47.7	74.3	76.8	1090	232
Nd	µg/g	61.9	1570	195	321	229	3500	753
Sm	µg/g	11.8	140	19.7	42.9	19.5	329	70.2
Eu	µg/g	2.92	30.3	3.34	7.93	4.54	59.4	11.2
Gd	µg/g	9.11	93.6	7.83	20.2	10.2	145	32.2
Tb	µg/g	1.45	7.39	0.480	1.72	0.770	7.08	1.30
Dy	µg/g	8.58	22.9	1.41	6.91	2.86	16.7	3.03
Ho	µg/g	1.69	1.59	0.160	0.900	0.330	0.170	0.0500
Er	µg/g	3.99	1.39	0.430	2.35	0.750	0.980	0.240
Tm	µg/g	0.450	0.160	0.0400	0.310	0.0900	0.190	0.0700
Yb	µg/g	2.51	1.18	0.320	2.10	0.490	1.96	0.510
Lu	µg/g	0.290	0.100	0.0400	0.270	0.0600	0.150	0.0600
Ni	µg/g	235	90.0	139	125	61.0	98.0	121
Mo	µg/g	3.39	0.0600	0.250	0.320	21.7	57.7	1.32

Sample		FR-154	LEQ-130	MOS-135	MOS-136	FRS-003	FRS-004	YW-145
Rock type		mag-bio dyke	mag-bio dyke	mag-bio dyke	mag-bio dyke	mag-bio dyke	mag-bio dyke	mag-bio dyke
Cu	µg/g	133	3.44	2.11	4.34	5.42	13.2	2.57
Pb	µg/g	516	40.8	10.4	14.2	998	2070	14.1
Zn	µg/g	1560	337	576	470	1400	4010	542
Ag	µg/g	447	36.0	9.00	42.0	30.0	12.0	25.0
Co	µg/g	57.4	27.4	60.8	37.1	40.5	35.8	43.4
As	µg/g	0.700	0.300	0.600	0.300	0.600	3.30	1.30
Au	µg/g	1.4	bdl	0.200	bdl	0.900	bdl	0.200
Cd	µg/g	0.750	0.0200	bdl	0.0100	0.720	2.07	0.150
Sb	µg/g	bdl	bdl	bdl	bdl	0.0300	0.0800	0.0400
Bi	µg/g	0.0500	0.0200	bdl	bdl	1.47	2.67	0.0400
Cr	µg/g	130	18.4	187	125	8.20	3.00	4.50
B	µg/g	3.00	bdl	bdl	bdl	bdl	48.00	2.00
Tl	µg/g	0.680	0.330	0.930	0.710	0.700	0.2000	0.380
Hg	µg/g	6.00	bdl	bdl	6.00	93.0	bdl	bdl
Se	µg/g	bdl	bdl	bdl	bdl	bdl	bdl	bdl
Te	µg/g	bdl	bdl	bdl	bdl	0.0400	bdl	bdl
Ge	µg/g	0.700	0.500	0.500	0.500	0.400	0.100	1.50
In	µg/g	0.420	bdl	0.0400	0.110	1.02	1.2	0.380
Re	µg/g	bdl	bdl	bdl	bdl	3.00	bdl	bdl
Be	µg/g	16.8	2.50	2.20	2.40	25.1	4.60	13.6
Li	µg/g	1520	280	515	561	712	6.50	1240
Pd	µg/g	bdl	bdl	bdl	bdl	bdl	bdl	bdl
Pt	µg/g	4.00	bdl	bdl	bdl	bdl	bdl	bdl
F	µg/g	25700	3840	37000	26700	8370	777	19700
TOT/C	wt.%	0.0500	0.0300	0.0300	0.0300	0.0800	0.110	0.0400
TOT/S	wt.%	0.0300	bdl	0.0100	0.0100	0.150	0.210	0.0100
LOI	wt.%	3.90	1.10	0.800	1.50	1.40	8.10	2.60

Sample		YW61-8
Rock type		mag-bio dyke
SiO2	wt.%	24.6
Al2O3	wt.%	9.91
Fe2O3	wt.%	42.1
MgO	wt.%	6.25
CaO	wt.%	0.190
Na2O	wt.%	0.0400
K2O	wt.%	6.16
TiO2	wt.%	0.630
P2O5	wt.%	2.20
MnO	wt.%	0.160
Cr2O3	wt.%	0.0180
Sum	wt.%	94.3
Ba	µg/g	1150
Sc	µg/g	52.0
Cs	µg/g	52.9
Ga	µg/g	29.5
Hf	µg/g	0.300
Nb	µg/g	77.4
Rb	µg/g	767
Sn	µg/g	8.00
Sr	µg/g	133
Ta	µg/g	2.70
Th	µg/g	1570
U	µg/g	5.40
V	µg/g	194
W	µg/g	1.90
Zr	µg/g	10.9
Y	µg/g	164
La	µg/g	7230
Ce	µg/g	17800
Pr	µg/g	2370
Nd	µg/g	8830
Sm	µg/g	1340
Eu	µg/g	315
Gd	µg/g	705
Tb	µg/g	44.1
Dy	µg/g	104
Ho	µg/g	1.49
Er	µg/g	0.590
Tm	µg/g	0.460
Yb	µg/g	7.56
Lu	µg/g	0.550
Ni	µg/g	78.0
Mo	µg/g	3.61

Sample		YW61-8
Rock type		mag-bio dyke
Cu	µg/g	2.37
Pb	µg/g	9.21
Zn	µg/g	551
Ag	µg/g	34.0
Co	µg/g	27.2
As	µg/g	0.300
Au	µg/g	0.300
Cd	µg/g	0.0200
Sb	µg/g	bdl
Bi	µg/g	bdl
Cr	µg/g	15.0
B	µg/g	bdl
Tl	µg/g	3.54
Hg	µg/g	bdl
Se	µg/g	bdl
Te	µg/g	bdl
Ge	µg/g	0.500
In	µg/g	0.150
Re	µg/g	bdl
Be	µg/g	4.10
Li	µg/g	371
Pd	µg/g	bdl
Pt	µg/g	bdl
F	µg/g	7490
TOT/C	wt.%	0.0200
TOT/S	wt.%	bdl
LOI	wt.%	1.90

2.B.2 – Bulk rock geochemistry detection limits

Element	concentration	detection limit
SiO_2	wt.%	0.01
Al_2O_3	wt.%	0.01
Fe_2O_3	wt.%	0.04
MgO	wt.%	0.01
CaO	wt.%	0.01
Na_2O	wt.%	0.01
K_2O	wt.%	0.04
TiO_2	wt.%	0.01
P_2O_5	wt.%	0.01
MnO	wt.%	0.01
Cr_2O_3	wt.%	0.002
Sum	wt.%	-
Ba	µg/g	5
Sc	µg/g	1
Cs	µg/g	0.1
Ga	µg/g	0.5
Hf	µg/g	0.1
Nb	µg/g	0.1
Rb	µg/g	0.1
Sn	µg/g	1
Sr	µg/g	0.5
Ta	µg/g	0.1
Th	µg/g	0.2
U	µg/g	0.1
V	µg/g	8
W	µg/g	0.5
Zr	µg/g	0.1
Y	µg/g	0.1
La	µg/g	0.1
Ce	µg/g	0.1
Pr	µg/g	0.02
Nd	µg/g	0.3
Sm	µg/g	0.05
Eu	µg/g	0.02
Gd	µg/g	0.05
Tb	µg/g	0.01
Dy	µg/g	0.05
Ho	µg/g	0.02
Er	µg/g	0.03
Tm	µg/g	0.01
Yb	µg/g	0.05
Lu	µg/g	0.01
Ni	µg/g	10

Element	concentration	detection limit
Mo	µg/g	0.01
Cu	µg/g	0.01
Pb	µg/g	0.01
Zn	µg/g	0.1
Ag	µg/g	2
Co	µg/g	0.1
As	µg/g	0.1
Au	µg/g	0.2
Cd	µg/g	0.01
Sb	µg/g	0.02
Bi	µg/g	0.02
Cr	µg/g	0.5
B	µg/g	1
Tl	µg/g	0.02
Hg	µg/g	5
Se	µg/g	0.1
Te	µg/g	0.02
Ge	µg/g	0.1
In	µg/g	0.02
Re	µg/g	1
Be	µg/g	0.1
Li	µg/g	0.1
Pd	µg/g	10
Pt	µg/g	5
F	µg/g	10
LOI	wt.%	0.01
TOT/C	wt.%	0.02
TOT/S	wt.%	0.02

Appendix 2.C – Carbon-Oxygen Isotope Data

Identifier	Carbonate mineral	$\delta^{13}C$‰VPDB	$\delta^{18}O$ ‰VSMOW
LRS-016	dolomite	-5.4	10.3
YN49-58.5	siderite	-7.1	10.8
LRS-001	dolomite	-4.9	19.4
LRS-125	dolomite	-4.4	26.6
LRS-149AG	dolomite	-5.4	10.5
LRS-119BB	calcite	-5.6	9.2
YN49-61.6	siderite	-6.4	11.1
LRS-15AG	dolomite	-5.1	10.6
LRS-117	dolomite	-5.0	10.8
LRS-151	dolomite	-5.1	10.6
YN50-48.6	siderite	-6.1	10.4
LRS-121	calcite	-5.4	10.1
LRS-140	dolomite	-5.3	10.5
LRS-15BB	dolomite	-5.1	10.2
LRS-23	dolomite	-5.7	10.7
LRS-149BB	dolomite	-5.4	10.2

Chapter 3 Appendices

Appendix 3.A – Apatite EPMA Analyses

Note 1: EPMA data consists of 3 parts: 1) measurements and 2) APFU results.

Note 2: In order to plot the apatite atoms per formula units (apfu) for all REY, the average REY values obtained from the laser data for each CL zone were calculated. These values were then normalized to the Ce value to get a calculation factor (e.g., Pr/Ce). These factors were then multiplied by the Ce values obtained from EMPA (in ppm) to extrapolate the rest of the REE values for each EMP spot analysis.

Sample	dmcy139_ap_dk_zn	dmcy139_ap_dk_zn	dmcy139_ap_dk_zn	dmcy139_ap_dk_zn	dmcy139_ap_dk_zn	dmcy139_ap_dk_zn	dmcy139_ap_dk_zn
CL Zone	green rim	green rim	green rim	green rim	green rim	green rim	green rim
Anaysis No.	2	12	13	14	24	25	26
P2O5	39.6	39.6	39.1	39.4	39.4	38.6	39.3
CaO	53.7	52.3	51.7	51.2	52.8	53.2	52.9
Nd2O3	0.214	0.323	0.235	0.434	0.268	0.196	0.217
Na2O	0.063	0.049	0.030	0.085	0.042	0.058	0.080
F	3.97	4.12	3.98	4.12	4.13	4.10	4.25
SiO2	n/a	na/	n/a	n/a	n/a	n/a	n/a
Cl	0.00500	0.00800	0.00200	0.00400	0.00200	0.01300	0.00700
Ce2O3	0.083	0.125	0.091	0.168	0.104	0.076	0.084
SrO	4.69	4.29	4.23	4.62	4.08	4.36	4.30
Total	101	99.0	97.9	98.2	99.1	98.9	99.5
-O=(F+CL)2	1.67	1.74	1.68	1.74	1.74	1.73	1.79
New Total	99.1	97.3	96.2	96.4	97.3	97.2	97.7
APFU							
P	2.78	2.81	2.81	2.82	2.79	2.76	2.79
Ca	4.78	4.69	4.70	4.64	4.74	4.82	4.74
Nd	0.00635	0.00965	0.00712	0.0131	0.00804	0.00592	0.00648
Na	0.0101	0.00795	0.00494	0.0139	0.00683	0.00950	0.0130

Sample	dmcy139_ap_dk_zn	dmcy139_ap_dk_zn	dmcy139_ap_dk_zn	dmcy139_ap_dk_zn	dmcy139_ap_dk_zn	dmcy139_ap_dk_zn	dmcy139_ap_dk_zn
CL Zone	green rim	green rim	green rim	green rim	green rim	green rim	green rim
Anaysis No.	2	12	13	14	24	25	26
F	1.04	1.09	1.07	1.10	1.09	1.10	1.12
Si	0	0	0	0	0	0	0
Cl	0.000704	0.00114	0.000288	0.000573	0.000284	0.00186	0.000992
Ce	0.00252	0.00383	0.00283	0.00520	0.00319	0.00235	0.00257
Sr	0.226	0.208	0.208	0.227	0.198	0.213	0.208
Y	0.000540	0.000820	0.000606	0.00111	0.000683	0.000503	0.000551
La	0.000205	0.000311	0.000230	0.000422	0.000259	0.000191	0.000209
Pr	0.000914	0.00139	0.00102	0.00188	0.00116	0.000851	0.000931
Sm	0.00117	0.00177	0.00131	0.00240	0.00147	0.00109	0.00119
Eu	0.000198	0.000301	0.000222	0.000408	0.000251	0.000185	0.000202
Ho	0.0000107	0.0000163	0.0000120	0.0000221	0.0000135	0.0000100	0.0000109
Er	0.0000235	0.0000357	0.0000263	0.0000484	0.0000297	0.0000219	0.0000240
Tm	0.00000289	0.00000438	0.00000323	0.00000595	0.00000365	0.00000269	0.00000294
Yb	0.0000178	0.0000271	0.0000200	0.0000367	0.0000225	0.0000166	0.0000182
Lu	0.00000236	0.00000358	0.00000264	0.00000485	0.00000298	0.00000219	0.00000240
REY sum	0.0124	0.0189	0.0139	0.0256	0.0157	0.0116	0.0127

Sample	dmcy139_ap_dk_zn	dmcy139_ap_ltzn	dmcy139_ap_ltzn	dmcy139_ap_ltzn	dmcy139_ap_ltzn	dmcy139_ap_ltzn	dmcy139_ap_ltzn
CL Zone	green rim	red cores/zone	red cores/zone	red cores/zone	red cores/zone	red cores/zone	red cores/zone
Anaysis No.	31	4	3	9	10	11	18
P2O5	39.4	39.1	39.6	39.2	38.9	39.1	39.5
CaO	51.9	53.4	51.3	50.6	50.5	50.3	50.8
Nd2O3	0.049	0.481	1.26	0.767	0.896	0.995	0.709
Na2O	0.035	0.117	0.214	0.138	0.150	0.190	0.161
F	3.37	4.24	3.89	4.10	4.81	3.94	4.80
SiO2	n/a	n/a	n/a	n/a	n/a	n/a	n/a
Cl	0.00000	0.00700	0.04300	0.00800	0.00000	0.00100	0.0120
Ce2O3	0.019	0.219	0.573	0.349	0.408	0.453	0.323
SrO	4.00	4.98	5.80	5.37	4.98	5.19	5.25
Total	97.7	101	101	98.6	98.4	98.2	99.5
-O=(F+CL)2	1.42	1.78	1.65	1.73	2.03	1.66	2.03
New Total	96.3	99.1	99.0	96.9	96.4	96.6	97.5
APFU							
P	2.84	2.75	2.92	2.81	2.78	2.81	2.80
Ca	4.74	4.76	4.78	4.58	4.57	4.57	4.55
Nd	0.00149	0.0143	0.0391	0.0232	0.0270	0.0302	0.0212
Na	0.00578	0.0189	0.0361	0.0226	0.0246	0.0313	0.0261
F	0.907	1.11	1.07	1.10	1.29	1.06	1.27
Si	0	0	0	0	0	0	0
Cl	0	0.000987	0.00634	0.00115	0	0.000144	0.00170
Ce	0.000592	0.00667	0.0182	0.0108	0.0126	0.0141	0.00988
Sr	0.198	0.240	0.293	0.263	0.244	0.256	0.254
Y	0.000127	0.000757	0.00207	0.00123	0.00143	0.00160	0.00112
La	0.0000481	0.000583	0.00159	0.000944	0.00110	0.00123	0.000863

Sample	dmcy139_ap_dk_zn	dmcy139_ap_ltzn	dmcy139_ap_ltzn	dmcy139_ap_ltzn	dmcy139_ap_ltzn	dmcy139_ap_ltzn	dmcy139_ap_ltzn
CL Zone	green rim	red cores/zone	red cores/zone	red cores/zone	red cores/zone	red cores/zone	red cores/zone
Anaysis No.	31	4	3	9	10	11	18
Pr	0.000215	0.00227	0.00620	0.00367	0.00429	0.00479	0.00336
Sm	0.000274	0.00196	0.00535	0.00317	0.00370	0.00413	0.00289
Eu	0.000047	0.000299	0.000819	0.000485	0.000566	0.000632	0.000443
Ho	0.00000251	0.0000143	0.0000390	0.0000231	0.0000270	0.0000301	0.0000211
Er	0.00000552	0.0000319	0.0000872	0.0000516	0.0000603	0.0000673	0.0000472
Tm	0.00000068	0.00000401	0.0000110	0.00000649	0.00000757	0.00000846	0.00000593
Yb	0.00000418	0.0000274	0.0000749	0.0000444	0.0000518	0.0000578	0.0000405
Lu	0.00000055	0.00000390	0.0000107	0.00000633	0.00000738	0.00000824	0.00000578
REY sum	0.00292	0.0276	0.0754	0.0447	0.0521	0.0582	0.0408

Sample	dmcy139_ap_ltzn	dmcy139_ap_ltzn	dmcy139_ap_ltzn	dmcy139_ap_ltzn	dmcy139_ap_ltzn	dmcy139_ap_ltzn	dmcy139_ap_ltzn
CL Zone	red cores/zone	red cores/zone	red cores/zone	red cores/zone	red cores/zone	red cores/zone	red cores/zone
Anaysis No.	19	20	21	22	23	32	1
P2O5	39.1	39.1	39.2	39.8	38.9	38.5	39.3
CaO	51.3	50.9	50.6	52.3	51.0	51.6	52.1
Nd2O3	0.909	0.727	0.668	0.558	0.883	0.582	1.18
Na2O	0.183	0.129	0.161	0.158	0.191	0.173	0.311
F	3.83	5.01	3.77	4.47	5.23	4.66	2.48
SiO2	n/a	n/a	n/a	n/a	n/a	n/a	n/a
Cl	bdl	bdl	bdl	bdl	0.00300	0.0110	bdl
Ce2O3	0.414	0.331	0.304	0.254	0.402	0.265	0.536
SrO	5.19	5.70	4.82	5.21	5.31	4.73	5.11
Total	98.9	99.8	98.0	101	99.4	98.7	99.8
-O=(F+CL)2	1.61	2.11	1.59	1.88	2.20	1.96	1.04
New Total	97.3	97.7	96.4	98.9	97.2	96.7	98.8
APFU							
P	2.80	2.77	2.83	2.79	2.75	2.76	2.82
Ca	4.65	4.57	4.61	4.63	4.57	4.68	4.73
Nd	0.0275	0.0217	0.0203	0.0165	0.0264	0.0176	0.0356
Na	0.0300	0.0209	0.0266	0.0253	0.0310	0.0284	0.0511
F	1.02	1.33	1.02	1.17	1.38	1.25	0.665
Si	0	0	0	0	0	0	0
Cl	0	0	0	0	0.000426	0.00158	0
Ce	0.0128	0.0101	0.00948	0.00769	0.0123	0.00821	0.0166
Sr	0.254	0.276	0.238	0.250	0.258	0.232	0.251
Y	0.00145	0.00115	0.00108	0.00087	0.00140	0.000932	0.00189
La	0.00112	0.000886	0.000828	0.000672	0.00108	0.000717	0.00145

Sample	dmcy139_ap_ltzn	dmcy139_ap_ltzn	dmcy139_ap_ltzn	dmcy139_ap_ltzn	dmcy139_ap_ltzn	dmcy139_ap_ltzn	dmcy139_ap_ltzn
CL Zone	red cores/zone	red cores/zone	red cores/zone	red cores/zone	red cores/zone	red cores/zone	red cores/zone
Anaysis No.	19	20	21	22	23	32	1
Pr	0.00436	0.00344	0.00322	0.00261	0.00419	0.00279	0.00565
Sm	0.00376	0.00297	0.00278	0.00225	0.00361	0.00241	0.00487
Eu	0.000575	0.000455	0.000425	0.000345	0.000553	0.000369	0.000747
Ho	0.0000274	0.0000217	0.0000203	0.0000164	0.0000263	0.0000175	0.0000355
Er	0.0000612	0.0000484	0.0000453	0.0000367	0.0000589	0.0000392	0.0000795
Tm	0.00000770	0.00000609	0.00000569	0.00000462	0.00000740	0.00000493	0.00000998
Yb	0.0000526	0.0000416	0.0000389	0.0000316	0.0000506	0.0000337	0.0000683
Lu	0.00000750	0.00000593	0.00000555	0.00000450	0.00000721	0.00000480	0.00000973
REY sum	0.0530	0.0419	0.0392	0.0318	0.0509	0.0339	0.0687

Sample	dmcy138_dkcore	dmcy138_dkcore	dmcy138_ltzn	dmcy138_ltzn	dmcy138_ltzn	dmcy138_ltzn	dmcy138_ltzn	dmcy138_ltzn	dmcy138_ltzn
CL Zone	blue-violet core	blue-violet core	pink rim/zone	pink rim/zone	pink rim/zone	pink rim/zone	pink rim/zone	pink rim/zone	pink rim/zone
Anaysis No.	16	19	17	18	21	22	23	24	20
P2O5	40.1	40.5	40.2	39.8	40.4	40.4	40.3	39.7	40.1
CaO	54.4	55.5	52.5	52.5	52.7	53.4	54.1	53.5	53.5
Nd2O3	0.505	0.357	0.870	0.664	0.636	0.763	0.555	0.740	0.532
Na2O	0.143	0.205	0.159	0.162	0.132	0.099	0.151	0.120	0.120
F	3.59	4.05	4.06	3.91	3.52	3.51	3.78	4.65	3.84
SiO2	0.014	0.023	0.025	0.063	0.008	0.028	0.002	0.111	0.030
Cl	0.00300	0.0140	bdl	bdl	0.0140	0.00600	0.00700	0.00400	0.0110
Ce2O3	0.597	0.422	0.342	0.261	0.250	0.300	0.218	0.291	0.209
SrO	1.90	1.48	4.47	4.74	4.67	4.60	4.77	4.70	4.55
Total	99.5	101	101	100	101	102	102	102	101
-O=(F+CL)2	1.51	1.71	1.71	1.65	1.49	1.48	1.59	1.96	1.62
New Total	98.0	99.1	99.0	98.8	99.3	100.0	100.8	99.6	99.6
APFU									
P	2.81	2.80	2.81	2.80	2.83	2.82	2.79	2.76	2.80
Ca	4.83	4.85	4.65	4.68	4.67	4.71	4.75	4.70	4.73
Nd	0.0149	0.0104	0.0256	0.0197	0.0188	0.0224	0.0162	0.0217	0.0157
Na	0.0230	0.0324	0.0254	0.0261	0.0212	0.0158	0.0240	0.0191	0.0192
F	0.940	1.04	1.06	1.03	0.921	0.914	0.979	1.21	1.00
Si	0.000580	0.000938	0.00103	0.00262	0.000331	0.00115	0.0000819	0.00455	0.00124
Cl	0.000421	0.00193	0	0	0.00196	0.000837	0.000971	0.000556	0.00154
Ce	0.0181	0.0126	0.0103	0.00794	0.00757	0.00904	0.00654	0.00874	0.00631
Sr	0.0914	0.0699	0.214	0.229	0.224	0.220	0.226	0.223	0.217
Y	0.000574	0.000399	0.00233	0.00179	0.00170	0.00203	0.00147	0.00197	0.00142
La	0.00439	0.00305	0.00102	0.000786	0.000749	0.000894	0.000646	0.000864	0.000624

Sample	dmcy138_dkcore	dmcy138_dkcore	dmcy138_ltzn	dmcy138_ltzn	dmcy138_ltzn	dmcy138_ltzn	dmcy138_ltzn	dmcy138_ltzn	dmcy138_ltzn
CL Zone	blue-violet core	blue-violet core	pink rim/zone	pink rim/zone	pink rim/zone	pink rim/zone	pink rim/zone	pink rim/zone	pink rim/zone
Anaysis No.	16	19	17	18	21	22	23	24	20
Pr	0.00340	0.00236	0.00379	0.00291	0.00277	0.00331	0.00240	0.00320	0.00231
Sm	0.00127	0.000881	0.00412	0.00316	0.00302	0.00360	0.00260	0.00348	0.00251
Eu	0.000185	0.000129	0.000749	0.000576	0.000549	0.000655	0.000474	0.000633	0.000457
Ho	0.0000125	0.00000873	0.0000491	0.0000378	0.0000360	0.0000430	0.0000311	0.0000415	0.0000300
Er	0.0000300	0.0000209	0.0001030	0.0000792	0.0000755	0.0000901	0.0000652	0.0000871	0.0000629
Tm	0.00000374	0.00000260	0.0000120	0.00000925	0.00000881	0.0000105	0.00000761	0.0000102	0.00000734
Yb	0.0000260	0.0000181	0.0000698	0.0000537	0.0000512	0.0000611	0.0000442	0.0000591	0.0000426
Lu	0.00000378	0.00000263	0.00000868	0.00000667	0.00000636	0.00000759	0.00000549	0.00000734	0.00000530
REY sum	0.0434	0.0302	0.0499	0.0384	0.0366	0.0437	0.0316	0.0422	0.0305

Sample	dmcy138_ltzn	frs4_ap_ltzn	frs4_ap_dkzn	frs4_ap_dkzn	frs4_ap_dkzn	frs4_ap_dkzn	frs4_ap_ltzn	frs4_ap_dkzn	frs4_ap_ltzn	frs4_ap_ltzn
CL Zone	pink rim/zone	pink zone	blue zone	blue zone	blue zone	blue zone	pink zone	blue zone	pink zone	pink zone
Anaysis No.	25	21	24	25	27	29	30	32	23	26
P2O5	39.9	40.5	40.3	40.1	40.4	40.4	40.2	40.9	39.4	39.2
CaO	51.8	56.1	55.9	55.0	55.2	55.7	54.8	56.1	52.7	51.4
Nd2O3	0.778	0.314	0.518	0.385	0.310	0.379	0.429	0.137	3.23	4.95
Na2O	0.136	0.111	0.182	0.095	0.076	0.107	0.143	0.117	0.780	1.082
F	3.73	3.83	4.64	4.07	3.36	3.78	3.58	3.66	4.74	3.49
SiO2	0.024	0.024	0.039	0.029	bdl	bdl	0.008	0.015	0.004	bdl
Cl	0.00700	bdl	bdl	0.00400	bdl	bdl	0.0100	0.00400	bdl	0.00500
Ce2O3	0.306	0.158	0.261	0.194	0.156	0.191	0.216	0.069	1.63	2.49
SrO	5.89	1.22	1.70	1.46	1.48	1.33	1.80	1.49	1.47	0.479
Total	101	100	101	99.6	99.7	100	99.5	101	100	98.2
-O=(F+CL)2	1.57	1.61	1.95	1.71	1.41	1.59	1.51	1.54	2.00	1.47
New Total	99.0	98.8	99.5	97.9	98.3	98.7	98.0	99.7	98.1	96.7
APFU										
P	2.81	2.80	2.76	2.80	2.82	2.80	2.81	2.82	2.71	2.73
Ca	4.62	4.90	4.84	4.85	4.89	4.89	4.85	4.89	4.59	4.52
Nd	0.0231	0.00915	0.0150	0.0113	0.00914	0.0111	0.0126	0.00398	0.0938	0.145
Na	0.0219	0.0176	0.0285	0.0152	0.0122	0.0170	0.0229	0.0184	0.1230	0.1722
F	0.980	0.989	1.19	1.06	0.878	0.979	0.936	0.941	1.22	0.905
Si	0.000999	0.000980	0.00158	0.00119	0	0	0.000330	0.000610	0.000163	0
Cl	0.000987	0	0	0.000558	0	0	0.00140	0.000551	0	0.000695
Ce	0.00932	0.00472	0.00773	0.00585	0.00472	0.00573	0.00653	0.00205	0.0485	0.0749
Sr	0.284	0.0576	0.0795	0.0697	0.0708	0.0632	0.0860	0.0700	0.0692	0.0228
Y	0.00210	0.00242	0.00396	0.00300	0.00242	0.00294	0.00335	0.00105	0.0249	0.0384
La	0.000922	0.000502	0.000821	0.000622	0.000502	0.000609	0.000694	0.000218	0.00515	0.00797

Sample	dmcy138_ltzn	frs4_ap_ltzn	frs4_ap_dkzn	frs4_ap_dkzn	frs4_ap_dkzn	frs4_ap_dkzn	frs4_ap_ltzn	frs4_ap_dkzn	frs4_ap_ltzn	frs4_ap_ltzn
CL Zone	pink rim/zone	pink zone	blue zone	blue zone	blue zone	blue zone	pink zone	blue zone	pink zone	pink zone
Anaysis No.	25	21	24	25	27	29	30	32	23	26
Pr	0.00342	0.00137	0.00223	0.00169	0.00136	0.00166	0.00189	0.000594	0.0140	0.0217
Sm	0.00371	0.00317	0.00519	0.00393	0.00317	0.00385	0.00439	0.00138	0.0325	0.0503
Eu	0.000676	0.000841	0.00138	0.00104	0.000840	0.00102	0.00116	0.000366	0.00862	0.0133
Ho	0.0000443	0.0000574	0.0000939	0.0000711	0.0000573	0.0000696	0.0000793	0.0000250	0.000589	0.000910
Er	0.0000929	0.0000823	0.000135	0.000102	0.0000822	0.0000997	0.000114	0.0000358	0.000844	0.00131
Tm	0.0000109	0.00000564	0.00000922	0.00000698	0.00000563	0.00000684	0.00000780	0.00000245	0.0000578	0.0000894
Yb	0.0000630	0.0000245	0.0000401	0.0000304	0.0000245	0.0000297	0.0000339	0.0000107	0.000252	0.000389
Lu	0.00000783	0.00000251	0.00000411	0.00000311	0.00000251	0.00000304	0.00000347	0.00000109	0.0000258	0.0000398
REY sum	0.0450	0.0254	0.0415	0.0314	0.0253	0.0307	0.0351	0.0110	0.260	0.402

Sample	frs4_ap_ltzn	frs4_ap_ltzn	bh224_ap_ltcore	bh224_ap_ltcore	bh224_ap_ltcore	bh224_ap_ltcore	bh224_ap_ltcore	bh224_ap_ltcore	bh224_ap_ltcore
CL Zone	pink zone	pink zone	pink core	pink core	pink core	pink core	pink core	pink core	pink core
Anaysis No.	28	31	26	27	28	37	38	43	44
P2O5	39.3	39.6	39.6	39.4	39.2	39.5	39.2	39.9	39.7
CaO	50.4	52.4	52.8	52.5	52.4	52.2	52.2	53.1	52.6
Nd2O3	3.43	2.96	1.22	1.58	1.52	1.20	1.60	0.753	0.753
Na2O	1.030	0.842	0.528	0.707	0.694	0.748	0.717	0.617	0.635
F	3.56	4.05	3.84	3.88	3.99	3.68	3.60	3.87	3.86
SiO2	0.005	bdl	0.036	0.032	0.036	0.008	0.021	0.045	0.054
Cl	bdl	0.00400	0.0130	0.00300	0.00900	0.00700	0.00900	0.0280	bdl
Ce2O3	1.73	1.49	0.932	1.21	1.16	0.919	1.22	0.576	0.576
SrO	1.47	0.17	0.426	0.421	0.462	0.391	0.530	0.940	0.621
Total	97.9	98.5	98.0	98.1	97.9	97.7	97.2	98.7	97.7
-O=(F+CL)2	1.50	1.70	1.62	1.63	1.68	1.55	1.52	1.64	1.62
New Total	96.4	96.8	96.4	96.4	96.2	96.1	95.7	97.1	96.0
APFU									
P	2.78	2.76	2.82	2.80	2.79	2.82	2.81	2.82	2.83
Ca	4.51	4.63	4.74	4.72	4.72	4.73	4.73	4.75	4.74
Nd	0.102	0.0872	0.0365	0.0473	0.0456	0.0363	0.0483	0.0225	0.0226
Na	0.1668	0.1345	0.0859	0.1150	0.1132	0.1226	0.1176	0.0999	0.1036
F	0.940	1.05	1.02	1.03	1.06	0.983	0.964	1.02	1.03
Si	0.000209	0	0.00151	0.00134	0.00151	0.000338	0.000888	0.00188	0.00227
Cl	0	0.000559	0.00185	0.000427	0.00128	0.00100	0.00129	0.00396	0
Ce	0.0529	0.0450	0.0286	0.0371	0.0358	0.0284	0.0379	0.0176	0.0177
Sr	0.0710	0.00831	0.0207	0.0205	0.0225	0.0192	0.0260	0.0455	0.0303
Y	0.0271	0.0231	0.00510	0.00661	0.00637	0.00507	0.00675	0.00314	0.00316
La	0.00562	0.00479	0.00512	0.00664	0.00640	0.00509	0.00678	0.00315	0.00318

Sample	frs4_ap_ltzn	frs4_ap_ltzn	bh224_ap_ltcore	bh224_ap_ltcore	bh224_ap_ltcore	bh224_ap_ltcore	bh224_ap_ltcore	bh224_ap_ltcore	bh224_ap_ltcore
CL Zone	pink zone	pink zone	pink core	pink core	pink core	pink core	pink core	pink core	pink core
Anaysis No.	28	31	26	27	28	37	38	43	44
Pr	0.0153	0.0130	0.00684	0.00886	0.00854	0.00679	0.00905	0.00421	0.00424
Sm	0.0355	0.0302	0.00544	0.00706	0.00680	0.00541	0.00720	0.00335	0.00337
Eu	0.00941	0.00802	0.00121	0.00157	0.00151	0.00120	0.00160	0.000744	0.000749
Ho	0.000643	0.000547	0.000132	0.000172	0.000165	0.000132	0.000175	0.0000815	0.0000821
Er	0.0009215	0.000785	0.000211	0.000273	0.000263	0.000209	0.000279	0.000130	0.000130
Tm	0.0000631	0.0000538	0.0000170	0.0000220	0.0000212	0.0000169	0.0000225	0.0000104	0.0000105
Yb	0.000275	0.000234	0.0000816	0.000106	0.000102	0.0000810	0.000108	0.0000502	0.0000506
Lu	0.0000281	0.0000239	0.00000923	0.0000120	0.0000115	0.00000917	0.0000122	0.00000568	0.00000572
REY sum	0.284	0.242	0.0938	0.122	0.117	0.0932	0.124	0.0577	0.0581

Sample	bh224_ap_dkrim	bh224_ap_dkrim	bh224_ap_dkrim	bh224_ap_dkrim	bh224_ap_dkrim	bh224_ap_dkrim	bh224_ap_dkrim	bh224_ap_dkrim
CL Zone	indigo rim	indigo rim	indigo rim	indigo rim	indigo rim	indigo rim	indigo rim	indigo rim
Anaysis No.	29	30	31	34	35	39	40	41
P2O5	40.4	40.4	40.3	40.1	40.5	40.4	40.5	40.3
CaO	55.9	55.4	55.5	56.4	57.0	55.9	55.0	55.4
Nd2O3	0.081	0.183	bdl	0.090	0.076	0.183	0.025	0.273
Na2O	0.005	0.008	0.005	0.005	0.005	0.005	0.005	0.005
F	4.04	4.02	3.94	4.44	4.84	3.87	4.02	3.88
SiO2	0.028	0.024	0.007	0.209	0.045	0.046	0.034	0.073
Cl	0.0120	0.00500	0.0120	0.00100	0.00300	bdl	bdl	bdl
Ce2O3	0.035	0.079	0.000	0.039	0.033	0.079	0.011	0.118
SrO	0.307	0.336	0.251	0.321	0.555	0.301	0.262	0.266
Total	99.3	98.8	98.5	99.7	101	99.0	98.2	98.4
-O=(F+CL)2	1.70	1.69	1.66	1.87	2.04	1.63	1.69	1.63
New Total	97.6	97.1	96.9	97.8	98.9	97.4	96.5	96.8
APFU								
P	2.81	2.82	2.82	2.78	2.76	2.81	2.83	2.81
Ca	4.92	4.88	4.92	4.94	4.93	4.92	4.87	4.89
Nd	0.0024	0.00537	0	0.00263	0.00220	0.00537	0.000752	0.00804
Na	0.000796	0.00128	0.000801	0.000792	0.000782	0.000796	0.000801	0.000799
F	1.05	1.05	1.03	1.15	1.23	1.01	1.05	1.01
Si	0.00115	0.000987	0.000289	0.00854	0.00182	0.00189	0.00141	0.00301
Cl	0.00167	0.000697	0.00168	0.000138	0.000410	0	0	0
Ce	0.00105	0.00238	0	0.00117	0.000975	0.00238	0.000333	0.00356
Sr	0.0146	0.0160	0.0120	0.0152	0.0260	0.0143	0.0126	0.0127
Y	0.00328	0.00742	0	0.00364	0.00304	0.00741	0.00104	0.0111
La	0.000160	0.000362	0	0.000178	0.000149	0.000362	0.0000507	0.000543

Sample	bh224_ap_dkrim	bh224_ap_dkrim	bh224_ap_dkrim	bh224_ap_dkrim	bh224_ap_dkrim	bh224_ap_dkrim	bh224_ap_dkrim	bh224_ap_dkrim
CL Zone	indigo rim	indigo rim	indigo rim	indigo rim	indigo rim	indigo rim	indigo rim	indigo rim
Anaysis No.	29	30	31	34	35	39	40	41
Pr	0.000319	0.000720	0	0.000353	0.000295	0.000720	0.000101	0.00108
Sm	0.00076	0.00172	0	0.000844	0.000705	0.00172	0.000241	0.00258
Eu	0.000223	0.000505	0	0.000248	0.000207	0.000505	0.0000707	0.000756
Ho	0.0000663	0.0001500	0	0.0000735	0.0000615	0.000150	0.0000210	0.000224
Er	0.000117	0.000264	0	0.000130	0.000108	0.000264	0.0000370	0.000396
Tm	0.00000987	0.0000223	0	0.0000109	0.00000915	0.0000223	0.00000312	0.0000334
Yb	0.0000452	0.000102	0	0.0000501	0.0000419	0.000102	0.0000143	0.000153
Lu	0.00000515	0.0000116	0	0.00000570	0.00000477	0.0000116	0.00000163	0.0000174
REY sum	0.00989	0.0224	0	0.0110	0.00916	0.0223	0.00313	0.0335

Sample	yw61_ap_ltzn	yw61_ap_ltzn	yw61_ap_ltzn	yw61_ap_ltzn	yw61_ap_ltzn	yw61_ap_ltzn	yw61_ap_dkzn	yw61_ap_dkzn	yw61_ap_dkzn
CL Zone	light violet zone	light violet zone	light violet zone	light violet zone	light violet zone	light violet zone	blue rim	blue rim	blue rim
Anaysis No.	33	34	35	40	43	47	36	37	38
P2O5	40.3	40.0	40.2	40.6	39.6	39.9	41.3	40.9	40.9
CaO	53.4	53.5	54.2	54.5	52.5	53.7	58.0	57.7	57.5
Nd2O3	0.214	0.559	0.938	0.289	0.263	0.554	0.148	0.135	0.103
Na2O	0.204	0.380	0.469	0.191	0.158	0.301	bdl	0.006	bdl
F	3.55	4.51	3.90	4.87	3.75	4.62	3.13	3.23	4.09
SiO2	0.004	0.037	0.043	bdl	bdl	0.022	bdl	0.015	0.010
Cl	bdl	0.0140	0.00700	bdl	0.00400	0.00100	bdl	bdl	bdl
Ce2O3	0.092	0.240	0.403	0.124	0.113	0.238	0.097	0.088	0.067
SrO	2.134	2.945	1.269	3.280	3.780	3.155	0.467	0.549	0.433
Total	98.5	100	99.6	102	98.5	100	102	101	101
-O=(F+CL)2	1.49	1.90	1.64	2.05	1.58	1.94	1.32	1.36	1.72
New Total	97.0	98.5	98.0	99.8	96.9	98.5	100.4	99.8	99.6
APFU									
P	2.84	2.77	2.78	2.77	2.81	2.76	2.82	2.81	2.79
Ca	4.76	4.69	4.75	4.72	4.72	4.71	5.00	5.01	4.96
Nd	0.00637	0.0163	0.0274	0.00832	0.00788	0.0162	0.00427	0.00390	0.00295
Na	0.0329	0.0603	0.0744	0.0299	0.0257	0.0477	0.0000	0.000942	0.0000
F	0.934	1.17	1.01	1.24	1.00	1.19	0.798	0.828	1.04
Si	0.000167	0.00152	0.00176	0	0	0.000900	0	0.000608	0.000403
Cl	0	0.00194	0.000970	0	0.000569	0.000139	0	0	0
Ce	0.00280	0.00720	0.0121	0.00366	0.00347	0.00713	0.00286	0.00261	0.00197
Sr	0.103	0.140	0.060	0.153	0.184	0.150	0.0218	0.0258	0.0202
Y	0.00716	0.0184	0.0308	0.00935	0.00886	0.0182	0.00809	0.00738	0.00559
La	0.000436	0.00112	0.00187	0.000569	0.000539	0.00111	0.000552	0.000504	0.000381

Sample	yw61_ap_ltzn	yw61_ap_ltzn	yw61_ap_ltzn	yw61_ap_ltzn	yw61_ap_ltzn	yw61_ap_ltzn	yw61_ap_dkzn	yw61_ap_dkzn	yw61_ap_dkzn
CL Zone	light violet zone	light violet zone	light violet zone	light violet zone	light violet zone	light violet zone	blue rim	blue rim	blue rim
Anaysis No.	33	34	35	40	43	47	36	37	38
Pr	0.000805	0.002066	0.00346	0.00105	0.000996	0.002046	0.000654	0.000598	0.000452
Sm	0.00366	0.00940	0.0158	0.00479	0.00453	0.00931	0.00212	0.00194	0.00147
Eu	0.00135	0.00346	0.00581	0.00176	0.00167	0.00343	0.000834	0.000761	0.000576
Ho	0.000164	0.000421	0.000706	0.000214	0.000203	0.000417	0.000161	0.000147	0.000111
Er	0.000244	0.000625	0.00105	0.000318	0.0003015	0.000619	0.000276	0.000252	0.000190
Tm	0.0000196	0.0000502	0.0000842	0.0000256	0.0000242	0.0000497	0.0000236	0.0000215	0.0000163
Yb	0.0000904	0.000232	0.000389	0.0001181	0.000112	0.000230	0.000114	0.000104	0.0000788
Lu	0.00000992	0.0000255	0.0000427	0.0000130	0.0000123	0.0000252	0.0000124	0.0000114	0.00000859
REY sum	0.0294	0.0755	0.126	0.0384	0.0364	0.0747	0.0245	0.0223	0.0169

Sample	yw61_ap_dkzn	yw61_ap_dkzn	yw61_ap_dkzn	yn50_ap_dkzn	yn50_ap_dkzn	yn50_ap_dkzn	yn50_ap_dkzn	yn50_ap_ltzn	yn50_ap_ltzn
CL Zone	blue rim	blue rim	blue rim	dark blue zone	dark blue zone	dark blue zone	dark blue zone	dark blue zone	dark blue zone
Anaysis No.	39	41	44	48	49	55	54	50	52
P2O5	40.5	40.2	40.4	40.0	40.1	40.3	40.0	39.8	39.6
CaO	56.3	56.2	57.0	56.1	56.1	56.1	55.8	53.8	53.1
Nd2O3	0.049	bld	0.012	0.117	bld	bdl	0.008	0.193	0.089
Na2O	bdl	0.008	bdl	bdl	bdl	0.006	0.006	0.086	0.151
F	4.14	4.30	4.79	3.63	4.42	4.46	4.01	3.77	3.78
SiO2	bdl	bdl	0.052	0.012	bdl	0.042	0.015	0.029	0.048
Cl	0.0160	0.00900	0.00100	bdl	bdl	0.00300	0.0100	0.00600	0.00400
Ce2O3	0.032	bdl	0.008	0.083	bdl	bdl	0.006	0.150	0.069
SrO	0.395	0.961	0.549	0.605	0.423	0.839	0.755	2.77	3.16
Total	99.7	99.9	101	98.8	99.2	100	98.9	99.0	98.6
-O=(F+CL)2	1.74	1.81	2.02	1.53	1.86	1.88	1.69	1.59	1.59
New Total	97.9	98.1	98.8	97.3	97.4	98.1	97.2	97.4	97.0
APFU									
P	2.80	2.79	2.77	2.80	2.79	2.79	2.80	2.80	2.81
Ca	4.93	4.93	4.94	4.97	4.93	4.91	4.94	4.80	4.77
Nd	0.00143	0	0.000354	0.00345	0	0	0.000249	0.00572	0.00265
Na	0.0000	0.00127	0.0000	0.0000	0.0000	0.000950	0.000961	0.0139	0.0245
F	1.07	1.11	1.22	0.950	1.15	1.15	1.05	0.992	1.00
Si	0	0	0.00210	0.000496	0	0.00172	0.000619	0.00121	0.00201
Cl	0.00221	0.00125	0.000137	0	0	0.000415	0.00140	0.000846	0.000568
Ce	0.00096	0	0.000237	0.00251	0	0	0.000181	0.00457	0.00212
Sr	0.0187	0.0456	0.0257	0.0290	0.0201	0.0397	0.0362	0.133	0.153
Y	0.00271	0	0.000670	0.00812	0	0	0.000586	0.0144	0.00667
La	0.000185	0	0.0000458	0.000461	0	0	0.0000333	0.000873	0.000405

Sample	yw61_ap_dkzn	yw61_ap_dkzn	yw61_ap_dkzn	yn50_ap_dkzn	yn50_ap_dkzn	yn50_ap_dkzn	yn50_ap_dkzn	yn50_ap_ltzn	yn50_ap_ltzn
CL Zone	blue rim	blue rim	blue rim	dark blue zone	dark blue zone	dark blue zone	dark blue zone	dark blue zone	dark blue zone
Anaysis No.	39	41	44	48	49	55	54	50	52
Pr	0.000219	0	0.0000542	0.000553	0	0	0.0000400	0.000979	0.000454
Sm	0.000711	0	0.000176	0.00177	0	0	0.000128	0.00254	0.00118
Eu	0.000279	0	0.0000691	0.000631	0	0	0.0000456	0.000958	0.000444
Ho	0.0000540	0	0.0000134	0.000216	0.0000000	0.0000000	0.0000156	0.000377	0.000175
Er	0.0000923	0	0.0000228	0.000362	0	0	0.0000261	0.000714	0.000331
Tm	0.00000789	0	0.00000195	0.0000310	0	0	0.00000224	0.0000682	0.0000316
Yb	0.0000382	0	0.00000945	0.000140	0	0	0.0000101	0.000321	0.000149
Lu	0.00000416	0	0.00000103	0.0000148	0	0	0.00000107	0.0000320	0.0000149
REY sum	0.00819	0	0.00203	0.0232	0	0	0.00168	0.0387	0.0179

Sample	yn50_ap_ltzn	le1_ap_dkcore	le1_ap_dkcore	le1_ap_dkcore	le1_ap_dkcore	le1_ap_dkcore	le1_ap_dkcore	le1_ap_dkcore	le1_ap_dkcore
CL Zone	dark blue zone	green core	green core	green core	green core	green core	green core	green core	green core
Anaysis No.	53	2	3	4	7	8	9	10	15
P2O5	39.4	40.0	39.9	39.9	40.3	39.9	39.6	39.8	39.5
CaO	53.0	57.7	56.9	57.2	57.0	56.4	55.9	55.5	56.0
Nd2O3	0.279	0.090	0.084	0.084	0.209	0.060	0.246	0.088	0.155
Na2O	0.174	0.061	bdl	0.045	0.051	0.056	0.129	0.026	0.138
F	3.74	3.62	4.34	4.77	4.30	4.48	4.20	3.86	4.04
SiO2	bdl	0.204	0.231	0.134	0.136	0.162	0.289	0.172	0.369
Cl	bdl	0.00300	bdl	0.00900	0.00300	bdl	bdl	bdl	0.00500
Ce2O3	0.217	0.048	0.045	0.045	0.112	0.032	0.132	0.047	0.083
SrO	3.28	0.00200	0.010	0.028	0.032	0.003	0.024	0.004	0.007
Total	98.5	100	99.6	100	100	99.2	98.6	97.9	98.5
-O=(F+CL)2	1.57	1.53	1.83	2.01	1.81	1.89	1.77	1.63	1.70
New Total	97.0	98.7	97.8	98.1	98.4	97.3	96.9	96.2	96.8
APFU									
P	2.79	2.77	2.76	2.74	2.77	2.77	2.76	2.80	2.76
Ca	4.76	5.06	4.98	4.98	4.95	4.96	4.94	4.94	4.96
Nd	0.00835	0.00261	0.00245	0.00244	0.00605	0.00175	0.00724	0.00260	0.00458
Na	0.0283	0.0097	0.0000	0.00709	0.00801	0.00891	0.0206	0.00419	0.0221
F	0.991	0.936	1.12	1.23	1.10	1.16	1.09	1.01	1.06
Si	0	0.00834	0.00945	0.00544	0.00551	0.00664	0.0119	0.00715	0.0153
Cl	0	0.000416	0	0.00124	0.000412	0	0	0	0.000701
Ce	0.00666	0.00144	0.00135	0.00134	0.00332	0.000961	0.00398	0.00143	0.00252
Sr	0.159	0.0000948	0.000474	0.00132	0.00150	0.000143	0.00115	0.000193	0.000336
Y	0.0210	0.0103	0.00969	0.00963	0.0239	0.00691	0.0286	0.0103	0.0181
La	0.00127	0.000294	0.000276	0.000274	0.000680	0.000197	0.000814	0.000293	0.000515

Sample	yn50_ap_ltzn	le1_ap_dkcore	le1_ap_dkcore	le1_ap_dkcore	le1_ap_dkcore	le1_ap_dkcore	le1_ap_dkcore	le1_ap_dkcore	le1_ap_dkcore
CL Zone	dark blue zone	green core	green core	green core	green core	green core	green core	green core	green core
Anaysis No.	53	2	3	4	7	8	9	10	15
Pr	0.00143	0.000357	0.000335	0.000332	0.000825	0.000239	0.000988	0.000355	0.000624
Sm	0.00371	0.00117	0.00110	0.00109	0.00272	0.00079	0.00325	0.00117	0.00206
Eu	0.00140	0.000163	0.000153	0.000152	0.000378	0.000109	0.000453	0.000163	0.000286
Ho	0.000550	0.000207	0.000194	0.000193	0.000479	0.000139	0.000574	0.000206	0.000363
Er	0.001041	0.000560	0.000525	0.000522	0.00129	0.000374	0.00155	0.000557	0.000980
Tm	0.0000995	0.0000687	0.0000644	0.0000640	0.000159	0.0000459	0.0001903	0.0000684	0.000120
Yb	0.000468	0.000421	0.000395	0.000393	0.000975	0.000282	0.00117	0.000420	0.000738
Lu	0.0000467	0.0000544	0.0000510	0.0000507	0.000126	0.0000364	0.000151	0.0000541	0.0000952
REY sum	0.0565	0.0204	0.0191	0.0190	0.0471	0.0136	0.0564	0.0203	0.0357

Sample	le1_ap_dkcore	le1_ap_dkcore	le1_ap_ltrim pink and	le1_ap_ltrim pink and	le1_ap_ltrim pink and	le1_ap_ltrim pink and	lrs150_dkcore blue-violet	lrs150_ltrim	lrs150_dkcore blue-violet
CL Zone	green core	green core	purple rim	purple rim	purple rim	purple rim	core	red rim	core
Anaysis No.	16	17	5	11	13	14	1	6	5
P2O5	39.5	39.5	39.5	39.8	39.3	40.0	39.6	39.5	39.6
CaO	56.5	56.6	52.9	52.9	53.4	53.5	53.7	52.9	53.2
Nd2O3	0.084	0.159	0.834	0.542	0.490	0.763	0.194	0.181	0.014
Na2O	0.072	0.139	0.331	0.212	0.197	0.256	0.189	0.185	0.137
F	4.83	4.13	4.83	3.91	3.80	4.83	3.47	3.94	3.45
SiO2	0.338	0.328	0.042	bdl	0.048	0.051	0.005	0.045	0.056
Cl	0.00100	0.00100	0.0130	0.00700	0.0110	bdl	bdl	0.00600	0.00700
Ce2O3	0.045	0.085	0.385	0.250	0.226	0.352	0.162	0.444	0.300
SrO	0.011	0.144	2.91	3.29	3.20	2.89	2.31	2.25	2.84
Total	99.3	99.4	99.5	99.1	98.8	100	98.2	97.8	98.2
-O=(F+CL)2	2.03	1.74	2.04	1.65	1.60	2.03	1.46	1.66	1.45
New Total	97.3	97.6	97.5	97.4	97.2	98.2	96.7	96.1	96.7
APFU									
P	2.74	2.75	2.76	2.80	2.78	2.76	2.82	2.82	2.77
Ca	4.96	4.99	4.67	4.71	4.78	4.68	4.84	4.80	4.74
Nd	0.00246	0.00466	0.0245	0.0161	0.0146	0.0222	0.00191	0.00354	0.0118
Na	0.0114	0.0222	0.0529	0.0342	0.0319	0.0405	0.0308	0.0224	0.0585
F	1.25	1.08	1.26	1.03	1.00	1.25	0.924	0.918	1.15
Si	0.0138	0.0135	0.00173	0	0.00201	0.00208	0.000210	0.00236	0.00333
Cl	0.000139	0.000139	0.00181	0.000986	0.00156	0	0	0.00100	0.00113
Ce	0.00135	0.00256	0.0116	0.00761	0.00692	0.0105	0.00499	0.00924	0.0209
Sr	0.000522	0.00687	0.139	0.159	0.155	0.137	0.112	0.138	0.125
Y	0.00970	0.0184	0.0183	0.0120	0.0109	0.0166	0.000353	0.000654	0.00309
La	0.000276	0.000524	0.00153	0.00100	0.000913	0.00139	0.00280	0.00518	0.00923

Sample	le1_ap_dkcore	le1_ap_dkcore	le1_ap_ltrim	le1_ap_ltrim	le1_ap_ltrim	le1_ap_ltrim	lrs150_dkcore	lrs150_ltrim	lrs150_dkcore
CL Zone	green core	green core	pink and purple rim	pink and purple rim	pink and purple rim	pink and purple rim	blue-violet core	red rim	blue-violet core
Anaysis No.	16	17	5	11	13	14	1	6	5
Pr	0.000335	0.000636	0.00342	0.00224	0.00204	0.00310	0.000534	0.000990	0.00277
Sm	0.00110	0.00209	0.01190	0.00780	0.00709	0.01079	0.000519	0.000961	0.00389
Eu	0.000154	0.000291	0.00395	0.00259	0.00235	0.00358	0.000128	0.000237	0.00101
Ho	0.000195	0.000369	0.000444	0.000291	0.000264	0.000402	0.00000738	0.0000137	0.0000644
Er	0.000526	0.000998	0.000654	0.000429	0.000390	0.000593	0.0000176	0.0000325	0.000130
Tm	0.0000645	0.000122	0.0000502	0.0000329	0.0000299	0.0000455	0.00000195	0.00000362	0.0000137
Yb	0.000396	0.000751	0.000232	0.000152	0.000138	0.000211	0.0000124	0.0000230	0.0000719
Lu	0.0000511	0.0000970	0.0000254	0.0000167	0.0000151	0.0000230	0.00000165	0.00000307	0.00000758
REY sum	0.0191	0.0363	0.0949	0.0622	0.0566	0.0860	0.0116	0.0216	0.0561

Sample	lrs150_ltrim	lrs150_ltrim
CL Zone	red rim	red rim
Anaysis No.	4	7
P2O5	39.3	39.5
CaO	53.1	51.7
Nd2O3	0.446	0.364
Na2O	0.362	0.452
F	4.36	4.03
SiO2	0.080	0.033
Cl	0.00800	0.00600
Ce2O3	0.684	1.006
SrO	2.58	2.30
Total	99.1	97.7
-O=(F+CL)2	1.84	1.70
New Total	97.3	96.0
APFU		
P	2.81	2.81
Ca	4.66	4.76
Nd	0.0175	0.00773
Na	0.0737	0.0302
F	1.07	1.05
Si	0.00139	0.00189
Cl	0.000855	0.000855
Ce	0.0310	0.0137
Sr	0.112	0.110
Y	0.00459	0.00202
La	0.0137	0.00605

Sample	lrs150_ltrim	lrs150_ltrim
CL Zone	red rim	red rim
Anaysis No.	4	7
Pr	0.00411	0.00181
Sm	0.00578	0.00255
Eu	0.00149	0.000659
Ho	0.0000956	0.0000422
Er	0.000193	0.0000853
Tm	0.0000204	0.00000899
Yb	0.000107	0.0000471
Lu	0.0000113	0.00000497
REY sum	0.0832	0.0367

Appendix 3.B – Apatite LA-ICP-MS Analyses

Note 1: The REY values were C1-normalized using chondrite values from Sun and McDonough (1995). These values were plotted against the ionic radius of the REE and Y based on a nine-fold coordination number. Nine-fold coordination was chosen on the assumption that the REY in apatite preferentially substitute for Ca(II) in the nine-fold coordination site (Gaft et al., 2015). Yttrium was plotted before Ho on the REE-normalized plots as these two elements are geochemical twins due to their nearly identical ionic radii (107.5 pm and 107.2 pm for Y and Ho with a CN=9, respectively).

Note 2: The λ values are calculated using the free Excel Macro provided by O'Neill (2016) in the Appendices. The λ values are calculated by determining the orthogonal coefficients for the 0-4th order polynomial equations that best fit the C1-normalized REE values. For further details, we refer the reader to O'Neill (2016).

Note 3: Spot numbers correlate to numbers in manuscript figures, where present.

Note 4: LA-ICP-MS tables consist of 3 parts: 1) spot data, 2) 1σ error, and 3) detection limits.

File **CL Colour**		yn50_aplz_44-1 light blue zone	yn50_apdz_44-2 dark blue zone	yn50_apdz_44-3 dark blue zone	yn50_aplz_44-4 light blue zone	yn50_apdz_44-5 dark blue zone	yn50_aplz_44-6 light blue zone	yn50_aplz_44-7 light blue zone	yn50_aplz_44-8 light blue zone
SiO_2	wt.%	bdl	bdl	bdl	bdl	bdl	bdl	bdl	bdl
TiO_2	wt.%	bdl	bdl	bdl	bdl	bdl	bdl	bdl	bdl
Al_2O_3	wt.%	bdl	bdl	bdl	bdl	bdl	bdl	bdl	0.0373
MnO	wt.%	0.0245	0.0355	0.0483	0.0279	0.0220	0.0233	0.0293	0.0196
CaO	wt.%	56.0	56.0	56.0	56.0	56.0	56.0	56.0	56.0
P_2O_5	wt.%	47.9	47.7	50.2	47.5	47.7	50.4	49.5	48.4
^{66}Zn	µg/g	bdl	bdl	bdl	bdl	bdl	bdl	bdl	bdl
^{75}As	µg/g	bdl	bdl	bdl	3.45	3.31	bdl	bdl	bdl
^{85}Rb	µg/g	0.12	bdl	bdl	bdl	bdl	bdl	bdl	1.3
^{88}Sr	µg/g	10300	5690	13900	11100	4510	11500	10600	6080
^{89}Y	µg/g	598	512	917	631	507	594	745	580
^{90}Zr	µg/g	bdl	bdl	bdl	bdl	bdl	bdl	bdl	bdl
^{93}Nb	µg/g	bdl	bdl	bdl	bdl	bdl	bdl	0.026	0.064
^{118}Sn	µg/g	0.33	bdl	bdl	bdl	bdl	bdl	bdl	bdl
^{133}Cs	µg/g	0.049	bdl	bdl	bdl	0.027	bdl	0.053	0.062
^{137}Ba	µg/g	3.54	2.00	2.95	2.69	10.3	2.20	16.1	6.80
^{139}La	µg/g	55.7	41.0	80.9	61.3	35.7	60.2	67.5	54.7
^{140}Ce	µg/g	313	233	432	321	205	321	368	303
^{141}Pr	µg/g	71.2	49.0	92.3	68.3	47.3	68.3	81.6	67.6
^{143}Nd	µg/g	467	288	540	420	306	415	548	440
^{147}Sm	µg/g	267	134	240	221	163	226	332	211
^{151}Eu	µg/g	96.0	53.5	97.8	79.1	65.3	80.7	108	76.6

File CL Colour		yn50_aplz_44-1 light blue zone	yn50_apdz_44-2 dark blue zone	yn50_apdz_44-3 dark blue zone	yn50_aplz_44-4 light blue zone	yn50_apdz_44-5 dark blue zone	yn50_aplz_44-6 light blue zone	yn50_aplz_44-7 light blue zone	yn50_aplz_44-8 light blue zone
^{157}Gd	µg/g	445	188	371	400	281	400	592	336
^{159}Tb	µg/g	62.8	29.8	59.0	59.8	43.7	59.7	85.3	49.1
^{163}Dy	µg/g	267	153	299	267	201	264	361	223
^{165}Ho	µg/g	30.7	22.2	42.9	31.7	24.5	31.2	40.6	27.6
^{167}Er	µg/g	47.0	42.7	85.6	50.9	41.8	48.4	62.5	48.3
^{169}Tm	µg/g	3.82	4.02	8.52	4.06	3.60	3.99	5.07	4.23
^{171}Yb	µg/g	16.7	19.1	42.1	18.2	17.0	17.8	21.9	19.4
^{175}Lu	µg/g	1.81	2.22	4.41	1.85	1.69	1.88	2.44	2.13
^{178}Hf	µg/g	0.036	bdl	0.047	0.047	0.036	bdl	0.052	bdl
^{181}Ta	µg/g	bdl	bdl	bdl	bdl	bdl	bdl	bdl	bdl
^{208}Pb	µg/g	8.06	7.28	12.6	6.47	3.53	5.92	8.65	4.00
^{232}Th	µg/g	0.349	11.2	0.207	0.123	0.185	5.99	12.8	1.22
^{238}U	µg/g	bdl	bdl	bdl	bdl	bdl	bdl	bdl	bdl
λ_0		6.19	5.77	6.53	6.18	5.90	6.18	6.44	6.13
λ_1		7.02	3.39	4.12	6.65	4.66	6.72	6.17	6.28
λ_2		-345	-229	-242	-322	-316	-323	-348	-302
λ_3		808	1220	393	1060	748	999	972	514
λ_4		13700	4970	486	9360	7420	10800	15900	8360
1σ error									
SiO_2	wt.%	bdl	bdl	bdl	bdl	bdl	bdl	bdl	bdl
TiO_2	wt.%	bdl	bdl	bdl	bdl	bdl	bdl	bdl	bdl
Al_2O_3	wt.%	bdl	bdl	bdl	bdl	bdl	bdl	bdl	0.00473
MnO	wt.%	0.00050	0.00078	0.0011	0.00039	0.00023	0.00060	0.00097	0.00034
CaO	wt.%	1.24	1.63	1.62	1.14	1.08	1.48	1.12	0.77
P_2O_5	wt.%	0.99	1.62	1.84	1.08	1.26	1.99	0.69	0.95
^{66}Zn	µg/g	bdl	bdl	bdl	bdl	bdl	bdl	bdl	bdl
^{75}As	µg/g	bdl	bdl	bdl	1.56	1.68	bdl	bdl	bdl
^{85}Rb	µg/g	0.057	bdl	bdl	bdl	bdl	bdl	bdl	0.13
^{88}Sr	µg/g	222	183	544	231	90.9	336	229	130
^{89}Y	µg/g	7.60	5.64	31.6	15.5	10.6	16.0	14.3	13.2
^{90}Zr	µg/g	bdl	bdl	bdl	bdl	bdl	bdl	bdl	bdl
^{93}Nb	µg/g	bdl	bdl	bdl	bdl	bdl	bdl	0.011	0.026
^{118}Sn	µg/g	0.13	bdl	bdl	bdl	bdl	bdl	bdl	bdl
^{133}Cs	µg/g	0.016	bdl	bdl	bdl	0.012	bdl	0.014	0.014
^{137}Ba	µg/g	0.23	0.45	0.27	0.23	0.97	0.24	1.13	0.51
^{139}La	µg/g	0.93	0.45	3.45	1.28	1.18	1.16	3.05	1.27
^{140}Ce	µg/g	5.28	6.83	20.2	5.90	4.22	7.30	13.2	7.13
^{141}Pr	µg/g	1.22	0.795	3.73	1.35	1.09	1.79	2.68	1.69
^{143}Nd	µg/g	6.84	13.3	23.4	8.86	7.40	11.2	16.2	13.9
^{147}Sm	µg/g	3.76	5.43	9.69	3.83	3.24	4.52	7.12	5.29
^{151}Eu	µg/g	1.42	0.867	3.41	1.50	1.09	1.90	1.82	2.29
^{157}Gd	µg/g	5.02	5.10	13.9	6.89	5.02	9.20	9.49	8.40

File CL Colour		yn50_aplz_44-1 light blue zone	yn50_apdz_44-2 dark blue zone	yn50_apdz_44-3 dark blue zone	yn50_aplz_44-4 light blue zone	yn50_apdz_44-5 dark blue zone	yn50_aplz_44-6 light blue zone	yn50_aplz_44-7 light blue zone	yn50_aplz_44-8 light blue zone
^{159}Tb	µg/g	0.75	0.72	2.04	1.12	0.69	1.30	1.41	1.17
^{163}Dy	µg/g	3.12	3.00	10.8	5.71	3.38	3.94	7.21	5.15
^{165}Ho	µg/g	0.37	0.45	1.56	0.60	0.46	0.65	1.02	0.62
^{167}Er	µg/g	0.62	0.57	3.03	1.06	0.81	0.89	1.31	1.24
^{169}Tm	µg/g	0.069	0.056	0.33	0.11	0.068	0.10	0.12	0.11
^{171}Yb	µg/g	0.34	0.74	1.95	0.47	0.43	0.52	0.65	0.57
^{175}Lu	µg/g	0.046	0.095	0.21	0.051	0.048	0.074	0.089	0.066
^{178}Hf	µg/g	0.011	bdl	0.016	0.017	0.014	bdl	0.012	bdl
^{181}Ta	µg/g	bdl	bdl	bdl	bdl	bdl	bdl	bdl	bdl
^{208}Pb	µg/g	0.27	0.36	0.35	0.27	0.14	0.23	0.24	0.16
^{232}Th	µg/g	0.034	0.85	0.025	0.015	0.025	0.16	0.64	0.069
^{238}U	µg/g	bdl	bdl	bdl	bdl	bdl	bdl	bdl	bdl
Detection Limit									
SiO_2	wt.%	1.00	1.64	1.18	1.11	1.04	1.26	1.27	1.19
TiO_2	wt.%	0.000357	0.000501	0.000413	0.000369	0.000326	0.000449	0.000418	0.000421
Al_2O_3	wt.%	0.00155	0.00220	0.00191	0.00173	0.00163	0.00197	0.00197	0.00184
MnO	wt.%	0.0000953	0.000134	0.000115	0.000103	0.0000993	0.000117	0.000119	0.000106
CaO	wt.%	0.0304	0.0453	0.0369	0.0333	0.0330	0.0396	0.0382	0.0377
P_2O_5	wt.%	0.0108	0.0148	0.0126	0.0113	0.0105	0.0130	0.0130	0.0116
^{66}Zn	µg/g	3.44	4.81	4.08	3.68	3.60	4.11	4.84	3.84
^{75}As	µg/g	3.05	4.64	3.71	3.20	3.07	3.73	4.03	3.65
^{85}Rb	µg/g	0.0965	0.150	0.120	0.114	0.114	0.135	0.142	0.122
^{88}Sr	µg/g	0.0370	0.0651	0.0662	0.0568	0.0431	0.0608	0.0595	0.0502
^{89}Y	µg/g	0.0389	0.0735	0.0507	0.0471	0.0450	0.0515	0.0691	0.0482
^{90}Zr	µg/g	0.105	0.151	0.124	0.112	0.113	0.137	0.149	0.123
^{93}Nb	µg/g	0.0199	0.0509	0.0260	0.0100	0.0100	0.0158	0.0179	0.0351
^{118}Sn	µg/g	0.265	0.428	0.340	0.300	0.298	0.323	0.339	0.321
^{133}Cs	µg/g	0.0123	0.0382	0.0257	0.0203	0.0242	0.0266	0.0249	0.0192
^{137}Ba	µg/g	0.110	0.170	0.154	0.092	0.086	0.145	0.165	0.095
^{139}La	µg/g	0.00385	0.0271	0.0153	0.0115	0.00483	0.0182	0.00862	0.0119
^{140}Ce	µg/g	0.0124	0.0221	0.0130	0.0148	0.0173	0.00789	0.00895	0.0153
^{141}Pr	µg/g	0.0105	0.0154	0.0114	0.00778	0.00877	0.0123	0.0127	0.00810
^{143}Nd	µg/g	0.0269	0.148	0.0874	0.0338	0.0923	0.127	0.129	0.103
^{147}Sm	µg/g	0.0554	0.0769	0.0885	0.0664	0.0279	0.0870	0.0498	0.0848
^{151}Eu	µg/g	0.0164	0.0323	0.0097	0.0163	0.0154	0.0220	0.0353	0.0170
^{157}Gd	µg/g	0.0433	0.148	0.0575	0.0522	0.0777	0.123	0.128	0.102
^{159}Tb	µg/g	0.00777	0.0187	0.00850	0.00931	0.00730	0.0147	0.00698	0.0109
^{163}Dy	µg/g	0.0395	0.0700	0.0346	0.0379	0.0468	0.0598	0.0514	0.0484
^{165}Ho	µg/g	0.00980	0.0201	0.0115	0.0106	0.00989	0.0149	0.0128	0.00813
^{167}Er	µg/g	0.0139	0.0833	0.0205	0.0470	0.0326	0.0657	0.0621	0.0485
^{169}Tm	µg/g	0.00849	0.0191	0.00975	0.0111	0.00838	0.0131	0.0122	0.00927

File		yn50_aplz_44-1	yn50_apdz_44-2	yn50_apdz_44-3	yn50_aplz_44-4	yn50_apdz_44-5	yn50_aplz_44-6	yn50_aplz_44-7	yn50_aplz_44-8
CL Colour		light blue zone	dark blue zone	dark blue zone	light blue zone	dark blue zone	light blue zone	light blue zone	light blue zone
^{171}Yb	µg/g	0.0621	0.0761	0.0999	0.0545	0.0690	0.0735	0.0979	0.0679
^{175}Lu	µg/g	0.00664	0.0206	0.0155	0.00964	0.00902	0.00637	0.0155	0.0141
^{178}Hf	µg/g	0.0316	0.0669	0.0445	0.0446	0.0351	0.0437	0.0452	0.0345
^{181}Ta	µg/g	0.0172	0.0128	0.0120	0.0046	0.0103	0.0174	0.0149	0.0161
^{208}Pb	µg/g	0.0215	0.0605	0.0531	0.0318	0.0295	0.0405	0.0412	0.0326
^{232}Th	µg/g	0.0162	0.0206	0.0149	0.00468	0.0162	0.0199	0.0083	0.0141
^{238}U	µg/g	0.0133	0.0183	0.0186	0.0111	0.0136	0.0161	0.0232	0.0140

File		yn50_apdz_44-11	yn50_aplz_44-13	yn50_aplz_44-14	yn50_aplz_44-9	yn50_aplz_44-10	bh224_aplz_24-10	bh224_aplz_24-11	bh224_aplz_24-12
CL Colour		dark blue zone	light blue zone	light blue zone	light blue zone	light blue zone	pink core	pink core	pink core
SiO_2	wt.%	bdl	bdl	bdl	bdl	bdl	bdl	bdl	bdl
TiO_2	wt.%	bdl	bdl	bdl	bdl	bdl	bdl	0.00196	bdl
Al_2O_3	wt.%	bdl	bdl	bdl	bdl	bdl	bdl	bdl	bdl
MnO	wt.%	0.0361	0.0321	0.1539	0.0378	0.0286	0.0395	0.0266	0.0464
CaO	wt.%	56.0	56.0	56.0	53.3	53.3	52.5	52.5	52.5
P_2O_5	wt.%	49.1	48.5	47.0	46.6	44.6	47.3	48.6	48.4
^{66}Zn	µg/g	bdl	bdl	bdl	bdl	bdl	bdl	bdl	bdl
^{75}As	µg/g	bdl	3.77	bdl	bdl	bdl	38.9	36.5	43.7
^{85}Rb	µg/g	bdl	bdl	0.270	bdl	bdl	bdl	bdl	bdl
^{88}Sr	µg/g	3410	6590	8410	6220	8150	4440	4590	4700
^{89}Y	µg/g	528	549	607	506	446	1090	1010	1170
^{90}Zr	µg/g	bdl	bdl	bdl	bdl	bdl	0.75	2.8	bdl
^{93}Nb	µg/g	bdl	0.07	0.527	0.038	bdl	0.19	0.62	0.44
^{118}Sn	µg/g	bdl	bdl	bdl	bdl	bdl	bdl	bdl	bdl
^{133}Cs	µg/g	bdl	0.034	0.092	0.061	0.066	0.24	bdl	0.21
^{137}Ba	µg/g	3.37	5.42	28.9	21.5	11.3	89.4	50.9	21.4
^{139}La	µg/g	35.6	65.9	41.4	54.9	41.5	1610	1220	2410
^{140}Ce	µg/g	216	331	242	273	230	8630	7020	12240
^{141}Pr	µg/g	48.8	70.9	59.0	58.0	51.4	2010	1810	2810
^{143}Nd	µg/g	301	438	411	347	320	1130	10100	14000
^{147}Sm	µg/g	160	194	245	164	155	1700	1650	1990
^{151}Eu	µg/g	56.0	73.1	88.3	61.2	54.0	384	373	427
^{157}Gd	µg/g	243	286	389	267	239	1000	974	1100
^{159}Tb	µg/g	36.7	40.6	55.4	41.6	35.6	115	111	123
^{163}Dy	µg/g	175	186	250	195	164	449	430	467
^{165}Ho	µg/g	23.2	25.6	30.9	25.1	22.9	51.8	49.7	52.9
^{167}Er	µg/g	45.4	48.4	55.1	47.6	41.3	86.5	81.6	85.9
^{169}Tm	µg/g	4.54	4.43	4.69	4.49	3.83	7.45	6.62	7.29
^{171}Yb	µg/g	22.9	20.8	22.5	21.6	17.3	36.8	32.8	36.3
^{175}Lu	µg/g	2.61	2.12	2.27	2.23	1.56	4.42	3.62	4.24
^{178}Hf	µg/g	bdl	bdl	0.0449	bdl	bdl	bdl	0.165	bdl
^{181}Ta	µg/g	bdl	bdl	bdl	bdl	bdl	bdl	bdl	bdl
^{208}Pb	µg/g	5.82	8.46	14.1	11.6	9.08	292	183	416
^{232}Th	µg/g	0.112	0.51	27.3	8.70	9.88	2540	1600	4220
^{238}U	µg/g	bdl	bdl	0.0299	bdl	bdl	1.43	2.43	1.60

File		yn50_apdz_44-11	yn50_aplz_44-13	yn50_aplz_44-14	yn50_aplz_44-9	yn50_aplz_44-10	bh224_aplz_24-10	bh224_aplz_24-11	bh224_aplz_24-12
CL Colour		dark blue zone	light blue zone	light blue zone	light blue zone	light blue zone	pink core	pink core	pink core
λ_0		5.95	6.11	6.16	6.04	5.88	7.77	7.66	7.89
λ_1		3.40	6.97	4.22	5.38	5.64	25.2	24.7	27.7
λ_2		-271	-271	-328	-268	-291	-247	-271	-241
λ_3		159	428	525	627	608	-1720	-1690	-1720
λ_4		7320	5040	11200	6180	1640	-1070	-2510	-1510
1σ error									
SiO_2	wt.%	bdl	bdl	bdl	bdl	bdl	bdl	bdl	bdl
TiO_2	wt.%	bdl	bdl	bdl	bdl	bdl	bdl	0.000922	bdl
Al_2O_3	wt.%	bdl	bdl	bdl	bdl	bdl	bdl	bdl	bdl
MnO	wt.%	0.00093	0.00046	0.020	0.00067	0.00049	0.0036	0.0012	0.0019
CaO	wt.%	2.75	1.20	2.73	1.31	1.41	5.34	4.73	2.09
P_2O_5	wt.%	2.28	1.72	2.25	1.18	1.73	4.76	4.31	1.87
^{66}Zn	µg/g	bdl	bdl	bdl	bdl	bdl	bdl	bdl	bdl
^{75}As	µg/g	bdl	1.57	bdl	bdl	bdl	10.4	12.0	8.47
^{85}Rb	µg/g	bdl	bdl	0.160	bdl	bdl	bdl	bdl	bdl
^{88}Sr	µg/g	228	117	558	149	205	370	337	151
^{89}Y	µg/g	27.7	10.1	32.4	12.0	7.52	168	112	65.0
^{90}Zr	µg/g	bdl	bdl	bdl	bdl	bdl	0.52	0.87	bdl
^{93}Nb	µg/g	bdl	0.043	0.15	0.021	bdl	0.12	0.23	0.10
^{118}Sn	µg/g	bdl	bdl	bdl	bdl	bdl	bdl	bdl	bdl
^{133}Cs	µg/g	bdl	0.018	0.024	0.017	0.019	0.086	bdl	0.051
^{137}Ba	µg/g	0.43	0.42	2.34	0.64	1.25	39.9	11.0	2.05
^{139}La	µg/g	1.69	1.81	1.50	2.29	0.82	280	146	169
^{140}Ce	µg/g	13.7	8.70	7.68	10.3	6.26	1520	870	855
^{141}Pr	µg/g	3.16	1.89	2.27	2.06	0.754	355	231	177
^{143}Nd	µg/g	21.7	11.7	18.2	11.5	10.6	2090	1360	851
^{147}Sm	µg/g	13.4	4.97	10.8	4.57	3.34	315	234	121
^{151}Eu	µg/g	3.93	1.81	5.18	1.82	0.94	69.3	49.9	27.0
^{157}Gd	µg/g	21.7	5.31	20.8	6.92	2.77	172	125	65.0
^{159}Tb	µg/g	2.81	0.90	3.19	1.08	0.39	18.9	14.0	7.61
^{163}Dy	µg/g	11.5	3.99	13.8	4.51	1.62	70.6	51.1	27.7
^{165}Ho	µg/g	1.27	0.63	1.70	0.55	0.35	8.05	5.63	3.14
^{167}Er	µg/g	2.26	1.05	2.91	1.18	0.92	13.3	9.11	4.93
^{169}Tm	µg/g	0.23	0.077	0.23	0.12	0.13	1.10	0.68	0.39

File		yn50_apdz_44-11	yn50_aplz_44-13	yn50_aplz_44-14	yn50_aplz_44-9	yn50_aplz_44-10	bh224_aplz_24-10	bh224_aplz_24-11	bh224_aplz_24-12
CL Colour		dark blue zone	light blue zone	light blue zone	light blue zone	light blue zone	pink core	pink core	pink core
^{171}Yb	µg/g	0.99	0.67	1.26	0.62	0.32	6.11	3.27	2.21
^{175}Lu	µg/g	0.14	0.067	0.11	0.054	0.063	0.75	0.38	0.31
^{178}Hf	µg/g	bdl	bdl	0.014	bdl	bdl	bdl	0.054	bdl
^{181}Ta	µg/g	bdl	bdl	bdl	bdl	bdl	0.017	bdl	bdl
^{208}Pb	µg/g	0.73	0.45	0.72	0.32	0.23	42.0	17.0	34.2
^{232}Th	µg/g	0.023	0.033	1.76	0.37	0.54	423	187	374
^{238}U	µg/g	bdl	bdl	0.014	bdl	bdl	0.16	0.31	0.15
Detection Limit									
SiO_2	wt.%	1.51	1.32	1.41	1.07	1.49	6.97	6.60	5.34
TiO_2	wt.%	0.000496	0.000414	0.000445	0.000406	0.000495	0.00204	0.00177	0.00146
Al_2O_3	wt.%	0.00232	0.00203	0.00222	0.00187	0.00223	0.0105	0.0107	0.00829
MnO	wt.%	0.000134	0.000115	0.000128	0.000108	0.000124	0.000559	0.000565	0.000437
CaO	wt.%	0.0422	0.0371	0.0413	0.0360	0.0438	0.201	0.185	0.149
P_2O_5	wt.%	0.0140	0.0124	0.0136	0.0128	0.0141	0.0620	0.0595	0.0486
^{66}Zn	µg/g	4.94	4.13	4.46	3.57	4.9	19.3	18.0	14.0
^{75}As	µg/g	4.46	3.59	4.18	3.50	4.30	18.1	16.9	13.8
^{85}Rb	µg/g	0.143	0.141	0.152	0.117	0.158	0.684	0.682	0.587
^{88}Sr	µg/g	0.0655	0.0619	0.0773	0.0513	0.0792	0.273	0.290	0.225
^{89}Y	µg/g	0.0714	0.0604	0.0646	0.0484	0.0693	0.276	0.284	0.192
^{90}Zr	µg/g	0.162	0.134	0.147	0.123	0.151	0.667	0.740	0.454
^{93}Nb	µg/g	0.0166	0.0441	0.0160	0.0268	0.0459	0.137	0.129	0.0388
^{118}Sn	µg/g	0.424	0.357	0.350	0.322	0.364	1.63	1.65	1.25
^{133}Cs	µg/g	0.0320	0.0275	0.0198	0.0189	0.0291	0.109	0.110	0.0651
^{137}Ba	µg/g	0.133	0.113	0.127	0.103	0.302	0.623	0.478	0.561
^{139}La	µg/g	0.00796	0.0170	0.0159	0.0129	0.0188	0.0293	0.0600	0.0442
^{140}Ce	µg/g	0.0173	0.00750	0.0200	0.0166	0.0114	0.0807	0.0760	0.0654
^{141}Pr	µg/g	0.0115	0.0172	0.0145	0.0105	0.0167	0.0520	0.0490	0.0408
^{143}Nd	µg/g	0.117	0.0989	0.111	0.166	0.131	0.205	0.192	0.536
^{147}Sm	µg/g	0.0965	0.0817	0.111	0.0921	0.127	0.452	0.159	0.256
^{151}Eu	µg/g	0.0285	0.0310	0.0271	0.0219	0.0375	0.0915	0.115	0.101
^{157}Gd	µg/g	0.102	0.105	0.132	0.0873	0.103	0.349	0.368	0.384
^{159}Tb	µg/g	0.0151	0.0137	0.0109	0.0129	0.0166	0.0513	0.0592	0.0403
^{163}Dy	µg/g	0.0550	0.0466	0.0523	0.0525	0.0543	0.276	0.197	0.165
^{165}Ho	µg/g	0.0137	0.00591	0.0145	0.0130	0.0179	0.0635	0.0547	0.0447

File		yn50_apdz_44-11	yn50_aplz_44-13	yn50_aplz_44-14	yn50_aplz_44-9	yn50_aplz_44-10	bh224_aplz_24-10	bh224_aplz_24-11	bh224_aplz_24-12
CL Colour		dark blue zone	light blue zone	light blue zone	light blue zone	light blue zone	pink core	pink core	pink core
^{167}Er	µg/g	0.0603	0.0693	0.0573	0.0576	0.0793	0.320	0.242	0.227
^{169}Tm	µg/g	0.0110	0.00562	0.0161	0.00830	0.0171	0.0646	0.0567	0.0386
^{171}Yb	µg/g	0.0806	0.0968	0.131	0.0909	0.125	0.405	0.446	0.358
^{175}Lu	µg/g	0.0304	0.0142	0.0113	0.00450	0.0213	0.0648	0.0769	0.0367
^{178}Hf	µg/g	0.0588	0.0857	0.0221	0.0531	0.0543	0.183	0.144	0.170
^{181}Ta	µg/g	0.0194	0.0183	0.0152	0.0152	0.0105	0.0277	0.0259	0.0520
^{208}Pb	µg/g	0.0562	0.0423	0.0613	0.0285	0.0586	0.209	0.197	0.0937
^{232}Th	µg/g	0.0244	0.0162	0.0152	0.0153	0.0234	0.0584	0.0251	0.0579
^{238}U	µg/g	0.0177	0.0190	0.0195	0.0138	0.0157	0.0571	0.0536	0.0447

File		bh224_aplz_24-13	bh224_aplz_24-14	bh224_aplz_24-19	bh224_aplz_24-20	bh224_aplz_24-21	bh224_apdr_24-2	bh224_apdr_24-4	bh224_apdr_24-5
CL Colour		pink core	pink core	pink core	pink core	pink core	indigo rim	indigo rim	indigo rim
SiO_2	wt.%	bdl	bdl	bdl	bdl	bdl	bdl	bdl	bdl
TiO_2	wt.%	bdl	0.0029	bdl	bdl	bdl	bdl	bdl	bdl
Al_2O_3	wt.%	0.090	bdl	bdl	0.15	bdl	bdl	bdl	bdl
MnO	wt.%	0.0470	0.0559	0.0415	0.0544	0.0205	0.0468	0.0453	0.0479
CaO	wt.%	52.5	52.5	52.5	52.5	52.5	56.0	56.0	56.0
P_2O_5	wt.%	48.4	47.9	49.2	50.1	48.1	52.9	51.2	50.7
^{66}Zn	µg/g	bdl	20.0	bdl	bdl	bdl	bdl	bdl	bdl
^{75}As	µg/g	42.3	35.3	43.3	64.4	48.6	bdl	bdl	bdl
^{85}Rb	µg/g	bdl	0.704	0.671	5.54	bdl	bdl	bdl	bdl
^{88}Sr	µg/g	5150	4710	4220	5100	3820	2990	2470	2440
^{89}Y	µg/g	1060	940	1190	1280	1280	488	804	489
^{90}Zr	µg/g	18.1	bdl	bdl	36.8	bdl	bdl	bdl	bdl
^{93}Nb	µg/g	1.17	0.619	0.505	3.34	1.04	bdl	bdl	bdl
^{118}Sn	µg/g	bdl	bdl	bdl	bdl	bdl	bdl	bdl	bdl
^{133}Cs	µg/g	0.36	0.23	0.23	bdl	0.098	bdl	bdl	bdl
^{137}Ba	µg/g	330	18.4	36.3	209	11.4	1.75	2.91	bdl
^{139}La	µg/g	2130	1630	1410	2500	1220	30.8	72.3	36.6
^{140}Ce	µg/g	10700	8700	8900	14800	8580	187	437	227
^{141}Pr	µg/g	2370	2130	2410	3080	2520	55.5	124	68.0
^{143}Nd	µg/g	12900	10600	13700	16600	15500	412	912	509
^{147}Sm	µg/g	1870	1430	2330	2370	2920	161	297	183
^{151}Eu	µg/g	415	311	546	514	677	47.5	90.6	55.0
^{157}Gd	µg/g	1070	793	1400	1280	1710	192	363	225
^{159}Tb	µg/g	111	93.8	149	138	179	27.1	51.9	31.8
^{163}Dy	µg/g	418	377	546	531	644	130	239	139
^{165}Ho	µg/g	48.8	43.7	59.4	60.5	66.8	16.9	30.2	17.9
^{167}Er	µg/g	80.5	73.8	90.2	103	97.6	32.0	57.1	31.6
^{169}Tm	µg/g	6.13	6.47	7.33	8.13	7.52	2.79	4.59	2.67
^{171}Yb	µg/g	30.3	32.3	34.7	43.1	33.9	14.8	19.6	12.5
^{175}Lu	µg/g	3.67	3.48	4.12	4.58	3.96	1.50	2.38	1.48
^{178}Hf	µg/g	1.04	bdl	bdl	1.89	0.18	0.089	bdl	bdl
^{181}Ta	µg/g	bdl	bdl	0.049	bdl	bdl	bdl	bdl	bdl
^{208}Pb	µg/g	642	293	176	569	161	10.1	8.13	7.50
^{232}Th	µg/g	4840	2560	1670	6570	1370	4.24	0.70	0.063
^{238}U	µg/g	13.1	1.06	1.20	19.8	0.55	bdl	bdl	bdl

File		bh224_aplz_24-13	bh224_aplz_24-14	bh224_aplz_24-19	bh224_aplz_24-20	bh224_aplz_24-21	bh224_apdr_24-2	bh224_apdr_24-4	bh224_apdr_24-5
CL Colour		pink core	pink core	pink core	pink core	pink core	indigo rim	indigo rim	indigo rim
λ_0		7.78	7.64	7.87	8.02	7.95	5.73	6.36	5.82
λ_1		27.7	26.5	25.5	27.6	25.2	6.47	8.89	8.04
λ_2		-251	-236	-298	-247	-335	-303	-310	-319
λ_3		-1650	-1770	-1820	-1810	-1840	-426	-306	-432
λ_4		444	-7040	1210	-3960	2390	3580	930	4970
1σ error									
SiO_2	wt.%	bdl	bdl	bdl	bdl	bdl	bdl	bdl	bdl
TiO_2	wt.%	bdl	0.0014	bdl	bdl	0.0019	bdl	bdl	bdl
Al_2O_3	wt.%	0.019	bdl	bdl	0.014	bdl	bdl	bdl	bdl
MnO	wt.%	0.0031	0.0042	0.0024	0.0017	0.0007	0.0023	0.0017	0.0019
CaO	wt.%	5.31	2.01	2.60	1.83	2.32	1.73	2.33	2.51
P_2O_5	wt.%	3.72	1.59	2.47	2.07	1.93	1.66	2.16	1.88
^{66}Zn	µg/g	bdl	9.44	bdl	bdl	bdl	bdl	bdl	bdl
^{75}As	µg/g	13.6	9.65	7.25	13.4	7.84	bdl	bdl	bdl
^{85}Rb	µg/g	bdl	0.327	0.257	4.60	bdl	bdl	bdl	bdl
^{88}Sr	µg/g	297	146	208	175	119	63.1	81.2	101
^{89}Y	µg/g	139	34.7	49.9	40.8	79.3	13.4	34.6	20.5
^{90}Zr	µg/g	3.70	bdl	bdl	4.00	bdl	bdl	bdl	bdl
^{93}Nb	µg/g	0.202	0.207	0.251	0.996	0.203	bdl	bdl	bdl
^{118}Sn	µg/g	bdl	bdl	bdl	bdl	bdl	bdl	bdl	bdl
^{133}Cs	µg/g	0.091	0.097	0.063	bdl	0.049	bdl	bdl	bdl
^{137}Ba	µg/g	51.9	2.91	8.56	27.6	1.21	0.45	0.56	bdl
^{139}La	µg/g	410	81	92.2	83.4	40.3	1.73	3.24	1.80
^{140}Ce	µg/g	2010	427	491	1010	328	8.61	17.6	9.64
^{141}Pr	µg/g	442	95.8	95.5	214	93.5	2.00	4.94	2.69
^{143}Nd	µg/g	2490	451	392	1180	632	17.5	42.2	22.1
^{147}Sm	µg/g	339	63.0	51.5	146	163	6.65	15.3	8.28
^{151}Eu	µg/g	71.6	12.6	11.9	32.9	38.3	1.76	3.98	2.18
^{157}Gd	µg/g	186	33.4	24.9	57.6	100	7.13	16.6	9.56
^{159}Tb	µg/g	16.8	3.34	3.27	6.29	10.6	1.05	2.19	1.37
^{163}Dy	µg/g	59.3	13.5	15.6	17.5	38.3	4.64	11.9	6.57
^{165}Ho	µg/g	6.20	1.40	2.32	1.64	3.93	0.57	1.45	0.76
^{167}Er	µg/g	10.2	2.71	4.16	3.62	5.76	1.09	2.38	1.52
^{169}Tm	µg/g	0.74	0.263	0.48	0.35	0.471	0.15	0.21	0.15

File		bh224_aplz_24-13	bh224_aplz_24-14	bh224_aplz_24-19	bh224_aplz_24-20	bh224_aplz_24-21	bh224_apdr_24-2	bh224_apdr_24-4	bh224_apdr_24-5
CL Colour		pink core	pink core	pink core	pink core	pink core	indigo rim	indigo rim	indigo rim
^{171}Yb	µg/g	3.68	1.28	2.05	2.36	2.01	0.60	1.28	0.62
^{175}Lu	µg/g	0.40	0.171	0.29	0.42	0.25	0.090	0.11	0.069
^{178}Hf	µg/g	0.23	bdl	bdl	0.40	0.063	bdl	bdl	bdl
^{181}Ta	µg/g	bdl	bdl	0.0271	bdl	bdl	bdl	bdl	bdl
^{208}Pb	µg/g	108	11.1	15.7	51.6	5.31	0.65	0.59	0.38
^{232}Th	µg/g	907	171	141	526	41.3	1.32	0.080	0.031
^{238}U	µg/g	1.10	0.12	0.12	1.20	0.049	bdl	bdl	bdl
Detection Limit									
SiO_2	wt.%	7.94	6.22	5.77	10.1	6.06	6.10	5.39	5.40
TiO_2	wt.%	0.00244	0.00180	0.00146	0.00327	0.00152	0.00168	0.00151	0.00137
Al_2O_3	wt.%	0.0114	0.0104	0.00924	0.0143	0.00983	0.00868	0.00829	0.00940
MnO	wt.%	0.000598	0.000557	0.000480	0.000752	0.000507	0.000475	0.000450	0.000501
CaO	wt.%	0.200	0.185	0.160	0.275	0.184	0.163	0.152	0.161
P_2O_5	wt.%	0.0664	0.0607	0.0507	0.0813	0.0584	0.0558	0.0500	0.0574
^{66}Zn	µg/g	20.6	17.4	15.5	24.5	16.0	17.3	14.3	16.7
^{75}As	µg/g	20.1	17.6	14.2	24.2	15.4	15.5	13.9	16.0
^{85}Rb	µg/g	0.675	0.614	0.484	0.914	0.616	0.558	0.468	0.571
^{88}Sr	µg/g	0.334	0.278	0.241	0.408	0.287	0.261	0.222	0.281
^{89}Y	µg/g	0.310	0.268	0.198	0.467	0.223	0.244	0.240	0.257
^{90}Zr	µg/g	0.889	0.618	0.546	1.04	0.602	0.510	0.526	0.585
^{93}Nb	µg/g	0.168	0.158	0.106	0.266	0.0353	0.0660	0.0552	0.0344
^{118}Sn	µg/g	1.90	1.43	1.22	2.09	1.41	1.34	1.33	1.32
^{133}Cs	µg/g	0.159	0.121	0.063	0.166	0.0854	0.0896	0.105	0.0743
^{137}Ba	µg/g	0.623	0.733	0.156	0.978	0.396	0.564	0.589	0.387
^{139}La	µg/g	0.0782	0.0289	0.0196	0.151	0.0162	0.0591	0.0258	0.0161
^{140}Ce	µg/g	0.0467	0.0299	0.0506	0.0862	0.0512	0.0320	0.0618	0.0640
^{141}Pr	µg/g	0.0638	0.0418	0.0454	0.100	0.0132	0.0577	0.0550	0.0131
^{143}Nd	µg/g	0.548	0.424	0.495	0.861	0.114	0.495	0.419	0.620
^{147}Sm	µg/g	0.262	0.167	0.284	0.711	0.288	0.461	0.346	0.281
^{151}Eu	µg/g	0.133	0.157	0.069	0.190	0.0846	0.101	0.0850	0.0827
^{157}Gd	µg/g	0.427	0.402	0.429	0.857	0.271	0.387	0.327	0.305
^{159}Tb	µg/g	0.0860	0.0543	0.0325	0.112	0.0320	0.0570	0.0208	0.0391
^{163}Dy	µg/g	0.225	0.199	0.133	0.456	0.163	0.233	0.233	0.221
^{165}Ho	µg/g	0.0792	0.0235	0.0573	0.107	0.0403	0.0576	0.0449	0.0548

File		bh224_aplz_24-13	bh224_aplz_24-14	bh224_aplz_24-19	bh224_aplz_24-20	bh224_aplz_24-21	bh224_apdr_24-2	bh224_apdr_24-4	bh224_apdr_24-5
CL Colour		pink core	pink core	pink core	pink core	pink core	indigo rim	indigo rim	indigo rim
^{167}Er	µg/g	0.281	0.315	0.176	0.498	0.205	0.235	0.179	0.223
^{169}Tm	µg/g	0.0602	0.0394	0.0427	0.120	0.0439	0.0505	0.0426	0.0374
^{171}Yb	µg/g	0.604	0.341	0.314	0.692	0.280	0.288	0.382	0.275
^{175}Lu	µg/g	0.0808	0.0693	0.0507	0.109	0.0473	0.0588	0.0356	0.0403
^{178}Hf	µg/g	0.330	0.210	0.159	0.317	0.142	0.0889	0.143	0.160
^{181}Ta	µg/g	0.0739	0.0571	0.0462	0.116	0.0468	0.0755	0.0639	0.0587
^{208}Pb	µg/g	0.236	0.1555	0.15	0.317	0.255	0.127	0.209	0.132
^{232}Th	µg/g	0.0714	0.0670	0.0177	0.136	0.0146	0.0287	0.0551	0.0570
^{238}U	µg/g	0.0868	0.0743	0.0580	0.146	0.0648	0.0643	0.0666	0.104

File		bh224_apdr_24-6	bh224_apdr_24-8	bh224_apdr_24-9	bh224_apdr_24-16	bh224_apdr_24-17	bh224_apdr_24-18	bh224_apdr_24-1	bh224_apdr_24-14
CL Colour		indigo rim	indigo rim	indigo rim	indigo rim	indigo rim	indigo rim	indigo rim	indigo rim
SiO_2	wt.%	bdl	bdl	bdl	bdl	bdl	bdl	bdl	bdl
TiO_2	wt.%	bdl	bdl	bdl	bdl	bdl	bdl	bdl	bdl
Al_2O_3	wt.%	bdl	bdl	bdl	9.94	bdl	bdl	bdl	bdl
MnO	wt.%	0.0440	0.0477	0.0490	0.0564	0.0421	0.0493	0.0451	0.0474
CaO	wt.%	56.0	56.0	56.0	56.0	56.0	56.0	56.0	55.6
P_2O_5	wt.%	49.1	45.4	50.6	47.6	52.7	50.5	56.5	48.5
^{66}Zn	µg/g	bdl	bdl	bdl	bdl	bdl	bdl	bdl	bdl
^{75}As	µg/g	bdl	bdl	bdl	bdl	bdl	bdl	bdl	bdl
^{85}Rb	µg/g	bdl	bdl	bdl	171	bdl	bdl	bdl	bdl
^{88}Sr	µg/g	2360	3570	2620	4260	3350	2520	2580	6280
^{89}Y	µg/g	574	458	437	496	534	446	545	698
^{90}Zr	µg/g	bdl	bdl	bdl	34.5	bdl	1.40	bdl	bdl
^{93}Nb	µg/g	bdl	0.120	bdl	3.80	bdl	0.190	bdl	bdl
^{118}Sn	µg/g	bdl	bdl	bdl	bdl	bdl	bdl	bdl	bdl
^{133}Cs	µg/g	bdl	bdl	bdl	0.978	bdl	bdl	bdl	bdl
^{137}Ba	µg/g	bdl	20.3	3.03	16500	0.81	2.45	bdl	17.9
^{139}La	µg/g	40.6	30.3	32.5	65.4	34.2	32.6	39.3	68.4
^{140}Ce	µg/g	259	175	201	274	217	195	247	619
^{141}Pr	µg/g	79.8	55.8	58.8	69.2	60.0	57.2	72.2	211
^{143}Nd	µg/g	582	414	458	468	500	435	540	1660
^{147}Sm	µg/g	218	155	165	156	184	163	192	427
^{151}Eu	µg/g	63.6	51.4	48.9	50.1	56.6	47.8	61.0	114
^{157}Gd	µg/g	260	185	201	182	228	188	240	380
^{159}Tb	µg/g	37.4	28.1	28.9	28.2	31.9	25.9	34.1	52.2
^{163}Dy	µg/g	168	129	125	147	146	119	158	230
^{165}Ho	µg/g	21.8	17.1	16.3	18.8	19.0	15.8	20.5	29.6
^{167}Er	µg/g	39.0	31.7	29.6	36.2	32.7	28.9	36.2	48.0
^{169}Tm	µg/g	3.47	2.74	2.52	3.11	2.82	2.66	2.93	4.07
^{171}Yb	µg/g	15.6	13.3	11.2	14.1	13.8	12.3	14.0	19.6
^{175}Lu	µg/g	1.75	1.61	1.27	1.58	1.72	1.34	1.57	2.25
^{178}Hf	µg/g	bdl	bdl	bdl	2.18	bdl	0.0937	bdl	bdl
^{181}Ta	µg/g	bdl	bdl	bdl	bdl	bdl	bdl	bdl	bdl
^{208}Pb	µg/g	7.02	11.3	8.51	1740	11.0	12.6	6.39	20.2
^{232}Th	µg/g	bdl	24.3	0.59	135	0.30	44.8	0.082	11.7
^{238}U	µg/g	bdl	0.26	bdl	22.1	bdl	0.285	bdl	bdl

File		bh224_apdr_24-6	bh224_apdr_24-8	bh224_apdr_24-9	bh224_apdr_24-16	bh224_apdr_24-17	bh224_apdr_24-18	bh224_apdr_24-1	bh224_apdr_24-14
CL Colour		indigo rim	indigo rim	indigo rim	indigo rim	indigo rim	indigo rim	indigo rim	indigo rim
λ_0		5.99	5.72	5.71	5.88	5.83	5.69	5.90	6.47
λ_1		7.50	6.36	7.88	8.87	7.01	7.56	7.79	11.6
λ_2		-319	-304	-321	-262	-315	-307	-318	-337
λ_3		-426	-445	-358	171	-462	-459	-322	-1470
λ_4		2410	4770	3630	1830	7370	3910	2430	-4770
1σ error									
SiO_2	wt.%	bdl	bdl	bdl	bdl	bdl	bdl	bdl	bdl
TiO_2	wt.%	bdl	bdl	bdl	bdl	bdl	bdl	bdl	bdl
Al_2O_3	wt.%	bdl	bdl	bdl	0.484	bdl	0.0049	bdl	bdl
MnO	wt.%	0.0013	0.0015	0.0018	0.0043	0.0008	0.0015	0.0010	0.0013
CaO	wt.%	2.90	1.87	2.06	3.75	1.88	1.84	1.57	2.90
P_2O_5	wt.%	1.95	1.22	1.93	2.66	1.49	1.81	2.46	1.95
^{66}Zn	µg/g	bdl	bdl	bdl	bdl	bdl	bdl	bdl	bdl
^{75}As	µg/g	bdl	bdl	bdl	bdl	bdl	bdl	bdl	bdl
^{85}Rb	µg/g	bdl	bdl	bdl	7.40	bdl	bdl	bdl	bdl
^{88}Sr	µg/g	72.6	20.6	88.0	147	84.3	68.4	85.5	72.6
^{89}Y	µg/g	31.2	20.9	17.6	24.8	13.4	16.4	18.1	31.2
^{90}Zr	µg/g	bdl	bdl	bdl	5.02	bdl	0.32	bdl	bdl
^{93}Nb	µg/g	bdl	0.056	bdl	0.87	bdl	0.067	bdl	bdl
^{118}Sn	µg/g	bdl	bdl	bdl	bdl	bdl	bdl	bdl	bdl
^{133}Cs	µg/g	bdl	bdl	bdl	bdl	bdl	bdl	bdl	bdl
^{137}Ba	µg/g	bdl	3.33	0.80	769	0.33	0.70	bdl	bdl
^{139}La	µg/g	1.94	1.41	1.34	4.85	1.25	1.46	1.95	1.94
^{140}Ce	µg/g	14.2	4.57	6.26	17.0	8.04	8.27	11.2	14.2
^{141}Pr	µg/g	4.52	0.976	1.98	3.21	1.74	1.96	2.74	4.52
^{143}Nd	µg/g	29.2	14.6	15.5	28.9	20.3	15.8	15.5	29.2
^{147}Sm	µg/g	12.1	5.38	6.07	5.20	3.57	6.12	7.31	12.1
^{151}Eu	µg/g	2.58	1.00	1.55	2.49	2.84	1.84	1.75	2.58
^{157}Gd	µg/g	12.0	7.34	6.18	12.6	7.69	6.68	6.63	12.0
^{159}Tb	µg/g	1.83	0.69	0.94	1.24	1.19	1.06	1.20	1.83
^{163}Dy	µg/g	7.37	1.49	3.98	6.62	5.19	4.18	4.96	7.37
^{165}Ho	µg/g	0.90	0.60	0.58	0.90	0.41	0.52	0.59	0.90
^{167}Er	µg/g	2.18	1.65	1.18	3.34	0.68	1.17	1.33	2.18
^{169}Tm	µg/g	0.20	0.13	0.14	0.26	0.15	0.099	0.11	0.20

File		bh224_apdr_24-6	bh224_apdr_24-8	bh224_apdr_24-9	bh224_apdr_24-16	bh224_apdr_24-17	bh224_apdr_24-18	bh224_apdr_24-1	bh224_apdr_24-14
CL Colour		indigo rim	indigo rim	indigo rim	indigo rim	indigo rim	indigo rim	indigo rim	indigo rim
^{171}Yb	µg/g	1.01	0.92	0.84	2.33	0.85	0.58	0.53	1.01
^{175}Lu	µg/g	0.15	0.087	0.078	0.27	0.094	0.071	0.080	0.15
^{178}Hf	µg/g	bdl	bdl	bdl	0.57	bdl	0.044	bdl	bdl
^{181}Ta	µg/g	bdl	bdl	bdl	bdl	bdl	bdl	bdl	bdl
^{208}Pb	µg/g	0.49	1.29	0.43	97.8	0.67	0.85	0.40	0.49
^{232}Th	µg/g	bdl	3.03	0.13	9.47	0.088	1.47	0.022	bdl
^{238}U	µg/g	bdl	0.047	bdl	1.75	bdl	0.061	bdl	bdl
Detection Limit									
SiO_2	wt.%	5.86	7.04	5.38	28.2	6.63	5.59	3.30	7.82
TiO_2	wt.%	0.00202	0.00229	0.00175	0.00880	0.00195	0.00146	0.000892	0.00266
Al_2O_3	wt.%	0.00905	0.00951	0.00849	0.0395	0.00981	0.00921	0.00448	0.0122
MnO	wt.%	0.000507	0.000525	0.000461	0.00207	0.000527	0.000479	0.000261	0.000653
CaO	wt.%	0.157	0.180	0.151	0.737	0.170	0.159	0.089	0.223
P_2O_5	wt.%	0.0563	0.0559	0.0484	0.2453	0.0559	0.0518	0.0303	0.0726
^{66}Zn	µg/g	14.6	19.4	14.6	69.3	17.7	16.9	8.80	22.0
^{75}As	µg/g	16.1	17.3	14.4	69.8	16.4	15.5	8.12	20.2
^{85}Rb	µg/g	0.511	0.657	0.521	2.54	0.640	0.581	0.286	0.768
^{88}Sr	µg/g	0.269	0.335	0.223	1.10	0.253	0.269	0.159	0.333
^{89}Y	µg/g	0.255	0.315	0.253	1.03	0.255	0.225	0.118	0.363
^{90}Zr	µg/g	0.618	0.669	0.446	2.84	0.630	0.541	0.327	0.745
^{93}Nb	µg/g	0.137	0.108	0.0372	0.835	0.0804	0.0643	0.0347	0.0815
^{118}Sn	µg/g	1.68	1.58	1.37	6.28	1.53	1.14	0.710	1.91
^{133}Cs	µg/g	0.119	0.110	0.0912	0.427	0.107	0.0913	0.0465	0.163
^{137}Ba	µg/g	0.508	0.402	0.423	2.79	0.606	0.708	0.388	0.732
^{139}La	µg/g	0.0319	0.0505	0.0531	0.592	0.0371	0.0755	0.0162	0.0378
^{140}Ce	µg/g	0.0659	0.0934	0.0631	0.315	0.0785	0.0692	0.0428	0.0785
^{141}Pr	µg/g	0.0628	0.0693	0.0287	0.286	0.0621	0.0583	0.0337	0.0529
^{143}Nd	µg/g	0.723	0.551	0.372	1.36	0.595	0.470	0.215	0.729
^{147}Sm	µg/g	0.184	0.575	0.307	1.13	0.215	0.325	0.094	0.440
^{151}Eu	µg/g	0.109	0.145	0.0822	0.519	0.137	0.0505	0.0452	0.156
^{157}Gd	µg/g	0.388	0.494	0.233	2.191	0.416	0.264	0.257	0.597
^{159}Tb	µg/g	0.0571	0.0765	0.0343	0.282	0.0569	0.0451	0.0213	0.0680
^{163}Dy	µg/g	0.210	0.166	0.212	1.21	0.122	0.184	0.121	0.302
^{165}Ho	µg/g	0.0519	0.0773	0.0466	0.158	0.0525	0.0393	0.0250	0.0746

File		bh224_apdr_24-6	bh224_apdr_24-8	bh224_apdr_24-9	bh224_apdr_24-16	bh224_apdr_24-17	bh224_apdr_24-18	bh224_apdr_24-1	bh224_apdr_24-14
CL Colour		indigo rim	indigo rim	indigo rim	indigo rim	indigo rim	indigo rim	indigo rim	indigo rim
^{167}Er	µg/g	0.229	0.324	0.153	1.26	0.289	0.256	0.132	0.273
^{169}Tm	µg/g	0.0547	0.0766	0.0409	0.234	0.0435	0.0580	0.0302	0.0707
^{171}Yb	µg/g	0.401	0.481	0.273	1.54	0.365	0.378	0.174	0.429
^{175}Lu	µg/g	0.0452	0.0887	0.0354	0.306	0.0630	0.0514	0.0344	0.0702
^{178}Hf	µg/g	0.156	0.244	0.152	1.00	0.230	0.0846	0.105	0.185
^{181}Ta	µg/g	0.0906	0.0744	0.0403	0.2877	0.0350	0.0529	0.0392	0.0868
^{208}Pb	µg/g	0.164	0.107	0.0906	0.737	0.220	0.141	0.0788	0.220
^{232}Th	µg/g	0.0880	0.0911	0.0677	0.317	0.0335	0.0506	0.0382	0.0692
^{238}U	µg/g	0.069	0.081	0.0432	0.290	0.0746	0.0695	0.0375	0.0971

File		dmcy139_apdz_24-1	dmcy139_apdz_24-2	dmcy139_aplz_24-6	dmcy139_apdz_24-8	dmcy139_apdz_24-4	dmcy139_aplz_24-5	dmcy139_aplz_24-7
CL Colour		green rim	green rim	red rim	green rim	green rim	red rim	red rim
SiO_2	wt.%	bdl	bdl	bdl	bdl	bdl	bdl	bdl
TiO_2	wt.%	bdl	bdl	bdl	bdl	bdl	bdl	bdl
Al_2O_3	wt.%	bdl	bdl	bdl	bdl	bdl	0.011	0.010
MnO	wt.%	0.0585	0.0914	0.0929	0.0746	0.0838	0.0979	0.0805
CaO	wt.%	52.2	52.2	51.5	52.2	52.7	51.3	51.3
P_2O_5	wt.%	51.2	49.9	48.9	48.3	49.3	49.7	46.8
^{66}Zn	µg/g	bdl	bdl	50.6	bdl	bdl	bdl	bdl
^{75}As	µg/g	bdl	18.5	21.2	12.3	bdl	22.2	bdl
^{85}Rb	µg/g	bdl	bdl	bdl	bdl	bdl	bdl	bdl
^{88}Sr	µg/g	37100	39100	41600	37400	35300	43000	37000
^{89}Y	µg/g	166	152	159	176	167	81.7	141
^{90}Zr	µg/g	bdl	bdl	bdl	bdl	bdl	bdl	bdl
^{93}Nb	µg/g	bdl	bdl	bdl	bdl	bdl	bdl	bdl
^{118}Sn	µg/g	bdl	bdl	bdl	bdl	bdl	bdl	bdl
^{133}Cs	µg/g	bdl	bdl	bdl	bdl	bdl	bdl	bdl
^{137}Ba	µg/g	26.2	41.0	89.1	34.5	40.0	118	58.3
^{139}La	µg/g	62.2	96.9	213	50.3	63.7	279	107
^{140}Ce	µg/g	856	1200	2270	780	941	3020	1350
^{141}Pr	µg/g	323	418	771	319	367	952	525
^{143}Nd	µg/g	2400	2850	4990	2550	2860	5640	3670
^{147}Sm	µg/g	515	518	765	575	618	613	600
^{151}Eu	µg/g	98.0	85.8	121	101	109	83.5	95.8
^{157}Gd	µg/g	195	177	212	201	213	135	175
^{159}Tb	µg/g	14.0	12.0	13.4	13.7	13.9	7.30	11.6
^{163}Dy	µg/g	48.2	43.4	44.7	48.8	48.8	22.0	40.1
^{165}Ho	µg/g	6.30	5.33	6.02	6.36	6.16	2.60	5.24
^{167}Er	µg/g	14.2	12.6	12.4	13.7	14.3	5.81	10.9
^{169}Tm	µg/g	1.76	1.58	1.68	1.65	1.65	0.87	1.45
^{171}Yb	µg/g	10.3	9.70	10.7	11.1	10.9	6.76	10.1
^{175}Lu	µg/g	1.50	1.31	1.34	1.42	1.46	1.19	1.56
^{178}Hf	µg/g	bdl	0.067	bdl	bdl	bdl	bdl	bdl
^{181}Ta	µg/g	bdl	bdl	bdl	bdl	bdl	bdl	bdl
^{208}Pb	µg/g	79.8	71.5	48.0	56.0	60.1	34.6	37.2
^{232}Th	µg/g	2.23	2.66	8.13	1.60	1.78	5.50	3.02
^{238}U	µg/g	bdl	bdl	0.13	bdl	bdl	0.11	bdl

File		dmcy139_apdz_24-1	dmcy139_apdz_24-2	dmcy139_aplz_24-6	dmcy139_apdz_24-8	dmcy139_apdz_24-4	dmcy139_aplz_24-5	dmcy139_aplz_24-7
CL Colour		green rim	green rim	red rim	green rim	green rim	red rim	red rim
λ_0		5.93	5.96	6.23	5.92	5.98	5.93	6.01
λ_1		19.8	22.8	27.1	19.3	20.6	32.5	24.0
λ_2		-287	-260	-243	-306	-297	-191	-254
λ_3		-4680	-4780	-5040	-4950	-4970	-6270	-5410
λ_4		5610	3830	4530	5690	6790	13400	7660
1σ error								
SiO_2	wt.%	bdl	bdl	bdl	bdl	bdl	bdl	bdl
TiO_2	wt.%	bdl	bdl	bdl	bdl	bdl	bdl	bdl
Al_2O_3	wt.%	bdl	bdl	bdl	bdl	bdl	bdl	bdl
MnO	wt.%	0.0014	0.0018	0.0038	0.0022	0.0039	0.0073	0.0089
CaO	wt.%	1.95	1.47	1.50	1.92	1.74	4.97	5.94
P_2O_5	wt.%	1.59	1.46	1.74	1.94	1.33	5.02	5.07
^{66}Zn	µg/g	bdl	bdl	40.7	bdl	bdl	bdl	bdl
^{75}As	µg/g	bdl	6.58	7.22	6.57	bdl	6.91	bdl
^{85}Rb	µg/g	bdl	bdl	bdl	bdl	bdl	bdl	bdl
^{88}Sr	µg/g	1030	1270	1420	1500	814	4420	4310
^{89}Y	µg/g	6.96	6.07	6.74	6.24	6.91	8.10	10.2
^{90}Zr	µg/g	bdl	bdl	bdl	bdl	bdl	bdl	bdl
^{93}Nb	µg/g	bdl	bdl	bdl	bdl	bdl	bdl	bdl
^{118}Sn	µg/g	bdl	bdl	bdl	bdl	bdl	bdl	bdl
^{133}Cs	µg/g	bdl	bdl	0.073	bdl	bdl	bdl	bdl
^{137}Ba	µg/g	1.37	2.34	5.13	1.66	2.99	10.7	9.15
^{139}La	µg/g	1.62	1.84	14.3	2.62	2.05	29.1	21.1
^{140}Ce	µg/g	21.5	20.2	147	33.9	28.4	264	247
^{141}Pr	µg/g	10.6	8.51	43.6	13.3	11.4	95.0	92.9
^{143}Nd	µg/g	91.9	78.1	262.6	96.2	93.2	599	601
^{147}Sm	µg/g	24.0	16.0	34.4	22.0	26.5	69.1	76.4
^{151}Eu	µg/g	4.54	3.06	4.92	3.84	4.30	9.01	10.5
^{157}Gd	µg/g	7.66	6.25	9.06	8.25	8.16	15.7	16.7
^{159}Tb	µg/g	0.68	0.45	0.63	0.49	0.50	0.90	0.94
^{163}Dy	µg/g	2.60	1.60	2.48	1.86	1.83	2.52	2.92
^{165}Ho	µg/g	0.25	0.20	0.28	0.26	0.30	0.29	0.44
^{167}Er	µg/g	0.73	0.70	0.78	0.59	0.54	0.64	0.82
^{169}Tm	µg/g	0.12	0.091	0.13	0.094	0.12	0.097	0.12

File		dmcy139_apdz_24-1	dmcy139_apdz_24-2	dmcy139_aplz_24-6	dmcy139_apdz_24-8	dmcy139_apdz_24-4	dmcy139_aplz_24-5	dmcy139_aplz_24-7
CL Colour		green rim	green rim	red rim	green rim	green rim	red rim	red rim
^{171}Yb	µg/g	0.79	0.50	0.64	0.55	0.69	0.74	1.10
^{175}Lu	µg/g	0.092	0.091	0.091	0.066	0.090	0.14	0.19
^{178}Hf	µg/g	bdl	0.032	bdl	bdl	bdl	bdl	bdl
^{181}Ta	µg/g	bdl	bdl	bdl	bdl	bdl	bdl	bdl
^{208}Pb	µg/g	2.28	2.29	1.18	2.31	2.97	2.41	1.57
^{232}Th	µg/g	0.15	0.17	0.83	0.082	0.17	0.68	0.35
^{238}U	µg/g	bdl	bdl	0.024	bdl	bdl	0.029	bdl
Detection Limit								
SiO_2	wt.%	5.26	5.23	5.16	5.19	5.35	8.11	6.83
TiO_2	wt.%	0.00149	0.00151	0.00175	0.00129	0.00164	0.00226	0.00200
Al_2O_3	wt.%	0.00772	0.00860	0.00855	0.00807	0.00922	0.0115	0.0105
MnO	wt.%	0.000395	0.000439	0.000430	0.000414	0.000474	0.000595	0.000533
CaO	wt.%	0.136	0.153	0.147	0.122	0.160	0.202	0.169
P_2O_5	wt.%	0.0455	0.0472	0.0469	0.0458	0.0514	0.0654	0.0569
^{66}Zn	µg/g	13.3	13.8	13.8	12.8	15.6	17.4	16.8
^{75}As	µg/g	12.4	13.8	13.1	11.9	14.4	17.0	15.8
^{85}Rb	µg/g	0.447	0.500	0.490	0.478	0.461	0.651	0.618
^{88}Sr	µg/g	0.149	0.194	0.221	0.210	0.210	0.252	0.266
^{89}Y	µg/g	0.175	0.203	0.169	0.168	0.176	0.294	0.266
^{90}Zr	µg/g	0.475	0.551	0.572	0.384	0.521	0.675	0.556
^{93}Nb	µg/g	0.110	0.0461	0.104	0.0291	0.0470	0.0765	0.129
^{118}Sn	µg/g	1.13	1.18	1.09	1.07	1.36	1.59	1.38
^{133}Cs	µg/g	0.0693	0.0705	0.0922	0.0754	0.0846	0.138	0.0819
^{137}Ba	µg/g	0.332	0.169	0.379	0.497	0.547	0.804	0.468
^{139}La	µg/g	0.0209	0.0212	0.0220	0.0133	0.0600	0.0922	0.0875
^{140}Ce	µg/g	0.0215	0.0218	0.0684	0.0575	0.0502	0.0700	0.0606
^{141}Pr	µg/g	0.0510	0.0396	0.0327	0.0354	0.0397	0.0285	0.0411
^{143}Nd	µg/g	0.147	0.341	0.409	0.266	0.151	0.573	0.560
^{147}Sm	µg/g	0.292	0.347	0.276	0.0770	0.283	0.473	0.341
^{151}Eu	µg/g	0.0356	0.0827	0.0909	0.0738	0.0830	0.139	0.111
^{157}Gd	µg/g	0.369	0.221	0.318	0.324	0.433	0.412	0.436
^{159}Tb	µg/g	0.0502	0.0390	0.0428	0.0246	0.0440	0.0468	0.0523
^{163}Dy	µg/g	0.165	0.180	0.132	0.101	0.160	0.191	0.232
^{165}Ho	µg/g	0.0376	0.0172	0.0472	0.0422	0.0556	0.0706	0.0611

File		dmcy139_apdz_24-1	dmcy139_apdz_24-2	dmcy139_aplz_24-6	dmcy139_apdz_24-8	dmcy139_apdz_24-4	dmcy139_aplz_24-5	dmcy139_aplz_24-7
CL Colour		green rim	green rim	red rim	green rim	green rim	red rim	red rim
^{167}Er	µg/g	0.214	0.196	0.170	0.186	0.174	0.270	0.270
^{169}Tm	µg/g	0.0273	0.0372	0.0308	0.0367	0.0312	0.0577	0.0541
^{171}Yb	µg/g	0.303	0.363	0.226	0.270	0.274	0.382	0.424
^{175}Lu	µg/g	0.0517	0.0452	0.0332	0.0253	0.0533	0.0561	0.0485
^{178}Hf	µg/g	0.162	0.060	0.178	0.136	0.206	0.248	0.167
^{181}Ta	µg/g	0.0474	0.0564	0.0548	0.0125	0.0202	0.0329	0.0553
^{208}Pb	µg/g	0.119	0.158	0.0989	0.115	0.142	0.169	0.122
^{232}Th	µg/g	0.0450	0.0189	0.0196	0.0495	0.0677	0.0605	0.0708
^{238}U	µg/g	0.0468	0.0475	0.0462	0.0412	0.0594	0.0651	0.0649

File		dmcy139_aplz_24-9	dmcy139_aplz_24-19	dmcy139_aplz_24-3	dmcy138_apdz_44-1	dmcy138_apdz_44-2	dmcy138_apdz_44-4	dmcy138_apdz_44-7
CL Colour		red rim	red rim	red rim	blue-violet core	blue-violet core	blue-violet core	blue-violet core
SiO_2	wt.%	bdl	bdl	bdl	bdl	bdl	bdl	bdl
TiO_2	wt.%	bdl	bdl	bdl	bdl	bdl	bdl	bdl
Al_2O_3	wt.%	0.0082	0.0085	0.0091	0.0011	0.0012	0.0016	0.18
MnO	wt.%	0.0676	0.0726	0.0770	0.0427	0.0444	0.0592	0.0557
CaO	wt.%	51.3	51.3	51.3	54.7	54.7	54.7	54.7
P_2O_5	wt.%	42.6	48.0	50.4	46.5	46.1	47.9	48.6
^{66}Zn	µg/g	bdl	bdl	bdl	bdl	bdl	bdl	10.4
^{75}As	µg/g	bdl	bdl	15.8	11.8	13.6	9.50	11.2
^{85}Rb	µg/g	bdl	bdl	bdl	bdl	bdl	bdl	0.496
^{88}Sr	µg/g	39100	39700	42400	15100	15500	15900	16800
^{89}Y	µg/g	154	170	132	53.0	54.5	90.3	113
^{90}Zr	µg/g	bdl	bdl	bdl	bdl	bdl	bdl	bdl
^{93}Nb	µg/g	bdl	bdl	bdl	0.00830	bdl	bdl	0.0284
^{118}Sn	µg/g	bdl	bdl	bdl	bdl	bdl	bdl	0.976
^{133}Cs	µg/g	bdl	bdl	bdl	bdl	0.0181	bdl	bdl
^{137}Ba	µg/g	64.7	65.6	70.8	69.1	77.5	58.1	1200
^{139}La	µg/g	144	111	175	959	984	841	723
^{140}Ce	µg/g	1710	1360	1990	4090	4020	3610	2880
^{141}Pr	µg/g	580	475	689	763	742	682	620
^{143}Nd	µg/g	3830	3310	4330	3450	3290	3040	3040
^{147}Sm	µg/g	625	538	587	259	246	321	335
^{151}Eu	µg/g	101	88.8	89.6	34.5	33.6	49.4	55.5
^{157}Gd	µg/g	187	157	153	62.3	61.1	88.7	97.8
^{159}Tb	µg/g	11.8	12.4	9.82	4.50	4.32	7.02	8.05
^{163}Dy	µg/g	40.0	45.0	34.2	15.7	15.5	26.0	30.8
^{165}Ho	µg/g	5.54	6.03	4.29	2.27	2.33	3.65	4.28
^{167}Er	µg/g	12.3	14.2	10.5	5.40	5.58	8.91	10.7
^{169}Tm	µg/g	1.44	1.60	1.47	0.701	0.72	1.08	1.34
^{171}Yb	µg/g	10.5	10.7	9.75	4.86	5.09	7.60	8.87
^{175}Lu	µg/g	1.46	1.34	1.33	0.72	0.76	1.05	1.27
^{178}Hf	µg/g	bdl	bdl	bdl	bdl	bdl	bdl	bdl
^{181}Ta	µg/g	bdl	bdl	bdl	0.00390	bdl	bdl	bdl
^{208}Pb	µg/g	38.9	36.9	30.7	397	466	535	550
^{232}Th	µg/g	2.26	2.92	3.78	2160	2610	3730	4070
^{238}U	µg/g	0.09	bdl	0.11	1.3	1.5	1.4	1.6

File		dmcy139_aplz_24-9	dmcy139_aplz_24-19	dmcy139_aplz_24-3	dmcy138_apdz_44-1	dmcy138_apdz_44-2	dmcy138_apdz_44-4	dmcy138_apdz_44-7
CL Colour		red rim	red rim	red rim	blue-violet core	blue-violet core	blue-violet core	blue-violet core
λ_0		6.08	6.02	6.04	5.71	5.71	5.96	6.02
λ_1		25.2	23.3	27.0	36.6	36.3	32.7	30.5
λ_2		-242	-251	-218	-69	-60	-89	-99
λ_3		-51440	-4810	-5460	-4370	-4310	-3800	-3720
λ_4		6000	-2000	2400	2410	2130	4070	5330
1σ error								
SiO_2	wt.%	bdl	bdl	bdl	bdl	bdl	bdl	bdl
TiO_2	wt.%	bdl	bdl	bdl	bdl	bdl	bdl	0.00046
Al_2O_3	wt.%	bdl	bdl	bdl	bdl	bdl	bdl	0.026
MnO	wt.%	0.0043	0.0036	0.0025	0.00100	0.00093	0.0016	0.0014
CaO	wt.%	2.70	1.83	1.77	1.20	1.27	1.80	1.73
P_2O_5	wt.%	2.50	1.62	1.95	1.25	1.30	1.70	1.08
^{66}Zn	µg/g	bdl	bdl	bdl	bdl	bdl	bdl	2.85
^{75}As	µg/g	bdl	bdl	7.19	1.26	1.57	2.27	3.05
^{85}Rb	µg/g	bdl	bdl	bdl	bdl	bdl	bdl	0.12
^{88}Sr	µg/g	2450	1380	1620	319	335	354	296
^{89}Y	µg/g	5.73	4.47	2.23	1.02	0.939	1.50	2.40
^{90}Zr	µg/g	bdl	bdl	bdl	bdl	bdl	bdl	bdl
^{93}Nb	µg/g	bdl	bdl	bdl	0.00426	bdl	bdl	0.015
^{118}Sn	µg/g	bdl	bdl	bdl	bdl	bdl	bdl	bdl
^{133}Cs	µg/g	bdl	bdl	bdl	bdl	0.0089	bdl	bdl
^{137}Ba	µg/g	6.19	7.34	3.79	1.75	1.90	1.81	169
^{139}La	µg/g	19.8	12.8	11.83	17.53	18.82	28.76	20.39
^{140}Ce	µg/g	185	144	91.0	92.1	86.3	85.1	84.5
^{141}Pr	µg/g	53.0	39.0	31.5	14.1	12.0	16.0	16.5
^{143}Nd	µg/g	262	254.0	164.9	61.1	56.3	57.3	81.9
^{147}Sm	µg/g	21.7	24.7	17.6	4.51	4.34	6.81	8.47
^{151}Eu	µg/g	3.38	2.91	2.21	0.623	0.656	1.07	1.43
^{157}Gd	µg/g	6.07	4.75	3.17	1.25	1.22	1.59	1.90
^{159}Tb	µg/g	0.59	0.31	0.38	0.098	0.086	0.145	0.181
^{163}Dy	µg/g	2.27	1.30	0.74	0.35	0.36	0.60	0.57
^{165}Ho	µg/g	0.30	0.15	0.13	0.048	0.062	0.079	0.11
^{167}Er	µg/g	0.76	0.76	0.68	0.126	0.16	0.22	0.41
^{169}Tm	µg/g	0.10	0.07	0.067	0.024	0.021	0.037	0.064

File		dmcy139_aplz_24-9	dmcy139_aplz_24-19	dmcy139_aplz_24-3	dmcy138_apdz_44-1	dmcy138_apdz_44-2	dmcy138_apdz_44-4	dmcy138_apdz_44-7
CL Colour		red rim	red rim	red rim	blue-violet core	blue-violet core	blue-violet core	blue-violet core
^{171}Yb	µg/g	0.58	0.42	0.36	0.15	0.16	0.28	0.39
^{175}Lu	µg/g	0.083	0.064	0.066	0.022	0.019	0.043	0.047
^{178}Hf	µg/g	bdl	bdl	bdl	bdl	bdl	bdl	bdl
^{181}Ta	µg/g	bdl	bdl	bdl	0.00166	bdl	bdl	bdl
^{208}Pb	µg/g	2.10	1.19	1.48	10.2	8.67	11.9	11.3
^{232}Th	µg/g	0.451	0.45	0.27	57.4	47.4	68.9	99.8
^{238}U	µg/g	0.023	bdl	0.032	0.040	0.044	0.040	0.10
Detection Limit								
SiO_2	wt.%	5.51	5.72	5.95	0.96	0.93	1.30	1.94
TiO_2	wt.%	0.00105	0.00168	0.00189	0.000189	0.000316	0.000432	0.000524
Al_2O_3	wt.%	0.00818	0.00853	0.00908	0.00106	0.00125	0.00157	0.00247
MnO	wt.%	0.000402	0.000424	0.000463	0.0000795	0.0000933	0.000112	0.000166
CaO	wt.%	0.138	0.129	0.156	0.0256	0.0300	0.0365	0.0549
P_2O_5	wt.%	0.0437	0.0447	0.0504	0.0102	0.0117	0.0137	0.0199
^{66}Zn	µg/g	13.9	12.6	14.9	2.14	2.56	3.35	5.72
^{75}As	µg/g	13.3	13.0	14.7	2.32	2.50	3.67	5.35
^{85}Rb	µg/g	0.471	0.467	0.430	0.089	0.090	0.137	0.191
^{88}Sr	µg/g	0.204	0.223	0.273	0.0208	0.0198	0.0470	0.0836
^{89}Y	µg/g	0.200	0.216	0.149	0.0302	0.0380	0.0523	0.0925
^{90}Zr	µg/g	0.526	0.527	0.500	0.067	0.077	0.125	0.162
^{93}Nb	µg/g	0.181	0.147	0.130	0.00450	0.0187	0.0329	0.0256
^{118}Sn	µg/g	1.11	1.02	1.35	0.282	0.337	0.403	0.603
^{133}Cs	µg/g	0.0726	0.105	0.0936	0.0166	0.0136	0.0292	0.0355
^{137}Ba	µg/g	0.503	0.466	0.226	0.0176	0.0285	0.128	0.178
^{139}La	µg/g	0.0534	0.0482	0.0597	0.0022	0.0036	0.0160	0.0223
^{140}Ce	µg/g	0.0651	0.0495	0.0292	0.00229	0.00951	0.0196	0.0232
^{141}Pr	µg/g	0.0436	0.0439	0.0412	0.00582	0.00744	0.00756	0.0200
^{143}Nd	µg/g	0.209	0.467	0.419	0.0153	0.0637	0.0648	0.156
^{147}Sm	µg/g	0.447	0.340	0.346	0.0127	0.0206	0.109	0.0717
^{151}Eu	µg/g	0.0909	0.0820	0.114	0.0141	0.0156	0.0158	0.0479
^{157}Gd	µg/g	0.321	0.294	0.276	0.0391	0.0568	0.120	0.122
^{159}Tb	µg/g	0.0428	0.0327	0.0584	0.00745	0.00609	0.0153	0.0101
^{163}Dy	µg/g	0.153	0.158	0.166	0.00724	0.0247	0.0621	0.0870
^{165}Ho	µg/g	0.0433	0.0389	0.0410	0.00677	0.00615	0.00761	0.0216

File		dmcy139_aplz_24-9	dmcy139_aplz_24-19	dmcy139_aplz_24-3	dmcy138_apdz_44-1	dmcy138_apdz_44-2	dmcy138_apdz_44-4	dmcy138_apdz_44-7
CL Colour		red rim	red rim	red rim	blue-violet core	blue-violet core	blue-violet core	blue-violet core
^{167}Er	µg/g	0.210	0.192	0.296	0.0390	0.0272	0.0724	0.0888
^{169}Tm	µg/g	0.0484	0.0367	0.0387	0.00785	0.00588	0.00727	0.0174
^{171}Yb	µg/g	0.355	0.270	0.284	0.0326	0.0430	0.0805	0.151
^{175}Lu	µg/g	0.0484	0.0481	0.0493	0.00601	0.0111	0.0135	0.0299
^{178}Hf	µg/g	0.235	0.116	0.222	0.0208	0.0267	0.0410	0.0714
^{181}Ta	µg/g	0.0594	0.0548	0.0684	0.00211	0.00878	0.00892	0.03311
^{208}Pb	µg/g	0.130	0.149	0.124	0.0210	0.0261	0.0588	0.0667
^{232}Th	µg/g	0.0731	0.0509	0.0253	0.00218	0.00906	0.0159	0.0122
^{238}U	µg/g	0.0503	0.0587	0.0517	0.0022	0.0139	0.0139	0.0289

File		dmcy138_apdz_44-9	dmcy138_aplz_44-3	dmcy138_aplz_44-6	dmcy138_aplz_44-8	dmcy138_aplz_44-10	lefn1_apc_24-1	lefn1_apc_24-2
CL Colour		blue-violet core	pink rim	pink rim	pink rim	pink rim	green core	green core
SiO_2	wt.%	bdl	bdl	bdl	bdl	bdl	bdl	bdl
TiO_2	wt.%	bdl	bdl	bdl	bdl	bdl	bdl	bdl
Al_2O_3	wt.%	0.0017	0.0014	0.0015	0.0024	0.0025	0.0084	0.0094
MnO	wt.%	0.0443	0.0871	0.0709	0.0799	0.0906	0.129	0.145
CaO	wt.%	54.7	53.0	53.0	53.0	53.0	56.6	56.6
P_2O_5	wt.%	53.4	46.6	48.3	45.0	47.4	53.0	50.0
^{66}Zn	µg/g	bdl	bdl	bdl	bdl	4.80	bdl	bdl
^{75}As	µg/g	7.7	17.8	12.4	24.8	19.1	bdl	bdl
^{85}Rb	µg/g	bdl	bdl	bdl	bdl	bdl	bdl	bdl
^{88}Sr	µg/g	12300	35400	36300	34900	35600	480	490
^{89}Y	µg/g	55.3	212	268	230	263	1510	1890
^{90}Zr	µg/g	bdl	bdl	bdl	bdl	bdl	0.694	1.72
^{93}Nb	µg/g	0.022	bdl	bdl	bdl	bdl	0.112	0.179
^{118}Sn	µg/g	bdl	bdl	bdl	bdl	bdl	bdl	bdl
^{133}Cs	µg/g	bdl	0.0492	bdl	bdl	bdl	bdl	bdl
^{137}Ba	µg/g	53.0	67.3	39.1	73.0	79.0	8.50	12.1
^{139}La	µg/g	864	162	71.6	242	193	63.3	80.2
^{140}Ce	µg/g	3610	1720	823	2150	2130	312	420
^{141}Pr	µg/g	625	628	320	770	796	78.3	108
^{143}Nd	µg/g	2640	4360	2500	5050	5510	631	766
^{147}Sm	µg/g	204	690	565	800	861	283	362
^{151}Eu	µg/g	28.7	124	116	140	156	35.5	45.2
^{157}Gd	µg/g	51.8	202	214	239	262	356	432
^{159}Tb	µg/g	3.82	16.4	19.6	19.1	21.5	50.9	63.6
^{163}Dy	µg/g	14.6	62.1	79.7	69.4	79.3	304	379
^{165}Ho	µg/g	2.31	8.05	10.9	9.00	10.2	57.5	68.8
^{167}Er	µg/g	5.39	17.1	23.5	19.0	21.6	160	191
^{169}Tm	µg/g	0.70	1.96	2.76	2.25	2.61	19.0	23.8
^{171}Yb	µg/g	5.84	11.8	16.1	13.6	15.5	121	145
^{175}Lu	µg/g	0.940	1.51	2.11	1.72	1.82	16.1	19.6
^{178}Hf	µg/g	bdl	bdl	bdl	bdl	bdl	bdl	bdl
^{181}Ta	µg/g	bdl	bdl	0.0069	bdl	bdl	0.028	0.044
^{208}Pb	µg/g	382	33.0	53.8	31.0	25.3	7.46	8.82
^{232}Th	µg/g	2380	5.26	1.82	14.3	7.95	9.97	28.8
^{238}U	µg/g	1.04	0.086	0.058	0.089	0.12	8.53	16.8

File		dmcy138_apdz_44-9	dmcy138_aplz_44-3	dmcy138_aplz_44-6	dmcy138_aplz_44-8	dmcy138_aplz_44-10	lefn1_apc_24-1	lefn1_apc_24-2
CL Colour		blue-violet core	pink rim	pink rim	pink rim	pink rim	green core	green core
λ_0		5.64	6.27	6.20	6.44	6.50	6.80	7.02
λ_1		34.8	24.1	16.9	25.0	23.9	-2.63	-2.14
λ_2		-34	-259	-281	-246	-264	-170	-169
λ_3		-4400	-4530	-4040	-4370	-4520	-810	-874
λ_4		3340	-1480	170	1730	-3030	5260	3710
1σ error								
SiO_2	wt.%	bdl	bdl	bdl	bdl	bdl	bdl	bdl
TiO_2	wt.%	bdl	bdl	bdl	bdl	bdl	bdl	bdl
Al_2O_3	wt.%	bdl	bdl	bdl	bdl	0.00095	bdl	bdl
MnO	wt.%	0.0011	0.0020	0.0023	0.0015	0.0024	0.0044	0.0055
CaO	wt.%	1.28	1.34	1.02	1.24	1.26	1.43	2.11
P_2O_5	wt.%	2.74	1.42	1.41	1.66	1.43	2.56	1.36
^{66}Zn	µg/g	bdl	bdl	bdl	bdl	1.53	bdl	bdl
^{75}As	µg/g	1.72	1.42	1.66	3.73	2.36	bdl	bdl
^{85}Rb	µg/g	bdl	bdl	bdl	bdl	bdl	bdl	bdl
^{88}Sr	µg/g	292	870	1100	683	960	14.2	31.5
^{89}Y	µg/g	0.92	3.12	7.96	3.68	7.09	66.9	143
^{90}Zr	µg/g	bdl	bdl	bdl	bdl	bdl	0.34	0.34
^{93}Nb	µg/g	0.013	bdl	bdl	bdl	bdl	0.061	0.085
^{118}Sn	µg/g	bdl	bdl	bdl	bdl	bdl	bdl	bdl
^{133}Cs	µg/g	bdl	0.021	bdl	bdl	bdl	bdl	bdl
^{137}Ba	µg/g	1.09	1.87	1.98	5.05	2.85	1.28	1.66
^{139}La	µg/g	25.97	3.91	7.57	2.49	4.02	2.67	5.41
^{140}Ce	µg/g	98.1	39.7	49.6	51.9	62.8	13.0	29.51
^{141}Pr	µg/g	12.1	11.6	13.8	10.1	12.5	2.44	6.82
^{143}Nd	µg/g	44.6	82.3	89.6	69.9	130.5	28.1	52.7
^{147}Sm	µg/g	2.94	8.83	14.1	7.97	22.5	10.3	26.5
^{151}Eu	µg/g	0.661	2.01	3.01	2.24	3.87	1.07	2.16
^{157}Gd	µg/g	0.79	3.13	4.29	3.28	7.43	17.9	22.5
^{159}Tb	µg/g	0.098	0.29	0.37	0.33	0.65	2.34	4.03
^{163}Dy	µg/g	0.26	1.30	1.65	1.05	2.63	14.8	24.0
^{165}Ho	µg/g	0.047	0.12	0.24	0.125	0.30	2.41	4.68
^{167}Er	µg/g	0.13	0.34	0.46	0.69	0.66	8.09	12.1
^{169}Tm	µg/g	0.023	0.057	0.065	0.035	0.091	1.07	1.59

File		dmcy138_apdz_44-9	dmcy138_aplz_44-3	dmcy138_aplz_44-6	dmcy138_aplz_44-8	dmcy138_aplz_44-10	lefn1_apc_24-1	lefn1_apc_24-2
CL Colour		blue-violet core	pink rim	pink rim	pink rim	pink rim	green core	green core
^{171}Yb	µg/g	0.19	0.28	0.53	0.41	0.45	7.01	11.2
^{175}Lu	µg/g	0.036	0.038	0.086	0.057	0.072	1.04	1.19
^{178}Hf	µg/g	bdl	bdl	bdl	bdl	bdl	bdl	bdl
^{181}Ta	µg/g	bdl	bdl	0.0037	bdl	bdl	0.020	0.017
^{208}Pb	µg/g	10.7	1.81	1.42	1.05	0.69	0.44	1.07
^{232}Th	µg/g	89.6	0.15	0.32	0.42	0.27	0.81	3.14
^{238}U	µg/g	0.033	0.011	0.0085	0.011	0.017	0.70	1.83
Detection Limit								
SiO_2	wt.%	1.28	1.11	1.16	1.86	1.41	8.03	8.94
TiO_2	wt.%	0.000401	0.000274	0.000333	0.000551	0.000390	0.00170	0.00132
Al_2O_3	wt.%	0.00168	0.00141	0.00147	0.00240	0.00201	0.00838	0.00938
MnO	wt.%	0.000109	0.000104	0.0000986	0.000157	0.000130	0.000420	0.000448
CaO	wt.%	0.0375	0.0304	0.0313	0.0536	0.0414	0.137	0.149
P_2O_5	wt.%	0.0129	0.0123	0.0116	0.0178	0.0150	0.0495	0.0538
^{66}Zn	µg/g	3.64	3.14	3.33	5.93	4.29	11.8	13.4
^{75}As	µg/g	3.36	2.96	3.03	4.91	4.17	12.0	13.9
^{85}Rb	µg/g	0.133	0.106	0.099	0.188	0.144	0.506	0.516
^{88}Sr	µg/g	0.0455	0.0276	0.0407	0.0649	0.0508	0.216	0.278
^{89}Y	µg/g	0.0490	0.0425	0.0516	0.0793	0.0545	0.205	0.220
^{90}Zr	µg/g	0.123	0.0809	0.0946	0.160	0.110	0.459	0.541
^{93}Nb	µg/g	0.0150	0.0287	0.0257	0.0246	0.0326	0.0607	0.125
^{118}Sn	µg/g	0.346	0.365	0.352	0.509	0.413	1.23	1.26
^{133}Cs	µg/g	0.0193	0.0181	0.0191	0.0367	0.0282	0.0741	0.105
^{137}Ba	µg/g	0.0578	0.0435	0.0999	0.219	0.173	0.375	0.517
^{139}La	µg/g	0.0166	0.0115	0.0169	0.0209	0.0158	0.0621	0.0725
^{140}Ce	µg/g	0.0144	0.0120	0.0130	0.0256	0.0199	0.0276	0.0667
^{141}Pr	µg/g	0.00973	0.00793	0.00876	0.0170	0.0109	0.0481	0.0396
^{143}Nd	µg/g	0.0969	0.0380	0.0453	0.172	0.0536	0.474	0.225
^{147}Sm	µg/g	0.0959	0.0919	0.0721	0.158	0.0909	0.274	0.3222
^{151}Eu	µg/g	0.0204	0.0166	0.0289	0.0420	0.0269	0.0701	0.129
^{157}Gd	µg/g	0.103	0.0532	0.0684	0.135	0.112	0.282	0.331
^{159}Tb	µg/g	0.0135	0.0093	0.0137	0.0186	0.0142	0.0471	0.0519
^{163}Dy	µg/g	0.0393	0.0462	0.0412	0.0688	0.0519	0.169	0.181
^{165}Ho	µg/g	0.0126	0.0123	0.0114	0.0201	0.0110	0.0500	0.0489

File		dmcy138_apdz_44-9	dmcy138_aplz_44-3	dmcy138_aplz_44-6	dmcy138_aplz_44-8	dmcy138_aplz_44-10	lefn1_apc_24-1	lefn1_apc_24-2
CL Colour		blue-violet core	pink rim	pink rim	pink rim	pink rim	green core	green core
^{167}Er	µg/g	0.0262	0.0417	0.0502	0.0756	0.0485	0.184	0.215
^{169}Tm	µg/g	0.00932	0.00762	0.00508	0.0192	0.0160	0.0511	0.0549
^{171}Yb	µg/g	0.0682	0.0312	0.0858	0.157	0.100	0.346	0.338
^{175}Lu	µg/g	0.0140	0.0108	0.00904	0.0153	0.0147	0.0424	0.0593
^{178}Hf	µg/g	0.0516	0.0375	0.0313	0.0760	0.0458	0.156	0.183
^{181}Ta	µg/g	0.00694	0.01348	0.00624	0.0200	0.0183	0.0250	0.0298
^{208}Pb	µg/g	0.0374	0.0363	0.0340	0.0555	0.0486	0.0939	0.110
^{232}Th	µg/g	0.0162	0.0139	0.00641	0.0117	0.0211	0.0527	0.0615
^{238}U	µg/g	0.0172	0.0149	0.0136	0.0204	0.0153	0.0480	0.0450

File		lefn1_apc_24-3	lefn1_apc_24-4	lefn1_apc_24-5	lefn1_apr_24-6	lefn1_apr_44-7	lefn1_apr_44-8	lefn1_apr_44-9	lefn1_apr_44-10
CL Colour		green core	green core	green core	pink/purple rim	pink/purple rim	pink/purple rim	pink/purple rim	pink/purple rim
SiO_2	wt.%	bdl	bdl	bdl	bdl	bdl	bdl	bdl	bdl
TiO_2	wt.%	0.0023	bdl	bdl	0.0081	bdl	bdl	bdl	bdl
Al_2O_3	wt.%	2.5	0.055	bdl	bdl	0.051	0.0090	0.020	0.14
MnO	wt.%	0.148	0.122	0.0917	0.0239	0.0303	0.0222	0.0259	0.0289
CaO	wt.%	56.6	56.6	56.6	54.0	54.0	54.0	54.0	54.0
P_2O_5	wt.%	51.6	49.3	51.8	47.9	55.8	52.4	47.6	46.0
^{66}Zn	µg/g	bdl	bdl	bdl	bdl	bdl	bdl	5.21	14.2
^{75}As	µg/g	bdl	bdl	bdl	bdl	7.44	bdl	bdl	bdl
^{85}Rb	µg/g	0.66	bdl	bdl	bdl	1.21	bdl	0.21	3.75
^{88}Sr	µg/g	581	1040	1590	5650	8000	18600	6030	4900
^{89}Y	µg/g	2080	2450	2710	554	536	760	413	465
^{90}Zr	µg/g	4.28	10.7	1.19	1.93	1.1	0.339	0.837	3.97
^{93}Nb	µg/g	2.53	0.682	0.150	0.176	0.197	0.121	0.106	5.92
^{118}Sn	µg/g	bdl	bdl	bdl	bdl	bdl	bdl	bdl	bdl
^{133}Cs	µg/g	bdl	bdl	bdl	bdl	bdl	bdl	bdl	0.45
^{137}Ba	µg/g	32.5	40.9	24.2	26.8	41.7	25.3	37.6	86.5
^{139}La	µg/g	108	106	116	47.1	43.7	89.1	41.4	179
^{140}Ce	µg/g	504	485	612	408	387	912	329	988
^{141}Pr	µg/g	118	132	146	132	135	292	104	227
^{143}Nd	µg/g	884	971	1120	1030	1010	2190	791	1480
^{147}Sm	µg/g	387	488	526	557	569	1050	456	577
^{151}Eu	µg/g	56.1	69.7	81.2	187	199	354	152	179
^{157}Gd	µg/g	467	586	658	657	639	1080	500	559
^{159}Tb	µg/g	69.6	84.5	98.6	65.8	72.0	102	55.9	59.5
^{163}Dy	µg/g	398	472	551	231	247	351	189	206
^{165}Ho	µg/g	76.6	89.6	103.2	23.3	26.2	35.0	19.8	21.6
^{167}Er	µg/g	216	239	279	35.3	40.7	54.3	28.1	31.2
^{169}Tm	µg/g	27.7	29.5	34.3	2.73	3.02	4.36	2.04	2.68
^{171}Yb	µg/g	172	189	218	12.6	14.2	22.2	10.4	12.7
^{175}Lu	µg/g	22.5	22.8	29.2	1.33	1.56	2.48	1.06	1.58
^{178}Hf	µg/g	0.25	0.60	bdl	bdl	0.070	0.088	bdl	0.20
^{181}Ta	µg/g	bdl	bdl	bdl	bdl	bdl	bdl	bdl	0.050
^{208}Pb	µg/g	19.0	24.6	19.9	9.85	11.0	10.3	15.9	75.9
^{232}Th	µg/g	48.5	103	92.3	43.1	26.4	8.64	22.0	512
^{238}U	µg/g	18.9	30.6	30.1	0.125	0.073	0.089	0.075	3.3

File		lefn1_apc_24-3	lefn1_apc_24-4	lefn1_apc_24-5	lefn1_apr_24-6	lefn1_apr_44-7	lefn1_apr_44-8	lefn1_apr_44-9	lefn1_apr_44-10
CL Colour		green core	green core	green core	pink/purple rim	pink/purple rim	pink/purple rim	pink/purple rim	pink/purple rim
λ_0		7.15	7.26	7.40	6.27	6.32	6.85	6.06	6.48
λ_1		-1.76	-2.15	-2.38	11.3	10.2	12.9	11.4	17.2
λ_2		-152	-178	-171	-426	-424	-413	-423	-336
λ_3		-780	-739	-805	-720	-758	-1360	-553	-595
λ_4		4530	7050	5900	19100	17200	18100	20900	21900
1σ error									
SiO_2	wt.%	bdl	bdl	bdl	bdl	bdl	bdl	bdl	bdl
TiO_2	wt.%	0.0012	bdl	bdl	0.00347	bdl	bdl	bdl	bdl
Al_2O_3	wt.%	0.16	0.011	bdl	bdl	0.0083	0.00182	0.0057	0.034
MnO	wt.%	0.0032	0.0036	0.0022	0.00072	0.00073	0.00021	0.0015	0.0024
CaO	wt.%	2.03	1.41	1.79	1.34	1.79	2.85	0.63	6.18
P_2O_5	wt.%	1.68	3.26	1.54	1.19	2.52	2.79	3.04	4.89
^{66}Zn	µg/g	bdl	bdl	bdl	bdl	bdl	bdl	2.39	4.47
^{75}As	µg/g	bdl	bdl	bdl	bdl	2.1	bdl	bdl	bdl
^{85}Rb	µg/g	0.24	bdl	bdl	bdl	0.27	bdl	0.076	1.28
^{88}Sr	µg/g	23.2	66.0	35.3	445	357	485	233	638
^{89}Y	µg/g	52.8	98.9	51.0	9.63	15.3	23.3	24.5	52.5
^{90}Zr	µg/g	0.53	0.49	0.30	0.70	0.10	0.14	0.28	0.97
^{93}Nb	µg/g	0.310	0.12	0.061	0.072	0.023	0.062	0.047	1.24
^{118}Sn	µg/g	bdl	bdl	bdl	bdl	bdl	bdl	bdl	bdl
^{133}Cs	µg/g	bdl	bdl	bdl	bdl	bdl	bdl	bdl	0.093
^{137}Ba	µg/g	2.03	6.79	2.83	2.72	1.51	2.11	2.42	12.5
^{139}La	µg/g	5.94	2.53	2.42	7.04	2.23	3.11	5.14	50.7
^{140}Ce	µg/g	28.1	28.3	13.3	25.8	19.2	26.7	14.9	259
^{141}Pr	µg/g	7.66	6.90	3.17	8.71	4.50	11.1	8.29	56.1
^{143}Nd	µg/g	47.5	37.4	30.6	56.5	29.6	61.1	58.2	337
^{147}Sm	µg/g	14.5	51.7	10.1	19.4	12.2	22.9	18.7	105
^{151}Eu	µg/g	4.04	5.54	1.58	7.17	5.84	8.28	4.08	29.1
^{157}Gd	µg/g	14.6	40.0	18.5	15.3	7.23	27.3	15.5	75.7
^{159}Tb	µg/g	2.68	6.02	2.21	2.21	1.87	3.73	2.49	7.50
^{163}Dy	µg/g	12.9	20.3	9.29	5.50	6.02	9.45	4.67	24.0
^{165}Ho	µg/g	2.48	6.31	2.96	0.86	0.60	1.16	0.778	2.70
^{167}Er	µg/g	6.41	15.8	4.87	1.88	1.03	2.22	1.16	3.76
^{169}Tm	µg/g	0.88	2.45	0.92	0.19	0.094	0.154	0.11	0.35

File		lefn1_apc_24-3	lefn1_apc_24-4	lefn1_apc_24-5	lefn1_apr_24-6	lefn1_apr_44-7	lefn1_apr_44-8	lefn1_apr_44-9	lefn1_apr_44-10
CL Colour		green core	green core	green core	pink/purple rim	pink/purple rim	pink/purple rim	pink/purple rim	pink/purple rim
^{171}Yb	µg/g	6.88	23.3	5.54	0.71	0.541	1.34	0.56	1.85
^{175}Lu	µg/g	0.68	2.61	1.21	0.18	0.060	0.11	0.070	0.21
^{178}Hf	µg/g	0.070	0.13	bdl	bdl	0.017	0.040	bdl	0.058
^{181}Ta	µg/g	bdl	bdl	bdl	bdl	bdl	bdl	bdl	0.034
^{208}Pb	µg/g	1.25	4.20	1.39	1.29	0.40	0.843	1.61	15.8
^{232}Th	µg/g	3.96	9.71	4.80	10.8	0.65	0.682	2.40	174
^{238}U	µg/g	0.64	1.88	1.36	0.057	0.011	0.019	0.013	1.3
Detection Limit									
SiO_2	wt.%	10.9	16.5	13.2	15.2	3.02	3.65	3.46	3.84
TiO_2	wt.%	0.00141	0.00323	0.00225	0.00319	0.000553	0.000747	0.000549	0.000605
Al_2O_3	wt.%	0.0117	0.0150	0.0147	0.0156	0.00313	0.00404	0.00368	0.00437
MnO	wt.%	0.000569	0.000735	0.000671	0.000732	0.000144	0.000190	0.000165	0.000197
CaO	wt.%	0.187	0.243	0.237	0.275	0.0460	0.0645	0.0576	0.0657
P_2O_5	wt.%	0.0657	0.0868	0.0813	0.0821	0.0168	0.0222	0.0184	0.0229
^{66}Zn	µg/g	16.0	21.6	20.6	23.5	3.92	5.70	4.95	5.40
^{75}As	µg/g	17.2	21.2	21.2	22.3	4.24	5.77	5.43	5.61
^{85}Rb	µg/g	0.612	0.910	0.691	0.974	0.156	0.225	0.182	0.239
^{88}Sr	µg/g	0.283	0.426	0.326	0.397	0.075	0.100	0.106	0.0948
^{89}Y	µg/g	0.253	0.441	0.285	0.347	0.0602	0.0963	0.0963	0.0906
^{90}Zr	µg/g	0.554	1.03	0.840	0.862	0.152	0.224	0.218	0.258
^{93}Nb	µg/g	0.144	0.205	0.102	0.159	0.0354	0.0588	0.0622	0.0568
^{118}Sn	µg/g	1.47	1.93	1.85	1.95	0.378	0.481	0.441	0.529
^{133}Cs	µg/g	0.128	0.160	0.129	0.0716	0.0269	0.0425	0.0308	0.0333
^{137}Ba	µg/g	0.782	1.24	0.644	0.901	0.124	0.205	0.216	0.258
^{139}La	µg/g	0.0984	0.129	0.108	0.132	0.00819	0.0258	0.0301	0.0249
^{140}Ce	µg/g	0.0654	0.132	0.0830	0.116	0.00838	0.0361	0.0241	0.0255
^{141}Pr	µg/g	0.0777	0.112	0.0727	0.113	0.017	0.0210	0.0360	0.0227
^{143}Nd	µg/g	0.593	1.01	0.570	0.798	0.131	0.181	0.166	0.148
^{147}Sm	µg/g	0.371	0.748	0.626	0.660	0.0905	0.150	0.137	0.162
^{151}Eu	µg/g	0.0945	0.154	0.163	0.236	0.0316	0.0505	0.0400	0.0358
^{157}Gd	µg/g	0.411	0.881	0.442	0.672	0.085	0.199	0.164	0.144
^{159}Tb	µg/g	0.0672	0.0936	0.0765	0.105	0.011	0.0261	0.0203	0.0198
^{163}Dy	µg/g	0.376	0.449	0.230	0.329	0.0563	0.0913	0.0771	0.0689
^{165}Ho	µg/g	0.0710	0.116	0.0717	0.0810	0.0160	0.0207	0.0189	0.0148

File		lefn1_apc_24-3	lefn1_apc_24-4	lefn1_apc_24-5	lefn1_apr_24-6	lefn1_apr_44-7	lefn1_apr_44-8	lefn1_apr_44-9	lefn1_apr_44-10
CL Colour		green core	green core	green core	pink/purple rim	pink/purple rim	pink/purple rim	pink/purple rim	pink/purple rim
^{167}Er	µg/g	0.284	0.417	0.316	0.248	0.0551	0.0914	0.0520	0.0820
^{169}Tm	µg/g	0.0483	0.0889	0.0726	0.0761	0.0117	0.0224	0.0178	0.0159
^{171}Yb	µg/g	0.200	0.804	0.249	0.560	0.0958	0.128	0.152	0.138
^{175}Lu	µg/g	0.0617	0.0960	0.0728	0.0926	0.0140	0.0188	0.0171	0.0189
^{178}Hf	µg/g	0.179	0.329	0.227	0.318	0.037	0.0781	0.0586	0.0908
^{181}Ta	µg/g	0.0701	0.196	0.0752	0.0648	0.00759	0.0239	0.0218	0.0231
^{208}Pb	µg/g	0.195	0.309	0.248	0.286	0.0306	0.0506	0.0462	0.0545
^{232}Th	µg/g	0.0930	0.108	0.0681	0.122	0.0175	0.0248	0.0197	0.00985
^{238}U	µg/g	0.0612	0.121	0.0905	0.1055	0.0124	0.0237	0.0240	0.0198

File		lefn1_apr_44-13	lefn1_apr_44-11	lefn1_apr_44-12	lrs150_apc_24-1	lrs150_apc_24-2	lrs150_apc_24-3	lrs150_apr_24-4	lrs150_apr_24-5
CL Colour		pink/purple rim	pink/purple rim	pink/purple rim	blue-violet core	blue-violet core	blue-violet core	red rim	red rim
SiO_2	wt.%	bdl	bdl	bdl	bdl	bdl	bdl	bdl	bdl
TiO_2	wt.%	bdl	bdl	bdl	bdl	bdl	bdl	0.175	bdl
Al_2O_3	wt.%	0.019	0.0089	bdl	bdl	bdl	bdl	bdl	0.021
MnO	wt.%	0.0214	0.0195	0.0232	0.0917	0.0550	0.0744	0.0528	0.0892
CaO	wt.%	54.0	57.2	57.2	53.4	53.4	53.4	53.1	51.7
P_2O_5	wt.%	55.6	49.3	45.5	49.9	47.8	49.9	50.5	48.2
^{66}Zn	µg/g	bdl	bdl	bdl	bdl	bdl	bdl	bdl	20.9
^{75}As	µg/g	bdl	bdl	bdl	bdl	bdl	bdl	bdl	bdl
^{85}Rb	µg/g	bdl	bdl	bdl	bdl	bdl	bdl	bdl	bdl
^{88}Sr	µg/g	3340	2070	2260	15700	19200	21500	22400	28200
^{89}Y	µg/g	289	180	241	68.4	92.3	75.2	362	352
^{90}Zr	µg/g	0.75	0.588	bdl	46.3	7.01	123	769	44.9
^{93}Nb	µg/g	0.16	0.063	0.053	0.29	bdl	0.18	90.7	0.77
^{118}Sn	µg/g	bdl	bdl	bdl	bdl	bdl	bdl	bdl	bdl
^{133}Cs	µg/g	bdl	bdl	bdl	bdl	bdl	bdl	bdl	bdl
^{137}Ba	µg/g	39.0	19.6	9.24	22.1	12.7	26.1	14.2	21.1
^{139}La	µg/g	19.6	15.1	13.9	819	1090	1010	2150	2670
^{140}Ce	µg/g	169	124	115	1500	2150	1600	5000	5370
^{141}Pr	µg/g	51.6	38.5	35.7	157	255	153	627	632
^{143}Nd	µg/g	388	289	291	592	925	558	2670	2620
^{147}Sm	µg/g	236	165	171	162	262	163	875	808
^{151}Eu	µg/g	82.4	51.5	61.0	41.2	63.7	41.5	227	205
^{157}Gd	µg/g	301	206	226	93.6	145	97.2	566	507
^{159}Tb	µg/g	34.0	21.3	25.1	6.42	10.1	7.48	40.0	35.7
^{163}Dy	µg/g	118	72.3	89.5	21.7	29.4	23.3	116	112
^{165}Ho	µg/g	12.3	6.99	9.28	2.62	3.61	2.92	13.9	13.8
^{167}Er	µg/g	18.0	9.85	13.3	5.92	8.16	8.01	28.8	29.0
^{169}Tm	µg/g	1.38	0.727	0.954	0.723	0.792	0.964	3.19	3.33
^{171}Yb	µg/g	5.67	3.32	3.76	4.13	5.50	6.51	15.6	18.0
^{175}Lu	µg/g	0.69	0.30	0.39	0.60	0.79	0.79	1.76	2.09
^{178}Hf	µg/g	0.054	bdl	bdl	0.785	bdl	2.00	11.7	1.00
^{181}Ta	µg/g	bdl	bdl	bdl	bdl	bdl	bdl	0.21	bdl
^{208}Pb	µg/g	13.8	4.19	3.63	211	84.9	149	79.6	122
^{232}Th	µg/g	25.6	15.4	5.04	1770	687	1270	663	878
^{238}U	µg/g	0.11	0.049	0.035	0.88	0.33	1.09	2.12	0.95

File		lefn1_apr_44-13	lefn1_apr_44-11	lefn1_apr_44-12	lrs150_apc_24-1	lrs150_apc_24-2	lrs150_apc_24-3	lrs150_apr_24-4	lrs150_apr_24-5
CL Colour		pink/purple rim	pink/purple rim	pink/purple rim	blue-violet core	blue-violet core	blue-violet core	red rim	red rim
λ_0		5.49	5.03	5.15	5.40	5.75	5.55	6.88	6.90
λ_1		9.76	12.2	10.1	29.7	30.6	28.2	28.4	28.5
λ_2		-427	-443	-447	-86	-110	-54	-172	-138
λ_3		-349	-301	-66.7	-981	-1210	-765	-665	-680
λ_4		19200	18900	16300	35700	38800	36300	32500	33600
1σ error									
SiO_2	wt.%	bdl	bdl	bdl	bdl	bdl	bdl	bdl	bdl
TiO_2	wt.%	bdl	bdl	bdl	bdl	bdl	bdl	0.073	bdl
Al_2O_3	wt.%	0.0023	0.0012	bdl	bdl	bdl	bdl	bdl	0.013
MnO	wt.%	0.00075	0.00064	0.00060	0.0027	0.0025	0.0017	0.0093	0.0037
CaO	wt.%	2.78	1.12	1.10	1.93	1.38	1.31	5.88	2.10
P_2O_5	wt.%	3.21	1.43	1.02	2.21	0.718	2.40	5.55	1.76
^{66}Zn	µg/g	bdl	bdl	bdl	bdl	bdl	bdl	bdl	bdl
^{75}As	µg/g	bdl	bdl	bdl	bdl	bdl	bdl	bdl	bdl
^{85}Rb	µg/g	bdl	bdl	bdl	bdl	bdl	bdl	bdl	bdl
^{88}Sr	µg/g	118	50.2	78.4	1160	531	441	3520	1300
^{89}Y	µg/g	5.64	5.11	6.11	2.17	1.42	1.97	30.4	13.8
^{90}Zr	µg/g	0.15	0.096	bdl	4.94	0.95	16.8	204	5.04
^{93}Nb	µg/g	0.037	0.017	0.020	0.071	bdl	0.090	40.7	0.20
^{118}Sn	µg/g	bdl	bdl	bdl	bdl	bdl	bdl	bdl	bdl
^{133}Cs	µg/g	bdl	bdl	bdl	bdl	bdl	bdl	bdl	bdl
^{137}Ba	µg/g	1.69	0.67	0.66	1.49	1.23	1.86	2.85	1.41
^{139}La	µg/g	0.84	0.38	0.41	40.5	35.7	26.9	374	109
^{140}Ce	µg/g	7.22	3.45	3.52	64.1	63.5	66.7	843	194
^{141}Pr	µg/g	1.22	1.01	1.03	6.19	5.70	4.66	91.4	24.1
^{143}Nd	µg/g	10.7	6.56	7.77	19.4	26.7	24.0	341	93.0
^{147}Sm	µg/g	8.30	4.21	5.17	4.77	13.6	7.80	88.0	27.0
^{151}Eu	µg/g	1.64	1.24	2.95	1.29	1.44	1.52	18.2	7.22
^{157}Gd	µg/g	5.42	4.04	6.00	3.48	2.62	5.34	44.6	15.8
^{159}Tb	µg/g	0.73	0.50	0.53	0.28	0.50	0.18	3.37	1.26
^{163}Dy	µg/g	2.84	2.26	2.23	0.82	0.78	0.90	10.6	4.27
^{165}Ho	µg/g	0.38	0.20	0.30	0.11	0.068	0.16	1.33	0.59
^{167}Er	µg/g	0.64	0.42	0.33	0.34	0.44	0.46	3.34	1.38
^{169}Tm	µg/g	0.074	0.029	0.052	0.048	0.098	0.060	0.37	0.21

File		lefn1_apr_44-13	lefn1_apr_44-11	lefn1_apr_44-12	lrs150_apc_24-1	lrs150_apc_24-2	lrs150_apc_24-3	lrs150_apr_24-4	lrs150_apr_24-5
CL Colour		pink/purple rim	pink/purple rim	pink/purple rim	blue-violet core	blue-violet core	blue-violet core	red rim	red rim
^{171}Yb	µg/g	0.33	0.18	0.24	0.33	0.84	0.56	2.29	0.94
^{175}Lu	µg/g	0.044	0.023	0.019	0.043	0.090	0.063	0.23	0.14
^{178}Hf	µg/g	0.018	bdl	bdl	0.13	bdl	0.13	3.17	0.18
^{181}Ta	µg/g	bdl	bdl	bdl	bdl	bdl	bdl	0.10	bdl
^{208}Pb	µg/g	1.72	0.15	0.26	4.05	4.16	5.44	11.1	3.81
^{232}Th	µg/g	1.24	0.53	0.18	27.0	55.0	46.1	133	44.3
^{238}U	µg/g	0.0118	0.0074	0.012	0.072	0.071	0.10	0.50	0.088
Detection Limit									
SiO_2	wt.%	2.76	2.09	3.46	10.1	10.7	10.9	10.7	12.4
TiO_2	wt.%	0.000494	0.000410	0.000673	0.00184	0.00227	0.00231	0.00196	0.00243
Al_2O_3	wt.%	0.00323	0.00266	0.00402	0.0114	0.0128	0.0139	0.0143	0.0170
MnO	wt.%	0.000150	0.000119	0.000181	0.000498	0.000560	0.000638	0.000641	0.000728
CaO	wt.%	0.0497	0.0368	0.0637	0.179	0.189	0.198	0.195	0.241
P_2O_5	wt.%	0.0156	0.0134	0.0195	0.0573	0.0632	0.0699	0.0702	0.0816
^{66}Zn	µg/g	4.20	3.62	5.32	14.2	17.3	18.8	18.5	20.0
^{75}As	µg/g	4.39	3.31	5.35	14.93	17.92	18.81	18.64	20.76
^{85}Rb	µg/g	0.176	0.128	0.214	0.534	0.636	0.742	0.649	0.742
^{88}Sr	µg/g	0.0860	0.0591	0.104	0.214	0.311	0.349	0.303	0.385
^{89}Y	µg/g	0.0622	0.0490	0.101	0.227	0.285	0.338	0.313	0.371
^{90}Zr	µg/g	0.163	0.108	0.231	0.595	0.715	0.742	0.696	0.899
^{93}Nb	µg/g	0.0228	0.0244	0.0237	0.0412	0.219	0.177	0.199	0.0583
^{118}Sn	µg/g	0.307	0.287	0.511	1.22	1.46	1.57	1.44	1.74
^{133}Cs	µg/g	0.0234	0.0172	0.0393	0.0673	0.120	0.112	0.109	0.0956
^{137}Ba	µg/g	0.162	0.120	0.161	0.332	0.584	0.612	0.310	0.582
^{139}La	µg/g	0.0174	0.0107	0.0104	0.0592	0.0736	0.0448	0.0975	0.0734
^{140}Ce	µg/g	0.0178	0.0109	0.0249	0.0606	0.0879	0.0458	0.0399	0.0750
^{141}Pr	µg/g	0.0167	0.0154	0.0142	0.0483	0.0655	0.0738	0.0318	0.0761
^{143}Nd	µg/g	0.160	0.146	0.143	0.126	0.518	0.542	0.275	0.179
^{147}Sm	µg/g	0.101	0.0975	0.0605	0.345	0.255	0.526	0.424	0.148
^{151}Eu	µg/g	0.0387	0.0205	0.0382	0.101	0.125	0.143	0.136	0.143
^{157}Gd	µg/g	0.124	0.0825	0.150	0.323	0.602	0.460	0.397	0.645
^{159}Tb	µg/g	0.0138	0.0105	0.0138	0.0411	0.0723	0.0538	0.0639	0.0706
^{163}Dy	µg/g	0.0623	0.0394	0.0568	0.114	0.241	0.221	0.238	0.240
^{165}Ho	µg/g	0.0153	0.0141	0.0181	0.0447	0.0645	0.0769	0.0645	0.0476

File		lefn1_apr_44-13	lefn1_apr_44-11	lefn1_apr_44-12	lrs150_apc_24-1	lrs150_apc_24-2	lrs150_apc_24-3	lrs150_apr_24-4	lrs150_apr_24-5
CL Colour		pink/purple rim	pink/purple rim	pink/purple rim	blue-violet core	blue-violet core	blue-violet core	red rim	red rim
^{167}Er	µg/g	0.0616	0.0690	0.0796	0.167	0.304	0.239	0.258	0.260
^{169}Tm	µg/g	0.0180	0.00806	0.0170	0.0446	0.0647	0.0681	0.0605	0.0790
^{171}Yb	µg/g	0.0966	0.0734	0.113	0.309	0.409	0.739	0.446	0.329
^{175}Lu	µg/g	0.0155	0.0190	0.0183	0.0421	0.0700	0.0686	0.0793	0.0597
^{178}Hf	µg/g	0.0486	0.0337	0.0768	0.132	0.240	0.189	0.258	0.220
^{181}Ta	µg/g	0.0161	0.0122	0.0320	0.0387	0.0681	0.0836	0.0901	0.0678
^{208}Pb	µg/g	0.0195	0.0356	0.0588	0.128	0.167	0.150	0.222	0.163
^{232}Th	µg/g	0.0170	0.0110	0.00864	0.0491	0.0790	0.0904	0.0806	0.0695
^{238}U	µg/g	0.0151	0.0113	0.0266	0.0408	0.0512	0.0713	0.0728	0.0621

File		lrs150_apr_24-6	frs4_ap_mot_24-1	frs4_ap_mot_24-6	frs4_ap_mot_24-10	frs4_ap_mot_24-2	frs4_ap_mot_24-4
CL Colour		red rim	"mottled" = mixed zones	"mottled" = mixed zones	"mottled" = mixed zones	"mottled" = mixed zones	"mottled" = mixed zones
SiO_2	wt.%	bdl	bdl	bdl	bdl	bdl	bdl
TiO_2	wt.%	bdl	bdl	bdl	bdl	bdl	bdl
Al_2O_3	wt.%	bdl	bdl	bdl	bdl	bdl	bdl
MnO	wt.%	0.0138	0.0647	0.0503	0.0457	0.0606	0.0539
CaO	wt.%	53.1	51.7	51.7	51.7	51.7	55.5
P_2O_5	wt.%	48.0	48.2	46.4	45.9	46.7	48.2
^{66}Zn	µg/g	bdl	bdl	bdl	bdl	bdl	bdl
^{75}As	µg/g	bdl	bdl	bdl	bdl	bdl	bdl
^{85}Rb	µg/g	bdl	bdl	bdl	bdl	bdl	bdl
^{88}Sr	µg/g	18900	13200	11200	10600	11900	15300
^{89}Y	µg/g	607	451	344	349	359	455
^{90}Zr	µg/g	43.2	bdl	bdl	bdl	bdl	bdl
^{93}Nb	µg/g	1.11	bdl	bdl	bdl	bdl	bdl
^{118}Sn	µg/g	bdl	bdl	bdl	bdl	bdl	bdl
^{133}Cs	µg/g	bdl	bdl	bdl	bdl	bdl	bdl
^{137}Ba	µg/g	6.98	33.5	14.1	19.2	23.8	33.5
^{139}La	µg/g	1340	125	104	124	159	113
^{140}Ce	µg/g	3700	1410	966	1120	1350	1240
^{141}Pr	µg/g	618	444	275	313	362	412
^{143}Nd	µg/g	2900	3230	1910	2080	2430	3000
^{147}Sm	µg/g	1130	1150	705	757	781	1200
^{151}Eu	µg/g	304	299	190	198	210	329
^{157}Gd	µg/g	747	854	509	555	579	939
^{159}Tb	µg/g	59.2	63.9	41.8	45.2	46.9	72.9
^{163}Dy	µg/g	184	205	136	152	153	228
^{165}Ho	µg/g	23.3	19.5	14.7	15.2	15.9	22.0
^{167}Er	µg/g	46.9	26.2	22.1	23.5	24.5	28.0
^{169}Tm	µg/g	4.63	1.87	1.64	1.70	1.59	1.85
^{171}Yb	µg/g	26.2	7.94	7.50	7.25	6.84	8.61
^{175}Lu	µg/g	2.52	0.80	0.91	0.66	0.73	0.96
^{178}Hf	µg/g	1.50	bdl	bdl	bdl	bdl	bdl
^{181}Ta	µg/g	bdl	bdl	bdl	bdl	bdl	bdl
^{208}Pb	µg/g	20.6	148	91.3	144	67.3	203
^{232}Th	µg/g	123	0.15	0.27	0.16	0.27	0.14
^{238}U	µg/g	0.47	0.25	bdl	bdl	0.096	0.078

File		lrs150_apr_24-6	frs4_ap_mot_24-1	frs4_ap_mot_24-6	frs4_ap_mot_24-10	frs4_ap_mot_24-2	frs4_ap_mot_24-4
CL Colour		red rim	"mottled" = mixed zones	"mottled" = mixed zones	"mottled" = mixed zones	"mottled" = mixed zones	"mottled" = mixed zones
λ_0		7.10	6.55	6.25	6.30	6.37	6.58
λ_1		23.8	21.9	20.0	21.4	22.6	20.5
λ_2		-213	-450	-394	-408	-399	-458
λ_3		-700	-1740	-1730	-1350	1370	-1680
λ_4		28500	12500	15700	9840	11100	17800
1σ error							
SiO_2	wt.%	bdl	bdl	bdl	bdl	bdl	bdl
TiO_2	wt.%	bdl	bdl	bdl	bdl	bdl	bdl
Al_2O_3	wt.%	bdl	bdl	bdl	bdl	bdl	bdl
MnO	wt.%	0.00047	0.0029	0.0015	0.0013	0.0016	0.0015
CaO	wt.%	3.68	2.16	1.52	1.42	1.91	2.13
P_2O_5	wt.%	2.68	2.14	1.26	1.61	1.87	1.79
^{66}Zn	µg/g	bdl	bdl	bdl	bdl	bdl	bdl
^{75}As	µg/g	bdl	bdl	bdl	bdl	bdl	bdl
^{85}Rb	µg/g	bdl	bdl	bdl	bdl	bdl	bdl
^{88}Sr	µg/g	1350	568	313	333	476	488
^{89}Y	µg/g	40.0	13.9	14.3	9.77	12.1	15.6
^{90}Zr	µg/g	8.90	bdl	bdl	bdl	bdl	bdl
^{93}Nb	µg/g	0.25	bdl	bdl	bdl	bdl	bdl
^{118}Sn	µg/g	bdl	bdl	bdl	bdl	bdl	bdl
^{133}Cs	µg/g	bdl	bdl	bdl	bdl	bdl	bdl
^{137}Ba	µg/g	0.95	1.66	1.07	1.54	1.00	2.12
^{139}La	µg/g	68.7	7.32	3.14	4.04	2.96	6.20
^{140}Ce	µg/g	207	63.8	32.3	34.1	37.4	53.2
^{141}Pr	µg/g	43.7	17.9	9.87	6.56	10.2	14.2
^{143}Nd	µg/g	137	115	79.4	53.9	91.1	89.7
^{147}Sm	µg/g	78.3	36.3	32.2	12.6	29.2	30.2
^{151}Eu	µg/g	17.4	11.3	8.56	4.82	7.43	6.89
^{157}Gd	µg/g	40.1	26.9	22.7	14.8	20.8	19.9
^{159}Tb	µg/g	3.12	1.61	1.86	1.16	1.56	1.80
^{163}Dy	µg/g	12.5	4.63	6.04	3.93	4.39	5.54
^{165}Ho	µg/g	1.40	1.04	0.64	0.36	0.42	0.53
^{167}Er	µg/g	2.59	1.72	1.02	1.00	0.94	0.90
^{169}Tm	µg/g	0.27	0.17	0.10	0.076	0.074	0.098

File		lrs150_apr_24-6	frs4_ap_mot_24-1	frs4_ap_mot_24-6	frs4_ap_mot_24-10	frs4_ap_mot_24-2	frs4_ap_mot_24-4
CL Colour		red rim	"mottled" = mixed zones	"mottled" = mixed zones	"mottled" = mixed zones	"mottled" = mixed zones	"mottled" = mixed zones
^{171}Yb	µg/g	1.88	0.75	0.52	0.56	0.42	0.39
^{175}Lu	µg/g	0.18	0.071	0.064	0.079	0.045	0.063
^{178}Hf	µg/g	0.37	bdl	bdl	bdl	bdl	bdl
^{181}Ta	µg/g	bdl	bdl	bdl	bdl	bdl	bdl
^{208}Pb	µg/g	1.07	5.23	4.76	2.09	4.33	8.11
^{232}Th	µg/g	4.23	0.050	0.054	0.043	0.058	0.035
^{238}U	µg/g	0.094	0.048	bdl	bdl	0.018	0.017
Detection Limit							
SiO_2	wt.%	11.6	17.8	10.2	10.3	6.87	7.66
TiO_2	wt.%	0.00251	0.00400	0.00190	0.00245	0.00130	0.00152
Al_2O_3	wt.%	0.0150	0.0208	0.0131	0.0129	0.00910	0.00950
MnO	wt.%	0.000644	0.000922	0.000600	0.000565	0.000404	0.000429
CaO	wt.%	0.231	0.289	0.190	0.187	0.130	0.139
P_2O_5	wt.%	0.0704	0.110	0.0622	0.0623	0.0471	0.0486
^{66}Zn	µg/g	19.2	28.1	16.0	14.0	11.8	11.6
^{75}As	µg/g	19.00	28.42	16.93	17.24	11.25	12.44
^{85}Rb	µg/g	0.723	1.26	0.613	0.685	0.442	0.457
^{88}Sr	µg/g	0.291	0.561	0.302	0.272	0.224	0.229
^{89}Y	µg/g	0.306	0.439	0.281	0.248	0.138	0.190
^{90}Zr	µg/g	0.815	1.13	0.629	0.617	0.418	0.519
^{93}Nb	µg/g	0.100	0.278	0.149	0.188	0.0391	0.0374
^{118}Sn	µg/g	1.53	2.60	1.54	1.43	1.08	1.06
^{133}Cs	µg/g	0.114	0.191	0.104	0.0958	0.0754	0.0402
^{137}Ba	µg/g	0.614	0.547	0.420	0.748	0.338	0.389
^{139}La	µg/g	0.0436	0.144	0.0529	0.0669	0.0425	0.0394
^{140}Ce	µg/g	0.0933	0.164	0.0540	0.0682	0.0175	0.0167
^{141}Pr	µg/g	0.0791	0.109	0.0433	0.0616	0.0347	0.0267
^{143}Nd	µg/g	0.307	0.485	0.162	0.582	0.374	0.441
^{147}Sm	µg/g	0.254	0.710	0.309	0.390	0.248	0.329
^{151}Eu	µg/g	0.115	0.207	0.127	0.114	0.0291	0.0959
^{157}Gd	µg/g	0.422	0.375	0.357	0.483	0.232	0.289
^{159}Tb	µg/g	0.0615	0.0967	0.0518	0.0444	0.0278	0.0313
^{163}Dy	µg/g	0.278	0.224	0.194	0.0964	0.138	0.128
^{165}Ho	µg/g	0.0682	0.107	0.0422	0.0532	0.0339	0.0422

File		lrs150_apr_24-6	frs4_ap_mot_24-1	frs4_ap_mot_24-6	frs4_ap_mot_24-10	frs4_ap_mot_24-2	frs4_ap_mot_24-4
CL Colour		red rim	"mottled" = mixed zones	"mottled" = mixed zones	"mottled" = mixed zones	"mottled" = mixed zones	"mottled" = mixed zones
^{167}Er	µg/g	0.323	0.471	0.230	0.197	0.170	0.139
^{169}Tm	µg/g	0.0582	0.108	0.0489	0.0418	0.0128	0.0422
^{171}Yb	µg/g	0.538	0.740	0.329	0.309	0.235	0.247
^{175}Lu	µg/g	0.0629	0.109	0.0571	0.0454	0.0392	0.0430
^{178}Hf	µg/g	0.255	0.297	0.166	0.156	0.0978	0.110
^{181}Ta	µg/g	0.0403	0.0636	0.0212	0.0274	0.0564	0.0791
^{208}Pb	µg/g	0.177	0.314	0.188	0.183	0.119	0.0770
^{232}Th	µg/g	0.0753	0.0572	0.0541	0.0244	0.0507	0.0467
^{238}U	µg/g	0.0667	0.106	0.0622	0.0439	0.0337	0.0352

File		frs4_ap_mot_24-5	frs4_ap_mot_24-7	frs4_ap_mot_24-8	frs4_ap_mot_24-11	yw61_apdz_32-1	yw61_apdz_32-2
CL Colour		"mottled" = mixed zones	"mottled" = mixed zones	"mottled" = mixed zones	"mottled" = mixed zones	blue rim	blue rim
SiO_2	wt.%	bdl	bdl	bdl	bdl	bdl	bdl
TiO_2	wt.%	bdl	bdl	bdl	bdl	bdl	bdl
Al_2O_3	wt.%	bdl	bdl	bdl	bdl	bdl	bdl
MnO	wt.%	0.040	0.043	0.050	0.078	0.062	0.055
CaO	wt.%	55.5	55.5	55.5	55.5	57.1	57.1
P_2O_5	wt.%	52.6	50.1	49.0	49.5	45.3	43.8
^{66}Zn	µg/g	bdl	bdl	bdl	bdl	bdl	bdl
^{75}As	µg/g	bdl	bdl	bdl	bdl	bdl	bdl
^{85}Rb	µg/g	bdl	bdl	bdl	bdl	bdl	bdl
^{88}Sr	µg/g	16200	13300	15200	16800	7910	4700
^{89}Y	µg/g	509	462	444	484	578	395
^{90}Zr	µg/g	bdl	bdl	bdl	bdl	bdl	bdl
^{93}Nb	µg/g	bdl	bdl	bdl	bdl	bdl	bdl
^{118}Sn	µg/g	bdl	bdl	bdl	bdl	bdl	bdl
^{133}Cs	µg/g	bdl	bdl	bdl	bdl	bdl	bdl
^{137}Ba	µg/g	21.0	21.2	30.3	47.1	1.66	0.79
^{139}La	µg/g	150	131	167	178	41.0	36.6
^{140}Ce	µg/g	1440	1290	1510	1520	218	192
^{141}Pr	µg/g	406	378	419	437	48.4	46.0
^{143}Nd	µg/g	2720	2570	2790	2890	324	309
^{147}Sm	µg/g	966	1020	963	1010	192	175
^{151}Eu	µg/g	256	282	256	269	78.0	67.8
^{157}Gd	µg/g	712	782	698	745	273	234
^{159}Tb	µg/g	59.3	63.5	56.9	60.1	36.5	31.2
^{163}Dy	µg/g	201	206	189	199	165	130
^{165}Ho	µg/g	21.3	20.7	19.7	20.5	20.6	15.3
^{167}Er	µg/g	34.4	28.2	29.4	30.1	38.4	26.2
^{169}Tm	µg/g	2.37	1.99	1.95	2.10	3.32	2.27
^{171}Yb	µg/g	11.3	8.70	8.67	9.20	15.7	11.7
^{175}Lu	µg/g	1.02	0.958	0.909	0.925	1.69	1.35
^{178}Hf	µg/g	bdl	bdl	bdl	bdl	bdl	bdl
^{181}Ta	µg/g	bdl	bdl	bdl	0.079	bdl	bdl
^{208}Pb	µg/g	96.5	107	98.2	90.5	9.31	8.02
^{232}Th	µg/g	0.29	0.30	0.67	0.897	0.081	bdl
^{238}U	µg/g	bdl	5.16	0.059	1.03	bdl	bdl

File		frs4_ap_mot_24-5	frs4_ap_mot_24-7	frs4_ap_mot_24-8	frs4_ap_mot_24-11	yw61_apdz_32-1	yw61_apdz_32-2
CL Colour		"mottled" = mixed zones	"mottled" = mixed zones	"mottled" = mixed zones	"mottled" = mixed zones	blue rim	blue rim
λ_0		6.60	6.53	6.54	6.59	5.87	5.68
λ_1		20.3	20.6	21.9	21.8	5.90	7.38
λ_2		-399	-427	-405	-406	-307	-316
λ_3		-1500	-1460	-1440	-1400	445	150
λ_4		8230	15100	11300	12100	13400	18900
1σ error							
SiO_2	wt.%	bdl	bdl	bdl	bdl	bdl	bdl
TiO_2	wt.%	bdl	bdl	bdl	bdl	bdl	bdl
Al_2O_3	wt.%	bdl	bdl	bdl	bdl	bdl	bdl
MnO	wt.%	0.0017	0.0013	0.0018	0.0065	0.0017	0.00131
CaO	wt.%	2.01	1.48	1.93	4.20	1.64	1.92
P_2O_5	wt.%	1.97	1.25	1.55	3.36	1.25	0.871
^{66}Zn	µg/g	bdl	bdl	bdl	bdl	bdl	bdl
^{75}As	µg/g	bdl	bdl	bdl	bdl	bdl	bdl
^{85}Rb	µg/g	bdl	bdl	bdl	bdl	bdl	bdl
^{88}Sr	µg/g	586	385	445	1020	217	115
^{89}Y	µg/g	18.7	14.7	15.0	35.1	14.6	8.78
^{90}Zr	µg/g	bdl	bdl	bdl	bdl	bdl	bdl
^{93}Nb	µg/g	bdl	bdl	bdl	bdl	bdl	bdl
^{118}Sn	µg/g	bdl	bdl	bdl	bdl	bdl	bdl
^{133}Cs	µg/g	bdl	bdl	bdl	bdl	bdl	bdl
^{137}Ba	µg/g	1.67	1.41	2.35	5.41	0.362	0.185
^{139}La	µg/g	4.31	5.07	4.35	13.3	1.41	1.20
^{140}Ce	µg/g	45.7	48.5	46.2	100	6.86	4.13
^{141}Pr	µg/g	12.1	12.5	13.4	30.5	1.13	1.05
^{143}Nd	µg/g	79.5	87.3	80.5	191	8.79	9.15
^{147}Sm	µg/g	24.8	38.6	32.2	66.0	5.05	5.16
^{151}Eu	µg/g	6.89	10.3	8.29	17.4	1.47	1.13
^{157}Gd	µg/g	23.7	30.8	23.6	53.4	5.03	5.22
^{159}Tb	µg/g	1.79	2.26	1.84	3.97	0.69	0.79
^{163}Dy	µg/g	7.88	7.24	6.45	13.7	3.99	3.52
^{165}Ho	µg/g	0.73	0.82	0.67	1.3	0.53	0.33
^{167}Er	µg/g	1.45	1.15	0.98	2.27	1.20	0.68
^{169}Tm	µg/g	0.12	0.100	0.10	0.17	0.13	0.11

File		frs4_ap_mot_24-5	frs4_ap_mot_24-7	frs4_ap_mot_24-8	frs4_ap_mot_24-11	yw61_apdz_32-1	yw61_apdz_32-2
CL Colour		"mottled" = mixed zones	"mottled" = mixed zones	"mottled" = mixed zones	"mottled" = mixed zones	blue rim	blue rim
^{171}Yb	µg/g	0.52	0.51	0.53	0.73	0.62	0.60
^{175}Lu	µg/g	0.094	0.052	0.062	0.12	0.076	0.10
^{178}Hf	µg/g	bdl	bdl	bdl	bdl	bdl	bdl
^{181}Ta	µg/g	bdl	bdl	bdl	0.0519	bdl	bdl
^{208}Pb	µg/g	2.21	3.09	3.60	4.01	0.43	0.49
^{232}Th	µg/g	0.063	0.055	0.076	0.12	0.019	bdl
^{238}U	µg/g	bdl	0.37	0.015	0.14	bdl	bdl
Detection Limit							
SiO_2	wt.%	14.4	8.31	7.74	9.72	4.58	4.31
TiO_2	wt.%	0.00252	0.00138	0.00165	0.00189	0.000912	0.00117
Al_2O_3	wt.%	0.0176	0.00962	0.0106	0.0125	0.00925	0.0112
MnO	wt.%	0.000780	0.000443	0.000468	0.000563	0.000356	0.000424
CaO	wt.%	0.256	0.140	0.152	0.179	0.113	0.132
P_2O_5	wt.%	0.0819	0.0479	0.0487	0.0601	0.0294	0.0333
^{66}Zn	µg/g	22.9	12.2	13.0	15.8	13.3	17.8
^{75}As	µg/g	21.83	12.52	14.27	16.41	11.58	14.41
^{85}Rb	µg/g	0.948	0.407	0.513	0.599	0.278	0.412
^{88}Sr	µg/g	0.394	0.253	0.207	0.369	0.177	0.246
^{89}Y	µg/g	0.334	0.198	0.187	0.235	0.268	0.368
^{90}Zr	µg/g	0.949	0.483	0.578	0.656	0.459	0.549
^{93}Nb	µg/g	0.164	0.121	0.0904	0.138	0.0740	0.0585
^{118}Sn	µg/g	1.82	1.16	1.19	1.26	0.612	0.798
^{133}Cs	µg/g	0.150	0.0540	0.0604	0.111	0.0497	0.0827
^{137}Ba	µg/g	0.706	0.348	0.472	0.822	0.305	0.195
^{139}La	µg/g	0.0303	0.0600	0.0667	0.0305	0.0522	0.0698
^{140}Ce	µg/g	0.0732	0.0220	0.0126	0.0311	0.0493	0.0653
^{141}Pr	µg/g	0.0783	0.0433	0.0323	0.0595	0.0338	0.0578
^{143}Nd	µg/g	0.506	0.152	0.279	0.426	0.268	0.450
^{147}Sm	µg/g	0.418	0.309	0.0719	0.526	0.255	0.142
^{151}Eu	µg/g	0.122	0.0901	0.0672	0.103	0.0532	0.111
^{157}Gd	µg/g	0.645	0.289	0.249	0.330	0.431	0.687
^{159}Tb	µg/g	0.0705	0.0501	0.0471	0.0409	0.0546	0.0568
^{163}Dy	µg/g	0.289	0.142	0.128	0.293	0.136	0.212
^{165}Ho	µg/g	0.0708	0.0297	0.0440	0.0480	0.0332	0.0518

File		frs4_ap_mot_24-5	frs4_ap_mot_24-7	frs4_ap_mot_24-8	frs4_ap_mot_24-11	yw61_apdz_32-1	yw61_apdz_32-2
CL Colour		"mottled" = mixed zones	"mottled" = mixed zones	"mottled" = mixed zones	"mottled" = mixed zones	blue rim	blue rim
^{167}Er	µg/g	0.285	0.154	0.160	0.212	0.180	0.202
^{169}Tm	µg/g	0.0536	0.0279	0.0295	0.0228	0.0196	0.0433
^{171}Yb	µg/g	0.329	0.293	0.280	0.285	0.198	0.269
^{175}Lu	µg/g	0.0875	0.0460	0.0370	0.0543	0.0540	0.0777
^{178}Hf	µg/g	0.267	0.122	0.165	0.229	0.154	0.171
^{181}Ta	µg/g	0.0821	0.0490	0.0365	0.0558	0.0362	0.0609
^{208}Pb	µg/g	0.140	0.117	0.115	0.117	0.0640	0.0982
^{232}Th	µg/g	0.0594	0.0178	0.0490	0.0677	0.0110	0.0537
^{238}U	µg/g	0.0700	0.0446	0.0310	0.0569	0.0355	0.0461

File		yw61_apdz_32-3	yw61_apdz_32-4	yw61_apdz_32-5	yw61_aplz_32-6	yw61_aplz_32-7	yw61_aplz_32-8	yw61_aplz_32-9	yw61_aplz_32-10
CL Colour		blue rim	blue rim	blue rim	light violet zone	light violet zone	light violet zone	light violet zone	light violet zone
SiO_2	wt.%	bdl	bdl	bdl	bdl	bdl	bdl	bdl	bdl
TiO_2	wt.%	bdl	bdl	bdl	bdl	bdl	bdl	bdl	bdl
Al_2O_3	wt.%	bdl	bdl	bdl	bdl	bdl	bdl	bdl	bdl
MnO	wt.%	0.043	0.034	0.040	0.022	0.047	0.041	0.042	0.042
CaO	wt.%	57.1	57.1	57.1	53.6	53.6	53.6	53.6	53.6
P_2O_5	wt.%	46.4	45.8	46.1	39.9	42.5	45.5	42.1	43.1
^{66}Zn	µg/g	bdl	bdl	bdl	143	bdl	bdl	bdl	59.0
^{75}As	µg/g	bdl	bdl	bdl	bdl	bdl	bdl	bdl	bdl
^{85}Rb	µg/g	bdl	bdl	bdl	bdl	bdl	bdl	bdl	bdl
^{88}Sr	µg/g	4690	4350	4630	4810	9770	13600	15000	7110
^{89}Y	µg/g	379	298	431	495	449	918	1050	604
^{90}Zr	µg/g	bdl	bdl	bdl	10.6	bdl	bdl	bdl	12.2
^{93}Nb	µg/g	bdl	bdl	bdl	bdl	bdl	bdl	bdl	bdl
^{118}Sn	µg/g	bdl	bdl	bdl	bdl	bdl	bdl	bdl	bdl
^{133}Cs	µg/g	bdl	bdl	bdl	bdl	bdl	bdl	bdl	0.095
^{137}Ba	µg/g	0.43	3.07	bdl	18.0	3.17	13.5	6.84	9.11
^{139}La	µg/g	41.7	47.6	55.1	53.1	69.0	93.0	64.2	55.0
^{140}Ce	µg/g	217	258	274	162	433	693	578	303
^{141}Pr	µg/g	49.7	60.6	62.2	39.8	103	198	190	95.9
^{143}Nd	µg/g	327	425	396	248	748	1610	1660	809
^{147}Sm	µg/g	155	210	191	143	381	846	1120	549
^{151}Eu	µg/g	63.4	81.7	75.7	62.3	132	332	409	198
^{157}Gd	µg/g	216	278	252	241	427	1060	1260	678
^{159}Tb	µg/g	28.2	30.7	31.9	30.0	48.5	110	134	71.4
^{163}Dy	µg/g	118	113	131	137	182	399	466	265
^{165}Ho	µg/g	14.3	11.6	15.3	16.9	19.6	39.7	46.5	26.7
^{167}Er	µg/g	25.6	17.0	26.3	27.8	29.1	57.0	70.7	40.5
^{169}Tm	µg/g	2.15	1.47	2.31	2.23	2.13	4.97	5.91	3.00
^{171}Yb	µg/g	11.8	5.70	12.3	10.8	9.49	22.7	27.9	15.5
^{175}Lu	µg/g	1.20	0.61	1.46	1.27	0.96	2.75	3.01	1.60
^{178}Hf	µg/g	bdl	bdl	bdl	bdl	bdl	bdl	bdl	bdl
^{181}Ta	µg/g	bdl	bdl	bdl	bdl	bdl	bdl	bdl	bdl
^{208}Pb	µg/g	9.16	6.12	9.32	44.8	10.3	11.7	7.58	14.3
^{232}Th	µg/g	bdl	0.99	0.11	21.3	2.32	11.0	0.935	9.03
^{238}U	µg/g	bdl	0.28	bdl	232	bdl	bdl	0.101	82.9

File		yw61_apdz_32-3	yw61_apdz_32-4	yw61_apdz_32-5	yw61_aplz_32-6	yw61_aplz_32-7	yw61_aplz_32-8	yw61_aplz_32-9	yw61_aplz_32-10
CL Colour		blue rim	blue rim	blue rim	light violet zone	light violet zone	light violet zone	light violet zone	light violet zone
λ_0		5.65	5.58	5.80	5.65	6.06	6.81	6.89	6.29
λ_1		8.46	13.1	9.50	7.39	13.2	10.8	8.60	9.23
λ_2		-301	-371	-297	-297	-381	-400	-436	-411
λ_3		144	272	5.16	1060	35.3	-568	-768	-73.4
λ_4		14000	19600	18800	23600	16800	24000	24200	29700
1σ error									
SiO_2	wt.%	bdl	bdl	bdl	bdl	bdl	bdl	bdl	bdl
TiO_2	wt.%	bdl	bdl	bdl	bdl	bdl	bdl	bdl	bdl
Al_2O_3	wt.%	bdl	bdl	bdl	bdl	bdl	bdl	bdl	bdl
MnO	wt.%	0.0011	0.0013	0.0011	0.00068	0.000937	0.003	0.00097	0.0011
CaO	wt.%	1.65	1.35	1.66	1.85	1.49	1.15	1.24	1.58
P_2O_5	wt.%	1.19	1.59	1.47	1.45	1.02	1.56	1.37	1.10
^{66}Zn	µg/g	bdl	bdl	bdl	19.2	bdl	bdl	bdl	7.32
^{75}As	µg/g	bdl	bdl	bdl	bdl	bdl	bdl	bdl	bdl
^{85}Rb	µg/g	bdl	bdl	bdl	bdl	bdl	bdl	bdl	bdl
^{88}Sr	µg/g	111	109	112	112	437	201	384	350
^{89}Y	µg/g	10.3	12.5	12.3	17.3	24.5	31.2	27.9	38.2
^{90}Zr	µg/g	bdl	bdl	bdl	1.14	bdl	bdl	bdl	1.33
^{93}Nb	µg/g	bdl	bdl	bdl	bdl	bdl	bdl	bdl	bdl
^{118}Sn	µg/g	bdl	bdl	bdl	bdl	bdl	bdl	bdl	bdl
^{133}Cs	µg/g	bdl	bdl	bdl	bdl	bdl	bdl	bdl	0.056
^{137}Ba	µg/g	0.20	0.56	bdl	1.01	0.72	3.26	1.54	1.15
^{139}La	µg/g	1.70	1.49	1.67	2.64	3.92	4.51	1.75	1.90
^{140}Ce	µg/g	7.72	4.13	8.15	4.13	32.8	24.8	18.1	16.8
^{141}Pr	µg/g	1.71	1.02	1.74	1.14	8.02	5.79	4.34	6.64
^{143}Nd	µg/g	11.5	12.4	12.6	6.45	62.6	57.8	36.4	59.7
^{147}Sm	µg/g	4.74	6.95	6.26	6.93	32.4	26.9	28.1	41.3
^{151}Eu	µg/g	2.08	1.64	2.31	1.88	9.83	5.53	9.12	17.7
^{157}Gd	µg/g	5.89	6.03	7.74	8.15	35.2	14.1	24.9	48.8
^{159}Tb	µg/g	0.71	0.93	0.95	0.87	3.55	1.46	2.54	4.74
^{163}Dy	µg/g	2.95	4.81	4.19	4.1	11.7	5.54	9.58	18.5
^{165}Ho	µg/g	0.31	0.54	0.42	0.59	1.39	0.71	1.39	1.98
^{167}Er	µg/g	0.52	1.48	0.82	1.67	2.06	1.94	2.13	2.79
^{169}Tm	µg/g	0.068	0.35	0.099	0.15	0.21	0.18	0.18	0.18

File		yw61_apdz_32-3	yw61_apdz_32-4	yw61_apdz_32-5	yw61_aplz_32-6	yw61_aplz_32-7	yw61_aplz_32-8	yw61_aplz_32-9	yw61_aplz_32-10
CL Colour		blue rim	blue rim	blue rim	light violet zone	light violet zone	light violet zone	light violet zone	light violet zone
^{171}Yb	µg/g	0.54	0.75	0.55	0.78	0.82	1.15	1.18	1.32
^{175}Lu	µg/g	0.064	0.069	0.069	0.13	0.12	0.20	0.14	0.14
^{178}Hf	µg/g	bdl	bdl	bdl	bdl	bdl	bdl	bdl	bdl
^{181}Ta	µg/g	bdl	bdl	bdl	bdl	bdl	bdl	bdl	bdl
^{208}Pb	µg/g	0.47	0.32	0.38	2.33	0.70	0.85	0.73	0.58
^{232}Th	µg/g	bdl	0.38	0.020	0.86	0.60	1.09	0.11	0.59
^{238}U	µg/g	bdl	0.075	bdl	18.9	bdl	bdl	0.040	8.37
Detection Limit									
SiO_2	wt.%	4.72	6.23	4.81	7.63	6.21	6.78	4.74	5.41
TiO_2	wt.%	0.000827	0.00114	0.00119	0.00154	0.00112	0.00162	0.00127	0.00140
Al_2O_3	wt.%	0.0105	0.0120	0.0106	0.0141	0.0119	0.0138	0.0111	0.0110
MnO	wt.%	0.000407	0.000473	0.000413	0.000560	0.000459	0.000538	0.000420	0.000434
CaO	wt.%	0.115	0.133	0.115	0.175	0.133	0.159	0.122	0.118
P_2O_5	wt.%	0.0298	0.0355	0.0293	0.0405	0.0330	0.0395	0.0296	0.0288
^{66}Zn	µg/g	16.5	20.1	16.8	23.9	19.9	22.5	18.1	16.9
^{75}As	µg/g	12.79	16.61	13.25	20.28	17.03	20.49	14.84	15.60
^{85}Rb	µg/g	0.383	0.407	0.381	0.577	0.469	0.539	0.464	0.381
^{88}Sr	µg/g	0.217	0.293	0.237	0.328	0.276	0.401	0.265	0.251
^{89}Y	µg/g	0.329	0.385	0.330	0.473	0.431	0.426	0.344	0.365
^{90}Zr	µg/g	0.550	0.658	0.536	0.761	0.615	0.773	0.626	0.546
^{93}Nb	µg/g	0.0872	0.145	0.0285	0.188	0.164	0.116	0.164	0.109
^{118}Sn	µg/g	0.827	0.861	0.731	1.28	0.809	1.13	0.877	0.815
^{133}Cs	µg/g	0.0569	0.100	0.0680	0.119	0.0715	0.104	0.0657	0.0561
^{137}Ba	µg/g	0.403	0.487	0.380	0.702	0.606	0.687	0.211	0.213
^{139}La	µg/g	0.0707	0.0728	0.0472	0.1003	0.0623	0.0937	0.0697	0.0709
^{140}Ce	µg/g	0.0610	0.0795	0.0588	0.0962	0.0769	0.114	0.0710	0.0674
^{141}Pr	µg/g	0.0414	0.0602	0.0337	0.0749	0.0544	0.0772	0.0499	0.0476
^{143}Nd	µg/g	0.311	0.366	0.372	0.707	0.602	0.602	0.616	0.384
^{147}Sm	µg/g	0.258	0.353	0.188	0.642	0.466	0.283	0.401	0.407
^{151}Eu	µg/g	0.0914	0.131	0.0818	0.128	0.107	0.139	0.129	0.122
^{157}Gd	µg/g	0.600	0.658	0.482	0.832	0.656	0.945	0.638	0.603
^{159}Tb	µg/g	0.0614	0.0650	0.0550	0.107	0.0691	0.109	0.0658	0.0693
^{163}Dy	µg/g	0.156	0.249	0.190	0.319	0.256	0.328	0.227	0.198
^{165}Ho	µg/g	0.0294	0.0489	0.0260	0.0778	0.0624	0.0825	0.0452	0.0544

File		yw61_apdz_32-3	yw61_apdz_32-4	yw61_apdz_32-5	yw61_aplz_32-6	yw61_aplz_32-7	yw61_aplz_32-8	yw61_aplz_32-9	yw61_aplz_32-10
CL Colour		blue rim	blue rim	blue rim	light violet zone	light violet zone	light violet zone	light violet zone	light violet zone
^{167}Er	µg/g	0.188	0.215	0.145	0.278	0.232	0.299	0.233	0.177
^{169}Tm	µg/g	0.0383	0.0461	0.0359	0.0658	0.0399	0.0674	0.0501	0.0476
^{171}Yb	µg/g	0.315	0.383	0.251	0.493	0.455	0.584	0.340	0.410
^{175}Lu	µg/g	0.0471	0.0722	0.0583	0.0937	0.0587	0.102	0.0603	0.0636
^{178}Hf	µg/g	0.186	0.206	0.162	0.245	0.263	0.251	0.215	0.191
^{181}Ta	µg/g	0.0607	0.0693	0.0589	0.0647	0.0656	0.106	0.0601	0.0572
^{208}Pb	µg/g	0.0918	0.126	0.0845	0.206	0.155	0.175	0.142	0.0540
^{232}Th	µg/g	0.0502	0.0436	0.0100	0.0888	0.0523	0.0940	0.0626	0.0388
^{238}U	µg/g	0.0408	0.0570	0.0407	0.0897	0.0534	0.0725	0.0426	0.0553

Chapter 4 Appendices

Appendix 4.A – Monazite U–Pb Results

Source file	$^{238}U/^{206}Pb$	2σ	$^{207}Pb/^{206}Pb$	2σ	$^{207}Pb/^{235}U$	2σ	$^{207}Pb/^{206}Pb$ Age	2σ	$^{206}Pb/^{238}U$ Age	2σ	$^{207}Pb/^{235}U$ Age	2σ	U µg/g	2σ	Th µg/g	2σ	Th/U
DMCY139-2	5.190	0.19	0.372	0.012	9.640	0.50	3796	49	1131	35	2397	48	21.6	0.28	39600	640	1830
DMCY139-6	5.542	0.14	0.2471	0.0098	6.050	0.27	3160	64	1072	23	1977	38	25.6	0.68	46600	790	1820
DMCY139-8	4.720	0.16	0.533	0.018	15.16	0.51	4335	50	1227	36	2822	32	13.9	0.17	46400	740	3340
DMCY139-13	4.800	0.19	0.486	0.020	13.82	0.66	4203	57	1213	41	2741	42	8.1	0.14	45600	580	5700
DMCY139-15	5.230	0.15	0.315	0.013	7.980	0.31	3536	62	1122	28	2241	36	28.3	0.36	44500	590	1570
DMCY139-16	5.320	0.18	0.34	0.016	8.580	0.48	3653	71	1108	32	2288	51	20.7	0.36	47200	730	2280
DMCY139-17	5.060	0.22	0.444	0.017	11.81	0.64	4072	62	1171	46	2594	54	21.6	0.32	51900	850	2400
DMCY139-18	4.940	0.16	0.422	0.016	11.44	0.44	3982	58	1192	34	2557	37	14.1	0.24	34500	460	2440
DMCY139-21	4.950	0.15	0.431	0.017	11.37	0.46	4015	59	1190	33	2560	41	23.3	0.46	47200	610	2030
DMCY139-23	4.740	0.18	0.498	0.026	13.74	0.65	4223	76	1240	42	2727	45	16.7	0.28	47400	740	2850
DMCY139-25	4.360	0.19	0.592	0.025	17.87	0.73	4482	64	1328	49	2980	40	14.1	0.46	31300	570	2220
DMCY139-28	4.640	0.17	0.468	0.013	13.18	0.58	4139	41	1264	40	2698	44	12.6	0.16	34800	530	2760
DMCY139-30	5.600	0.16	0.2165	0.0084	5.180	0.22	2940	64	1054	26	1851	35	31.8	0.47	31900	310	1000
HK1-1	4.260	0.13	0.296	0.013	9.610	0.42	3413	67	1358	35	2397	40	3.1	0.06	5870	80	1900
HK1-2	4.460	0.17	0.251	0.015	7.650	0.46	3169	93	1306	44	2183	54	4.9	0.10	9890	190	2000
HK1-4	4.580	0.2	0.245	0.019	7.480	0.55	3140	120	1274	52	2169	63	3.9	0.24	7990	470	2100
HK1-5	4.810	0.15	0.191	0.010	5.590	0.31	2735	95	1220	34	1921	48	5.1	0.10	8240	160	1600
HK1-6	4.910	0.16	0.166	0.011	4.610	0.31	2500	110	1203	34	1748	58	5.8	0.13	8380	150	1500
HK1-7	4.690	0.18	0.182	0.014	5.270	0.37	2660	120	1256	44	1862	57	4.2	0.07	5710	78	1400
HK1-8	5.138	0.12	0.1106	0.0042	2.990	0.14	1805	72	1143	24	1400	34	23.1	0.79	4260	130	185
HK1-9	5.355	0.11	0.1063	0.0031	2.672	0.09	1725	54	1104	20	1320	24	30.3	0.5	4720	60	156
HK1-10	5.270	0.16	0.1034	0.0048	2.580	0.14	1671	85	1123	30	1290	40	26.9	0.44	5260	60	195
HK1-11	4.360	0.18	0.283	0.012	8.720	0.41	3382	67	1331	48	2320	38	4.4	0.09	6620	140	1500
HK1-12	4.660	0.19	0.246	0.017	6.810	0.40	3120	110	1259	46	2095	51	5.6	0.11	7090	100	1300
HK1-13	3.660	0.19	0.366	0.029	13.63	0.97	3740	120	1552	62	2713	67	3.0	0.06	4260	80	1400

Source file	$^{238}U/^{206}Pb$	2σ	$^{207}Pb/^{206}Pb$	2σ	$^{207}Pb/^{235}U$	2σ	$^{207}Pb/^{206}Pb$ Age	2σ	$^{206}Pb/^{238}U$ Age	2σ	$^{207}Pb/^{235}U$ Age	2σ	U µg/g	2σ	Th µg/g	2σ	Th/U
HK1-15	4.540	0.22	0.216	0.013	6.270	0.50	2970	110	1270	55	2021	70	3.8	0.12	6710	150	1800
HK1-17	4.640	0.16	0.205	0.010	5.760	0.29	2845	84	1259	38	1945	44	4.8	0.08	7340	90	1500
HK1-24	3.110	0.14	0.457	0.035	20.30	1.20	4110	130	1811	70	3101	57	6.2	0.09	7740	100	1200
HK1-26	4.060	0.18	0.309	0.021	10.21	0.68	3500	100	1430	58	2445	61	3.7	0.09	6840	50	1800
HK1-28	3.910	0.18	0.351	0.030	11.69	0.79	3670	130	1454	57	2570	64	4.8	0.08	9200	140	1900
LEQ130-1	5.510	0.17	0.1047	0.0057	2.500	0.14	1670	100	1078	30	1276	40	16.5	0.21	6940	90	422
LEQ130-2	4.770	0.15	0.193	0.011	5.250	0.31	2747	95	1231	35	1887	49	9.9	0.25	6730	110	680
LEQ130-3	5.100	0.2	0.166	0.015	4.440	0.47	2500	140	1160	41	1686	84	12.0	0.23	5420	90	451
LEQ130-4	5.280	0.16	0.1262	0.0087	3.170	0.22	1910	120	1111	29	1420	51	5.1	0.07	2550	30	500
LEQ130-5	5.690	0.23	0.0883	0.0098	2.080	0.26	1460	220	1049	39	1129	84	15.1	0.33	7950	130	527
LEQ130-6	3.610	0.13	0.388	0.019	14.16	0.75	3853	76	1567	49	2750	51	5.3	0.08	5750	180	1100
LEQ130-7	5.070	0.18	0.1435	0.0096	3.880	0.29	2220	130	1161	37	1601	62	4.6	0.09	2440	40	530
LEQ130-8	5.310	0.16	0.1075	0.0058	2.690	0.14	1735	97	1107	30	1330	38	18.1	0.41	8670	140	479
LEQ130-9	1.816	0.065	0.664	0.017	48.80	1.6	4654	39	2848	82	3965	33	11.5	0.25	8170	130	713
LEQ130-11	5.600	0.15	0.0926	0.0039	2.241	0.10	1515	74	1056	24	1199	31	17.2	0.24	8270	110	482
LEQ130-12	5.590	0.2	0.1053	0.0071	2.620	0.20	1750	130	1066	33	1299	55	14.6	0.26	8850	170	605
LEQ130-13	5.100	0.27	0.152	0.015	4.070	0.39	2360	180	1166	54	1655	83	6.4	0.13	3219	40	510
LEQ130-14	5.150	0.16	0.1258	0.0091	3.310	0.24	1980	130	1135	33	1478	57	12.3	0.26	11500	180	933
LEQ130-15	4.920	0.22	0.19	0.017	5.440	0.47	2780	150	1187	46	1879	73	5.5	0.14	8000	90	1400
LEQ130-16	5.120	0.2	0.197	0.014	4.990	0.25	2800	110	1146	44	1813	41	16.2	0.62	9010	140	558
LEQ130-17	5.350	0.15	0.1153	0.0067	2.920	0.16	1916	95	1111	28	1401	40	5.5	0.09	2600	40	470
LEQ130-18	5.380	0.2	0.132	0.011	3.260	0.23	2030	150	1115	38	1475	63	5.9	0.09	2940	40	500
LEQ130-19	5.540	0.22	0.126	0.010	3.130	0.23	2100	130	1078	38	1444	57	5.9	0.13	2690	40	460
LEQ130-20	5.090	0.16	0.1646	0.0092	4.430	0.28	2488	95	1157	30	1704	52	11.7	0.17	7280	110	624
LEQ130-21	4.780	0.26	0.208	0.015	5.870	0.36	2900	130	1236	62	1965	58	9.6	0.17	3050	70	320
LEQ130-22	5.600	0.21	0.0964	0.008	2.300	0.19	1520	150	1063	35	1201	56	6.9	0.13	7040	140	1000
LEQ130-23	3.540	0.14	0.385	0.019	14.41	0.75	3856	82	1611	56	2782	50	6.4	0.14	6550	70	1000

Source file	$^{238}U/^{206}Pb$	2σ	$^{207}Pb/^{206}Pb$	2σ	$^{207}Pb/^{235}U$	2σ	$^{207}Pb/^{206}Pb$ Age	2σ	$^{206}Pb/^{238}U$ Age	2σ	$^{207}Pb/^{235}U$ Age	2σ	U µg/g	2σ	Th µg/g	2σ	Th/U
LEQ130-24	4.840	0.25	0.201	0.019	5.420	0.49	2770	160	1209	58	1899	80	6.1	0.11	8490	150	1400
LEQ130-25	4.190	0.18	0.288	0.019	9.230	0.79	3407	98	1379	56	2343	82	10.5	0.21	7890	150	752
LEQ130-26	2.670	0.17	0.529	0.070	26.20	3.1	4290	200	2060	120	3340	110	3.7	0.08	19100	420	5100
LEQ130-28	3.360	0.15	0.394	0.018	15.95	0.57	3894	64	1691	68	2872	35	14.8	0.41	17700	340	1200
LEQ130-29	2.220	0.17	0.613	0.044	37.50	2.9	4520	110	2440	150	3710	72	4.4	0.07	19600	310	4400
LEQ130-30	2.950	0.16	0.535	0.043	23.90	2.5	4320	120	1878	93	3260	110	7.3	0.13	28900	380	4000
LEQ130-31	5.560	0.25	0.083	0.012	2.010	0.29	1180	300	1060	39	1100	100	8.9	0.19	8080	170	910
FRS4-2	2.149	0.051	0.6150	0.013	38.26	1.1	4541	30	2469	46	3727	28	6.7	0.12	7610	160	1100
FRS4-3	4.100	0.17	0.3000	0.018	9.720	0.65	3445	92	1419	49	2414	62	2.5	0.04	8730	90	3500
FRS4-4	4.330	0.15	0.2670	0.017	8.280	0.48	3280	110	1349	43	2260	55	2.7	0.04	11040	130	4100
FRS4-5	1.628	0.066	0.7120	0.025	57.40	2.6	4763	56	3083	91	4136	42	2.9	0.07	10140	100	3500
FRS4-6	3.232	0.11	0.4310	0.021	17.39	0.63	4036	73	1735	47	2954	34	6.6	0.12	12040	160	1800
FRS4-7	3.870	0.15	0.3140	0.020	10.86	0.81	3513	100	1493	52	2518	69	2.7	0.07	13400	250	5000
FRS4-8	1.591	0.041	0.7200	0.014	61.00	2.1	4782	33	3150	60	4188	35	7.9	0.11	8530	80	1100
FRS4-9	4.250	0.18	0.2460	0.013	7.890	0.52	3187	86	1366	49	2216	58	4.2	0.08	16400	230	3900
FRS4-10	5.010	0.15	0.1210	0.013	3.320	0.34	1930	200	1176	30	1487	78	8.9	0.16	14600	290	1700
FRS4-11	1.525	0.059	0.7140	0.027	63.60	2.7	4778	58	3257	92	4227	42	1.6	0.06	15900	180	9900
FRS4-12	4.690	0.19	0.1850	0.016	5.250	0.43	2640	150	1265	46	1861	70	1.2	0.02	10200	110	8300
FRS4-13	3.540	0.17	0.3960	0.039	15.00	1.2	3830	140	1585	69	2808	81	1.6	0.04	9220	120	5700
FRS4-15	4.900	0.23	0.1680	0.021	4.660	0.52	2560	210	1213	55	1749	95	2.3	0.06	8450	130	3640
FRS4-16	1.364	0.05	0.7410	0.034	72.9	1.8	4829	76	3554	98	4369	25	6.1	0.19	6760	90	1100
FRS4-17	1.862	0.096	0.6510	0.047	46.8	3.6	4630	120	2750	110	3927	78	1.0	0.04	11400	250	11000
FRS4-18	0.5740	0.035	0.8670	0.040	206	13	5113	90	6540	240	5421	70	1.2	0.04	15400	310	13000
FRS4-19	1.330	0.10	0.7370	0.067	75.5	6.3	4810	160	3680	210	4422	82	1.5	0.03	9630	150	6500
FRS4--20	0.6120	0.019	0.8690	0.019	193.8	6.4	5118	43	6233	110	5350	33	3.5	0.14	10100	190	2900
FRS4-21	1.010	0.027	0.8260	0.022	111.6	4.6	5021	49	4444	83	4792	42	6.7	0.14	10000	130	1500
FRS4-22	1.597	0.074	0.6940	0.033	59.6	2.6	4722	75	3160	120	4174	47	4.3	0.12	13500	190	3130

Source file	$^{238}U/^{206}Pb$	2σ	$^{207}Pb/^{206}Pb$	2σ	$^{207}Pb/^{235}U$	2σ	$^{207}Pb/^{206}Pb$ Age	2σ	$^{206}Pb/^{238}U$ Age	2σ	$^{207}Pb/^{235}U$ Age	2σ	U µg/g	2σ	Th µg/g	2σ	Th/U
FRS4-23	4.700	0.23	0.1840	0.023	5.30	0.62	2590	220	1254	52	1840	100	1.7	0.06	8560	110	4900
FRS4-24	3.140	0.16	0.4600	0.038	19.8	1.5	4080	120	1790	76	3080	70	1.1	0.03	9480	110	8500
FRS4-25	0.6060	0.018	0.8600	0.023	190.1	6.4	5097	52	6298	110	5330	34	1.5	0.03	8810	110	5800
FRS4-26	1.244	0.054	0.7890	0.037	87.9	5.5	4936	82	3820	120	4548	63	2.6	0.06	10700	150	4200
FRS4-27	1.644	0.078	0.7390	0.030	61.5	2.9	4824	68	3080	110	4194	48	6.7	0.28	10900	150	1600
FRS4-28	4.380	0.24	0.2490	0.020	7.64	0.58	3170	130	1348	64	2182	70	2.2	0.04	12200	160	5600
FRS4-29	0.4110	0.013	0.9110	0.024	300.3	9.5	5212	54	7960	140	5794	32	4.0	0.061	12100	230	3100
FRS4-30	0.5036	0.012	0.8890	0.012	237.5	6.3	5163	27	7048	100	5563	29	3.5	0.05	10100	90	2900
FRS4-31	4.680	0.18	0.2020	0.013	5.76	0.37	2810	100	1257	41	1931	56	9.8	0.17	7310	110	750
FRS4-33	3.254	0.11	0.4450	0.020	18.5	0.67	4073	62	1725	49	3013	35	10.2	0.16	8270	130	812
FRS4-34	4.243	0.11	0.2450	0.011	7.69	0.39	3148	69	1362	29	2207	45	8.7	0.16	9990	130	1200
FRS4-35	3.400	0.093	0.3920	0.015	15.43	0.67	3879	58	1666	38	2837	40	14.3	0.26	11000	170	768
FRS4-36	3.177	0.098	0.4300	0.021	18.6	1.1	4002	72	1770	45	3009	57	9.2	0.18	10300	160	1100
FRS4-37	0.5780	0.017	0.8940	0.034	206.8	8.3	5174	77	6484	120	5416	41	2.8	0.06	11200	200	3900
FRS4-38	0.6420	0.02	0.8840	0.026	184.5	8	5152	59	6031	110	5300	44	4.1	0.11	11500	150	2800
FRS4-39	3.558	0.10	0.3440	0.014	13.08	0.67	3686	58	1601	40	2680	47	10.6	0.22	12200	210	1150
FRS4-40	4.300	0.18	0.2480	0.013	7.83	0.36	3175	77	1348	48	2218	46	6.1	0.13	10300	200	1700
FRS4-32	4.360	0.19	0.2540	0.023	7.79	0.72	3160	150	1335	55	2186	80	5.0	0.12	9430	160	1900
YN49-6	3.170	0.22	0.4500	0.054	18.9	2	4050	180	1787	100	3034	99	0.75	0.03	7760	120	10000
YN49-7	4.140	0.19	0.3450	0.029	11.09	0.8	3650	130	1398	58	2517	69	4.7	0.07	20600	270	4400
YN49-8	1.354	0.091	0.7860	0.051	76.2	4.4	4930	120	3550	210	4404	59	1.8	0.04	23600	390	13000
YN49-9	5.110	0.23	0.1140	0.012	2.93	0.3	1820	220	1142	52	1383	80	11.4	0.35	10000	310	877
YN49-11	5.550	0.19	0.0889	0.008	2.1	0.19	1310	180	1078	34	1146	61	7.3	0.12	4320	60	590
YN49-13	4.880	0.30	0.2420	0.026	6.37	0.74	3080	190	1198	67	2035	96	6.2	0.38	23300	410	3800
YN49-14	3.240	0.22	0.4550	0.043	19.4	1.9	4070	150	1780	100	3040	110	2.7	0.12	25900	510	9500
YN49-16	2.090	0.15	0.6710	0.054	43.1	3.6	4650	140	2500	140	3837	76	1.4	0.09	11600	220	8200
YN49-18	2.640	0.17	0.5400	0.051	27.5	2.8	4320	140	2090	120	3375	88	1.2	0.04	17300	250	15000
YN49-19	2.550	0.16	0.5990	0.044	31.2	2.2	4490	110	2150	110	3519	67	2.5	0.11	19800	330	7800

Source file	$^{238}U/^{206}Pb$	2σ	$^{207}Pb/^{206}Pb$	2σ	$^{207}Pb/^{235}U$	2σ	$^{207}Pb/^{206}Pb$ Age	2σ	$^{206}Pb/^{238}U$ Age	2σ	$^{207}Pb/^{235}U$ Age	2σ	U µg/g	2σ	Th µg/g	2σ	Th/U
YN49-22	2.590	0.29	0.5480	0.083	29.7	3.9	4460	270	2140	190	3480	120	0.43	0.02	7030	80	16000
YN49-24	2.810	0.18	0.5030	0.046	24.9	1.9	4220	130	2000	110	3280	76	2.1	0.08	7910	160	3800
YN49-29	5.240	0.20	0.1620	0.014	4.41	0.52	2480	140	1131	38	1691	97	9.0	0.21	12300	200	1400
YN49-30	5.360	0.21	0.1180	0.011	2.99	0.26	1870	170	1110	39	1395	66	6.4	0.15	10000	220	1600
BH224-2	7.420	0.15	0.0659	0.0064	1.37	0.13	580	190	811	15	840	55	24.5	0.73	26700	730	1090
BH224-5	6.710	0.21	0.1590	0.013	3.71	0.30	2430	130	901	26	1572	67	48.7	0.95	23300	950	479
BH224-7	6.360	0.23	0.2320	0.019	5.53	0.49	3060	120	947	32	1918	80	34.6	1.4	13900	1500	402
BH224-8	7.400	0.18	0.0940	0.0081	1.97	0.16	1440	160	829	21	1085	54	21.3	0.37	18000	380	845
BH224-15	7.000	0.17	0.1054	0.0085	2.32	0.18	1730	140	856	21	1211	57	30.3	0.71	34900	590	1150
BH224-16	7.280	0.26	0.0870	0.0063	1.81	0.13	1380	150	836	27	1051	47	28.4	0.58	23600	330	830
BH224-17	6.160	0.22	0.2230	0.014	5.46	0.33	2971	100	969	30	1901	52	28.7	0.33	28500	410	994
BH224-18	7.440	0.15	0.0604	0.0048	1.223	0.093	550	170	818	16	808	42	32.0	0.53	26300	450	823
BH224-19	7.450	0.20	0.0592	0.0049	1.23	0.096	530	190	811	19	811	45	35.0	0.57	27100	500	774
BH224-23	7.370	0.25	0.0817	0.010	1.75	0.21	1100	260	820	29	1004	81	51.3	1.5	41100	990	801
BH224-24	6.420	0.27	0.1890	0.015	4.61	0.35	2700	140	934	34	1751	64	29.3	0.75	57700	1600	1967
BH224-325	6.460	0.28	0.1610	0.014	3.81	0.31	2490	160	934	39	1599	73	21.2	0.78	17600	700	829
BH224-26	5.170	0.33	0.3540	0.032	10.7	0.88	3670	140	1168	63	2488	76	9.4	0.67	14600	540	1600
BH224-27	7.220	0.3	0.0830	0.012	1.79	0.26	1200	290	843	32	1018	93	39.8	1.1	40100	590	1010
BH224-28	6.490	0.42	0.2340	0.047	5.5	1	2990	340	923	52	1830	180	11.0	0.37	2270	120	207
BH224-29	6.530	0.17	0.1700	0.013	3.84	0.26	2540	130	921	23	1613	59	37.3	0.68	47700	680	1280
YN50-2	3.370	0.15	0.2980	0.021	12.22	0.76	3440	110	1683	65	2617	59	6.6	0.36	31400	500	4700
YN50-3	2.228	0.088	0.5790	0.025	35.8	1.6	4439	66	2395	77	3673	42	1.7	0.05	26200	290	15000
YN50-4	2.081	0.094	0.5800	0.026	40	1.8	4465	67	2565	95	3760	46	1.3	0.05	23400	330	19000
YN50-5	4.310	0.19	0.1579	0.0081	5	0.42	2440	94	1329	55	1806	71	6.7	0.18	21800	290	3270
YN50-7	1.940	0.069	0.6200	0.033	44.2	2.4	4545	79	2693	80	3861	54	1.5	0.04	28800	400	20000
YN50-8	1.760	0.063	0.6530	0.023	52.1	2.1	4626	54	2922	85	4026	41	2.0	0.06	28000	410	14000
YN50-9	1.859	0.062	0.6490	0.03	47.9	2.4	4625	75	2775	74	3956	53	1.5	0.05	29500	440	20000
YN50-12	4.095	0.097	0.2187	0.0082	7.23	0.33	2955	61	1404	30	2138	40	10.5	0.21	18200	240	1740

Source file	$^{238}U/^{206}Pb$	2σ	$^{207}Pb/^{206}Pb$	2σ	$^{207}Pb/^{235}U$	2σ	$^{207}Pb/^{206}Pb$ Age	2σ	$^{206}Pb/^{238}U$ Age	2σ	$^{207}Pb/^{235}U$ Age	2σ	U µg/g	2σ	Th µg/g	2σ	Th/U
YN50-13	1.955	0.086	0.6190	0.027	43.5	2.3	4545	64	2667	92	3845	52	1.3	0.03	20500	300	16000
YN50-14	4.225	0.11	0.1625	0.0076	5.22	0.25	2464	81	1373	32	1868	40	15.4	0.29	11300	220	736
YN50-16	2.590	0.14	0.5230	0.048	28.1	2.2	4270	140	2100	98	3427	71	2.4	0.09	16600	340	6900
YN50-17	3.066	0.088	0.3690	0.013	16.67	0.60	3782	53	1820	45	2910	34	5.8	0.13	17600	210	3100
YN50-18	3.400	0.15	0.3600	0.016	14.53	0.84	3769	68	1661	65	2788	57	7.6	0.16	16000	210	2100
YN50-19	2.650	0.11	0.4810	0.023	24.5	1.3	4187	64	2052	77	3300	52	1.9	0.06	17800	260	9200
YN50-20	3.980	0.17	0.2250	0.012	7.81	0.46	3022	80	1433	50	2202	52	7.2	0.2	20700	420	2900
YN50-21	2.010	0.11	0.6050	0.038	42.4	2.4	4503	93	2630	110	3830	52	1.4	0.0270	28900	390	21000
YN50-24	2.058	0.086	0.5750	0.029	38.7	2.4	4446	70	2554	92	3738	60	2.5	0.08	32700	330	13000
YN50-26	1.419	0.044	0.7040	0.026	68	2.5	4754	58	3421	90	4301	34	1.5	0.03	34300	400	23000
YN50-27	4.540	0.11	0.1118	0.0064	3.39	0.18	1820	100	1286	29	1505	44	17.4	0.35	39100	750	2250
YN50-28	4.499	0.09	0.1072	0.0034	3.274	0.11	1730	59	1297	24	1470	26	17.4	0.23	25800	270	1480
YN50-29	2.055	0.097	0.5870	0.025	39.6	1.9	4469	61	2557	96	3755	49	1.8	0.05	28900	380	16000
LE1-1	3.870	0.26	0.2800	0.022	9.93	0.85	3370	130	1477	93	2456	79	6.7	0.2	40900	590	6100
LE1-3	2.380	0.15	0.5460	0.029	32	2.4	4361	76	2280	120	3542	71	6.2	0.26	37500	910	6100
LE1-4	2.955	0.13	0.3930	0.019	18.7	1.3	3872	74	1884	73	3018	69	10.0	0.38	42400	870	4230
LE1-5	3.431	0.15	0.3450	0.012	14.16	0.77	3691	53	1661	66	2754	53	8.4	0.12	31100	510	3700
LE1-7	3.250	0.14	0.3980	0.016	17.12	0.93	3888	62	1738	66	2936	53	12.1	0.22	50800	770	4210
LE1-8	4.780	0.22	0.1013	0.0053	3	0.19	1620	100	1232	52	1404	49	52.1	1.1	43200	690	829
LE1-9	3.530	0.17	0.3070	0.013	12.05	0.76	3498	66	1616	65	2602	59	8.3	0.25	45200	1100	5400
LE1-11	3.091	0.13	0.3820	0.015	17.09	0.9	3856	60	1802	65	2936	51	12.6	0.3	56800	1200	4500
LE1-12	4.520	0.20	0.1790	0.011	5.39	0.39	2680	100	1293	52	1876	62	26.1	0.93	33700	400	1290
LE1-14	3.045	0.13	0.3910	0.021	18.1	1.3	3877	86	1828	72	2981	71	5.9	0.23	26600	690	4500
LE1-16	3.340	0.19	0.3450	0.025	13.8	1.2	3680	120	1703	84	2722	80	5.1	0.09	22500	390	4400
LE1--18	3.330	0.18	0.3650	0.021	14.91	1.1	3751	93	1694	84	2800	70	4.6	0.15	25500	290	5500
LE1-21	4.770	0.19	0.1080	0.0038	3.12	0.18	1758	67	1223	48	1434	44	53.8	1.2	49300	1600	916
LE1-27	3.450	0.19	0.3750	0.025	14.68	1.1	3790	100	1635	84	2814	74	8.8	0.22	30400	510	3500
LRS150-1	5.350	0.32	0.1390	0.022	3.49	0.56	2100	320	1133	59	1450	140	8.2	0.29	106000	3600	13000

Source file	$^{238}U/^{206}Pb$	2σ	$^{207}Pb/^{206}Pb$	2σ	$^{207}Pb/^{235}U$	2σ	$^{207}Pb/^{206}Pb$ Age	2σ	$^{206}Pb/^{238}U$ Age	2σ	$^{207}Pb/^{235}U$ Age	2σ	U µg/g	2σ	Th µg/g	2σ	Th/U
LRS150-2	5.400	0.31	0.1440	0.022	4.03	0.59	2120	330	1126	63	1610	120	6.6	0.37	107000	2700	16000
LRS150-3	3.760	0.32	0.3970	0.044	17	3	3840	170	1590	130	2800	170	3.5	0.17	43300	1300	12000
LRS150-5	2.770	0.19	0.5840	0.080	30.1	3.5	4380	260	2050	140	3520	110	2.3	0.11	117000	1700	52000
LRS150-10	1.199	0.089	0.6650	0.069	78	10	4650	170	3880	210	4400	140	1.4	0.08	68200	2100	48000
LRS150-12	0.3230	0.014	0.8570	0.018	366	15	5091	40	9160	210	6000	42	5.0	0.24	63700	1500	13000
LRS150-13	0.8160	0.047	0.7750	0.026	133.1	6.7	4906	59	5240	200	4961	53	10.6	0.68	112000	1600	10600
YW61-1	4.070	0.18	0.3370	0.023	11.53	0.93	3660	110	1424	55	2556	75	6.8	0.28	19500	360	2900
YW61-2	3.474	0.11	0.3890	0.016	15.79	0.66	3872	63	1641	46	2862	39	5.3	0.08	18900	230	3600
YW61-4	5.520	0.24	0.1534	0.0092	3.87	0.27	2360	100	1084	43	1599	55	5.7	0.13	16800	200	3000
YW61-5	4.430	0.13	0.2690	0.012	8.68	0.37	3317	78	1316	37	2300	38	9.7	0.25	16680	450	1700
YW61-6	4.723	0.11	0.2480	0.0059	7.29	0.2	3192	36	1239	27	2149	26	11.2	0.16	19100	160	1710
YW61-11	5.820	0.14	0.1099	0.0061	2.6	0.13	1770	110	1022	23	1293	38	13.6	0.22	16800	170	1240
YW61-13	6.070	0.16	0.08770	0.0044	1.99	0.11	1376	88	982	26	1114	34	31.1	1	6820	110	219
YW61-15	6.023	0.11	0.07780	0.0014	1.79	0.043	1138	36	989.6	17	1040	16	57.9	0.83	5830	40	101
YW61-16	5.983	0.10	0.08290	0.0014	1.91	0.048	1255	34	997.7	17	1084	16	34.7	0.54	7350	170	212
YW61-17	6.027	0.12	0.07940	0.0017	1.79	0.049	1176	42	992	19	1042	19	55.4	0.82	5790	70	105
YW61-19	5.931	0.11	0.07910	0.0013	1.852	0.046	1171	34	1004.5	18	1064	17	58.2	0.53	4360	80	74.9
YW61-20	6.024	0.12	0.08310	0.0020	1.916	0.060	1274	49	992	19	1087	21	55.2	1.3	5750	130	104
YW61-21	6.020	0.15	0.08010	0.0032	1.836	0.060	1185	78	993	24	1062	23	89.0	3.4	4560	280	51.2
YW61-22	5.890	0.14	0.07620	0.0019	1.794	0.064	1090	50	1014	23	1041	23	104	2.0	3160	40	30.3
YW61-26	5.857	0.12	0.07610	0.0015	1.785	0.048	1087	40	1017	19	1040	18	89.5	2.5	4070	30	45.5
YW61-28	6.020	0.15	0.08560	0.0035	1.968	0.080	1331	87	993	23	1107	26	61.5	0.84	7180	90	117
YW61-29	6.024	0.12	0.07480	0.0014	1.712	0.043	1062	40	992	18	1015	16	64.6	0.55	6170	70	95.6
YW61-30	6.012	0.11	0.08070	0.0016	1.867	0.046	1212	36	991.9	18	1068	16	82.2	1.2	4200	50	51.1

Appendix 4.B – Sm–Nd Data

Note: Ages used for initial $^{143}Nd/^{144}Nd(t)$ ratios and $\varepsilon Nd(t)$ calculations are based on Sm–Nd dates from respective sample. Sm and Nd concentrations can be found in Ch. 3 for apatite and Ch. 5 for monazite.

4.B.1 – Monazite Sm-Nd results

Sample	$^{147}Sm/^{144}Nd$	2σ	$^{143}Nd/^{144}Nd$	2σ	isochron age (Ma)	CHUR (*t*)	$^{143}Nd/^{144}Nd(t)$	εNd(*t*)	2σ
BH224-63b_mnz_10	0.0603	0.0013	0.511315	0.000016	1284	0.510980	0.510806	-3.4	0.32
BH224-63b_mnz_11	0.0623	0.0024	0.511326	0.000021	1284	0.510980	0.510800	-3.5	0.42
BH224-63b_mnz_12	0.0760	0.0003	0.511438	0.000012	1284	0.510980	0.510797	-3.6	0.23
BH224-63b_mnz_14	0.0311	0.0003	0.511080	0.000011	1284	0.510980	0.510818	-3.2	0.21
BH224-63b_mnz_7	0.0488	0.0010	0.511215	0.000015	1284	0.510980	0.510803	-3.5	0.29
BH224-63b_mnz_9	0.0727	0.0019	0.511444	0.000013	1284	0.510980	0.510832	-2.9	0.26
BH224-63b_mnz_dk_3	0.0366	0.0002	0.511139	0.000016	1284	0.510980	0.510830	-2.9	0.31
BH224-63b_mnz_dk_4	0.0359	0.0003	0.511113	0.000011	1284	0.510980	0.510810	-3.3	0.22
BH224-63b_mnz_lt_1	0.0780	0.0002	0.511451	0.000012	1284	0.510980	0.510794	-3.6	0.24
DMCY139_mnz_24_1	0.0320	0.0001	0.511107	0.000014	1217	0.511067	0.510851	-4.24	0.27
DMCY139_mnz_24_2	0.0324	0.0001	0.511109	0.000013	1217	0.511067	0.510850	-4.24	0.25
DMCY139_mnz_24_5	0.0321	0.0002	0.511108	0.000013	1217	0.511067	0.510852	-4.21	0.25
DMCY139_mnz_24_7	0.0323	0.0002	0.511105	0.000014	1217	0.511067	0.510847	-4.30	0.27
DMCY139_mnz_24_8	0.0321	0.0001	0.511110	0.000013	1217	0.511067	0.510853	-4.18	0.26
DMCY139_mnz_24_dz_3	0.0334	0.0001	0.511113	0.000013	1217	0.511067	0.510846	-4.32	0.26
DMCY139_mnz_24_dz_4	0.0347	0.0002	0.511126	0.000014	1217	0.511067	0.510849	-4.27	0.27
DMCY139_mnz_24_dz_6	0.0299	0.0004	0.511093	0.000016	1217	0.511067	0.510854	-4.16	0.31
LRS150_mnz_24_1	0.0818	0.0006	0.511414	0.000017	1192	0.511099	0.510773	-6.38	0.34
LRS150_mnz_24_2	0.0841	0.0004	0.511442	0.000016	1192	0.511099	0.510783	-6.18	0.31
LRS150_mnz_24_3	0.0840	0.0003	0.511449	0.000015	1192	0.511099	0.510791	-6.03	0.29
LRS150_mnz_24_4	0.0769	0.0005	0.511397	0.000027	1192	0.511099	0.510795	-5.95	0.52

Sample	$^{147}Sm/^{144}Nd$	2σ	$^{143}Nd/^{144}Nd$	2σ	isochron age (Ma)	CHUR (*t*)	$^{143}Nd/^{144}Nd(t)$	εNd(*t*)	2σ
LRS150_mnz_24_5	0.0809	0.0005	0.511423	0.000017	1192	0.511099	0.510790	-6.05	0.32
LRS150_mnz_24_6	0.0754	0.0006	0.511377	0.000022	1192	0.511099	0.510787	-6.11	0.43
FRS4_mnz_24_dk	0.0460	0.0003	0.511151	0.000014	1252	0.511022	0.510773	-4.86	0.28
FRS4_mnz_24_dk_1	0.0423	0.0003	0.511120	0.000013	1252	0.511022	0.510772	-4.88	0.25
FRS4_mnz_24_dk_12	0.0433	0.0012	0.511135	0.000018	1252	0.511022	0.510779	-4.75	0.35
FRS4_mnz_24_dk_2	0.0426	0.0003	0.511139	0.000014	1252	0.511022	0.510789	-4.56	0.28
FRS4_mnz_24_dk_4	0.0445	0.0004	0.511151	0.000014	1252	0.511022	0.510785	-4.63	0.27
FRS4_mnz_24_dk_5	0.0487	0.0005	0.511188	0.000014	1252	0.511022	0.510788	-4.57	0.26
FRS4_mnz_24_lt_10	0.0435	0.0009	0.511145	0.000014	1252	0.511022	0.510787	-4.59	0.27
FRS4_mnz_24_lt_11	0.0365	0.0007	0.511080	0.000014	1252	0.511022	0.510780	-4.72	0.26
FRS4_mnz_24_lt_6	0.0439	0.0005	0.511143	0.000014	1252	0.511022	0.510782	-4.69	0.27
FRS4_mnz_24_lt_7	0.0422	0.0002	0.511128	0.000015	1252	0.511022	0.510781	-4.71	0.28
FRS4_mnz_24_lt_8	0.0440	0.0001	0.511138	0.000015	1252	0.511022	0.510777	-4.80	0.28
FRS4_mnz_24_lt_9	0.0352	0.0003	0.511071	0.000016	1252	0.511022	0.510782	-4.69	0.30
YN49-61a_mnz24_dk_1	0.0656	0.0006	0.511356	0.000013	1283	0.510981	0.510803	-3.49	0.25
YN49-61a_mnz24_dk_10	0.0695	0.0003	0.511381	0.000014	1283	0.510981	0.510795	-3.65	0.27
YN49-61a_mnz24_dk_11	0.0608	0.0002	0.511305	0.000014	1283	0.510981	0.510793	-3.70	0.27
YN49-61a_mnz24_dk_15	0.0583	0.0002	0.511287	0.000015	1283	0.510981	0.510795	-3.64	0.29
YN49-61a_mnz24_dk_16	0.0604	0.0002	0.511305	0.000013	1283	0.510981	0.510797	-3.62	0.25
YN49-61a_mnz24_dk_2	0.0654	0.0003	0.511354	0.000014	1283	0.510981	0.510803	-3.49	0.28
YN49-61a_mnz24_dk_3	0.0615	0.0002	0.511316	0.000013	1283	0.510981	0.510798	-3.58	0.25
YN49-61a_mnz24_dk_4	0.0648	0.0002	0.511341	0.000012	1283	0.510981	0.510796	-3.64	0.24
YN49-61a_mnz24_dk_9	0.0586	0.0002	0.511293	0.000015	1283	0.510981	0.510800	-3.56	0.30
YN49-61a_mnz24_lt_12	0.0868	0.0009	0.511530	0.000014	1283	0.510981	0.510799	-3.57	0.27
YN49-61a_mnz24_lt_13	0.0702	0.0002	0.511392	0.000013	1283	0.510981	0.510800	-3.55	0.26
YN49-61a_mnz24_lt_14	0.0795	0.0013	0.511464	0.000018	1283	0.510981	0.510795	-3.66	0.36
YN49-61a_mnz24_lt_18	0.0650	0.0003	0.511352	0.000014	1283	0.510981	0.510804	-3.46	0.28

Sample	$^{147}Sm/^{144}Nd$	2σ	$^{143}Nd/^{144}Nd$	2σ	isochron age (Ma)	CHUR (*t*)	$^{143}Nd/^{144}Nd(t)$	εNd(*t*)	2σ
YN49-61a_mnz24_lt_5	0.0717	0.0002	0.511401	0.000013	1283	0.510981	0.510797	-3.61	0.25
YN49-61a_mnz24_lt_6	0.0728	0.0006	0.511404	0.000012	1283	0.510981	0.510791	-3.72	0.24
YN49-61a_mnz24_lt_7	0.0704	0.0002	0.511392	0.000015	1283	0.510981	0.510798	-3.58	0.29
YN49-61a_mnz24_lt_8	0.0714	0.0007	0.511405	0.000014	1283	0.510981	0.510803	-3.49	0.28
YN50-49-mnz-1	0.1053	0.0014	0.511692	0.000016	1262	0.511009	0.510820	-3.69	0.30
YN50-49-mnz-2	0.0886	0.0010	0.511555	0.000015	1262	0.511009	0.510820	-3.68	0.30
YN50-49-mnz-3	0.0899	0.0010	0.511565	0.000014	1262	0.511009	0.510820	-3.70	0.28
YN50-49-mnz-4	0.0898	0.0010	0.511561	0.000014	1262	0.511009	0.510817	-3.76	0.28
YN50-49-mnz-5	0.0874	0.0009	0.511541	0.000016	1262	0.511009	0.510816	-3.77	0.31
YN50-49-mnz-6	0.0904	0.0010	0.511567	0.000015	1262	0.511009	0.510817	-3.74	0.29
YN50-49-mnz-7	0.0872	0.0009	0.511538	0.000015	1262	0.511009	0.510815	-3.78	0.30
YN50-49-mnz-8	0.0896	0.0011	0.511568	0.000016	1262	0.511009	0.510826	-3.58	0.30
YN50-49-mnz-9	0.0868	0.0009	0.511541	0.000016	1262	0.511009	0.510822	-3.66	0.32
YN50-49-mnz-10	0.0879	0.0013	0.511542	0.000018	1262	0.511009	0.510814	-3.81	0.35
FRS9_104_1	0.0548	0.0005	0.511254	0.000016	1270	0.510998	0.510797	-3.94	0.32
FRS9_104_2	0.0574	0.0002	0.511285	0.000018	1270	0.510998	0.510806	-3.76	0.36
FRS9_104_3	0.0540	0.0002	0.511248	0.000016	1270	0.510998	0.510797	-3.93	0.30
FRS9_104_4	0.0603	0.0002	0.511332	0.000024	1270	0.510998	0.510829	-3.32	0.48
FRS9_104_5	0.0550	0.0002	0.511261	0.000015	1270	0.510998	0.510802	-3.84	0.30
FRS9_104_6	0.0496	0.0002	0.511218	0.000017	1270	0.510998	0.510805	-3.79	0.34
FRS9_104_7	0.0558	0.0003	0.511267	0.000016	1270	0.510998	0.510802	-3.84	0.32
FRS9_104_8	0.0518	0.0003	0.511238	0.000016	1270	0.510998	0.510805	-3.77	0.32
FRS9_104_9	0.0615	0.0005	0.511319	0.000018	1270	0.510998	0.510806	-3.77	0.35
FRS9_104_10	0.0576	0.0003	0.511280	0.000018	1270	0.510998	0.510800	-3.88	0.35
FRS9_104_11	0.0525	0.0002	0.511243	0.000017	1270	0.510998	0.510805	-3.78	0.34
FRS9_104_12	0.0609	0.0002	0.511311	0.000019	1270	0.510998	0.510803	-3.82	0.36
FRS9_102_1	0.0500	0.0002	0.511254	0.000038	1270	0.510998	0.510837	-3.15	0.75

Sample	$^{147}Sm/^{144}Nd$	2σ	$^{143}Nd/^{144}Nd$	2σ	isochron age (Ma)	CHUR (*t*)	$^{143}Nd/^{144}Nd(t)$	εNd(*t*)	2σ
FRS9_102_2	0.0526	0.0002	0.511243	0.000029	1270	0.510998	0.510804	-3.80	0.56
FRS9_102_3	0.0352	0.0002	0.511140	0.000033	1270	0.510998	0.510847	-2.97	0.65
FRS9_102_4	0.0337	0.0001	0.511089	0.000022	1270	0.510998	0.510808	-3.72	0.43
FRS9_102_5	0.0336	0.0001	0.511081	0.000016	1270	0.510998	0.510801	-3.86	0.31
FRS9_102_6	0.0336	0.0001	0.511081	0.000016	1270	0.510998	0.510801	-3.86	0.31
FRS9_102_7	0.0337	0.0002	0.511077	0.000024	1270	0.510998	0.510796	-3.96	0.48
YW61-8A_Mnz_1	0.0722	0.0006	0.511378	0.000016	1085	0.511238	0.510864	-7.31	0.30
YW61-8A_Mnz_2	0.0725	0.0007	0.511393	0.000015	1085	0.511238	0.510876	-7.08	0.30
YW61-8A_Mnz_4	0.0708	0.0006	0.511374	0.000016	1085	0.511238	0.510869	-7.21	0.30
YW61-8A_Mnz_5	0.0708	0.0006	0.511372	0.000014	1085	0.511238	0.510867	-7.25	0.28
YW61-8A_Mnz_6	0.0718	0.0006	0.511381	0.000015	1085	0.511238	0.510870	-7.20	0.29
YW61-8A_Mnz_7	0.0791	0.0007	0.511444	0.000016	1085	0.511238	0.510881	-6.99	0.32
YW61-8A_Mnz_8	0.0771	0.0007	0.511435	0.000014	1085	0.511238	0.510886	-6.89	0.27
YW61-8A_Mnz_9	0.0732	0.0007	0.511386	0.000015	1085	0.511238	0.510865	-7.30	0.30
YW61-8A_Mnz_10	0.0800	0.0008	0.511447	0.000017	1085	0.511238	0.510878	-7.05	0.34
YW61-8A_Mnz_11	0.0764	0.0007	0.511427	0.000015	1085	0.511238	0.510883	-6.95	0.30
YW61-8A_Mnz_12	0.0692	0.0008	0.511366	0.000016	1085	0.511238	0.510873	-7.15	0.31
YW61-8A_Mnz_13	0.0721	0.0007	0.511387	0.000017	1085	0.511238	0.510873	-7.14	0.34
YW61-8A_Mnz_14	0.0699	0.0007	0.511368	0.000016	1085	0.511238	0.510870	-7.20	0.31

4.B.2 – Apatite Sm-Nd results

Sample	$^{147}Sm/^{144}Nd$	2σ	$^{143}Nd/^{144}Nd$	2σ	isochron age (Ma)	CHUR (at *t*)	$^{143}Nd/^{144}Nd(t)$	ε Nd(*t*)	2σ
BH224-63b_ap_r_1	0.1305	0.0016	0.511931	0.000028	1284	0.510980	0.510830	-2.93	0.54
BH224-63b_ap_r_8	0.1202	0.0043	0.511851	0.000043	1284	0.510980	0.510838	-2.79	0.85
BH224-63b_ap_r_11	0.1088	0.0036	0.511733	0.000040	1284	0.510980	0.510815	-3.23	0.78
BH224-63b_ap_c_3	0.0843	0.0008	0.511504	0.000052	1284	0.510980	0.510793	-3.66	1.02
BH224-63b_ap_c_4	0.0917	0.0017	0.511610	0.000049	1284	0.510980	0.510838	-2.79	0.95
BH224-63b_ap_c_7	0.0847	0.0005	0.511520	0.000045	1284	0.510980	0.510805	-3.43	0.87
DMCY138_ap_60_dk_1	0.0539	0.0018	0.511252	0.000025	1308	0.510949	0.510789	-3.14	0.48
DMCY138_ap_60_dk_2	0.0501	0.0005	0.511206	0.000022	1308	0.510949	0.510775	-3.40	0.44
DMCY138_ap_60_dk_3	0.0484	0.0003	0.511208	0.000023	1308	0.510949	0.510792	-3.06	0.45
DMCY138_ap_60_dk_6	0.0516	0.0010	0.511223	0.000027	1308	0.510949	0.510779	-3.33	0.52
DMCY138_ap_60_dk_9	0.0797	0.0023	0.511458	0.000031	1308	0.510949	0.510773	-3.45	0.60
DMCY138_ap_60_lt_10	0.0896	0.0003	0.511558	0.000024	1308	0.510949	0.510788	-3.15	0.47
DMCY138_ap_60_lt_4	0.0898	0.0007	0.511568	0.000020	1308	0.510949	0.510796	-3.00	0.39
DMCY138_ap_60_lt_5	0.1095	0.0015	0.511719	0.000028	1308	0.510949	0.510778	-3.34	0.55
DMCY138_ap_60_lt_7	0.1054	0.0015	0.511687	0.000028	1308	0.510949	0.510782	-3.28	0.56
DMCY138_ap_60_lt_8	0.0949	0.0012	0.511590	0.000029	1308	0.510949	0.510774	-3.42	0.56
DMCY139_ap_44_c_10	0.1334	0.0010	0.511905	0.000034	1217	0.511067	0.510839	-4.46	0.66
DMCY139_ap_44_c_2	0.0857	0.0032	0.511522	0.000044	1217	0.511067	0.510837	-4.51	0.86
DMCY139_ap_44_c_3	0.0808	0.0012	0.511494	0.000030	1217	0.511067	0.510848	-4.29	0.59
DMCY139_ap_44_c_8	0.0877	0.0011	0.511555	0.000033	1217	0.511067	0.510854	-4.16	0.65
DMCY139_ap_44_c_9	0.0684	0.0003	0.511399	0.000030	1217	0.511067	0.510853	-4.19	0.59
DMCY139_ap_44_lz_11	0.0875	0.0026	0.511513	0.000035	1217	0.511067	0.510813	-4.96	0.68
DMCY139_ap_44_lz_13	0.1134	0.0023	0.511747	0.000038	1217	0.511067	0.510840	-4.44	0.73

Sample	$^{147}Sm/^{144}Nd$	2σ	$^{143}Nd/^{144}Nd$	2σ	isochron age (Ma)	CHUR (at *t*)	$^{143}Nd/^{144}Nd(t)$	ε Nd(*t*)	2σ
DMCY139_ap_44_r_5	0.1242	0.0005	0.511830	0.000039	1217	0.511067	0.510838	-4.48	0.77
DMCY139_ap_44_r_6	0.1477	0.0007	0.512035	0.000049	1217	0.511067	0.510855	-4.16	0.95
DMCY139_ap_60_14	0.1015	0.0012	0.511669	0.000026	1217	0.511067	0.510859	-4.08	0.51
DMCY139_ap_60_15	0.0919	0.0005	0.511594	0.000025	1217	0.511067	0.510859	-4.06	0.48
DMCY139_ap_60_16	0.1269	0.0013	0.511867	0.000031	1217	0.511067	0.510852	-4.20	0.60
DMCY139_ap_60_17	0.0926	0.0005	0.511596	0.000023	1217	0.511067	0.510856	-4.13	0.45
DMCY139_ap_60_18	0.1083	0.0005	0.511705	0.000020	1217	0.511067	0.510840	-4.45	0.39
DMCY139_ap_60_19	0.1291	0.0015	0.511902	0.000026	1217	0.511067	0.510871	-3.84	0.51
LRS150_ap_44_c_10	0.1802	0.0020	0.512195	0.000036	1192	0.511099	0.510785	-6.15	0.70
LRS150_ap_44_c_12a	0.1586	0.0010	0.512017	0.000058	1192	0.511099	0.510776	-6.33	1.13
LRS150_ap_44_c_12b	0.1973	0.0032	0.512330	0.000101	1192	0.511099	0.510786	-6.14	1.97
LRS150_ap_44_c_3	0.2132	0.0029	0.512487	0.000037	1192	0.511099	0.510819	-5.49	0.72
LRS150_ap_44_c_8	0.1632	0.0004	0.512020	0.000033	1192	0.511099	0.510742	-6.98	0.65
LRS150_ap_44_r_2	0.1768	0.0016	0.512162	0.000044	1192	0.511099	0.510779	-6.27	0.86
LRS150_ap_44_r_4b	0.1707	0.0008	0.512130	0.000034	1192	0.511099	0.510794	-5.97	0.67
LRS150_ap_44_r_5	0.2454	0.0034	0.512716	0.000041	1192	0.511099	0.510796	-5.95	0.81
FRS4_ap_60_1	0.2022	0.0007	0.512452	0.000026	1252	0.511022	0.510789	-4.54	0.50
FRS4_ap_60_10	0.1887	0.0019	0.512319	0.000033	1252	0.511022	0.510767	-4.98	0.64
FRS4_ap_60_11	0.2028	0.0030	0.512438	0.000033	1252	0.511022	0.510771	-4.90	0.65
FRS4_ap_60_12	0.2050	0.0015	0.512454	0.000025	1252	0.511022	0.510769	-4.95	0.48
FRS4_ap_60_2	0.2195	0.0011	0.512599	0.000030	1252	0.511022	0.510795	-4.44	0.58
FRS4_ap_60_3	0.2141	0.0012	0.512540	0.000031	1252	0.511022	0.510780	-4.73	0.61
FRS4_ap_60_4	0.2343	0.0008	0.512703	0.000023	1252	0.511022	0.510777	-4.79	0.45
FRS4_ap_60_6	0.2285	0.0031	0.512664	0.000032	1252	0.511022	0.510785	-4.64	0.62
FRS4_ap_60_7	0.2255	0.0013	0.512631	0.000028	1252	0.511022	0.510777	-4.78	0.54

Sample	$^{147}Sm/^{144}Nd$	2σ	$^{143}Nd/^{144}Nd$	2σ	isochron age (Ma)	CHUR (at *t*)	$^{143}Nd/^{144}Nd(t)$	ε Nd(*t*)	2σ
FRS4_ap_60_8	0.1609	0.0041	0.512104	0.000033	1252	0.511022	0.510781	-4.70	0.64
FRS4_ap_60_8	0.1924	0.0057	0.512375	0.000048	1252	0.511022	0.510793	-4.47	0.95
FRS4_ap_60_9	0.2019	0.0011	0.512449	0.000028	1252	0.511022	0.510789	-4.55	0.54
YN50-49-ap1	0.3339	0.0046	0.513603	0.000102	1262	0.511009	0.510835	-3.39	2.00
YN50-49-ap2	0.3298	0.0037	0.513605	0.000074	1262	0.511009	0.510872	-2.68	1.45
YN50-49-ap3	0.3311	0.0043	0.513570	0.000067	1262	0.511009	0.510826	-3.58	1.30
YN50-49-ap4	0.3045	0.0036	0.513384	0.000081	1262	0.511009	0.510861	-2.90	1.58
YN50-49-ap5	0.3034	0.0034	0.513260	0.000072	1262	0.511009	0.510746	-5.14	1.41
YN50-49-ap6	0.3338	0.0040	0.513580	0.000065	1262	0.511009	0.510814	-3.82	1.28
YN50-49-ap7	0.3702	0.0051	0.513885	0.000068	1262	0.511009	0.510818	-3.73	1.32
YN50-49-ap8	0.3017	0.0034	0.513301	0.000083	1262	0.511009	0.510801	-4.07	1.63
YN50-49-ap9	0.3087	0.0037	0.513348	0.000086	1262	0.511009	0.510789	-4.29	1.68
YN50-49-ap10	0.3186	0.0035	0.513461	0.000091	1262	0.511009	0.510820	-3.68	1.78
YW61-8A_Ap_8	0.3329	0.0029	0.513176	0.000041	1085	0.511238	0.510806	-8.5	0.80
YW61-8A_Ap_9	0.3311	0.0031	0.513249	0.000050	1085	0.511238	0.510891	-6.8	0.98
YW61-8A_Ap_11	0.3411	0.0029	0.513279	0.000048	1085	0.511238	0.510850	-7.6	0.93
YW61-8A_Ap_12	0.3329	0.0030	0.513305	0.000042	1085	0.511238	0.510934	-5.9	0.83
YW61-8A_Ap_13	0.3240	0.0028	0.513146	0.000045	1085	0.511238	0.510838	-7.8	0.89
YW61-8A_Ap_14	0.3356	0.0036	0.513208	0.000043	1085	0.511238	0.510818	-8.2	0.84
YW61-8A_Ap_15	0.3269	0.0049	0.513222	0.000044	1085	0.511238	0.510894	-6.7	0.86
YW61-8A_Ap_16	0.3180	0.0031	0.513145	0.000046	1085	0.511238	0.510881	-7.0	0.90
YW61-8A_Ap_17	0.3368	0.0033	0.513356	0.000044	1085	0.511238	0.510957	-5.5	0.85
YW61-8A_Ap_18	0.3215	0.0050	0.513142	0.000062	1085	0.511238	0.510853	-7.5	1.21

Appendix 4.C – Zircon Trace Element Analyses

Note: LA-ICP-MS tables consist of 3 parts: 1) spot data, 2) 1σ error, and 3) detection limits.

Sample		yn50-50_zrn_44_02	yn50-50_zrn_44_03	yn50-50_zrn_44_05	yn50-50_zrn_44_06	yn50-50_zrn_44_08	yn50-50_zrn_44_09	yn50-50_zrn_44_10
SiO_2	wt.%	41.0	42.1	40.7	35.4	43.2	42.8	45.8
TiO_2	wt.%	bdl	bdl	0.0004	0.0053	bdl	bdl	0.0056
Al_2O_3	wt.%	bdl	bdl	bdl	0.082	0.013	0.040	0.072
FeO	wt.%	0.09	0.58	bdl	0.14	0.03	0.08	0.19
MgO	wt.%	0.0030	0.0026	bdl	0.0113	bdl	0.0114	0.0111
Na_2O	wt.%	bdl	bdl	bdl	bdl	bdl	bdl	bdl
P_2O_5	wt.%	0.49	0.39	0.19	0.40	0.28	0.27	0.34
7Li	µg/g	207	227	217	208	249	171	225
^{53}Cr	µg/g	bdl	bdl	bdl	bdl	bdl	bdl	bdl
^{66}Zn	µg/g	bdl	bdl	bdl	8.89	bdl	5.16	4.02
^{85}Rb	µg/g	0.56	0.55	bdl	0.31	0.13	0.54	0.31
^{88}Sr	µg/g	7.76	20.0	0.97	28.7	5.02	14.1	19.8
^{89}Y	µg/g	3580	3430	1660	4190	2460	2010	2580
^{91}Zr	µg/g	431400	431400	431400	431400	431400	431400	431400
^{93}Nb	µg/g	904	1020	713	1840	822	590	669
^{118}Sn	µg/g	0.74	1.2	1.0	1.6	0.67	1.2	1.8
^{137}Ba	µg/g	38.3	55.1	1.24	43.8	12.8	14.1	33.4
^{139}La	µg/g	2.1	1.6	0.46	19.6	2.1	6.1	12.8
^{140}Ce	µg/g	21.9	13.1	5.1	163	19.3	54.1	115
^{141}Pr	µg/g	6.7	3.2	1.3	37.5	4.2	11.8	24.8
^{143}Nd	µg/g	69.3	37.9	15.8	271	39.2	89.6	169
^{147}Sm	µg/g	142	84.9	45.8	221	66.4	106	137
^{151}Eu	µg/g	102	63.3	34.0	130	46.2	65.3	78.2
^{157}Gd	µg/g	542	369	197	718	273	345	419
^{159}Tb	µg/g	144	105	55.1	174	76.8	84.3	102
^{163}Dy	µg/g	980	780	399	1080	580	546	670
^{165}Ho	µg/g	158	140	66.1	172	106	87.6	112
^{167}Er	µg/g	315	326	146	339	248	186	234
^{169}Tm	µg/g	34.9	39.2	16.4	34.4	29.3	20.5	25.7
^{171}Yb	µg/g	220	263	107	199	197	122	154
^{175}Lu	µg/g	26.9	37.4	15.4	25.3	28.4	15.9	21.2

Sample		yn50-50_zrn_44_02	yn50-50_zrn_44_03	yn50-50_zrn_44_05	yn50-50_zrn_44_06	yn50-50_zrn_44_08	yn50-50_zrn_44_09	yn50-50_zrn_44_10
^{177}Hf	µg/g	12300	4990	5220	7290	3800	18000	8150
^{181}Ta	µg/g	61.2	93.9	85.9	152	88.3	66.5	71.7
^{208}Pb	µg/g	247	237	105	268	138	152	218
^{232}Th	µg/g	1940	1860	705	2320	937	1010	1560
^{238}U	µg/g	786	1190	823	1100	1170	568	847
1σ Error								
SiO_2	wt.%	1.75	3.40	1.46	2.21	1.64	1.88	2.70
TiO_2	wt.%	0.00022	0.00045	0.00017	0.00066	0.00019	0.00023	0.00071
Al_2O_3	wt.%	0.0013	0.0022	0.0024	0.0022	0.0016	0.0022	0.0027
FeO	wt.%	0.0078	0.0536	0.0042	0.0114	0.0024	0.0039	0.010
MgO	wt.%	0.0007	0.0013	0.0023	0.0012	0.0019	0.0015	0.0016
Na_2O	wt.%	0.17	0.24	0.22	0.17	0.18	0.22	0.31
P_2O_5	wt.%	0.012	0.035	0.010	0.008	0.010	0.011	0.018
7Li	µg/g	6.1	14.1	3.1	4.9	4.6	3.6	7.0
^{53}Cr	µg/g	3.5	5.3	4.7	4.0	3.8	4.6	6.3
^{66}Zn	µg/g	1.6	1.9	1.6	1.4	1.4	1.2	1.4
^{85}Rb	µg/g	0.057	0.122	0.114	0.040	0.048	0.202	0.081
^{88}Sr	µg/g	0.46	2.7	0.20	0.90	0.34	0.29	1.1
^{89}Y	µg/g	96.9	323	58.0	54.6	39.4	27.7	109
^{91}Zr	µg/g	12740	33200	9080	12680	7140	7630	13700
^{93}Nb	µg/g	25.4	72.3	21.5	58.3	29.5	12.1	27.3
^{118}Sn	µg/g	0.14	0.34	0.13	0.19	0.15	0.21	0.24
^{137}Ba	µg/g	1.14	4.35	0.351	1.80	1.39	0.59	1.35
^{139}La	µg/g	0.11	0.27	0.11	0.73	0.18	0.22	0.63
^{140}Ce	µg/g	1.01	2.12	0.820	6.99	1.20	1.18	5.39
^{141}Pr	µg/g	0.61	0.54	0.22	1.77	0.23	0.33	1.06
^{143}Nd	µg/g	3.56	5.39	1.58	9.99	1.91	1.54	7.05
^{147}Sm	µg/g	5.96	8.21	0.86	3.68	1.54	2.05	5.57
^{151}Eu	µg/g	3.42	6.20	0.80	1.95	0.95	1.02	3.40
^{157}Gd	µg/g	13.9	35.1	4.58	12.5	6.06	3.76	18.2
^{159}Tb	µg/g	4.66	10.0	1.40	3.52	1.50	0.86	4.35
^{163}Dy	µg/g	27.0	78.4	8.37	20.6	10.1	5.61	28.8
^{165}Ho	µg/g	3.95	12.8	1.71	2.50	1.44	1.08	4.59
^{167}Er	µg/g	7.85	28.9	2.75	6.23	3.75	2.57	9.82
^{169}Tm	µg/g	0.91	3.38	0.43	0.63	0.48	0.33	1.13

Sample		yn50-50_zrn_44_02	yn50-50_zrn_44_03	yn50-50_zrn_44_05	yn50-50_zrn_44_06	yn50-50_zrn_44_08	yn50-50_zrn_44_09	yn50-50_zrn_44_10
^{171}Yb	µg/g	4.74	21.2	2.80	4.41	2.56	2.22	6.00
^{175}Lu	µg/g	0.70	2.43	0.41	0.517	0.49	0.30	0.81
^{177}Hf	µg/g	427	487	144	302	115	319	196
^{181}Ta	µg/g	1.50	5.66	3.43	6.61	3.43	1.18	2.66
^{208}Pb	µg/g	5.34	22.8	2.64	3.23	2.07	2.85	8.38
^{232}Th	µg/g	46.8	194	31.5	51.3	18.5	23.5	59.8
^{238}U	µg/g	33.0	71.5	25.0	25.9	18.6	8.20	31.0
Detection Limit								
SiO_2	wt.%	1.12	1.28	1.44	1.20	1.15	1.43	1.85
TiO_2	wt.%	0.000310	0.000310	0.000342	0.000254	0.000246	0.000263	0.000443
Al_2O_3	wt.%	0.00181	0.00264	0.00238	0.00192	0.00196	0.00245	0.00346
FeO	wt.%	0.00311	0.00447	0.00419	0.00332	0.00339	0.00418	0.00591
MgO	wt.%	0.00173	0.00251	0.00227	0.00185	0.00186	0.00231	0.00323
Na_2O	wt.%	0.169	0.238	0.216	0.173	0.176	0.218	0.306
P_2O_5	wt.%	0.0105	0.0147	0.0137	0.0109	0.0108	0.0134	0.0184
7Li	µg/g	1.75	2.56	2.14	1.80	1.77	2.22	3.08
^{53}Cr	µg/g	3.46	5.35	4.70	3.97	3.82	4.61	6.27
^{66}Zn	µg/g	1.55	1.89	1.62	1.41	1.43	1.55	2.35
^{85}Rb	µg/g	0.0781	0.119	0.114	0.0858	0.0952	0.110	0.147
^{88}Sr	µg/g	0.0156	0.0297	0.0322	0.0263	0.0197	0.0232	0.0369
^{89}Y	µg/g	0.0251	0.0321	0.0319	0.0311	0.0247	0.0290	0.0437
^{91}Zr	µg/g	0.146	0.255	0.211	0.170	0.154	0.229	0.181
^{93}Nb	µg/g	0.0169	0.0322	0.0253	0.0117	0.0154	0.0205	0.0313
^{118}Sn	µg/g	0.232	0.364	0.308	0.263	0.256	0.308	0.417
^{137}Ba	µg/g	0.100	0.129	0.139	0.094	0.094	0.082	0.124
^{139}La	µg/g	0.00439	0.0141	0.0205	0.0100	0.00932	0.00459	0.0179
^{140}Ce	µg/g	0.0105	0.0147	0.0181	0.0147	0.0110	0.0119	0.0129
^{141}Pr	µg/g	0.00718	0.00991	0.0137	0.00996	0.00902	0.00865	0.0132
^{143}Nd	µg/g	0.0616	0.103	0.106	0.0730	0.0681	0.0912	0.0366
^{147}Sm	µg/g	0.0571	0.0794	0.0889	0.0536	0.0467	0.0698	0.0758
^{151}Eu	µg/g	0.0172	0.0182	0.0251	0.0216	0.0157	0.0230	0.0229
^{157}Gd	µg/g	0.0603	0.0842	0.0868	0.0699	0.0667	0.0746	0.0742
^{159}Tb	µg/g	0.00886	0.0124	0.0152	0.0124	0.00818	0.00403	0.00440
^{163}Dy	µg/g	0.0157	0.0415	0.0447	0.0418	0.0273	0.0446	0.0553
^{165}Ho	µg/g	0.00744	0.0141	0.01107	0.00514	0.00822	0.00897	0.0190

Sample		yn50-50_zrn_44_02	yn50-50_zrn_44_03	yn50-50_zrn_44_05	yn50-50_zrn_44_06	yn50-50_zrn_44_08	yn50-50_zrn_44_09	yn50-50_zrn_44_10
^{167}Er	µg/g	0.0440	0.0545	0.0484	0.0618	0.0139	0.0177	0.0765
^{169}Tm	µg/g	0.00960	0.00479	0.0106	0.00842	0.00786	0.00387	0.0150
^{171}Yb	µg/g	0.0577	0.0802	0.0775	0.0617	0.0576	0.0706	0.0870
^{175}Lu	µg/g	0.0106	0.00528	0.0135	0.0109	0.00985	0.0116	0.00465
^{177}Hf	µg/g	0.0403	0.0766	0.0695	0.0478	0.0446	0.0220	0.0240
^{181}Ta	µg/g	0.00924	0.0155	0.0159	0.0110	0.00839	0.0137	0.0136
^{208}Pb	µg/g	0.0338	0.0333	0.0483	0.0276	0.0180	0.0293	0.0578
^{232}Th	µg/g	0.0105	0.0147	0.00804	0.0135	0.0110	0.0129	0.00519
^{238}U	µg/g	0.00870	0.0165	0.0165	0.0155	0.0096	0.0146	0.0182

Sample		ynyn61-12_zrn_44_01	yn61-12_zrn_44_02	yn61-12_zrn_44_03	yn61-12_zrn_44_04	yn61-12_zrn_44_05	yn61-12_zrn_44_06	yn61-12_zrn_44_07
SiO_2	wt.%	42.1	43.5	40.5	43.3	45.6	40.8	44.1
TiO_2	wt.%	0.028	0.0052	0.0062	bdl	0.015	0.0058	0.0039
Al_2O_3	wt.%	0.067	0.017	0.17	0.015	0.23	0.18	0.10
FeO	wt.%	1.5	0.26	0.76	0.024	0.67	1.0	0.13
MgO	wt.%	0.24	0.11	0.043	bdl	0.15	0.039	0.023
Na_2O	wt.%	bdl	bdl	bdl	bdl	bdl	bdl	bdl
P_2O_5	wt.%	0.46	0.49	0.59	0.57	0.64	0.55	0.60
^{7}Li	µg/g	378	295	274	217	349	228	225
^{53}Cr	µg/g	bdl	bdl	bdl	bdl	bdl	bdl	bdl
^{66}Zn	µg/g	12.7	17.1	67.9	5.03	59.0	46.4	27.9
^{85}Rb	µg/g	2.0	0.36	2.0	0.69	15.4	2.7	3.2
^{88}Sr	µg/g	4.3	11.2	55.9	0.78	37.2	38.1	33.9
^{89}Y	µg/g	3870	3780	4670	3600	4300	4160	3970
^{91}Zr	µg/g	431400	431400	431400	431400	431400	431400	431400
^{93}Nb	µg/g	1280	1450	1430	1060	1330	1220	270
^{118}Sn	µg/g	1.3	0.47	1.0	0.58	0.83	0.95	0.58
^{137}Ba	µg/g	10.0	9.19	44.5	3.24	35.0	30.8	53.0
^{139}La	µg/g	1.4	2.9	18.2	0.17	9.2	10.2	5.3
^{140}Ce	µg/g	13.1	31.3	189	6.5	120	176	63.7
^{141}Pr	µg/g	3.6	6.5	32.0	3.2	15.5	21.0	10.5
^{143}Nd	µg/g	61.6	86.9	309	70.0	156	210	128
^{147}Sm	µg/g	201	227	469	217	297	369	279
^{151}Eu	µg/g	153	162	278	160	198	227	191
^{157}Gd	µg/g	809	845	1240	825	945	1010	921
^{159}Tb	µg/g	188	189	241	178	210	206	197
^{163}Dy	µg/g	1130	1110	1310	1080	1230	1170	1170
^{165}Ho	µg/g	170	166	195	160	185	175	173
^{167}Er	µg/g	309	310	395	308	359	347	335
^{169}Tm	µg/g	29.8	29.5	40.5	30.1	36.6	36.0	34.3
^{171}Yb	µg/g	163	168	232	173	203	213	195
^{175}Lu	µg/g	20.6	21.6	30.2	22.5	25.8	27.0	24.7
^{177}Hf	µg/g	6580	6480	10700	7930	7140	10600	8050
^{181}Ta	µg/g	46.7	50.8	58.0	39.7	52.9	45.1	47.7
^{208}Pb	µg/g	475	490	394	486	384	388	508
^{232}Th	µg/g	3500	3520	3820	3490	3190	3220	3870
^{238}U	µg/g	393	474	582	413	548	486	491

Sample		yn61-12_zrn_44_01	yn61-12_zrn_44_02	yn61-12_zrn_44_03	yn61-12_zrn_44_04	yn61-12_zrn_44_05	yn61-12_zrn_44_06	yn61-12_zrn_44_07
1σ Error								
SiO_2	wt.%	2.52	2.38	2.29	2.19	4.17	2.41	2.36
TiO_2	wt.%	0.0041	0.00061	0.00063	0.00042	0.0039	0.00053	0.00084
Al_2O_3	wt.%	0.0047	0.0044	0.021	0.0039	0.048	0.017	0.0074
FeO	wt.%	0.040	0.021	0.057	0.0038	0.084	0.16	0.018
MgO	wt.%	0.022	0.0064	0.0054	0.0025	0.034	0.0018	0.0018
Na_2O	wt.%	0.15	0.19	0.16	0.23	0.30	0.16	0.23
P_2O_5	wt.%	0.015	0.035	0.044	0.014	0.063	0.021	0.024
^{7}Li	µg/g	18.6	14.6	18.9	4.88	41.1	5.40	7.59
^{53}Cr	µg/g	3.89	4.23	3.96	5.43	7.32	3.90	5.80
^{66}Zn	µg/g	1.26	3.65	7.22	1.90	10.0	3.30	2.27
^{85}Rb	µg/g	0.20	0.062	0.34	0.15	5.29	0.27	0.28
^{88}Sr	µg/g	0.200	2.638	6.369	0.114	4.01	1.64	3.19
^{89}Y	µg/g	119	203	319	62.4	432	133	72.6
^{91}Zr	µg/g	12800	22700	22600	4600	27100	13500	7360
^{93}Nb	µg/g	39.8	93.0	85.4	13.5	105	23.7	14.5
^{118}Sn	µg/g	0.18	0.16	0.25	0.22	0.24	0.11	0.17
^{137}Ba	µg/g	0.459	1.06	4.86	0.342	4.69	1.01	6.46
^{139}La	µg/g	0.188	0.72	1.97	0.031	1.04	0.33	0.26
^{140}Ce	µg/g	0.47	7.23	19.2	0.25	15.0	6.14	3.85
^{141}Pr	µg/g	0.16	1.26	3.21	0.10	1.96	0.77	0.41
^{143}Nd	µg/g	2.51	12.3	30.7	1.57	20.6	5.61	5.14
^{147}Sm	µg/g	7.44	21.8	41.9	3.64	38.0	9.84	5.00
^{151}Eu	µg/g	5.52	12.8	24.3	1.96	24.4	6.15	3.64
^{157}Gd	µg/g	27.5	59.8	105	10.8	103	26.2	15.0
^{159}Tb	µg/g	6.23	10.9	19.1	2.47	23.4	5.02	3.74
^{163}Dy	µg/g	35.3	59.2	96.4	17.2	131	35.5	18.8
^{165}Ho	µg/g	4.87	8.38	13.9	1.72	18.5	4.88	3.37
^{167}Er	µg/g	9.83	15.8	28.6	5.29	34.7	11.3	5.48
^{169}Tm	µg/g	0.95	1.42	2.64	0.56	3.57	1.30	0.56
^{171}Yb	µg/g	5.15	8.08	16.0	3.29	19.4	7.35	4.34
^{175}Lu	µg/g	0.57	0.97	2.05	0.321	2.13	1.09	0.57
^{177}Hf	µg/g	307	536	451	265	657	444	261
^{181}Ta	µg/g	1.37	3.73	3.36	0.82	4.06	1.22	0.97
^{208}Pb	µg/g	12.6	27.0	21.1	9.47	39.1	4.74	10.7
^{232}Th	µg/g	141	203	290	77.2	310	89.5	83.6

Sample		yn61-12_zrn_44_01	yn61-12_zrn_44_02	yn61-12_zrn_44_03	yn61-12_zrn_44_04	yn61-12_zrn_44_05	yn61-12_zrn_44_06	yn61-12_zrn_44_07
^{238}U	µg/g	8.59	24.0	51.3	6.89	36.2	14.0	12.4
Detection Limit								
SiO_2	wt.%	1.30	1.40	1.07	1.58	2.28	1.36	1.80
TiO_2	wt.%	0.000235	0.000346	0.000261	0.000418	0.000485	0.000267	0.000287
Al_2O_3	wt.%	0.00182	0.00221	0.00194	0.00270	0.00352	0.00193	0.00275
FeO	wt.%	0.00336	0.00392	0.00335	0.00484	0.00639	0.00341	0.00496
MgO	wt.%	0.00169	0.00205	0.00178	0.00250	0.00327	0.00175	0.00258
Na_2O	wt.%	0.153	0.190	0.162	0.227	0.298	0.164	0.230
P_2O_5	wt.%	0.0104	0.0125	0.0111	0.0152	0.0194	0.0107	0.0154
^{7}Li	µg/g	1.56	1.81	1.65	2.12	2.95	1.58	2.30
^{53}Cr	µg/g	3.89	4.23	3.96	5.43	7.32	3.90	5.80
^{66}Zn	µg/g	1.47	1.65	1.40	2.10	2.58	1.63	1.96
^{85}Rb	µg/g	0.0856	0.0934	0.0855	0.123	0.147	0.0964	0.128
^{88}Sr	µg/g	0.0323	0.0275	0.0244	0.0334	0.0434	0.0237	0.0363
^{89}Y	µg/g	0.0260	0.0264	0.0304	0.0445	0.0544	0.0299	0.0369
^{91}Zr	µg/g	0.161	0.186	0.131	0.297	0.364	0.185	0.258
^{93}Nb	µg/g	0.00860	0.0207	0.0182	0.0294	0.0383	0.00901	0.0262
^{118}Sn	µg/g	0.237	0.308	0.260	0.385	0.445	0.258	0.387
^{137}Ba	µg/g	0.0976	0.111	0.0397	0.144	0.201	0.0691	0.104
^{139}La	µg/g	0.00819	0.0102	0.0120	0.0179	0.0190	0.0045	0.0157
^{140}Ce	µg/g	0.0136	0.0121	0.0131	0.0170	0.0210	0.0121	0.0150
^{141}Pr	µg/g	0.00835	0.00715	0.00766	0.01392	0.01352	0.00731	0.0133
^{143}Nd	µg/g	0.0720	0.0852	0.0785	0.0897	0.171	0.0328	0.0477
^{147}Sm	µg/g	0.0678	0.0711	0.0608	0.0892	0.1076	0.0452	0.0796
^{151}Eu	µg/g	0.0151	0.0155	0.0166	0.0268	0.0429	0.0175	0.0266
^{157}Gd	µg/g	0.0661	0.0825	0.0678	0.0869	0.139	0.0567	0.0934
^{159}Tb	µg/g	0.00718	0.00896	0.00789	0.0128	0.0139	0.0102	0.0114
^{163}Dy	µg/g	0.0293	0.0415	0.0322	0.0585	0.0831	0.0307	0.0560
^{165}Ho	µg/g	0.00864	0.00355	0.00434	0.01073	0.00748	0.0112	0.01556
^{167}Er	µg/g	0.0427	0.0448	0.0412	0.0252	0.0730	0.0397	0.0603
^{169}Tm	µg/g	0.00931	0.0108	0.00899	0.0122	0.0210	0.00976	0.0109
^{171}Yb	µg/g	0.0683	0.0580	0.0660	0.0899	0.117	0.0530	0.0801
^{175}Lu	µg/g	0.0121	0.00777	0.00987	0.0151	0.0175	0.00950	0.00598
^{177}Hf	µg/g	0.0578	0.0659	0.0235	0.0581	0.0901	0.0212	0.0842
^{181}Ta	µg/g	0.00465	0.00920	0.0131	0.00715	0.02326	0.0127	0.00708

Sample		yn61-12_zrn_44_01	yn61-12_zrn_44_02	yn61-12_zrn_44_03	yn61-12_zrn_44_04	yn61-12_zrn_44_05	yn61-12_zrn_44_06	yn61-12_zrn_44_07
^{208}Pb	µg/g	0.0258	0.0344	0.0249	0.0380	0.0440	0.0295	0.0363
^{232}Th	µg/g	0.0044	0.0142	0.0110	0.0197	0.0218	0.0105	0.0181
^{238}U	µg/g	0.00829	0.0140	0.0108	0.0123	0.0253	0.0138	0.0179

Sample		yn61-12_zrn_44_08	yn61-12_zrn_44_09	yn61-12_zrn_44_10	yn61-12_zrn_44_11	FR152_zrn_44_01	FR152_zrn_44_02	FR152_zrn_44_03
SiO_2	wt.%	41.2	39.8	44.9	45.6	40.9	50.5	45.8
TiO_2	wt.%	bdl	bdl	0.0015	0.0060	0.010	0.024	0.016
Al_2O_3	wt.%	0.009	0.028	0.16	0.32	0.061	0.19	0.49
FeO	wt.%	0.040	0.13	0.26	1.0	0.20	0.32	0.70
MgO	wt.%	0.0068	0.026	0.055	0.16	0.011	0.072	0.082
Na_2O	wt.%	bdl	bdl	bdl	bdl	bdl	bdl	bdl
P_2O_5	wt.%	0.43	0.54	1.1	1.6	0.56	1.1	0.81
^{7}Li	µg/g	213	244	269	464	158	183	148
^{53}Cr	µg/g	bdl	bdl	bdl	bdl	bdl	40.6	21.9
^{66}Zn	µg/g	3.7	10.2	94.9	203	7.5	33.0	84.8
^{85}Rb	µg/g	0.11	0.25	0.29	1.29	0.28	2.05	5.58
^{88}Sr	µg/g	5.9	11.5	82.6	184.3	1.2	31.9	249.3
^{89}Y	µg/g	3860	4180	5270	8000	6070	2900	1840
^{91}Zr	µg/g	431400	431400	431400	431400	431400	431400	431400
^{93}Nb	µg/g	1550	1210	1210	1100	1720	1080	586
^{118}Sn	µg/g	0.41	0.53	0.62	0.66	bdl	1.19	0.80
^{137}Ba	µg/g	6.3	9.0	42.2	93.6	5.5	93.5	279
^{139}La	µg/g	1.0	2.6	19.9	45.0	2.3	15.2	27.8
^{140}Ce	µg/g	12.4	43.9	318	592	17.9	106	145
^{141}Pr	µg/g	3.4	7.4	35.3	75.7	3.4	13.2	15.3
^{143}Nd	µg/g	60.2	111	342	691	39.7	145	144
^{147}Sm	µg/g	210	286	526	1020	90.7	341	227
^{151}Eu	µg/g	158	199	326	615	66.7	199	128
^{157}Gd	µg/g	836	974	1440	2650	427	885	554
^{159}Tb	µg/g	188	208	278	487	121	142	84.1
^{163}Dy	µg/g	1140	1240	1510	2470	1090	733	451
^{165}Ho	µg/g	170	182	219	342	235	114	72.0
^{167}Er	µg/g	322	345	416	625	522	242	160
^{169}Tm	µg/g	31.5	32.4	40.6	58.1	45.6	25.8	18.1
^{171}Yb	µg/g	178	194	225	303	186	141	107
^{175}Lu	µg/g	22.1	23.7	28.5	37.4	17.6	18.0	14.0
^{177}Hf	µg/g	6180	7970	9490	8300	4160	9320	10100
^{181}Ta	µg/g	59.8	49.1	53.1	60.9	15.3	9.1	5.70
^{208}Pb	µg/g	467	554	545	429	435	418	488
^{232}Th	µg/g	3620	4420	4330	5300	3280	3660	3620
^{238}U	µg/g	485	448	722	930	519	237	153

Sample		yn61-12_zrn_44_08	yn61-12_zrn_44_09	yn61-12_zrn_44_10	yn61-12_zrn_44_11	FR152_zrn_44_01	FR152_zrn_44_02	FR152_zrn_44_03
1σ Error								
SiO_2	wt.%	2.01	1.68	2.58	3.17	1.88	2.40	2.99
TiO_2	wt.%	0.00057	0.00038	0.00023	0.00062	0.00086	0.00193	0.00244
Al_2O_3	wt.%	0.0014	0.0050	0.0034	0.0062	0.0060	0.0169	0.014
FeO	wt.%	0.0065	0.032	0.006	0.022	0.024	0.017	0.13
MgO	wt.%	0.0015	0.0019	0.0022	0.0047	0.0016	0.0081	0.0052
Na_2O	wt.%	0.16	0.18	0.23	0.35	0.19	0.28	0.30
P_2O_5	wt.%	0.015	0.015	0.029	0.040	0.031	0.049	0.023
^{7}Li	µg/g	8.98	5.87	8.94	12.7	4.06	5.21	9.36
^{53}Cr	µg/g	3.69	4.48	5.60	8.76	4.48	3.91	4.43
^{66}Zn	µg/g	0.90	1.85	4.64	9.38	1.14	5.57	6.46
^{85}Rb	µg/g	0.047	0.083	0.056	0.32	0.059	0.19	0.60
^{88}Sr	µg/g	0.40	1.218	1.358	4.106	0.15	1.398	20.8
^{89}Y	µg/g	118	79.4	107	131	174	99.1	55.2
^{91}Zr	µg/g	16000	14900	13000	6480	12000	5200	16400
^{93}Nb	µg/g	45.2	59.0	39.1	12.7	47.6	19.4	35.4
^{118}Sn	µg/g	0.12	0.17	0.16	0.29	0.33	0.28	0.23
^{137}Ba	µg/g	0.31	1.01	0.77	2.01	0.71	4.18	19.6
^{139}La	µg/g	0.09	0.30	0.32	0.87	0.26	1.16	3.65
^{140}Ce	µg/g	0.78	4.17	3.35	7.03	1.61	3.43	5.13
^{141}Pr	µg/g	0.19	0.42	0.52	1.30	0.37	0.63	0.70
^{143}Nd	µg/g	3.51	4.30	5.61	12.4	3.50	5.85	5.85
^{147}Sm	µg/g	11.3	7.59	8.30	14.6	4.81	9.57	6.01
^{151}Eu	µg/g	7.61	5.18	5.94	9.01	3.02	5.26	4.5
^{157}Gd	µg/g	34.4	17.6	24.1	40.2	14.6	23.7	14.7
^{159}Tb	µg/g	7.89	5.16	5.44	6.22	3.95	4.25	2.63
^{163}Dy	µg/g	40.4	26.5	29.9	28.9	26.3	22.5	7.56
^{165}Ho	µg/g	5.64	3.18	4.50	3.93	6.36	3.58	1.69
^{167}Er	µg/g	12.3	7.64	8.43	7.92	12.8	7.64	2.99
^{169}Tm	µg/g	1.18	0.912	1.02	0.88	1.48	0.89	0.48
^{171}Yb	µg/g	6.87	4.63	5.35	3.77	4.85	4.97	4.89
^{175}Lu	µg/g	0.70	0.81	0.81	0.44	0.49	0.64	0.57
^{177}Hf	µg/g	366	348	372	174	161	124	754
^{181}Ta	µg/g	1.90	2.09	1.97	0.96	0.54	0.20	0.334
^{208}Pb	µg/g	11.9	10.1	19.8	8.01	11.3	5.45	24.0
^{232}Th	µg/g	135	82.1	110	138	81.0	79.3	189

Sample		yn61-12_zrn_44_08	yn61-12_zrn_44_09	yn61-12_zrn_44_10	yn61-12_zrn_44_11	FR152_zrn_44_01	FR152_zrn_44_02	FR152_zrn_44_03
^{238}U	µg/g	9.63	18.3	14.9	19.6	13.9	4.81	1.58
Detection Limit								
SiO_2	wt.%	1.11	1.44	1.64	2.61	1.52	2.00	2.44
TiO_2	wt.%	0.000260	0.000334	0.000359	0.000554	0.000325	0.000400	0.000373
Al_2O_3	wt.%	0.00190	0.00222	0.00285	0.00428	0.00226	0.00353	0.00373
FeO	wt.%	0.00342	0.00401	0.00489	0.00755	0.00400	0.00616	0.00647
MgO	wt.%	0.00173	0.00205	0.00259	0.00390	0.00206	0.00316	0.00335
Na_2O	wt.%	0.157	0.184	0.230	0.349	0.187	0.285	0.300
P_2O_5	wt.%	0.0105	0.0128	0.0149	0.0235	0.0124	0.0195	0.0204
^{7}Li	µg/g	1.56	1.84	2.30	3.68	1.80	2.71	2.86
^{53}Cr	µg/g	3.69	4.48	5.60	8.76	4.48	6.95	7.18
^{66}Zn	µg/g	1.27	1.56	1.97	3.52	1.71	2.91	2.90
^{85}Rb	µg/g	0.0857	0.112	0.104	0.186	0.106	0.159	0.169
^{88}Sr	µg/g	0.0228	0.0268	0.0292	0.0523	0.0338	0.0555	0.0357
^{89}Y	µg/g	0.0264	0.0343	0.0348	0.0578	0.0370	0.0425	0.0558
^{91}Zr	µg/g	0.162	0.232	0.177	0.469	0.166	0.077	0.155
^{93}Nb	µg/g	0.0225	0.0140	0.00780	0.0454	0.0137	0.0263	0.0216
^{118}Sn	µg/g	0.260	0.299	0.337	0.545	0.327	0.491	0.475
^{137}Ba	µg/g	0.0656	0.140	0.148	0.244	0.138	0.105	0.154
^{139}La	µg/g	0.00815	0.0144	0.00978	0.0186	0.0134	0.0187	0.0107
^{140}Ce	µg/g	0.0094	0.0111	0.0137	0.0165	0.0147	0.0169	0.0219
^{141}Pr	µg/g	0.00837	0.0104	0.00832	0.0158	0.00578	0.0177	0.0193
^{143}Nd	µg/g	0.0599	0.0897	0.0900	0.188	0.0839	0.119	0.0786
^{147}Sm	µg/g	0.0249	0.0426	0.0750	0.127	0.0863	0.0798	0.117
^{151}Eu	µg/g	0.0150	0.0246	0.00714	0.0292	0.0229	0.0240	0.0197
^{157}Gd	µg/g	0.0626	0.0906	0.0933	0.123	0.0985	0.0963	0.125
^{159}Tb	µg/g	0.00355	0.0107	0.0107	0.0163	0.0140	0.00461	0.00933
^{163}Dy	µg/g	0.0351	0.0248	0.0349	0.0804	0.0408	0.0579	0.0904
^{165}Ho	µg/g	0.00356	0.00609	0.00339	0.0163	0.0158	0.0142	0.0167
^{167}Er	µg/g	0.0156	0.0469	0.0470	0.0867	0.0569	0.0203	0.106
^{169}Tm	µg/g	0.00826	0.00584	0.01026	0.0214	0.0124	0.0136	0.0160
^{171}Yb	µg/g	0.0687	0.0939	0.0815	0.1389	0.0820	0.0909	0.103
^{175}Lu	µg/g	0.00751	0.0147	0.0130	0.00845	0.0136	0.00485	0.0253
^{177}Hf	µg/g	0.0467	0.0825	0.0463	0.1208	0.0321	0.0614	0.119
^{181}Ta	µg/g	0.00442	0.00757	0.01064	0.02026	0.0161	0.0176	0.0116

Sample		yn61-12_zrn_44_08	yn61-12_zrn_44_09	yn61-12_zrn_44_10	yn61-12_zrn_44_11	FR152_zrn_44_01	FR152_zrn_44_02	FR152_zrn_44_03
^{208}Pb	µg/g	0.0228	0.0371	0.0424	0.0830	0.0264	0.0431	0.0584
^{232}Th	µg/g	0.0083	0.0124	0.0125	0.0260	0.0135	0.0165	0.0280
^{238}U	µg/g	0.0123	0.0161	0.0196	0.0227	0.0149	0.0208	0.0297

Sample		FR152_zrn_44_04	FR152_zrn_44_05	FR152_zrn_44_06	FR152_zrn_44_07	FR152_zrn_44_08	FR152_zrn_44_09	FR152_zrn_44_10
SiO_2	wt.%	46.0	39.5	46.9	39.1	43.0	44.0	51.3
TiO_2	wt.%	0.085	0.014	0.025	0.0052	0.0085	0.020	0.015
Al_2O_3	wt.%	0.33	0.09	0.42	0.025	0.11	0.44	0.54
FeO	wt.%	1.9	0.80	0.42	0.37	0.21	0.17	0.16
MgO	wt.%	0.11	0.073	0.088	0.040	0.12	0.05	0.17
Na_2O	wt.%	bdl	bdl	bdl	bdl	bdl	bdl	bdl
P_2O_5	wt.%	1.1	0.34	2.41	0.46	1.1	3.9	1.7
^{7}Li	µg/g	162	233	180	200	233	219	205
^{53}Cr	µg/g	189	11.1	64.5	bdl	12.9	47.0	bdl
^{66}Zn	µg/g	80.9	34.9	151	11.0	24.9	82.4	47.6
^{85}Rb	µg/g	3.9	1.8	1.5	0.45	0.75	0.75	1.3
^{88}Sr	µg/g	34	2.9	5.1	1.9	6.7	7.3	1.6
^{89}Y	µg/g	3420	4150	5450	5670	6600	7560	6850
^{91}Zr	µg/g	431400	431400	431400	431400	431400	431400	431400
^{93}Nb	µg/g	869	1450	1230	1710	1760	1680	1440
^{118}Sn	µg/g	1.4	0.77	0.98	0.45	bdl	0.60	0.71
^{137}Ba	µg/g	37.0	26.5	34.8	8.0	15.8	27.6	14.2
^{139}La	µg/g	18.7	2.72	25.8	0.792	0.055	6.88	51.5
^{140}Ce	µg/g	203	19.6	327	16.1	1.5	150	280
^{141}Pr	µg/g	18.9	4.0	36.5	2.2	0.25	10.1	42.9
^{143}Nd	µg/g	205	53.7	404	35	9.0	101	394
^{147}Sm	µg/g	436	162	657	138	71.6	238	647
^{151}Eu	µg/g	239	118	356	101	66.6	153	350
^{157}Gd	µg/g	1030	696	1500	550	450	816	1590
^{159}Tb	µg/g	167	159	233	129	136	177	289
^{163}Dy	µg/g	835	1020	1200	1020	1220	1320	1630
^{165}Ho	µg/g	128	161	186	215	253	269	250
^{167}Er	µg/g	277	296	416	529	571	701	505
^{169}Tm	µg/g	28.6	23.8	45.3	52.3	49.7	76.7	49.7
^{171}Yb	µg/g	159	106	257	249	210	411	256
^{175}Lu	µg/g	19.6	10.3	33.0	25.7	20.7	51.4	31.1
^{177}Hf	µg/g	8020	5500	8620	3250	4400	3410	6160
^{181}Ta	µg/g	7.1	11.5	9.9	12.3	15.7	13.1	11.5
^{208}Pb	µg/g	402	540	523	612	506	516	474
^{232}Th	µg/g	4120	4950	5540	4460	3930	5230	5960
^{238}U	µg/g	267	489	403	511	547	539	492

Sample		FR152_zrn_44_04	FR152_zrn_44_05	FR152_zrn_44_06	FR152_zrn_44_07	FR152_zrn_44_08	FR152_zrn_44_09	FR152_zrn_44_10
1σ Error								
SiO_2	wt.%	3.60	1.63	2.91	1.49	1.59	1.63	2.04
TiO_2	wt.%	0.023	0.0013	0.0014	0.00051	0.00067	0.0012	0.0013
Al_2O_3	wt.%	0.045	0.012	0.0097	0.0029	0.0050	0.011	0.014
FeO	wt.%	0.42	0.053	0.026	0.056	0.012	0.0077	0.012
MgO	wt.%	0.011	0.0088	0.0019	0.010	0.011	0.0043	0.012
Na_2O	wt.%	0.22	0.16	0.22	0.17	0.19	0.25	0.33
P_2O_5	wt.%	0.12	0.016	0.054	0.024	0.045	0.10	0.037
^{7}Li	µg/g	10.9	7.66	6.97	8.20	6.66	6.56	9.84
^{53}Cr	µg/g	43.1	2.26	5.15	4.30	1.86	3.73	8.48
^{66}Zn	µg/g	12.0	4.67	4.54	2.64	2.64	3.36	2.96
^{85}Rb	µg/g	0.53	0.24	0.095	0.10	0.091	0.083	0.13
^{88}Sr	µg/g	16.9	0.33	0.31	0.17	0.33	0.32	0.09
^{89}Y	µg/g	373	167	142	84.7	141	138	183
^{91}Zr	µg/g	43200	15700	17600	12500	10300	7980	6600
^{93}Nb	µg/g	70.2	62.1	32.0	43.4	40.3	33.4	38.5
^{118}Sn	µg/g	0.27	0.17	0.16	0.15	0.30	0.21	0.25
^{137}Ba	µg/g	7.73	4.73	1.83	0.62	0.90	0.87	0.93
^{139}La	µg/g	2.20	0.33	0.58	0.091	0.011	0.21	1.39
^{140}Ce	µg/g	19.2	2.00	6.86	2.60	0.12	3.72	7.10
^{141}Pr	µg/g	1.85	0.43	1.60	0.28	0.035	0.30	1.15
^{143}Nd	µg/g	19.9	4.80	20.4	2.96	0.58	2.95	12.4
^{147}Sm	µg/g	44.3	8.65	22.2	4.22	2.40	5.60	19.9
^{151}Eu	µg/g	23.7	5.63	11.4	2.42	1.38	3.39	10.6
^{157}Gd	µg/g	104	30.4	38.9	11.6	7.42	15.5	45.9
^{159}Tb	µg/g	17.8	6.22	5.85	2.54	2.62	3.80	7.02
^{163}Dy	µg/g	89.9	37.1	30.9	21.2	23.9	26.0	38.0
^{165}Ho	µg/g	14.2	6.15	5.10	4.40	4.67	5.91	5.29
^{167}Er	µg/g	28.1	11.7	10.6	8.69	11.6	15.2	12.1
^{169}Tm	µg/g	3.06	0.96	1.14	1.16	1.05	1.81	1.24
^{171}Yb	µg/g	16.4	4.27	6.78	4.85	3.18	8.20	6.63
^{175}Lu	µg/g	1.92	0.27	0.66	0.35	0.41	1.35	0.72
^{177}Hf	µg/g	794	182	424	67.3	92.6	51.9	80.8
^{181}Ta	µg/g	0.69	0.62	0.34	0.30	0.35	0.29	0.34
^{208}Pb	µg/g	27.0	14.1	16.5	6.88	6.42	9.29	8.37
^{232}Th	µg/g	420	326	192	68.5	90.7	123	126

Sample		FR152_zrn_44_04	FR152_zrn_44_05	FR152_zrn_44_06	FR152_zrn_44_07	FR152_zrn_44_08	FR152_zrn_44_09	FR152_zrn_44_10
^{238}U	µg/g	22.1	18.6	14.0	7.15	12.1	11.7	9.17
Detection Limit								
SiO_2	wt.%	1.61	1.17	1.73	1.31	1.42	1.94	2.34
TiO_2	wt.%	0.000367	0.000252	0.000388	0.000333	0.000338	0.000334	0.000619
Al_2O_3	wt.%	0.00271	0.00192	0.00278	0.00216	0.00245	0.00323	0.00423
FeO	wt.%	0.00461	0.00341	0.00498	0.00393	0.00435	0.00567	0.00740
MgO	wt.%	0.00238	0.00174	0.00248	0.00195	0.00216	0.00287	0.00370
Na_2O	wt.%	0.216	0.156	0.223	0.173	0.194	0.253	0.328
P_2O_5	wt.%	0.0146	0.0107	0.0154	0.0118	0.0133	0.0173	0.0218
^{7}Li	µg/g	2.16	1.57	2.07	1.64	1.84	2.45	3.29
^{53}Cr	µg/g	5.06	3.44	5.54	4.30	4.92	6.29	8.48
^{66}Zn	µg/g	1.92	1.41	2.01	1.81	1.96	2.66	3.21
^{85}Rb	µg/g	0.111	0.0839	0.115	0.0994	0.116	0.116	0.190
^{88}Sr	µg/g	0.0338	0.0232	0.0263	0.0311	0.0353	0.0396	0.0370
^{89}Y	µg/g	0.0436	0.0271	0.0342	0.0268	0.0354	0.0484	0.0617
^{91}Zr	µg/g	0.244	0.122	0.205	0.217	0.193	0.265	0.288
^{93}Nb	µg/g	0.0310	0.0203	0.0103	0.0195	0.0112	0.0100	0.0146
^{118}Sn	µg/g	0.346	0.247	0.346	0.286	0.301	0.410	0.518
^{137}Ba	µg/g	0.146	0.100	0.130	0.0777	0.143	0.116	0.183
^{139}La	µg/g	0.0136	0.00841	0.0142	0.0115	0.0111	0.0144	0.0251
^{140}Ce	µg/g	0.0101	0.00749	0.0119	0.0150	0.0128	0.0181	0.0168
^{141}Pr	µg/g	0.0116	0.00964	0.0152	0.0109	0.0128	0.00424	0.0138
^{143}Nd	µg/g	0.113	0.0321	0.0376	0.0842	0.0981	0.122	0.119
^{147}Sm	µg/g	0.0834	0.0617	0.0589	0.0701	0.0816	0.0882	0.122
^{151}Eu	µg/g	0.0231	0.0154	0.0177	0.0210	0.0226	0.0265	0.0365
^{157}Gd	µg/g	0.0807	0.0497	0.0765	0.0885	0.0977	0.0975	0.126
^{159}Tb	µg/g	0.00507	0.00380	0.0156	0.00469	0.00487	0.0101	0.0173
^{163}Dy	µg/g	0.0548	0.0359	0.0182	0.0192	0.0475	0.0178	0.0577
^{165}Ho	µg/g	0.00507	0.00733	0.0123	0.0122	0.00963	0.0101	0.0198
^{167}Er	µg/g	0.0647	0.0323	0.0441	0.0371	0.0424	0.0633	0.0279
^{169}Tm	µg/g	0.0114	0.00843	0.0118	0.00450	0.0111	0.00417	0.00608
^{171}Yb	µg/g	0.0696	0.0660	0.0993	0.0703	0.0679	0.0884	0.0994
^{175}Lu	µg/g	0.0154	0.00399	0.00468	0.0105	0.0151	0.0106	0.0182
^{177}Hf	µg/g	0.0641	0.0474	0.0540	0.0454	0.0625	0.0234	0.1064
^{181}Ta	µg/g	0.0167	0.0109	0.0124	0.0124	0.0120	0.0156	0.0175

Sample		FR152_zrn_44_04	FR152_zrn_44_05	FR152_zrn_44_06	FR152_zrn_44_07	FR152_zrn_44_08	FR152_zrn_44_09	FR152_zrn_44_10
^{208}Pb	µg/g	0.0314	0.0286	0.0411	0.0344	0.0435	0.0419	0.0521
^{232}Th	µg/g	0.0156	0.0126	0.00517	0.00976	0.0152	0.0166	0.0200
^{238}U	µg/g	0.0136	0.0134	0.0162	0.0128	0.0150	0.0165	0.0198

Sample		FR152_zrn_44_11	FR152_zrn_44_12	LRS_zrn_44_01	LR9_zrn_44_02	LRS9_zrn_44_03	LRS9_zrn_44_04	LRS9_zrn_44_05
SiO_2	wt.%	41.4	40.1	45.0	41.4	39.7	44.4	42.3
TiO_2	wt.%	0.022	0.028	0.057	0.041	0.029	0.029	0.028
Al_2O_3	wt.%	0.44	0.13	0.0022	bdl	bdl	bdl	bdl
FeO	wt.%	0.36	0.52	1.00	0.69	0.19	0.33	0.25
MgO	wt.%	0.11	0.030	0.63	0.41	0.093	0.23	0.19
Na_2O	wt.%	bdl	bdl	0.24	bdl	bdl	bdl	bdl
P_2O_5	wt.%	2.18	0.53	0.46	0.43	0.47	0.48	0.52
^{7}Li	µg/g	225	120	527	447	343	468	457
^{53}Cr	µg/g	15.6	19.8	bdl	bdl	bdl	bdl	bdl
^{66}Zn	µg/g	63.6	22.0	181	38.2	27.1	60.6	41.6
^{85}Rb	µg/g	2.21	2.13	0.89	0.92	0.13	0.47	0.35
^{88}Sr	µg/g	2.36	11.0	3.9	4.7	2.7	5.1	3.5
^{89}Y	µg/g	7170	4440	40.7	47.0	37.7	45.3	34.8
^{91}Zr	µg/g	431400	431400	431400	431400	431400	431400	431400
^{93}Nb	µg/g	1250	974	2700	2320	3230	2990	3240
^{118}Sn	µg/g	1.29	0.853	6.726	0.675	7.16	1.18	6.11
^{137}Ba	µg/g	25.0	14.1	45.9	42.9	37.3	46.0	42.5
^{139}La	µg/g	18.5	2.8	2.3	1.3	2.4	2.1	2.2
^{140}Ce	µg/g	373	43.1	63.5	49.5	80.3	70.2	81.6
^{141}Pr	µg/g	34.75	4.5	34.8	29.7	47.4	41.1	47.5
^{143}Nd	µg/g	429	56.5	545	503	701	647	713
^{147}Sm	µg/g	936	128	279	300	327	313	303
^{151}Eu	µg/g	498	74.8	66.6	66.6	69.5	66.2	62.9
^{157}Gd	µg/g	2080	404	121	130	127	122	111
^{159}Tb	µg/g	342	97.5	7.89	8.31	7.81	7.81	6.74
^{163}Dy	µg/g	1800	782	20.2	22.4	18.8	20.7	16.5
^{165}Ho	µg/g	272	160	1.70	2.20	1.67	2.07	1.52
^{167}Er	µg/g	581	367	2.59	3.61	2.46	3.29	2.44
^{169}Tm	µg/g	62.1	34.6	0.23	0.33	0.21	0.32	0.23
^{171}Yb	µg/g	341	160	1.3	1.9	1.2	1.9	1.4
^{175}Lu	µg/g	41.2	17.3	0.145	0.220	0.129	0.221	0.160
^{177}Hf	µg/g	7790	4860	7280	2570	7240	3180	6670
^{181}Ta	µg/g	10.5	9.49	25.8	24.3	32.7	30.2	32.0
^{208}Pb	µg/g	501	229	326	327	380	376	389
^{232}Th	µg/g	5360	1690	2300	2310	2840	2620	2750
^{238}U	µg/g	592	320	13.5	12.2	15.7	13.8	14.3

Sample		FR152_zrn_44_11	FR152_zrn_44_12	LRS9_zrn_44_01	LRS9_zrn_44_02	LRS9_zrn_44_03	LRS9_zrn_44_04	LRS9_zrn_44_05
1σ Error								
SiO_2	wt.%	2.17	2.07	1.59	1.62	1.74	1.56	1.43
TiO_2	wt.%	0.00139	0.012	0.0022	0.0021	0.0010	0.00090	0.00075
Al_2O_3	wt.%	0.0095	0.0093	0.00068	0.0016	0.0015	0.0017	0.0016
FeO	wt.%	0.016	0.087	0.036	0.026	0.0062	0.0094	0.0073
MgO	wt.%	0.0032	0.0053	0.029	0.017	0.0051	0.0075	0.0063
Na_2O	wt.%	0.16	0.19	0.074	0.15	0.15	0.16	0.15
P_2O_5	wt.%	0.040	0.0099	0.013	0.018	0.0091	0.012	0.015
^{7}Li	µg/g	8.08	3.32	20.2	14.7	8.60	10.4	12.3
^{53}Cr	µg/g	2.28	3.69	3.01	3.24	3.01	3.33	3.02
^{66}Zn	µg/g	2.56	2.11	5.87	2.12	1.47	2.60	2.13
^{85}Rb	µg/g	0.13	0.34	0.082	0.075	0.039	0.065	0.052
^{88}Sr	µg/g	0.07	2.01	0.17	0.32	0.13	0.12	0.13
^{89}Y	µg/g	231	151	0.994	1.30	0.92	1.08	0.912
^{91}Zr	µg/g	19200	13000	8720	11100	12400	9100	10400
^{93}Nb	µg/g	55.6	30.6	71.6	67.9	61.4	42.5	43.3
^{118}Sn	µg/g	0.14	0.18	0.28	0.13	0.24	0.13	0.22
^{137}Ba	µg/g	0.99	1.23	1.79	1.58	1.47	0.70	0.93
^{139}La	µg/g	0.69	0.14	0.06	0.060	0.098	0.068	0.060
^{140}Ce	µg/g	9.92	0.91	1.29	2.22	1.81	1.18	1.97
^{141}Pr	µg/g	1.38	0.15	0.80	1.52	1.17	0.66	1.35
^{143}Nd	µg/g	15.1	1.06	12.7	22.3	17.9	12.3	20.1
^{147}Sm	µg/g	32.7	3.11	7.26	11.1	8.77	7.50	7.79
^{151}Eu	µg/g	16.9	2.20	1.77	2.14	1.96	1.69	1.52
^{157}Gd	µg/g	59.6	12.6	3.34	3.78	3.72	3.12	2.79
^{159}Tb	µg/g	10.3	3.60	0.26	0.29	0.24	0.19	0.19
^{163}Dy	µg/g	58.0	25.0	0.62	0.75	0.60	0.54	0.53
^{165}Ho	µg/g	8.08	5.58	0.063	0.072	0.060	0.061	0.057
^{167}Er	µg/g	18.2	12.4	0.11	0.20	0.11	0.14	0.10
^{169}Tm	µg/g	2.25	1.12	0.018	0.027	0.014	0.013	0.013
^{171}Yb	µg/g	13.7	5.62	0.076	0.088	0.065	0.086	0.074
^{175}Lu	µg/g	1.42	0.686	0.012	0.017	0.012	0.014	0.011
^{177}Hf	µg/g	386	135	126	65.5	214	33.4	153
^{181}Ta	µg/g	0.533	0.47	0.75	0.73	0.96	0.65	0.52
^{208}Pb	µg/g	14.8	7.49	5.89	9.35	7.57	7.90	11.0
^{232}Th	µg/g	173	68.3	48.0	91.2	72.4	67.8	85.4

Sample		FR152_zrn_44_11	FR152_zrn_44_12	LRS9_zrn_44_01	LRS9_zrn_44_02	LRS9_zrn_44_03	LRS9_zrn_44_04	LRS9_zrn_44_05
^{238}U	µg/g	16.3	11.5	0.32	0.42	0.40	0.34	0.33
Detection Limit								
SiO_2	wt.%	1.16	1.48	1.03	0.980	0.854	0.900	0.849
TiO_2	wt.%	0.000211	0.000273	0.000161	0.000159	0.000148	0.000152	0.000154
Al_2O_3	wt.%	0.00201	0.00236	0.00152	0.00156	0.00149	0.00171	0.00156
FeO	wt.%	0.00356	0.00420	0.00275	0.00283	0.00268	0.00315	0.00266
MgO	wt.%	0.00178	0.00209	0.00151	0.00152	0.00146	0.00166	0.00152
Na_2O	wt.%	0.158	0.185	0.155	0.152	0.146	0.164	0.152
P_2O_5	wt.%	0.0109	0.0127	0.0102	0.00983	0.00882	0.0100	0.00907
^{7}Li	µg/g	1.47	1.78	1.54	1.51	1.50	1.68	1.56
^{53}Cr	µg/g	3.85	4.93	3.01	3.24	3.01	3.33	3.02
^{66}Zn	µg/g	1.62	1.81	1.07	1.03	0.95	0.98	1.09
^{85}Rb	µg/g	0.0845	0.107	0.0720	0.0686	0.0801	0.0781	0.0671
^{88}Sr	µg/g	0.0184	0.0306	0.0189	0.0173	0.0134	0.0157	0.0155
^{89}Y	µg/g	0.0290	0.0394	0.0165	0.0192	0.0150	0.0194	0.0165
^{91}Zr	µg/g	0.158	0.203	0.136	0.147	0.084	0.123	0.094
^{93}Nb	µg/g	0.0140	0.0212	0.0047	0.0120	0.0117	0.0037	0.0102
^{118}Sn	µg/g	0.228	0.286	0.229	0.224	0.212	0.232	0.219
^{137}Ba	µg/g	0.0794	0.0849	0.0685	0.0483	0.0586	0.0588	0.0608
^{139}La	µg/g	0.0127	0.0141	0.00590	0.00599	0.00583	0.00570	0.00511
^{140}Ce	µg/g	0.0108	0.0130	0.00829	0.00625	0.00502	0.00685	0.00734
^{141}Pr	µg/g	0.00929	0.01397	0.00503	0.00870	0.00201	0.00726	0.00553
^{143}Nd	µg/g	0.0875	0.0778	0.0434	0.0440	0.0428	0.0137	0.0618
^{147}Sm	µg/g	0.0481	0.0355	0.0412	0.0368	0.0358	0.0350	0.0314
^{151}Eu	µg/g	0.0170	0.0214	0.00439	0.0166	0.0108	0.00847	0.0108
^{157}Gd	µg/g	0.0547	0.0686	0.0474	0.0402	0.0433	0.0111	0.0419
^{159}Tb	µg/g	0.00859	0.0122	0.00208	0.00744	0.00207	0.00640	0.00569
^{163}Dy	µg/g	0.0107	0.0501	0.0262	0.0302	0.0208	0.0260	0.00647
^{165}Ho	µg/g	0.00859	0.0109	0.00834	0.00750	0.00208	0.00645	0.00573
^{167}Er	µg/g	0.0330	0.0539	0.0285	0.0328	0.0281	0.0330	0.0251
^{169}Tm	µg/g	0.00250	0.00881	0.00621	0.00218	0.00613	0.00615	0.00432
^{171}Yb	µg/g	0.0427	0.0648	0.0493	0.0582	0.0450	0.0284	0.0363
^{175}Lu	µg/g	0.0100	0.00528	0.00793	0.00691	0.00781	0.00681	0.00605
^{177}Hf	µg/g	0.0403	0.0657	0.0113	0.0488	0.0279	0.0407	0.0245
^{181}Ta	µg/g	0.00930	0.0165	0.00646	0.00656	0.00796	0.00625	0.00199

Sample		FR152_zrn_44_11	FR152_zrn_44_12	LRS9_zrn_44_01	LRS9_zrn_44_02	LRS9_zrn_44_03	LRS9_zrn_44_04	LRS9_zrn_44_05
^{208}Pb	µg/g	0.0226	0.0376	0.0175	0.0242	0.0199	0.00442	0.0303
^{232}Th	µg/g	0.0136	0.0141	0.00994	0.00779	0.00765	0.00600	0.00538
^{238}U	µg/g	0.0127	0.0105	0.00890	0.00984	0.00760	0.00762	0.00534

Sample		LRS9_zrn_44_06	LRS9_zrn_44_07	LRS9_zrn_44_08	LRS9_zrn_44_09	LRS9_zrn_44_10
SiO_2	wt.%	42.9	42.2	41.8	38.0	41.3
TiO_2	wt.%	0.027	0.022	0.018	0.031	0.021
Al_2O_3	wt.%	bdl	bdl	0.00472	0.00378	bdl
FeO	wt.%	0.20	0.16	0.20	0.50	0.17
MgO	wt.%	0.15	0.13	0.13	0.29	0.13
Na_2O	wt.%	bdl	bdl	bdl	bdl	bdl
P_2O_5	wt.%	0.50	0.51	0.42	0.35	0.49
^{7}Li	µg/g	437	399	370	396	402
^{53}Cr	µg/g	bdl	bdl	bdl	bdl	bdl
^{66}Zn	µg/g	32.5	33.8	23.9	13.3	34.6
^{85}Rb	µg/g	0.31	0.23	0.28	0.75	0.22
^{88}Sr	µg/g	2.9	2.6	1.9	1.2	2.6
^{89}Y	µg/g	33.7	32.5	59.4	62.3	40.7
^{91}Zr	µg/g	431400	431400	431400	431400	431400
^{93}Nb	µg/g	3290	2970	2660	2360	2720
^{118}Sn	µg/g	6.5	7.0	0.76	0.73	6.0
^{137}Ba	µg/g	31.9	40.0	19.3	18.4	32.0
^{139}La	µg/g	1.8	2.4	2.1	2.0	1.9
^{140}Ce	µg/g	79.7	78.5	68.5	47.6	69.8
^{141}Pr	µg/g	46.6	45.8	38.6	25.5	41.7
^{143}Nd	µg/g	703	680	639	444	648
^{147}Sm	µg/g	297	295	350	291	321
^{151}Eu	µg/g	61.1	61.3	74.0	65.1	70.2
^{157}Gd	µg/g	109	108	143	135	134
^{159}Tb	µg/g	6.6	6.6	9.3	9.0	8.2
^{163}Dy	µg/g	15.7	15.8	26.1	25.0	21.6
^{165}Ho	µg/g	1.5	1.4	2.7	2.7	1.8
^{167}Er	µg/g	2.48	1.98	4.40	4.94	2.70
^{169}Tm	µg/g	0.21	0.20	0.48	0.48	0.23
^{171}Yb	µg/g	1.3	1.1	2.7	3.2	1.2
^{175}Lu	µg/g	0.16	0.16	0.38	0.39	0.15
^{177}Hf	µg/g	6820	7480	2380	2280	7370
^{181}Ta	µg/g	31.9	28.2	32.7	28.2	26.2
^{208}Pb	µg/g	391	399	383	277	385
^{232}Th	µg/g	2770	2800	2760	2060	2850
^{238}U	µg/g	14.5	14.3	18.4	14.7	15.5

Sample		LRS9_zrn_44_06	LRS9_zrn_44_07	LRS9_zrn_44_08	LRS9_zrn_44_09	LRS9_zrn_44_10
1σ Error						
SiO_2	wt.%	1.42	1.44	1.65	1.43	2.26
TiO_2	wt.%	0.0011	0.00076	0.00079	0.0014	0.0014
Al_2O_3	wt.%	0.0017	0.0018	0.00089	0.00066	0.0018
FeO	wt.%	0.014	0.012	0.0078	0.0088	0.0045
MgO	wt.%	0.011	0.010	0.0062	0.0060	0.0026
Na_2O	wt.%	0.16	0.17	0.15	0.16	0.17
P_2O_5	wt.%	0.013	0.013	0.014	0.012	0.022
^{7}Li	µg/g	15.6	14.3	10.7	5.66	16.2
^{53}Cr	µg/g	3.24	3.50	3.04	3.16	3.43
^{66}Zn	µg/g	2.71	3.23	1.29	1.25	1.62
^{85}Rb	µg/g	0.040	0.046	0.039	0.072	0.044
^{88}Sr	µg/g	0.17	0.12	0.089	0.051	0.14
^{89}Y	µg/g	0.89	0.89	1.17	2.83	1.52
^{91}Zr	µg/g	10300	9560	10700	11500	19900
^{93}Nb	µg/g	67.5	61.9	56.0	54.8	159
^{118}Sn	µg/g	0.20	0.29	0.10	0.12	0.39
^{137}Ba	µg/g	1.28	1.05	0.840	0.509	1.59
^{139}La	µg/g	0.069	0.067	0.044	0.16	0.12
^{140}Ce	µg/g	2.27	2.11	1.89	2.14	3.95
^{141}Pr	µg/g	1.22	1.14	1.16	1.03	2.31
^{143}Nd	µg/g	19.1	19.4	18.5	17.7	35.1
^{147}Sm	µg/g	7.27	8.06	9.99	9.70	15.3
^{151}Eu	µg/g	1.50	1.77	2.01	2.08	3.08
^{157}Gd	µg/g	2.54	3.08	3.71	4.88	5.44
^{159}Tb	µg/g	0.18	0.21	0.26	0.33	0.31
^{163}Dy	µg/g	0.48	0.47	0.68	1.07	0.78
^{165}Ho	µg/g	0.049	0.059	0.065	0.14	0.087
^{167}Er	µg/g	0.10	0.087	0.14	0.29	0.18
^{169}Tm	µg/g	0.014	0.013	0.016	0.028	0.020
^{171}Yb	µg/g	0.057	0.051	0.078	0.20	0.098
^{175}Lu	µg/g	0.013	0.012	0.018	0.025	0.015
^{177}Hf	µg/g	128	178	59.8	39.1	362
^{181}Ta	µg/g	0.737	0.661	0.729	0.853	1.70
^{208}Pb	µg/g	8.25	9.38	8.81	6.23	15.5
^{232}Th	µg/g	65.7	75.4	76.6	62.8	129

Sample		LRS9_zrn_44_06	LRS9_zrn_44_07	LRS9_zrn_44_08	LRS9_zrn_44_09	LRS9_zrn_44_10
^{238}U	µg/g	0.33	0.46	0.32	0.64	0.79
Detection Limit						
SiO_2	wt.%	0.947	0.951	1.01	0.970	1.01
TiO_2	wt.%	0.000240	0.000219	0.000140	0.000247	0.000264
Al_2O_3	wt.%	0.00165	0.00183	0.00158	0.00167	0.00183
FeO	wt.%	0.00287	0.00325	0.00265	0.00287	0.00316
MgO	wt.%	0.00158	0.00177	0.00153	0.00163	0.00176
Na_2O	wt.%	0.159	0.174	0.152	0.159	0.171
P_2O_5	wt.%	0.00960	0.0106	0.00938	0.00983	0.0104
^{7}Li	µg/g	1.56	1.88	1.52	1.60	1.63
^{53}Cr	µg/g	3.24	3.50	3.04	3.16	3.43
^{66}Zn	µg/g	1.08	1.19	0.957	1.24	1.18
^{85}Rb	µg/g	0.0709	0.0817	0.0650	0.0737	0.0883
^{88}Sr	µg/g	0.0148	0.0169	0.0145	0.0175	0.0212
^{89}Y	µg/g	0.0145	0.0215	0.0218	0.0177	0.0194
^{91}Zr	µg/g	0.152	0.114	0.0971	0.120	0.130
^{93}Nb	µg/g	0.0108	0.0123	0.0105	0.0136	0.0181
^{118}Sn	µg/g	0.210	0.247	0.218	0.229	0.230
^{137}Ba	µg/g	0.0435	0.0906	0.0777	0.0845	0.0833
^{139}La	µg/g	0.00184	0.00916	0.00524	0.0105	0.00729
^{140}Ce	µg/g	0.00716	0.00819	0.00700	0.00594	0.0101
^{141}Pr	µg/g	0.00460	0.00525	0.00821	0.00709	0.00621
^{143}Nd	µg/g	0.0396	0.0452	0.0493	0.0611	0.0535
^{147}Sm	µg/g	0.0458	0.0435	0.0371	0.0467	0.0447
^{151}Eu	µg/g	0.0165	0.0145	0.0112	0.0154	0.0112
^{157}Gd	µg/g	0.0506	0.0547	0.0313	0.0597	0.0538
^{159}Tb	µg/g	0.00473	0.00180	0.00460	0.00833	0.00640
^{163}Dy	µg/g	0.0285	0.0280	0.0187	0.0242	0.0112
^{165}Ho	µg/g	0.00477	0.00811	0.00149	0.00273	0.00797
^{167}Er	µg/g	0.0209	0.0304	0.0304	0.0263	0.0443
^{169}Tm	µg/g	0.00579	0.00663	0.00442	0.00260	0.00265
^{171}Yb	µg/g	0.0383	0.0382	0.0453	0.0191	0.0452
^{175}Lu	µg/g	0.00640	0.00575	0.00626	0.00633	0.00680
^{177}Hf	µg/g	0.0088	0.0376	0.0321	0.0454	0.0494
^{181}Ta	µg/g	0.00591	0.00675	0.00860	0.00912	0.00988

Sample		LRS9_zrn_44_06	LRS9_zrn_44_07	LRS9_zrn_44_08	LRS9_zrn_44_09	LRS9_zrn_44_10
^{208}Pb	µg/g	0.0232	0.0146	0.0159	0.0269	0.0244
^{232}Th	µg/g	0.00566	0.00825	0.00704	0.0110	0.0120
^{238}U	µg/g	0.00833	0.00641	0.00545	0.00864	0.0129

Appendix 4.D – Zircon U–Pb Results

Note: all zircons analysed with 32 µm spot size. 2σ is uncertainty for ages and concentrations.

Analysis	$^{238}U/^{206}Pb$	2σ	$^{207}Pb/^{206}Pb$	2σ	$^{207}Pb/^{235}U$	2σ	$^{207}Pb/^{206}Pb$ Age	2σ	$^{206}Pb/^{238}U$ Age	2σ	$^{207}Pb/^{235}U$ Age	2σ	U (µg/g)	2σ	Th (µg/g)	2σ	Th/U
LRS9_2	3.7286	0.13	0.1685	0.0085	6.150	0.33	2540	88	1530	46	2008	47	12.4	0.24	2480	41	200
LRS9_4	3.7979	0.10	0.1566	0.0065	5.630	0.27	2414	70	1505	35	1918	42	11.0	0.23	2630	65	239
LRS9_5	3.9526	0.14	0.1482	0.0090	5.220	0.35	2320	110	1452	46	1861	57	12.8	0.18	2930	58	229
LRS9_6	3.9448	0.14	0.1189	0.0089	4.110	0.32	1890	140	1454	47	1648	62	11.0	0.26	2610	50	237
LRS9_7	3.9293	0.13	0.1451	0.0094	4.680	0.31	2280	110	1468	40	1764	57	18.0	0.58	4050	150	226
LRS9_8	3.9510	0.14	0.1145	0.0088	3.990	0.28	1860	150	1454	47	1637	61	15.5	0.35	3360	84	217
LRS9_10	4.1305	0.13	0.1162	0.0080	3.840	0.26	1880	120	1397	39	1605	52	12.1	0.27	2920	66	242
LRS9_13	3.7037	0.18	0.1700	0.012	6.290	0.52	2560	130	1541	68	2004	74	14.7	0.29	4860	94	332
LRS9_14	3.4014	0.14	0.2480	0.016	10.09	0.56	3175	100	1661	60	2436	53	12.3	0.22	3070	34	250
LRS9_15	4.0502	0.16	0.1122	0.0078	3.890	0.32	1840	130	1430	52	1620	66	12.2	0.24	4070	90	333
LRS9_16	3.9370	0.12	0.1310	0.0093	4.400	0.30	2080	120	1458	41	1722	55	17.3	0.50	4760	130	276
LRS9_17	4.0900	0.12	0.1221	0.0061	4.120	0.24	1997	88	1409	36	1658	47	13.6	0.39	3860	120	284
LRS9_18	4.0502	0.14	0.1063	0.0075	3.570	0.25	1740	130	1421	45	1528	57	15.9	0.61	4290	150	270
LRS9_19	4.0306	0.12	0.1263	0.0067	4.340	0.26	1995	95	1427	39	1691	49	9.59	0.23	2430	52	253
LRS9_21	3.7341	0.14	0.1757	0.010	6.780	0.43	2630	110	1528	53	2072	57	14.7	0.30	4370	81	297
LRS9_24	3.8760	0.11	0.1471	0.0076	5.280	0.27	2322	84	1478	38	1872	44	13.5	0.31	4440	100	330
LRS9_29	3.4904	0.093	0.2259	0.0093	8.770	0.40	3016	64	1623	38	2313	44	20.5	0.81	5570	210	271
LRS9_31	3.3864	0.13	0.2700	0.014	10.86	0.66	3326	96	1666	54	2506	58	11.7	0.16	3850	85	329
LRS9_33	3.5753	0.12	0.2150	0.012	8.240	0.49	2935	87	1588	47	2256	55	11.3	0.21	4580	64	404
LRS9_35	3.4722	0.14	0.2320	0.012	8.800	0.46	3074	84	1629	58	2316	46	14.5	0.51	4800	200	330
LRS9_36	4.0420	0.16	0.1093	0.0083	3.680	0.28	1750	140	1423	49	1565	61	11.6	0.18	4230	68	366
LRS9_37	3.7979	0.13	0.1794	0.0084	6.480	0.37	2636	78	1505	45	2039	49	18.3	0.50	5910	150	323
LRS9_38	4.2141	0.18	0.1090	0.011	3.170	0.30	1780	190	1371	52	1480	77	22.4	1.0	9590	460	428

Analysis	$^{238}U/^{206}Pb$	2σ	$^{207}Pb/^{206}Pb$	2σ	$^{207}Pb/^{235}U$	2σ	$^{207}Pb/^{206}Pb$ Age	2σ	$^{206}Pb/^{238}U$ Age	2σ	$^{207}Pb/^{235}U$ Age	2σ	U (µg/g)	2σ	Th (µg/g)	2σ	Th/U
LRS9_40	3.2563	0.099	0.2610	0.013	10.92	0.54	3245	76	1725	46	2513	46	12.1	0.20	4050	84	335
FR-152_32_08	4.2159	0.085	0.08743	0.0013	2.861	0.061	1369	28	1372	25	1372	16	412	12	5170	140	12.5
FR-152_32_09	4.1789	0.087	0.08820	0.0015	2.903	0.064	1384	32	1384	26	1383	17	516	15	5410	150	10.5
FR-152_32_10	4.1789	0.087	0.08700	0.0014	2.899	0.067	1363	31	1383	26	1380	17	469	12	6310	230	13.5
FR-152_32_11	4.2772	0.093	0.08686	0.0015	2.788	0.062	1352	33	1354	26	1351	17	375	7.8	6170	150	16.4
FR-152_32_12	4.1824	0.11	0.08760	0.0018	2.918	0.081	1369	39	1381	32	1385	21	522	15	9050	250	17.3
FR-152_32_19	4.2319	0.098	0.08780	0.0016	2.988	0.077	1382	35	1367	29	1403	19	678	17	6250	190	9.22
FR-152_32_38	4.2105	0.11	0.08810	0.0022	2.872	0.086	1387	49	1373	32	1373	23	414	6.5	4350	110	10.5
YN50-50_32_01	4.3459	0.11	0.08603	0.0014	2.742	0.066	1339	31	1334	29	1339	18	1010	27	2670	110	2.64
YN50-50_32_03	4.1859	0.096	0.08756	0.0014	2.909	0.070	1370	30	1381	28	1385	19	1070	52	4120	200	3.85
YN50-50_32_06	4.2918	0.098	0.08732	0.0014	2.797	0.063	1365	30	1350	28	1354	17	1650	57	3320	56	2.01
YN50-50_32_08	4.3687	0.094	0.08539	0.0013	2.703	0.060	1322	29	1329	26	1329	16	1180	27	1190	20	1.01
YN50-50_32_14	4.1946	0.097	0.08780	0.0015	2.892	0.068	1375	34	1378	29	1379	18	715	19	3200	88	4.48
YN50-50_32_16	4.1964	0.088	0.08744	0.0013	2.875	0.060	1369	29	1378	26	1375	16	801	30	2170	93	2.71
YN50-50_32_18	4.2845	0.099	0.08780	0.0019	2.877	0.071	1375	41	1352	28	1375	19	708	22	824	19	1.16
YN50-50_32_27	4.1152	0.098	0.08810	0.0015	2.987	0.075	1382	34	1402	30	1403	19	305	4.3	6860	150	22.5
YN50-50_32_30	4.2937	0.094	0.08726	0.0013	2.786	0.063	1366	30	1349	26	1352	17	893	26	2120	48	2.37
YN61-12_32_03	4.2937	0.10	0.08703	0.0015	2.780	0.069	1358	33	1349	29	1353	18	352	6.6	3580	100	10.2
YN61-12_32_06	4.3103	0.089	0.08628	0.0014	2.746	0.061	1346	31	1345	25	1343	16	445	9.1	5720	160	12.8
YN61-12_32_07	4.3497	0.10	0.08710	0.0017	2.747	0.069	1358	38	1334	29	1342	18	345	5.6	5080	98	14.7
YN61-12_32_08	4.1859	0.10	0.08720	0.0016	2.963	0.076	1362	35	1381	30	1397	20	580	17	6380	230	11.0
YN61-12_32_09	4.1118	0.11	0.08900	0.0021	3.044	0.078	1408	48	1403	35	1418	20	507	27	5640	350	11.1
YN61-12_32_16	4.3141	0.11	0.08780	0.0017	2.772	0.068	1379	38	1344	30	1347	18	509	7.0	5500	150	10.8
YN61-12_32_26	4.2882	0.092	0.08695	0.0014	2.782	0.060	1360	31	1351	26	1350	16	403	4.4	3880	78	9.62
YN61-12_32_30	4.1580	0.093	0.08610	0.0016	2.974	0.084	1336	36	1389	28	1402	21	716	21	4910	150	6.86

Appendix 4.E – Zircon Lu–Hf Results

Sample	$^{176}Lu/^{177}Hf$	2σ	$^{176}Hf/^{177}Hf$	2σ	Age (Ma)	Initial $^{176}Hf/^{177}Hf(t)$	εHf(*t*)	2σ	$T_{(DM)}$
FR151-01	0.000715	0.000008	0.281898	0.000025	1370	0.281879	-1.26	0.90	1890
FR151-02	0.000917	0.000032	0.281936	0.000017	1370	0.281912	-0.076	0.60	1850
FR151-03	0.001359	0.000017	0.281976	0.000015	1370	0.281941	0.938	0.54	1800
FR151-04	0.000788	0.000014	0.281878	0.000021	1370	0.281858	-2.01	0.74	1920
FR151-05	0.000916	0.000016	0.281916	0.000013	1370	0.281892	-0.805	0.45	1870
FR151-06	0.000237	0.000016	0.281836	0.000008	1370	0.281830	-3.00	0.29	1950
FR151-07	0.000258	0.000010	0.281826	0.000016	1370	0.281820	-3.37	0.58	1960
FR151-08	0.000704	0.000011	0.281877	0.000016	1370	0.281859	-1.98	0.55	1920
FR151-09	0.000673	0.000005	0.281867	0.000019	1370	0.281849	-2.31	0.68	1930
FR151-10	0.000736	0.000042	0.281886	0.000017	1370	0.281867	-1.68	0.59	1910
FR151-11	0.000490	0.000007	0.281894	0.000012	1370	0.281881	-1.19	0.41	1880
FR151-12	0.000546	0.000016	0.281860	0.000012	1370	0.281846	-2.42	0.44	1930
FR151-13	0.000305	0.000004	0.281831	0.000016	1370	0.281824	-3.23	0.56	1960
FR151-14	0.000336	0.000016	0.281860	0.000014	1370	0.281851	-2.25	0.50	1920
FR151-15	0.000271	0.000008	0.281872	0.000014	1370	0.281865	-1.74	0.49	1900
FR151-16	0.000427	0.000002	0.281846	0.000016	1370	0.281835	-2.82	0.57	1950
FR151-17	0.001424	0.000004	0.281881	0.000024	1370	0.281844	-2.49	0.87	1950
FR151-18	0.002352	0.000041	0.281976	0.000017	1370	0.281915	0.019	0.61	1860
FR151-19	0.001265	0.000021	0.281951	0.000015	1370	0.281918	0.124	0.52	1840
FR151-20	0.001174	0.000023	0.281941	0.000014	1370	0.281911	-0.126	0.48	1850
FR151-21	0.001143	0.000024	0.281918	0.000012	1370	0.281889	-0.912	0.44	1880
YN50-49.9-01	0.000905	0.000044	0.281841	0.000030	1370	0.281818	-3.43	1.05	1980
YN50-49.9-02	0.000672	0.000025	0.281798	0.000023	1370	0.281781	-4.75	0.81	2020
YN50-49.9-03	0.000878	0.000088	0.281828	0.000021	1370	0.281805	-3.88	0.73	1990
YN50-49.9-04	0.000346	0.000011	0.281798	0.000018	1370	0.281789	-4.45	0.65	2010

Sample	$^{176}Lu/^{177}Hf$	2σ	$^{176}Hf/^{177}Hf$	2σ	Age (Ma)	Initial $^{176}Hf/^{177}Hf(t)$	εHf(*t*)	2σ	$T_{(DM)}$
YN50-49.9-06	0.002452	0.000064	0.281882	0.000024	1370	0.281818	-3.41	0.84	2000
YN50-49.9-08	0.000356	0.000018	0.281787	0.000017	1370	0.281778	-4.84	0.60	2020
YN50-49.9-09	0.000424	0.000008	0.281782	0.000019	1370	0.281771	-5.08	0.66	2030
YN50-49.9-12	0.001086	0.000049	0.281809	0.000016	1370	0.281781	-4.73	0.57	2030
YN50-49.9-13	0.000831	0.000124	0.281794	0.000019	1370	0.281772	-5.04	0.66	2040
YN50-49.9-14	0.001068	0.000077	0.281870	0.000018	1370	0.281842	-2.57	0.62	1950
YN50-49.9-15	0.000700	0.000034	0.281865	0.000014	1370	0.281847	-2.39	0.51	1930
YN50-49.9-16	0.000995	0.000041	0.281902	0.000014	1370	0.281876	-1.37	0.50	1900
YN50-49.9-17	0.000270	0.000010	0.281821	0.000015	1370	0.281814	-3.56	0.53	1970
YN50-49.9-18	0.000483	0.000021	0.281785	0.000020	1370	0.281772	-5.04	0.71	2030
YN50-49.9-19	0.001090	0.000027	0.281868	0.000025	1370	0.281840	-2.64	0.88	1950
YN50-49.9-20	0.000840	0.000047	0.281891	0.000016	1370	0.281869	-1.61	0.56	1900
YN61-12-01	0.000380	0.000010	0.281806	0.000016	1370	0.281796	-4.19	0.56	2000
YN61-12-02	0.000462	0.000015	0.281813	0.000016	1370	0.281801	-4.02	0.56	1990
YN61-12-03	0.000273	0.000004	0.281776	0.000016	1370	0.281769	-5.16	0.56	2030
YN61-12-04	0.000415	0.000010	0.281817	0.000015	1370	0.281806	-3.85	0.55	1980
YN61-12-05	0.000532	0.000011	0.281842	0.000016	1370	0.281828	-3.07	0.55	1960
YN61-12-06	0.000511	0.000032	0.281830	0.000023	1370	0.281817	-3.48	0.80	1970
YN61-12-07	0.000426	0.000003	0.281809	0.000019	1370	0.281798	-4.14	0.68	2000
YN61-12-08	0.000548	0.000018	0.281806	0.000017	1370	0.281792	-4.34	0.60	2000
YN61-12-09	0.000407	0.000011	0.281795	0.000017	1370	0.281784	-4.62	0.61	2010
YN61-12-10	0.000474	0.000012	0.281815	0.000022	1370	0.281802	-3.97	0.80	1990
YN61-12-11	0.000516	0.000014	0.281814	0.000021	1370	0.281800	-4.05	0.74	1990
YN61-12-12	0.000396	0.000011	0.281775	0.000022	1370	0.281765	-5.31	0.79	2040
YN61-12-13	0.000424	0.000010	0.281805	0.000013	1370	0.281794	-4.28	0.45	2000
YN61-12-14	0.000433	0.000012	0.281803	0.000017	1370	0.281792	-4.36	0.59	2000
YN61-12-15	0.000476	0.000009	0.281839	0.000018	1370	0.281826	-3.12	0.62	1960

Sample	$^{176}Lu/^{177}Hf$	2σ	$^{176}Hf/^{177}Hf$	2σ	Age (Ma)	Initial $^{176}Hf/^{177}Hf(t)$	εHf(*t*)	2σ	$T_{(DM)}$
YN61-12-16	0.000462	0.000016	0.281814	0.000018	1370	0.281802	-3.98	0.63	1990
YN61-12-17	0.000384	0.000013	0.281818	0.000019	1370	0.281808	-3.77	0.67	1980
YN61-12-18	0.000428	0.000015	0.281793	0.000018	1370	0.281782	-4.69	0.64	2020
YN61-12-19	0.000278	0.000003	0.281803	0.000015	1370	0.281796	-4.22	0.53	2000
YN61-12-20	0.000179	0.000011	0.281779	0.000013	1370	0.281775	-4.96	0.45	2020
YN61-12-21	0.000568	0.000018	0.281830	0.000020	1370	0.281815	-3.52	0.70	1970
LR9CB-1-1Z	0.000004	0.000000	0.281839	0.000012	1370	0.281839	-2.67	0.42	1930
LR9CB-1-2Z	0.000003	0.000000	0.281836	0.000014	1370	0.281836	-2.78	0.49	1940
LR9CB-1-3Z	0.000002	0.000000	0.281851	0.000009	1370	0.281851	-2.26	0.33	1920
LR9CB-1-4Z	0.000004	0.000000	0.281857	0.000020	1370	0.281857	-2.05	0.70	1910
LR9CB-1-6Z	0.000005	0.000000	0.281853	0.000014	1370	0.281853	-2.17	0.50	1910
LR9CB-1-7Z	0.000003	0.000000	0.281841	0.000013	1370	0.281841	-2.62	0.46	1930
LR9CB-1-10Z	0.000004	0.000000	0.281854	0.000014	1370	0.281854	-2.16	0.51	1910
LR9CB-1-11Z	0.000005	0.000000	0.281840	0.000011	1370	0.281840	-2.64	0.40	1930
LR9CB-1-12Z	0.000003	0.000000	0.281850	0.000011	1370	0.281850	-2.30	0.38	1920
LR9CB-1-14Z	0.000003	0.000000	0.281835	0.000012	1370	0.281835	-2.83	0.42	1940
LR9CB-1-15Z	0.000005	0.000000	0.281848	0.000016	1370	0.281848	-2.35	0.56	1920
LR9CB-1-17Z	0.000003	0.000000	0.281838	0.000012	1370	0.281838	-2.70	0.42	1930
LR9CB-1-20Z	0.000026	0.000001	0.281857	0.000030	1370	0.281856	-2.08	1.07	1910
LR9CB-1-21Z	0.000003	0.000000	0.281844	0.000015	1370	0.281844	-2.49	0.52	1930
LR9CB-1-22Z	0.000005	0.000000	0.281840	0.000016	1370	0.281839	-2.66	0.56	1930
LR9CB-1-23Z	0.000020	0.000001	0.281833	0.000019	1370	0.281833	-2.90	0.66	1940
LR9CB-1-25Z	0.000003	0.000000	0.281849	0.000012	1370	0.281849	-2.33	0.44	1920
LR9CB-1-26Z	0.000003	0.000000	0.281853	0.000015	1370	0.281853	-2.18	0.52	1910
LR9CB-1-28Z	0.000003	0.000000	0.281828	0.000012	1370	0.281828	-3.08	0.42	1950
LR9CB-1-30Z	0.000004	0.000000	0.281864	0.000009	1370	0.281864	-1.78	0.32	1990
LR9CB-1-32Z	0.000004	0.000000	0.281844	0.000010	1370	0.281844	-2.50	0.36	1930

Sample	$^{176}Lu/^{177}Hf$	2σ	$^{176}Hf/^{177}Hf$	2σ	Age (Ma)	Initial $^{176}Hf/^{177}Hf(t)$	εHf(*t*)	2σ	$T_{(DM)}$
LR9CB-1-33Z	0.000017	0.000001	0.281833	0.000018	1370	0.281833	-2.90	0.64	1940
LR9CB-1-36Z	0.000036	0.000000	0.281852	0.000021	1370	0.281851	-2.26	0.75	1920
LR9CB-1-38Z	0.000035	0.000001	0.281839	0.000023	1370	0.281839	-2.69	0.81	1930
LR9CB-1-39Z	0.000005	0.000000	0.281843	0.000011	1370	0.281843	-2.53	0.37	1930
LR9CB-1-40Z	0.000003	0.000000	0.281848	0.000010	1370	0.281848	-2.36	0.34	1920
LR9CB-1-41	0.000005	0.000000	0.281828	0.000010	1370	0.281828	-3.08	0.35	1950
LR9CB-1-42	0.000072	0.000002	0.281844	0.000020	1370	0.281842	-2.58	0.70	1930
LR9CB-1-43	0.000004	0.000000	0.281850	0.000011	1370	0.281850	-2.28	0.39	1920
LR9CB-1-44	0.000045	0.000000	0.281868	0.000023	1370	0.281867	-1.69	0.80	1900
LR9CB-1-45	0.000004	0.000000	0.281839	0.000012	1370	0.281839	-2.69	0.44	1930
LR9CB-1-46	0.000004	0.000000	0.281844	0.000014	1370	0.281844	-2.50	0.48	1930
LR9CB-1-47	0.000003	0.000000	0.281840	0.000010	1370	0.281840	-2.64	0.36	1930
LR9CB-1-48	0.000021	0.000001	0.281829	0.000023	1370	0.281828	-3.07	0.80	1950
LR9CB-1-49	0.000004	0.000000	0.281828	0.000009	1370	0.281827	-3.09	0.32	1950
LR9CB-1-50	0.000003	0.000000	0.281841	0.000009	1370	0.281841	-2.60	0.34	1930
LR9CB-1-51	0.000003	0.000000	0.281847	0.000013	1370	0.281847	-2.38	0.46	1920
LR9CB-1-52	0.000005	0.000000	0.281861	0.000015	1370	0.281861	-1.90	0.52	1900
LR9CB-1-53	0.000021	0.000001	0.281834	0.000017	1370	0.281834	-2.87	0.61	1940
LR9CB-1-54	0.000004	0.000000	0.281850	0.000010	1370	0.281850	-2.27	0.35	1920
LR9CB-1-55	0.000052	0.000001	0.281833	0.000015	1370	0.281832	-2.94	0.54	1940
LR9CB-1-56	0.000029	0.000001	0.281824	0.000026	1370	0.281823	-3.25	0.92	1960
LR9CB-1-57	0.000004	0.000000	0.281833	0.000012	1370	0.281833	-2.91	0.43	1940
LR9CB-1-58	0.000003	0.000000	0.281832	0.000012	1370	0.281831	-2.94	0.42	1940
LR9CB-1-59	0.000003	0.000000	0.281838	0.000014	1370	0.281838	-2.73	0.48	1940
LR9CB-1-60	0.000003	0.000000	0.281839	0.000011	1370	0.281839	-2.69	0.40	1930

Chapter 5 Appendices

Appendix 5.A – Bulk Rock Transect Geochemistry

5.A.1 – Bulk rock transect geochemistry results

Sample Number		**FT-1**	**FT-2**	**FT1-4**	**FT-3**	**FT-8**	**FT-7**
Rock type		ironstone	ironstone next to granite contact	fenite-granite	fenite-granite	granite	granite
Latitude		429894	429913	429913	429913	429926	429926
Longitude		7350903	7350912	7350912	7350912	7350811	7350811
Distance to ironstone (m)		0	0.1	0.2	0.35	20	50
SiO_2	*wt.%*	11.2	49.2	63.6	62.5	73.6	70.7
TiO_2	*wt.%*	0.0500	0.590	0.630	0.360	0.150	0.350
Al_2O_3	*wt.%*	3.99	10.7	13.4	15.7	14.3	15.4
Fe_2O_3T	*wt.%*	60.6	25.5	8.49	5.15	0.870	2.59
MnO	*wt.%*	0.0800	0.0200	0.0100	0.0200	0.0300	0.0500
MgO	*wt.%*	bdl	0.590	0.100	0.630	0.270	0.800
CaO	*wt.%*	0.180	0.0600	0.0500	0.0600	0.500	1.94
Na_2O	*wt.%*	0.0600	0.170	0.180	0.230	2.99	3.36
K_2O	*wt.%*	0.400	7.84	10.8	12.6	6.13	4.32
P_2O_5	*wt.%*	5.05	1.12	0.230	0.150	0.120	0.0900
LOI	*wt.%*	11.8	3.11	0.750	0.940	0.800	0.990
Total (major)	*wt.%*	93.5	98.9	98.3	98.5	99.8	101
Be	µg/g	16.1	5.96	5.17	6.09	3.03	0.335
Sc	µg/g	12.9	46.2	68.6	17.9	0.790	6.37
Cr	µg/g	26.7	208	86.5	28.9	24.4	23.5
Co	µg/g	48.2	45.3	67.4	50.5	45.4	32.1
Ni	µg/g	117	67.9	9.50	19.4	10.1	10.9
Cu	µg/g	23.1	22.3	14.1	10.8	3.49	5.99
Zn	µg/g	836	382	96.8	189	11.8	28.6
Ga	µg/g	177	67.4	99.6	145	14.1	19.5
Ge	µg/g	5.92	6.45	3.09	1.59	2.18	1.91
As	µg/g	7.43	4.00	1.39	3.11	3.16	2.54
Rb	µg/g	9.51	175	218	314	184	145
Sr	µg/g	1110	333	92.0	82.8	190	262

Sample Number		**FT-1**	**FT-2**	**FT1-4**	**FT-3**	**FT-8**	**FT-7**
Rock type		ironstone	ironstone next to granite contact	fenite-granite	fenite-granite	granite	granite
Latitude		429894	429913	429913	429913	429926	429926
Longitude		7350903	7350912	7350912	7350912	7350811	7350811
Distance to ironstone (m)		0	0.1	0.2	0.35	20	50
Y	µg/g	50.2	37.4	9.75	17.0	6.75	7.64
Zr	µg/g	5.71	58.9	24.5	926	61.5	155
Nb	µg/g	16.0	32.5	67.1	43.4	4.96	8.64
Mo	µg/g	17.1	3.06	2.53	1.42	1.82	0.831
Sn	µg/g	2.24	33.56	225	120	2.55	3.15
Sb	µg/g	0.449	0.505	0.438	0.499	0.662	0.389
Cs	µg/g	0.073	1.37	0.912	1.97	4.26	4.01
Ba	µg/g	20500	5880	10900	16700	653	666
La	µg/g	179.0	82.3	10.0	11.9	12.3	43.9
Ce	µg/g	972	561	38.4	50.9	24.1	87.4
Pr	µg/g	206	140	9.04	12.0	2.69	9.34
Nd	µg/g	912	714	50.1	70.7	9.12	34.0
Sm	µg/g	89.1	93.3	8.89	12.8	1.80	5.49
Eu	µg/g	17.2	20.6	2.43	3.17	0.739	1.05
Gd	µg/g	47.9	51.8	6.55	9.14	1.60	3.64
Tb	µg/g	5.29	5.94	0.873	1.21	0.198	0.418
Dy	µg/g	19.7	20.6	3.70	5.17	1.36	1.88
Ho	µg/g	2.20	2.05	0.456	0.691	0.222	0.308
Er	µg/g	3.29	2.69	0.751	1.46	0.647	0.697
Tm	µg/g	0.308	0.256	0.0831	0.214	0.121	0.121
Yb	µg/g	1.48	1.06	0.304	0.813	0.624	0.536
Lu	µg/g	0.195	0.137	0.0408	0.106	0.0780	0.0857
Hf	µg/g	0.258	2.19	1.39	27.9	2.13	4.57
Ta	µg/g	0.208	0.463	0.755	0.705	1.11	1.20
Pb	µg/g	714	917	933	225	42.1	34.0
Th	µg/g	106	87.4	8.27	10.8	6.59	23.7
U	µg/g	10.2	9.17	4.34	1.93	2.84	2.36

Sample Number		**EGT-5**	**EGT-2**	**EGT-3**	**EGT-4**	**TT-1**	**TT-2**	**TT-3**	**TT-5**	**TT-4**
Rock type		ironstone	ironstone next to granite contact	fenite? - quartzite	quartzite	ironstone	ironstone	fenite-schist	fenite-schist	fenite
Latitude		411310	411310	411310	411312	413947	413943	413943	413943	413955
Longitude		7350106	7350106	7350106	7350099	7356294	7356292	7356292	7356290	7356267
Distance to ironstone (m)		0	0.1	0.5	7	0	0	0.1	0.3	2
SiO_2	*wt.%*	7.08	47.2	94.6	93.6	2.44	1.99	52.5	62.4	57.3
TiO_2	*wt.%*	4.40	2.47	0.300	0.250	bdl	0.0300	0.750	0.640	0.640
Al_2O_3	*wt.%*	3.5	2.06	2.2	2.53	0.530	1.62	15.8	18.3	17.4
Fe_2O_3T	*wt.%*	71.4	39.8	1.25	0.950	81.4	80.3	13.3	4.59	5.29
MnO	*wt.%*	0.0700	0.0600	bdl	bdl	0.0900	0.0800	bdl	0.0300	bdl
MgO	*wt.%*	0.0300	0.0400	0.140	0.0100	bdl	bdl	0.0100	2.42	2.23
CaO	*wt.%*	0.110	0.120	0.0200	0.0300	0.0400	0.0400	0.0200	1.20	0.0300
Na_2O	*wt.%*	0.0100	0.0200	0.0200	0.0300	0.0200	0.0100	0.160	3.94	0.200
K_2O	*wt.%*	0.0100	0.0500	0.560	1.91	bdl	bdl	13.4	3.12	14.2
P_2O_5	*wt.%*	2.20	1.26	0.0400	0.0200	2.60	2.67	0.530	0.0600	0.0800
TOT/S	*wt.%*	0.0400	0.0900	bdl	bdl	0.0200	0.0100	bdl	bdl	0.0100
Cr_2O_3	*wt.%*	0.0760	0.0570	0.00400	0.00400	0.00700	0.0100	0.00700	0.0170	0.0180
LOI	*wt.%*	10.7	6.60	0.900	0.700	12.3	12.2	3.30	1.20	3.00
Total	*wt.%*	99.6	99.8	100	100	99.5	99.0	99.6	98.6	99.7
Be	µg/g	4.40	0.400	0.100	8.60	7.50	14.6	3.2	1.7	2.9
Sc	µg/g	22.0	15.0	3.00	1.00	12.0	24.0	2.00	16.0	11.0
Cr	µg/g	203	206	13.2	11.6	12.6	26.4	6.10	80.1	113
Co	µg/g	9.10	7.10	1.30	0.800	26.4	34.1	5.00	12.4	16.7
Ni	µg/g	226	138	5.90	3.20	118	164	32.2	44.2	46.7
Cu	µg/g	52.7	72.2	12.7	6.34	44.6	72.3	21.5	4.28	5.09
Zn	µg/g	179	124	13.9	6.40	787	1050	375	79.1	149
Ga	µg/g	9.50	5.30	1.60	1.80	0.70	2.30	22.9	21.0	18.9
Ge	µg/g	0.200	bdl	bdl	bdl	0.500	0.600	bdl	bdl	0.300
As	µg/g	28.8	28.3	1.30	2.20	47.8	60.1	27.0	0.600	0.900
Rb	µg/g	0.400	2.40	77.3	27.9	0.100	0.400	337	207	535
Sr	µg/g	22.2	44.9	24.9	5.40	19.2	32.8	101	239	54.2
Y	µg/g	50.5	25.8	2.60	1.70	8.30	39.3	14.4	23.4	6.00
Zr	µg/g	474	244	22.3	8.70	7.70	1280	24.0	129	95.3

Sample Number		**EGT-5**	**EGT-2**	**EGT-3**	**EGT-4**	**TT-1**	**TT-2**	**TT-3**	**TT-5**	**TT-4**
Rock type		ironstone	ironstone next to granite contact	fenite - quartzite	quartzite	ironstone	ironstone	fenite-schist	fenite-schist	fenite
Latitude		411310	411310	411310	411312	413947	413943	413943	413943	413955
Longitude		7350106	7350106	7350106	7350099	7356294	7356292	7356292	7356290	7356267
Distance to ironstone (m)		0	0.1	0.5	7	0	0	0.1	0.3	2
Nb	µg/g	215	108	61.5	73.9	3.40	248	172	11.2	63.3
Mo	µg/g	1.1	1.27	2.31	0.530	6.88	13.0	3.59	0.400	0.390
Sn	µg/g	2.00	bdl	bdl	bdl	bdl	bdl	bdl	2.00	2.00
Sb	µg/g	0.160	0.650	0.0700	0.0900	bdl	bdl	bdl	bdl	bdl
Cs	µg/g	0.100	0.300	10.1	0.300	0.100	0.100	1.40	17.9	7.90
Ba	µg/g	87	325	130	50	589	331	2050	1270	11900
La	µg/g	254	133	6.40	4.00	34.2	118	11.2	39.3	18.6
Ce	µg/g	497	255	11.1	7.80	131	491	63.3	78.8	34.0
Pr	µg/g	54.3	27.8	1.42	0.930	27.3	113	20.5	9.08	4.49
Nd	µg/g	196	97.5	6.30	4.00	172	755	187	33.6	21.3
Sm	µg/g	30.0	14.6	1.40	1.19	36.9	206	80.5	5.67	4.82
Eu	µg/g	7.96	4.27	0.260	0.270	6.67	41.7	19.0	1.14	1.17
Gd	µg/g	21.3	10.3	0.860	0.670	13.0	81.5	40.1	4.92	2.79
Tb	µg/g	2.35	1.16	0.100	0.0800	0.750	4.75	2.41	0.690	0.230
Dy	µg/g	11.5	5.81	0.530	0.470	2.38	13.6	6.69	4.22	1.03
Ho	µg/g	1.77	0.930	0.100	0.0600	0.130	0.670	0.230	0.770	0.170
Er	µg/g	4.5	2.71	0.250	0.210	0.600	1.99	0.540	2.35	0.390
Tm	µg/g	0.590	0.390	0.0400	0.0200	0.100	0.410	0.120	0.350	0.0600
Yb	µg/g	3.47	2.65	0.260	0.160	0.740	3.16	0.860	2.17	0.400
Lu	µg/g	0.460	0.350	0.0400	0.0200	0.100	0.400	0.0900	0.330	0.0500
Hf	µg/g	13.0	6.80	0.600	0.300	0.200	34.4	0.800	3.60	2.50
Ta	µg/g	14.4	7.70	0.500	0.400	0.100	1.50	1.30	1.10	1.00
Pb	µg/g	4.49	2.62	3.48	2.40	333	647	28.5	3.28	24.7
Th	µg/g	40.9	31.5	4.20	3.10	57.9	263	104	17.3	11.8
U	µg/g	8.40	7.30	0.300	0.300	7.30	19.9	2.70	4.40	0.600

5.A.2 – Detection limits for transect analyses

		DL for EGT & TT	DL for FT
SiO_2	*wt.%*	0.01	
TiO_2	*wt.%*	0.01	
Al_2O_3	*wt.%*	0.01	
Fe_2O_3T	*wt.%*	0.04	
MnO	*wt.%*	0.01	
MgO	*wt.%*	0.01	
CaO	*wt.%*	0.01	
Na_2O	*wt.%*	0.01	
K_2O	*wt.%*	0.04	
P_2O_5	*wt.%*	0.01	
TOT/S	*wt.%*	0.02	
Cr_2O_3	*wt.%*	0.002	
LOI	*wt.%*	0.01	
Be	µg/g	0.1	0.5
Sc	µg/g	1	0.4
Cr	µg/g	0.5	3
Co	µg/g	0.1	0.4
Ni	µg/g	0.1	3
Cu	µg/g	0.01	2
Zn	µg/g	0.1	1
Ga	µg/g	0.5	0.2
Ge	µg/g	0.1	1
As	µg/g	0.1	1
Rb	µg/g	0.1	0.2
Sr	µg/g	0.5	0.04
Y	µg/g	0.1	0.03
Zr	µg/g	0.1	0.1
Nb	µg/g	0.1	0.03
Mo	µg/g	0.01	0.05
Sn	µg/g	1	0.2
Sb	µg/g	0.02	0.07
Cs	µg/g	0.1	0.01
Ba	µg/g	5	0.1
La	µg/g	0.1	0.01
Ce	µg/g	0.1	0.02
Pr	µg/g	0.02	0.006
Nd	µg/g	0.3	0.05
Sm	µg/g	0.05	0.02
Eu	µg/g	0.02	0.01
Gd	µg/g	0.05	0.03
Tb	µg/g	0.01	0.003
Dy	µg/g	0.05	0.02
Ho	µg/g	0.02	0.004
Er	µg/g	0.03	0.02
Tm	µg/g	0.01	0.003
Yb	µg/g	0.05	0.02
Lu	µg/g	0.01	0.003
Hf	µg/g	0.1	0.01
Ta	µg/g	0.1	0.004
Pb	µg/g	0.01	0.04
Th	µg/g	0.2	0.02
U	µg/g	0.1	0.01

5.A.3 – Supplementary fenite isocon diagrams

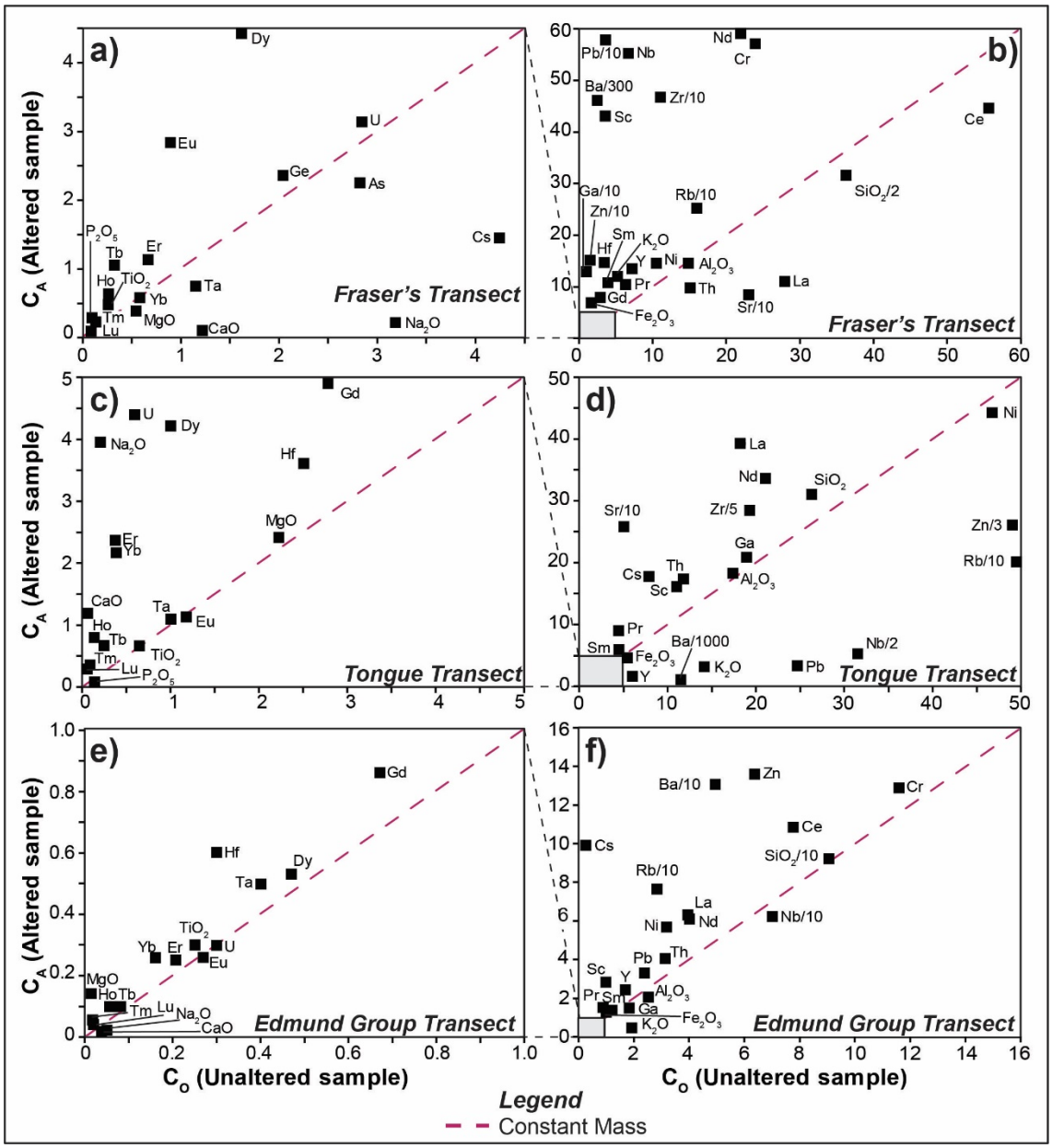

Supplementary Figure 5.A.1. Diagrams comparing the fenites from Fraser's (a,b), Tongue (c,d), and in the Edmund Group (e,f) with the least-altered host rock for granite, schist, and quartzite, respectively. Line of constant mass is plotted for reference. Grey boxes in b,d,andf are subset locations for a,c, and e, respectively.

Appendix 5.B – Monazite and rhabdophane EPMA Data

Comment	YW61-8A Mnz 1	YW61-8A Mnz 2	YW61-8A Mnz 3	YW61-8A Mnz 4	YW61-8A Mnz 5	YW61-8A Mnz 6	YW61-8A Mnz 7	YW61-8A Mnz 8
Mineral	monazite	monazite	monazite	monazite	monazite	monazite	monazite	monazite
deposit	Yangibana West	Yangibana West	Yangibana West	Yangibana West	Yangibana West	Yangibana West	Yangibana West	Yangibana West
Rock type	mag-bio dyke	mag-bio dyke	mag-bio dyke	mag-bio dyke	mag-bio dyke	mag-bio dyke	mag-bio dyke	mag-bio dyke
SiO2	0.235	bdl	0.259	0.000500	bdl	0.695	0.295	0.146
P2O5	29.6	30.8	29.9	30.3	30.7	29.3	29.8	30.0
CaO	0.0776	0.0094	0.105	0.00300	0.0181	0.114	0.113	0.147
SrO	N.A.	N.A.	N.A.	N.A.	N.A.	N.A.	N.A.	N.A.
Y2O3	0.104	0.163	bdl	0.279	0.204	bdl	bdl	0.298
La2O3	12.7	15.9	12.9	14.9	16.7	11.8	12.5	12.4
Ce2O3	30.1	34.2	33.5	33.1	33.8	32.3	32.5	30.2
Pr2O3	4.13	4.02	3.77	3.86	3.56	4.27	4.32	4.04
Nd2O3	16.2	11.9	14.3	13.1	12.2	14.8	13.8	15.5
Sm2O3	0.467	0.0862	0.237	0.321	0.217	0.205	0.323	0.479
Gd2O3	1.44	0.896	0.539	1.01	1.04	0.541	0.588	1.33
Dy2O3	0.248	0.118	bdl	0.199	0.225	bdl	0.155	0.418
ThO2	1.71	0.298	1.80	0.454	0.214	3.91	3.36	1.75
Total	96.9	98.4	97.3	97.6	98.9	97.9	97.8	96.7
APFU								
Si	0.00943	0	0.0103	0	0	0.0278	0.0117	0.00584
P	1.01	1.02	1.01	1.02	1.02	0.990	1.01	1.02
Ca	0.00334	0.00039	0.00450	0.000127	0.000758	0.00486	0.00482	0.00630
Sr	0	0	0	0	0	0	0	0
Y	0.00222	0.00339	0	0.0058796	0.00424	0	0	0.00634
La	0.188	0.229	0.190	0.218	0.240	0.174	0.184	0.183
Ce	0.443	0.490	0.489	0.481	0.483	0.472	0.474	0.443
Pr	0.0605	0.0573	0.0548	0.0558	0.0507	0.0621	0.0627	0.0589
Nd	0.232	0.166	0.204	0.186	0.171	0.211	0.196	0.221
Sm	0.00647	0.00116	0.00326	0.00439	0.00292	0.00282	0.00444	0.00659
Gd	0.0192	0.0116	0.00712	0.0133	0.0135	0.00716	0.00777	0.0176
Dy	0.0032131	0.00149	0	0.00254	0.00283	0	0.00199	0.00538
Th	0.0156	0.00265	0.0163	0.00410	0.00191	0.0355	0.0305	0.0159

Comment	YW61-8A Mnz 9	YW61-8A Mnz 10	YW61-8A Mnz 11	50-49A Mnz 1	50-49A Mnz 2	50-49A Mnz 3	50-49A Mnz 4
Mineral	monazite	monazite	monazite	monazite	monazite	monazite	monazite
deposit	Yangibana West	Yangibana West	Yangibana West	Yangibana North	Yangibana North	Yangibana North	Yangibana North
Rock type	mag-bio dyke	mag-bio dyke	mag-bio dyke	ank-sid carbonatite	ank-sid carbonatite	ank-sid carbonatite	ank-sid carbonatite
SiO2	0.0283	0.187	0.0179	0.0788	0.238	0.0208	0.0386
P2O5	30.6	30.0	30.3	30.1	30.3	29.9	30.1
CaO	0.0846	0.0830	0.0450	0.209	0.0771	0.188	0.166
SrO	N.A.	N.A.	N.A.	N.A.	N.A.	N.A.	N.A.
Y2O3	0.105	0.0271	0.0298	bdl	0.221	bdl	bdl
La2O3	16.5	13.4	16.0	10.1	12.1	13.6	12.9
Ce2O3	35.0	32.1	34.6	30.4	32.0	32.9	32.5
Pr2O3	3.77	3.88	3.97	3.76	4.01	3.74	4.20
Nd2O3	12.3	14.5	12.5	16.2	15.8	13.1	13.9
Sm2O3	0.136	0.476	0.159	0.354	0.499	0.204	0.302
Gd2O3	0.367	1.07	0.345	1.18	1.24	0.846	0.924
Dy2O3	bdl	0.222	0.147	0.0232	0.180	0.426	0.146
ThO2	0.339	1.39	0.404	3.93	1.59	1.96	2.07
Total	99.2	97.3	98.4	96.4	98.1	96.9	97.2
APFU							
Si	0.00111	0.00743	0.000706	0.00316	0.00940	0.000833	0.0015402
P	1.01	1.01	1.01	1.02	1.01	1.02	1.02
Ca	0.00354	0.00354	0.00190	0.00899	0.00326	0.00809	0.00708
Sr	0	0	0	0	0	0	0
Y	0.00219	0.000574	0.000626	0	0.00465	0	0
La	0.238	0.196	0.232	0.150	0.175	0.201	0.189
Ce	0.501	0.468	0.500	0.446	0.462	0.482	0.475
Pr	0.0537	0.0563	0.0571	0.0550	0.0576	0.0546	0.0611
Nd	0.172	0.206	0.176	0.232	0.222	0.187	0.198
Sm	0.00183	0.00653	0.00216	0.00490	0.00678	0.00281	0.00415
Gd	0.00476	0.0141	0.00451	0.0157	0.0162	0.0112	0.0122
Dy	0	0.00285	0.00186	0.000300	0.00228	0.00549	0.00188
Th	0.0030	0.0126	0.00363	0.0359	0.0143	0.0179	0.0188

Comment	50-49A Mnz 5	50-49A Mnz 6	50-49A Mnz 7	50-49A Mnz 8	50-49A Mnz 9	50-49A Mnz 10	50-49A Mnz 11
Mineral	monazite	monazite	monazite	monazite	monazite	monazite	monazite
deposit	Yangibana North	Yangibana North	Yangibana North	Yangibana North	Yangibana North	Yangibana North	Yangibana North
Rock type	ank-sid carbonatite	ank-sid carbonatite	ank-sid carbonatite	ank-sid carbonatite	ank-sid carbonatite	ank-sid carbonatite	ank-sid carbonatite
SiO2	0.0350	0.0550	0.0569	0.0338	bdl	bdl	0.0105
P2O5	30.3	30.4	30.2	30.5	30.4	30.5	30.4
CaO	0.169	0.193	0.179	0.264	0.227	0.230	0.160
SrO	N.A.	N.A.	N.A.	N.A.	N.A.	N.A.	N.A.
Y2O3	0.181	bdl	0.0701	bdl	bdl	0.0135	bdl
La2O3	8.28	13.2	13.2	12.4	12.1	10.8	11.8
Ce2O3	26.4	32.4	32.7	31.7	31.6	30.2	32.1
Pr2O3	4.41	3.62	3.66	3.90	3.96	3.95	3.93
Nd2O3	19.4	13.4	13.9	13.5	14.6	15.0	13.9
Sm2O3	0.824	0.201	0.328	0.113	0.436	0.529	0.378
Gd2O3	2.20	0.964	1.12	0.618	0.961	1.38	1.10
Dy2O3	0.194	0.109	0.0101	bdl	0.105	0.278	0.161
ThO2	2.63	3.18	2.12	4.28	2.48	2.85	2.61
Total	95.0	97.7	97.5	97.3	96.9	95.6	96.6
APFU							
Si	0.00141	0.0021801	0.0022603	0.0013402	0	0	0.000418
P	1.03	1.02	1.02	1.02	1.02	1.03	1.03
Ca	0.00731	0.00818	0.00764	0.0112	0.00968	0.00986	0.00681
Sr	0	0	0	0	0	0	0
Y	0.00389	0	0.00148	0	0	0.000288	0
La	0.123	0.194	0.193	0.181	0.178	0.160	0.174
Ce	0.390	0.470	0.475	0.460	0.460	0.442	0.468
Pr	0.0648	0.0523	0.0530	0.0563	0.0574	0.0577	0.0570
Nd	0.279	0.190	0.197	0.191	0.208	0.214	0.198
Sm	0.0115	0.00275	0.00449	0.00155	0.00598	0.00730	0.00518
Gd	0.0294	0.0127	0.0147	0.0081	0.0127	0.0183	0.0145
Dy	0.00252	0.00139	0.000129	0	0.00134	0.00359	0.00207
Th	0.0241	0.0287	0.0192	0.0386	0.0225	0.0260	0.0237

Comment	LR26 Mnz 1	LR26 Mnz 2	LR26 Mnz 3	LR26 Mnz 4	LR26 Mnz 5	LR26 Mnz 6	LR26 Mnz 7	LR26 Mnz 8
Mineral	monazite	monazite	monazite	monazite	monazite	monazite	monazite	monazite
deposit	Yangibana North	Yangibana North	Yangibana North	Yangibana North	Yangibana North	Yangibana North	Yangibana North	Yangibana North
Rock type	Amph-dol vnlt	Amph-dol vnlt	Amph-dol vnlt	Amph-dol vnlt	Amph-dol vnlt	Amph-dol vnlt	Amph-dol vnlt	Amph-dol vnlt
SiO2	0.750	0.311	0.589	0.461	0.489	0.567	0.687	0.234
P2O5	28.9	29.4	29.4	29.6	29.7	29.3	28.6	29.7
CaO	0.670	0.422	0.402	0.484	0.414	0.436	0.676	0.319
SrO	N.A.	N.A.	N.A.	N.A.	N.A.	N.A.	N.A.	N.A.
Y2O3	bdl	bdl	bdl	bdl	bdl	bdl	bdl	bdl
La2O3	17.2	16.0	17.7	17.9	17.8	17.4	17.3	18.9
Ce2O3	28.8	30.0	30.5	30.5	30.9	31.0	28.5	30.8
Pr2O3	2.40	2.94	2.67	2.72	2.67	2.74	2.35	2.61
Nd2O3	6.68	9.20	7.18	7.47	7.30	7.10	6.05	7.87
Sm2O3	bdl	0.0431	bdl	bdl	0.0186	bdl	bdl	0.174
Gd2O3	0.0265	0.317	0.00850	0.119	0.222	0.0943	bdl	0.0191
Dy2O3	bdl	0.269	0.0857	bdl	bdl	bdl	0.167	bdl
ThO2	10.1	6.68	8.41	7.64	7.81	8.19	10.1	6.78
Total	95.6	95.6	96.9	96.8	97.3	96.9	94.4	97.5
APFU								
Si	0.0306	0.0126	0.0237	0.0185	0.0196	0.0228	0.0283	0.00938
P	1.00	1.01	1.00	1.00	1.00	1.00	1.00	1.01
Ca	0.0292	0.0184	0.0173	0.0208	0.0177	0.0188	0.0299	0.0137
Sr	0	0	0	0	0	0	0	0
Y	0	0	0	0	0	0	0	0
La	0.259	0.240	0.263	0.264	0.262	0.259	0.263	0.279
Ce	0.430	0.445	0.449	0.449	0.453	0.456	0.431	0.452
Pr	0.0356	0.0435	0.0391	0.0398	0.0389	0.0402	0.0353	0.0381
Nd	0.0972	0.133	0.103	0.107	0.104	0.102	0.0891	0.113
Sm	0	0.000603	0	0	0.00026	0	0	0.00240
Gd	0.000358	0.004260	0.000113	0.00158	0.00294	0.00126	0	0.000253466
Dy	0	0.00351	0.001110059	0	0	0	0.002216498	0
Th	0.0940	0.0617	0.0769	0.0698	0.0711	0.0750	0.0952	0.0618

Comment	LR26 Mnz 9	LE1 Mnz 1	LE1 Mnz 2	LE1 Mnz 3	LE1 Mnz 4	LE1 Mnz 5	LE1 Mnz 6	LE1 Mnz 7	LE1 Mnz 8
Mineral	monazite	monazite	monazite	monazite	monazite	monazite	monazite	monazite	monazite
deposit	Yangibana North	Lion's Ear	Lion's Ear	Lion's Ear	Lion's Ear	Lion's Ear	Lion's Ear	Lion's Ear	Lion's Ear
Rock type	Amph-dol vnlt	fenite	fenite	fenite	fenite	fenite	fenite	fenite	fenite
SiO2	0.0906	0.456	0.421	0.310	0.477	0.167	0.110	0.404	0.266
P2O5	30.2	29.2	29.0	28.9	29.3	29.7	30.0	29.8	30.1
CaO	0.300	0.182	0.200	0.248	0.191	0.116	0.0739	0.150	0.198
SrO	N.A.	N.A.	N.A.	N.A.	N.A.	N.A.	N.A.	N.A.	N.A.
Y2O3	bdl	0.593	0.132	0.0258	0.288	0.191	0.119	0.377	0.474
La2O3	18.3	6.64	6.55	5.00	6.09	4.82	6.89	6.38	6.45
Ce2O3	30.9	25.0	25.6	23.0	24.9	23.1	26.1	25.2	25.3
Pr2O3	2.57	4.34	4.69	4.91	4.87	4.76	4.93	4.66	4.47
Nd2O3	8.40	21.9	22.2	24.2	22.7	25.9	22.6	22.4	22.7
Sm2O3	0.00590	0.819	0.758	1.00	0.838	1.20	0.854	0.735	0.822
Gd2O3	0.18860	2.31	1.72	2.03	2.02	2.53	1.99	2.36	2.59
Dy2O3	0.114	0.377	0.176	0.172	0.257	0.260	0.0902	0.265	0.359
ThO2	5.96	2.76	2.75	2.94	3.32	1.23	1.34	2.90	1.96
Total	97.0	94.6	94.2	92.7	95.1	93.9	95.0	95.6	95.7
APFU									
Si	0.00361	0.0186	0.0173	0.0129	0.0194	0.00685	0.00443	0.0163	0.0107
P	1.02	1.01	1.01	1.02	1.01	1.03	1.03	1.02	1.02
Ca	0.0128	0.00796	0.00881	0.0111	0.00832	0.00508	0.00320	0.00649	0.00849
Sr	0	0	0	0	0	0	0	0	0
Y	0	0.01289	0.00289	0.000572	0.006238058	0.00415	0.00256	0.00810	0.0101
La	0.269	0.100	0.0993	0.0769	0.0915	0.0727	0.103	0.0949	0.0954
Ce	0.451	0.375	0.385	0.351	0.371	0.345	0.387	0.372	0.372
Pr	0.0373	0.0646	0.0702	0.0746	0.0723	0.0710	0.0727	0.0685	0.0653
Nd	0.120	0.320	0.326	0.360	0.330	0.378	0.326	0.323	0.325
Sm	0.0000811	0.0115	0.0107	0.0144	0.0118	0.0169	0.0119	0.0102	0.0114
Gd	0.00249	0.0313	0.0234	0.0280	0.0273	0.0343	0.0267	0.0315	0.0344
Dy	0.00146	0.00497	0.00233	0.00231	0.00337	0.00342957	0.00118	0.00344	0.00463
Th	0.0541	0.0257	0.0257	0.0279	0.0308	0.0115	0.0123	0.0266	0.0179

Comment	LR23 Mnz 4	LR23 Mnz 5	LR25 Mnz 1	LR25 Mnz 2	LR25 Mnz 3	LR25 Mnz 4	LR25 Mnz 5	LR25 Mnz 7
Mineral	monazite	monazite	monazite	monazite	monazite	monazite	monazite	monazite
deposit	*Windarrie Pool	*Windarrie Pool	*Windarrie Pool	*Windarrie Pool	*Windarrie Pool	*Windarrie Pool	*Windarrie Pool	*Windarrie Pool
Rock type	dol carbonatite	dol carbonatite	dol carbonatite	dol carbonatite	dol carbonatite	dol carbonatite	dol carbonatite	dol carbonatite
SiO2	0.250	0.161	0.0921	0.521	0.237	0.738	0.110	0.299
P2O5	28.9	28.9	28.7	28.7	28.7	29.0	29.0	30.2
CaO	0.266	0.049	0.756	0.836	0.831	0.515	0.546	0.263
SrO	N.A.	N.A.	N.A.	N.A.	N.A.	N.A.	N.A.	N.A.
Y2O3	bdl	bdl	bdl	bdl	bdl	bdl	bdl	bdl
La2O3	15.8	16.8	14.8	14.9	14.9	15.4	15.3	15.2
Ce2O3	33.7	34.5	27.7	27.1	26.7	28.3	27.8	30.6
Pr2O3	3.65	3.47	3.22	2.48	2.61	2.80	3.01	3.34
Nd2O3	12.6	12.5	9.05	9.14	9.21	10.1	10.1	11.4
Sm2O3	0.235	0.264	0.146	0.287	0.282	0.210	0.0780	0.219
Gd2O3	0.388	0.382	0.531	0.504	0.563	0.623	0.638	0.734
Dy2O3	bdl	0.0801	bdl	0.163	bdl	0.312	bdl	0.0401
ThO2	1.01	1.08	9.05	9.58	10.0	6.68	7.27	3.84
Total	96.9	98.1	94.1	94.2	94.0	94.7	93.8	96.0
APFU								
Si	0.0101	0.00649	0.003830086	0.021499799	0.00983	0.0301	0.00455	0.0120
P	0.991	0.987	1.01	1.00	1.01	1.00	1.02	1.02
Ca	0.0116	0.00211	0.0337	0.0370	0.0370	0.0225	0.0242	0.0113
Sr	0	0	0	0	0	0	0	0
Y	0	0	0	0	0	0	0	0
La	0.236	0.250	0.227	0.226	0.228	0.232	0.233	0.224
Ce	0.500	0.509	0.422	0.409	0.407	0.422	0.421	0.447
Pr	0.0539	0.0510	0.0488	0.0373	0.0395	0.0416	0.0454	0.0487
Nd	0.183	0.179	0.134	0.135	0.137	0.147	0.149	0.162
Sm	0.00327	0.00367	0.00210	0.00408	0.00404	0.00295	0.00111	0.00302
Gd	0.00521	0.00510	0.00732	0.00689	0.00776	0.00842	0.00876	0.00973
Dy	0	0.001040458	0	0.00217	0	0.00410	0	0.000516
Th	0.00932	0.00994	0.0856	0.0900	0.0949	0.0620	0.0685	0.0349

Comment	LR25 Mnz 8	LR25 Mnz 9	LR25 Mnz 10	LR25 Mnz 11	LR27 Mnz 3	LR27 Mnz 4	LR27 Mnz 5	LR27 Mnz 6
Mineral	monazite	monazite	monazite	monazite	monazite	monazite	monazite	monazite
deposit	*Windarrie Pool	*Windarrie Pool	*Windarrie Pool	*Windarrie Pool	*Windarrie Pool	*Windarrie Pool	*Windarrie Pool	*Windarrie Pool
Rock type	dol carbonatite	dol carbonatite	dol carbonatite	dol carbonatite	dol carbonatite	dol carbonatite	dol carbonatite	dol carbonatite
SiO2	0.634	0.882	0.324	0.881	0.381	0.178	0.0346	0.174
P2O5	29.0	29.5	30.2	29.3	30.3	30.3	30.7	30.6
CaO	0.338	0.290	0.211	0.624	0.392	0.844	0.225	0.273
SrO	N.A.	N.A.	N.A.	N.A.	N.A.	N.A.	N.A.	N.A.
Y2O3	bdl	bdl	bdl	0.0823	0.0361	0.198	0.309	0.275
La2O3	15.0	15.0	17.3	12.5	16.6	16.6	19.8	20.4
Ce2O3	30.1	29.1	31.3	27.1	31.0	31.6	31.5	30.9
Pr2O3	3.01	3.05	2.96	3.39	3.07	3.03	2.76	2.95
Nd2O3	10.9	10.2	10.5	12.8	11.0	11.6	9.60	9.58
Sm2O3	0.244	0.196	0.273	0.327	0.261	0.274	0.0938	0.102
Gd2O3	0.731	0.818	0.605	1.39	0.862	0.941	0.519	0.630
Dy2O3	0.0372	0.0578	bdl	0.0892	bdl	0.111	0.168	0.127
ThO2	5.92	6.71	3.73	7.09	2.85	2.62	1.53	1.15
Total	95.8	95.8	97.5	95.5	96.7	98.2	97.2	97.1
APFU								
Si	0.0258	0.0355	0.0128	0.0356	0.0151	0.00698	0.00136	0.00684
P	1.00	1.00	1.01	1.00	1.02	1.01	1.02	1.02
Ca	0.0147	0.0125	0.00894	0.0270	0.0166	0.0355	0.0095	0.0115
Sr	0	0	0	0	0	0	0	0
Y	0	0	0	0.00177	0.000761805	0.00414	0.00647	0.00577
La	0.225	0.223	0.253	0.186	0.243	0.240	0.288	0.296
Ce	0.447	0.428	0.454	0.400	0.451	0.454	0.455	0.445
Pr	0.0446	0.0447	0.0427	0.0499	0.0444	0.0434	0.0397	0.0424
Nd	0.158	0.147	0.149	0.185	0.155	0.163	0.135	0.135
Sm	0.00342	0.00272	0.00372	0.00456	0.00357	0.00371	0.00127	0.00138
Gd	0.00985	0.0109	0.00794	0.0186	0.0113	0.0123	0.00678	0.00823
Dy	0.000487	0.000749	0	0.00116	0	0.00140	0.00213	0.00161
Th	0.0548	0.0614	0.0336	0.0652	0.0257	0.0234	0.0137	0.0103

Comment	LR27 Mnz 7	LR27 Mnz 8	LR27 Mnz 9	LR27 Mnz 10	LR27 Mnz 11	LR27 Mnz 12	LR265 Mnz 1	LR265 Mnz 2
Mineral	monazite	monazite	monazite	monazite	monazite	monazite	monazite	monazite
deposit	*Windarrie Pool	*Windarrie Pool	*Windarrie Pool	*Windarrie Pool	*Windarrie Pool	*Windarrie Pool	*Windarrie Pool	*Windarrie Pool
Rock type	dol carbonatite	dol carbonatite	dol carbonatite	dol carbonatite	dol carbonatite	dol carbonatite	ironstone	ironstone
SiO2	0.212	0.0822	0.332	0.359	0.220	0.545	0.429	bdl
P2O5	30.3	30.4	30.1	30.0	30.2	29.6	29.5	29.0
CaO	0.427	0.364	0.640	0.593	0.811	0.302	0.820	1.09
SrO	N.A.	N.A.	N.A.	N.A.	N.A.	N.A.	N.A.	N.A.
Y2O3	0.0370	0.0719	0.115	bdl	0.0530	bdl	0.0612	0.0446
La2O3	16.3	14.7	17.2	16.2	17.5	12.9	5.93	6.39
Ce2O3	29.1	28.8	30.7	27.9	29.5	27.0	18.9	19.5
Pr2O3	2.87	3.30	2.85	2.86	2.71	2.85	4.04	4.18
Nd2O3	10.8	11.9	10.7	11.3	10.5	12.9	22.2	21.7
Sm2O3	0.358	0.335	0.376	0.301	0.398	0.551	1.05	1.05
Gd2O3	1.08	1.18	0.884	0.945	0.975	1.65	2.41	2.33
Dy2O3	0.0389	0.324	0.117	0.0324	bdl	0.183	0.362	0.339
ThO2	4.43	4.77	3.25	6.03	4.47	5.72	7.90	4.85
Total	96.0	96.2	97.2	96.6	97.3	94.1	93.6	90.4
APFU								
Si	0.00847	0.00329	0.0132	0.0143	0.00871	0.0222	0.0176	0
P	1.02	1.03	1.01	1.01	1.01	1.02	1.02	1.04
Ca	0.0183	0.0156	0.0272	0.0254	0.03440	0.0132	0.0361	0.0493
Sr	0	0	0	0	0	0	0	0
Y	0.000787	0.00153	0.00243	0	0.00112	0	0.00134	0.00100
La	0.240	0.217	0.251	0.239	0.255	0.193	0.0897	0.0995
Ce	0.426	0.422	0.445	0.407	0.427	0.403	0.285	0.301
Pr	0.0418	0.0481	0.0411	0.0416	0.0391	0.0423	0.0604	0.0643
Nd	0.155	0.169	0.152	0.161	0.148	0.187	0.325	0.326
Sm	0.00493	0.00461	0.00514	0.00413	0.00543	0.00774	0.0149	0.0153
Gd	0.0143	0.0156	0.0116	0.0125	0.0128	0.0223	0.0328	0.0326
Dy	0.000501	0.00417	0.00150	0.000417	0	0.00241	0.00479	0.00461
Th	0.0403	0.0434	0.0293	0.0548	0.0403	0.0530	0.0738	0.0466

Comment	LR265 Mnz 3	LR265 Mnz 4	LR265 Mnz 5	LR265 Mnz 6	LR265 Mnz 7	yn49-61a_mnz_dk_zn	yn49-61a_mnz_dkzn_2
Mineral	monazite	monazite	monazite	monazite	monazite	monazite	monazite
deposit	*Windarrie Pool	*Windarrie Pool	*Windarrie Pool	*Windarrie Pool	*Windarrie Pool	Yangibana North	Yangibana North
Rock type	ironstone	ironstone	ironstone	ironstone	ironstone	ank-sid carbonatite	ank-sid carbonatite
SiO2	0.918	0.478	bdl	bdl	0.472	0.127	0.0847
P2O5	28.7	29.3	29.6	29.5	29.6	30.5	30.3
CaO	0.479	0.462	0.949	0.891	0.485	0.0481	0.0735
SrO	N.A.	N.A.	N.A.	N.A.	N.A.	bdl	0.218
Y2O3	0.173	0.106	bdl	0.102	0.0865	bdl	0.130
La2O3	6.32	6.15	7.47	7.94	6.05	14.3	15.9
Ce2O3	19.9	19.9	23.3	22.9	20.1	33.4	32.4
Pr2O3	4.36	4.07	4.52	4.33	4.22	4.24	4.06
Nd2O3	22.1	22.3	22.4	23.0	22.6	13.1	12.5
Sm2O3	0.957	0.939	0.712	0.719	0.760	0.888	1.17
Gd2O3	2.47	2.65	1.42	1.54	2.59	N.A.	N.A.
Dy2O3	0.466	0.277	0.112	0.471	0.530	N.A.	N.A.
ThO2	7.36	6.71	3.30	2.80	6.68	0.478	0.578
Total	94.2	93.2	93.7	94.1	94.1	97.1	97.2
APFU							
Si	0.0378	0.0197	0	0	0.01930	0.00501	0.00336
P	1.00	1.02	1.03	1.02	1.02	1.02	1.02
Ca	0.0211	0.0204	0.0417	0.0391	0.0212	0.00204	0.00313
Sr	0	0	0	0	0	0	0
Y	0.00379	0.00233	0	0.00221	0.00188	0	0.00274
La	0.0959	0.0936	0.113	0.120	0.0912	0.208	0.233
Ce	0.300	0.300	0.349	0.343	0.301	0.484	0.471
Pr	0.0654	0.0612	0.0675	0.0646	0.0628	0.0611	0.0587
Nd	0.324	0.328	0.328	0.336	0.329	0.185	0.177
Sm	0.0136	0.0133	0.0100	0.0102	0.0107	0.0121	0.0160
Gd	0.0337	0.0362	0.0193	0.0209	0.0351	0	0
Dy	0.00618	0.00368	0.001479864	0.00621	0.00697	0	0
Th	0.0689	0.0630	0.0308	0.0261	0.0621	0.00430	0.00522

Comment	yn49-61a_mnz_dkzn_3	yn49-61a_mnz_dkzn_4	yn49-61a_mnz_dkzn_5	yn49-61a_mnz_lt_zn_6	yn49-61a_mnz_lt_zn_7	yn49-61a_mnz_lt_zn_8
Mineral	monazite	monazite	monazite	monazite	monazite	monazite
deposit	Yangibana North	Yangibana North	Yangibana North	Yangibana North	Yangibana North	Yangibana North
Rock type	ank-sid carbonatite	ank-sid carbonatite	ank-sid carbonatite	ank-sid carbonatite	ank-sid carbonatite	ank-sid carbonatite
SiO2	0.0204	0.0144	0.0257	0.103	0.297	0.227
P2O5	30.6	30.7	30.7	30.6	30.0	30.2
CaO	0.0197	bdl	0.0210	0.0768	0.125	0.0575
SrO	bdl	0.0821	0.154	0.144	0.301	0.0266
Y2O3	0.0765	0.0725	bdl	0.134	0.0614	0.0458
La2O3	16.3	16.2	17.4	15.0	13.2	14.8
Ce2O3	33.3	33.0	33.3	31.5	31.3	32.7
Pr2O3	3.74	3.79	3.73	3.87	3.94	3.83
Nd2O3	12.3	12.4	11.6	12.7	14.1	13.1
Sm2O3	0.952	1.08	1.00	1.34	1.67	1.15
Gd2O3	N.A.	N.A.	N.A.	N.A.	N.A.	N.A.
Dy2O3	N.A.	N.A.	N.A.	N.A.	N.A.	N.A.
ThO2	0.427	0.413	0.284	1.03	1.56	1.45
Total	97.7	97.7	97.9	96.2	96.3	97.6
APFU						
Si	0.000804	0.000567	0.00101	0.00407	0.0119	0.00899
P	1.02	1.02	1.02	1.03	1.02	1.01
Ca	0.00083	0	0.000885	0.00327	0.00533	0.00244
Sr	0	0	0.00501	0	0.001873404	0.003513223
Y	0.00160	0.00152	0	0.00283	0.00131	0.000964848
La	0.236	0.236	0.252	0.219	0.195	0.216
Ce	0.480	0.476	0.479	0.457	0.459	0.474
Pr	0.0537	0.0544	0.0534	0.0560	0.0574	0.0552
Nd	0.173	0.174	0.162	0.180	0.201	0.185
Sm	0.0129	0.0147	0.0136	0.0183	0.0230	0.0156
Gd	0	0	0	0	0	0
Dy	0	0	0	0	0	0
Th	0.00383	0.00370	0.00254	0.00927	0.0142	0.0131

Comment	yn49-61a_mnz_lt_zn_9	yn49-61a_mnz_lt_zn_10	leq130_mnz_ltzn_1	leq130_mnz_ltzn_2	leq130_mnz_ltzn_3	leq130_mnz_ltzn_4	leq130_mnz_ltzn_5
Mineral	monazite	monazite	monazite	monazite	monazite	monazite	monazite
deposit	Yangibana North	Yangibana North	Leceq	Leceq	Leceq	Leceq	Leceq
Rock type	ank-sid carbonatite	ank-sid carbonatite	mag-bio dyke	mag-bio dyke	mag-bio dyke	mag-bio dyke	mag-bio dyke
SiO2	0.303	0.327	0.397	0.480	0.125	0.185	0.481
P2O5	30.3	29.7	29.9	29.9	30.3	30.5	29.9
CaO	0.0642	bdl	0.0747	0.0561	0.0179	0.0224	0.0381
SrO	0.0156	0.0305	0.371	0.178	0.0477	0.0637	0.126
Y2O3	bdl	0.000200	0.204	0.0730	0.160	0.300	0.144
La2O3	14.2	14.3	17.0	16.3	17.1	17.1	16.1
Ce2O3	33.4	33.6	33.0	33.8	34.4	33.5	33.4
Pr2O3	4.04	4.08	3.43	3.70	3.75	3.56	3.77
Nd2O3	13.7	13.2	11.4	11.7	12.0	12.6	12.2
Sm2O3	1.38	0.975	0.819	0.859	0.818	0.945	0.980
Gd2O3	N.A.	N.A.	N.A.	N.A.	N.A.	N.A.	N.A.
Dy2O3	N.A.	N.A.	N.A.	N.A.	N.A.	N.A.	N.A.
ThO2	1.17	1.5	2.08	2.49	0.582	0.930	2.32
Total	98.6	97.7	98.3	99.4	99.3	99.6	99.4
APFU							
Si	0.0119	0.0130	0.0157	0.0189	0.0049	0.0071965	0.0189
P	1.01	1.00	1.00	0.994	1.01	1.01	0.995
Ca	0.00270	0	0.00316	0.00236	0.000751	0.000935	0.00160
Sr	0.003319501	0.006955116	0.000611	0.000355	0.000705	0.00847	0.00406
Y	0	0	0.00428	0.00153	0.00333	0.00622	0.00301
La	0.206	0.210	0.248	0.236	0.247	0.245	0.234
Ce	0.480	0.490	0.478	0.486	0.494	0.478	0.480
Pr	0.0578	0.0592	0.0494	0.0529	0.0535	0.0505	0.0539
Nd	0.192	0.187	0.161	0.165	0.168	0.175	0.171
Sm	0.0187	0.0134	0.0112	0.0116	0.0110	0.0127	0.0133
Gd	0	0	0	0	0	0	0
Dy	0	0	0	0	0	0	0
Th	0.0105	0.0136	0.0187	0.0223	0.0052	0.00824	0.0207

Comment	leq130_mnz_dkzn_6	leq130_mnz_dkzn_7	leq130_mnz_dkzn_8	leq130_mnz_dkzn_9	yg4_mnz_dk_zn_1	yg4_mnz_dk_zn_2	yg4_mnz_dk_zn_3	yg4_mnz_dk_zn_4
Mineral	monazite	monazite	monazite	monazite	monazite	monazite	monazite	monazite
deposit	Leceq	Leceq	Leceq	Leceq	Fraser's	Fraser's	Fraser's	Fraser's
Rock type	mag-bio dyke	mag-bio dyke	mag-bio dyke	mag-bio dyke	mag-bio dyke	mag-bio dyke	mag-bio dyke	mag-bio dyke
SiO2	0.0873	0.150	0.101	0.0903	0.0114	bdl	0.0113	0.0421
P2O5	30.4	30.7	30.6	30.5	30.5	30.9	30.6	30.6
CaO	0.0256	0.0565	0.0105	0.0291	0.174	0.200	0.126	0.206
SrO	0.117	0.227	0.0188	0.0250	0.255	0.351	0.304	0.317
Y2O3	0.179	0.185	0.138	0.308	bdl	bdl	bdl	bdl
La2O3	19.8	18.3	17.8	17.9	11.7	12.3	13.7	11.5
Ce2O3	34.1	33.9	33.8	33.8	38.8	37.5	38.2	37.9
Pr2O3	3.34	3.50	3.72	3.86	4.41	4.42	4.17	4.44
Nd2O3	10.9	11.6	11.9	12.1	14.0	13.4	12.1	13.6
Sm2O3	0.635	0.618	0.673	0.766	0.566	0.796	0.569	0.743
Gd2O3	N.A.	N.A.	N.A.	N.A.	N.A.	N.A.	N.A.	N.A.
Dy2O3	N.A.	N.A.	N.A.	N.A.	N.A.	N.A.	N.A.	N.A.
ThO2	0.133	0.404	0.228	0.243	0.847	0.925	0.653	0.802
Total	99.6	99.4	98.9	99.5	101	100	100	99.7
APFU								
Si	0.00341	0.00582	0.00397	0.00352	0.000442	0	0.000440	0.001642004
P	1.00	1.01	1.01	1.01	1.00	1.01	1.01	1.01
Ca	0.00107	0.00236	0.000440	0.00122	0.00722	0.00831	0.005270275	0.00860
Sr	0.00108	0.00144	0.00286	0.00265	0.00512	0.000426	0.000566	0.00572
Y	0.00371	0.003840037	0.00286	0.00640	0	0	0	0
La	0.285	0.262	0.257	0.257	0.167	0.175	0.196	0.165
Ce	0.488	0.483	0.483	0.482	0.551	0.531	0.544	0.541
Pr	0.0476	0.0496	0.0530	0.0549	0.0624	0.0623	0.0591	0.0631
Nd	0.152	0.161	0.166	0.168	0.194	0.186	0.169	0.189
Sm	0.00856	0.00829	0.00907	0.0103	0.00756	0.0106	0.00763	0.00999
Gd	0	0	0	0	0	0	0	0
Dy	0	0	0	0	0	0	0	0
Th	0.0012	0.0036	0.00203	0.00216	0.00748	0.00815	0.00578	0.00712

Comment	yg4_mnz_dk_zn_5	yg4_mnz_lt_zn_6	yg4_mnz_lt_zn_7	yg4_mnz_lt_zn_8	yg4_mnz_lt_zn_9	yg4_mnz_lt_zn_10	dmcy139_mnz_dk_zn_1	dmcy139_mnz_dk_zn_2
Mineral	monazite	monazite	monazite	monazite	monazite	monazite	monazite	monazite
deposit	Fraser's	Fraser's	Fraser's	Fraser's	Fraser's	Fraser's	Demarcay	Demarcay
Rock type	mag-bio dyke	mag-bio dyke	mag-bio dyke	mag-bio dyke	mag-bio dyke	mag-bio dyke	mag-bio dyke	mag-bio dyke
SiO2	0.0128	0.0022	0.0311	0.0157	0.0445	0.0292	0.0712	0.0535
P2O5	30.6	30.9	30.8	30.6	30.5	30.6	30.3	30.4
CaO	0.128	0.0869	0.114	0.0613	0.112	0.0856	0.217	0.0796
SrO	0.290	0.207	0.360	0.187	0.248	0.250	0.868	0.716
Y2O3	bdl	bdl	bdl	bdl	bdl	bdl	bdl	bdl
La2O3	11.3	11.1	10.7	11.3	11.0	11.7	6.56	7.22
Ce2O3	37.3	37.5	38.2	37.9	37.1	37.8	32.6	33.6
Pr2O3	4.32	4.58	4.44	4.45	4.86	4.64	5.86	5.96
Nd2O3	14.4	13.5	13.9	13.9	13.9	14.0	19.8	19.7
Sm2O3	0.792	0.832	0.934	0.659	0.621	0.450	0.461	0.670
Gd2O3	N.A.	N.A.	N.A.	N.A.	N.A.	N.A.	N.A.	N.A.
Dy2O3	N.A.	N.A.	N.A.	N.A.	N.A.	N.A.	N.A.	N.A.
ThO2	0.943	1.44	1.63	1.15	1.39	1.08	3.09	2.42
Total	99.7	99.9	101	100	99.5	100	98.9	100
APFU								
Si	0.000500	0	0.00120	0.000612	0.00174	0.00113	0.00281	0.00209
P	1.01	1.02	1.01	1.01	1.01	1.01	1.01	1.01
Ca	0.00536	0.00362	0.00471	0.00256	0.00468	0.00356	0.00918	0.00334
Sr	0.00786	0.00685	0.00716	0.00655	0.00467	0.00805	0.00421	0.00562
Y	0	0	0	0	0	0	0	0
La	0.162	0.159	0.153	0.162	0.159	0.167	0.095	0.104
Ce	0.533	0.533	0.541	0.541	0.531	0.538	0.471	0.482
Pr	0.0614	0.0648	0.0626	0.0632	0.0693	0.0657	0.0842	0.0850
Nd	0.200	0.187	0.193	0.193	0.194	0.194	0.279	0.275
Sm	0.0107	0.0111	0.0124	0.00885	0.00837	0.00602	0.00627	0.00903
Gd	0	0	0	0	0	0	0	0
Dy	0	0	0	0	0	0	0	0
Th	0.00837	0.0127	0.0143	0.0102	0.0124	0.00955	0.0277	0.0215

Comment	dmcy139_mnz_dk_zn_3	dmcy139_mnz_dk_zn_4	dmcy139_mnz_dk_zn_5	dmcy139_mnz_lt_zn_6	dmcy139_mnz_lt_zn_7	dmcy139_mnz_lt_zn_8	dmcy139_mnz_lt_zn_9
Mineral	monazite	monazite	monazite	monazite	monazite	monazite	monazite
deposit	Demarcay	Demarcay	Demarcay	Demarcay	Demarcay	Demarcay	Demarcay
Rock type	mag-bio dyke	mag-bio dyke	mag-bio dyke	mag-bio dyke	mag-bio dyke	mag-bio dyke	mag-bio dyke
SiO2	0.163	0.0938	0.0509	0.735	0.700	0.631	0.609
P2O5	30.1	30.2	30.0	29.4	29.4	29.4	29.4
CaO	0.117	0.0984	0.0984	0.158	0.147	0.183	0.145
SrO	0.689	0.646	0.606	0.530	0.730	0.769	0.438
Y2O3	bdl	bdl	bdl	bdl	0.000200	bdl	bdl
La2O3	6.24	6.75	6.62	5.08	5.85	5.94	5.41
Ce2O3	32.5	34.5	33.7	30.5	30.1	30.2	29.7
Pr2O3	5.96	5.69	5.90	5.97	5.60	5.99	5.90
Nd2O3	20.9	20.3	20.9	22.9	22.0	22.5	23.0
Sm2O3	0.772	0.575	0.518	1.02	1.03	0.887	1.16
Gd2O3	N.A.	N.A.	N.A.	N.A.	N.A.	N.A.	N.A.
Dy2O3	N.A.	N.A.	N.A.	N.A.	N.A.	N.A.	N.A.
ThO2	2.76	2.17	2.18	4.24	4.53	4.34	3.48
Total	99.5	100	100	100	99.3	100	98.8
APFU							
Si	0.00640	0.00368	0.00200	0.0290	0.0278	0.0249	0.0242
P	1.00	1.00	1.00	0.982	0.986	0.983	0.989
Ca	0.00494	0.00413	0.004149746	0.00666	0.00626	0.00775	0.00617
Sr	0.00562	0.0198	0.0162	0.0157	0.0146	0.0138	0.0121
Y	0	0	0	0	0	0	0
La	0.0906	0.0975	0.0961	0.0739	0.0855	0.0865	0.0793
Ce	0.468	0.495	0.486	0.441	0.436	0.437	0.432
Pr	0.0855	0.0812	0.0846	0.0858	0.0809	0.0862	0.0854
Nd	0.294	0.284	0.294	0.322	0.312	0.317	0.327
Sm	0.0105	0.00777	0.00703	0.0139	0.0140	0.0121	0.0159
Gd	0	0	0	0	0	0	0
Dy	0	0	0	0	0	0	0
Th	0.0247	0.0193	0.0195	0.0380	0.0409	0.0390	0.0315

Comment	dmcy139_mnz_lt_zn_10	bh224-63b_mnz_lt_zn_2	bh224-63b_mnz_lt_zn_3	bh224-63b_mnz_lt_zn_4	bh224-63b_mnz_lt_zn_5	bh224-63b_mnz_dk_zn_1
Mineral	monazite	monazite	monazite	monazite	monazite	monazite
deposit	Demarcay	Bald Hill	Bald Hill	Bald Hill	Bald Hill	Bald Hill
Rock type	mag-bio dyke	mag-bio dyke	mag-bio dyke	mag-bio dyke	mag-bio dyke	mag-bio dyke
SiO2	0.689	0.402	0.424	0.327	0.587	0.490
P2O5	29.5	30.0	30.0	30.2	29.8	29.8
CaO	0.146	0.152	0.289	0.178	0.062	0.145
SrO	0.482	0.0264	bdl	0.0280	0.0576	bdl
Y2O3	bdl	0.414	0.470	0.300	bdl	0.538
La2O3	5.43	9.00	8.01	8.86	8.88	8.56
Ce2O3	30.2	28.0	25.0	27.3	31.7	27.5
Pr2O3	5.89	4.84	4.70	4.76	5.20	4.82
Nd2O3	23.4	21.9	23.1	22.9	20.4	22.5
Sm2O3	0.952	2.54	3.23	2.39	1.22	2.39
Gd2O3	N.A.	N.A.	N.A.	N.A.	N.A.	N.A.
Dy2O3	N.A.	N.A.	N.A.	N.A.	N.A.	N.A.
ThO2	3.84	1.98	2.50	1.88	2.37	2.45
Total	100	99.2	97.7	99.1	100	99.2
APFU						
Si	0.0271	0.0158	0.0168	0.0128	0.0230	0.0193
P	0.985	1.00	1.01	1.00	0.989	0.994
Ca	0.00616	0.00642	0.01226	0.00747	0.00260	0.00611
Sr	0.0167	0.0175	0.0101	0.0110	0.000602	0
Y	0	0.00867	0.00991	0.00627	0	0.0113
La	0.0789	0.131	0.117	0.128	0.128	0.124
Ce	0.435	0.403	0.363	0.393	0.454	0.396
Pr	0.0845	0.0694	0.0679	0.0681	0.0743	0.0692
Nd	0.328	0.307	0.327	0.320	0.285	0.317
Sm	0.0129	0.0344	0.0441	0.0323	0.0165	0.0324
Gd	0	0	0	0	0	0
Dy	0	0	0	0	0	0
Th	0.0344	0.0177	0.0226	0.0168	0.0211	0.0220

Comment	bh224-63b_mnz_dk_zn_2	bh224-63b_mnz_dk_zn_3	bh224-63b_mnz_dk_zn_4	lrs150_mnz_1	lrs150_mnz_2	lrs150_mnz_3	lrs150_mnz_4
Mineral	monazite	monazite	monazite	monazite	monazite	monazite	monazite
deposit	Bald Hill	Bald Hill	Bald Hill	*Windarrie Pool	*Windarrie Pool	*Windarrie Pool	*Windarrie Pool
Rock type	mag-bio dyke	mag-bio dyke	mag-bio dyke	Amph-dol vnlt	Amph-dol vnlt	Amph-dol vnlt	Amph-dol vnlt
SiO2	0.466	0.414	0.494	0.349	0.364	0.0443	0.116
P2O5	29.9	30.0	29.8	29.4	29.6	30.2	30.0
CaO	0.210	0.192	0.324	0.649	0.909	0.275	0.247
SrO	0.0444	bdl	0.0537	1.95	2.26	2.36	2.58
Y2O3	0.486	0.413	0.443	bdl	bdl	bdl	bdl
La2O3	9.79	7.88	8.27	19.7	20.9	17.0	15.3
Ce2O3	28.7	26.9	26.1	29.0	27.7	29.6	29.5
Pr2O3	4.59	4.92	4.67	2.13	2.28	2.80	2.88
Nd2O3	21.3	21.8	22.8	6.44	5.48	10.3	10.5
Sm2O3	2.46	2.39	3.08	0.283	0.305	0.987	1.07
Gd2O3	N.A.	N.A.	N.A.	N.A.	N.A.	N.A.	N.A.
Dy2O3	N.A.	N.A.	N.A.	N.A.	N.A.	N.A.	N.A.
ThO2	2.30	1.92	3.10	8.01	9.35	7.09	6.93
Total	100	96.9	99.0	96.0	96.8	98.2	96.5
APFU							
Si	0.0182	0.0165	0.0195	0.0141	0.0146	0.00176	0.00465
P	0.990	1.01	0.995	1.01	1.01	1.02	1.02
Ca	0.00881	0.00818	0.0137	0.0281	0.0391	0.011699503	0.0106
Sr	0.000638	0.00131	0	0.00101	0	0.00123	0.0452
Y	0.0101	0.00875	0.00930	0	0	0	0
La	0.141	0.116	0.120	0.294	0.309	0.248	0.227
Ce	0.411	0.393	0.377	0.429	0.406	0.429	0.434
Pr	0.0654	0.0714	0.0672	0.0314	0.0333	0.0405	0.0422
Nd	0.298	0.310	0.321	0.0930	0.0785	0.146	0.150
Sm	0.0331	0.0328	0.0419	0.0039	0.0042	0.0135	0.0149
Gd	0	0	0	0	0	0	0
Dy	0	0	0	0	0	0	0
Th	0.0205	0.0174	0.0278	0.0737	0.0854	0.0640	0.0634

Comment	lrs150_mnz_5	lrs150_mnz_dk_zn_6	lrs150_mnz_dk_zn_7	lrs150_mnz_dk_zn_8	lrs150_mnz_dk_zn_9	lrs150_mnz_in_rt	lrs150_mnz_in_rt_2
Mineral	monazite	monazite	monazite	monazite	monazite	monazite	monazite
deposit	*Windarrie Pool	*Windarrie Pool	*Windarrie Pool	*Windarrie Pool	*Windarrie Pool	*Windarrie Pool	*Windarrie Pool
Rock type	Amph-dol vnlt	Amph-dol vnlt	Amph-dol vnlt	Amph-dol vnlt	Amph-dol vnlt	Amph-dol vnlt	Amph-dol vnlt
SiO2	0.255	0.375	0.0831	0.121	0.0807	0.834	0.872
P2O5	29.8	29.8	30.1	30.2	30.3	29.5	29.5
CaO	0.433	0.348	0.356	0.338	0.489	0.485	0.526
SrO	2.65	0.578	2.71	2.55	3.12	1.26	1.97
Y2O3	bdl	bdl	bdl	bdl	bdl	bdl	bdl
La2O3	16.0	17.0	15.2	14.3	15.4	21.1	19.6
Ce2O3	29.5	32.4	28.4	29.3	28.3	30.2	29.4
Pr2O3	2.86	2.77	2.89	3.01	2.81	2.25	2.29
Nd2O3	9.99	10.8	10.5	10.7	9.51	7.55	7.09
Sm2O3	1.00	1.21	1.17	1.27	0.897	0.667	0.675
Gd2O3	N.A.	N.A.	N.A.	N.A.	N.A.	N.A.	N.A.
Dy2O3	N.A.	N.A.	N.A.	N.A.	N.A.	N.A.	N.A.
ThO2	8.32	4.08	8.15	7.83	9.20	6.96	7.92
Total	98.1	98.7	96.8	97.0	96.9	99.5	97.9
APFU							
Si	0.0102	0.0148	0.00333	0.00485	0.00323	0.0328	0.0346
P	1.01	1.00	1.02	1.02	1.02	0.982	0.992
Ca	0.0185	0.0147	0.0153	0.0145	0.0209	0.0205	0.0223
Sr	0.0519	0.0536	0.0593	0.0604	0.0132	0.0620	0.0583
Y	0	0	0	0	0	0	0
La	0.236	0.248	0.225	0.211	0.227	0.306	0.287
Ce	0.431	0.469	0.417	0.428	0.414	0.436	0.427
Pr	0.0416	0.0400	0.0422	0.0439	0.0409	0.0323	0.0331
Nd	0.142	0.152	0.151	0.153	0.136	0.106	0.100
Sm	0.0138	0.0165	0.0162	0.0175	0.0123	0.00905	0.00923
Gd	0	0	0	0	0	0	0
Dy	0	0	0	0	0	0	0
Th	0.0756	0.0368	0.0744	0.0713	0.0837	0.0624	0.0715

Comment	lrs150_mnz_in_rt_3	fr9-104-mnz1	fr9-104-mnz2	fr9-104-mnz3	fr9-104-mnz4	fr9-104-mnz5	fr9-104-mnz6	fr9-104-mnz7
Mineral	monazite	monazite	monazite	monazite	monazite	monazite	monazite	monazite
deposit	*Windarrie Pool	Fraser's	Fraser's	Fraser's	Fraser's	Fraser's	Fraser's	Fraser's
Rock type	Amph-dol vnlt	ironstone	ironstone	ironstone	ironstone	ironstone	ironstone	ironstone
SiO2	0.529	0.122	0.128	0.0931	0.0503	0.142	0.135	0.121
P2O5	29.5	29.6	29.7	29.7	29.5	29.5	29.6	29.8
CaO	0.802	0.165	0.117	0.209	0.190	0.0978	0.147	0.135
SrO	1.48	0.291	0.316	0.330	0.284	0.222	0.397	0.391
Y2O3	bdl	0.304	0.457	0.236	0.456	0.285	0.250	0.231
La2O3	21.8	6.68	6.13	6.61	5.59	6.21	6.30	5.91
Ce2O3	28.5	30.3	29.7	31.4	29.6	30.9	30.0	29.8
Pr2O3	2.24	5.55	5.41	5.58	5.76	5.47	5.70	5.48
Nd2O3	5.84	21.6	21.3	21.0	22.1	21.4	22.2	22.4
Sm2O3	0.270	1.46	1.81	1.44	2.09	1.61	1.75	2.00
Gd2O3	N.A.	N.A.	N.A.	N.A.	N.A.	N.A.	N.A.	N.A.
Dy2O3	N.A.	N.A.	N.A.	N.A.	N.A.	N.A.	N.A.	N.A.
ThO2	6.37	0.694	1.28	0.525	0.687	0.720	0.880	0.980
Total	95.8	96.5	96.0	96.8	96.0	96.3	96.9	96.8
APFU								
Si	0.0213	0.00492	0.005170293	0.00373	0.00203	0.00571	0.00541	0.004829882
P	1.00	1.01	1.01	1.01	1.01	1.01	1.00	1.01
Ca	0.0346	0.00712	0.00505	0.00897	0.00821	0.00423	0.00632	0.00577
Sr	0.0710	0.0286	0.0448	0.0342	0.00666	0.00520	0.009233774	0.009079752
Y	0	0.00649	0.00980	0.00502	0.00980	0.00612	0.00535	0.00491
La	0.324	0.0990	0.0910	0.0976	0.0833	0.0924	0.0932	0.0873
Ce	0.420	0.446	0.438	0.460	0.438	0.456	0.440	0.437
Pr	0.0328	0.0813	0.0794	0.0814	0.0848	0.0804	0.0833	0.0800
Nd	0.0839	0.310	0.306	0.300	0.319	0.308	0.318	0.320
Sm	0.00375	0.0202	0.0251	0.0199	0.0291	0.0224	0.0242	0.0276
Gd	0	0	0	0	0	0	0	0
Dy	0	0	0	0	0	0	0	0
Th	0.0583	0.00635	0.0117	0.00479	0.00632	0.00660	0.00804	0.00893

Comment	fr9-104-mnz8	fr9-104-mnz9	fr9-104-lt-mnz16	fr9-104-lt-mnz17	fr9-104-dk-mnz18	fr63_15-2_mnz1	fr63_15-2_mnz2	fr63_15-2_mnz3
Mineral	monazite	monazite	monazite	monazite	monazite	monazite	monazite	monazite
deposit	Fraser's	Fraser's	Fraser's	Fraser's	Fraser's	Fraser's	Fraser's	Fraser's
Rock type	ironstone	ironstone	ironstone	ironstone	ironstone	ironstone	ironstone	ironstone
SiO2	0.143	0.188	0.440	0.543	0.116	0.464	0.444	0.515
P2O5	30.0	29.7	29.3	29.4	29.9	29.5	29.6	29.8
CaO	0.166	0.182	0.242	0.141	0.161	0.0227	0.0319	0.0538
SrO	0.338	0.380	0.514	0.381	bdl	0	0.0202	bdl
Y2O3	0.297	0.264	0.170	0.508	0.534	0.0754	0.106	bdl
La2O3	6.14	5.92	5.21	5.09	5.70	6.46	7.29	7.90
Ce2O3	30.1	28.5	27.9	27.1	29.4	31.0	31.3	32.5
Pr2O3	5.54	5.39	5.38	5.36	5.42	5.82	5.86	5.69
Nd2O3	22.0	22.4	22.4	22.1	22.4	22.7	22.8	21.0
Sm2O3	1.81	1.88	2.37	2.29	2.23	1.09	0.905	0.655
Gd2O3	N.A.	N.A.	N.A.	N.A.	N.A.	N.A.	N.A.	N.A.
Dy2O3	N.A.	N.A.	N.A.	N.A.	N.A.	N.A.	N.A.	N.A.
ThO2	1.30	1.71	3.21	2.92	0.560	1.40	1.15	1.18
Total	97.5	96.2	96.6	95.4	96.4	98.6	99.5	99.2
APFU								
Si	0.00568	0.00756	0.0177	0.0219	0.00463	0.0184	0.0176	0.0203
P	1.01	1.01	1.00	1.00	1.01	0.993	0.989	0.993
Ca	0.00707	0.00782	0.0104	0.00608	0.00689	0.00096677	0.001350165	0.00227
Sr	0.00780	0.00886	0.0120	0.00893	0.00606	0	0.000463	0
Y	0.00628	0.00564	0.00364	0.0109	0.0114	0.00159	0.002219833	0
La	0.0901	0.0877	0.0773	0.0759	0.0842	0.0947	0.106	0.115
Ce	0.438	0.419	0.410	0.401	0.431	0.451	0.453	0.468
Pr	0.0803	0.0789	0.0788	0.0789	0.0791	0.0843	0.0843	0.0817
Nd	0.313	0.322	0.322	0.319	0.320	0.322	0.322	0.295
Sm	0.0248	0.0260	0.0328	0.0319	0.0308	0.0149	0.0123	0.00890
Gd	0	0	0	0	0	0	0	0
Dy	0	0	0	0	0	0	0	0
Th	0.0118	0.0156	0.0294	0.0269	0.00510	0.0127	0.0103	0.0106

Comment	fr63_15-2_mnz4	hk4-14_mnz_1	hk4-14_mnz_2	hk4-14_mnz_3	hk4-14_mnz_4	hk4-14_mnz_dk_5	hk4-14_mnz_dk_6	hk4-14_mnz_dk_8
Mineral	monazite	monazite	monazite	monazite	monazite	monazite	monazite	monazite
deposit	Fraser's	Hook	Hook	Hook	Hook	Hook	Hook	Hook
Rock type	ironstone	ironstone	ironstone	ironstone	ironstone	ironstone	ironstone	ironstone
SiO2	0.595	0.189	0.0904	0.144	0.252	0.119	0.123	0.133
P2O5	29.2	29.9	30.4	30.1	29.8	30.1	30.2	29.8
CaO	0.0408	0.149	0.0647	0.0726	0.0633	0.0705	0.0793	0.0582
SrO	0.0431	0.356	0.0666	0.0779	0.0958	0.207	0.158	0.0299
Y2O3	bdl	0.202	0.0942	0.0697	0.00450	0.0983	0.0381	0.0506
La2O3	6.22	9.73	11.7	10.0	10.2	9.33	10.4	9.96
Ce2O3	30.6	32.4	36.9	34.1	34.6	34.7	34.8	34.5
Pr2O3	5.56	4.65	4.54	5.06	4.80	4.98	4.80	4.99
Nd2O3	23.3	17.1	14.8	16.7	16.3	16.7	16.5	17.2
Sm2O3	0.898	1.61	1.03	1.45	1.35	1.51	1.24	1.10
Gd2O3	N.A.	N.A.	N.A.	N.A.	N.A.	N.A.	N.A.	N.A.
Dy2O3	N.A.	N.A.	N.A.	N.A.	N.A.	N.A.	N.A.	N.A.
ThO2	2.04	1.63	0.647	0.652	1.29	0.908	0.995	0.730
Total	98.5	97.6	100.2	98.4	98.7	98.5	99.1	98.6
APFU								
Si	0.0238	0.00751	0.00353	0.00570	0.00998	0.00471	0.00481	0.00527
P	0.986	1.01	1.00	1.01	1.00	1.01	1.01	1.00
Ca	0.00175	0.00633	0.00270	0.00307	0.00269	0.00299	0.00334	0.00247
Sr	0.00100	0.00820	0.00151	0.00178	0.00220	0.00475	0.00360	0.000688
Y	0	0.004269751	0.00195	0.00147	0	0.00207	0.000797	0.00107
La	0.0916	0.143	0.168	0.146	0.149	0.136	0.150	0.146
Ce	0.448	0.471	0.526	0.493	0.503	0.502	0.500	0.501
Pr	0.0809	0.0673	0.0645	0.0728	0.0693	0.0717	0.0687	0.0721
Nd	0.333	0.242	0.207	0.236	0.231	0.235	0.232	0.244
Sm	0.0124	0.0220	0.0139	0.0197	0.0184	0.0206	0.0168	0.0151
Gd	0	0	0	0	0	0	0	0
Dy	0	0	0	0	0	0	0	0
Th	0.0185	0.0147	0.00574	0.0059	0.0116	0.00817	0.00890	0.00659

Comment	hk4-14_mnz_dk_9	hk4-14_mnz_dk_10	hk4-14_mnz_lt_12	hk4-14_mnz_lt_13	hk4-14_mnz_lt_14	hk4-14_mnz_lt_15	hk4-14_mnz_lt_16
Mineral	monazite	monazite	monazite	monazite	monazite	monazite	monazite
deposit	Hook	Hook	Hook	Hook	Hook	Hook	Hook
Rock type	ironstone	ironstone	ironstone	ironstone	ironstone	ironstone	ironstone
SiO2	0.0846	0.118	0.420	0.524	0.422	0.301	0.282
P2O5	30.0	30.3	29.6	29.8	29.7	29.8	29.9
CaO	0.0793	0.129	0.0604	0.0647	0.0497	0.0643	0.0475
SrO	0.135	0.186	0.165	0.151	0.126	0.0656	0.0922
Y2O3	0.0379	0.185	0.0832	0.00430	0.0575	0.0325	0.171
La2O3	9.65	10.4	9.34	9.96	9.95	10.1	9.57
Ce2O3	34.6	34.5	33.8	33.8	33.5	34.0	34.7
Pr2O3	4.77	4.56	4.70	5.00	4.57	4.53	4.74
Nd2O3	17.2	16.4	17.2	16.7	16.9	16.7	16.9
Sm2O3	1.38	1.40	1.30	1.26	1.45	1.10	1.32
Gd2O3	N.A.	N.A.	N.A.	N.A.	N.A.	N.A.	N.A.
Dy2O3	N.A.	N.A.	N.A.	N.A.	N.A.	N.A.	N.A.
ThO2	0.732	0.942	1.87	1.88	1.65	1.56	1.22
Total	98.5	98.9	98.3	98.9	98.3	98.1	98.8
APFU							
Si	0.00335	0.00465	0.0167	0.0207	0.0167	0.0120	0.0112
P	1.01	1.01	0.995	0.994	1.00	1.00	1.00
Ca	0.00336	0.00541	0.00257	0.00273	0.00211	0.00274	0.00201
Sr	0.00311	0.00425	0.00380	0.00345	0.00290	0.00151	0.00211
Y	0.000798	0.00387	0.00176	0	0.00121	0.000687	0.00360
La	0.141	0.151	0.137	0.145	0.146	0.149	0.139
Ce	0.501	0.497	0.492	0.488	0.486	0.494	0.502
Pr	0.0688	0.0653	0.0680	0.0718	0.0660	0.0656	0.0682
Nd	0.243	0.230	0.243	0.234	0.240	0.236	0.239
Sm	0.0188	0.0190	0.0178	0.0171	0.0198	0.0150	0.0180
Gd	0	0	0	0	0	0	0
Dy	0	0	0	0	0	0	0
Th	0.00659	0.00842	0.0169	0.0169	0.0149	0.0141	0.0110

Comment	hk4-14_mnz_lt_17	hk4-14_mnz_inmag_lt_18	hk4-14_mnz_inmag_lt_19	hk4-14_mnz_inmag_lt_20	hk4-14_mnz_inmag_dk_21	fr63_15-7b_mnz_lt_1
Mineral	monazite	monazite	monazite	monazite	monazite	monazite
deposit	Hook	Hook	Hook	Hook	Hook	Fraser's
Rock type	ironstone	ironstone	ironstone	ironstone	ironstone	ironstone
SiO2	0.116	0.305	0.341	0.390	0.113	0.740
P2O5	30.1	29.7	29.7	29.6	29.5	29.3
CaO	0.0909	0.111	0.161	0.136	0.134	0.0479
SrO	0.0624	0.264	0.374	0.337	0.389	bdl
Y2O3	0.171	0.200	0.142	0.149	0.0165	bdl
La2O3	9.42	7.90	9.00	8.37	10.1	5.92
Ce2O3	34.5	34.2	34.1	34.4	36.6	30.8
Pr2O3	4.70	5.07	4.77	4.79	4.55	5.65
Nd2O3	17.2	16.9	16.3	16.3	14.9	22.8
Sm2O3	1.37	1.21	1.28	1.34	0.884	1.17
Gd2O3	N.A.	N.A.	N.A.	N.A.	N.A.	N.A.
Dy2O3	N.A.	N.A.	N.A.	N.A.	N.A.	N.A.
ThO2	0.841	2.57	2.11	2.60	0.931	2.64
Total	98.5	98.2	97.8	98.0	97.7	99.1
APFU						
Si	0.00460	0.0121	0.0135	0.0155	0.004529829	0.0293
P	1.01	1.00	1.00	1.00	1.00	0.984
Ca	0.00385	0.00474	0.00684	0.00578	0.00572	0.00203
Sr	0.00143	0.00607521	0.008629629	0.007769569	0.00900	0
Y	0.00360	0.00422	0.00300	0.00316	0.000351	0
La	0.137	0.116	0.132	0.123	0.149	0.0865
Ce	0.499	0.497	0.496	0.500	0.535	0.448
Pr	0.0676	0.0734	0.0691	0.0694	0.0662	0.0816
Nd	0.242	0.240	0.232	0.232	0.212	0.323
Sm	0.0186	0.0166	0.0175	0.0184	0.0122	0.0160
Gd	0	0	0	0	0	0
Dy	0	0	0	0	0	0
Th	0.00755	0.0232	0.0191	0.0235	0.00846	0.0238

Comment	fr63_15-7b_mnz_lt_2	fr63_15-7b_mnz_dk_3	fr63_15-7b_mnz_dk_4	fr63_15-7b_mnz_dk_5
Mineral	monazite	monazite	monazite	monazite
deposit	Fraser's	Fraser's	Fraser's	Fraser's
Rock type	ironstone	ironstone	ironstone	ironstone
SiO2	0.733	0.395	0.422	0.350
P2O5	29.1	29.7	29.7	29.3
CaO	0.0504	0.0118	0.0531	0.0552
SrO	bdl	bdl	bdl	0.0513
Y2O3	bdl	0.0296	bdl	0.0218
La2O3	6.10	5.87	5.78	5.84
Ce2O3	31.4	32.3	32.5	34.6
Pr2O3	5.39	5.68	6.02	5.93
Nd2O3	22.7	23.3	22.6	20.7
Sm2O3	1.21	1.01	0.937	0.853
Gd2O3	N.A.	N.A.	N.A.	N.A.
Dy2O3	N.A.	N.A.	N.A.	N.A.
ThO2	2.44	1.20	0.876	1.48
Total	99.1	99.5	99.0	99.1
APFU				
Si	0.0291	0.0156	0.01670	0.0139
P	0.980	0.992	0.994	0.987
Ca	0.00215	0.00050	0.00225	0.00235
Sr	0	0	0	0.00118
Y	0	0.000622	0	0.000462
La	0.0894	0.0855	0.0843	0.0857
Ce	0.457	0.467	0.471	0.504
Pr	0.0781	0.0818	0.0868	0.0860
Nd	0.322	0.328	0.320	0.295
Sm	0.0166	0.0137	0.0128	0.0117
Gd	0	0	0	0
Dy	0	0	0	0
Th	0.0221	0.0108	0.00789	0.0134

Comment	fr9-102_fibrous-min1	fr9-102_fibrous-min2	fr9-102_fibrous-min3	fr9-102_fibrous-min4	fr63_15-7_ree-P_5	fr63_15-7_ree-P_6	fr63_15-7_ree-P_7
Mineral	rhabdophane	rhabdophane	rhabdophane	rhabdophane	rhabdophane	rhabdophane	rhabdophane
deposit	Fraser's	Fraser's	Fraser's	Fraser's	Fraser's	Fraser's	Fraser's
Rock type	ironstone	ironstone	ironstone	ironstone	ironstone	ironstone	ironstone
SiO2	0.00990	0.107	0.0116	0.00110	0.130	0.114	0.0741
P2O5	29.11	28.59	29.09	26.3	27	25.5	28.6
CaO	5.58	5.43	5.58	5.08	3.60	3.12	3.75
SrO	0.0116	0.0663	0.0220	0.0076	0.168	0.109	0.124
Y2O3	bdl	0.0524	bdl	bdl	0.00460	bdl	bdl
La2O3	4.39	3.91	4.29	4.15	5.22	6.38	5.35
Ce2O3	26.3	24.6	25.8	23.8	31.5	32.0	33.6
Pr2O3	4.93	5.10	5.27	4.70	4.18	4.60	4.33
Nd2O3	21.0	20.5	21.2	19.2	16.3	17.6	17.0
Sm2O3	1.09	0.959	1.27	1.06	0.788	0.612	0.547
Gd2O3	N.A.	N.A.	N.A.	N.A.	N.A.	N.A.	N.A.
Dy2O3	N.A.	N.A.	N.A.	N.A.	N.A.	N.A.	N.A.
ThO2	0.0745	0.0907	bdl	1.26	2.67	0.660	0.943
Total	92.5	89.4	92.5	85.6	91.6	90.7	94.3
APFU							
Si	0.000400	0.00444	0.000469	0.00	0.00553	0.00498	0.00301
P	1.00	1.00	1.00	0.984	0.970	0.946	0.985
Ca	0.242	0.241	0.242	0.241	0.164	0.147	0.163
Sr	0.000272	0.00159	0.000515	0.000195	0.00415	0.002769519	0.00291
Y	0	0.00115	0	0	0.000104	0	0
La	0.0654	0.0597	0.0639	0.0677	0.0817	0.103	0.080
Ce	0.388	0.373	0.381	0.386	0.490	0.514	0.500
Pr	0.0726	0.0770	0.0776	0.0757	0.0647	0.0735	0.0642
Nd	0.303	0.303	0.306	0.303	0.248	0.276	0.247
Sm	0.0152	0.0137	0.0177	0.0162	0.0115	0.00925	0.00766
Gd	0	0	0	0	0	0	0
Dy	0	0	0	0	0	0	0
Th	0.000685	0.000855	0	0.0127	0.0258	0.00658	0.00872

Comment	fr63_15-7b_mnz_alt_1	fr63_15-7b_mnz_alt_2	fr63_15-7b_mnz_alt_3	fr63_15-7b_mnz_alt_4	fr9-104b-unk11	fr9-104b-unk12	fr9-104b-unk13
Mineral	rhabdophane	rhabdophane	rhabdophane	rhabdophane	rhabdophane	rhabdophane	rhabdophane
deposit	Fraser's	Fraser's	Fraser's	Fraser's	Fraser's	Fraser's	Fraser's
Rock type	ironstone	ironstone	ironstone	ironstone	ironstone	ironstone	ironstone
SiO2	0.0183	0.0190	0.107	0.133	0.186	0.117	0.0737
P2O5	29.0	28.7	28.3	28.6	26.92	28.58	27.24
CaO	3.96	3.49	4.52	4.55	4.04	4.46	3.66
SrO	0.185	0.152	0.317	0.307	0.255	0.306	0.415
Y2O3	0.000700	bdl	0.0139	0.0129	0.103	0.0181	0.0957
La2O3	5.27	4.70	4.67	5.27	4.61	4.36	4.29
Ce2O3	32.7	38.8	29.3	29.9	25.7	25.4	25.7
Pr2O3	4.60	3.91	4.48	4.38	4.99	4.99	4.80
Nd2O3	16.7	13.0	15.4	15.7	20.0	19.5	19.7
Sm2O3	0.636	0.446	0.525	0.619	1.10	1.27	1.12
Gd2O3	N.A.	N.A.	N.A.	N.A.	N.A.	N.A.	N.A.
Dy2O3	N.A.	N.A.	N.A.	N.A.	N.A.	N.A.	N.A.
ThO2	1.94	1.26	4.31	4.15	0.769	1.19	1.54
Total	95.0	94.5	91.9	93.6	88.7	90.2	88.6
APFU							
Si	0.00074	0.00077	0.00441	0.00542	0.00801	0.00484	0.00317
P	0.988	0.988	0.990	0.986	0.981	1.00	0.992
Ca	0.171	0.152	0.200	0.199	0.186	0.198	0.169
Sr	0.00432	0.00357	0.00761	0.00725	0.00636	0.00735	0.0103
Y	0	0	0.000306	0.000280	0.00237	0.000400	0.00219
La	0.0783	0.0704	0.0712	0.0792	0.0732	0.0667	0.0681
Ce	0.483	0.577	0.443	0.446	0.406	0.385	0.405
Pr	0.0675	0.0579	0.0675	0.0650	0.0782	0.0754	0.0752
Nd	0.241	0.189	0.228	0.228	0.307	0.289	0.302
Sm	0.00883	0.00624	0.00749	0.00869	0.0163	0.0182	0.0166
Gd	0	0	0	0	0	0	0
Dy	0	0	0	0	0	0	0
Th	0.0178	0.0116	0.0406	0.0385	0.00753	0.0112	0.0151

Comment	fr9-104b-unk14	fr9-104b-unk15	fr63_15-2_fibrous-min5	fr63_15-2_fibrous-min6	fr63_15-2_fibrous-min7	fr63_15-2_fibrous-dkmin8
Mineral	rhabdophane	rhabdophane	rhabdophane	rhabdophane	rhabdophane	rhabdophane
deposit	Fraser's	Fraser's	Fraser's	Fraser's	Fraser's	Fraser's
Rock type	ironstone	ironstone	ironstone	ironstone	ironstone	ironstone
SiO2	0.0969	0.0679	0.0053	0.0408	0.0519	0.225
P2O5	28.04	27.62	27.67	27.47	27.88	26.64
CaO	3.80	3.00	0.603	0.765	0.682	0.680
SrO	0.457	0.243	bdl	bdl	bdl	bdl
Y2O3	0.150	0.192	0.0688	0.0290	0.0497	0.0201
La2O3	4.26	4.45	8.09	5.71	7.38	8.19
Ce2O3	25.2	24.8	6.9	23.6	13.5	8.09
Pr2O3	4.88	4.97	10.16	7.02	9.12	9.15
Nd2O3	19.8	20.9	35.9	25.2	31.9	34.7
Sm2O3	1.15	1.23	2.02	1.30	1.60	1.67
Gd2O3	N.A.	N.A.	N.A.	N.A.	N.A.	N.A.
Dy2O3	N.A.	N.A.	N.A.	N.A.	N.A.	N.A.
ThO2	1.30	1.10	0.412	0.518	1.11	0.755
Total	89.1	88.6	91.8	91.6	93.2	90.1
APFU						
Si	0.00410	0.00291	0.000227	0.00175	0.00219	0.00985
P	1.00	1.00	1.00	1.00	1.00	0.987
Ca	0.172	0.138	0.0277	0.0351	0.0308	0.0319
Sr	0.0112	0.00605	0	0	0	0
Y	0.00338	0.00438	0.00157	0.000661	0.00112	0.000468
La	0.0664	0.0704	0.128	0.0902	0.115	0.132
Ce	0.390	0.390	0.108	0.370	0.209	0.130
Pr	0.0751	0.0777	0.158	0.110	0.140	0.146
Nd	0.299	0.320	0.548	0.385	0.480	0.543
Sm	0.0168	0.0182	0.0298	0.0192	0.0233	0.0252
Gd	0	0	0	0	0	0
Dy	0	0	0	0	0	0
Th	0.0125	0.0108	0.00401	0.00504	0.0106	0.00752

Appendix 5.C – Supplementary Hyperspectral CL Monazite Data

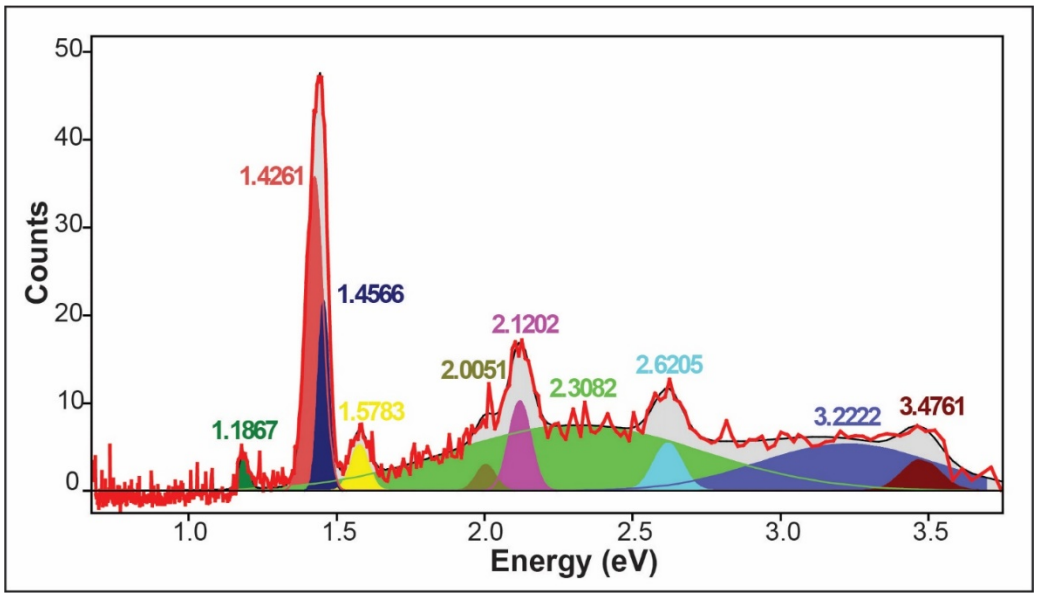

Supplementary Figure 5.C.1 Peak location and fitting for YW61 monazite analyses using CCD fitted to EPMA. Fitting was completed using OpticalFit 17.07 from CSIRO (Torpy and Wilson, 2008)

Supplementary Table 5.C.1. Peak data for Supplementary Figure 1 in OpticalFit 17.07. X-axis: eV. Number of peaks: 10.

Position	Fit	Height	Fit	FWHM	Fit	G/L	Fit	Colour
1.42615	1	35.7492	1	0.0688615	1	1	1	5050DC
2.30825	1	7.43497	1	0.993939	1	1	1	50DC50
3.22224	1	5.30251	1	0.693226	1	1	1	DC5050
3.47614	1	3.55931	1	0.149892	1	1	1	00007F
1.18666	1	4.15634	1	0.0396621	1	1	1	007F00
1.45661	1	21.6201	1	0.0428453	1	1	1	7F0000
1.57835	1	5.21449	1	0.0723736	1	1	1	00FFFF
2.12023	1	10.217	1	0.0883116	1	1	1	FF00FF
2.62052	1	5.38465	1	0.113433	1	1	1	FFFF00
2.00511	1	2.93335	1	0.076534	1	1	1	007F7F

Appendix 5.D – Monazite LA-ICP-MS Analyses

Note: LA-ICP-MS tables consist of 3 parts: 1) spot data, 2) 1σ error, and 3) detection limits. ^{140}Ce is internal standard.

File		yn49-61A_mnd_24-2	yn 49-61A_mnd_24-3	yn 49-61A_mnd_24-6	yn 49-61A_mnd_24-7	yn 49-61A_mnz_24-1	yn 49-61A_mnz_24-4	yn 49-61A_mnz_24-5
rock type		ank-sid carbonatite	ank-sid carbonatite	ank-sid carbonatite	ank-sid carbonatite	ank-sid carbonatite	ank-sid carbonatite	ank-sid carbonatite
SiO_2	wt.%	bdl	bdl	bdl	bdl	bdl	bdl	bdl
TiO_2	wt.%	bdl	bdl	bdl	bdl	bdl	bdl	bdl
Al_2O_3	wt.%	bdl	bdl	bdl	bdl	bdl	bdl	bdl
MnO	wt.%	bdl	bdl	bdl	bdl	bdl	bdl	bdl
CaO	wt.%	bdl	bdl	bdl	0.15	bdl	bdl	0.36
P_2O_5	wt.%	38.6	39.9	35.2	39.9	42.9	40.6	43.7
^{6}6Zn	µg/g	bdl	bdl	bdl	bdl	bdl	bdl	bdl
^{75}As	µg/g	334	376	332	370	362	375	471
^{85}Rb	µg/g	bdl	bdl	bdl	bdl	bdl	bdl	bdl
^{88}Sr	µg/g	71.3	1030	78.9	3120	2050	2710	6300
^{89}Y	µg/g	813	771	1050	2270	1450	962	1250
^{90}Zr	µg/g	1.39	1.27	1.36	1.31	1.54	1.22	1.24
^{93}Nb	µg/g	0.18	bdl	0.21	0.32	0.20	0.26	0.30
^{118}Sn	µg/g	bdl	bdl	bdl	bdl	bdl	bdl	bdl
^{133}Cs	µg/g	bdl	bdl	bdl	bdl	bdl	bdl	bdl
^{137}Ba	µg/g	7.05	2.56	bdl	59.2	10.8	16.5	68.9
^{139}La	µg/g	120000	123000	111000	127000	119000	118000	106000
^{140}Ce	µg/g	279945	279945	279945	279945	279945	279945	279945
^{141}Pr	µg/g	30900	32200	31000	31800	32400	32500	36600
^{143}Nd	µg/g	103000	113000	109000	114000	115000	116000	142000
^{147}Sm	µg/g	10400	13200	9990	13200	13500	14000	19100
^{151}Eu	µg/g	2110	2540	2290	2850	2790	2630	4330
^{157}Gd	µg/g	4350	5890	4670	7310	6990	6350	9880
^{159}Tb	µg/g	256	343	308	527	490	370	607
^{163}Dy	µg/g	570	740	758	1420	1200	799	1230

File		yn 49-61A_mnd_24-2	yn 49-61A_mnd_24-3	yn 49-61A_mnd_24-6	yn 49-61A_mnd_24-7	yn 49-61A_mnz_24-1	yn 49-61A_mnz_24-4	yn 49-61A_mnz_24-5
rock type		ank-sid carbonatite	ank-sid carbonatite	ank-sid carbonatite	ank-sid carbonatite	ank-sid carbonatite	ank-sid carbonatite	ank-sid carbonatite
^{165}Ho	µg/g	44.0	52.0	59.4	123	90.1	57.3	77.6
^{167}Er	µg/g	46.0	51.1	65.2	153	90.6	58.5	68.2
^{169}Tm	µg/g	2.47	2.86	3.54	10.1	4.15	3.07	3.06
^{171}Yb	µg/g	8.68	12.6	11.9	37.1	12.2	12.3	12.8
^{175}Lu	µg/g	0.50	1.15	0.74	2.9	0.69	0.87	0.82
^{178}Hf	µg/g	0.14	0.12	0.13	0.19	0.15	bdl	0.20
^{181}Ta	µg/g	bdl	0.023	0.034	0.051	0.051	0.050	0.042
^{208}Pb	µg/g	250	327	373	1150	1600	1750	2430
^{232}Th	µg/g	1880	2570	3020	9140	13300	17300	20600
^{238}U	µg/g	0.40	8.20	0.24	22.7	0.75	6.84	2.15
1σ Error								
SiO_2	wt.%	bdl	bdl	bdl	bdl	bdl	bdl	bdl
TiO_2	wt.%	bdl	bdl	bdl	bdl	bdl	bdl	bdl
Al_2O_3	wt.%	bdl	bdl	bdl	bdl	bdl	bdl	bdl
MnO	wt.%	bdl	bdl	bdl	bdl	bdl	bdl	bdl
CaO	wt.%	bdl	bdl	bdl	0.0488	bdl	bdl	0.0623
P_2O_5	wt.%	2.76	1.25	1.21	1.20	2.07	1.03	1.82
^{6}6Zn	µg/g	bdl	bdl	bdl	bdl	bdl	bdl	bdl
^{75}As	µg/g	25.6	16.7	15.0	16.0	23.4	20.1	22.2
^{85}Rb	µg/g	bdl	bdl	bdl	bdl	bdl	bdl	bdl
^{88}Sr	µg/g	8.04	29.3	3.12	115	102	57.0	446
^{89}Y	µg/g	63.2	38.7	38.2	47.4	46.6	28.8	41.7
^{90}Zr	µg/g	0.26	0.23	0.21	0.18	0.30	0.24	0.19
^{93}Nb	µg/g	0.064	0.12	0.062	0.057	0.052	0.047	0.050
^{118}Sn	µg/g	bdl	bdl	bdl	bdl	bdl	bdl	bdl
^{133}Cs	µg/g	bdl	bdl	bdl	bdl	bdl	bdl	bdl
^{137}Ba	µg/g	1.88	0.200	bdl	5.84	0.94	1.02	5.29
^{139}La	µg/g	9770	4720	3830	4120	6180	2620	2110

File		yn 49-61A_mnd_24-2	yn 49-61A_mnd_24-3	yn 49-61A_mnd_24-6	yn 49-61A_mnd_24-7	yn 49-61A_mnz_24-1	yn 49-61A_mnz_24-4	yn 49-61A_mnz_24-5
rock type		ank-sid carbonatite	ank-sid carbonatite	ank-sid carbonatite	ank-sid carbonatite	ank-sid carbonatite	ank-sid carbonatite	ank-sid carbonatite
^{140}Ce	µg/g	25100	11400	12000	9470	16700	8020	13400
^{141}Pr	µg/g	2490	1090	1170	1050	1900	637	1710
^{143}Nd	µg/g	8030	3800	3820	4020	6860	2940	6920
^{147}Sm	µg/g	767	399	221	343	644	286	917
^{151}Eu	µg/g	161	90.8	73.8	77.4	120	61.8	188
^{157}Gd	µg/g	326	215	155	184	313	152	433
^{159}Tb	µg/g	18.6	12.6	10.7	12.4	21.0	7.68	27.2
^{163}Dy	µg/g	40.6	29.8	24.6	35.1	46.3	21.8	46.9
^{165}Ho	µg/g	3.27	2.32	1.83	2.75	2.86	1.68	2.45
^{167}Er	µg/g	3.66	2.38	2.19	2.92	2.45	1.91	1.76
^{169}Tm	µg/g	0.15	0.14	0.14	0.23	0.15	0.14	0.09
^{171}Yb	µg/g	0.71	0.60	0.36	0.74	0.51	0.65	0.49
^{175}Lu	µg/g	0.064	0.057	0.035	0.081	0.039	0.061	0.040
^{178}Hf	µg/g	0.040	0.028	0.028	0.038	0.029	bdl	0.037
^{181}Ta	µg/g	bdl	0.0097	0.0096	0.019	0.022	0.019	0.017
^{208}Pb	µg/g	19.6	9.50	11.2	39.4	84.2	51.0	126
^{232}Th	µg/g	112	71.1	135	379	898	488	923
^{238}U	µg/g	0.057	0.36	0.021	0.51	0.054	0.14	0.064
Detection Limit								
SiO_2	wt.%	6.09	4.69	3.74	4.20	4.73	5.92	4.27
TiO_2	wt.%	0.00158	0.00100	0.000838	0.00111	0.00116	0.001408	0.000884
Al_2O_3	wt.%	0.00793	0.00658	0.00478	0.00591	0.00663	0.00768	0.00573
MnO	wt.%	0.000411	0.000329	0.000240	0.000303	0.000351	0.000402	0.000297
CaO	wt.%	0.140	0.104	0.0844	0.0942	0.111	0.130	0.0904
P_2O_5	wt.%	0.0321	0.0259	0.0192	0.0229	0.0285	0.0319	0.0236
$^{6}6Zn$	µg/g	9.13	6.94	5.11	5.56	7.66	8.38	6.16
^{75}As	µg/g	9.85	7.80	6.03	7.15	8.14	9.39	6.83
^{85}Rb	µg/g	0.400	0.318	0.261	0.305	0.310	0.372	0.271

File		yn49-61A_mnd_24-2	yn 49-61A_mnd_24-3	yn 49-61A_mnd_24-6	yn 49-61A_mnd_24-7	yn 49-61A_mnz_24-1	yn 49-61A_mnz_24-4	yn 49-61A_mnz_24-5
rock type		ank-sid carbonatite	ank-sid carbonatite	ank-sid carbonatite	ank-sid carbonatite	ank-sid carbonatite	ank-sid carbonatite	ank-sid carbonatite
^{88}Sr	µg/g	0.146	0.0678	0.0967	0.0927	0.120	0.127	0.0834
^{89}Y	µg/g	0.129	0.135	0.110	0.120	0.142	0.186	0.133
^{90}Zr	µg/g	0.448	0.342	0.258	0.306	0.325	0.420	0.274
^{93}Nb	µg/g	0.104	0.122	0.0593	0.0531	0.0613	0.0377	0.0195
^{118}Sn	µg/g	0.988	0.771	0.633	0.662	0.835	0.929	0.681
^{133}Cs	µg/g	0.0664	0.0510	0.0380	0.0413	0.0471	0.0665	0.0521
^{137}Ba	µg/g	0.278	0.174	0.193	0.173	0.283	0.308	0.233
^{139}La	µg/g	0.0430	0.0222	0.0246	0.0220	0.0254	0.0323	0.0298
^{140}Ce	µg/g	0.0362	0.0292	0.00980	0.0280	0.0369	0.0331	0.0264
^{141}Pr	µg/g	0.0136	0.0354	0.0234	0.0072	0.0250	0.0257	0.0186
^{143}Nd	µg/g	0.117	0.0467	0.0656	0.188	0.074	0.221	0.0553
^{147}Sm	µg/g	0.0950	0.124	0.112	0.122	0.141	0.218	0.0449
^{151}Eu	µg/g	0.0277	0.0360	0.0327	0.0295	0.0342	0.0584	0.0274
^{157}Gd	µg/g	0.206	0.186	0.167	0.154	0.133	0.188	0.146
^{159}Tb	µg/g	0.0590	0.0168	0.0199	0.0189	0.0193	0.0297	0.0195
^{163}Dy	µg/g	0.132	0.0209	0.0293	0.0763	0.0962	0.0989	0.0631
^{165}Ho	µg/g	0.0130	0.0169	0.00727	0.0138	0.0193	0.0245	0.00613
^{167}Er	µg/g	0.118	0.104	0.075	0.0833	0.0958	0.108	0.111
^{169}Tm	µg/g	0.0253	0.0159	0.0200	0.0157	0.0363	0.0112	0.0184
^{171}Yb	µg/g	0.225	0.134	0.105	0.115	0.150	0.256	0.146
^{175}Lu	µg/g	0.0302	0.0238	0.0154	0.0139	0.0219	0.0300	0.0179
^{178}Hf	µg/g	0.0922	0.0669	0.0525	0.0770	0.0747	0.128	0.0775
^{181}Ta	µg/g	0.0720	0.0193	0.0083	0.0274	0.0312	0.0340	0.0224
^{208}Pb	µg/g	0.0791	0.0409	0.0452	0.0580	0.0736	0.110	0.0379
^{232}Th	µg/g	0.0276	0.0173	0.0191	0.0273	0.0281	0.0122	0.0201
^{238}U	µg/g	0.0347	0.0167	0.0241	0.0222	0.0159	0.0206	0.0127

File		yn 49-61A_mnz_24-8	bh224-63b_mnd24-2	bh224-63b_mnd24-3	bh224-63b_mnd24-4	bh224-63b_mnd24-7	bh224-63b_mnd24-10	bh224-63b_mnz24-1
rock type		ank-sid carbonatite	mag-bio dyke	mag-bio dyke	mag-bio dyke	mag-bio dyke	mag-bio dyke	mag-bio dyke
SiO_2	wt.%	bdl	bdl	bdl	bdl	bdl	bdl	bdl
TiO_2	wt.%	bdl	bdl	bdl	bdl	bdl	bdl	bdl
Al_2O_3	wt.%	bdl	0.013	bdl	bdl	bdl	bdl	bdl
MnO	wt.%	bdl	0.0020	0.00073	0.00031	0.00088	0.0048	bdl
CaO	wt.%	bdl	bdl	0.122	0.092	bdl	0.15	0.17
P_2O_5	wt.%	40.5	37.6	40.2	38.0	34.0	36.2	48.5
^{6}6Zn	µg/g	bdl	bdl	bdl	bdl	bdl	bdl	bdl
^{75}As	µg/g	359	591	513	524	605	563	690
^{85}Rb	µg/g	bdl	bdl	bdl	bdl	bdl	bdl	bdl
^{88}Sr	µg/g	580	337	664	234	292	1800	324
^{89}Y	µg/g	1860	696	1620	1240	456	1170	4790
^{90}Zr	µg/g	1.48	2.11	3.60	7.91	1.46	2.89	1.13
^{93}Nb	µg/g	0.19	0.52	0.34	0.33	0.67	0.50	0.40
^{118}Sn	µg/g	bdl	bdl	bdl	bdl	bdl	bdl	bdl
^{133}Cs	µg/g	bdl	bdl	bdl	0.0416	bdl	bdl	bdl
^{137}Ba	µg/g	2.28	35.6	11.8	18.7	27.1	133	1.13
^{139}La	µg/g	129000	58100	64200	58700	59900	68600	74400
^{140}Ce	µg/g	279945	231160	231160	231160	231160	231160	231160
^{141}Pr	µg/g	31000	38800	39700	39600	40300	38400	41700
^{143}Nd	µg/g	106000	165000	160000	162000	160000	154000	207000
^{147}Sm	µg/g	12500	9140	9170	9500	7440	10800	24900
^{151}Eu	µg/g	2780	1270	1760	1820	729	1620	4770
^{157}Gd	µg/g	6340	3120	3590	3580	1890	4010	13000
^{159}Tb	µg/g	459	201	321	297	109	277	1040
^{163}Dy	µg/g	1230	446	933	801	250	658	2630
^{165}Ho	µg/g	101	33.1	78.5	62.7	22.6	53.5	205
^{167}Er	µg/g	114	32.9	84.0	63.9	26.5	64.4	217
^{169}Tm	µg/g	5.75	1.65	4.25	3.00	1.24	4.19	11.2

File		yn 49-61A_mnz_24-8 ank-sid	bh224-63b_mnd24-2	bh224-63b_mnd24-3	bh224-63b_mnd24-4	bh224-63b_mnd24-7	bh224-63b_mnd24-10	bh224-63b_mnz24-1
rock type		carbonatite	mag-bio dyke	mag-bio dyke	mag-bio dyke	mag-bio dyke	mag-bio dyke	mag-bio dyke
^{171}Yb	µg/g	19.0	5.54	12.8	9.37	3.95	16.7	36.2
^{175}Lu	µg/g	1.11	0.35	0.83	0.68	0.25	1.45	2.66
^{178}Hf	µg/g	0.19	0.090	0.25	0.34	bdl	0.19	0.40
^{181}Ta	µg/g	0.050	0.033	0.063	0.059	bdl	0.052	0.051
^{208}Pb	µg/g	1030	1040	1040	695	817	1800	2050
^{232}Th	µg/g	7510	10700	10800	7640	8410	18600	20700
^{238}U	µg/g	1.02	4.35	21.2	16.1	2.12	10.0	43.9
1σ Error								
SiO_2	wt.%	bdl	bdl	bdl	bdl	bdl	bdl	bdl
TiO_2	wt.%	bdl	bdl	bdl	bdl	bdl	bdl	bdl
Al_2O_3	wt.%	bdl	0.0055	bdl	bdl	bdl	bdl	bdl
MnO	wt.%	bdl	0.00035	0.00015	0.00014	0.00025	0.00062	bdl
CaO	wt.%	bdl	bdl	0.044	0.038	bdl	0.063	0.052
P_2O_5	wt.%	1.39	1.06	1.30	1.19	1.49	1.25	2.30
^{6}6Zn	µg/g	bdl	bdl	bdl	bdl	bdl	bdl	bdl
^{75}As	µg/g	18.3	21.1	20.9	21.7	24.4	23.2	37.1
^{85}Rb	µg/g	bdl	bdl	bdl	bdl	bdl	bdl	bdl
^{88}Sr	µg/g	22.1	36.2	17.2	13.2	9.5	234	23.0
^{89}Y	µg/g	30.1	94.4	33.0	36.7	12.7	32.1	226
^{90}Zr	µg/g	0.40	0.36	0.35	1.29	0.18	0.72	0.24
^{93}Nb	µg/g	0.079	0.070	0.053	0.048	0.20	0.081	0.047
^{118}Sn	µg/g	bdl	bdl	bdl	bdl	bdl	bdl	bdl
^{133}Cs	µg/g	bdl	bdl	bdl	0.0180	bdl	bdl	bdl
^{137}Ba	µg/g	0.57	2.72	0.85	2.23	2.18	24.0	0.21
^{139}La	µg/g	3940	2110	2150	1930	847	3790	4380
^{140}Ce	µg/g	7160	9970	8230	9840	7180	13700	13800
^{141}Pr	µg/g	900	853	1470	1330	643	1940	2290

File		yn 49-61A_mnz_24-8 ank-sid	bh224-63b_mnd24-2	bh224-63b_mnd24-3	bh224-63b_mnd24-4	bh224-63b_mnd24-7	bh224-63b_mnd24-10	bh224-63b_mnz24-1
rock type		carbonatite	mag-bio dyke	mag-bio dyke	mag-bio dyke	mag-bio dyke	mag-bio dyke	mag-bio dyke
^{143}Nd	µg/g	3350	4730	6010	5560	4140	7370	10900
^{147}Sm	µg/g	297	512	317	264	299	299	1370
^{151}Eu	µg/g	52.5	129	58.9	52.2	14.0	34.9	243
^{157}Gd	µg/g	103	309	112	111	31.0	101	585
^{159}Tb	µg/g	8.29	24.2	9.15	8.27	0.90	7.82	55.1
^{163}Dy	µg/g	22.1	62.1	22.4	21.3	5.25	18.4	139
^{165}Ho	µg/g	1.76	4.05	1.74	1.70	0.45	1.36	10.9
^{167}Er	µg/g	2.28	3.59	1.75	2.14	0.99	1.71	10.2
^{169}Tm	µg/g	0.26	0.17	0.10	0.13	0.058	0.097	0.56
^{171}Yb	µg/g	0.82	0.70	0.30	0.41	0.44	0.86	1.97
^{175}Lu	µg/g	0.076	0.049	0.027	0.049	0.029	0.078	0.15
^{178}Hf	µg/g	0.071	0.024	0.027	0.059	bdl	0.047	0.062
^{181}Ta	µg/g	0.020	0.015	0.011	0.015	bdl	0.016	0.017
^{208}Pb	µg/g	20.3	28.5	24.6	28.4	17.3	58.5	104
^{232}Th	µg/g	181	383	304	391	293	597	1130
^{238}U	µg/g	0.075	0.67	0.53	0.92	0.13	0.36	2.3
Detection Limit								
SiO_2	wt.%	8.18	3.64	4.07	3.45	4.91	4.60	6.32
TiO_2	wt.%	0.00217	0.00100	0.000950	0.000848	0.00143	0.000971	0.00132
Al_2O_3	wt.%	0.01078	0.00528	0.00537	0.00498	0.00640	0.00610	0.00743
MnO	wt.%	0.000561	0.000266	0.000270	0.000254	0.000342	0.000324	0.000381
CaO	wt.%	0.187	0.0915	0.0950	0.0825	0.121	0.110	0.136
P_2O_5	wt.%	0.0443	0.0243	0.0240	0.0222	0.0292	0.0271	0.0347
^{6}6Zn	µg/g	11.5	7.20	6.31	6.33	8.22	7.42	10.0
^{75}As	µg/g	13.1	7.00	6.52	6.35	8.75	8.07	10.2
^{85}Rb	µg/g	0.566	0.301	0.234	0.246	0.333	0.280	0.352
^{88}Sr	µg/g	0.157	0.0600	0.0744	0.0939	0.138	0.112	0.118

File		yn 49-61A_mnz_24-8	bh224-63b_mnd24-2	bh224-63b_mnd24-3	bh224-63b_mnd24-4	bh224-63b_mnd24-7	bh224-63b_mnd24-10	bh224-63b_mnz24-1
rock type		ank-sid carbonatite	mag-bio dyke	mag-bio dyke	mag-bio dyke	mag-bio dyke	mag-bio dyke	mag-bio dyke
^{89}Y	µg/g	0.257	0.108	0.118	0.0927	0.156	0.141	0.148
^{90}Zr	µg/g	0.573	0.303	0.284	0.257	0.356	0.342	0.369
^{93}Nb	µg/g	0.141	0.0717	0.0403	0.0184	0.111	0.0733	0.0277
^{118}Sn	µg/g	1.386	0.596	0.580	0.596	0.796	0.814	0.867
^{133}Cs	µg/g	0.0962	0.0475	0.0331	0.0335	0.0666	0.0496	0.0477
^{137}Ba	µg/g	0.565	0.260	0.217	0.141	0.425	0.238	0.0898
^{139}La	µg/g	0.0490	0.0144	0.00567	0.0255	0.0263	0.0249	0.0114
^{140}Ce	µg/g	0.0264	0.0369	0.0284	0.0184	0.0270	0.0120	0.0299
^{141}Pr	µg/g	0.0431	0.0175	0.0132	0.0177	0.0320	0.0289	0.0231
^{143}Nd	µg/g	0.335	0.202	0.114	0.152	0.275	0.170	0.199
^{147}Sm	µg/g	0.507	0.183	0.0925	0.157	0.256	0.138	0.234
^{151}Eu	µg/g	0.0683	0.0447	0.0218	0.0242	0.0702	0.0403	0.0472
^{157}Gd	µg/g	0.376	0.155	0.121	0.141	0.211	0.146	0.191
^{159}Tb	µg/g	0.0319	0.0210	0.0102	0.0137	0.0306	0.0247	0.0182
^{163}Dy	µg/g	0.150	0.0674	0.0706	0.0550	0.111	0.0762	0.0892
^{165}Ho	µg/g	0.0320	0.0225	0.0145	0.0154	0.0410	0.0189	0.0221
^{167}Er	µg/g	0.141	0.0990	0.0449	0.0946	0.145	0.101	0.0800
^{169}Tm	µg/g	0.0387	0.0212	0.00962	0.0212	0.0259	0.0084	0.0208
^{171}Yb	µg/g	0.220	0.075	0.120	0.0779	0.240	0.146	0.152
^{175}Lu	µg/g	0.0322	0.0227	0.0103	0.0155	0.0332	0.0303	0.0223
^{178}Hf	µg/g	0.152	0.0376	0.0148	0.0625	0.105	0.0726	0.0952
^{181}Ta	µg/g	0.0224	0.0285	0.00490	0.0155	0.0348	0.0102	0.00986
^{208}Pb	µg/g	0.175	0.0546	0.0509	0.0522	0.106	0.0857	0.0940
^{232}Th	µg/g	0.0456	0.0259	0.0193	0.0200	0.0359	0.0237	0.0228
^{238}U	µg/g	0.0495	0.0273	0.0145	0.0113	0.0274	0.0159	0.0182

File		bh224-63b_mnz24-5	bh224-63b_mnz24-6	bh224-63b_mnz24-8	bh224-63b_mnz24-9	dmcy139_mnz_24-1	dmcy139_mnz_24-2	dmcy139_mnz_24-3
rock type		mag-bio dyke	mag-bio dyke	mag-bio dyke	mag-bio dyke	mag-bio dyke	mag-bio dyke	mag-bio dyke
SiO_2	wt.%	bdl	bdl	bdl	bdl	bdl	bdl	bdl
TiO_2	wt.%	bdl	0.0022	bdl	bdl	bdl	bdl	bdl
Al_2O_3	wt.%	bdl	0.0085	bdl	bdl	0.014	bdl	bdl
MnO	wt.%	bdl	0.0013	bdl	bdl	0.00083	0.0014	0.00145
CaO	wt.%	0.22	0.23	0.17	0.21	0.40	0.46	0.36
P_2O_5	wt.%	40.5	45.4	44.6	42.7	45.6	50.7	50.6
^{6}6Zn	µg/g	bdl	bdl	bdl	bdl	12.4	bdl	bdl
^{75}As	µg/g	570	680	684	581	802	735	796
^{85}Rb	µg/g	bdl	bdl	bdl	bdl	bdl	bdl	bdl
^{88}Sr	µg/g	1120	413	297	1740	5320	5880	4900
^{89}Y	µg/g	1980	4720	4270	2100	374	319	331
^{90}Zr	µg/g	1.01	4.75	1.13	1.24	1.09	1.49	1.44
^{93}Nb	µg/g	0.28	1.38	0.42	0.58	0.59	0.44	0.32
^{118}Sn	µg/g	bdl	bdl	bdl	bdl	bdl	bdl	bdl
^{133}Cs	µg/g	bdl	bdl	bdl	bdl	bdl	bdl	bdl
^{137}Ba	µg/g	22.7	24.6	3.27	38.3	90.0	99.3	95.1
^{139}La	µg/g	65000	74400	73500	70200	51200	50800	52500
^{140}Ce	µg/g	231160	231160	231160	231160	271160	271160	271160
^{141}Pr	µg/g	40500	43800	42600	41900	51900	52000	52200
^{143}Nd	µg/g	171000	212000	207000	180000	215000	220000	227000
^{147}Sm	µg/g	12900	24900	23900	15500	12000	11400	13100
^{151}Eu	µg/g	2660	4650	4410	2910	1440	1280	1420
^{157}Gd	µg/g	6050	12800	11700	7190	2790	2470	2660
^{159}Tb	µg/g	489	1070	1010	530	125	114	119
^{163}Dy	µg/g	1190	2740	2450	1280	181	158	174
^{165}Ho	µg/g	87.3	215	195	92.4	16.3	14.0	15.6
^{167}Er	µg/g	84.4	234	200	96.2	23.8	21.1	21.8
^{169}Tm	µg/g	4.10	12.1	10.5	4.63	1.66	1.51	1.67

File		bh224-63b_mnz24-5	bh224-63b_mnz24-6	bh224-63b_mnz24-8	bh224-63b_mnz24-9	dmcy139_mnz_24-1	dmcy139_mnz_24-2	dmcy139_mnz_24-3
rock type		mag-bio dyke	mag-bio dyke	mag-bio dyke	mag-bio dyke	mag-bio dyke	mag-bio dyke	mag-bio dyke
^{171}Yb	µg/g	13.4	39.8	34.8	15.3	8.09	6.65	7.46
^{175}Lu	µg/g	0.917	2.95	2.56	1.01	0.64	0.51	0.54
^{178}Hf	µg/g	0.17	0.71	0.37	0.21	bdl	bdl	0.035
^{181}Ta	µg/g	0.039	0.094	0.058	0.059	0.071	bdl	0.054
^{208}Pb	µg/g	2030	2060	2300	1930	3460	3650	3250
^{232}Th	µg/g	21300	21900	24000	18500	41400	42200	37200
^{238}U	µg/g	11.2	50.6	44.3	15.3	10.6	20.7	9.09
1σ Error								
SiO_2	wt.%	bdl	bdl	bdl	bdl	bdl	bdl	bdl
TiO_2	wt.%	bdl	0.00060	bdl	bdl	bdl	bdl	bdl
Al_2O_3	wt.%	bdl	0.0031	bdl	bdl	0.0054	bdl	bdl
MnO	wt.%	bdl	0.00020	bdl	bdl	0.00026	0.00031	0.00030
CaO	wt.%	0.058	0.062	0.052	0.069	0.10	0.090	0.066
P_2O_5	wt.%	1.33	1.25	1.79	1.29	1.87	3.90	2.04
^{6}6Zn	µg/g	bdl	bdl	bdl	bdl	3.60	bdl	bdl
^{75}As	µg/g	21.0	21.5	33.4	21.9	39.5	67.1	41.5
^{85}Rb	µg/g	bdl	bdl	bdl	bdl	bdl	bdl	bdl
^{88}Sr	µg/g	87.1	11.8	10.5	64.6	157	449	195
^{89}Y	µg/g	140	139	130	66.7	18.1	26.8	16.0
^{90}Zr	µg/g	0.15	0.43	0.28	0.31	0.15	0.35	0.22
^{93}Nb	µg/g	0.054	0.15	0.15	0.15	0.061	0.073	0.060
^{118}Sn	µg/g	bdl	bdl	bdl	bdl	bdl	bdl	bdl
^{133}Cs	µg/g	bdl	bdl	bdl	bdl	bdl	bdl	bdl
^{137}Ba	µg/g	2.29	1.19	0.59	3.20	7.48	4.26	3.74
^{139}La	µg/g	1660	1880	2930	873	1840	4620	2560
^{140}Ce	µg/g	7780	6320	8950	2690	15000	26400	12700
^{141}Pr	µg/g	1140	1230	1340	651	1660	4740	2340

File		bh224-63b_mnz24-5	bh224-63b_mnz24-6	bh224-63b_mnz24-8	bh224-63b_mnz24-9	dmcy139_mnz_24-1	dmcy139_mnz_24-2	dmcy139_mnz_24-3
rock type		mag-bio dyke	mag-bio dyke	mag-bio dyke	mag-bio dyke	mag-bio dyke	mag-bio dyke	mag-bio dyke
^{143}Nd	µg/g	5490	6230	7180	2880	9990	20400	11000
^{147}Sm	µg/g	626	678	853	363	481	832	447
^{151}Eu	µg/g	143	144	174	38.4	39.3	112	62.0
^{157}Gd	µg/g	331	316	485	109	93.5	218	128
^{159}Tb	µg/g	30.7	33.0	35.4	8.36	4.88	10.2	5.25
^{163}Dy	µg/g	78.5	85.8	62.9	24.7	6.1	14.7	8.06
^{165}Ho	µg/g	6.06	6.74	6.43	1.95	0.50	1.28	0.79
^{167}Er	µg/g	5.90	7.43	7.00	2.15	1.37	2.01	1.13
^{169}Tm	µg/g	0.28	0.41	0.31	0.15	0.075	0.14	0.10
^{171}Yb	µg/g	0.98	1.11	1.31	0.83	0.49	0.53	0.49
^{175}Lu	µg/g	0.075	0.127	0.132	0.061	0.052	0.053	0.037
^{178}Hf	µg/g	0.035	0.084	0.069	0.087	bdl	bdl	0.015
^{181}Ta	µg/g	0.017	0.021	0.026	0.0203	0.029	bdl	0.018
^{208}Pb	µg/g	69.8	60.0	69.7	27.5	62.9	295	128
^{232}Th	µg/g	955	585	724	332	792	3480	1700
^{238}U	µg/g	0.731	1.58	1.30	0.469	0.314	1.47	0.489
Detection Limit								
SiO_2	wt.%	3.97	5.10	5.28	6.58	5.92	6.12	5.67
TiO_2	wt.%	0.000923	0.00122	0.000981	0.00164	0.00144	0.00142	0.00133
Al_2O_3	wt.%	0.00527	0.00666	0.00658	0.00857	0.00694	0.00743	0.00750
MnO	wt.%	0.000270	0.000341	0.000347	0.000434	0.000399	0.000418	0.000400
CaO	wt.%	0.0917	0.117	0.120	0.161	0.153	0.138	0.136
P_2O_5	wt.%	0.0244	0.0298	0.0303	0.0385	0.0432	0.0427	0.0403
$^{6}6Zn$	µg/g	6.28	8.30	7.77	10.9	8.23	9.76	9.38
^{75}As	µg/g	7.22	8.64	8.82	10.9	11.3	10.7	11.0
^{85}Rb	µg/g	0.237	0.322	0.378	0.410	0.359	0.351	0.370
^{88}Sr	µg/g	0.0719	0.116	0.111	0.163	0.0967	0.0955	0.0989

File		bh224-63b_mnz24-5	bh224-63b_mnz24-6	bh224-63b_mnz24-8	bh224-63b_mnz24-9	dmcy139_mnz_24-1	dmcy139_mnz_24-2	dmcy139_mnz_24-3
rock type		mag-bio dyke	mag-bio dyke	mag-bio dyke	mag-bio dyke	mag-bio dyke	mag-bio dyke	mag-bio dyke
^{89}Y	µg/g	0.117	0.131	0.161	0.189	0.168	0.159	0.151
^{90}Zr	µg/g	0.223	0.336	0.321	0.463	0.388	0.360	0.336
^{93}Nb	µg/g	0.0496	0.0774	0.101	0.0603	0.0561	0.0740	0.109
^{118}Sn	µg/g	0.609	0.746	0.927	1.14	0.983	1.026	0.856
^{133}Cs	µg/g	0.0361	0.0505	0.0654	0.0628	0.0488	0.0558	0.0567
^{137}Ba	µg/g	0.161	0.092	0.248	0.447	0.376	0.294	0.278
^{139}La	µg/g	0.0084	0.0117	0.0316	0.0249	0.0404	0.0305	0.0448
^{140}Ce	µg/g	0.0210	0.0120	0.0179	0.0445	0.0491	0.0143	0.0293
^{141}Pr	µg/g	0.0185	0.0255	0.0219	0.0346	0.0378	0.0111	0.0486
^{143}Nd	µg/g	0.201	0.250	0.256	0.424	0.325	0.0950	0.0825
^{147}Sm	µg/g	0.114	0.145	0.0971	0.241	0.128	0.0773	0.158
^{151}Eu	µg/g	0.0333	0.0519	0.0680	0.0704	0.0657	0.0495	0.0197
^{157}Gd	µg/g	0.107	0.168	0.208	0.283	0.186	0.160	0.283
^{159}Tb	µg/g	0.0177	0.0089	0.0303	0.0452	0.0177	0.0262	0.0246
^{163}Dy	µg/g	0.0520	0.0980	0.0535	0.133	0.0707	0.0786	0.0726
^{165}Ho	µg/g	0.0194	0.0198	0.0208	0.0361	0.0175	0.0357	0.0244
^{167}Er	µg/g	0.0686	0.0871	0.116	0.145	0.118	0.115	0.108
^{169}Tm	µg/g	0.0147	0.0210	0.0249	0.0178	0.0253	0.0245	0.0204
^{171}Yb	µg/g	0.107	0.114	0.144	0.199	0.211	0.179	0.0633
^{175}Lu	µg/g	0.0196	0.0199	0.0242	0.0291	0.0366	0.0263	0.0219
^{178}Hf	µg/g	0.0666	0.105	0.0907	0.113	0.0926	0.0896	0.0317
^{181}Ta	µg/g	0.0221	0.0225	0.0324	0.0442	0.0348	0.0524	0.0104
^{208}Pb	µg/g	0.0155	0.0590	0.0773	0.114	0.0981	0.107	0.0651
^{232}Th	µg/g	0.0200	0.00912	0.0137	0.0445	0.0319	0.0335	0.0224
^{238}U	µg/g	0.0156	0.0277	0.0284	0.0431	0.0342	0.0309	0.0271

File		dmcy139_mnz_24-8	dmcy139_mnz_24-9	dmcy139_mnzdk_24-4	dmcy139_mnzdk_24-5	dmcy139_mnzdk_24-6	dmcy139_mnzdk_24-7
rock type		mag-bio dyke	mag-bio dyke	mag-bio dyke	mag-bio dyke	mag-bio dyke	mag-bio dyke
SiO_2	wt.%	bdl	bdl	bdl	bdl	bdl	bdl
TiO_2	wt.%	0.0030	bdl	bdl	0.0021	bdl	bdl
Al_2O_3	wt.%	0.011	0.021	bdl	0.0096	bdl	bdl
MnO	wt.%	0.00098	0.00060	bdl	0.0013	bdl	bdl
CaO	wt.%	0.52	0.38	0.45	0.84	0.73	0.65
P_2O_5	wt.%	53.8	53.0	55.5	48.4	46.2	49.5
^{6}6Zn	µg/g	bdl	12.8	bdl	16.9	bdl	bdl
^{75}As	µg/g	734	772	759	752	686	663
^{85}Rb	µg/g	bdl	bdl	bdl	bdl	bdl	bdl
^{88}Sr	µg/g	7950	5400	6860	7980	13000	9850
^{89}Y	µg/g	284	353	251	105	66.2	126
^{90}Zr	µg/g	1.31	1.33	1.44	1.27	1.44	0.988
^{93}Nb	µg/g	0.93	0.33	0.31	0.45	0.38	0.40
^{118}Sn	µg/g	bdl	bdl	bdl	bdl	bdl	bdl
^{133}Cs	µg/g	bdl	0.0493	bdl	bdl	bdl	bdl
^{137}Ba	µg/g	105	45.3	41.4	167	160	106
^{139}La	µg/g	51300	52700	49100	47800	44000	50500
^{140}Ce	µg/g	271160	271160	271160	271160	271160	271160
^{141}Pr	µg/g	52700	52800	52000	50800	49500	50800
^{143}Nd	µg/g	227000	227000	222000	230000	213000	207000
^{147}Sm	µg/g	13100	12900	12600	11400	9410	9830
^{151}Eu	µg/g	1320	1390	1220	1250	1110	885
^{157}Gd	µg/g	2520	2540	2350	2280	1940	1810
^{159}Tb	µg/g	107	114	103	88.2	70.2	75.6
^{163}Dy	µg/g	150	170	134	88.0	48.3	75.9
^{165}Ho	µg/g	13.1	15.6	11.9	6.87	3.76	6.05
^{167}Er	µg/g	18.5	22.4	17.1	8.26	4.57	9.07
^{169}Tm	µg/g	1.29	1.63	1.30	0.50	0.23	0.58

File		dmcy139_mnz_24-8	dmcy139_mnz_24-9	dmcy139_mnzdk_24-4	dmcy139_mnzdk_24-5	dmcy139_mnzdk_24-6	dmcy139_mnzdk_24-7
rock type		mag-bio dyke	mag-bio dyke	mag-bio dyke	mag-bio dyke	mag-bio dyke	mag-bio dyke
^{171}Yb	µg/g	7.04	8.18	6.35	2.21	1.21	3.09
^{175}Lu	µg/g	0.57	0.61	0.46	0.18	0.10	0.21
^{178}Hf	µg/g	bdl	bdl	bdl	bdl	bdl	bdl
^{181}Ta	µg/g	0.040	bdl	0.039	0.051	bdl	0.042
^{208}Pb	µg/g	4840	4010	4520	3220	5110	4520
^{232}Th	µg/g	50500	42200	49100	32300	47000	43000
^{238}U	µg/g	47.9	15.8	44.3	27.4	25.6	29.8
1σ Error							
SiO_2	wt.%	bdl	bdl	bdl	bdl	bdl	bdl
TiO_2	wt.%	0.0011	bdl	bdl	0.00079	bdl	bdl
Al_2O_3	wt.%	0.0049	0.0049	bdl	0.0032	bdl	bdl
MnO	wt.%	0.00027	0.00019	bdl	0.00026	bdl	bdl
CaO	wt.%	0.095	0.078	0.073	0.15	0.060	0.084
P_2O_5	wt.%	1.32	2.18	1.56	1.60	1.55	1.24
^{6}6Zn	µg/g	bdl	4.88	bdl	7.48	bdl	bdl
^{75}As	µg/g	26.8	43.5	26.2	21.8	32.6	22.8
^{85}Rb	µg/g	bdl	bdl	bdl	bdl	bdl	bdl
^{88}Sr	µg/g	170	217	192	223	313	174
^{89}Y	µg/g	6.03	20.8	7.14	2.19	1.66	10.3
^{90}Zr	µg/g	0.28	0.27	0.29	0.22	0.30	0.20
^{93}Nb	µg/g	0.16	0.080	0.070	0.12	0.083	0.084
^{118}Sn	µg/g	bdl	bdl	bdl	bdl	bdl	bdl
^{133}Cs	µg/g	bdl	0.023	bdl	bdl	bdl	bdl
^{137}Ba	µg/g	7.73	3.56	2.84	7.15	7.22	2.80
^{139}La	µg/g	1510	2650	1460	1960	1610	1190
^{140}Ce	µg/g	6500	13300	10700	15500	14100	9460
^{141}Pr	µg/g	1410	2390	1450	1470	1630	1480

File		dmcy139_mnz_24-8	dmcy139_mnz_24-9	dmcy139_mnzdk_24-4	dmcy139_mnzdk_24-5	dmcy139_mnzdk_24-6	dmcy139_mnzdk_24-7
rock type		mag-bio dyke	mag-bio dyke	mag-bio dyke	mag-bio dyke	mag-bio dyke	mag-bio dyke
^{143}Nd	µg/g	5610	10900	5550	11200	8810	7010
^{147}Sm	µg/g	293	618	295	639	615	414
^{151}Eu	µg/g	29.8	69.4	28.0	55.7	12.9	45.3
^{157}Gd	µg/g	60.5	127	53.5	88.4	43.6	80.7
^{159}Tb	µg/g	2.59	5.86	2.63	3.51	1.93	3.31
^{163}Dy	µg/g	3.30	9.40	3.05	2.76	1.52	5.24
^{165}Ho	µg/g	0.32	0.90	0.36	0.46	0.15	0.49
^{167}Er	µg/g	0.62	1.520	0.71	0.39	0.33	0.71
^{169}Tm	µg/g	0.060	0.13	0.075	0.045	0.026	0.049
^{171}Yb	µg/g	0.50	0.57	0.41	0.19	0.27	0.34
^{175}Lu	µg/g	0.039	0.050	0.037	0.034	0.025	0.024
^{178}Hf	µg/g	bdl	bdl	bdl	bdl	bdl	bdl
^{181}Ta	µg/g	0.014	bdl	0.013	0.026	bdl	0.018
^{208}Pb	µg/g	93.9	171	86.2	61.8	190	83.1
^{232}Th	µg/g	1320	2030	1200	998	1080	1430
^{238}U	µg/g	1.58	1.17	0.75	1.47	1.16	2.46
Detection Limit							
SiO_2	wt.%	7.05	5.85	6.32	5.13	6.16	5.17
TiO_2	wt.%	0.00171	0.00117	0.00128	0.00123	0.00200	0.00140
Al_2O_3	wt.%	0.00965	0.00785	0.00825	0.00657	0.00797	0.00708
MnO	wt.%	0.000505	0.000414	0.000434	0.000347	0.000423	0.000367
CaO	wt.%	0.166	0.130	0.157	0.125	0.154	0.128
P_2O_5	wt.%	0.0473	0.0384	0.0424	0.0346	0.0404	0.0348
^{6}6Zn	µg/g	13.2	10.4	11.1	9.33	10.9	10.1
^{75}As	µg/g	12.8	10.2	11.5	9.03	11.1	9.78
^{85}Rb	µg/g	0.513	0.332	0.428	0.342	0.404	0.329
^{88}Sr	µg/g	0.116	0.129	0.115	0.126	0.168	0.119

File		dmcy139_mnz_24-8	dmcy139_mnz_24-9	dmcy139_mnzdk_24-4	dmcy139_mnzdk_24-5	dmcy139_mnzdk_24-6	dmcy139_mnzdk_24-7
rock type		mag-bio dyke	mag-bio dyke	mag-bio dyke	mag-bio dyke	mag-bio dyke	mag-bio dyke
^{89}Y	µg/g	0.192	0.157	0.191	0.174	0.208	0.147
^{90}Zr	µg/g	0.476	0.383	0.407	0.401	0.408	0.368
^{93}Nb	µg/g	0.109	0.101	0.0782	0.0845	0.149	0.0649
^{118}Sn	µg/g	1.17	1.06	0.894	0.849	0.932	0.870
^{133}Cs	µg/g	0.0585	0.0473	0.0578	0.0658	0.0875	0.0493
^{137}Ba	µg/g	0.408	0.365	0.309	0.319	0.440	0.296
^{139}La	µg/g	0.0517	0.0363	0.0445	0.0348	0.0559	0.0267
^{140}Ce	µg/g	0.0464	0.0300	0.0332	0.0461	0.0502	0.0387
^{141}Pr	µg/g	0.0242	0.0232	0.0286	0.0277	0.0467	0.0299
^{143}Nd	µg/g	0.353	0.317	0.334	0.144	0.333	0.0813
^{147}Sm	µg/g	0.203	0.0669	0.247	0.193	0.311	0.183
^{151}Eu	µg/g	0.0669	0.0537	0.0636	0.0501	0.0954	0.0534
^{157}Gd	µg/g	0.287	0.127	0.189	0.183	0.277	0.118
^{159}Tb	µg/g	0.0279	0.0185	0.0321	0.0327	0.0402	0.0204
^{163}Dy	µg/g	0.0481	0.101	0.0987	0.124	0.150	0.143
^{165}Ho	µg/g	0.0231	0.0184	0.0338	0.0160	0.0465	0.0203
^{167}Er	µg/g	0.173	0.0977	0.0914	0.117	0.147	0.0895
^{169}Tm	µg/g	0.0348	0.0173	0.0258	0.0221	0.0456	0.0192
^{171}Yb	µg/g	0.0820	0.173	0.205	0.212	0.292	0.207
^{175}Lu	µg/g	0.0280	0.00923	0.0301	0.0344	0.0429	0.0271
^{178}Hf	µg/g	0.0955	0.0764	0.0941	0.106	0.146	0.0786
^{181}Ta	µg/g	0.0135	0.0252	0.0133	0.0349	0.0421	0.0416
^{208}Pb	µg/g	0.138	0.0539	0.0595	0.0643	0.0587	0.0493
^{232}Th	µg/g	0.0123	0.0328	0.0253	0.0318	0.0384	0.00936
^{238}U	µg/g	0.0346	0.0223	0.0276	0.0291	0.0450	0.0205

File		yg4_mnz_24-5	yg4_mnz_24-6	yg4_mnz_24-7	yg4_mnz_24-8	yg4_mnzdk_24-1	yg4_mnzdk_24-2	yg4_mnzdk_24-3	yg4_mnzdk_24-4
rock type		mag-bio dyke	mag-bio dyke	mag-bio dyke	mag-bio dyke	mag-bio dyke	mag-bio dyke	mag-bio dyke	mag-bio dyke
SiO_2	wt.%	bdl	bdl	bdl	bdl	bdl	bdl	bdl	bdl
TiO_2	wt.%	bdl	bdl	bdl	bdl	bdl	bdl	bdl	bdl
Al_2O_3	wt.%	bdl	bdl	bdl	bdl	bdl	bdl	bdl	bdl
MnO	wt.%	bdl	bdl	bdl	0.00096	0.00040	bdl	bdl	bdl
CaO	wt.%	0.23	0.19	0.10	0.29	0.28	0.11	0.22	0.26
P_2O_5	wt.%	39.4	39.2	37.1	39.7	40.5	39.5	41.1	39.7
^{6}6Zn	µg/g	bdl	bdl	bdl	bdl	bdl	bdl	bdl	bdl
^{75}As	µg/g	380	395	319	385	383	368	379	410
^{85}Rb	µg/g	bdl	bdl	bdl	bdl	bdl	bdl	bdl	bdl
^{88}Sr	µg/g	2810	3020	1570	2950	3590	2180	2550	3380
^{89}Y	µg/g	77.5	87.9	22.3	75.5	119	61.7	80.0	143
^{90}Zr	µg/g	1.22	1.33	1.37	2.06	1.51	1.55	1.53	1.60
^{93}Nb	µg/g	0.22	0.24	0.16	0.37	0.24	0.29	0.19	0.31
^{118}Sn	µg/g	bdl	bdl	bdl	bdl	bdl	bdl	bdl	0.82
^{133}Cs	µg/g	bdl	0.023	bdl	bdl	bdl	bdl	bdl	bdl
^{137}Ba	µg/g	77.4	1410	24.4	220	497	49.4	112	144
^{139}La	µg/g	95500	96800	105000	94900	100100	98800	99300	101000
^{140}Ce	µg/g	322821	322821	322821	322821	322821	322821	322821	322821
^{141}Pr	µg/g	39700	38800	34900	39800	38800	37900	38700	39100
^{143}Nd	µg/g	131000	129000	106000	131000	126000	123000	128000	130000
^{147}Sm	µg/g	10300	10100	6670	10200	9970	8690	10000	10600
^{151}Eu	µg/g	1450	1430	833	1460	1490	1210	1450	1590
^{157}Gd	µg/g	2700	2710	1560	2710	2870	2280	2740	3090
^{159}Tb	µg/g	101	102	48.3	98.4	111	80.6	104	122
^{163}Dy	µg/g	125	130	38.6	115	144	95.1	126	176
^{165}Ho	µg/g	5.76	6.48	1.74	5.41	7.37	4.57	5.94	10.0
^{167}Er	µg/g	3.28	3.89	1.35	3.48	5.66	2.77	3.34	6.59
^{169}Tm	µg/g	0.080	0.096	0.04	0.13	0.24	0.054	0.097	0.18

File		yg4_mnz_24-5	yg4_mnz_24-6	yg4_mnz_24-7	yg4_mnz_24-8	yg4_mnzdk_24-1	yg4_mnzdk_24-2	yg4_mnzdk_24-3	yg4_mnzdk_24-4
rock type		mag-bio dyke	mag-bio dyke	mag-bio dyke	mag-bio dyke	mag-bio dyke	mag-bio dyke	mag-bio dyke	mag-bio dyke
^{171}Yb	µg/g	1.30	1.23	0.63	1.35	1.79	0.87	1.09	1.33
^{175}Lu	µg/g	0.075	0.054	bdl	0.066	0.100	0.046	0.056	0.064
^{178}Hf	µg/g	bdl	bdl	bdl	bdl	0.077	bdl	bdl	0.068
^{181}Ta	µg/g	0.053	0.033	bdl	bdl	0.028	0.038	0.032	bdl
^{208}Pb	µg/g	1750	1880	1150	1820	1320	1380	1380	1750
^{232}Th	µg/g	13400	14400	8800	14100	10600	10900	10500	13800
^{238}U	µg/g	7.47	10.4	1.86	5.35	7.19	5.47	3.63	18.1
1σ Error									
SiO_2	wt.%	bdl	bdl	bdl	bdl	bdl	bdl	bdl	bdl
TiO_2	wt.%	bdl	bdl	bdl	bdl	bdl	bdl	bdl	bdl
Al_2O_3	wt.%	bdl	bdl	bdl	bdl	bdl	bdl	bdl	bdl
MnO	wt.%	bdl	bdl	bdl	0.00019	0.00014	bdl	bdl	bdl
CaO	wt.%	0.057	0.050	0.040	0.064	0.056	0.055	0.048	0.057
P_2O_5	wt.%	1.34	1.04	0.994	1.90	1.11	1.30	1.29	1.00
^{6}6Zn	µg/g	bdl	bdl	bdl	bdl	bdl	bdl	bdl	bdl
^{75}As	µg/g	17.6	16.3	12.8	21.6	14.6	18.0	16.3	16.4
^{85}Rb	µg/g	bdl	bdl	bdl	bdl	bdl	bdl	bdl	bdl
^{88}Sr	µg/g	95.4	92.4	44.5	126	108	75.8	110	89.3
^{89}Y	µg/g	3.07	2.82	0.79	2.47	3.10	2.33	3.60	2.47
^{90}Zr	µg/g	0.23	0.20	0.20	0.25	0.23	0.21	0.18	0.22
^{93}Nb	µg/g	0.049	0.053	0.039	0.076	0.053	0.062	0.047	0.071
^{118}Sn	µg/g	bdl	bdl	bdl	bdl	bdl	bdl	bdl	0.381
^{133}Cs	µg/g	bdl	0.011	bdl	bdl	bdl	bdl	bdl	bdl
^{137}Ba	µg/g	3.00	489	1.38	5.25	18.2	2.34	5.31	2.34
^{139}La	µg/g	3620	2960	2900	4940	3110	4200	3130	3010
^{140}Ce	µg/g	16000	11300	9850	19700	10600	15400	11000	9130
^{141}Pr	µg/g	1660	1180	944	2200	1100	1640	1220	1090

File		yg4_mnz_24-5	yg4_mnz_24-6	yg4_mnz_24-7	yg4_mnz_24-8	yg4_mnzdk_24-1	yg4_mnzdk_24-2	yg4_mnzdk_24-3	yg4_mnzdk_24-4
rock type		mag-bio dyke	mag-bio dyke	mag-bio dyke	mag-bio dyke	mag-bio dyke	mag-bio dyke	mag-bio dyke	mag-bio dyke
^{143}Nd	µg/g	5220	4420	3060	6860	3970	5300	4570	3630
^{147}Sm	µg/g	418	336	180	484	292	360	371	303
^{151}Eu	µg/g	56.3	48.5	24.2	68.6	43.8	52.2	57.3	40.8
^{157}Gd	µg/g	103	83.8	42.9	128	91.4	92.6	107	84.1
^{159}Tb	µg/g	4.12	3.19	1.23	4.45	3.21	3.42	4.16	2.85
^{163}Dy	µg/g	5.12	4.41	1.23	4.16	4.22	3.92	5.53	3.87
^{165}Ho	µg/g	0.21	0.23	0.080	0.19	0.21	0.17	0.29	0.21
^{167}Er	µg/g	0.19	0.17	0.099	0.27	0.27	0.22	0.21	0.25
^{169}Tm	µg/g	0.015	0.011	0.010	0.018	0.022	0.0094	0.011	0.018
^{171}Yb	µg/g	0.14	0.13	0.067	0.13	0.15	0.10	0.13	0.12
^{175}Lu	µg/g	0.014	0.0097	0.036	0.013	0.012	0.011	0.011	0.012
^{178}Hf	µg/g	bdl	bdl	bdl	bdl	0.024	bdl	bdl	0.027
^{181}Ta	µg/g	0.013	0.012	bdl	bdl	0.0080	0.012	0.013	bdl
^{208}Pb	µg/g	65.7	54.9	32.2	93.0	38.0	51.7	50.1	63.5
^{232}Th	µg/g	555	440	261	804	319	468	419	516
^{238}U	µg/g	0.30	0.39	0.11	0.18	0.20	0.11	0.23	0.51
Detection Limit									
SiO_2	wt.%	4.86	4.22	4.01	5.32	4.37	3.89	4.40	4.78
TiO_2	wt.%	0.00127	0.00101	0.000851	0.00121	0.00104	0.000975	0.000881	0.00127
Al_2O_3	wt.%	0.00680	0.00593	0.00568	0.00751	0.00581	0.00616	0.00627	0.00626
MnO	wt.%	0.000334	0.000299	0.000281	0.000383	0.000291	0.000315	0.000310	0.000307
CaO	wt.%	0.109	0.0932	0.0895	0.112	0.0976	0.101	0.0984	0.101
P_2O_5	wt.%	0.0246	0.0218	0.0197	0.0273	0.0225	0.0234	0.0220	0.0235
^{6}6Zn	µg/g	7.69	6.43	5.94	8.30	6.44	6.59	6.67	6.71
^{75}As	µg/g	7.96	6.97	6.61	8.12	6.72	7.90	7.78	7.74
^{85}Rb	µg/g	0.252	0.279	0.239	0.389	0.249	0.286	0.275	0.314
^{88}Sr	µg/g	0.126	0.0788	0.103	0.117	0.111	0.117	0.117	0.100

File		yg4_mnz_24-5	yg4_mnz_24-6	yg4_mnz_24-7	yg4_mnz_24-8	yg4_mnzdk_24-1	yg4_mnzdk_24-2	yg4_mnzdk_24-3	yg4_mnzdk_24-4
rock type		mag-bio dyke	mag-bio dyke	mag-bio dyke	mag-bio dyke	mag-bio dyke	mag-bio dyke	mag-bio dyke	mag-bio dyke
^{89}Y	µg/g	0.136	0.106	0.117	0.129	0.111	0.154	0.112	0.140
^{90}Zr	µg/g	0.422	0.299	0.280	0.381	0.312	0.362	0.317	0.310
^{93}Nb	µg/g	0.0267	0.0612	0.0504	0.0257	0.0519	0.0559	0.0643	0.0751
^{118}Sn	µg/g	0.807	0.649	0.691	0.831	0.650	0.689	0.673	0.707
^{133}Cs	µg/g	0.0460	0.0202	0.0399	0.0550	0.0386	0.0480	0.0505	0.0402
^{137}Ba	µg/g	0.257	0.232	0.205	0.224	0.169	0.258	0.165	0.281
^{139}La	µg/g	0.0329	0.0200	0.0209	0.0107	0.00804	0.0287	0.00779	0.0399
^{140}Ce	µg/g	0.0270	0.0338	0.0268	0.0367	0.0220	0.0237	0.0272	0.0318
^{141}Pr	µg/g	0.0413	0.0203	0.0209	0.0228	0.0250	0.0228	0.0137	0.0226
^{143}Nd	µg/g	0.225	0.137	0.143	0.196	0.147	0.197	0.145	0.213
^{147}Sm	µg/g	0.183	0.0381	0.146	0.0593	0.0447	0.129	0.118	0.173
^{151}Eu	µg/g	0.0484	0.0261	0.0277	0.0462	0.0284	0.0312	0.0279	0.0333
^{157}Gd	µg/g	0.197	0.144	0.184	0.230	0.128	0.136	0.110	0.162
^{159}Tb	µg/g	0.0200	0.0151	0.0180	0.0216	0.0222	0.0234	0.0202	0.0235
^{163}Dy	µg/g	0.0673	0.0702	0.0640	0.128	0.0246	0.0709	0.0647	0.0866
^{165}Ho	µg/g	0.0201	0.0152	0.0199	0.0247	0.0133	0.0176	0.0202	0.0215
^{167}Er	µg/g	0.110	0.0922	0.0698	0.188	0.0268	0.103	0.0806	0.0834
^{169}Tm	µg/g	0.0235	0.0182	0.0188	0.0204	0.0210	0.0138	0.0123	0.0202
^{171}Yb	µg/g	0.172	0.120	0.0419	0.170	0.128	0.161	0.110	0.130
^{175}Lu	µg/g	0.0229	0.0175	0.0356	0.0218	0.0187	0.0200	0.0221	0.0191
^{178}Hf	µg/g	0.0855	0.0420	0.0445	0.0936	0.0457	0.0746	0.0752	0.0536
^{181}Ta	µg/g	0.00962	0.0173	0.0228	0.0313	0.00697	0.00856	0.0231	0.0217
^{208}Pb	µg/g	0.0770	0.0467	0.0728	0.113	0.0849	0.0605	0.0634	0.0572
^{232}Th	µg/g	0.0206	0.0230	0.0236	0.0361	0.0167	0.0180	0.0207	0.0078
^{238}U	µg/g	0.0198	0.0206	0.0196	0.0291	0.0161	0.0196	0.0058	0.0154

File		leq130A_mnz-1	leq130A_mnz-2	leq130A_mnz-3	leq130A_mnz-4	leq130A_mnz-5	leq130A_mnz-6	leq130A_mnz-7	leq130A_mnz-8
rock type		mag-bio dyke	mag-bio dyke	mag-bio dyke	mag-bio dyke	mag-bio dyke	mag-bio dyke	mag-bio dyke	mag-bio dyke
SiO_2	wt.%	bdl	bdl	bdl	bdl	bdl	bdl	bdl	bdl
TiO_2	wt.%	bdl	bdl	bdl	bdl	bdl	bdl	bdl	bdl
Al_2O_3	wt.%	bdl	bdl	bdl	bdl	bdl	bdl	bdl	bdl
MnO	wt.%	bdl	bdl	bdl	bdl	0.0010	bdl	bdl	bdl
CaO	wt.%	0.0889	bdl	bdl	bdl	0.21	0.11	0.084	0.24
P_2O_5	wt.%	35.6	34.8	34.9	35.5	35.4	35.1	34.4	36.1
^{6}6Zn	µg/g	bdl	4.94	bdl	bdl	10.8	bdl	bdl	bdl
^{75}As	µg/g	449	431	429	464	434	409	397	439
^{85}Rb	µg/g	bdl	0.275	bdl	bdl	0.277	bdl	bdl	bdl
^{88}Sr	µg/g	1310	1250	723	1170	3610	1990	1580	3970
^{89}Y	µg/g	3500	3490	1830	2300	2890	2670	2490	3300
^{90}Zr	µg/g	1.73	1.32	1.12	1.53	1.68	1.12	1.40	1.71
^{93}Nb	µg/g	0.18	0.16	0.18	0.21	0.16	0.20	0.27	0.26
^{118}Sn	µg/g	bdl	bdl	bdl	bdl	bdl	bdl	bdl	bdl
^{133}Cs	µg/g	bdl	bdl	bdl	bdl	0.215	bdl	bdl	bdl
^{137}Ba	µg/g	16.7	24.0	4.54	7.94	40.3	26.9	23.7	55.7
^{139}La	µg/g	143000	138000	147000	143000	143000	157000	157000	147000
^{140}Ce	µg/g	288132	288132	288132	288132	288132	288132	288132	288132
^{141}Pr	µg/g	32200	32600	33400	33500	33000	31800	32100	33700
^{143}Nd	µg/g	111000	112000	110000	115000	113000	105000	106000	119000
^{147}Sm	µg/g	10500	10800	9570	10800	10800	9880	9220	11800
^{151}Eu	µg/g	2350	2346	1910	2320	2280	2040	1960	2360
^{157}Gd	µg/g	6560	6450	5080	6430	6350	5500	5160	6850
^{159}Tb	µg/g	620	603	412	560	560	478	455	610
^{163}Dy	µg/g	2160	2060	1200	1810	1890	1560	1480	2050
^{165}Ho	µg/g	219	206	106	172	182	146	139	194
^{167}Er	µg/g	245	232	103	183	191	164	149	209
^{169}Tm	µg/g	10.0	9.63	3.67	6.88	7.14	6.81	5.75	7.72
^{171}Yb	µg/g	20.8	21.6	7.94	14.1	13.9	14.9	12.3	15.4

File		leq130A_mnz-1	leq130A_mnz-2	leq130A_mnz-3	leq130A_mnz-4	leq130A_mnz-5	leq130A_mnz-6	leq130A_mnz-7	leq130A_mnz-8
rock type		mag-bio dyke	mag-bio dyke	mag-bio dyke	mag-bio dyke	mag-bio dyke	mag-bio dyke	mag-bio dyke	mag-bio dyke
^{175}Lu	µg/g	1.16	1.23	0.44	0.82	0.83	0.82	0.66	0.80
^{178}Hf	µg/g	0.39	0.27	0.22	0.27	0.25	0.33	0.25	0.30
^{181}Ta	µg/g	0.076	0.066	0.058	0.068	0.049	0.074	0.042	0.040
^{208}Pb	µg/g	556	648	933	1230	3260	647	289	3650
^{232}Th	µg/g	4430	4930	7260	9330	29000	5010	2410	28700
^{238}U	µg/g	14.2	23.1	15.6	32.9	14.8	10.5	8.98	15.5
1σ Error									
SiO_2	wt.%	bdl	bdl	bdl	bdl	bdl	bdl	bdl	bdl
TiO_2	wt.%	bdl	bdl	bdl	bdl	bdl	bdl	bdl	bdl
Al_2O_3	wt.%	bdl	bdl	bdl	bdl	bdl	bdl	bdl	bdl
MnO	wt.%	bdl	bdl	bdl	bdl	0.00024	bdl	bdl	bdl
CaO	wt.%	0.028	bdl	bdl	bdl	0.036	0.036	0.034	0.047
P_2O_5	wt.%	0.95	0.84	1.06	0.80	1.98	0.99	0.93	0.99
^{6}6Zn	µg/g	bdl	1.99	bdl	bdl	3.07	bdl	bdl	bdl
^{75}As	µg/g	17.4	16.4	18.4	14.5	24.5	13.7	13.1	12.9
^{85}Rb	µg/g	bdl	0.108	bdl	bdl	0.131	bdl	bdl	bdl
^{88}Sr	µg/g	44.5	40.7	21.4	50.1	192	47.9	64.5	112
^{89}Y	µg/g	97.3	87.0	60.6	52.7	176	80.6	64.7	51.4
^{90}Zr	µg/g	0.17	0.16	0.16	0.17	0.21	0.14	0.20	0.22
^{93}Nb	µg/g	0.053	0.033	0.042	0.036	0.054	0.036	0.048	0.050
^{118}Sn	µg/g	bdl	bdl	bdl	bdl	bdl	bdl	bdl	bdl
^{133}Cs	µg/g	bdl	bdl	bdl	bdl	0.0468	bdl	bdl	bdl
^{137}Ba	µg/g	1.15	1.67	0.43	0.60	4.19	0.85	1.34	3.28
^{139}La	µg/g	3920	3920	4730	3810	7810	5320	4790	3820
^{140}Ce	µg/g	11000	11500	9840	8530	18100	10500	9610	6800
^{141}Pr	µg/g	853	997	991	916	1960	990	956	855
^{143}Nd	µg/g	3200	3640	3350	3100	6710	3380	3330	2800
^{147}Sm	µg/g	324	314	270	274	586	301	276	252

File		leq130A_mnz-1	leq130A_mnz-2	leq130A_mnz-3	leq130A_mnz-4	leq130A_mnz-5	leq130A_mnz-6	leq130A_mnz-7	leq130A_mnz-8
rock type		mag-bio dyke	mag-bio dyke	mag-bio dyke	mag-bio dyke	mag-bio dyke	mag-bio dyke	mag-bio dyke	mag-bio dyke
^{151}Eu	µg/g	56.5	72.1	56.5	63.5	138	61.5	58.8	48.7
^{157}Gd	µg/g	166	193	146	168	385	163	153	126
^{159}Tb	µg/g	16.5	18.1	11.9	14.7	35.6	14.7	13.7	11.2
^{163}Dy	µg/g	62.1	62.2	34.2	43.6	129	45.8	43.2	32.5
^{165}Ho	µg/g	6.13	6.36	3.22	3.66	12.5	4.19	4.09	2.84
^{167}Er	µg/g	7.74	6.95	3.32	3.79	13.6	4.15	4.39	3.82
^{169}Tm	µg/g	0.34	0.295	0.14	0.16	0.50	0.22	0.20	0.18
^{171}Yb	µg/g	1.135	0.788	0.41	0.63	1.138	0.56	0.51	0.59
^{175}Lu	µg/g	0.073	0.052	0.030	0.038	0.069	0.054	0.038	0.050
^{178}Hf	µg/g	0.055	0.036	0.029	0.044	0.049	0.049	0.045	0.054
^{181}Ta	µg/g	0.019	0.018	0.017	0.019	0.015	0.021	0.021	0.019
^{208}Pb	µg/g	15.8	22.9	23.9	39.6	194	9.09	7.49	85.0
^{232}Th	µg/g	147	180	189	371	1630	80.9	58.8	875
^{238}U	µg/g	0.38	0.64	0.59	0.55	1.37	0.24	0.28	0.41
Detection Limit									
SiO_2	wt.%	2.55	2.57	2.57	2.64	3.26	2.85	2.76	3.93
TiO_2	wt.%	0.000751	0.000638	0.000719	0.000767	0.000680	0.000670	0.000711	0.00112
Al_2O_3	wt.%	0.00272	0.00268	0.00290	0.00311	0.00341	0.00332	0.00345	0.00481
MnO	wt.%	0.000250	0.000245	0.000253	0.000266	0.000279	0.000256	0.000263	0.000361
CaO	wt.%	0.0696	0.0720	0.0735	0.0762	0.0847	0.0754	0.0787	0.102
P_2O_5	wt.%	0.0214	0.0200	0.0204	0.0212	0.0216	0.0197	0.0197	0.0263
^{6}6Zn	µg/g	4.95	3.98	5.54	6.01	6.01	5.38	4.96	6.16
^{75}As	µg/g	5.69	5.69	5.44	5.67	6.20	5.35	5.54	7.36
^{85}Rb	µg/g	0.217	0.213	0.248	0.264	0.265	0.235	0.242	0.299
^{88}Sr	µg/g	0.108	0.0664	0.0723	0.0723	0.0955	0.0570	0.0774	0.116
^{89}Y	µg/g	0.115	0.0717	0.105	0.108	0.117	0.104	0.103	0.105
^{90}Zr	µg/g	0.196	0.229	0.221	0.209	0.200	0.245	0.225	0.267
^{93}Nb	µg/g	0.0536	0.0168	0.0621	0.0193	0.0740	0.0179	0.0612	0.0298

File		leq130A_mnz-1	leq130A_mnz-2	leq130A_mnz-3	leq130A_mnz-4	leq130A_mnz-5	leq130A_mnz-6	leq130A_mnz-7	leq130A_mnz-8
rock type		mag-bio dyke	mag-bio dyke	mag-bio dyke	mag-bio dyke	mag-bio dyke	mag-bio dyke	mag-bio dyke	mag-bio dyke
^{118}Sn	µg/g	0.750	0.749	0.789	0.738	0.776	0.757	0.761	0.950
^{133}Cs	µg/g	0.0435	0.0490	0.0384	0.0343	0.0402	0.0395	0.0333	0.0529
^{137}Ba	µg/g	0.0924	0.170	0.234	0.269	0.223	0.0658	0.0605	0.260
^{139}La	µg/g	0.0118	0.0318	0.0238	0.0238	0.0126	0.0224	0.0287	0.0335
^{140}Ce	µg/g	0.0121	0.0282	0.0245	0.0095	0.0362	0.00867	0.0343	0.0142
^{141}Pr	µg/g	0.0095	0.0199	0.0218	0.0156	0.0258	0.0374	0.0230	0.0111
^{143}Nd	µg/g	0.0820	0.151	0.0634	0.165	0.199	0.059	0.199	0.0965
^{147}Sm	µg/g	0.148	0.124	0.135	0.195	0.162	0.159	0.127	0.0783
^{151}Eu	µg/g	0.0437	0.0417	0.0501	0.0154	0.0538	0.0373	0.0519	0.0630
^{157}Gd	µg/g	0.142	0.183	0.147	0.175	0.231	0.153	0.181	0.226
^{159}Tb	µg/g	0.0207	0.0198	0.0334	0.0189	0.0301	0.0202	0.0205	0.0300
^{163}Dy	µg/g	0.0848	0.0578	0.0774	0.0878	0.114	0.0988	0.0591	0.155
^{165}Ho	µg/g	0.0237	0.0201	0.0219	0.0157	0.0102	0.0180	0.0063	0.0269
^{167}Er	µg/g	0.0935	0.0781	0.0854	0.0698	0.0857	0.0801	0.0807	0.120
^{169}Tm	µg/g	0.0168	0.0062	0.0208	0.0247	0.0247	0.0172	0.00596	0.0212
^{171}Yb	µg/g	0.146	0.122	0.109	0.243	0.197	0.102	0.102	0.187
^{175}Lu	µg/g	0.00982	0.0206	0.0248	0.0197	0.0237	0.0211	0.0214	0.0277
^{178}Hf	µg/g	0.0632	0.0628	0.0263	0.0777	0.0687	0.0807	0.0646	0.0956
^{181}Ta	µg/g	0.0248	0.0207	0.0227	0.0226	0.0120	0.0212	0.0316	0.0317
^{208}Pb	µg/g	0.0253	0.0464	0.0956	0.100	0.0739	0.0679	0.0846	0.0855
^{232}Th	µg/g	0.0246	0.0076	0.0280	0.00854	0.0325	0.0333	0.0261	0.0431
^{238}U	µg/g	0.0319	0.0164	0.0219	0.0293	0.0258	0.0228	0.0276	0.0364

File		leq130A_mnz-9	leq130A_mnz-10	lrs150_mnz_24-1	lrs150_mnz_24-2	lrs150_mnz_24-3	lrs150_mnz_24-4	yn 50-49A-MNZ-24-1	yn 50-49A-MNZ-24-2
rock type		mag-bio dyke	mag-bio dyke	amph-dol vnlt	amph-dol vnlt	amph-dol vnlt	amph-dol vnlt	ank-sid carbonatite	ank-sid carbonatite
SiO_2	wt.%	bdl	bdl	bdl	bdl	bdl	bdl	bdl	bdl
TiO_2	wt.%	bdl	bdl	0.0013	bdl	0.0095	0.032	bdl	bdl
Al_2O_3	wt.%	bdl	bdl	bdl	bdl	0.26	0.84	bdl	bdl
MnO	wt.%	bdl	bdl	0.0013	bdl	0.040	0.024	bdl	0.0017
CaO	wt.%	0.085	0.26	0.64	1.20	2.03	1.89	0.30	0.34
P_2O_5	wt.%	34.4	35.8	33.7	34.6	34.8	38.6	33.7	31.9
^{6}6Zn	µg/g	bdl	bdl	20.0	bdl	145	269	bdl	bdl
^{75}As	µg/g	395	401	416	399	367	373	368	376
^{85}Rb	µg/g	bdl	0.215	bdl	bdl	4.71	53.7	bdl	bdl
^{88}Sr	µg/g	1540	3670	8150	10600	12500	19500	2910	3010
^{89}Y	µg/g	3010	3390	379	533	297	167	1880	2150
^{90}Zr	µg/g	1.40	1.35	4.97	1.47	241	291	1.45	1.20
^{93}Nb	µg/g	0.28	0.24	0.97	0.22	12.4	11.8	0.22	0.25
^{118}Sn	µg/g	bdl	bdl	bdl	bdl	2.96	2.51	bdl	bdl
^{133}Cs	µg/g	bdl	bdl	0.054	bdl	0.30	3.87	bdl	0.096
^{137}Ba	µg/g	24.4	53.4	52.1	69.7	97.3	309	19.9	28.6
^{139}La	µg/g	149000	150000	137000	138000	150000	165000	112000	107000
^{140}Ce	µg/g	288132	288132	247790	247790	247790	247790	273339	273339
^{141}Pr	µg/g	31900	32900	26000	26600	23400	23600	35300	35700
^{143}Nd	µg/g	107000	114000	95400	97800	77900	80700	134000	139000
^{147}Sm	µg/g	9740	10900	13300	12300	10900	11500	19500	20700
^{151}Eu	µg/g	2060	2260	2090	2050	2030	1670	3760	4170
^{157}Gd	µg/g	5540	6280	3160	3140	3200	2520	9940	11000
^{159}Tb	µg/g	506	575	114	124	124	68.9	672	767
^{163}Dy	µg/g	1690	1970	221	271	206	103	1570	1840
^{165}Ho	µg/g	163	194	18.4	24.8	15.1	7.73	104	131
^{167}Er	µg/g	182	208	22.8	32.1	18.9	11.9	92.8	122
^{169}Tm	µg/g	7.34	7.61	1.28	1.71	1.27	0.872	4.23	5.65

File		leq130A_mnz-9	leq130A_mnz-10	lrs150_mnz_24-1	lrs150_mnz_24-2	lrs150_mnz_24-3	lrs150_mnz_24-4	yn 50-49A-MNZ-24-1	yn 50-49A-MNZ-24-2
rock type		mag-bio dyke	mag-bio dyke	amph-dol vnlt	amph-dol vnlt	amph-dol vnlt	amph-dol vnlt	ank-sid carbonatite	ank-sid carbonatite
^{171}Yb	µg/g	15.9	15.8	4.40	5.25	5.43	4.33	11.4	17.1
^{175}Lu	µg/g	0.88	0.80	0.34	0.30	0.38	0.41	0.72	1.16
^{178}Hf	µg/g	0.25	0.33	0.16	0.089	5.0	8.02	bdl	0.13
^{181}Ta	µg/g	0.061	0.071	bdl	bdl	0.14	bdl	0.0497	0.032
^{208}Pb	µg/g	310	2620	5060	8030	7690	8910	2360	2590
^{232}Th	µg/g	2510	20300	49800	82500	72000	89000	23700	27400
^{238}U	µg/g	12.3	12.1	2.60	6.79	7.97	15.0	1.90	3.57
1σ Error									
SiO_2	wt.%	bdl	bdl	bdl	bdl	bdl	bdl	bdl	bdl
TiO_2	wt.%	bdl	bdl	0.00055	bdl	0.0013	0.0024	bdl	bdl
Al_2O_3	wt.%	bdl	bdl	bdl	bdl	0.024	0.031	bdl	bdl
MnO	wt.%	bdl	bdl	0.00027	bdl	0.0053	0.0017	bdl	0.00059
CaO	wt.%	0.033	0.041	0.079	0.078	0.12	0.13	0.12	0.072
P_2O_5	wt.%	0.97	0.87	1.60	0.88	0.86	1.02	1.22	1.79
^{6}6Zn	µg/g	bdl	bdl	7.07	bdl	23.4	22.4	bdl	bdl
^{75}As	µg/g	14.6	15.9	25.2	16.2	17.6	12.4	23.2	35.4
^{85}Rb	µg/g	bdl	0.098	bdl	bdl	0.716	1.63	bdl	bdl
^{88}Sr	µg/g	32.2	98.1	705	417	199	650	140	180
^{89}Y	µg/g	76.9	85.1	17.4	12.2	11.6	5.8	76.8	194
^{90}Zr	µg/g	0.162	0.19	0.68	0.38	27.2	31.9	0.38	0.23
^{93}Nb	µg/g	0.0545	0.036	0.16	0.064	1.15	0.721	0.13	0.081
^{118}Sn	µg/g	bdl	bdl	bdl	bdl	0.61	0.39	bdl	bdl
^{133}Cs	µg/g	bdl	bdl	0.023	bdl	0.059	0.26	bdl	0.040
^{137}Ba	µg/g	1.07	1.98	5.27	8.82	3.91	15.1	1.60	4.67
^{139}La	µg/g	4060	3740	6980	2300	4150	5720	3540	7290
^{140}Ce	µg/g	10500	9130	14900	7290	9460	8320	8420	19700
^{141}Pr	µg/g	900	885	1360	594	688	582	1380	2710

File		leq130A_mnz-9	leq130A_mnz-10	lrs150_mnz_24-1	lrs150_mnz_24-2	lrs150_mnz_24-3	lrs150_mnz_24-4	yn 50-49A-MNZ-24-1	yn 50-49A-MNZ-24-2
rock type		mag-bio dyke	mag-bio dyke	amph-dol vnlt	amph-dol vnlt	amph-dol vnlt	amph-dol vnlt	ank-sid carbonatite	ank-sid carbonatite
^{143}Nd	µg/g	3310	3090	4720	2280	2460	2370	6090	11500
^{147}Sm	µg/g	293	313	525	421	322	293	1020	1870
^{151}Eu	µg/g	57.5	55.4	107	38.8	69.8	41.5	159	354
^{157}Gd	µg/g	174	163	136	62.5	117	56.3	419	1010
^{159}Tb	µg/g	15.2	14.6	5.40	2.25	4.78	1.75	29.1	73.1
^{163}Dy	µg/g	50.7	52.3	11.0	5.79	7.79	3.61	68.1	165
^{165}Ho	µg/g	5.18	5.26	0.92	0.69	0.604	0.30	4.61	12.3
^{167}Er	µg/g	6.10	5.85	0.90	1.08	0.701	0.46	4.11	12.6
^{169}Tm	µg/g	0.23	0.22	0.092	0.074	0.060	0.065	0.21	0.63
^{171}Yb	µg/g	0.67	0.62	0.40	0.27	0.30	0.33	0.63	2.37
^{175}Lu	µg/g	0.035	0.043	0.031	0.035	0.027	0.049	0.064	0.17
^{178}Hf	µg/g	0.038	0.057	0.051	0.037	0.50	0.68	bdl	0.031
^{181}Ta	µg/g	0.017	0.014	bdl	bdl	0.037	bdl	0.0229	0.014
^{208}Pb	µg/g	6.77	67.4	221	235	101	192	50.6	167
^{232}Th	µg/g	52.3	531	3650	2070	1320	2710	869	2340
^{238}U	µg/g	0.45	0.42	0.23	0.25	0.47	0.86	0.19	0.23
Detection Limit									
SiO_2	wt.%	3.33	3.74	3.96	3.75	3.83	4.50	9.15	5.76
TiO_2	wt.%	0.000829	0.00102	0.000807	0.000767	0.000749	0.000830	0.00266	0.00150
Al_2O_3	wt.%	0.00377	0.00447	0.00822	0.00769	0.00858	0.0111	0.0271	0.0186
MnO	wt.%	0.000260	0.000299	0.000320	0.000303	0.000331	0.000424	0.000602	0.000406
CaO	wt.%	0.0719	0.0859	0.0892	0.0805	0.0940	0.128	0.224	0.142
P_2O_5	wt.%	0.0196	0.0210	0.0240	0.0196	0.0225	0.0280	0.0721	0.0404
$^{6}6Zn$	µg/g	5.13	6.09	13.0	12.3	12.9	18.5	29.2	22.1
^{75}As	µg/g	5.16	5.95	11.8	10.1	11.8	14.6	19.9	14.5
^{85}Rb	µg/g	0.236	0.207	0.268	0.281	0.333	0.361	0.567	0.369
^{88}Sr	µg/g	0.0520	0.0845	0.199	0.173	0.204	0.260	0.245	0.164

File		leq130A_mnz-9	leq130A_mnz-10	lrs150_mnz_24-1	lrs150_mnz_24-2	lrs150_mnz_24-3	lrs150_mnz_24-4	yn 50-49A-MNZ-24-1	yn 50-49A-MNZ-24-2
rock type		mag-bio dyke	mag-bio dyke	amph-dol vnlt	amph-dol vnlt	amph-dol vnlt	amph-dol vnlt	ank-sid carbonatite	ank-sid carbonatite
^{89}Y	µg/g	0.086	0.129	0.260	0.233	0.271	0.349	0.245	0.140
^{90}Zr	µg/g	0.228	0.278	0.404	0.396	0.521	0.550	0.482	0.290
^{93}Nb	µg/g	0.0632	0.0263	0.0857	0.0337	0.0713	0.111	0.174	0.0450
^{118}Sn	µg/g	0.751	0.772	0.679	0.585	0.667	0.894	1.07	0.676
^{133}Cs	µg/g	0.0433	0.0277	0.0506	0.0446	0.0726	0.0864	0.115	0.0645
^{137}Ba	µg/g	0.226	0.337	0.120	0.280	0.299	0.556	0.778	0.559
^{139}La	µg/g	0.0235	0.0278	0.0492	0.0554	0.0542	0.0772	0.0732	0.0386
^{140}Ce	µg/g	0.0240	0.0123	0.0422	0.0508	0.0476	0.0486	0.0539	0.0156
^{141}Pr	µg/g	0.0233	0.0494	0.0341	0.0341	0.0329	0.0471	0.0489	0.0272
^{143}Nd	µg/g	0.259	0.0836	0.212	0.277	0.298	0.276	0.351	0.191
^{147}Sm	µg/g	0.0543	0.0676	0.334	0.165	0.0817	0.311	0.336	0.150
^{151}Eu	µg/g	0.0160	0.0459	0.0579	0.0678	0.0640	0.0753	0.0771	0.0389
^{157}Gd	µg/g	0.171	0.150	0.491	0.393	0.507	0.591	0.440	0.268
^{159}Tb	µg/g	0.0210	0.0095	0.0520	0.0520	0.0558	0.0539	0.0439	0.0379
^{163}Dy	µg/g	0.0858	0.0896	0.160	0.135	0.130	0.155	0.271	0.118
^{165}Ho	µg/g	0.00775	0.0185	0.0360	0.0312	0.0334	0.0528	0.0402	0.0294
^{167}Er	µg/g	0.104	0.131	0.127	0.129	0.155	0.188	0.178	0.0836
^{169}Tm	µg/g	0.0148	0.0177	0.0273	0.0278	0.0277	0.0463	0.0407	0.0249
^{171}Yb	µg/g	0.0539	0.154	0.205	0.252	0.223	0.267	0.296	0.168
^{175}Lu	µg/g	0.0241	0.0258	0.0489	0.0375	0.0446	0.0479	0.0477	0.0313
^{178}Hf	µg/g	0.0756	0.0889	0.127	0.0802	0.118	0.186	0.168	0.0972
^{181}Ta	µg/g	0.0221	0.0113	0.0343	0.0271	0.0398	0.0686	0.0448	0.0244
^{208}Pb	µg/g	0.0886	0.102	0.113	0.0801	0.116	0.110	0.257	0.186
^{232}Th	µg/g	0.0209	0.0246	0.0381	0.0241	0.0355	0.0328	0.0491	0.0363
^{238}U	µg/g	0.0168	0.0237	0.0271	0.0334	0.0300	0.0384	0.0593	0.0417

File		yn 50-49A-MNZ-24-3	yn 50-49A-MNZ-24-4	YW61-MNZ-24-1	YW61-MNZ-24-2	YW61-MNZ-24-3	YW61-MNZ-24-4	YW61-MNZ-24-5
rock type		ank-sid carbonatite	ank-sid carbonatite	mag-bio dyke	mag-bio dyke	mag-bio dyke	mag-bio dyke	mag-bio dyke
SiO_2	wt.%	bdl	bdl	bdl	bdl	bdl	bdl	bdl
TiO_2	wt.%	bdl	bdl	bdl	bdl	bdl	bdl	bdl
Al_2O_3	wt.%	bdl	bdl	bdl	bdl	bdl	bdl	bdl
MnO	wt.%	0.00049	bdl	bdl	bdl	bdl	bdl	bdl
CaO	wt.%	0.18	0.23	bdl	0.16	0.18	bdl	0.15
P_2O_5	wt.%	31.0	29.7	31.5	30.8	30.9	31.1	30.8
^{6}6Zn	µg/g	bdl	bdl	bdl	bdl	bdl	bdl	bdl
^{75}As	µg/g	318	359	292	318	358	367	356
^{85}Rb	µg/g	bdl	bdl	0.247	bdl	bdl	bdl	bdl
^{88}Sr	µg/g	2080	1440	1420	1800	627	1540	1890
^{89}Y	µg/g	2000	2300	3140	2780	2170	1050	1300
^{90}Zr	µg/g	0.91	1.24	1.00	1.00	1.01	0.97	1.25
^{93}Nb	µg/g	0.15	0.14	0.11	0.16	0.13	0.18	0.16
^{118}Sn	µg/g	bdl	bdl	bdl	bdl	bdl	bdl	bdl
^{133}Cs	µg/g	bdl	bdl	0.0690	bdl	bdl	0.0444	bdl
^{137}Ba	µg/g	14.1	25.7	17.9	13.9	3.44	25.4	43.0
^{139}La	µg/g	108000	104000	139000	125000	116000	121000	120000
^{140}Ce	µg/g	273339	273339	282830	282830	282830	282830	282830
^{141}Pr	µg/g	34500	35000	32100	34000	35800	36900	36700
^{143}Nd	µg/g	130000	134000	111000	120000	143000	138000	137000
^{147}Sm	µg/g	18500	18800	14400	14000	22300	15300	16000
^{151}Eu	µg/g	3730	3940	4290	3970	5130	3060	3180
^{157}Gd	µg/g	9890	9560	8580	7480	10600	5920	6190
^{159}Tb	µg/g	699	682	726	635	674	347	373
^{163}Dy	µg/g	1720	1690	2060	1840	1500	771	869
^{165}Ho	µg/g	119	125	165	147	103	53.6	65.9
^{167}Er	µg/g	111	130	174	153	99.4	51.8	68.9
^{169}Tm	µg/g	5.00	7.08	8.63	7.56	5.00	2.27	3.27

File		yn50-49A-MNZ-24-3	yn50-49A-MNZ-24-4	YW61-MNZ-24-1	YW61-MNZ-24-2	YW61-MNZ-24-3	YW61-MNZ-24-4	YW61-MNZ-24-5
rock type		ank-sid carbonatite	ank-sid carbonatite	mag-bio dyke	mag-bio dyke	mag-bio dyke	mag-bio dyke	mag-bio dyke
^{171}Yb	µg/g	15.6	20.9	25.8	20.2	16.1	6.94	9.16
^{175}Lu	µg/g	0.98	1.33	1.58	1.17	1.06	0.38	0.53
^{178}Hf	µg/g	0.085	0.086	0.064	bdl	0.083	0.061	bdl
^{181}Ta	µg/g	0.031	0.016	0.017	0.035	bdl	0.020	bdl
^{208}Pb	µg/g	2040	2520	403	669	1540	1380	1210
^{232}Th	µg/g	21700	26100	4260	7130	17000	17500	13400
^{238}U	µg/g	2.48	1.84	117	105	20.5	8.08	9.39
1σ Error								
SiO_2	wt.%	bdl	bdl	bdl	bdl	bdl	bdl	bdl
TiO_2	wt.%	bdl	bdl	bdl	bdl	bdl	bdl	bdl
Al_2O_3	wt.%	bdl	bdl	bdl	bdl	bdl	bdl	bdl
MnO	wt.%	0.00017	bdl	bdl	bdl	bdl	bdl	bdl
CaO	wt.%	0.061	0.062	bdl	0.054	0.057	bdl	0.049
P_2O_5	wt.%	0.63	0.70	0.77	0.60	1.63	0.83	0.86
^{6}6Zn	µg/g	bdl	bdl	bdl	bdl	bdl	bdl	bdl
^{75}As	µg/g	11.9	11.0	13.7	14.5	27.9	17.3	19.5
^{85}Rb	µg/g	bdl	bdl	0.104	bdl	bdl	bdl	bdl
^{88}Sr	µg/g	19.4	23.2	36.8	21.2	16.6	40.4	48.2
^{89}Y	µg/g	77.4	52.0	74.2	41.2	85.5	36.4	23.3
^{90}Zr	µg/g	0.15	0.18	0.14	0.18	0.19	0.14	0.18
^{93}Nb	µg/g	0.040	0.050	0.024	0.050	0.045	0.037	0.044
^{118}Sn	µg/g	bdl	bdl	bdl	bdl	bdl	bdl	bdl
^{133}Cs	µg/g	bdl	bdl	0.024	bdl	bdl	0.0179	bdl
^{137}Ba	µg/g	0.75	1.20	0.63	0.77	0.83	1.18	2.97
^{139}La	µg/g	2450	2300	3410	1760	6940	3840	3800
^{140}Ce	µg/g	8000	8260	8000	5350	18600	8620	10300
^{141}Pr	µg/g	766	981	748	397	2330	1150	1190

File		yn50-49A-MNZ-24-3	yn50-49A-MNZ-24-4	YW61-MNZ-24-1	YW61-MNZ-24-2	YW61-MNZ-24-3	YW61-MNZ-24-4	YW61-MNZ-24-5
rock type		ank-sid carbonatite	ank-sid carbonatite	mag-bio dyke	mag-bio dyke	mag-bio dyke	mag-bio dyke	mag-bio dyke
^{143}Nd	µg/g	2930	4220	2500	1290	9150	4460	4180
^{147}Sm	µg/g	353	572	352	182	1540	557	471
^{151}Eu	µg/g	79.4	132	103	51.8	305	107	70.4
^{157}Gd	µg/g	208	279	171	95.2	620	203	123
^{159}Tb	µg/g	17.3	23.5	16.1	9.13	32.9	12.2	7.17
^{163}Dy	µg/g	59.0	47.6	44.4	30.2	59.8	26.7	16.0
^{165}Ho	µg/g	4.96	3.28	3.97	2.70	3.48	1.79	1.24
^{167}Er	µg/g	5.65	3.34	4.06	2.42	2.78	1.79	1.43
^{169}Tm	µg/g	0.30	0.40	0.22	0.12	0.18	0.089	0.068
^{171}Yb	µg/g	1.18	0.56	0.58	0.63	0.41	0.31	0.33
^{175}Lu	µg/g	0.073	0.072	0.047	0.042	0.062	0.027	0.033
^{178}Hf	µg/g	0.030	0.029	0.021	bdl	0.022	0.019	bdl
^{181}Ta	µg/g	0.010	0.0094	0.0056	0.011	bdl	0.0077	bdl
^{208}Pb	µg/g	35.9	64.9	8.61	14.2	58.1	44.2	45.3
^{232}Th	µg/g	364	748	101	127	837	565	496
^{238}U	µg/g	0.12	0.053	2.27	2.06	0.61	0.27	0.18
Detection Limit								
SiO_2	wt.%	5.11	5.52	4.07	4.67	5.44	4.49	4.28
TiO_2	wt.%	0.00166	0.00127	0.000930	0.00140	0.00129	0.00110	0.00139
Al_2O_3	wt.%	0.0167	0.0151	0.0121	0.0163	0.0154	0.0135	0.0157
MnO	wt.%	0.000349	0.000340	0.000279	0.000368	0.000337	0.000292	0.000336
CaO	wt.%	0.120	0.113	0.0888	0.115	0.112	0.0906	0.104
P_2O_5	wt.%	0.0386	0.0350	0.0339	0.0426	0.0347	0.0315	0.0343
^{6}6Zn	µg/g	18.3	18.5	13.5	18.5	18.7	15.4	18.1
^{75}As	µg/g	11.8	11.4	9.19	13.3	12.0	10.7	11.8
^{85}Rb	µg/g	0.282	0.298	0.219	0.339	0.295	0.270	0.319
^{88}Sr	µg/g	0.124	0.118	0.108	0.142	0.107	0.079	0.135

File		yn50-49A-MNZ-24-3	yn50-49A-MNZ-24-4	YW61-MNZ-24-1	YW61-MNZ-24-2	YW61-MNZ-24-3	YW61-MNZ-24-4	YW61-MNZ-24-5
rock type		ank-sid carbonatite	ank-sid carbonatite	mag-bio dyke	mag-bio dyke	mag-bio dyke	mag-bio dyke	mag-bio dyke
^{89}Y	µg/g	0.117	0.135	0.102	0.131	0.144	0.103	0.124
^{90}Zr	µg/g	0.257	0.221	0.172	0.279	0.209	0.155	0.223
^{93}Nb	µg/g	0.0292	0.0386	0.0181	0.0699	0.0693	0.0172	0.0740
^{118}Sn	µg/g	0.614	0.597	0.479	0.590	0.609	0.473	0.554
^{133}Cs	µg/g	0.0588	0.0527	0.0405	0.0426	0.0605	0.0370	0.0571
^{137}Ba	µg/g	0.471	0.453	0.294	0.403	0.422	0.279	0.502
^{139}La	µg/g	0.0314	0.0421	0.0224	0.0354	0.0454	0.0319	0.0367
^{140}Ce	µg/g	0.0281	0.0376	0.0199	0.0391	0.0284	0.0202	0.0291
^{141}Pr	µg/g	0.0218	0.0252	0.0231	0.0224	0.0220	0.0229	0.0281
^{143}Nd	µg/g	0.148	0.166	0.0402	0.188	0.0800	0.104	0.132
^{147}Sm	µg/g	0.0517	0.0683	0.0316	0.0594	0.0628	0.0300	0.0436
^{151}Eu	µg/g	0.0155	0.0337	0.0199	0.0408	0.0435	0.0309	0.0131
^{157}Gd	µg/g	0.232	0.270	0.192	0.259	0.272	0.191	0.249
^{159}Tb	µg/g	0.0247	0.0285	0.0177	0.0304	0.0221	0.0224	0.0291
^{163}Dy	µg/g	0.0572	0.0844	0.0540	0.0798	0.0908	0.0701	0.0757
^{165}Ho	µg/g	0.00754	0.0190	0.0046	0.0178	0.0195	0.0136	0.0172
^{167}Er	µg/g	0.0847	0.0723	0.0429	0.0384	0.0781	0.0602	0.0672
^{169}Tm	µg/g	0.0136	0.0156	0.0255	0.0144	0.00874	0.00924	0.0120
^{171}Yb	µg/g	0.0987	0.0690	0.102	0.0599	0.135	0.104	0.118
^{175}Lu	µg/g	0.0233	0.0249	0.0192	0.0209	0.0281	0.0132	0.0287
^{178}Hf	µg/g	0.0834	0.0627	0.0592	0.0953	0.0739	0.0533	0.0616
^{181}Ta	µg/g	0.00838	0.0111	0.00511	0.0239	0.0234	0.0132	0.0208
^{208}Pb	µg/g	0.140	0.142	0.0962	0.141	0.128	0.0887	0.133
^{232}Th	µg/g	0.0268	0.0212	0.0242	0.0199	0.0319	0.0161	0.0240
^{238}U	µg/g	0.0354	0.0303	0.0227	0.0343	0.0302	0.0284	0.0243

File		LE1FN-MNZ-24-1	LE1FN-MNZ-24-2	LE1FN-MNZ-24-3	LE1FN-MNZ-24-4	LE1FN-MNZ-24-5	LE1FN-MNZ-24-6
rock type		fenite	fenite	fenite	fenite	fenite	fenite
SiO_2	wt.%	bdl	bdl	bdl	bdl	bdl	bdl
TiO_2	wt.%	bdl	bdl	0.0065	bdl	bdl	bdl
Al_2O_3	wt.%	0.040	0.55	0.42	bdl	bdl	0.0186
MnO	wt.%	0.00070	0.00075	0.0052	0.00039	0.0015	0.00099
CaO	wt.%	bdl	bdl	0.440	0.501	0.285	0.460
P_2O_5	wt.%	27.7	28.2	32.0	26.4	27.7	23.1
^{6}6Zn	µg/g	bdl	bdl	bdl	bdl	bdl	bdl
^{75}As	µg/g	523	543	562	418	447	415
^{85}Rb	µg/g	0.63	24.2	bdl	bdl	bdl	bdl
^{88}Sr	µg/g	609	919	7350	6550	1950	3200
^{89}Y	µg/g	1970	2710	1730	1290	1450	1180
^{90}Zr	µg/g	1.59	4.83	11.7	1.17	1.54	4.04
^{93}Nb	µg/g	3.51	20.5	539	0.678	0.977	1.32
^{118}Sn	µg/g	bdl	bdl	bdl	bdl	bdl	bdl
^{133}Cs	µg/g	bdl	0.192	bdl	0.0362	bdl	bdl
^{137}Ba	µg/g	21.0	186	156	57.5	77.8	222
^{139}La	µg/g	62300	55200	50300	55000	61200	52800
^{140}Ce	µg/g	216736	216736	216736	216736	216736	216736
^{141}Pr	µg/g	38700	40000	41200	36700	35900	35300
^{143}Nd	µg/g	193000	198000	208000	164000	164000	162000
^{147}Sm	µg/g	35700	37400	34500	22000	26700	24000
^{151}Eu	µg/g	6210	7450	6850	4300	5140	4310
^{157}Gd	µg/g	16500	17600	14000	7920	11700	9700
^{159}Tb	µg/g	913	1030	790	431	658	529
^{163}Dy	µg/g	1780	2100	1600	899	1270	1010
^{165}Ho	µg/g	107	133	101	62.6	74.5	62.0
^{167}Er	µg/g	90.2	120	96.3	65.3	64.3	56.3
^{169}Tm	µg/g	3.79	5.63	5.05	3.73	3.16	2.91

File		LE1FN-MNZ-24-1	LE1FN-MNZ-24-2	LE1FN-MNZ-24-3	LE1FN-MNZ-24-4	LE1FN-MNZ-24-5	LE1FN-MNZ-24-6
rock type		fenite	fenite	fenite	fenite	fenite	fenite
^{171}Yb	µg/g	12.8	20.7	19.0	13.6	10.3	10.3
^{175}Lu	µg/g	0.70	1.53	1.38	0.94	0.82	0.79
^{178}Hf	µg/g	0.17	0.20	0.70	0.077	bdl	0.15
^{181}Ta	µg/g	0.033	0.081	0.48	0.027	0.041	0.041
^{208}Pb	µg/g	1850	1910	5080	5500	3740	4290
^{232}Th	µg/g	17400	20400	48700	52200	36000	52000
^{238}U	µg/g	6.78	11.2	90.9	40.5	4.94	24.2
1σ Error							
SiO_2	wt.%	bdl	bdl	bdl	bdl	bdl	bdl
TiO_2	wt.%	bdl	bdl	0.0015	bdl	bdl	bdl
Al_2O_3	wt.%	0.011	0.082	0.028	bdl	bdl	0.0064
MnO	wt.%	0.00023	0.00032	0.00093	0.00012	0.00031	0.00025
CaO	wt.%	bdl	bdl	0.075	0.078	0.071	0.064
P_2O_5	wt.%	0.51	2.61	0.95	0.63	1.64	0.55
^{6}6Zn	µg/g	bdl	bdl	bdl	bdl	bdl	bdl
^{75}As	µg/g	18.8	67.8	24.8	14.6	35.7	11.6
^{85}Rb	µg/g	0.26	3.09	bdl	bdl	bdl	bdl
^{88}Sr	µg/g	22.5	31.8	279	347	263	354
^{89}Y	µg/g	31.5	259	49.9	14.3	97.0	18.1
^{90}Zr	µg/g	0.271	0.814	1.74	0.156	0.254	1.07
^{93}Nb	µg/g	0.311	3.83	35.3	0.18	0.17	0.59
^{118}Sn	µg/g	bdl	bdl	bdl	bdl	bdl	bdl
^{133}Cs	µg/g	bdl	0.0462	bdl	0.0128	bdl	bdl
^{137}Ba	µg/g	1.74	21.2	3.50	3.29	11.1	14.9
^{139}La	µg/g	1430	5290	1380	1130	4520	1770
^{140}Ce	µg/g	5730	21900	9880	6680	16600	9630
^{141}Pr	µg/g	682	4120	1060	991	2530	1020

File		LE1FN-MNZ-24-1	LE1FN-MNZ-24-2	LE1FN-MNZ-24-3	LE1FN-MNZ-24-4	LE1FN-MNZ-24-5	LE1FN-MNZ-24-6
rock type		fenite	fenite	fenite	fenite	fenite	fenite
^{143}Nd	µg/g	3660	20000	4800	4490	10300	4344
^{147}Sm	µg/g	711	3900	853	814	1610	706
^{151}Eu	µg/g	144	826	132	161	330	105
^{157}Gd	µg/g	290	2020	427	283	686	300
^{159}Tb	µg/g	8.15	110	16.2	13.7	39.7	9.00
^{163}Dy	µg/g	17.8	208	42.2	21.3	77.9	13.5
^{165}Ho	µg/g	1.64	12.3	2.35	1.03	4.67	0.82
^{167}Er	µg/g	2.20	10.8	2.97	1.20	4.38	0.89
^{169}Tm	µg/g	0.11	0.42	0.17	0.097	0.25	0.15
^{171}Yb	µg/g	0.35	1.63	0.90	0.54	0.91	0.42
^{175}Lu	µg/g	0.047	0.124	0.12	0.052	0.086	0.047
^{178}Hf	µg/g	0.067	0.063	0.21	0.024	bdl	0.038
^{181}Ta	µg/g	0.012	0.033	0.038	0.012	0.019	0.012
^{208}Pb	µg/g	19.1	105	163	165	345	250
^{232}Th	µg/g	259	1000	1240	1890	4680	2850
^{238}U	µg/g	0.24	0.50	3.55	1.52	0.11	0.81
Detection Limit							
SiO_2	wt.%	7.64	8.46	8.66	4.01	5.22	4.79
TiO_2	wt.%	0.00182	0.00182	0.00271	0.00104	0.00165	0.00150
Al_2O_3	wt.%	0.0224	0.0243	0.0239	0.0122	0.0170	0.0137
MnO	wt.%	0.000498	0.000549	0.000549	0.000254	0.000363	0.000309
CaO	wt.%	0.180	0.189	0.197	0.0933	0.123	0.109
P_2O_5	wt.%	0.0528	0.0515	0.0571	0.0253	0.0356	0.0281
^{6}6Zn	µg/g	28.2	27.2	31.7	16.2	21.1	18.7
^{75}As	µg/g	18.4	20.3	18.8	8.83	13.4	10.8
^{85}Rb	µg/g	0.496	0.503	0.495	0.275	0.338	0.326
^{88}Sr	µg/g	0.212	0.195	0.250	0.113	0.143	0.146

File		LE1FN-MNZ-24-1	LE1FN-MNZ-24-2	LE1FN-MNZ-24-3	LE1FN-MNZ-24-4	LE1FN-MNZ-24-5	LE1FN-MNZ-24-6
rock type		fenite	fenite	fenite	fenite	fenite	fenite
^{89}Y	µg/g	0.193	0.206	0.243	0.0876	0.144	0.116
^{90}Zr	µg/g	0.357	0.315	0.447	0.176	0.274	0.246
^{93}Nb	µg/g	0.0634	0.103	0.0955	0.0259	0.0414	0.0998
^{118}Sn	µg/g	0.808	0.869	0.907	0.398	0.563	0.571
^{133}Cs	µg/g	0.0852	0.0741	0.108	0.0356	0.0551	0.0530
^{137}Ba	µg/g	0.624	0.633	0.741	0.334	0.452	0.398
^{139}La	µg/g	0.0593	0.0552	0.0652	0.0206	0.0448	0.0398
^{140}Ce	µg/g	0.0375	0.0178	0.0567	0.0175	0.0261	0.0173
^{141}Pr	µg/g	0.0318	0.0369	0.0547	0.0150	0.0255	0.0299
^{143}Nd	µg/g	0.318	0.339	0.402	0.169	0.168	0.199
^{147}Sm	µg/g	0.224	0.178	0.252	0.0887	0.0713	0.136
^{151}Eu	µg/g	0.0627	0.0595	0.0495	0.0228	0.0344	0.0470
^{157}Gd	µg/g	0.434	0.371	0.422	0.205	0.304	0.243
^{159}Tb	µg/g	0.0390	0.0439	0.0543	0.0183	0.0288	0.0282
^{163}Dy	µg/g	0.112	0.0532	0.0971	0.0713	0.0860	0.0970
^{165}Ho	µg/g	0.0328	0.0314	0.0368	0.0177	0.0193	0.0241
^{167}Er	µg/g	0.108	0.139	0.187	0.0693	0.0946	0.0883
^{169}Tm	µg/g	0.0440	0.0248	0.0230	0.0149	0.0159	0.0218
^{171}Yb	µg/g	0.110	0.231	0.290	0.0893	0.159	0.137
^{175}Lu	µg/g	0.0335	0.0404	0.0478	0.0179	0.0283	0.0232
^{178}Hf	µg/g	0.125	0.116	0.151	0.0728	0.0843	0.0784
^{181}Ta	µg/g	0.0176	0.0346	0.0406	0.0172	0.0213	0.0219
^{208}Pb	µg/g	0.209	0.207	0.212	0.0983	0.132	0.115
^{232}Th	µg/g	0.0391	0.0288	0.0424	0.0192	0.0278	0.0248
^{238}U	µg/g	0.0429	0.0449	0.0524	0.0200	0.0299	0.0250

Additional Materials

Publications (formatted in respective journal style):

Slezak, P., Spandler, C., and Blake, K. (2018) Ghosts of Apatite Past: Using Hyperspectral CL and Micro-geochemical Data to Reveal Multi-generational Apatite in the Gifford Creek Carbonatite Complex, Australia. *Canadian Mineralogist* **56(5),** 773-779. https://doi.org/10.3749/canmin.1800021

Slezak, P., Spandler, C., 2019. Carbonatites as recorders of mantle-derived magmatism and subsequent tectonic events: An example of the Gifford Creek Carbonatite Complex, Western Australia. Lithos 328-329, 212-227. https://doi.org/10.106/j.lithos.2019.01.028

The Canadian Mineralogist
Vol. 56, pp. 773-797 (2018)
DOI: 10.3749/canmin.1800021

GHOSTS OF APATITE PAST: USING HYPERSPECTRAL CATHODOLUMINESCENCE AND MICRO-GEOCHEMICAL DATA TO REVEAL MULTI-GENERATIONAL APATITE IN THE GIFFORD CREEK CARBONATITE COMPLEX, AUSTRALIA

PAUL SLEZAK[§] AND CARL SPANDLER

Department of Geoscience, James Cook University, Townsville, Queensland 4811 Australia

KEVIN BLAKE

Advanced Analytical Centre, James Cook University, Townsville, Queensland 4811 Australia

ABSTRACT

Apatite can host significant levels of trace elements, including REE, within its crystal lattice, making it particularly useful for deciphering geological events and processes. This study employs hyperspectral cathodoluminescence (CL) and *in situ* microchemical techniques to identify and characterize various generations of apatite occurring in the phoscorites, carbonatites, and fenites of the Gifford Creek Carbonatite Complex (GCCC), Western Australia. Hyperspectral CL revealed that apatite crystals in all samples have complex internal zoning, including multiple distinct generations, with zones of relatively bright CL generally having more complex spectra compared to darker CL zones. Most of the CL spectra have prominent sharp peaks at ~1.4 eV and ~2.1 eV as well as a broad peak between 2.3 eV and 3.5 eV. We relate these different peaks to individual REE activators and groups of activators, in particular Nd^{3+}, Eu^{3+}, Sm^{3+}, and Ce^{3+}.

Trace element analyses of apatite confirm the relative enrichment of REE in the CL brighter zones. Most apatite generations exhibit concave-down to sinusoidal REY patterns lacking Eu anomalies, but often feature distinct negative Y anomalies. The depletion in LREE is interpreted to be due to LREE sequestration into monazite, which is relatively abundant in most of the samples. Most apatite samples contain very low Si contents, but appreciable Na, so REE incorporation into apatite was primarily *via* a coupled substitution of REE + Na replacing 2Ca, which is consistent with the highly alkaline, low SiO_2 environment under which the apatite formed. Based on the combined trace-element signatures and CL textures, we interpret the multiple generations of apatite to reflect magmatic growth from alkaline magmas followed by recrystallization during subsequent metamorphic/hydrothermal events. The notable exception is the apatite core domains from a fenite sample that contain relatively high Si and Mn contents, low Sr, and relatively HREE-enriched REY patterns with distinct negative Eu anomalies. This apatite is interpreted to be relict from the granitic precursor to fenitization.

The apatite samples also show systematic compositional variations across the GCCC, with apatite from phoscorite samples from the southeast part of the complex containing higher Sr, lower Gd/Ce, and lower λ_3 values (normalized REE pattern inflections) compared to apatite from the northwest part of the complex. Recognition of these spatial variations in apatite compositions from the intra-grain micro-scale through to the district scale demonstrates the utility of combining advanced petrographic methods, such as hyperspectral CL, with micro-chemical analysis to reveal complex geological records preserved in apatite. As apatite is a common accessory mineral, these techniques may be more broadly applicable to igneous source tracing, understanding metamorphic and/or metasomatic processes, provenance studies from detrital mineral records, and studies of the evolution of ore systems.

Keywords: apatite, hyperspectral, cathodoluminescence, rare earth elements, phoscorite, carbonatite, Gifford Creek Carbonatite Complex.

[§] *Corresponding author e-mail address*: paul.slezak@my.jcu.edu.au

Introduction

Apatite [$Ca_5(PO_4)_3(OH,Cl,F)$] is a common accessory mineral in many rock types as well as a significant biogenic mineral in teeth and bone. The crystal structure of apatite allows numerous substitutions, including Na, Mn, Y, REE, As, Si, F, Cl, OH^-, and CO_3^{2-}, as well as the radioactive tracers Sr, U, Pb, and Nd (Pan & Fleet 2002, Hughes & Rakovan 2015). Apatite also readily undergoes recrystallization during post-formation hydrothermal alteration (Harlov & Förster 2003, Harlov 2015). This susceptibility to recrystallization together with an affinity for trace elements means that apatite geochemistry has great potential to monitor geological processes and events. In particular, radiogenic isotope ratios of apatite can be used to determine crystallization ages, modal ages, and source rock compositions (De Paolo 1981, Nelson & De Paolo 1985). In addition, the REE geochemistry of apatite can be used to decipher the environment and conditions of mineral formation and recrystallization.

The incorporation of REE into the apatite crystal lattice can occur *via* the following coupled substitutions (Portnov & Gorobets 1969, Roeder *et al*. 1987, Rønsbo 1989, Hughes *et al*. 1991, Fleet & Pan 1995, Mitchell *et al*. 1997, Cherniak 2000, Chen *et al*. 2002, Pan & Fleet 2002):

$$REE^{3+} + Si^{4+} = Ca^{2+} + P^{5+} \quad (1)$$

$$REE^{3+} + Na^{+} = 2Ca^{2+} \quad (2)$$

$$2REE^{3+} + \square = 3Ca^{2+} \quad (3)$$

$$REE^{3+} + O^{2-} = Ca^{2+} + F^{-} \quad (4)$$

where $\square$ corresponds to a site vacancy. At the individual grain scale, these substitutions may manifest as zoning or growth textures related to either primary apatite formation or recrystallization during secondary metamorphic or hydrothermal events. These secondary events may also present themselves as dissolution–reprecipitation of apatite to form a new generation of apatite and/or other minerals (e.g., monazite or xenotime; Pan et al. 1993, Pan 1997, Harlov & Förster 2003, Harlov 2015). Careful documentation of these textural features can provide insights to the causative geological events, provided the textures are appropriately interpreted with respect to the whole-rock phase petrology; in this case, detailed study of each apatite phase is required.

Cathodoluminescence (CL) is electromagnetic radiation emission produced by electron excitation of luminescent material (Marshall 1988, Pagel *et al*. 2000, Waychunas 2002, Götze *et al*. 2013). Cathodoluminescence can reveal hidden or cryptic textures in luminescent minerals that normally appear homogenous with optical microscopy or backscattered electron (BSE) imaging (Marshall 1988, Pagel *et al*. 2000, Waychunas 2002, Götze 2012, Götze *et al*. 2013). Apatite is among the more luminescent rock-forming minerals due to its capacity to incorporate REE and Mn into its crystal structure, elements that are considered to be the primary cause of luminescence in many minerals (Marshall 1988, Mitchell *et al*. 1997, Pagel *et al*. 2000, Waychunas 2002, Gaft *et al*. 2015). Additionally, apatite may luminesce due to defects in the crystal structure, which hereafter is referred to as "intrinsic" luminescence after MacRae & Wilson (2008). This luminescent character of apatite means that CL imaging can be used in complement to optical petrography, BSE, or element concentration mapping to delineate the micro-scale textural and chemical zoning in apatite.

Optical microscope CL and some SEM-CL setups operate in the visible spectrum. However, many minerals, especially apatite, emit luminescent bands in the ultraviolet (UV) and near-infrared (NIR) spectra, which are not normally visible to the human eye. Hyperspectral CL mapping with false color overlays gives the benefit of allowing one to visualize UV and NIR spectral data (MacRae *et al*. 2005, 2012, 2013, Edwards *et al*. 2007, Edwards & Lee 2014). For example, hyperspectral CL mapping was used to identify and help quantify Nd^{3+} in apatite, which occurs in the NIR spectrum (MacRae *et al*. 2012). Nevertheless, application of these techniques to natural apatite samples is in its infancy, and further work is required to better understand the geochemical/crystallographic controls on CL signatures of natural apatite for various geological settings.

In this study, we undertook hyperspectral CL mapping in combination with *in situ* geochemical analyses (*e.g*., WDS EPMA and LA-ICP-MS) of apatite from the Gifford Creek Carbonatite Complex (GCCC) in Western Australia. Our study focuses on multiple generations of apatite formed under different magmatic/hydrothermal conditions, with the primary goal of reaching a better understanding of trace element incorporation into—and the corresponding CL response of—apatite from alkaline magmatic/hydrothermal environments. The findings of this study have broad implications for REE mobility, Sm-Nd isotope systematics, and potential mechanisms for increasing ore tenor in REE deposits.

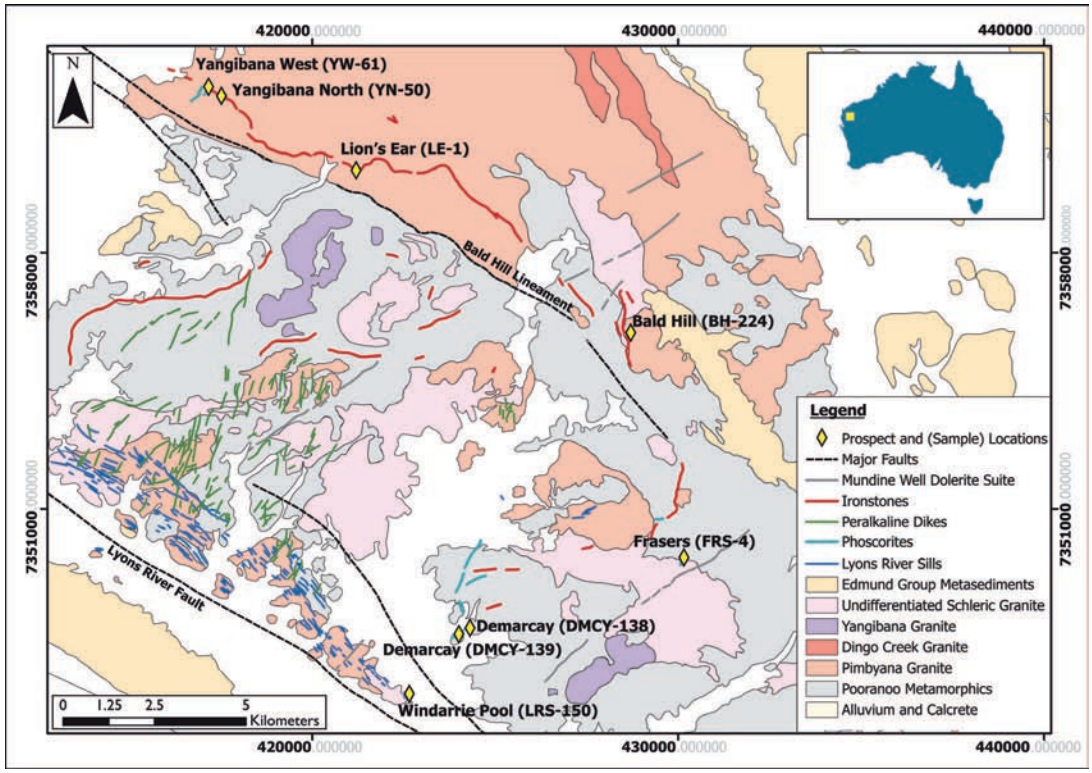

FIG. 1. Geologic map of the Gifford Creek Carbonatite Complex (modified from Pearson 1996).

GEOLOGIC SETTING AND SAMPLE DESCRIPTION

The Gifford Creek Carbonatite Complex (GCCC) is located in the Proterozoic Gascoyne Province of Western Australia (Fig. 1). The GCCC primarily consists of series or swarms of narrow dikes, sills, and veins that cut Mesoproterozoic metasedimentary and granitic rocks of the Pooranoo Metamorphics and Durlacher Supersuite, respectively. They also cut the Neoproterozoic Edmund Group metasediments that unconformably overlay the Mesoproterzoic rocks. Emplacement of the GCCC was controlled by regional faults such as the Lyons River Fault and the Bald Hill Lineament (Fig. 1; Pearson *et al*. 1996, Sheppard *et al*. 2010). Age determinations for the GCCC span a wide range from 1380 to 900 Ma based on U-Th-Pb dating of zircon and monazite (Slezak & Spandler 2016, Zi *et al*. 2017); this age range covers the initial onset of alkaline magmatism and multiple metamorphic and tectonic events, such as the Mutherbukin Tectonic Event (1320 to 1170 Ma; Korhonen *et al*. 2015), the Warakurna Large Igneous Province (*ca.* 1076 Ma; Wingate *et al*. 2004), and the Edmundian Orogeny (1030 to 950 Ma; Sheppard *et al*. 2007).

This area is of economic interest, as dikes/sills located along the Bald Hill Lineament and in the southeastern part of the complex (Fig. 1) contain significant resources of LREE (particularly Nd and Pr) totaling 21 million tonnes of ore at 1.17% total rare earth oxides (Hastings Technology Metals Limited 2017). The LREE are hosted mainly in monazite and apatite (Pirajno *et al*. 2014), and there is a distinct spatial variation in the REE ore compositions, with orebodies in the northwest part of the GCCC (along the Bald Hill Lineament; Fig. 1) having lower Nd/La values than those in the southeast (Fig. 2).

The GCCC consists of four primary rock types: (1) dolomitic carbonatites (also known as the Lyons River Sills); (2) peralkaline dikes; (3) phoscorites; and (4) ferrocarbonatites. Associated with these four main rock types are fenitized wall rocks ("fenites") and magmatic-hydrothermal veins that emanate from carbonatite dikes/sills. Weathered and oxidized surface outcrops of the four main rock types form "ironstones" (Fig. 1) rich in Fe-oxides and hydroxides, Fe-rich carbonates, and quartz. Although the precise protolith of each ironstone unit is difficult to ascertain, these rocks are of economic interest, as they are the main

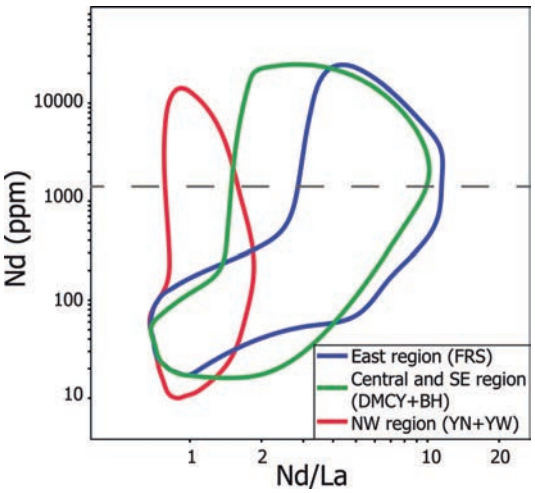

FIG. 2. Neodymium *versus* Nd/La of ore samples from the Gifford Creek Carbonatite Complex. Note the variation in ore composition with location across the GCCC, with ore samples from the northwest of the complex (Yangibana North: YN and Yangibana West: YW) having relatively low Nd/La values compared to ore samples from the center (Bald Hill: BH) and southeast (Demarcay: DMCY) of the complex, which in turn have lower Nd/La than ores from the easternmost (Frasers: FRS) regions of the complex. The dashed gray line is the minimum ore grade cut off. Ore composition fields were constructed from 15,272 analyses of drill core provided by Hastings Technology Metals Ltd.

host of REE mineralization. Detailed descriptions of all of these rock types will be presented in a companion paper (Slezak *et al*. in prep.). Here we present geochemical and textural analyses of apatite from eight rock samples: three phoscorites samples collected from outcrop (DMCY-138, DMCY-139, FRS-4), two phoscorite samples and one ferrocarbonatite sample taken from drill core (YW-61, BH-224, and YN-50, respectively), one sample of a magmatic-hydrothermal vein (LRS-150) taken from surface outcrop, and one sample taken from a surface outcrop of fenite adjacent to an "ironstone" (LE-1). These samples were selected for their apatite size, abundance, and proximity to the LREE deposits.

Phoscorites

The phoscorites form thin (0.1 to 1.5 m) dikes and sills throughout the field area, but are most abundant in the southeast and northwest corners of the complex, around the Demarcay/Frasers and Yangibana West prospects, respectively (Fig. 1). The phoscorites are seriate to equigranular in texture and are composed of biotite (phlogopite–annite series), magnetite, apatite, and monazite, although proportions of apatite and monazite vary greatly. Mineralogy and locations of the samples examined here are presented in Table 1 and Figure 1. Apatite is a major constituent of all of the samples and, generally, is present as large (up to 500 μm) anhedral to euhedral grain aggregates or clots. These apatite clots often contains inclusions of monazite and magnetite. In places, apatite grains are cut by small veinlets and fractures filled with iron oxides. The biotite ranges in size from 100 μm to 2 mm and often features radiation damage from included monazite. Biotite may be present as euhedral coarse grains or as an interstitial phase to the apatite and magnetite (*e.g.*, sample DMCY-139). Magnetite tends to be anhedral to subhedral (except sample FRS-4, where magnetite is euhedral) and may be up to 500 μm in size. Magnetite is variably altered to hematite along grain margins. Monazite is present in all samples and occurs both as large (up to 1 mm) anhedral to euhedral crystals, either individually or as splayed clusters of crystals, and as small ($<$10 μm) inclusions within the apatite. Minor amounts of late-stage quartz and iron oxides (most likely hematite and goethite) are occasionally present as infill between the magnetite, biotite, and phosphate minerals. These are considered post-magmatic alteration phases. Additional mineral phases include minor amounts of ragged and irregular potassium feldspar grains in sample BH-224, which likely represent entrained grains from the fenitized host rock, and fine ($\sim$10 μm) blebs of aegirine in sample FRS-4.

Ferrocarbonatites

Fresh ferrocarbonatites are only found as 5 cm veins to 1 m thick dikes at depth in drill core along the Bald Hill Lineament (Fig. 1). The veins and dikes are mantled by fenitic potassium feldspar alteration of the host granitic and metasedimentary rocks. Sample YN-50 is a ferrocarbonatite taken from drill core from the Yangibana North prospect. The main rock constituent is macro-crystalline ($>$2 mm) subhedral to euhedral siderite that transitions to finer-grained ankerite (20 to 200 μm) and then calcite (20 to 200 μm) proximal to a phosphate-silicate enclave found within the sample. The enclave is composed of magnetite, biotite, monazite, apatite, quartz, and trace plagioclase. Euhedral magnetite and biotite occur together along the contact between the carbonates and the enclave and range in size from 50 to 250 μm. Quartz crystals are typically large ($>$1000 μm), but have recrystallized along the grain margins as revealed by undulatory extinction. Apatite occurs as small anhedral to subhedral crystals (200 to 500 μm in length) that are

TABLE 1. LOCATION, ROCK TYPE, AND MINERALOGY OF THE SAMPLES ANALYZED IN THIS STUDY

Sample #	Rock type	Nearest prospect	Latitude	Longitude	Primary mineralogy (in order of abundance)
DMCY-139	Phoscorite	Demarcay	424026	7347653	Mag, Ap, Bio, Mnz
DMCY-138	Phoscorite	Demarcay	424026	7347653	Bio, Ap, Mag, Mnz, Qtz
FRS-4	Phoscorite	Frasers	430083	7349554	Mag, Aeg, Qtz, Hem, Mnz, Ap, Bio
BH-224	Phoscorite	Bald Hill	428503	7355090	Bio, Mag, Kfs, Ap, Mnz
YW-61	Phoscorite	Yangibana West	416152	7363045	Mag, Bio, Mnz, Ap
YN-50	Carbonatite	Yangibana North	417402	7362065	Sid, Ank, Bio, Mag, Mnz, Qtz, Ap, Kfs
LRS-150	Magmatic-hydrothermal vein	Windarrie Pool*	422586	7345898	Rbk, Arf, Rt, Dol, Qtz, Ap, Mag, Mnz
LE-1	Fenite	Lion's Ear	419997	7360600	Kfs, Qtz, Ap, Mnz, Hem, Zrn

Notes: Locations are recorded in UTM zone 51. Bio = biotite, Mag = magnetite, Mnz = monazite, Ap = apatite, Qtz = quartz, Aeg = aegirine, Rbk = riebeckite, Arf = arfvedsonite, Rt = rutile, Sid = siderite, Ank = ankerite, Cal = calcite, Dol = dolomite, Kfs = potassium feldspar, Hem = hematite, Zrn = zircon. Abbreviations from Whitney & Evans (2010). *Not a prospect, location name taken from Pearson (1996).

proximal to monazite, which itself occurs as large (up to 500 μm) lathlike crystals. Monazite is often found in the quartz, but in some cases the laths extend beyond the silicate enclave into the carbonate domain.

Magmatic-hydrothermal veins

The dolomitic carbonatite sills (known as the Lyon River Sills) that crop out to the northeast of the Lyons River Fault (Fig. 1) often have thin (typically 0.3 to 2 cm wide) veins that emanate from the sill into the fenitized wall rock over a distance of several tens of meters. These veins (referred to herein as magmatic-hydrothermal veins) have distinct pink potassium feldspar alteration halos that extend 1 cm to 3 cm outward from the veins. The magmatic-hydrothermal vein sample studied here (LRS-150) is composed of fine, feathery rutile (crystal masses up to 500 μm) and fine, fibrous riebeckite–arfvedsonite (crystal masses up to 2 mm) with lesser amounts of Fe-dolomite (100 to 200 μm in size) and iron oxides, mainly euhedral to subhedral magnetite (~100 μm in size) partly altered to hematite. Subhedral quartz (up to 200 μm) and

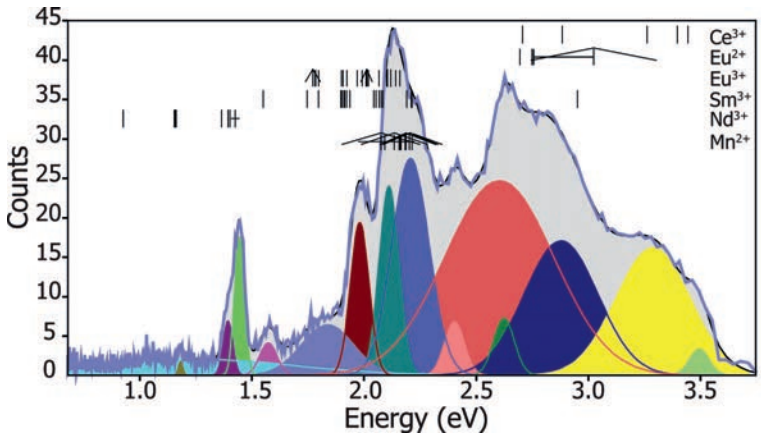

FIG. 3. A deconvoluted hyperspectral CL curve for the mottled pink and purple zones in the apatite from LE-1, constructed using the Optical Fit 17.07 software from CSIRO (Torpy & Wilson 2008). The total curve (purple) comprises the sum of Gaussian distributed peaks (multiple colors) of possible CL activators present across the energy spectra. Thin vertical lines indicate single activator locations. Thin horizontal lines indicate an activator present over a range of band values, and triangular hats depict the full width at half maximum (FWHM) for an activator (where data are available). The locations of the apatite activators are taken from MacRae & Wilson (2008) and references therein. More activators are present in apatite, but only these were shown in the interest of simplicity.

euhedral apatite (100 to 500 μm) are present, as are trace amounts of anhedral monazite as small (<100 μm) inclusions within the rutile and riebeckite–arfvedsonite.

Fenites

The phoscorites, ironstones, carbonatites, and related magmatic-hydrothermal veins are enveloped by K-rich fenite zones within the host metasedimentary or granitic rocks. The widths of the fenite zones are commensurate with the size of the dikes and veins (*i.e.*, 1 to 2 m dikes tend to have distinct fenite halos of 2 to 3 m width, while a 1 cm vein will tend to have a 1 to 3 cm fenite halo).

Sample LE-1 is fenite taken from an alteration zone of precursor granite around an ironstone dike near the Lions Ear prospect (Fig. 1). Sample LE-1 is primarily composed of potassium feldspar with lesser amounts of plagioclase, apatite, monazite, quartz, zircon, and hematite. Most of the primary plagioclase has been altered to ragged, irregular potassium feldspar grains that range in size from 20 to 300 μm. The quartz is mostly fine-grained (<50 μm) and exhibits undulose extinction and extensively recrystallized grain boundaries. The apatite grains are relatively large (500 μm in length) and are subhedral to euhedral in form. Monazite (up to 200 μm) occurs throughout the sample as interstitial grains to potassium feldspar, as fracture fillings, and as small inclusions (10 to 20 μm) in apatite. Hematite is present as veinlets that cross-cut the sample. Accessory zircon with oscillatory zoning is also present in this sample.

Methods

All samples were prepared as polished thin sections and 25 mm diameter polished pucks which contained the rock offcuts for the polished thin sections. Both thin sections and polished pucks were examined using a Leica DMRXP optical microscope. The apatite grains hosted in the rock samples (mounted in the polished pucks) were then analyzed *in situ* by electron probe microanalysis (EPMA) and laser ablation inductively coupled plasma mass spectrometry (LA-ICP-MS) at the Advanced Analytical Centre at James Cook University, Townsville, Australia.

In order to ascertain the nature of the apatite in each sample, a large region, usually 1.5 × 1.5 mm, was scanned using hyperspectral cathodoluminescence according to the methods described below to determine the luminescent nature of the apatites (*e.g.*, heterogeneity or homogeneity of spectra). Following this, higher-resolution CL scans were obtained from two to three individual apatite grains. One image and corresponding CL spectra for each sample that best illustrate the overall textures observed are presented in Figures 5–12.

Cathodoluminescence (CL) analyses of apatite were obtained using a JEOL XM-86440 CL spectrometer connected to the JEOL JXA-8200 EPMA *via* a 200 μm optic fiber cable. The effective wavelength range of the spectrometer is 350 to 1200 nm (*i.e.*, 3.54 to 1.03 eV). At >1200 nm the signal-to-noise ratio is too high for meaningful interpretation (MacRae *et al.* 2005). Samples were mapped *in situ* using a 1 to 5 μm spot size and 1 to 5 μm step (depending on apatite size) with a dwell time of 20 to 50 μm per spot. The beam was set to 20 kV and 20 nA. These data were compiled into raster images and then into RGB false-color images using the xCLent software from CSIRO and Chimage software, respectively (Harrowfield *et al.* 1993). Wavelength spectra for the different zones within the apatite were obtained using the XCL-image software. Deconvolution of these spectra was conducted using the Optical Fit 17.07 software from CSIRO (Fig. 3; Torpy & Wilson 2008). Each CL spectrum is considered to be the sum of a number of CL peaks with Gaussian distributions produced by the presence of CL activators. The Optical Fit software is used to approximate a "best fit" to the CL spectrum by assuming Gaussian peak profiles and matching peak locations to known activator band locations for apatite from the CSIRO luminescence database (Fig. 3; MacRae & Wilson 2008).

After CL analysis the samples were polished to remove the top few micrometers of the exposed surface of the samples in order to avoid potential electron beam damage from the previous analysis (see below). The samples were then carbon-coated again and analyzed for major/minor elements using a JEOL JXA-8200 WD/ED combined electron probe microanalyzer. Analysis locations were selected in various CL zones across multiple apatite grains within the regional CL maps acquire for each sample. The beam was set to a 2 to 5 μm spot size with an accelerating voltage of 15 kV and a current of 20 nA. All elements were analyzed for 20 s on peak with 10 s on background, except for F and Sr, which were analyzed using 40 s on peak with 20 s on background and 30 s on peak with 15 s on background, respectively. Element concentrations were quantified using well-characterized in-house standards as follows: Ca and Si (wollastonite), Na (albite), P and Ce ($CePO_4$), Nd ($NdPO_4$), F and Sr (SrF_2), and Cl (tugtupite). Analyses were then subject to a ZAF matrix correction procedure for data quantification, as it best fit our data due to the substantial levels of REE in some apatites.

The analysis of halogens in apatite is highly dependent on crystal orientation and electron beam

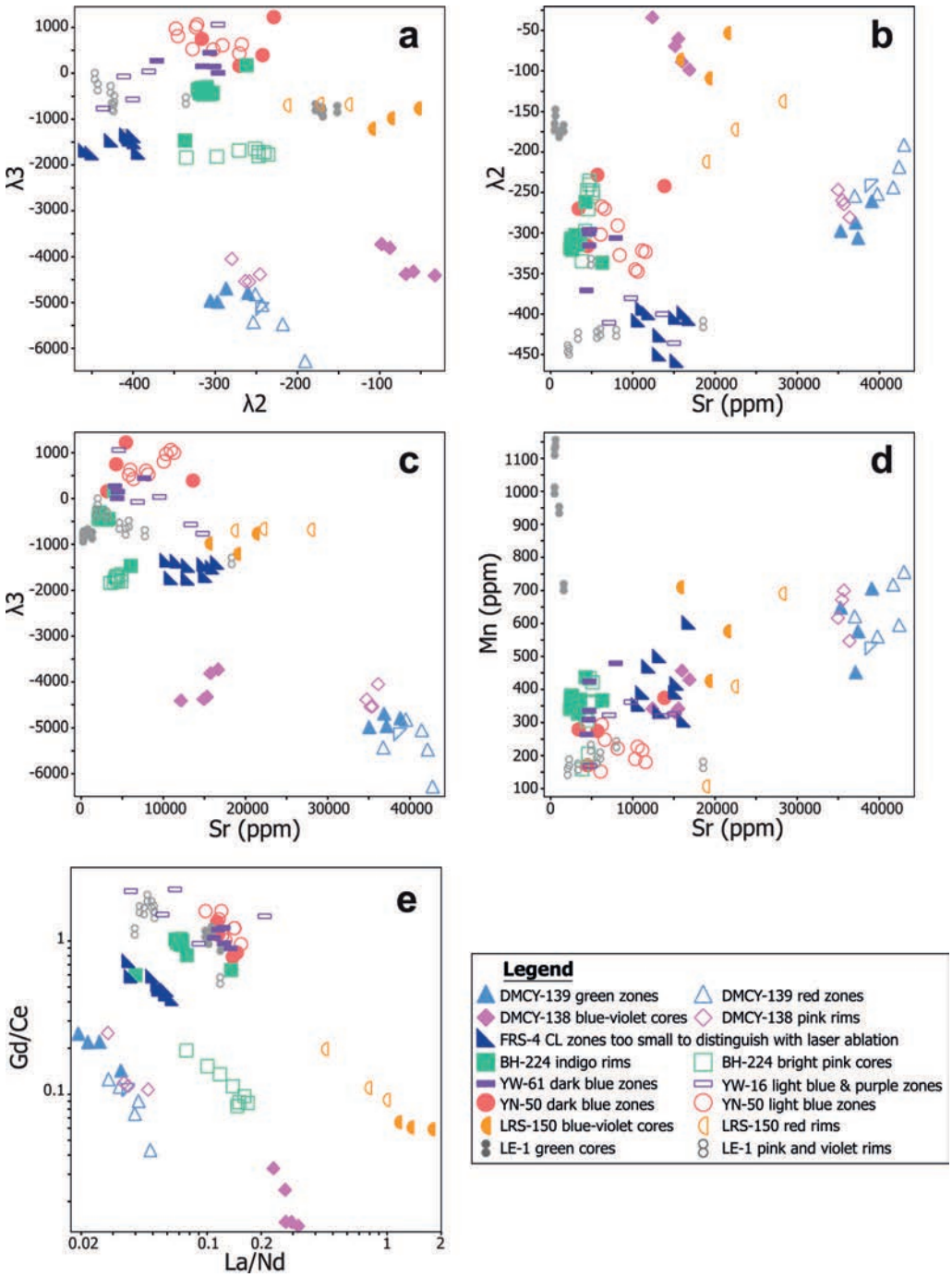

FIG. 4. Trace element characteristics of apatite from the GCCC. (a) REE compositional parameters λ_2 *versus* λ_3 of apatite. Definitions of λ_2 and λ_3 are outlined in O'Neill (2016). Both DMCY phoscorite samples from the southeastern region have low λ_3 values compared to other samples from this study. The blue-violet cores from DMCY-138, the green cores from fenite sample LE-1, and the magmatic-hydrothermal apatite from LRS-150 have relatively high λ_2 values. (b) Sr *versus* λ_2 of apatite. Apatites from the southeastern part of the GCCC (DMCY-138, DMCY-139, and LRS-150) have the highest Sr

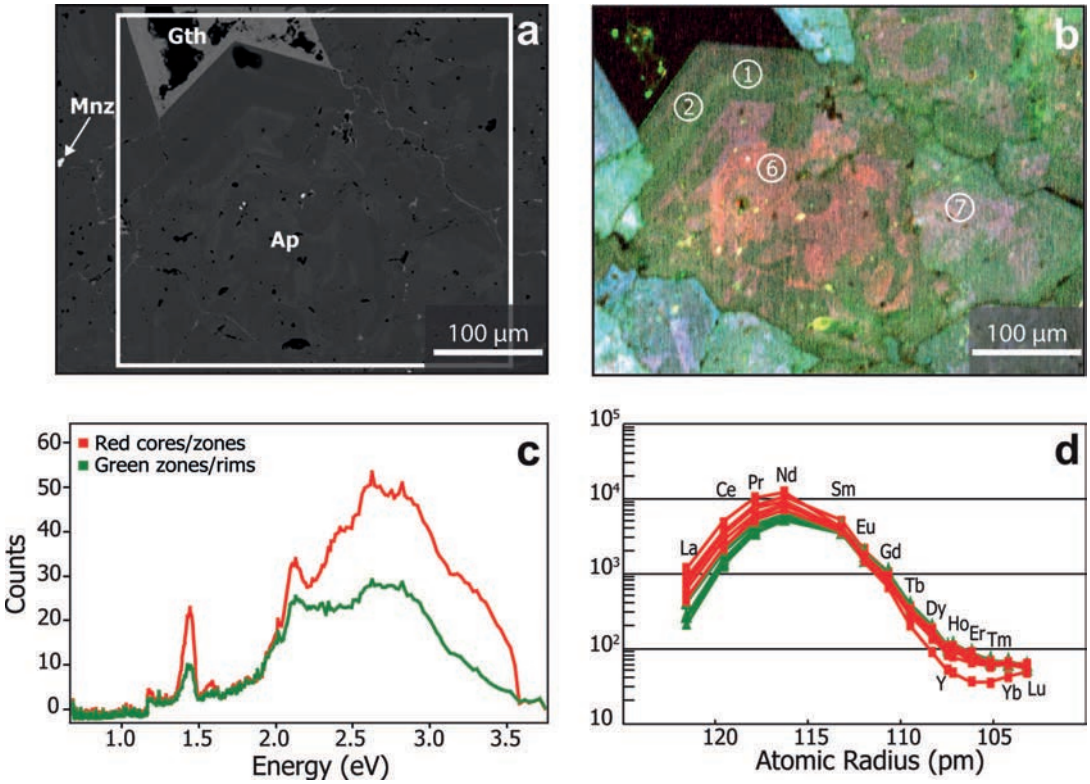

FIG. 5. (a) Backscattered electron image of apatite from the phoscorite sample DMCY-139. (b) Hyperspectral CL image of apatite showing zonation and internal variation, possibly from dissolution, in the apatite grain. Circles and numbers denote laser sampling locations (Appendix B) and sample number present in this image. Circles are actual spot size. (c) CL spectra of the apatite in (b). The red zones have slightly higher count rates and a more pronounced shoulder from 3.1 to 3.5 eV. The line colors of the spectra correlate to the apatite color in (b). (d) Chondrite-normalized REY patterns for both CL zones. Colors correspond to CL in (b). There is overlap in the zones, indicating only slight variations in REY content. Mineral abbreviations can be found in Table 1. Chondrite values are from McDonough & Sun (1995) and REY are plotted according to atomic radii assuming a coordination number of nine for apatite.

exposure. Fluorine in particular is susceptible to migration in the apatite crystal lattice due to exposure to an electron beam (Stormer *et al*. 1993, Pyle *et al*. 2002). For example, X-ray counts of F in apatite tend to increase substantially when F is analyzed by an electron beam parallel to the **c** axis of the crystal (Stormer *et al*. 1993, Goldoff *et al*. 2012). This migration of F can lead to erroneous values greater than 1.0 *apfu* or 3.77 wt.% F in fluorapatite (Pyle *et al*. 2002, Chakhmouradian *et al*. 2017). To monitor and correct for potential F migration during analysis, F counts were recorded with analysis time using a chart recorder. These time-resolved data were then used to extrapolate back to the F counts at time zero, as stipulated by Stormer & Pierson (1993), McCubbin *et al*. (2010), and Goldoff *et al*. (2012). The zero-intercept value was used as the raw F count rate for the

←

FIG. 4. (continued) values. (c) λ_3 *versus* Sr of apatite. Note the high Sr and low λ_3 of the phoscorite samples from the southeastern part of the GCCC. (d) Sr *versus* Mn concentration of apatite. The green CL apatite cores from the fenite (LE-1) have low Sr and high Mn, whereas apatite from the southeast phoscorite from the southeastern part of the complex has high Sr and moderate Mn contents. (e) Gd/Ce *versus* La/Nd of apatite. Samples from the southeastern region of the GCCC and the bright apatite cores from Bald Hill (BH-224) have much lower Gd/Ce ratios than the other samples.

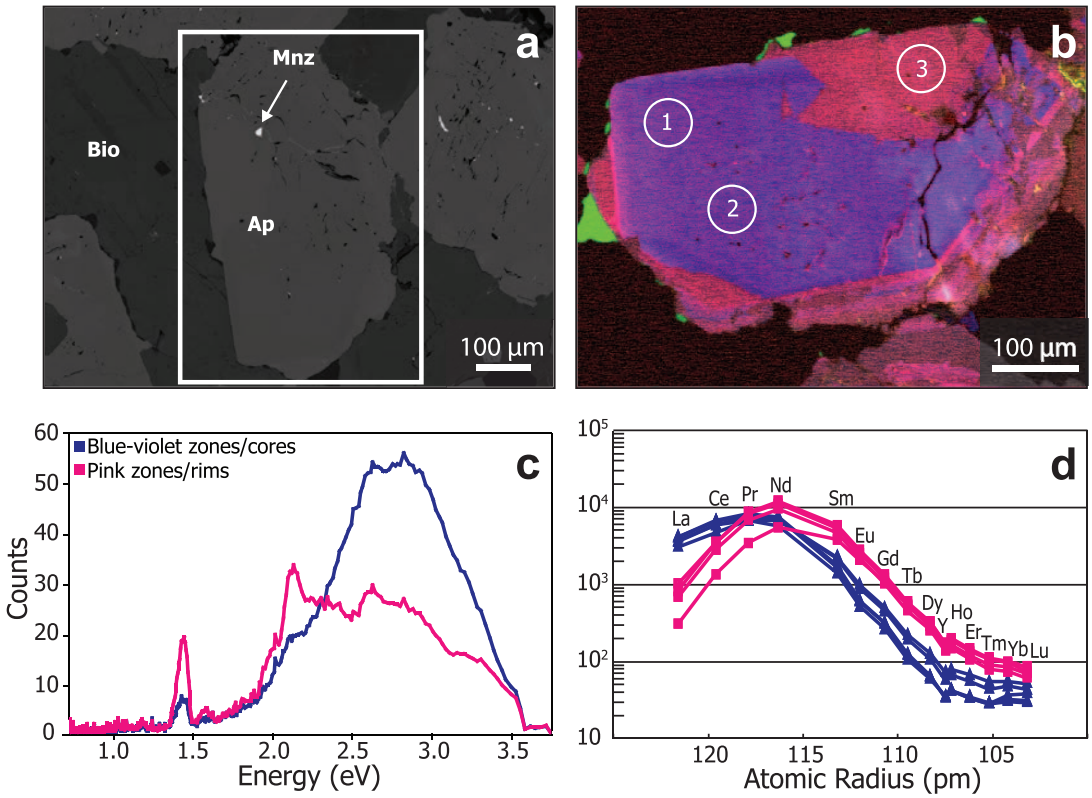

FIG. 6. (a) Backscattered electron image of apatite from the phoscorite sample DMCY-138. (b) Hyperspectral CL image of apatite highlighting zonation. Circles and numbers denote laser sampling location and sample number present in this image. Circles are actual spot size. (c) CL spectra of the apatite in (b). The bright pink rim has higher counts near 1.4 and 2.1 eV. The blue-violet core has higher counts, from 2.5 to 3.5 eV. The line colors of the spectra correlate to the apatite color in (b). (d) Chondrite-normalized REY patterns for both CL zones. Colors correspond to CL in (b). The blue-violet core is enriched in La and Ce whereas the pink rim is enriched in the REY from Nd to Lu. See Figure 5 for details on mineral abbreviations and REY plot style.

analysis prior to ZAF correction to calculated final element concentration values.

Transmitted light, CL images, and the EPMA WDS spot locations were used to determine suitable areas for trace element spot analysis by LA-ICP-MS. For each sample, multiple apatite crystals and their correlating CL zones were analyzed using laser spot analyses. As laser spot analyses also sample at depth, Sr and REE counts were monitored during data reduction and the appropriate signal intervals were selected according to each CL zone analyzed with EPMA and based on our CL images. Trace element analyses were conducted using a Coherent GeoLasPro 193 nm Excimer laser coupled to a Varian (now Bruker) 820-MS quadrupole ICP-MS. Laser spot sizes varied from 24 to 44 µm depending on the size of the target apatite zone. Samples were ablated using a surface energy density of 4 J/cm^2, as measured at the ablation site, and a repetition rate of 10 Hz. The rate of oxide production and plasma fractionation was monitored by keeping ThO/Th to around 0.5% and ^{238}U/^{232}Th sensitivity ≈ 1, respectively. The synthetic glasses NIST SRM 610 and 612 were used as the primary and secondary standards, respectively, with reference values taken from Spandler *et al*. (2011). The Ca content as determined by EPMA WDS was used as an internal standard, and data reduction was carried out using the SILLS program (Guillong *et al*. 2008). The error and detection limit were calculated in SILLS using the methods from Luo *et al*. (2007) and Pettke *et al*. (2012), respectively. The following isotopes were chosen for analysis: ^{27}Al, ^{31}P, ^{43}Ca,

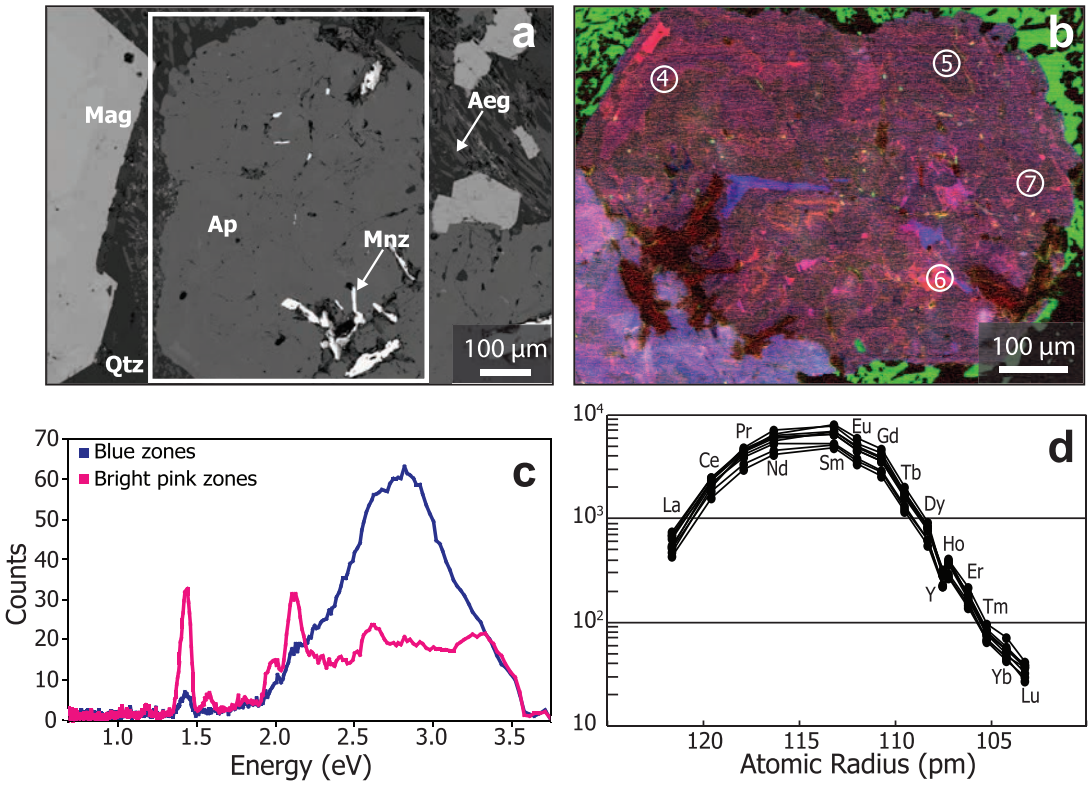

FIG. 7. (a) Backscattered electron image of apatite from the phoscorite sample FRS-4. (b) Hyperspectral CL image of apatite revealing complex internal structure. Circles and numbers denote laser sampling locations and sample numbers present in this image. Circles are actual spot size. (c) CL spectra of the apatite in (b). The bright pink zones have higher counts at peaks near 1.4, 2.0, and 2.1 eV. The blue-violet cores have higher counts from 2.3 to 3.3 eV. The line colors of the spectra correlate to the apatite color in (b). (d) Chondrite-normalized REY patterns for the apatite sample. See Figure 5 for details of mineral abbreviations and REY plot style.

^{44}Ca, ^{49}Ti, ^{55}Mn, ^{66}Zn, ^{75}As, ^{85}Rb, ^{88}Sr, ^{89}Y, ^{90}Zr, ^{93}Nb, ^{118}Sn, ^{133}Cs, ^{137}Ba, ^{139}La, ^{140}Ce, ^{141}Pr, ^{143}Nd, ^{147}Sm, ^{151}Eu, ^{157}Gd, ^{159}Tb, ^{163}Dy, ^{165}Ho, ^{167}Er, ^{169}Tm, ^{171}Yb, ^{175}Lu, ^{178}Hf, ^{181}Ta, ^{208}Pb, ^{232}Th, and ^{238}U.

Our examination of REE data utilizes standard chondrite-normalized REY plots, as well as the methods introduced by O'Neill (2016), who fitted polynomial equations to REE patterns and arranged the data in orthogonal form such that the coefficients of the equations (expressed as λ_n) represent a shape of the normalized REE pattern. O'Neill (2016) defined five coefficients that can be used to effectively describe the shape of REE patterns: λ_0 describes the overall height of the REE pattern (*i.e.*, the average concentration of REE); λ_1 describes the slope of the REE pattern; λ_2 describes the quadratic curvature of the REE pattern; λ_3 describes the inflections at either end of the REE patterns; and λ_4 describes the W-shape of the pattern. Analysis of our REE data revealed that λ_2 and λ_3 were effective at illustrating the differences across the apatite samples in this study (Fig. 4).

RESULTS

Cathodoluminescence and REY patterns

One of the advantages of hyperspectral CL over other CL methods is the ability to apply a false-color overlay to the measured CL spectra, including UV and NIR wavelengths. Red, green, and blue colors can be applied over specific CL wavelengths in order to highlight changes in peak position and intensity. In this study, red was mapped to the wavelengths ~830 to 930 nm (*i.e.*, 1.49 to 1.33 eV), green was mapped to ~525 to 650 nm (*i.e.*, 2.36 to 1.91 eV), and blue was mapped to ~350 to 500 nm (*i.e.*, 3.54 to 2.48 eV).

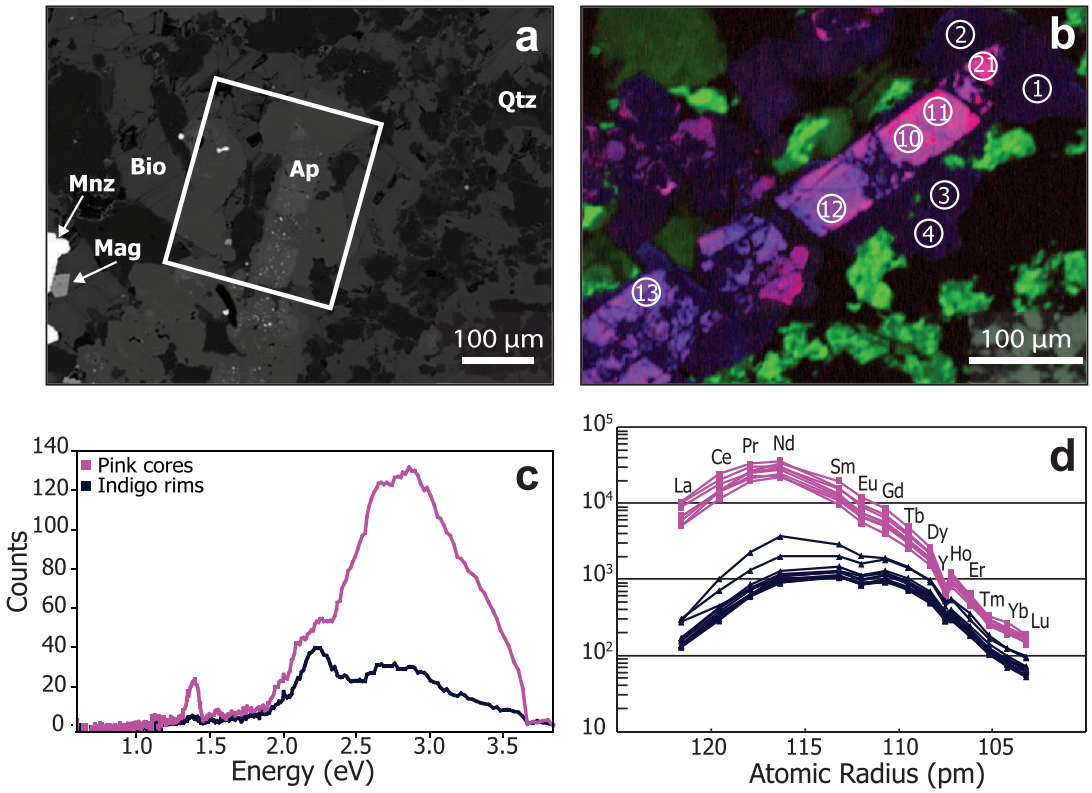

FIG. 8. (a) Backscattered electron image of apatite from the phoscorite sample BH-224. (b) Hyperspectral CL image of apatite showing bright pink cores with dark indigo rims. Circles and numbers denote laser sampling locations and sample numbers present in this image. Circles are actual spot size. (c) CL spectra of the apatite in (b). The bright pink core has much higher counts over the entire spectra compared to the dark indigo rim. The line colors of the spectra correlate to the apatite color in (b). (d) Chondrite-normalized REY patterns for both CL zones. Colors correspond to CL in (b). The pink core is enriched in the REY compared to the darker, indigo zone. See Figure 5 for details on mineral abbreviations and REY plot style.

"Brighter" zones refer to the longer wavelengths and correlate to the reds, pinks, and lighter color shades, and "darker" zones refer to the observed deep blues, greens, and indigos.

Overall, the CL spectra of the brighter zones show more peaks, greater peak intensity, and more complex spectra (Table 2). The darker zones (greens and blues) display spectra that have fewer, less intense peaks than the pink to light purple zones. Accordingly, the overall REE + Y contents for the brighter CL zones tend to be higher than for the CL dark zones.

Phoscorite sample DMCY-139. Backscattered electron imaging reveals two distinct domains of apatite in sample DMCY-139 (Fig. 5a). The inner cores of the apatite grains are colored bright red/pink in CL (using the RGB coding in this study). Although some aspects of the primary oscillatory zoning can be observed (Fig. 5b), much of this apatite phase is heavily embayed. The red core zones are mantled by CL green-colored apatite, which also exhibits distinct oscillatory zoning. Both the darker green and brighter red zones have comparable CL spectra; however, the red zones have more distinct peaks (*e.g.*, ~1.4, ~2.1, near 3.5 eV) of greater intensity (Fig. 5c; Table 2).

Chondrite-normalized REY patterns for both of these apatite domains feature a sinusoidal shape with an inflection from concave downward between La to Eu to concave upward from Gd to Lu (Fig. 5d), giving distinctly low λ_3 values (O'Neill 2016; Fig. 4a). The two domains have similar REY patterns and similar CL peak patterns, although the darker, green CL zones have slightly lower LREE contents (and lower CL peak heights) than the brighter, red CL zones.

Phoscorite sample DMCY-138. Apatite grains from sample DMCY-138 show nearly uniform BSE signals (Fig. 6a). Nevertheless, hyperspectral CL reveals two distinct apatite generations: (1) blue-violet core zones and (2) bright pink rim zones that mantle the cores and

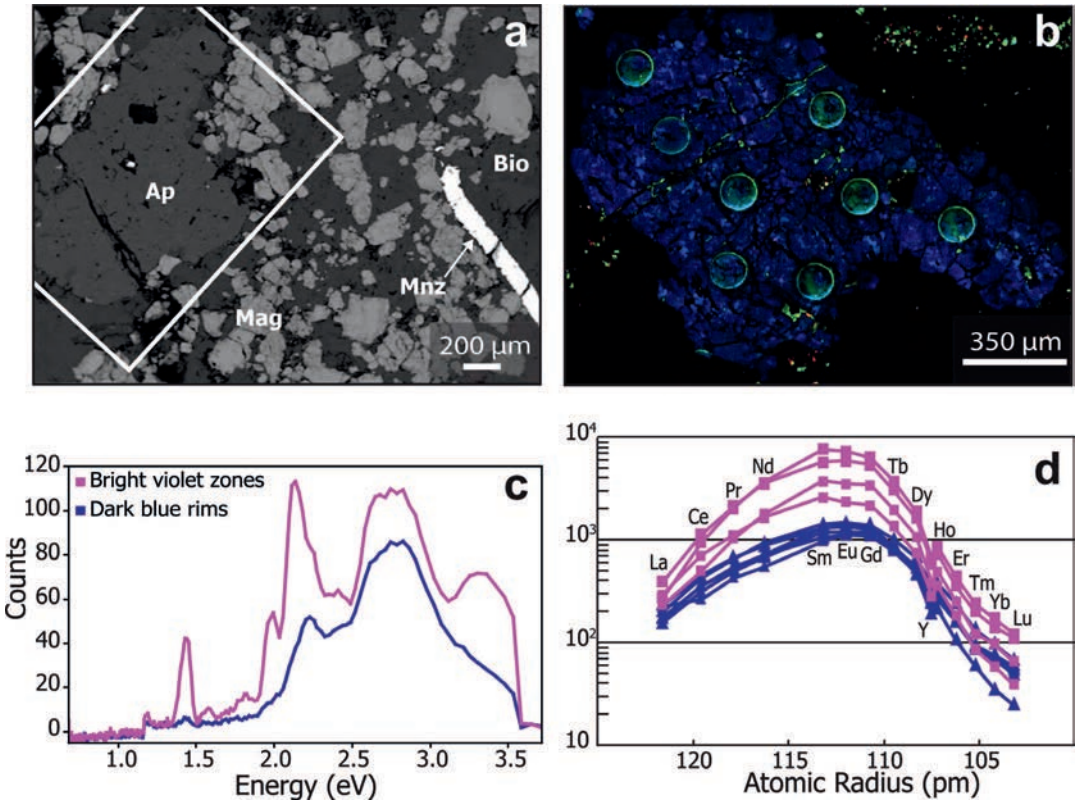

FIG. 9. (a) Backscattered electron image of apatite from the phoscorite sample YW-61. (b) Hyperspectral CL image of apatite showing internal zonation. Bubbles are laser spots for LA-MC-ICP-MS analyses for Sm-Nd isotopes. Trace element analyses were obtained from other apatites with the same CL spectra within the same rock sample. (c) CL spectra of the apatite in (b). The light violet zones have overall higher counts than the dark blue zones. The line colors of the spectra correlate to the apatite color in (b). (d) Chondrite-normalized REY patterns for both CL zones. Colors correspond to CL in (b). The light violet cores are enriched in all REY. See Figure 5 for details of mineral abbreviations and REY plot style.

occasionally display oscillatory zoning (Fig. 6b). The darker, blue-violet cores have relatively simple CL spectra with a small peak at 1.35 to 1.48 eV and a very wide and tall peak extending from 2.3 to 3.6 eV (Fig. 6c; Table 2). The pink zones have distinct CL spectra with taller peaks at 1.35 to 1.48 eV and around 2.1 eV but with shorter and wider peaks in the 2.3 to 3.6 eV range (Fig. 6c; Table 2).

As with sample DMCY-139, both apatite zones have sinusoidal REY patterns with inflections near Nd, low λ_3 values (Fig. 4a), and small, negative Y anomalies (Fig. 6d). The pink CL zones are enriched in the elements Sm to Lu but are relatively depleted in La and Ce compared to the blue-violet CL zones.

Phoscorite sample FRS-4. Despite a fairly homogeneous BSE response (Fig. 7a), CL analysis of apatite from FRS-4 reveals a wispy and mottled texture composed of bright pink zones swirled with darker, purple zones (Fig. 7b). Also present are bright pink zones with oscillatory zoning that are interpreted to be relict primary apatite and some discrete blue zones found in the center of the apatite grains (*e.g.*, Fig. 7b). The blue zone and the bright pink zones appear to be luminescent endmembers of the wispy, mottled pink and purple apatite textures.

Regarding CL spectra, the blue zones display a small peak from 1.35 to 1.48 eV and a tall, wide peak from 2.3 to 3.6 eV. The bright pink zones have more peaks that are distinct in their CL spectra (Fig. 7c; Table 2), with higher intensity peaks at approximately 1.4, 1.6, 2.0, and 2.2 eV. By contrast, the blue zones have greater peak intensities from 2.3 to 3.3 eV.

We could not determine the trace-element concentrations of the luminescent endmember apatite zones due to their complex nature and small size. The mottled (mixed?) zone has a strongly concave-

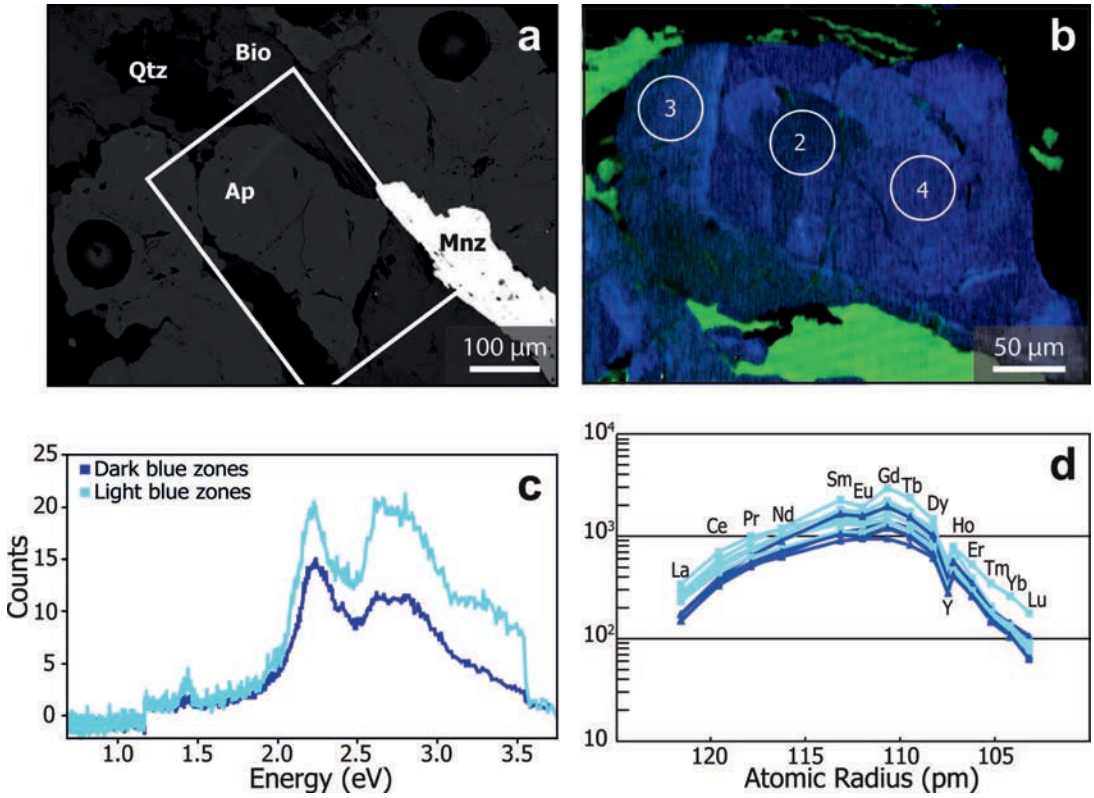

FIG. 10. (a) Backscattered electron image of apatite from the ferrocarbonatite sample YN-50. Dark bubbles are laser spots for LA-MC-ICP-MS analyses for Sm-Nd isotopes. (b) Hyperspectral CL image of apatite showing minor zonation and slight internal variation in the apatite grain. Circles and numbers denote laser sampling locations and sample numbers present in this image. Circles are actual spot size. (c) CL spectra of the apatite in panel (b). The light blue zones have slightly higher count rates; however, the overall counts for this sample are extremely low compared to other samples in this study. The line colors of the spectra correlate to the apatite color in (b). (d) Chondrite-normalized REY patterns for both CL zones. Colors correspond to CL in (b). There is some overlap in the zones, indicating only slight variations in REY content.

downward REY pattern (*i.e.*, low λ_2 values; Fig 4a) with the apex of the curve between Nd and Sm (Fig. 7d).

Phoscorite sample BH-224. Apatite grains in this sample contain core zones with monazite inclusions (~10 µm) mantled by BSE-darker, monazite-free apatite (Fig. 8a). The monazite-bearing core zones are bright pink in their CL response. The core zones are elongated and euhedral but appear to be fragmented and broken (Fig. 8b). The darker BSE apatite zones are a dark indigo color under CL. The bright pink zones have greater peak intensities, and more complex spectra, compared to the darker indigo zones that have simple spectra (*i.e.*, only two main peaks at 2.2 and 2.7 eV). The bright pink zones also feature a large peak centered at 2.5 to 2.7 eV that has multiple shoulders on either side (Fig. 8c; Table 2).

The REY patterns for the bright and dark CL zones both have concave-downward patterns, with the apex around Nd, and higher λ_3 values than the samples from the Demarcay prospect described above. However, the brighter, pink CL zones are distinctly enriched in LREE compared to the indigo zones (Fig. 8d). Both zones have a distinct negative Y anomaly.

Phoscorite sample YW-61. Much of the apatite in sample YW-61 appears homogenous in optical microscope and BSE images (Fig. 9a). By contrast, CL imaging reveals a heterogeneous texture within apatite grains and clusters. Small (<40 µm wide) light blue and lavender zones of apatite mottle the more common dark blue apatite zones (Fig. 9b). The dark blue zones display simpler CL spectra compared to the brighter, lavender zones. The lavender zones have many more distinct peaks (*e.g.*, the peaks at 1.35 to 1.48 eV and

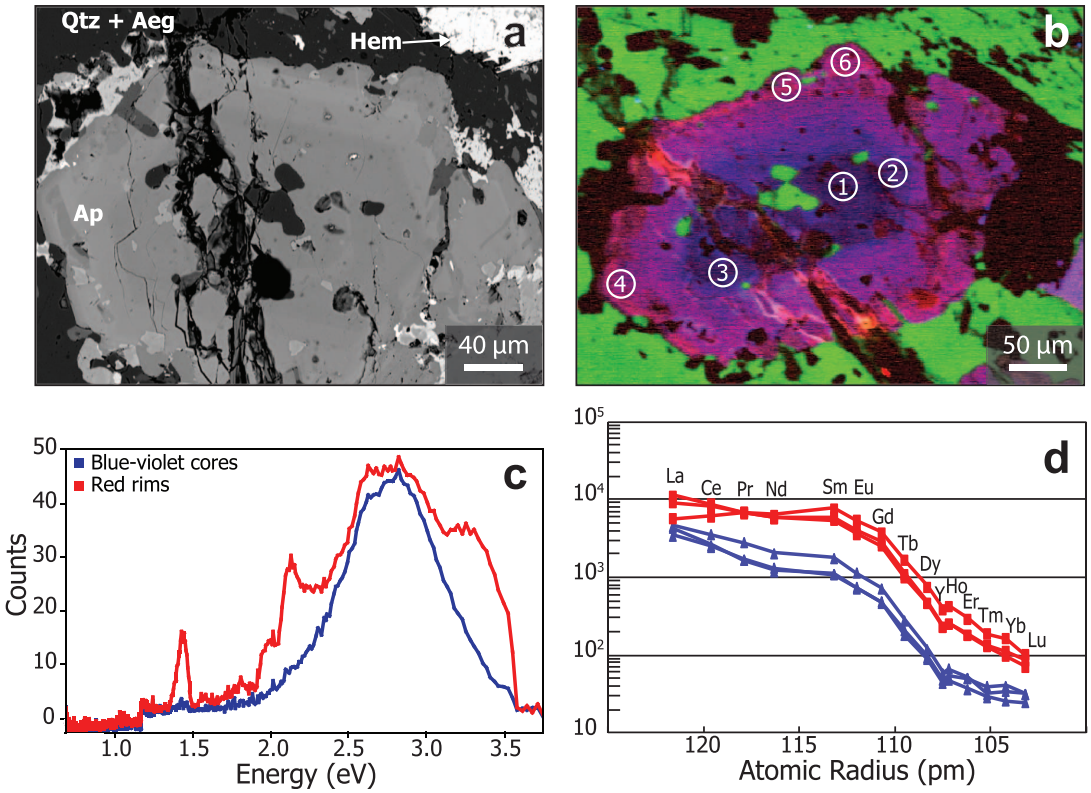

FIG. 11. (a) BSE images of apatite from the magmatic-hydrothermal vein sample (LRS-150; mineral abbreviations can be found in Table 1). (b) Hyperspectral CL image of apatite depicting zonation from a dark blue-violet core to a brighter pink/red rim. Circles and numbers denote laser sampling locations and sample numbers present in this image. Circles are actual spot size. (c) CL spectra of the apatite in (b). The red/pink rims have many more peaks (*e.g.*, 1.4 eV) compared to the darker, blue-violet core. The line colors of the spectra correlate to the apatite color in (b). (d) REY-normalized pattern for both CL. Colors correspond to CL in (b). The red rims are enriched in all REY compared to the darker blue-violet cores.

1.75 to 1.85 eV) with much higher counts (Fig. 9c; Table 2).

The dark blue and brighter violet CL zones share similar overall REY pattern shapes. Both zones display REY patterns that are concave downward with an apex centered on Eu, and both zones have a distinct negative Y anomaly (Fig. 9d) and high λ_3 values. The brighter lavender zones, however, are more enriched in REY, especially LREE and MREE, compared to the dark blue zones.

Ferrocarbonatite sample YN-50. The apatite in the ferrocarbonatite sample YN-50 has dark blue and light blue CL signals, based on the RGB color scheme used in this study. The texture of these apatite grains can be described as mottled, with minor growth rims (Fig. 10a, b). This dark blue apatite has two broad peaks: one from 2.1 to 2.5 eV with a small shoulder at 2.4 eV and another from 2.5 to 3.1 eV. The light blue zones display a slight increase in the relative peak intensities and exhibit more peaks than the dark blue zones (Fig. 10c; Table 2).

The REY patterns for the YN-50 apatite are concave-downward with the apex of the curve near Gd and a small negative Y anomaly (Fig. 10d). These patterns are similar in shape to those of phoscorite sample YW-61, but overall have a flatter shape and are not as HREE-depleted (*i.e.*, higher λ_2 and λ_3 than YW-61). Furthermore, the YN-50 apatite REY patterns also show a slight negative Eu anomaly. The light blue CL zones are slightly enriched in REY compared to the darker blue zones, but the differences are not as distinct when compared to other samples.

Magmatic-hydrothermal vein sample LRS-150. Apatite grains from the magmatic-hydrothermal vein (sample LRS-150; Fig. 11a) show a distinct CL color transition from dark blue-violet cores to bright red

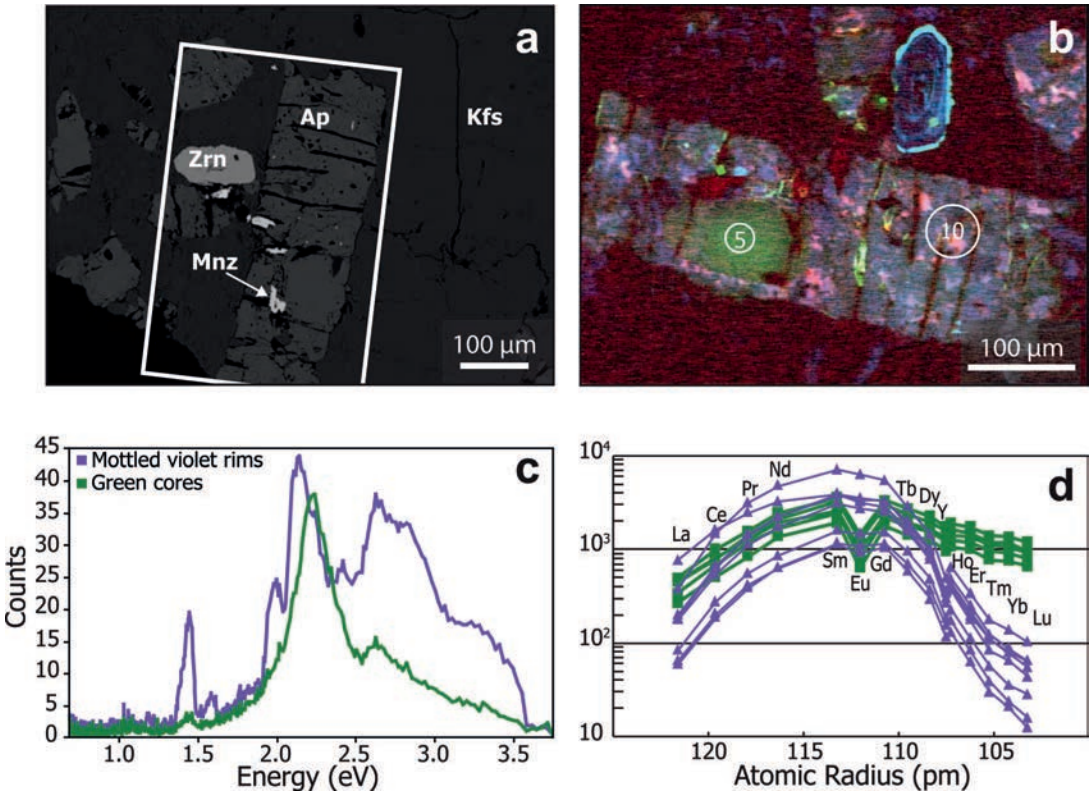

FIG. 12. (a) BSE images of apatite from the fenite sample (LE-1; mineral abbreviations can be found in Table 1). (b) Hyperspectral CL image of (a) highlighting the green apatite core and the mottled pink and violet rims. Circles and numbers denote laser sampling locations and sample numbers present in this image. Circles are actual spot size. (c) CL spectra of the apatite in (b). The green core has fewer peaks and the main peak is offset to the right of the main peak from the pink and violet rims. The line colors of the spectra correlate to the apatite color in (b). (d) REY-normalized pattern for both CL zones. Colors correspond to CL in (b). The green core shows a much flatter pattern, enriched in HREE.

rims (Fig. 11b). This transition is also evident in BSE images as slightly brighter rims compared to the cores (Fig. 11a). The CL spectrum for the dark blue-violet cores is simple, with one large broad peak from 2.0 to 3.5 eV (Fig. 11c). The red rims have more complicated spectra with multiple peaks (Table 2).

The REY patterns for both the red and blue-violet apatite zones are distinctively LREE rich and less concave (*i.e.*, high λ_2; Fig. 4a) compared to other studied apatite samples. Despite the similar pattern shape, the red CL zones are more enriched in all REY compared to the blue-violet zones.

Fenite sample LE-1. Apatite grains in the fenitized granite sample LE-1 appear homogenous in their BSE signal (Fig. 12a), whereas two distinct types are apparent from CL imaging: (1) rounded, green CL cores that are mantled by (2) mottled pink and violet-colored apatite marked by fractures and occasional monazite inclusions (Fig. 12b). The green cores have simple CL spectra with one substantial peak from 2.0 to 2.5 eV that is offset to higher eV than the distinct peak ~2.1 to ~2.2 eV that is commonly present in the bright pink-red/violet apatite zones of LE-1 and other samples. The pink/violet mottled rims in sample LE-1 have more complex spectra with multiple, taller peaks (Fig. 12c; Table 2).

The two apatite domains have very different REY patterns. The green CL apatite cores have REY patterns that are atypical of other apatite crystals examined in this study; they are enriched in HREE compared to the LREE, with a large, negative Eu anomaly (Fig. 12d) and relatively high λ_2 (Fig. 4a). The mottled CL pink/violet apatite rim zones have concave-downward REY patterns with an apex at Sm, no significant Eu anomaly, and a much more pronounced negative Y anomaly (Fig. 12d). These

TABLE 2. SUMMARY OF DESCRIPTIONS AND INTENSITY OF PEAKS COMPRISING THE CL SPECTRA OF APATITE DOMAINS (PEAK WIDTH DESCRIPTIONS ARE COMPARED RELATIVE TO EACH OTHER WITHIN EACH SAMPLE)

Sample	Rock type	Hyperspectral CL color	1.16–1.22	1.35–1.48	1.53–1.63	1.75–1.85	1.9–2.03	2.05–2.2	2.05–2.37	2.2–2.44	2.44–3.1	2.3–3.6	2.5–2.7	3.1–3.6
DMCY-139	Phoscorite	Red core	NP	NP	NP		NS	NP		WS	WP			WS
		Green rim	NP	NP	NP		NS	NP		NS	WP			
DMCY-138	Phoscorite	Pink rims	NP	NP	NP		NS	NP		WP	WP			WS
		Blue-violet cores	NP	NP			WS	WS				VWP		
FRS-4	Phoscorite	Pink zones	NP	NP	NP	WP	NP	NP		WP			NP	WP
		Blue zones		NP			WS	WS				VWP		WS
BH-224	Phoscorite	Pink core	NP	NP	NP		WS		WS			VWP		WS
		Indigo rim		NP			WS		WP		WP			
YW-61	Phoscorite	Light violet zones	NP	NP	NP	WP	NP	NP		NS	WP			WP
		Blue rims	NP	NP	WP		WP		NP		WP			WS
YN-50	Ferro-carbonatite	Light blue zones		NP			NS		NP		WP			WS
		Dark blue zones							WP		WP			
LRS-150	Magmatic-hydrothermal vein	Red rim	NP	NP	NP	WP	NS	NP			WP			WP
		Blue-violet core		NP								VWP		
LE-1	Fenite	Pink and purple rims	NP	NP	NP		NP	NP		NS	WP			WS
		Green cores		NP					NP				NP	

Note: Intensity is compared across samples. Darker shaded boxes are indicative of peak heights (*i.e.*, intensity, with darker colors corresponding to tall peaks). W = wide, N = narrow, V = very, S = shoulder to a peak (*i.e.*, "exposed" side peak), P = Peak.

rims are also depleted in HREE compared to the green cores.

Other minor and trace elements

Average F contents of the analyzed apatite ranges from 3.8 to 4.4 wt.% (at or above the stoichiometric limit) and Cl is at or below detection limit, which classifies all samples as fluorapatite. These values are greater than the expected stoichiometric value of 3.77 wt.% but are consistent with previously reported fluorapatite compositions (Bühn *et al*. 2001, Luo *et al*. 2011, Chakhmouradian *et al*. 2017). The REY contents negatively correlate with Ca + Sr (Fig. 13a) but show a positive correlation with Na content, with atomic Na to atomic (total) REY ratios near 1:1 (Fig. 13b). Apatite zones with brighter and more complex CL responses tend to have higher REY (and Na) contents. The SiO_2 contents are below or near detection limits (approximately 0.01 to 0.05 wt.% SiO_2) in all samples except in the green apatite cores from LE-1, where the average SiO_2 value is 0.24 wt.% (Fig. 13c, Appendix A[1]).

Strontium contents of the analyzed apatite can attain 5 wt.% with samples from the southeast of the study area (LRS-150, DMCY-138, DMCY-139) having the highest Sr contents and apatite cores from fenite sample LE-1 having the lowest Sr (Fig. 4b). Strontium shows a weak positive correlation with LREE content and a negative correlation with λ_3 (Fig. 4c) but does not display any significant correlations with MREE or HREE. Within each sample there is also correlation between Sr and the LREE with respect to bright CL zones and dark CL zones, respectively. Lead, Ba, and LREE all have a moderate positive correlations, with the brighter CL zones (*e.g.*, pinks and reds) typically having higher contents of these elements than the darker CL zones (*e.g.*, dark blues and indigos). Thorium and Ba also show a positive correlation trend; however, the distinction between different CL zones is not apparent. Arsenic was near, or below, detection limits for all samples.

[1] Supplementary Data is available from the Depository of Unpublished data on the MAC website (http://mineralogicalassociation.ca/), document "Apatite, CM56, 18-00021".

TABLE 3. SUMMARY OF DISCERNABLE CL ACTIVATORS AND THEIR EMISSION PEAK LOCATIONS IN APATITE FROM THIS STUDY

Activator	Peak location (eV)
Ce^{3+}	2.5–3.0, 3.1–3.6
Pr^{3+}	1.9–2.03
Nd^{3+}	1.16–1.22, 1.35–1.48
Sm^{3+}	1.53–1.63, 1.9–2.03
Eu^{2+}	2.5–3.0
Eu^{3+}	1.9–2.03
Tb^{3+}	2.5–3.0
Dy^{3+}	2.5–3.0
Tm^{3+}	2.5–3.0, 3.1–3.6
Mn^{2+}	1.9–2.03, 2.22
UO_2^{2+}	2.5–3.0
Intrinsic	3.1–3.6

Discussion

Cathodoluminescence of apatite

Cathodoluminescence imaging has proven highly effective for identifying internal zonation and textural variations in luminescent minerals (Götze 2012, Götze *et al*. 2013), as also demonstrated by our results for apatite. Our CL images reveal complex internal zonation in all of the examined apatite, even though many samples (DMCY-138, YW-61, FRS-4, and LE-1) show no significant variation in their BSE signals. Therefore, CL can be much more effective than BSE for imaging intra-grain chemical variations in apatite. Hyperspectral CL analysis, as used here, may provide yet more information on the chemical composition and lattice structure of apatite, provided the distinct features of CL spectra can be directly related to specific elemental or crystallographic features of apatite.

The CL spectral line is the total CL spectra combined over a range of wavelengths. In order to determine individual activators from a sample, the spectrum must be deconvoluted. Deconvolution involves transforming and scaling the spectra emitted by the sample from wavelength (nm) to energy (eV) using the Planck-Einstein relation:

$$E = \frac{hc}{\lambda} \quad (5)$$

where E is energy, h is Planck's constant, c is the speed of light, and λ is wavelength. This transformation transposes and scales the x axis, allowing the spectra to be expressed as a sum of Gaussian distributions. Each individual curve represents a probability of a luminescent center within the mineral, which allows identification of potential activators (Marshall 1988, Townsend & Rowlands 2000, Barbarand & Pagel 2001, MacRae et al. 2013).

For many minerals, apatite being a preeminent example, a CL spectrum can be quite complicated, as it involves multiple activators. For example, in apatite, Eu^{3+}, Sm^{3+}, Pr^{3+}, and Mn^{2+} are all potential activators near 1.9 eV (Roeder *et al*. 1987, Gaft *et al*. 1998, 2015, Götze 2000, Barbarand & Pagel 2001). Some activators such as Nd^{3+} and Yb^{3+} do not share overlapping activation energies with other activators, making their presence in apatite easily discernable in CL spectra. Activators such as Ce^{3+} have a wide spread of activation energies. Some of these energy bands may overlap with many other possible activators (*e.g*., Ce^{3+} at 2.88 eV overlaps with Eu^{2+}, Yb^{2+}, and one band of intrinsic luminescence; Gaft *et al*. 1998, 2015, Dorenbos 2003). Other energy bands may overlap with few or no other activators (*e.g*., Ce^{3+} at 3.39 eV is very close to Tm^{3+} at 3.40 eV but Ce^{3+} at 3.54 eV is alone; Gaft *et al*. 1998, Barbarand & Pagel 2001). To further complicate matters, some REE within apatite may have a synergistic effect that causes other activators to increase in intensity (Waychunas 2002). These overlapping bands make deconvolution of CL spectra in apatite better for some elements than others, particularly when examining natural samples. However, the peak interpretation can be assisted by trace element chemistry (especially REE), which is the approach taken in this study.

In the samples examined here, the apatite grains with pink, purple, and red (bright) colors all exhibit CL spectra with more peaks and with greater intensities than the CL spectra observed in the apatite with blue and indigo (dark) colors. In these brighter zones the peaks at 1.16 to 1.22 eV and 1.35 to 1.48 eV can be attributed to Nd^{3+} (MacRae *et al*. 2013). The peak from 1.35 to 1.48 eV is actually a composite of two overlapping Gaussian distributions related to Nd^{3+} as specific energy bands at 1.364, 1.393, and 1.403 eV and as a range from 1.40 to 1.44 eV (see Fig. 3 for an example of overlap). The small peaks at 1.16 to 1.22 eV have distribution curves that suggest that the peak is also caused by the Nd^{3+} energy bands at 1.161 and 1.163 eV (Table 3; Gaft *et al*. 1998, 2015 Kempe & Götze 2002).

Many of the bright zones also exhibit a distinct peak from 1.53 to 1.63 eV as well as a "shoulder" from 1.9 to 2.03 eV. The 1.53 to 1.63 eV peak has a probability distribution related to Sm^{3+} (Table 3), which has a known band at 1.55 eV (Kempe & Götze 2002). The shoulder at 1.9 to 2.03 eV has a distribution that is likely related to Eu^{3+} and/or Mn^{2+}, but it may also be affected by and/or related to Sm^{3+} and Pr^{3+}, which also have energy bands near that location (Table

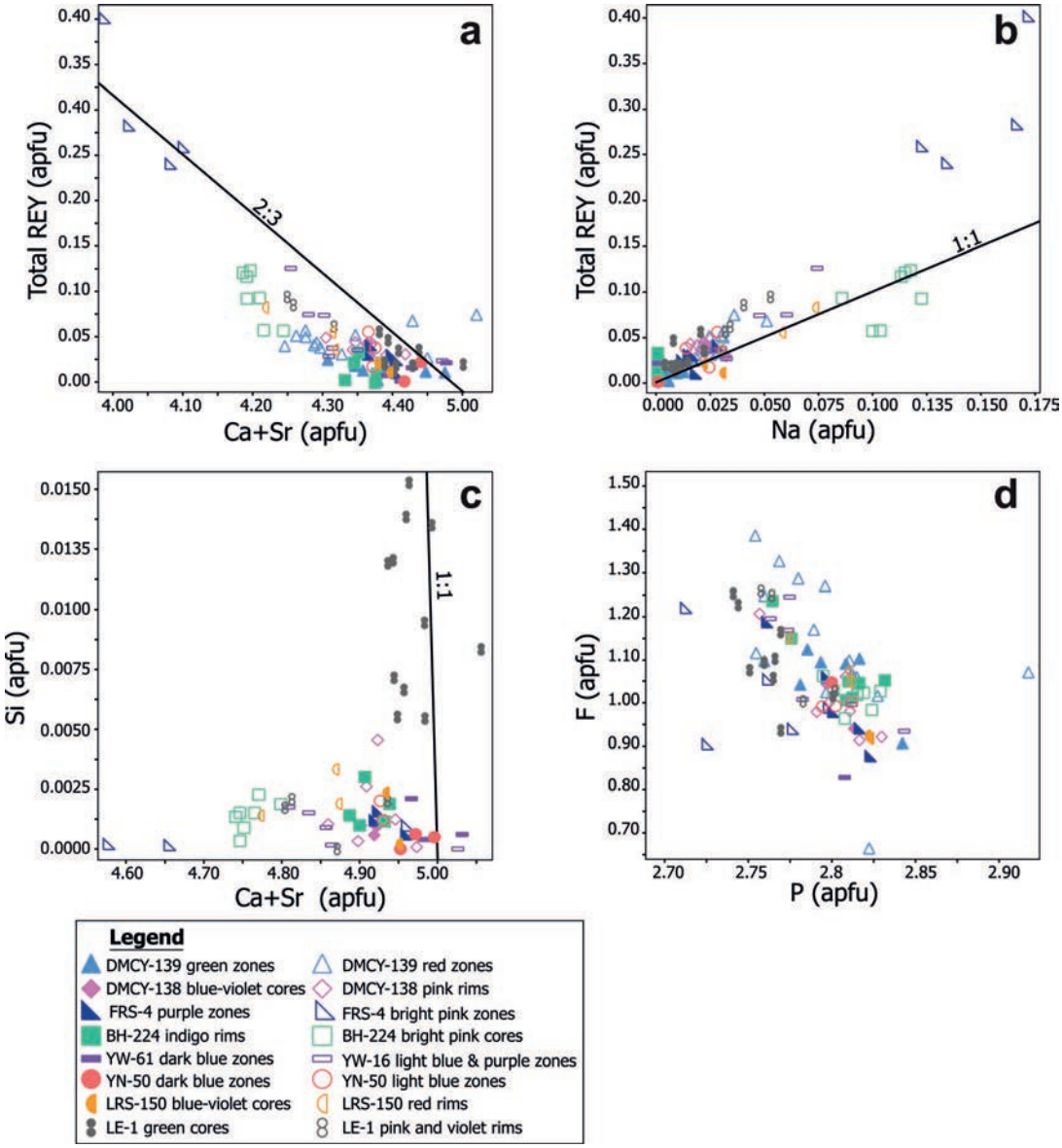

FIG. 13. (a) Atomic Ca + Sr *versus* atomic total REE + Y (REY) of apatite compositions. The 2:3 slope for some samples (*e.g.*, FRS-4) suggests some REY incorporation *via* a $2REY^{3+} + \square = 3Ca^{2+}$ mechanism. (b) Atomic Na *versus* atomic total REE + Y (REY) for apatite samples examined in this study. Compositions that plot close to the 1:1 line indicate REY incorporation into apatite *via* an $REY^{3+} + Na^{+} = 2Ca^{2+}$ substitution. Compositions plotting above the 1:1 line require an additional REY substitution mechanism. (c) Atomic Ca + Sr *versus* atomic Si of apatite compositions. All samples have low Si contents, except the core zones of apatite from fenite sample LE-1. (d) Atomic F *versus* atomic P of apatite compositions. The negative slope suggests that F and another anion (possibly CO_3^{2-} due to the carbonatite association) are substituting for PO_4^{3-}. This may account for the excess F (>1.0 *apfu*) measured in apatite in this study. Atomic formula unit values are presented in Appendix C.

3; Roeder *et al*. 1987, Gaft *et al*. 1998, 2015, Götze 2000, Barbarand & Pagel 2001). There is a notable increase in intensity of the peak(s) in the region between 2.5 and 3.0 eV in the bright pink, purple, and red zones. There are many activators in this area such as Ce^{3+}, Dy^{3+}, Eu^{2+}, Tb^{3+}, Tm^{3+}, and UO_2^{2+}, as well as several intrinsic luminescence bands (Table 3; Portnov & Gorobets 1969, Mariano & Ring 1975, Marshall 1988, Gaft *et al*.1998, Götze 2000, Barbarand & Pagel 2001, Kempe & Götze 2002, Dorenbos 2003, Czaja *et al*. 2010, 2013, Gaft *et al*. 2015). Due to the significant overlap of activators in this spectral region, it is difficult to determine the specific REE, or REEs, responsible for the luminescence.

The shoulder from 3.1 to 3.6 eV consists of several overlapping Gaussian distributions that may be attributed to Ce^{3+}, Tm^{3+}, and/or an intrinsic luminescence (Table 3). These activators have energy band locations at 3.263, 3.397, 3.444, and 3.542 eV for Ce^{3+}; 3.406 and 3.416 eV for Tm^{3+}; and 3.289 eV for the intrinsic luminescence (Portnov & Gorobets 1969, Gaft *et al*. 1998, 2015, Barbarand & Pagel 2001, Kempe & Götze 2002).

The darker CL apatite zones (blue and indigo) tend to have simpler spectra overall, with only one or two large peaks (*e.g*., YN-50 dark blue zone in Fig. 10b and LRS-150 blue zone in Fig. 11b). However, the peaks are located in spectral regions with the most activator overlap (2.0 to 3.0 eV). Attempts to deconvolute these spectra result in fewer Gaussian curves than in the brighter red zones. Nevertheless, the curves have a much wider distribution that captures multiple CL activators, resulting in similar difficulties in deciphering specific activators.

The green apatite cores from fenite sample LE-1 have a main peak centered at 2.22 eV, slightly to the right of the peak for the pink/violet rims, which is at 2.03 to 2.17 eV (Fig. 12c). As previously mentioned, this region contains multiple REE activators in addition to Mn^{2+} (Mariano & Ring 1975, Marshall 1988, Gaft *et al*. 1998, 2015, Götze 2000, Kempe & Götze 2002). However, we interpret this peak shift to be the result of Mn^{2+} exhibiting greater influence on the CL spectra than the REE in this region the trace element data collected in this study show that the green CL cores in the fenite contain more Mn than the other samples in this study (Fig. 4d; Appendix B).

Overall, apatite domains with higher CL counts across the spectra (*i.e*., brighter CL signals) tend to have higher overall REE contents (or λ_0 of O'Neill 2016), which means that hyperspectral CL analysis can be used as a qualitative tool for determining relative REE contents between apatite domains.

Element substitution mechanisms in apatite

Using our geochemical dataset, we can evaluate likely mechanisms of trace element substitution in apatite. The Si content is quite low for most of the apatite samples, and there is a clear positive relationship between REY and Na (Fig. 13b), as well as a negative correlation between REY and Ca. These features support REY incorporation in apatite by the reaction $REY^{3+} + Na^{+} = 2Ca^{2+}$, rather than through the reaction $REY^{3+} + Si^{4+} = Ca^{2+} + P^{5+}$ (Fig. 13c; Portnov & Gorobets 1969, Rønsbo 1989, Hughes *et al*. 1991, Fleet & Pan 1995, Mitchell *et al*. 1997). Some compositions fall above the 1:1 line for (atomic) REY *versus* Na, indicating that other substitution mechanisms may also be responsible for incorporating REE into the apatite structure. We observed no correlation between REY and F, which indicates that the reaction $REY^{3+} + O^{2-} = Ca^{2+} + F$ is unlikely to be important in this case. Instead we suggest that the reaction $2REY^{3+} + \square = 3Ca^{2+}$ (Fig. 13c; Pan & Fleet 2002) may account for the additional REE substitution in nearly all of the samples (except the apatite cores in LE-1; see below). Other minor reactions may also account for some REY substitution in apatite, but evaluation of these reactions is beyond the scope of this study.

The green apatite cores in fenite sample LE-1 contain higher SiO_2 and lower Na_2O and Sr values than the other analyzed apatite. These samples also plotted above the 1:1 line in atomic REY *versus* Na space (Fig. 13b) and hence have excess REY compared to Na. With high SiO_2 contents, we suggest that the reaction $REY^{3+} + Si^{4+} = Ca^{2+} + P^{5+}$ plays a role in REY incorporation in these apatite cores.

Roeder *et al*. (1987) and Rønsbo (1989) established that silica activity and alkalinity of fluid can affect REY incorporation into precipitating apatite. For example, in a silica-saturated system, the reaction $REY^{3+} + Si^{4+} = Ca^{2+} + P^{5+}$ will be the dominant mechanism of REE substitution in apatite, whereas in a silica-undersaturated, alkaline system, $REY^{3+} + Na^{+} = 2Ca^{2+}$ will be the dominant REY substitution mechanism. In our study, most of the examined grains are from peralkaline carbonatites and phoscorites, which are alkaline melts (or fluids) with low silica activity. These apatite grains contain low Si and incorporate REY primarily *via* the substitution $REY^{3+} + Na^{+} = 2Ca^{2+}$. The apatite cores from the fenite sample LE-1 are interpreted to be relict apatite grains from the granitic host rock (see below), and hence originally formed from silica-saturated granitic melt. In this case, the $REY^{3+} + Si^{4+} = Ca^{2+} + P^{5+}$ substitution plays an important role in REY incorporation into apatite. If these findings are more generally

applicable, then Na-Si-REY systematics of apatite may be used to evaluate the chemical environment from which the apatite crystallized, and may therefore be a powerful provenance-tracing tool.

The high Sr content of the apatite samples is a commonly observed feature of apatite from peralkaline and carbonatitic rocks. Strontium, Ba, and Pb are divalent, and thus can substitute for Ca without charge balance issues (Pan & Fleet 2002 and references therein, Chakhmouradian *et al*. 2002). Thorium correlates with these 2+ ions as well as the LREE and may be substituting for Ca *via* the process $Th^{4+} + \square = 2Ca^{2+}$ (Hughson & Sen Gupta 1964, Baumer *et al*. 1983, Pan & Fleet 2002), although further studies on this reaction are needed.

Based on the general apatite formula [$Ca_5(PO_4)_3(OH,Cl,F)$], the endmember fluorapatite is able to accommodate about 3.77 wt.% F (1.0 *apfu*) at "channel sites" dictated by the PO_4^{3-} tetrahedron and the $Ca(I)O_9$ and $Ca(II)O_6$ polyhedra (Hughes *et al*. 1989, 1990). The incorporation of F^- is usually at the expense of Cl^- and/or OH^-. Fluorine values above the presumed stoichiometric limit of 3.77 wt.% may be due to F incorporation at sites other than the nominal hydroxyl site of apatite. The coupled substitution $F^- + CO_3^{2-} = PO_4^{3-}$ (Binder & Troll 1989, Fleet & Liu 2008, Yi *et al*. 2013) is supported the negative correlation between F and P_2O_5 in Figure 13d and therefore is proposed to account for the high F values in our apatite analyses.

Composition and origin of apatite of the GCCC

Our CL imaging and chemical analysis reveal multiple generations of apatite present in alkaline magmatic/hydrothermal rocks from across the GCCC. These features are consistent with other reports of multiphase apatite from alkaline igneous rocks and REE ore deposits (Kempe & Götze 2002, Schoneveld *et al*. 2015, Chakhmouradian *et al*. 2017, Song *et al*. 2018). Chakhmouradian *et al*. (2017) describes several different cases to explain core–rim compositional variations within apatite from carbonatites: (1) precipitation of different mineral phases within a magma that cause re-saturation of apatite within the melt, creating REE-rich apatite rims; (2) hydrothermal fluid alteration of apatite either by *in situ* alteration or dissolution/re-precipitation onto existing grains; and (3) multiple intrusions of alkaline melt that precipitates re-equilibrated apatite onto the pre-existing cores.

We interpret the zoning features of the GCCC apatite to be a cryptic record of apatite crystallization and re-crystallization. Some zones in the grain interiors with regular or oscillatory zoning can be ascribed to original magmatic apatite, while the mottled or irregular rims and zones are likely to have formed *via* subsequent (and possibly multiple) recrystallization events related to later hydrothermal or magmatic activity. In many cases, a hydrothermal origin for the apatite rim zones can be inferred based on textural features (*e.g*., mottled textures) and the association of hydrothermal quartz and Fe-oxides (± K-feldspar, ± aegirine) in fractures and pores in the apatite.

The concept of multiple events forming different generations of apatite is consistent with the protracted (>300 m.y.) geological history of the GCCC (Slezak & Spandler 2016, Zi *et al*. 2017) that records the effects of an assortment of regional-scale tectonic events including the 1320 to 1170 Ma Mutherbukin Tectonic Event (Korhonen *et al*. 2015), the *ca*. 1076 Ma Warakurna Large Igneous Province (Wingate *et al*. 2004), and the 1030 to 950 Ma Edmundian Orogeny (Sheppard *et al*. 2007). We proposed that initial magmatism, followed by metamorphism or hydrothermal activity associated with these events, is responsible for forming the multiple apatite domains in our samples.

Despite these complexities, there are some commonalities in apatite between samples. Apatite from most samples feature convex-down REY patterns (or negative λ_2 values: Fig. 4a), with relatively depleted HREE contents, a notable negative Y anomaly, a very small to negligible Eu anomaly, and depleted LREE contents (Figs. 5–12). This convex-down pattern (negative λ_2) is consistent with the apatite/carbonatite melt partition coefficients that favor MREE over both LREE and HREE (Klemme & Dalpé 2003). At first, the depleted LREE patterns appear anomalous given that these rocks lie within an LREE ore field, but all analyzed apatite samples, except sample LRS-150, coexist with abundant monazite, which preferentially sequesters the LREE and is the dominant ore mineral of the GCCC. Only apatite from hydrothermal vein sample LRS-150 is enriched in LREE, and this sample only contains very rare monazite. Most of our samples are phoscorites, which have not previously been reported from the GCCC, but will be described in detail in a companion paper (Slezak *et al*. in prep.). Here we note that many of the distinctive features of apatite from the phoscorites are shared by apatite from the carbonatite (concave REY pattern, Y anomaly; Fig. 10d), which may be evidence to support direct genetic links between these rock units.

A more detailed evaluation of REY and other trace elements from our sample set reveals some systematic differences between samples. The REY patterns for DMCY-139 and DMCY-138 (Figs. 5d and 6d, respectively) both exhibit sinusoidal shapes (for both CL-defined zones), giving distinctly lower λ_3 values,

but somewhat higher λ_2 values compared to other samples (Fig. 4a). The hydrothermal vein sample (LRS-150; Fig. 11) also has relatively high λ_2 (Fig. 4a). All three samples are enriched in Sr and Mn, and they have lower Gd/Ce compared to the other samples (Fig. 4b–d). These three samples were collected from the southeastern part of the study area (Fig. 1), and, together with the spatial variation observed in ore composition (Fig. 2), are interpreted to reflect primary compositional variations in the alkaline magmatic rocks across the GCCC. The origin of this spatial variation in chemistry will be examined in detail using bulk rock geochemical and isotopic data in a subsequent paper (Slezak *et al*. in prep.).

Apatite grains from fenite sample LE-1 have notably different CL spectra and REY patterns. The dark green apatite core zones have simple CL spectra that suggest Mn^{2+} is also a key activator. The trace element composition of this apatite is quite distinct from all other samples: they are relatively enriched in HREE, Mn, and Si (Figs. 12d, 4d, 13c, respectively), depleted in Sr (Fig. 4b, c), and have distinct negative Eu anomalies. These cores lack the more complex multi-peak CL spectra and negative Y anomalies observed for most other apatite samples examined in this study. The REY pattern with the negative Eu anomaly of the green apatite is characteristic of apatite crystallized from a granitic rock in which apatite and feldspar crystallized from the same melt (Möller & Muecke 1984, Sha & Chappell 1999). The high SiO_2 content is consistent with apatite crystallized from silica-saturated magma (Rønsbo 1989, Sha & Chappell 1999). By contrast, the negative Y anomaly and HREE depletion in the mottled bright pink/violet apatite that envelopes the green cores is consistent with a carbonatite-phoscorite origin for these apatite rims as documented in this study (Figs. 5 to 10) and in Chakhmouradian *et al*. (2017). We interpret the zoning in these apatite grains to be the result of crystallization of apatite related to alkaline magmatism (*i.e*., fenitization) preferentially onto pre-existing apatite of the granitic protolith. This complex grain history is not made apparent from optical microscope or BSE imaging, which further highlights the value of hyperspectral CL imaging as a petrographic tool to guide micro-scale geochemical analysis, such as LA-ICP-MS.

Applications

Apatite is common in many rock types and forms in many geological environments and can incorporate a large range of trace elements that can be used for petrogenetic tracing and geochronology. However, apatite is also reactive to hydrothermal processes, and recrystallization may not be immediately apparent from routine petrographic analysis. Techniques such as optical or monochromatographic CL provide researchers with the ability to identify alteration, growth zoning, and multiple generations in luminescent minerals such as apatite. More advanced methods, such as hyperspectral CL mapping combined with elemental micro-analysis, hold even greater promise for understanding igneous and hydrothermal histories of rocks, or for provenance studies that use "out of context" minerals, such as detrital components of sediments or sedimentary rocks (*e.g*., Morton 1991). For example, apatite grains in fenite samples LE-1 comprise two domains each with distinct CL spectra and chemical compositions that are interpreted to have formed from two very different igneous sources (granitic and carbonatitic), as described above.

These techniques may also be used to improve understanding of ore systems and thus assist mineral exploration efforts. Despite the broad similarities in the CL spectra and composition of most apatite samples analyzed here, we could distinguish apatite collected from the southeast and east of the GCCC (Demarcay and Frasers, respectively) from those of Bald Hill and Yangibana in the north and northwest (Fig. 1). This spatial distinction is also seen in the REE tenor of ore samples from the region (Fig. 2) with the more sought-after Nd-rich ores (*i.e*., high Nd/La) found in the southeast. This coincidence of apatite and bulk ore chemistry across the region strongly indicates that the distinct REE compositions of the ores are inherited from protolithic igneous and hydrothermal rocks, rather than being a product of ironstone-forming weathering and alteration processes. In this case, analysis of apatite from suitable indicator rocks for mineralization (carbonatites, phoscorites) may aid in targeting the most prospective areas for exploration.

Accurate identification of different mineral generations and origins may also be crucial for guiding further *in situ* analysis such as Sm-Nd, Rb-Sr, and/or U-Pb isotopes for age dating and source tracing (*e.g*., De Paolo 1981). This is particularly relevant for REE-rich minerals such as apatite and monazite, as these minerals can now be analyzed *in situ* for their Sm-Nd isotope composition *via* LA-MC-ICP-MS (Fisher *et al*. 2011). Samarium-Nd isotope values determined for coexisting mineral phases, or rocks, can be used for age determinations provided that the minerals (or rocks) crystallized at the same time from a source with uniform isotopic composition and provided that isotopic ratios were not disturbed by subsequent metamorphic and hydrothermal events.

In this study, apatite and monazite from carbonatite sample YN-50 were interpreted to be co-genetic, based on their textural relationship, trace element content,

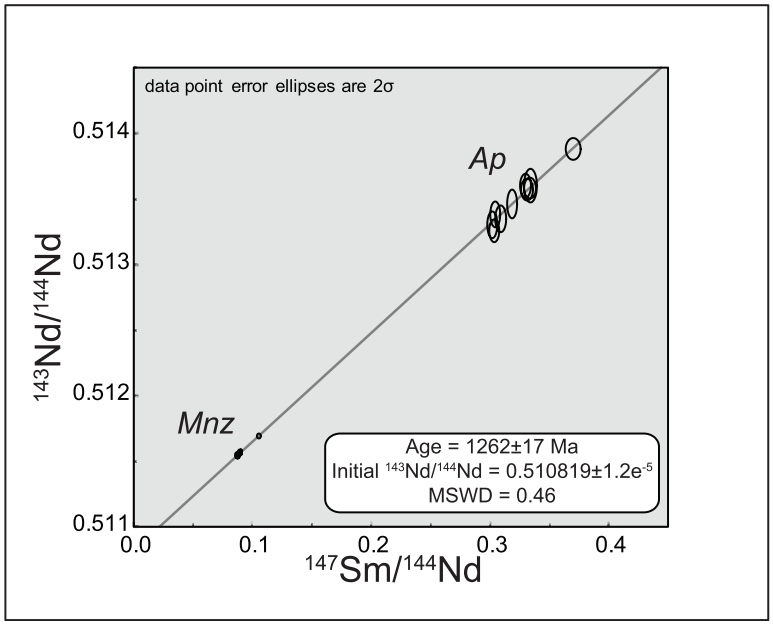

FIG. 14. Sm-Nd isochron for sample YN-50 using isotopic data obtained *in situ* from coexisting apatite and monazite.

and CL signatures (Fig. 10). The inferred contemporaneous formation and contrasting Sm/Nd ratio of these two minerals makes them well suited for Sm-Nd isochron dating *via in situ* micro-scale Sm-Nd isotope analyses. Guided by micro-textural features of these minerals, we undertook *in situ* Sm-Nd isotope analyses of monazite and apatite from YN-50 following the methodology of Hammerli *et al*. (2014). The analyses produced an isochron age of 1262 ± 17 Ma (Fig. 14), which is in agreement with our U-Pb age of 1250 ± 15 Ma for monazite from the same sample (Slezak *et al*. in prep.) and previous age determinations for the GCCC (Zi *et al*. 2017). This consistency of age determinations demonstrates the utility of *in situ* Sm-Nd isotope microanalysis of REE minerals for dating, provided co-genetic mineral phases can be accurately identified. This latter point is most effectively achieved with the aid of micro-textural/micro-chemical characterization of REE minerals, such as outlined in this paper.

ACKNOWLEDGMENTS

This study was supported by an ARC Future Fellowship (FT 120100198) to Carl Spandler. We thank Hasting Technology Metals Limited for their sample contributions and hospitality while conducting fieldwork. We also thank Shane Askew and Yi Hu from the JCU Advanced Analytical Centre for their help with the analytical equipment used in this study. Finally, we thank Colin MacRae and one anonymous reviewer for their comments, which improved this manuscript.

REFERENCES

BARBARAND, J. & PAGEL, M. (2001) Cathodoluminescence study of apatite crystals. *American Mineralogist* **86**, 473–484.

BAUMER, A., CARUBA, R., BIZZOUARD, H., & PECKETT, A. (1983) Chlorapatite de synthesis: substitution et inclusions de Mn, Ce, U et Th traces. *Canadian Mineralogist* **21**, 567–573 (in French).

BINDER, G. & TROLL, G. (1989) Coupled anion substitution in natural carbon-bearing apatites. *Contributions to Mineralogy and Petrology* **101**, 394–401.

BÜHN, B., WALL, F., & LE BAS, M.J. (2001) Rare-earth element systematics of carbonatitic fluorapatites and their significance for carbonatite magma evolution. *Contributions to Mineralogy and Petrology* **141**, 572–591.

CHAKHMOURADIAN, A.R., REGUIR, E.P., & MITCHELL, R.H. (2002) Strontium-apatite: New occurrences and the extent of Ca-Sr substitution in apatite-group minerals. *Canadian Mineralogist* **40**, 121–136.

CHAKHMOURADIAN, A.R., REGUIR, E.P., ZAITSEV, A.N., COUESLAN, C., XU, C., KYNICKY, J., MUMIN, A.H., &

Yang, P. (2017) Apatite in carbonatitic rocks: Compositional variation, zoning, element partitioning and petrogenetic significance. *Lithos* **274–275**, 188–213.

Chen, N., Pan, Y., & Weil, J.A. (2002) Electron paramagnetic resonance spectroscopic study of synthetic fluorapatite: Part I. Local structural environment and substitution mechanism of Gd33+ at the Ca2 site. *American Mineralogist* **87**, 37–46.

Cherniak, D.J. (2000) Rare earth element diffusion in apatite. *Geochemica et Cosmochemica Acta* **64**, 3871–3885.

Czaja, M., Bodyl, S., Lisiecki, R., & Mazurak, Z. (2010) Luminescence properties of Pr^{3+} and Sm^{3+} ions in natural apatite. *Physics and Chemistry of Minerals* **37**, 425–433.

Czaja, M., Bodyl-Gajowska, S., & Mazurak, Z. (2013) Steady-state luminescence measurement for qualitative identification of rare earth ions in minerals. *Journal of Mineralogical and Petrological Sciences* **108**, 47–54.

De Paolo, D.J. (1981) Neodymium isotopes in the Colorado Front Range and crust-mantle evolution in the Proterozoic. *Nature* **291**, 193–196.

Dorenbos, P. (2003) Anomalous luminescence of Eu^{2+} and Yb^{2+} in inorganic compounds. *Journal of Physics: Condensed Matter* **15**, 2645–2665.

Edwards, P.R. & Lee, M.R. (2014) Cathodoluminescence hyperspectral imaging. *In* Cathodoluminescence and its application to geoscience. Mineralogical Association of Canada, Québec, Canada (29–45).

Edwards, P.R., Martin, R.W., & Lee, M.R. (2007) Combined cathodoluminescence hyperspectral imaging and wavelength dispersive X-ray analysis of minerals. *American Mineralogist* **92**, 235–242.

Fisher, C.M., McFarlane, C.R.M., Hanchar, J.M., Schmitz, M.D., Sylvester, P.J., Lam, R., & Longerich, H.P. (2011) Sm-Nd isotope systematics by laser ablation-multicollector-inductively coupled plasma mass spectrometry: Methods and potential natural and synthetic reference materials. *Chemical Geology* **284**, 1–20.

Fleet, M.E. & Liu, X. (2008) Accommodation of the carbonate ion in fluorapatites synthesized at high pressure. *American Mineralogist* **93**, 1460–1469.

Fleet, M.E. & Pan, Y. (1995) Site preference of rare earth elements in fluorapatite. *American Mineralogist* **80**, 329–335.

Gaft, M., Reisfeld, R., Panczer, G., Blank, P., & Boulon, G. (1998) Laser-induced time-resolved luminescence of minerals. *Spectrochimica Acta* **54**, 2163–2175.

Gaft, G., Reisfeld, R., & Panczer, G. (2015) *Modern luminescence spectroscopy of minerals and materials*. Springer Mineralogy, Cham, Switzerland.

Goldoff, B., Webster, J.D., & Harlov, D.E. (2012) Characterization of fluor-chlorapatites by electron probe microanalysis with a focus on time-dependent intensity variation of halogens. *American Mineralogist* **97**, 1103–1115.

Götze, J. (2000) Materials characterization by cathodoluminescence microscopy and spectroscopy. *In* Proceedings of the Sixth International Congress on Applied Mineralogy in Research, Economy, Technology, Ecology and Culture. Gottingen, Germany (783–786).

Götze, J. (2012) Application of cathodoluminescence microscopy and spectroscopy in geosciences. *Microscopy and Microanalysis* **18**, 1270–1284.

Götze, J., Schertl, H.P., Neuser, R.D., Kempe, U., & Hanchar, J.M. (2013) Optical microscope-cathodoluminescence (OM-CL) imaging as a powerful tool to reveal internal textures of minerals. *Mineralogy and Petrology* **107**, 373–392.

Guillong, M., Meier, D.L., Allan, M.M., Heinrich, C.A., & Yardley, B.W.D. (2008) Appendix A6: SILLS: A MATLAB-based program for the reduction of laser ablation ICP-MS data of homogenous materials and inclusions. *In* Laser Ablation ICP-MS in the Earth Sciences: Current Practices and Outstanding Issues (P. Sylvester, ed.). Mineralogical Association of Canada, Vancouver, Canada (328–333).

Hammerli, J., Kemp, A.I.S., & Spandler, C. (2014) Neodymium isotope equilibration during crustal metamorphism revealed by *in situ* microanalysis of REE-rich accessory minerals. *Earth and Planetary Science Letters* **392**, 133–142.

Harlov, D.E. (2015) Apatite: a fingerprint for metasomatic processes. *Elements* **11**, 171–176.

Harlov, D.E. & Förster, H.J. (2003) Fluid-induced nucleation of (Y+REE)-phosphate minerals within apatite: nature and experiment. Part II. Fluorapatite. *American Mineralogist* **88**, 1209–1229.

Harrowfield, I.R., MacRae, C., & Wilson, N.C. (1993) Chemical imaging in electron microprobes. *In* Proceedings of the 27th Annual Microbeam Analysis Society (MAS) Meeting. Microbeam Analysis Society, Los Angeles, California (547–548).

Hastings Technology Metals Limited (2017) Yangibana Project: definitive feasibility study. Retrieved from http://hastingstechmetals.com/images/asx_latest/Hastings_DFS_Executive_Summary_Nov_2017_NEW.pdf [date accessed: December 20, 2017].

Hughes, J.M. & Rakovan, J. (2015) Structurally robust, chemically diverse: apatite and apatite supergroup minerals. *Elements* **11**, 165–170.

Hughes, J.M., Cameron, M., & Crowley, K.D. (1989) Structural variations in natural F, OH, and Cl apatites. *American Mineralogist* **74**, 870–876.

Hughes, J.M., Cameron, M., & Crowley, K.D. (1990) Crystal structures of natural ternary apatites: solid solution in the

$Ca_5(PO_4)_3X$ (X=F, OH, CL) system. *American Mineralogist* **75**, 295–304.

Hughes, J.M., Cameron, M., & Mariano, A.N. (1991) Rare-earth-element ordering and structural variations in natural rare-earth-bearing apatites. *American Mineralogist* **76**, 1165–1173.

Hughson, M.R. & Sen Gupta, J.G. (1964) A thorian intermediate member of the britholite-apatite series. *American Mineralogist* **49**, 937–951.

Kempe, U. & Götze, J. (2002) Cathodoluminescence (CL) behavior and crystal chemistry of apatite from rare-metal deposits. *Mineralogical Magazine* **66**, 151–172.

Klemme, S. & Dalpé, C. (2003) Trace-element partitioning between apatite and carbonatite melt. *American Mineralogist* **88**, 639–646.

Korhonen, F.J., Johnson, S.P., Fletcher, I.R., Rasmussen, B., Sheppard, S., Muhling, J.R., Dunkley, D.J., Wingate, M.T.D., Roberts, M.P., & Kirkland, C.L. (2015) *Pressure-temperature-time evolution of the Mutherbukin Tectonic Event, Capricorn Orogen*. Geological Survey of Western Australia, Perth, Australia.

Luo, Y., Gao, S., Longerich, H.P., Günter, D., Wunderli, S., Yuan, H-L., & Liu, X-M. (2007) The uncertainty budget of the multi-element analysis of glasses using LA-ICP-MS. *Journal of Analytical Atomic Spectrometry* **22**, 122–130.

Luo, Y., Rakovan, J., Tang, Y., Lupulescu, M., Hughes, J.M., & Pan, Y. (2011) Crystal chemistry of Th in fluorapatite. *American Mineralogist* **96**, 23–33.

MacRae, C.M. & Wilson, N.C. (2008) Luminescence database I–minerals and materials. *Microscopy and Microanalysis* **14**, 184–204.

MacRae, C.M., Wilson, N.C., Johnson, S.A., Phillips, P.L., & Otsuki, M. (2005) Hyperspectral mapping-combining cathodoluminescence and X-ray collection in an electron microprobe. *Microscopy Research and Technique* **67**, 271–277.

MacRae, C., Wilson, N.C., Torpy, A., & Davidson, C.J. (2012) Hyperspectral cathodoluminescence imaging and analysis extending from ultraviolet to near infrared. *Microscopy and Microanalysis* **18**, 1239–1245.

MacRae, C., Wilson, N.C., & Torpy, A. (2013) Hyperspectral cathodoluminescence. *Mineralogy and Petrology* **107**, 429–440.

Mariano, A.N. & Ring, P.J. (1975) Europium-activated cathodoluminescence in minerals. *Geochemica et Cosmochemica Acta* **39**, 649–660.

Marshall, D.J. (1988) *Cathodoluminescence of geological materials*. Unwin Hyman, Boston, United States.

McCubbin, F.M., Steele, A., Nekvasil, H., Schnieders, A., Rose, T., Fries, M., Carpenter, P.K., & Jolliff, B.L. (2010). Detection of structurally bound hydroxyl in fluorapatite from Apollo Mare basalt 15058,128 using TOF-SIMS. *American Mineralogist* **95**, 1141–1150.

McDonough, W.F. & Sun, S.S. (1995) The composition of the Earth. *Chemical Geology* **120**, 223–253.

Mitchell, R.H., Xiong, J., Mariano, A.N., & Fleet, M.E. (1997) Rare-earth-element-activated cathodoluminescence in apatite. *Canadian Mineralogist* **35**, 979–998.

Möller, P. & Muecke, G.K. (1984) Significance of Europium anomalies in silicate melts and crystal-melt equilibria: a review. *Contributions to Mineralogy and Metrology* **87**, 242–250.

Morton, A.C. (1991) Geochemical studies of detrital heavy minerals and their application to provenance research. *In* Developments in Sedimentary Provenance Studies (A.C. Morton, S.P. Todd, & P.D.W. Haughton, eds.). Geological Society Special Publications, London, United Kingdom.

Nelson, B.K. & De Paolo, D.J. (1985) Rapid production of continental crust 1.7 to 1.9 b.y. ago: Nd isotopic evidence from the basement of the North American mid-continent. *Geological Society of America Bulletin* **96**, 746–754.

O'Neill, H.S.C. (2016) The smoothness and shapes of chondrite-normalized rare earth element patterns in basalts. *Journal of Petrology* **57**, 1463–1508.

Pagel, M., Barbin, V., Blanc, P., & Ohnenstetter, D. (2000) Cathodoluminescence in geosciences: an introduction. *In* Cathodoluminescence in Geoscience (M. Pagel, V Barbin, P. Blanc, & D. Ohnenstetter, eds.). Springer, Berlin, Germany.

Pan, Y. (1997) Zircon- and monazite-forming metamorphic reactions at Manitouwadge, Ontario. *Canadian Mineralogist* **35**, 105–118.

Pan, Y. & Fleet, M.E. (2002) Compositions of the apatite-group minerals: substitution mechanisms and controlling factors. *In* Phosphates: Geochemical, Geobiological, and Materials Importance (M.J. Kohn, J. Rakovan, & J.M. Hughes, eds.). *Reviews in Mineralogy and Geochemistry* **48**, 13–49.

Pan, Y., Fleet, M.E., & MacRae, N.D. (1993) Oriented monazite inclusions in apatite porphyroblasts from the Hemlo gold deposit, Ontario, Canada. *Mineralogical Magazine* **57**, 697–707.

Pearson, J.M. (1996) *Alkaline rocks of the Gifford Creek Complex, Gascoyne Province, Western Australia: their petrogenetic and tectonic significance*. Ph.D. thesis, University of Western Australia, Perth, Australia.

Pearson, J.M., Taylor, W.R., & Barley, M.E. (1996) Geology of the alkaline Gifford Creek Complex, Gascoyne Complex, Western Australia. *Australian Journal of Earth Sciences* **43**, 299–309.

Pettke, T., Oberlie, F., Audétat, A., Guillong, M., Simon, A.C., Hanley, J.J., & Klemm, L.M. (2012) Recent

developments in element concentration and isotope ratio analysis of individual fluid inclusions by laser ablation single and multiple collector ICP-MS. *Ore Geology Reviews* **44**, 10–38.

Pirajno, F., González-Álvarez, I., Chen, W., Kyser, K.T., Simonetti, A., Leduc, E., & Legras, M. (2014) The Gifford Creek Ferrocarbonatite Complex, Gascoyne Province, Western Australia: associated fenitic alteration and a putative link with the ~1075 Ma Warakurna LIP. *Lithos* **202–203**, 100–119.

Portnov, A.M. & Gorobets, B.S. (1969) Luminescence of apatite from different rock types. *Doklady Akademii Nauk SSSR* **184**, 110–113.

Pyle, J.M., Spear, F.S., & Wark, D.A. (2002) Electron microprobe analysis of REE in apatite, monazite, and xenotime: protocols and pitfalls. *In* Phosphates: Geochemical, Geobiological, and Materials Importance (M.J. Kohn, J. Rakovan, & J.M. Hughes, eds.). *Reviews in Mineralogy and Geochemistry* **48**, 337–362.

Roeder, P.L., MacArthur, D., Ma, X., Palmer, G.R., & Mariano, A.N. (1987) Cathodoluminescence and microprobe study of rare-earth elements in apatite. *American Mineralogist* **72**, 801–811.

Rønsbo, J.G. (1989) Coupled substitutions involving REEs and Na and Si in apatites in alkaline rocks from the Ilimaussag intrusion, South Greenland, and the petrological implications. *American Mineralogist* **74**, 896–901.

Schoneveld, L., Spandler, C., & Hussey, K. (2015) Genesis of the central zone of the Nolans Bore rare earth element deposit, Northern Territory, Australia. *Contributions to Mineralogy and Petrology* **170**, 1–22.

Sha, L.-K. & Chappell, B.W. (1999) Apatite chemical composition, determined by electron microprobe and laser-ablation inductively coupled plasma mass spectrometry, as a probe into granite petrogenesis. *Geochemica et Cosmochemica Acta* **63**, 3861–3881.

Sheppard, S., Rasmussen, B., Muhling, J.R., Farrell, T.R., & Fletcher, I.R. (2007) Grenvillian-aged orogenesis in the Palaeoproterozoic Gascoyne Complex, Western Australia: 1030–950 Ma reworking of the Proterozoic Capricorn Orogen. *Journal of Metamorphic Geology* **25**, 477–494.

Sheppard, S., Johnson, S.P., Wingate, M.T.D., Kirkland, C.L., & Pirajno, F. (2010) *Explanatory notes for the Gascoyne Province*. Geological Survey of Western Australia, Perth, Western Australia.

Slezak, P. & Spandler, C. (2016) Age and origin of the Yangibana LREE deposit and associated ferrocarbonatites, Gascoyne Province, Western Australia. *In* Proceedings from the Goldschmidt 2016 conference. Geochemical Society, Yokohama, Japan, June 26th–July 1st, 2888.

Song, W., Xu, C., Smith, M.P., Chakhmouradian, A.R., Brenna, M., Kynický, J., Chen, W., Yang, Y., Deng, M., & Tang, H. (2018) Genesis of world's largest rare earth element deposit, Bayan Obo, China: Protracted mineralization evolution over ~1 b.y. *Geology* **46**, 323–326.

Spandler, C., Pettke, T., & Rubatto, D. (2011) Internal and external fluid sources for eclogite-facies veins in the Monviso meta-ophiolite, Western Alps: Implications for fluid flow in subduction zones. *Journal of Petrology* **52**, 1207–1236.

Stormer, J.C., Jr. & Pierson, M.L. (1993) Variation of F and Cl X-ray intensity due to anisotropic diffusion and electron microprobe analysis of apatite: an addendum. *American Mineralogist Supplemental Data* **78**. Available from http://www.minsocam.org/MSA/amMin/Supplemental_Data/Stormer.html [date accessed: February 12, 2016].

Stormer, J.C., Jr., Pierson, M.L., & Tacker, R.C. (1993) Variation of F and Cl on X-ray intensity due to anisotropic diffusion in apatite during electron microprobe analysis. *American Mineralogist* **78**, 641–648.

Torpy, A. & Wilson, N.C. (2008) OpticalFit Software by CSIRO Australia. Available from http://www.csiro.au/luminescence/opticalfit/ [downloaded: September 16, 2016].

Townsend, P.D. & Rowlands, A.P. (2000) Information encoded in cathodoluminescence emission spectra. *In* Cathodoluminescence in Geosciences (M. Pagel, V. Barbin, P. Blanc, & D. Ohnenstetter, eds.). Springer, Berlin, Germany.

Waychunas, G.A. (2002) Apatite luminescence. *In* Phosphates: Geochemical, Geobiological, and Materials Importance (M.J. Kohn, J. Rakovan, & J.M. Hughes, eds.). *Reviews in Mineralogy and Geochemistry* **48**, 701–742.

Whitney, D.L. & Evans, B.W. (2010) Abbreviations for names of rock-forming minerals. *American Mineralogist* **95**, 185–187.

Wingate, M.T.D., Pirajno, F., & Morris, P.A. (2004) Warakurna large igneous province: a new Mesoproterozoic large igneous province in west-central Australia. *Geology* **32**, 105–108.

Yi, H., Balan, E., Gervais, C., Segalen, L., Fayon, F., Roche, D., Person, A., Morin, G., Guillaumet, M., Blanchard, M., Lazzeri, M., & Baboneau, F. (2013) A carbonate-fluoride defect model for carbonate-rich fluorapatite. *American Mineralogist* **98**, 1066–1069.

Zi, J.W., Gregory, C., Rasmussen, B., Sheppard, S., & Muhling, J.R. (2017) Using monazite geochronology to test the plume model for carbonatites: The example of Gifford Creek Carbonatite Complex, Australia. *Chemical Geology* **463**, 50–60.

Received March 20, 2018. Revised manuscript accepted July 20, 2018.

Lithos 328–329 (2019) 212–227

Contents lists available at ScienceDirect

Lithos

journal homepage: www.elsevier.com/locate/lithos

Carbonatites as recorders of mantle-derived magmatism and subsequent tectonic events: An example of the Gifford Creek Carbonatite Complex, Western Australia

Paul Slezak *, Carl Spandler

Department of Geoscience, College of Science and Engineering, James Cook University, Townsville, QLD 4811, Australia

ARTICLE INFO

Article history:
Received 6 November 2018
Accepted 21 January 2019
Available online 25 January 2019

Keywords:
Geochronology
Radiogenic isotopes
Carbonatite
Phoscorite
Monazite
Gifford Creek Carbonatite Complex

ABSTRACT

The Gifford Creek Carbonatite Complex (GCCC), Western Australia contains a diverse suite of alkaline igneous rocks, including magnesiocarbonatites, ferrocarbonatites, phoscorites, fenites, magmatic-hydrothermal peralkaline dykes, and ironstones. This study employs U-Pb, Sm-Nd, and Lu-Hf radiogenic isotope techniques on monazite – (Ce), fluorapatite, and zircon to determine the origin, age, and history of the GCCC.

Zircon crystals found in glimmerite alteration selvages adjacent to ferrocarbonatites exhibit pyramidal crystal morphologies, εHf values of −1.8 to −4.3, high Th/U, and variable Zr/Hf, all of which are indicative of carbonatitic zircon sourced from an enriched mantle component. Uranium-Pb dating of these zircons returned a definitive magmatic age of ~1370 Ma for the GCCC. Monazite hosted in the ferrocarbonatites, phoscorites, and fenite alteration assemblages yielded variable U-Pb ages ranging from ca. 1250 Ma to 815 Ma. Neodymium isotope isochrons determined from coexisting monazite and apatite gave ages between ca. 1310 Ma to ca. 1190 Ma, but all with similar initial $^{143}Nd/^{144}Nd$ values of 0.51078–0.51087.

The 1370 Ma age of the GCCC does not correspond to any known mantle plume activity, but does broadly correlate with the separation of the North China Craton from the West Australian Craton as part of the greater breakup of Nuna. The monazite and apatite εNd data illustrate that the multiple younger U-Pb monazite and Nd isotope isochron ages are not recording multiple magmatic intrusions into the complex, but rather represent partial recrystallisation/resetting of REE-bearing minerals during the protracted tectonic history of the Western Australia Craton from ~1300 Ma to 815 Ma and its involvement in the breakup of Nuna and assembly and disassembly of Rodinia.

The age variability in the U-Pb and the Sm-Nd isotope systems in monazite and apatite reveal that tectonically-induced hydrothermalism can contribute to the isotopic resetting of phosphate minerals. This age resetting, if properly identified, can be used as a thorough geochronological record of tectonism affecting alkaline igneous complexes after initial magmatic emplacement.

1. Introduction

Carbonatites are uncommon igneous rocks that contain >30% primary carbonate minerals (Mitchell, 2005). Owing to their mantle origins, carbonatites are excellent recorders of mantle processes, mantle sources (Bell and Simonetti, 2010), and the tectonic processes that allow their emplacement in the crust (Woolley and Bailey, 2012). Therefore, the preserved carbonatite record has the potential to provide information on mantle upwelling and/or tectonic processes through time. This record may be particularly beneficial for understanding the Proterozoic Era, as Proterozoic carbonatites and their associated rock types are found in many cratons (Woolley and Bailey, 2012) where other evidence of contemporary mantle magmatism may be lacking. As well as their petrological significance, carbonatite complexes are prospective for critical metals, such as LREE, Nb, Ta, and Zr in addition to other commodities such as P and Fe (Mariano, 1989).

To fully exploit the petrological, tectonic and mineralogical record of carbonatites, accurate temporal constraints on carbonatite formation is needed. However, carbonatite complex geochronology has been problematic and the subject of debate in the literature. Efforts to date prominent rare metal-bearing carbonatite complexes using different dating methods have returned significant age discrepancies. For instance, Bayan Obo, the world's largest REE deposit, has been repeatedly dated using different methods ($^{40}Ar/^{39}Ar$, Rb-Sr, Re-Os, U-Pb, Th-Pb, Sm-Nd, La-Ba) over the last 25 years, with each radiogenic system returning different ages, ranging from Devonian to mid Proterozoic (Le Bas et al., 2007; Song et al., 2018; Yang et al., 2011; Yang et al., 2017; Zhu et al., 2015). The Southern Canadian Cordillera Carbonatites include fourteen carbonatite bodies, several of which, such as the Upper Fir carbonatites,

* Corresponding author.
E-mail address: paul.slezak@my.jcu.edu.au (P. Slezak).

https://doi.org/10.1016/j.lithos.2019.01.028
0024-4937/